"Searching for stochastic gravitational-wave backgrounds with LIGO and Virgo Detectors"

De Lillo, Federico

ABSTRACT

Gravitational-wave (GW) astronomy with ground-based interferometric detectors is rapidly entering its golden age. The first three observing runs of the LIGO-Virgo-KAGRA collaboration have detected and catalogued about 90 GW signals from compact binary coalescences (CBCs), and the ongoing fourth observing run, started on 23rd May 2023, is expected to detect a CBC signal every two to three days. Among the variety of GW signals that could be detected there is the stochastic gravitational-wave background (SGWB), which is expected to arise from the superposition of all the GW signals produced by sources that cannot be individually detectable and/or are unresolvable. An SGWB can be generated by a plethora of phenomena, either of astrophysical or cosmological origin, and its spectrum may span a broad range of frequencies. Detecting an SGWB would be extraordinarily valuable. On the one hand, the discovery of an astrophysical SGWB would allow for gaining a noticeable amount of information about astrophysical populations otherwise inaccessible to electromagnetic astronomy and about the cosmos stellar history. On the other hand, the discovery of a cosmological SGWB would enable the direct assessment of inflation-like and other cosmological scenarios and the probe of physical laws at extremely high energies beyond the reach of particle physics colliders. The search for different kinds of stochastic gravitational-wave backgrounds in the frequency range of LIGO and Virgo detectors using the data from the first three LVK observing runs is the main topic of this doctoral dissertation.

CITE THIS VERSION

UCLouvain

Searching for Stochastic Gravitational-Wave Backgrounds with LIGO and Virgo Detectors

Doctoral dissertation presented by

Federico De Lillo

in fulfilment of the requirements for the degree of Doctor in Sciences.

Thesis Jury

Prof. Giacomo Bruno	Supervisor	Université Catholique de Louvain
Prof. Fabio Maltoni	President	Université Catholique de Louvain
Prof. Christophe Ringeval	Secretary	Université Catholique de Louvain
Prof. Nick Van Remortel	Member	Universiteit Antwerpen
Prof. Nelson Christensen	Member	Université Côte d'Azur

Private defence: 25th March, 2024
Public defence: 27th May, 2024

Abstract

Gravitational-wave (GW) astronomy with ground-based interferometric detectors is rapidly entering its golden age. The first three observing runs of the LIGO-Virgo-KAGRA collaboration have detected and catalogued about 90 GW signals from compact binary coalescences (CBCs), and the ongoing fourth observing run, started on 23rd May 2023, is expected to detect a CBC signal every two to three days. Among the variety of GW signals that could be detected there is the stochastic gravitational-wave background (SGWB), which is expected to arise from the superposition of all the GW signals produced by sources that cannot be individually detectable and/or are unresolvable. An SGWB can be generated by a plethora of phenomena, either of astrophysical or cosmological origin, and its spectrum may span a broad range of frequencies. Detecting an SGWB would be extraordinarily valuable. On the one hand, the discovery of an astrophysical SGWB would allow for gaining a noticeable amount of information about astrophysical populations otherwise inaccessible to electromagnetic astronomy and about the cosmos stellar history. On the other hand, the discovery of a cosmological SGWB would enable the direct assessment of inflation-like and other cosmological scenarios and the probe of physical laws at extremely high energies beyond the reach of particle physics colliders. The search for different kinds of stochastic gravitational-wave backgrounds in the frequency range of LIGO and Virgo detectors using the data from the first three LVK observing runs is the main topic of this doctoral dissertation.

Associated Publications and Contributions

[1] R. Abbott et al., "Search for anisotropic gravitational-wave backgrounds using data from Advanced LIGO and Advanced Virgo's first three observing runs", *Phys. Rev. D*, vol. 104, no. 2, pp. 022005, 2021.

[2] Federico De Lillo, Jishnu Suresh, and Andrew L. Miller, "Stochastic gravitational-wave background searches and constraints on neutron-star ellipticity", *Mon. Not. Roy. Astron. Soc.*, vol. 513, no. 1, pp. 1105–1114, 2022.

[3] Federico De Lillo, Jishnu Suresh, Antoine Depasse, Magdalena Sieniawska, Andrew L. Miller, and Giacomo Bruno, "Probing ensemble properties of vortex-avalanche pulsar glitches with a stochastic gravitational-wave background search", *Phys. Rev. D*, 107(10):102001, 2023.

[4] Federico De Lillo and Jishnu Suresh,"Estimating Astrophysical Population Properties using a multi-component Stochastic Gravitational-Wave Background Search", accepted for publication by *Phys. Rev. D*

List of other works I have contributed to during my PhD that I am not presenting in this manuscript:

[5] Antonio Costantini, Federico De Lillo, Fabio Maltoni, Luca Mantani, Olivier Mattelaer, Richard Ruiz, and Xiaoran Zhao, "Vector boson fusion at multi-TeV muon colliders", *JHEP*, vol. 09, pp. 080, 2020.

[6] Andrew L. Miller, Sébastien Clesse, Federico De Lillo, Giacomo Bruno, Antoine Depasse, and Andres Tanasijczuk, "Probing planetary-mass primordial black holes with continuous gravitational waves", *Phys. Dark Univ.*, vol. 32, pp. 100836, 2021.

[7] Andrew L. Miller, Nancy Aggarwal, Sébastien Clesse, and Federico De Lillo, "Constraints on planetary and asteroid-mass primordial black holes from continuous gravitational-wave searches", *Phys. Rev. D*, vol. 105, no. 6, pp. 062008, 2022.

[8] Arianna I. Renzini et al. "pygwb: A Python-based Library for Gravitational-wave Background Searches" *Astrophys. J.*, 952(1):25, 2023.

Contents

Introduction

"... l'amor che move il sole e l'altre stelle."
Dante Alighieri, *Divina Commedia, Paradiso XXXIII, v. 145*

Gravity is the weakest among the four known fundamental interactions and the first one we experience as children, when we fall on the ground while learning how to walk. Gravity is also the main character of the first unification in the history of physics, when Sir Isaac Newton understood that the force that makes us fall back on the ground when jumping is the same that makes the Moon orbit around (or rather, constantly free-falling on) the Earth. Newton's gravity description was that of an action-at-a-distance force, instantly propagating in the absolute space and the absolute time he used to describe our reality in the XVII-XVIII century. Then, the study of electrodynamics and the discovery of electromagnetic waves in the XIX century made wonder whether gravity could actually propagate at finite speed in space and time as waves emitted by a massive body satisfying some condition, similarly to what happens to an accelerated charge emitting electromagnetic waves. This guess became a prediction in the first years of the XX century, after Einstein's general relativity theory formulation in 1915. Within this description of reality, gravity does not propagate in the Newtonian absolute space and absolute time, but it is rather the space-time itself, "telling matter how to move". In turn, "the matter tells space-time how to curve" and, under some conditions (namely a time-dependent quadrupolar pattern in the matter distribution), can produce *gravitational waves*, small ripples in the "space-time arena" propagating at the speed of light and carrying information about the source and the gravitational interaction. After almost one century from Einstein's general relativity formulation, together with the controversies about the existence of gravitational waves (see "Historical Prelude"), the detection of GW150914 by the LIGO and Virgo collaborations on 14th September 2015 confirmed that gravitational waves (GWs) do exist, in agreement with general relativity predictions, and marked the birth of gravitational-wave astronomy. Today, after three observing runs (O1, O2, and O3) and the detection of 90 GW signals consistent with the coalescence of binary systems of black holes/neutron stars, gravitational-wave astronomy is rapidly entering its golden age, with the fourth observing run (O4) started on 24th May 2023 expected to detect this class of GW signals every few days.

Among the variety of GW signals that could be detected there is the stochastic gravitational-wave background (SGWB), expected to arise from the superposition of all the GW signals produced by sources that cannot be individually detectable and/or are unresolvable. Two main classes of SGWB are usually considered to exist, namely

an astrophysical SGWB (AGWB) and a cosmological SGWB (CGWB), which can be considered to be the gravitational analogy of the cosmic infrared background and of the cosmic microwave background in electromagnetic astronomy, respectively, for a simpler visualisation. The AGWB is expected to be generated by the superposition of the GWs from the sources produced throughout the stellar formation history and to be anisotropic, following the spatial distribution of the sources. The discovery of an AGWB would allow gaining a noticeable amount of information about the astrophysical population of celestial objects otherwise inaccessible to electromagnetic astronomy and about the cosmos stellar history. On the other hand, the CGWB is the remnant of the GWs released in the very first instants of existence of the Universe, up to the Planck Era ($10^{-43} - 10^{-42}$ s after the Big Bang, when gravity decoupled from the other interactions), and it is expected to be predominantly isotropic. The discovery of a CGWB is often referred to as the "holy grail" of GW astronomy, given the impact it would have on our comprehension of the evolution of the primordial universe, allowing the assessment of inflation-like and other cosmological scenarios directly, together with probing physical laws at extremely high energies non-accessible to particle physics colliders.

The search for a stochastic gravitational-wave background with the LIGO-Virgo-KAGRA (LVK) detector network is the main topic of this doctoral dissertation. The structure of the thesis reflects the will to gather in a single standing document all that I have learnt during these four years and would like to have known when I first started the PhD as a total neophyte on this topic. There are many reviews in the literature covering in depth multiple aspects presented in the main text, but I really hope that this manuscript may be of help to some future students approaching the topic. Going into details, after a "Historical Prelude", this thesis is divided into three parts, or rather three levels:

- The first part (Chapters 1 and 2), thought for the newcomers to the GW field, provides an introduction to the theory of GWs (Chapter 1), from the linearised theory to the quadrupole formula, and then makes a transition to the ground-based inteferometric GW detector network and to how to detect GW via Michelson interferometry with the relative real-world complications (Chapter 2).

- The second part (Chapters 3, 4, and 5), thought for those already acquainted with GW theory and ground-based GW detectors, gives a more rigorous introduction to what an SGWB is, what the related sources are, and what the experimental status throughout the GW spectrum is (Chapter 3), followed by the search methods for isotropic (Chapter 4), anisotropic and more "exotic" SGWBs (Chapter 5) with ground-based GW detectors.

- The third and final part (Chapters 6, 7, 8, and 9), for those wanting to examine the contributions I have made to the topic during the PhD, starts with the LIGO-Virgo-KAGRA directional searches performed during the third observing run (Chapter 6), where I have been responsible for producing the results for the

broad-band radiometer analysis. This part continues with three chapters about projects in collaboration with members of the Centre for Cosmology, Particle Physics, and Phenomenology (CP3) at the Université catholique de Louvain, where I was the main investigator. The first two projects explore how to infer the ensemble properties of some astrophysical populations using the results of SGWB searches, and they focus on the ellipticity of galactic and extra-galactic neutron stars (Chapter 7) and the parameters of glitching pulsars (Chapter 8). The last project (Chapter 9) presents a strategy for the joint estimation of multiple SGWB spectral amplitudes, with particular attention for SGWBs from compact binary coalescences, r-mode instabilities in young rotating neutron stars, and magnetars.

Prelude: A brief History of Gravitational Waves

> 「俺の財宝か。欲しけりゃくれてやる。探せ！ この世の全てをそこに置いてきた！」
>
> ゴールド・ロジャー, ワンピース

Before entering the realm of GW theory and ground-based GW interferometric detectors, it is useful to write a story. A story lasting one century (and counting): the history of GW astronomy, from Einstein's prediction in 1916 to the announcement of the first GW direct detection by the LIGO collaboration on 11th February 2016. The story written here is far from being detailed and comprehensive enough: many more particulars can be found in specialised books, e.g. [9–12] and review articles [13–16]. This section is divided into three parts: the first two parts, based on [15] and [16], cover the first theoretical predictions and controversies about GWs nature and energy and the several experimental attempts to detect GWs until the LIGO-Virgo-KAGRA era, respectively; the third one offers a glimpse towards the future of GW astronomy throughout the GW spectrum and different experiments and sources. The idea of this "Prelude" is to better contextualise historically the content of the chapters 1 and 2, respectively, using a less formal style than the rest of this manuscript.

0.1 Do gravitational waves exist?

0.1.1 Forerunners

Before Einstein's general relativity (GR) theory final formulation in November 1915 [17, 18] and the later prediction about GW existence, this notion had already been explored by some forerunners, starting from Clifford's *curvatures waves* in the 1870s [19]. The first person to use the term "gravitational waves" was probably Poincaré with the *ondes graviques* in his work from 1905 [20] (soon after the formulation of Einstein's special relativity), where he speculated about (special) relativistic gravity having acceleration waves, a retarded attractive force propagating at the speed of light. The concept of waves propagating at light speed appeared also later in tentative Lorentz-covariant scalar theories generalising special relativity, such as the Nordström one in 1913 [21] (which however did not predict bending of light in a gravitational field, not respecting Einstein's *equivalence principle*).

0.1.2 The early years (1915-1955): GWs do not exist... Or do they?

In November 1915, Einstein presented his generally-covariant theory of gravity. Only three months later, on a similar line as Poincaré, Einstein conjectured about the existence of GWs, using the analogy with electromagnetic waves. Then, in an exchange with Schwarzschild in February 1916, Einstein claimed that "...there are no gravitational waves analogues to light waves." [22]. Perhaps surprisingly, the first Einstein's statement about GWs was actually about their non-existence, probably suggested from calculations showing that no gravity dipole radiation exists in attractive gravity [9]. However, like many scientists in the first fifty years of GR, Einstein changed his mind about the topic multiple times. Already a few months later, in June 1916, after some exchange with de Sitter about coordinate frames, he published the article "Approximate integration of the field equations of gravitation" [23], where he developed the weak-field linearised GR theory in a similar way to what is done in textbooks nowadays. In that work, using the appropriate gauge choice, he predicted the existence of GWs propagating at the speed of light from a source with a time-varying quadrupole moment and derived the quadrupole-radiation formula (up to some mistakes in the expressions). More specifically, he identified three kinds of waves (named later by Weyl as longitudinal-longitudinal, longitudinal-transverse, and transverse-transverse [24]), among which only the last category carries energy, while the other two are gauge artefacts. Some errors present in the manuscript were corrected later in Einstein's 1918 paper "On gravitational waves" [25], after a correspondence with Nordström.

In spite of Einstein's works, the existence of GWs was still a debated topic within the scientific community of that time (even Einstein was still doubtful), mainly due to the use of approximated field equations in dedicated articles. A confirmation to what had already been written by Einstein came from the 1922 work "The propagation of gravitational waves" by Eddington [26], who used a different approach and verified the spurious nature of longitudinal-longitudinal and longitudinal-transverse waves, which can propagate at any speed but in turn do not carry energy. Moreover, he also corrected Einstein's quadrupole formula by a factor of two and proved that transverse-transverse waves propagate at the speed of light in every coordinate system, not ruling out their existence. In addition to this work, in 1923, Eddington evaluated the quadrupole radiation emitted by a spinning rod through radiation reaction due to retardation[1] [27].

However, the dispute about GW existence was far from being over. After emigrating to the United States of America in 1933, Einstein and his collaborator Nathan Rosen submitted a manuscript to *Physical Review* in 1936, where they claimed that GWs do not exist (this can be inferred from a letter from Einstein to Max Born [28,29], since no original version of the manuscript exists today). The editor of *Physical Re-*

[1] In the following years, it was attempted to use the quadrupole formula to calculate the radiation from gravitating quadrupoles. This calculation, mainly due to the lack of a consistent and recognised formalism, would still have caused several controversies in the incoming years before the advent of the post-Newtonian framework.

view, J. Tate, sent the manuscript for review to H. P. Robertson, whose negative (yet correct) comments triggered the "Einstein versus Physical Review" [30] episode[2], which ended up with Einstein withdrawing his publication from *Physical Review* and publishing the work in the "Journal of the Franklin Society" with the new title "On gravitational waves" [31]. Nonetheless, after the interaction between Einstein's new assistant L. Infeld and Robertson, Einstein accepted Robertson's criticism, acknowledged his and Rosen's mistakes in their own work, and had to modify the galley proofs of the paper. In this way, the final conclusions of the work read the opposite than the initial ones, namely that they had proven the existence of *cylindrical gravity waves* [31] (nowadays often referred to as Einstein-Rosen waves), and, at the end, Einstein indeed became convinced of GW existence[3,4].

0.1.3 Two important conferences

Crucial steps in establishing the physical effects and nature of GWs were made in two conferences, which also marked the end of the period in history of GR known as "The low water mark of general relativity" [36], namely the Bern 1955 [37] and the Chapel Hill 1957 [38] conferences. During the Bern conference, F. Pirani presented the idea and the formula for geodesic deviation (followed by the 1956 paper "On the physical significance of the Riemann tensor" [39]). The formalism made it possible to derive physical observable quantities for GWs, such as the reaction of a ring of test masses to a GW passage[5].

If Pirani's work partially solved how to measure the physical effects of GWs, it was still an open problem whether GWs carried energy or not[6], since there were no

[2]Einstein's response to Tate [30] (Who has not dreamt to do this at least once?):
July 27, 1936
Dear Sir.
"We (Mr. Rosen and I) had sent you our manuscript for publication and had not authorized you to show it to specialists before it is printed. I see no reason to address the—in any case erroneous—comments of your anonymous expert. On the basis of this incident I prefer to publish the paper elsewhere."
Respectfully
Einstein
P.S. Mr. Rosen, who has left for the Soviet Union, has authorized me to represent him in this matter.

[3]The initial misunderstanding in the paper sent to *Physical Rewiew* was deriving from the fact that Einstein and Rosen had discovered the impossibility of having a metric for plane GWs in a coordinate system without any singularity. Much later, it would have been shown [32] that the singularity was just a coordinate singularity, hence removable, but Einstein-Rosen had interpreted it as physical, hence arguing for the non-existence of GWs.

[4]On the other hand, Rosen (who had emigrated to the Soviet Union in the meantime) remained sceptical, publishing in 1937 in a Soviet journal a paper about the non-existence of GWs due to a singularity in the solution [33], arguing in a 1955 conference that GWs do not transport energy [34], and publishing another article in 1979 titled "Does Gravitational Radiation exist?" [35].

[5]This is because, similarly to the Lorentz force in electrodynamics, the geodesic deviation equation allows to both "define the fields" [32] (Maxwell tensor in electrodynamics, Riemann curvature tensor in GR) and "predict the motion" (Lorentz force can cause charges to accelerate away from inertial motion, while geodesic deviation describes the relative "tidal" acceleration of two inertially moving particles).

[6]This problem is related to the fact that energy can only be conserved locally in GR, which was the source of several arguments at that time (see section 1.3 for the definition of GW energy).

experiments allowing to solve that riddle. A step towards the acceptance of GW carrying energy came thanks to Bondi and Feynman in the Chapel Hill conference. They have independently proposed a similar thought experiment, nowadays known as the "bead argument". Imagine having two bead rings that can freely slide on a "sticky" (i.e. with friction) bar. Suppose a GW crosses the bar transversally to its propagation direction. The GW (see section 1.2 to understand why) will generate tidal forces with respect to the centre of the bar, producing in turn a compressive stress on the bar. Meanwhile, in response to the tidal force, the two bead rings will slide first towards the bar extremes and then back to the bar centre. Due to friction, the movement will cause the beads and the bar to heat up, implying that energy was transferred to the bar system by the GW, showing that GWs do indeed carry energy [38]. Even though several people in the community kept remaining sceptical about the topic, this argument was historically accepted by many as the one making the case for GWs transporting energy.

0.1.4 Binary pulsars: Lighthouses in the GW sea

In spite of the "sticky bead" argument, the discussion on whether GWs carry energy or not continued, and the main source of confusion was the derivation of the GW energy loss rate in binary systems as a solution to the problem of motion, on a similar line as Eddington had done for a rotating rod [27]. Calculations between 1947 and 1970 were performed with several methods and intricate computations that led to a wide variety of results, often in disagreement with the quadrupole formula and the energy emission as GWs [9]. The theoretical controversy continued in the years until 1985 (see [9] for a detailed discussion), when the comparison of quadrupole formula (and finer GR) predictions with the evolution of motion of the binary pulsar PSR B1913+16 issued the verdict in agreement with GR theory, ending the dispute [40].

The binary pulsar PSR B1913+16, nowadays known as the Hulse-Taylor pulsar, was discovered in 1974 by Hulse and Taylor, who eventually were awarded the Nobel Prize in 1993. The first announcement of the pulsar parameters decaying in agreement with the quadrupole formula was given by Taylor in 1979 [41, 42]. At the time, this resulted in convincing indirect evidence for GW existence, the conjecture that they do carry energy, and the validity of the quadrupole formula for gravitating binaries, boosting the interest of the scientific community in the construction of experiments for direct GW detection. The agreement between binary pulsar PSR B1913+16 and GR predictions has been continuing being confirmed more and more precisely throughout the years, until nowadays [43]. Other pulsars, whose study of orbital parameters through pulsar timing techniques contributed to the evidence for GW existence through history, have been the double pulsar system PSR J0737-3039A/B [44], and the binary pulsar J1738+0333 [45].

0.2 The hunt for gravitational waves

0.2.1 100 years ago: GW strain and sensitivity

The main complication in the GW detection history has been (and still is) the extremely tiny effect of the GW passage in the matter. This effect is usually encoded in a dimensionless quantity $h(t)$, called "strain". Simplifying the picture, the strain can be related to the maximum displacement per unit length that would be induced by the passage of a given GW through a set of test masses. To better explain (see section 1.2 for more details), consider a couple of test masses laying in a plane separated by a distance L and a GW whose propagation direction is perpendicular to the plane. Then, because of the shift in the relative position of the masses ΔL from the GW crossing the plane, the strain can be defined as[7] $\Delta L/L$. In the case of astrophysical sources, such as a binary black hole coalescence emitting GWs in the 10-1000 Hz band, a representative value of the strain is $h \sim \mathcal{O}\big(10^{-21}\big)$[8]. For a comparison, the best strain sensitivity reachable one hundred years ago, when GW existence was predicted and debated, was around 10^{-5} [15] with the technology available at the time. This corresponds to a gap of sixteen orders of magnitude from the GW strain to be detected. How this gap was bridged in 100 years of GW history, together with the main steps and milestones in the process, are briefly presented in the following.

0.2.2 50 years of GR: Weber's bar experiments and "detections"

J. Weber was among the participants at the Chapel Hill conference in 1958. He remained fascinated by the GW topic and challenges, and soon began designing instruments to detect GWs. Together with his collaborators, D. Zipoy and R. L. Forward, he developed the technology necessary to realise a bar GW detector, as discussed in his 1960-61 works [46, 47]. The main idea was using a cylindrical metal bar as a sort of "antenna", and observing the resonant modes of the bar as a consequence of the GW passage. Eventually, Weber and his team finished the construction of the antenna in the mid-sixties and gave a detailed report of its properties in their work from 1966 "Observation of the Thermal Fluctuations of a Gravitational-Wave Detector" [48]. Weber's detector consisted of an aluminium bar about 66 cm in diameter and 153 cm in length, for a weight of around 3 tons. The bar was suspended through a steel wire to isolate it from environmental vibrations, and placed inside a vacuum chamber. Around the bar there were piezoelectric crystals, which acted as detectors of the GW-induced cylinder vibrations. The vibrations were then converted to impulses

[7] The characterisation of the strain is actually more complicated (see chapters 1 and 2), having to account for the kind of GW source, the GW frequency, polarisation, and the relative orientation and geometry of the experimental apparatus aiming to detect GWs.

[8] To get an idea of how tiny this quantity is, consider the case where $L \sim \mathcal{O}(\mathrm{km})$. This means that the variation in the length to be measured is $\Delta L \sim \mathcal{O}\big(10^{-18}\,\mathrm{m}\big)$, three orders of magnitude less than the "radius" of a proton!

by means of piezoelectric sensors. Weber's group actually built two copies of this detector model, one at the University of Maryland and the other one at the Argonne National Laboratory, 950 km away, near Chicago, in order to rule out spurious local noise. In the same work from 1966 [48], it was also stated that the detector was sensitive to strain down to $h \sim \mathcal{O}(10^{-16})$. In just fifty years, technology had already advanced enough to improve by ten orders of magnitude the initial sensitivity at the time when Einstein formalised GR.

In the incoming years, Weber claimed multiple GW detections. First, in 1969, he announced GW detection due to several coincidences in the two detectors [49]. Later, in 1970, he pointed out a strong anisotropy in GW intensity that peaked towards the Galactic Centre [50]. However, his results were in very strong contrast with theoretical studies performed within GR [51, 52] and were strongly questioned. Nonetheless, Weber's "detections" drew even more attention and enthusiasm to the searches for GWs, and some scientific groups started building their own version of Weber's detectors, looking for improvements. In this way, by the mid-seventies, there were several groups searching for GWs with first-generation bar detectors working at room temperature, such as those in Moscow State University [53–55]; the Bell laboratories Rochester-Holmdel [56]; IBM labs in Yorktown Heights [57], and Glasgow University. None of these groups ever had any evidence for a GW signal, definitely invalidating Weber's results. This urged researchers to find new research methods for GWs and rely on different technologies to build the related experiments.

Cryogenic resonant experiments

Before passing to nowadays interferometry-based detectors, there was a second generation of resonant detectors that was developed as an improvement to Weber's bar detector, namely the cryogenic resonant experiments [58,59]. These experiments shared the property of working at very low temperatures ($\ll 1$ K), mainly to reduce as much as possible the thermal noise affecting the resonant bars and increase their quality factor. They can be classified into two main groups: cryogenic resonant bar detectors like NAUTILUS [60], AURIGA [61], EXPLORER [62], ALLEGRO [63], and NIOBE [64]; and cryogenic spherical detectors for omnidirectional GW detection like MiniGRAIL [65] and the "Mario Schenberg" [66] ones. Most of these experiments operated in the late nineties and in the two-thousands.

0.2.3 Getting closer to modern era: Laser interferometry

Looking back in time, it appears that the first explicit suggestion about using laser interferometry to detect GWs was by Gertsenshtein and Pustovoid in USSR in 1962 [67] and again in USSR in 1966 by V. B. Braginskii [68]. However, these suggestions remained ideas and were not carried out behind the "Iron Curtain". Meanwhile, in Weber's group, the concept was considered (see laboratory notebook [10]) but not pursued, at least initially. One of Weber's collaborators, R. L. Forward (who would

also have had a major role in conceptualising resonant spheres as detectors [59]), resurrected the idea some years later, while working at the Hughes Research Laboratory in Malibu, California, and began the construction of a GW interferometer, later becoming the first scientist to assemble such a detector. The design of the apparatus became public in 1971 [69]. The interferometer had 8.5-m-long arms, and, in 1978, the results of 150 hours of observation and the correlation with the other bar detectors around the world were shared [70]. There was no GW observation. In the same work, Forward acknowledged the advice he received from P. Chapman and R. Weiss.

Independently of Forward, R. Weiss, influenced by Pirani's [39] and Chapman's works [71], was planning on building a laser interferometer at MIT in the early seventies. However, after starting to construct a 1.5-m interferometer using military funding, he was negated to continue his work due to a change in the US funding laws. This forced him to write a financing proposal to the NSF agency in 1974, asking to enlarge the construction of the interferometer prototype with 9-m long arms. This proposal, which eventually would have been approved in 1975, triggered a chain reaction that eventually led to the construction and assembly of the current worldwide interferometer network. The history of three of them is briefly sketched, continuing the main story.

GEO600

In 1974, the NSF sent Weiss' proposal [72] to P. Kafka in the Max Planck Institute in Garching, Munich, for a review. Kafka, a theoretician, asked the experimentalists in the group working with bar detectors for an opinion about the proposal. Perhaps to his surprise, the experimentalists showed enthusiasm for the proposal, and the group led by H. Billing decided to build its own prototype. To that end, they contacted Weiss, asking for advice and offering a job to one of his students who had experience with his 1.5-m prototype. This resulted in D. Shoemaker joining the Garching group and helping them in the design and construction of a German 3-m prototype in 1975 and, later in 1981, of a 30-m interferometer [73]. In 1985, they presented a proposal for a 3-km-long interferometer at the Marcel Grossmann Meeting in Rome [74] and subsequently presented it to German funding agencies. However, this proposal was rejected due to a lack of interest at the time. Meanwhile, in Glasgow, another group had developed experience in interferometric detectors. This group, initially led by R. Drever (who started working on interferometers after listening to a lecture by Kafka in 1975 in Erice, Sicily), developed a 10-m-long interferometer in the second half of the seventies. In 1979, Drever joined a working team at Caltech, and J. Hough replaced him. In 1986, the Glasgow group designed a Long Baseline Gravitational Wave Observatory [75], but they were denied funding as well.

As it often happens in science, having common interests brings different groups together. In 1989, the Glasgow and Garching groups presented a joint proposal [76] for an underground 3-km installation to be constructed in the Harz Mountains in Germany, but again the proposal was not funded. However, in 1994, in light of a new

proposal for a shorter interferometer, together with the donation from the University of Hannover and the State of Lower Saxony of ground to build a 600-m instrument in Ruthe (20 km south of Hannover), they finally received funding from both British and German agencies. GEO600 construction started in September 1995. In 2002, between August and September, there was the first official joint scientific run with the LIGO detectors, followed by a two-year-long one in November 2005. GEO600 has been operated by the Center for Gravitational Physics, of which the Max Planck Institute is a member, together with Leibniz Universität in Hannover and Glasgow and Cardiff Universities. In addition to its function as a GW observatory, GEO600 has been used as a testing and developing laboratory for technologies successfully integrated into other GW detectors on the world surface.

Virgo

The story of Virgo began in 1985 during the Marcel Grossmann Meeting in Rome (the same meeting where the German group first proposed the 3-km-long German interferometer), when two scientists, A. Brillet and A. Giazotto, met. Brillet, from Orsay UPMC, Paris, had had past visiting experiences at MIT between 1980 and 1981, during which he had established a good connection with Weiss that would have produced fruitful (informal and formal) collaboration in the incoming years. He was a strong supporter of interferometry as the best technique to detect GWs [77, 78]. Giazotto, from Pisa University, Italy, was working on suspension systems. During the meeting, Giazotto brought up concepts and results about his super-attenuators, seismic isolator devices to which interferometer mirros could be connected. In addition to that, J. Y. Vinet, Brillet's colleague, gave an exposition about Drever's theory of (laser power-) recycling, which could significantly reduce the laser power needed for a GW interferometer. The two (Brillet and Giazotto) agreed to form a partnership.

They first tried to join the Garching group with the perspective of a European collaboration for a large interferometer, but they received a negative response. They then initiated a parallel project with the final goal of realising a large GW interferometer. The name of the project was chosen after Virgo, the galaxy cluster at roughly 18 Mpc from Earth, to underline the will of reaching a sensitivity to observe extra-galactic GW signals. After a first refusal for funding from the CNRS (focused on financing the Very Large Telescope project in Chile), the two continued collaborating, including the groups of Naples and Frascati in 1989. Eventually, they submitted a request for funding to both CNRS and INFN, which were eventually approved in 1993 and 1994, respectively. The location chosen for the Virgo's site was the alluvial plain in Cascina, Pisa, Italy. Differently from LIGO, which used Caltech, MIT, and GE0600 to test technologies before implementing them in the actual detector, Virgo's strategy was to use the instrument both as its own prototype and actual detector. In this way, it would have been possible to tackle problems already at the interferometer scale.

The construction of Virgo should have started in 1996 but faced many difficulties (such as convincing the nearly 50 landlords to yield their part of the plain and adopt-

ing additional measures to counteract the risk of flooding [79]). Among the complications, between 1996 and 1999, there were many management problems, given the lack of unified leadership among the different institutes [12]. To improve the coordination, in December 2000, the CNRS and INFN assembled the European Gravitational Observatory (EGO consortium [80]), which would have been responsible for the Virgo site, the construction, the maintenance, the operation, and the upgrades of the detector. Eventually, the erection of the initial Virgo experiment [79] concluded in August 2003. Moreover, in 2007, a memorandum agreement between the LIGO and Virgo collaborations was signed, ensuring data exchange, joint analyses and co-authorship of all publications involving the two experiments. The agreement was followed by multiple joint science runs between 2007 and 2011, before the detectors started a new period of commissioning to be upgraded to their "advanced" configurations.

LIGO

In summer 1975, during a NASA conference (where the concept of "Laser Interferometer Space Antenna was also presented") in Washington, there was an important meeting between R. Weiss and K. Thorne, who at that time was not yet convinced about the potential of interferometry in GW searches (see, as an example, chapter 37 from [32]). During the meeting, Weiss converted Thorne to his cause, and Thorne decided to build a GW interferometer at Caltech. To this goal, under Weiss' advice, they hired the leader of the Glasgow group, R. Drever (part-time 1979, permanent in 1983), who already had experience with bar detectors [81] (Thorne's first choice would actually have been Braginskii, but Cold War prevented him from being hired). After a few years, in 1983, Caltech had a 40-m-long-arm interferometer, while Weiss had built a 1.5-m prototype at MIT (due to a smaller budget). Soon, a competition between Drever and Weiss started for the improvement of technologies and the interferometer sensitivity, such as increasing the laser power and the optical path travelled by light beam (Weiss advocated optical delay lines [82, 83], while Drever explored the usage of Fabry-Perot cavities [84, 85], which are still used today), with Caltech eventually taking the lead. In response to this, in October 1983, Weiss submitted to the NSF the document "A study of a long Baseline Gravitational Wave antenna", authored by himself, P. Saulson, and P. Linsay [86]. This milestone document is also known as "The Blue Book", and contains many discussions about the construction and operation of large-scale interferometers, asking for a $100 million budget to build two km-long interferometers in the United States. However, the NSF could not finance both MIT and Caltech for these two large-scale projects, and a "forced marriage" between Drever's (Caltech) and Weiss' (MIT) groups was necessary, with Thorne acting as mediator. This resulted in a joint "Caltech-MIT" project sent to NSF [87].

The official name of the project funded by the NSF was "Laser Interferometer Gravitational-Wave Observatory" (LIGO), with Thorne, Weiss, and Drever as initial leaders. Nonetheless, the strong frictions between Weiss and Drever caused delays between 1984 and 1985, and the NSF appointed a single project manager, E. Vogt, in

1986 [88]. The project was officially funded by the NSF in 1988. Slow progress led to a major restructuring of LIGO in 1992, with Drever no longer belonging to the project and B. C. Barish replacing Vogt as the new director. He reviewed and amended the old NSF proposal, planning to build LIGO as an evolutionary laboratory. The first stage, called "initial LIGO" (iLIGO), would have been a proof-of-concept and offered the chance of detecting GWs. The second stage, called "advanced LIGO" (aLIGO), would have made GW detection very likely. The two sites for building the observatories were chosen to be one in Hanford, Washington State, and one in Livingston, Louisiana. Their construction started in late 1994 and early 1995, respectively, and finished in 1997. At the end of the construction, under Barish's suggestion, two organisations were funded: the laboratory LIGO, responsible for laboratory administration, and the LIGO scientific collaboration (LSC), responsible for scientific and technological research with Weiss as head. LSC would have established active collaboration with GEO600 and Virgo, whose mutual synergy helped LIGO evolve to reach current sensitivity levels.

Initial LIGO operated between 2002 and 2010, not detecting any GW. In 2010, the upgrade of the detector started, and aLIGO came to light in February 2015 [89, 90]. Due to some delays in the upgrade, the start of the data-taking was pushed back to 18th September 2015. Before that date, tests were made with the instruments in "engineering run" mode, and, during the last of those tests between 13th September and 14th September 2015, something unexpected happened...

0.3 The birth of Gravitational-Wave astronomy: From first detection to future perspectives

0.3.1 After almost one century: The first direct GW detection

It was on Monday 14th September 2015, at 9:45:50 a.m. UTC. Three minutes later, at 11:48 a.m. CET [92], Marco Drago, a postdoctoral researcher at the Max Planck Institute for Gravitational Physics in Hannover, received an e-mail, automatically generated by the LIGO monitors. In the e-mail, there were links to two plots (see figure 1, top). Each of the plots contained a chirp-like signal emerging suddenly from the noise backgrounds of the Hanford and Livingston LIGO detectors. The signals were almost identical and had reached the detectors with a delay of 7 ms. Marco Drago has been the first person to see a GW signal, but he did not know it yet with certainty at that time. There was the possibility that the signal was fake, namely a "blind injection" of the signal in the data, performed to test the detection system procedure during the engineering run. After having ascertained that none of his colleagues in Hannover were aware of any injections, he sent an e-mail to the whole LIGO collaboration, asking the same question. Some hours later, when it was morning time in the US, a long day of

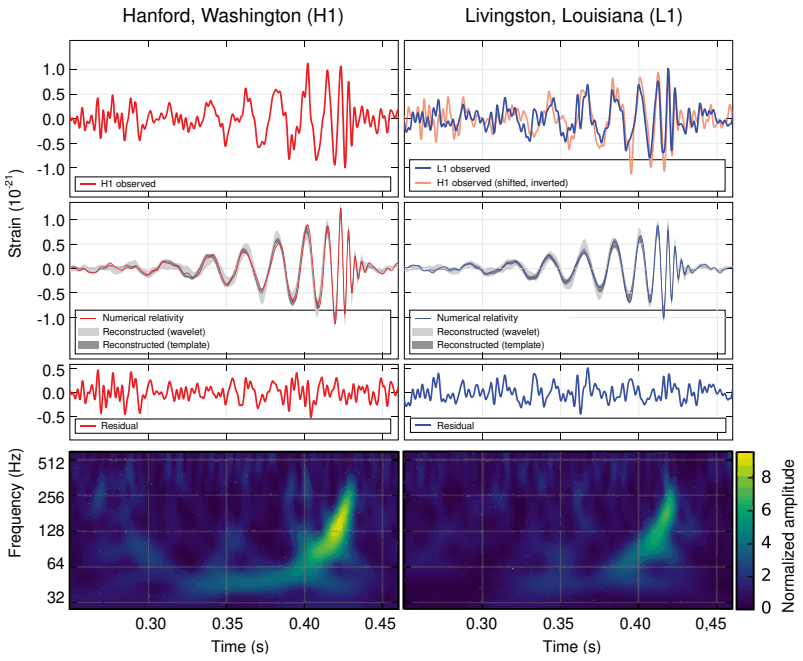

Figure 1: GW150914 [91]: Detector strains (top); comparison with GR predictions (mid); spectrogram in the two detectors (bottom).

e-mail exchanges and discussions started. As a result, it became evident at the end of the day that there hadn't been any blind injections. However, before performing any analysis about the nature of the signal, more data needed to be collected in order to collect more statistics about the noise distribution of the two detectors.

After one month of the (now known as) first LIGO observing run (O1), enough data were available, and the search about the signal nature was performed. It turned out that the signal waveform was matching the ones predicted by general relativity in the case of a binary-black-hole coalescence event. The possibility of a false detection was 1 in 203 000 years. The signal was real: two black holes, with masses around 35 and 29 solar masses, had merged around 1.3 billion years ago, forming a final black hole with a mass around 62 solar masses, meaning that two solar masses have been radiated away as GWs. Travelling through space and time, the waves had become tiny ripples, appearing in the detectors with a frequency between 35 and 350 Hz and a peak strain $h \sim 10^{-21}$. A paper soon followed the detection of this event, labelled GW150914, and was submitted to *Physical Review Letters* on 21st January 2016 and published on 11th February 2016 [91]. On the same day, LIGO held multiple conferences all around the world to make the official announcement. LIGO had made the first direct detection of a gravitational wave and observed for the first time a binary-black-hole merger, definitely proving the existence of these extreme objects. For this event, C. B. Barrish, K. Thorne, and R. Weiss would have received the Nobel Prize for physics in 2017. The era of gravitational-wave astronomy had officially begun.

0.3.2 100 years and counting: The first three observing runs

GW150914 has been the first of the 90 compact-binary-coalescence (CBC) GW signals observed during the first three observing runs (O1, O2, and O3) of the LIGO-Virgo-KAGRA collaboration between September 2015 and end-March 2020 [93]. During the years, Advanced Virgo [94] and KAGRA, Kamioka mine, Gifu-prefecture, Japan [95] (see [96–98] for more details about its design and construction history as successor of TAMA300 [99]) came into operation and joined LIGO (and GEO600) in the ground-based GW interferometers network.

During the first observing run O1, from 18th September 2015 to 19th January 2016 with only LIGO online, two other events associated with binary-black-hole (BBH) mergers were observed, namely GW151012 and GW151226, bringing the total number of observed events to three. This definitely established that GW150914 had not been a blunder and that GW astronomy was a reality.

The second observing run O2, from end November 2016 to 26th August 2017, started with only the LIGO detectors being active, while Virgo joined only during the last month of observation in August 2017. Even if for just a few weeks, Virgo presence was nonetheless extremely important. It helped in the triangulation procedure to locate the first joint detection of the network with the BBH signal GW170814 on 14th August 2017, restricting by almost two orders of magnitude the region of the sky associated with the event [100]. However, the most spectacular detection during O2 was GW170817 [101]. Not only was it the first detection of a binary-neutron-star (BNS) merger, but it also had an electromagnetic (EM) counterpart in the short gamma-ray burst GRB 170817A [102], observed by Fermi/GBM (Gamma-ray Burst Monitor) [103] and INTEGRAL (the International Gamma-ray Astrophysics Laboratory) [104], signing the birth of GW-EM multi-messenger astronomy. The double observation in the GW and EM domains also allowed to perform important tests of GR, such as probing the speed of propagation of GW [105], and measuring the Hubble parameter H_0 in a new way via the GW channel [106]. Up until today, GW170817 has been the only GW signal with an EM counterpart. At the end of the O2 run, with eight observations, the total number of observed events became eleven and was collected in the first Gravitational-Wave Transient Catalogue (GWTC-1) [107].

During the third observing run O3 (divided into two phases: O3a, from 1st April 2019 to 1st October 2019, and O3b, from 1st November 2019 to 27th March 2020), 79 additional events were observed, and KAGRA joined the network actively in February 2020. The highlights from this run are the events GW190412 (the first BBH event with a noticeable asymmetric mass ratio of the two components [108]); GW190425 (the second and last one BNS event until now [109]); GW190521 (event with the largest progenitors' masses [110]); GW190814 (where one of the two progenitors is in the mass gap and is not known whether to be the lightest BH, the lightest NS or anything more exotic [111]), and the first two signal from a binary-black-hole-neutron-star (BHNS) system GW200105 and GW200115 [112]. The events observed

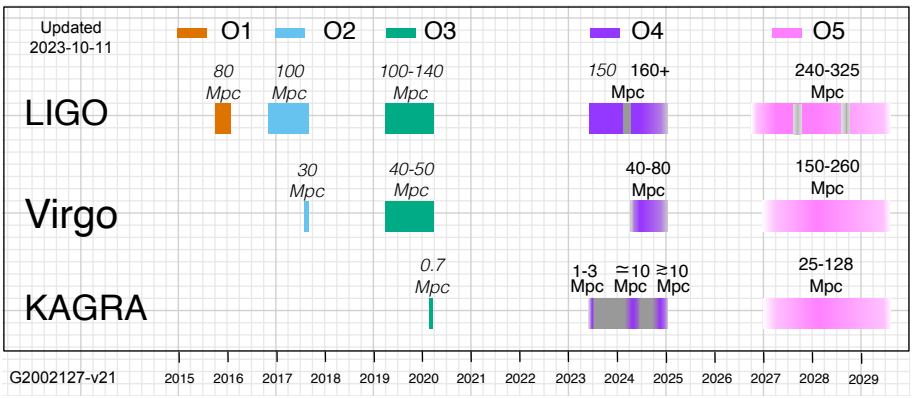

Figure 2: LVK observation timeline [LIGO-G2002127].

during O3 (76 BBH, 1 BNS, 2 BHNS) are reported in the GWTC-2 [113] and GWTC-2.1 [114]. The summary and implications from the 90 CBC events (86 BBH, 2 BNS, 2 BHNS) are collected in the GWTC-3 [93].

0.3.3 A glimpse towards the future

During the writing of this manuscript, the fourth observing run (O4) of the LVK collaborations started on Wednesday 24th May 2023 at 15:00 UTC. The duration of the run is set to last twenty months, including two months of commissioning after the first nine months of observation (see figure 2). The O4 run looks very promising, and the improved sensitivity of the detector network should enable CBC detection every few days. In addition to that, it could be possible to have access to and also detect for the first time signals that are different from CBCs (short-duration, modelled signals), namely GW bursts (short-duration, unmodelled signals, e.g. from core-collapse to supernova), continuous waves (quasi-monochromatic, persistent GW signals, e.g. from isolated, non-axisymmetric, rotating neutron stars), or stochastic gravitational-wave backgrounds (persistent, random GW signals resulting from the superposition of undetectable and unresolved GW signals from previous categories and the subject of this work).

After the end of O4, plans for further detector upgrades and a fifth observing run (O5, during which a fifth detector, LIGO India [115] could be ready to join the network) are already scheduled (see figure 2). Then, at the end of O5, the detectors will undergo a major final upgrade, reaching the limits of their sensitivities imposed by their infrastructures. Following this upgrade, the detector network is likely to enter a semi-continuous observation mode while waiting for the construction of the third-generation ground-based interferometers such as the Einstein Telescope [116] and the two Cosmic Explorers [117]. These interferometers, with 10-km arms in a triangular configuration, 20-km and 40km arms L-shaped, respectively, are expected to enter into operation in the second half of the 2030s. Their sensitivity is foreseen to improve

by one order of magnitude the design sensitivity of the second-generation detector network, giving access to GW signals from the very early universe.

This is not all, since the present and future of GW astronomy are not limited to ground-based interferometers, which are designed to detect GWs with frequencies between a few Hz and a few kHz. This frequency interval constitutes just a tiny fraction of the GW spectrum, spanning a range from aHz to above THz. Within this spectrum, a plethora of GW sources and signals are expected to exist, corresponding to a very rich phenomenology and approved or proposed experiments and detection techniques (see table 1 for an overview or the recent "Handbook of Graviational Wave Astronomy" [145]). Cosmic-microwave-background (CMB) polarisation B-modes searches for primordial GWs, pulsar timing arrays looking for GWs from supermassive black hole mergers, a future laser interferometer space antenna (LISA) looking for extreme-mass-ratio black hole coalescences and phase transitions from the very early universe, and others... The future is bright, and the (re)search continues!

Frequency range	Techniques	Present and future experiments
≥ 1 THz (ultra high frequency band)	Terahertz resonators; Optical resonators; Magnetic conversion detectors	
100 kHz $-$ 1 THz (very high frequency band)	Microwave resonator/wave guide detectors; Laser interferometers and Gaussian beam detectors	[118, 119], [120]; Review [120]; Fermi Lab Holometer [121]
10 Hz $-$ 100 kHz (high frequency band)	Low-temperature resonators; Ground-based laser-interferometric detectors	NAUTILUS [60], AURIGA [61], EXPLORER [62], ALLEGRO [63], NIOBE [64], MiniGRAIL [65], Schenberg [66]; TAMA [99], GEO600 [122], aLIGO [90], Virgo [94], KAGRA [95], ET [116], CE [117]
0.1 Hz $-$ 10 Hz (middle frequency band)	Space laser-interferometric detectors with arm length 1,000 km $-$ 60,000 km; Atom interferometers	DECIGO [123], BBO; [124] AION [125], MAGIS [126]
100 nHz $-$ 0.1 Hz (low frequency band)	Space laser-interferometric detectors with arm length longer than 60,000 km; Binary resonance	Cassini spacecraft Doppler tracking [127] LISA [128], TIANQIN [129], μAres [130]; Binary resonance [131, 132]
300 pHz $-$ 100 nHz (very low frequency band)	Pulsar timing arrays	NANOGrav [133], EPTA [134], PPTA [135], InPTA [136], IPTA [137], FAST [138], MeerKAT [139], SKA [140]
10 fHz $-$ 300 pHz (ultra low frequency band)	Astrometry of quasar proper motions	[141]
1 aHz $-$ 10 fHz (Hubble frequency band)	Cosmic microwave background experiments	Planck [142], BICEP2/Keck [143]
≤ 1 aHz (infra-Hubble frequency band)	Through verification of inflationary/ primordial cosmological models	

Table 1: Taxonomy of the GW spectrum [144] and experiments.

Part I

Gravitational Waves and Detectors

Chapter 1

Gravitational Waves

「か-め-は-め-波！」

孫悟空 , ドラゴンボール

This first chapter covers the basics of gravitational waves. After a brief introduction to the linearised version of general relativity, section 1.1 illustrates the derivation of the wave equation for physical modes of gravitational radiation in the transverse-traceless gauge. Then, section 1.2 discusses the interaction between gravitational waves and test masses, making clear that gravitational waves do carry energy and momentum. Consequently, section 1.3 examines the concept and the definition of the gravitational-wave energy-momentum tensor. Finally, sections 1.4 and 1.5 present the quadrupole formula for the gravitational-wave amplitude, radiated power, and related quantities, together with some simple examples of astrophysical interest (compact binary inspiral and rotating rigid body). This introductory chapter is far from covering all the relevant aspects of the gravitational-wave in linearised and full general relativity. The literature is full of excellent and comprehensive reviews that can be consulted, such as (but not limited to) [32, 145–150].

1.1 Gravitational Waves from linearised Einstein equations

1.1.1 Einstein equations and linearised theory

In 1915, Einstein published his work [17] about his theory of general relativity (GR). The tensor field equations of GR, also known as the *Einstein equations*, describe how the curvature of spacetime is related to the distribution of matter within it and read

$$R_{\mu\nu} - \frac{1}{2} R\, g_{\mu\nu} = \frac{8\pi G}{c^4}\, T_{\mu\nu}. \tag{1.1.1}$$

where $R_{\mu\nu}$ and R are, respectively, the Ricci tensor and Ricci curvature scalar, $g_{\mu\nu}$ is the spacetime metric, and $T_{\mu\nu}$ is the matter energy-momentum tensor. The left-hand side of the equation describes the properties of spacetime, depending only on the metric tensor and its first and second derivatives through the Ricci tensor and the Ricci scalar. The right-hand side describes the energy, the momentum, and the stress

distribution in spacetime. From left to right, the equations encode how the space-time structure determines the motion of the matter distribution, while from right to left they express how, in turn, the matter distribution affects the space-time metric. Equations (1.1.1), and hence the theory of GR, are invariant under the group of diffeomorphisms, namely coordinate transformations that are invertible, differentiable, and whose inverse is differentiable:

$$x^\mu \to x'^\mu(x), \qquad g_{\mu\nu}(x) \to g'_{\mu\nu}(x') = \frac{\partial x^\rho}{\partial x'^\mu}\frac{\partial x^\sigma}{\partial x'^\nu} g_{\rho\sigma}(x). \tag{1.1.2}$$

This gauge symmetry caused several controversies historically (see the prelude 0.1) on whether gravitational waves (GWs) can be properly defined within GR or if they are rather artefacts and can be gauged-away via a specific gauge-fixing procedure. As shown next in different contexts, GWs do indeed exist and are a prediction within GR.

The simplest approach to prove that GWs emerge from GR and explore their properties is within linearised theory of GR. This framework is set by expanding the metric about the flat Minkowski spacetime

$$g_{\mu\nu} = \eta_{\mu\nu} + h_{\mu\nu}, \qquad |h_{\mu\nu}| \ll 1, \tag{1.1.3}$$

and Einstein equations to linear order in $h_{\mu\nu}$ [1]. Equation (1.1.3) corresponds to the choice of a specific reference frame, hence breaking the symmetry of the full GR under coordinate transformation. Nonetheless, the linearised theory still has a residual gauge symmetry under *slowly varying diffeomorphisms*

$$x^\mu \to x'^\mu(x) = x^\mu + \xi^\mu(x), \qquad |\partial_\mu \xi_\nu| \sim \mathcal{O}(|h_{\mu\nu}|) \ll 1, \tag{1.1.4}$$

under which $h_{\mu\nu}(x)$ transforms as

$$h'_{\mu\nu}(x') = h_{\mu\nu}(x) - (\partial_\mu \xi_\nu + \partial_\nu \xi_\mu) + \mathcal{O}(\partial\xi\,\partial\xi) + \mathcal{O}(h\,\partial\xi) + \mathcal{O}(h\,\partial\xi\,\partial\xi). \tag{1.1.5}$$

Moreover, $h_{\mu\nu}$ transforms like a tensor under (global) Lorentz transformations[2] and is invariant under space-time translations. This implies that the linearised theory is also invariant under the finite Poincaré group transformations, in contrast to the full theory of GR (where flat spacetime does not play any special role).

To obtain Einstein linearised equations, it is useful to note that, to linear order in $h_{\mu\nu}$, the Riemann tensor can be expressed as[3]

$$R_{\mu\nu\rho\sigma} = \frac{1}{2}\left(\partial_\nu\partial_\rho h_{\mu\sigma} + \partial_\mu\partial_\sigma h_{\nu\rho} - \partial_\mu\partial_\rho h_{\nu\sigma} - \partial_\nu\partial_\sigma h_{\mu\rho}\right). \tag{1.1.6}$$

[1] Note that first it is defined $h_{\mu\nu}(x) \equiv g_{\mu\nu}(x) - \eta_{\mu\nu}$, and secondly the condition $|h_{\mu\nu}| \ll 1$ is enforced.

[2] Note that rotations always preserve the condition $|h_{\mu\nu}| \ll 1$, while this is not true for general boosts.

[3] Note that, in linearised GR, the Riemann tensor is *invariant* under slowly-varying diffeomorphisms. This difference from the full GR, where it is just covariant under general diffeomorphism, will be important in section 1.2 to simplify calculations when evaluating the effect of GWs on test masses in different frames.

After inserting the above expressions in the field equations of GR and retaining only terms linear in $h_{\mu\nu}$, the linearised Einstein equations are obtained as

$$\Box\bar{h}_{\mu\nu} + \eta_{\mu\nu}\partial^\rho\partial^\sigma\bar{h}_{\rho\sigma} - \partial^\rho\partial_\nu\bar{h}_{\mu\rho} - \partial^\rho\partial_\mu\bar{h}_{\nu\rho} = -\frac{16\pi\,G}{c^4}\,T_{\mu\nu}, \tag{1.1.7}$$

where $\Box \equiv \partial^\lambda\partial_\lambda$ is the flat-spacetime D'Alambertian. The above equation is written as a function of the trace-reversed metric perturbation $\bar{h}_{\mu\nu}$, which is defined as

$$h \equiv h_{\mu\nu}\,\eta^{\mu\nu}, \qquad h_{\mu\nu} = \bar{h}_{\mu\nu} - \frac{1}{2}\eta_{\mu\nu}\,h \tag{1.1.8}$$

and (at first order in $h_{\mu\nu}$) transforms as follows under slowly-varying diffeomorphisms:

$$\bar{h}_{\mu\nu}\,(x) \to \bar{h}'_{\mu\nu}\,(x') = \bar{h}_{\mu\nu}\,(x) - \left(\partial_\mu\xi_\nu + \partial_\nu\xi_\mu - \eta_{\mu\nu}\partial_\lambda\xi^\lambda\right). \tag{1.1.9}$$

1.1.2 The transverse-traceless gauge

At this stage, equation (1.1.7) does not resemble a wave equation for $\bar{h}_{\mu\nu}$, which as a consequence cannot be interpreted as GWs yet. Nonetheless, by using the gauge freedom in equation (1.1.5), it is possible to choose the Lorentz gauge (also known as De Donder or harmonic gauge) by imposing the condition[4]

$$\partial^\nu\bar{h}_{\mu\nu} = 0, \tag{1.1.10}$$

and then equation (1.1.7) becomes a standard wave equation:

$$\Box\bar{h}_{\mu\nu} = -\frac{16\pi\,G}{c^4}\,T_{\mu\nu}. \tag{1.1.11}$$

However, the properties of GWs cannot be characterised by only applying the Lorentz gauge: the four conditions in equation (1.1.10) reduce the number of independent components of $\bar{h}_{\mu\nu}$ from ten to six, and not all of them are guaranteed to be physical.

The verification of which degrees of freedom are physical can be easily performed in the absence of matter, where $T_{\mu\nu} = 0$.[5] The Lorentz gauge condition in equation (1.1.10) does not fix the gauge completely, not being violated by the transformations $x^\mu \to x^\mu + \xi^\mu$ with

$$\Box\xi_\mu = 0 = \Box\xi_{\mu\nu}, \qquad \xi_{\mu\nu} \equiv \partial_\mu\xi_\nu + \partial_\nu\xi_\mu - \eta_{\mu\nu}\partial_\lambda\xi^\lambda. \tag{1.1.12}$$

[4] To ensure equation (1.1.10) to be respected under the transformation (1.1.5), it is necessary to choose $\xi_\mu(x)$ such that $\Box\xi_\mu(x) = f_\mu(x)$, with $f_\mu(x)$ some function.

[5] Note that in the vacuum, linearised Einstein equations (1.1.11) imply that the speed of GWs $v_{\rm gw}$ is the same as the speed of light c. This is still true in full GR and constitutes a GR prediction. As an example, the detection of the electromagnetic counterpart of GW170817 [101, 102] has allowed to test $v_{\rm gw}/v_{\rm em} = 1$ to less than 5×10^{-16} precision [105].

This implies that it is possible to choose the four components of ξ^μ in such a way to impose four additional conditions on $h_{\mu\nu}$. Concretely, one can fix ξ^0 in such a way that the trace $\bar{h} = 0$, and consequently $\bar{h}_{\mu\nu} = h_{\mu\nu}$ from now on. In addition to this, one can select the three $\xi^i(x)$ so that $h^{0i}(x) = 0$. As a result, using this condition together with the $\mu = 0$ component of the Lorentz condition (1.1.10), one can deduce that $\partial^0 h_{00} = 0$, hence $h^{00} = 0$ and constant in time for a GW, which in turn must be related to time-varying parts of the spacetime. These additional conditions define the traceless-transverse (TT) gauge, which can be summarised as follows:

$$h^{0\mu} = 0, \qquad h^i_j = 0, \qquad \partial^i h_{ij} = 0. \tag{1.1.13}$$

The choice of the TT gauge completely fixes the gauge. As a consequence, $h_{\mu\nu}$ has only two independent radiative components. The physical meaning of the two remaining degrees of freedom can be understood when considering the plane-wave solution to equation (1.1.11):

$$h^{\mathrm{TT}}_{ij}(t, \vec{\boldsymbol{x}}) = e_{ij}(\vec{\boldsymbol{k}})\, e^{ik^\mu x_\mu}, \qquad k^\mu = \left(\frac{\omega}{c}, \vec{\boldsymbol{k}}\right), \quad \frac{\omega}{c} = \left|\vec{\boldsymbol{k}}\right|, \quad \hat{\boldsymbol{k}} = \frac{\vec{\boldsymbol{k}}}{\left|\vec{\boldsymbol{k}}\right|}, \tag{1.1.14}$$

where $e_{ij}(\vec{\boldsymbol{k}})$ is called the polarisation tensor and $\vec{\boldsymbol{k}}$ is the GW wave vector. In fact, by specialising the above equation to a GW propagating along $\hat{\boldsymbol{k}} = \hat{\boldsymbol{z}}$, one then obtains

$$h^{TT}_{ab}(t, z) = \begin{pmatrix} h_+ & h_\times \\ h_\times & -h_+ \end{pmatrix}_{ab} \cos\left[\omega\left(t - \frac{z}{c}\right)\right], \tag{1.1.15}$$

where $a, b = 1, 2$ are the components in the transverse (x, y) plane, and h_+ and $h_\times$ are the amplitudes of the "plus" and "cross" polarisation[6] of the GW, constituting the physical interpretation of the two degrees of freedom of $h_{\mu\nu}$.

In general, for a plane-wave solution $h_{\mu\nu}$, with propagation direction $\hat{\boldsymbol{k}}$ outside the source, in the Lorentz gauge but not yet in the TT gauge, the expression of the wave in the TT gauge can be obtained as follows by means of a projector. First, one introduces the transverse projector

$$P_{ij}(\hat{\boldsymbol{k}}) = \delta_{ij} - \hat{k}_i \hat{k}_j, \qquad \hat{k}^i P_{ij}(\hat{\boldsymbol{k}}) = 0, \qquad P_{ik} P_{jl} = P_{ij} \tag{1.1.16}$$

and uses it to assemble the TT projector

$$\Lambda_{ij,kl}(\hat{\boldsymbol{k}}) = P_{ik} P_{jl} - \frac{1}{2} P_{ij} P_{kl}, \tag{1.1.17}$$

$$\Lambda_{ij,mn}\Lambda_{mn,kl} = \Lambda_{ij,kl}, \qquad \hat{k}^i \Lambda_{ij,kl} = \hat{k}^j \Lambda_{ij,kl} = 0 = \Lambda_{ii,kl} = \Lambda_{ij,kk}, \tag{1.1.18}$$

[6] As it will become clearer later, h_+ and $h_\times$ are the components of one of the possible plane-wave expansion bases.

whose explicit form is

$$\Lambda_{ij,kl}(\hat{\boldsymbol{k}}) = \delta_{ik}\delta_{jl} - \frac{1}{2}\delta_{ij}\delta_{kl} - \hat{k}_j\hat{k}_l\delta_{ik} - \hat{k}_i\hat{k}_k\delta_{jl} + \frac{\delta_{ij}}{2}\hat{k}_k\hat{k}_l + \frac{\delta_{kl}}{2}\hat{k}_i\hat{k}_j + \frac{1}{2}\hat{k}_i\hat{k}_j\hat{k}_k\hat{k}_l. \tag{1.1.19}$$

Hence, the transformation to TT gauge is expressed in terms of the spatial components as

$$h_{ij}^{TT} = \Lambda_{ij,kl}\, h_{kl}. \tag{1.1.20}$$

This is a general result that can be applied to derive the transverse-traceless part of any symmetric tensor S_{ij}.

Eventually, by using the superposition principle, one can write any GW $h_{\mu\nu}^{TT}$ as a plane-wave expansion (see figure 1.1 for conventions):

$$h_{ij}^{\mathrm{TT}}(t,\vec{\boldsymbol{x}}) = \int \frac{\mathrm{d}^3k}{(2\pi)^3}\left(\mathcal{A}_{ij}(\vec{\boldsymbol{k}})\, e^{-ik^\mu x_\mu} + c.c.\right), \tag{1.1.21}$$

$$\hat{k}^i\mathcal{A}_{ij}(\vec{\boldsymbol{k}}) = 0 = \mathcal{A}_i^i(\vec{\boldsymbol{k}}), \tag{1.1.22}$$

where the conditions over the tensor amplitudes $\mathcal{A}_{ij}$ are a consequence of the TT gauge in the Fourier domain. The above expression can be recast in terms of "physical" frequencies $f \geq 0$ and the solid angle by observing $\mathrm{d}^3k = (2\pi/c)^3 f^2\,\mathrm{d}f\,\mathrm{d}\Omega$, and then expanded in the polarisation basis as

$$h_{ij}^{\mathrm{TT}}(t,\vec{\boldsymbol{x}}) = \sum_{A=+,\times}\int_{-\infty}^{+\infty}\mathrm{d}f\int \mathrm{d}^2\hat{\boldsymbol{n}}\,\tilde{h}_A(f,\hat{\boldsymbol{n}})\, e_{ij}^A(\hat{\boldsymbol{n}})\; e^{-2\pi i f\left(t+\frac{\hat{\boldsymbol{n}}\cdot\vec{\boldsymbol{x}}}{c}\right)}, \tag{1.1.23}$$

where $\mathrm{d}^2\hat{\boldsymbol{n}} = \mathrm{d}\cos\theta\,\mathrm{d}\phi$, $\hat{\boldsymbol{n}} = -\hat{\boldsymbol{k}}$, $\tilde{h}_A(-f,\hat{\boldsymbol{n}}) = \tilde{h}_A^*(f,\hat{\boldsymbol{n}})$, and

$$\frac{f^2}{c^3}\mathcal{A}_{ij}(f,\hat{\boldsymbol{n}}) = \sum_{A=+,\times}\tilde{h}_A(f,\hat{\boldsymbol{n}})\, e_{ij}^A(\hat{\boldsymbol{n}}). \tag{1.1.24}$$

The $e_{ij}^A(\hat{\boldsymbol{n}})$ quantities are the polarisation tensors and are defined as

$$e_{ij}^+(\hat{\boldsymbol{n}}) = \hat{l}_i\,\hat{l}_j - \hat{m}_i\,\hat{m}_j, \qquad e_{ij}^\times(\hat{\boldsymbol{n}}) = \hat{l}_i\,\hat{m}_j + \hat{m}_i\,\hat{l}_j, \tag{1.1.25}$$

$$e_{ij}^A(\hat{\boldsymbol{n}})\, e^{A',ij}(\hat{\boldsymbol{n}}) = 2\delta^{AA'}, \tag{1.1.26}$$

where

$$\begin{aligned}\hat{\boldsymbol{n}} &= (\sin\theta\,\cos\phi,\,\sin\theta\,\sin\phi,\,\cos\theta)\,,\\ \hat{\boldsymbol{l}} &= (\cos\theta\,\cos\phi,\,\cos\theta\,\cos\phi,\,-\sin\theta)\,,\\ \hat{\boldsymbol{m}} &= (-\sin\phi,\,\cos\phi,0)\,.\end{aligned} \tag{1.1.27}$$

As a final remark for this section, the $+$ and $\times$ polarisations are defined by choosing the axes in the transverse plane. If such an axes system is rotated by a polarisation

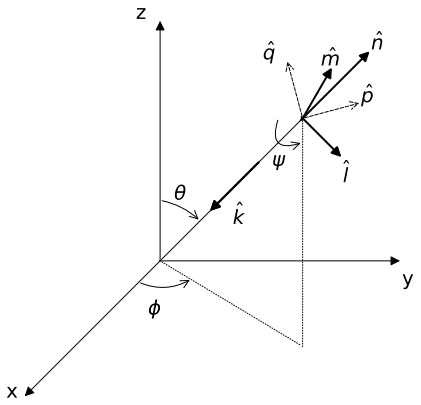

Figure 1.1: System of coordinates in the GW polarisation basis [`my_code`].

angle ψ, $\tilde{h}_+$ and $\tilde{h}_\times$ transform accordingly as

$$\begin{aligned} \tilde{h}_+ &\to \tilde{h}_+ \cos(2\psi) - \tilde{h}_\times \sin(2\psi) \\ \tilde{h}_\times &\to \tilde{h}_+ \sin(2\psi) + \tilde{h}_\times \cos(2\psi) \,. \end{aligned} \tag{1.1.28}$$

This makes clear the spin-2 (actually helicity h, whose ± 2 eigenstates are $(h_+ \mp i h_\times)$) nature of the massless quanta of the gravitational field.

1.2 Gravitational-wave interaction with test masses

After having shown in the previous section that GWs are not gauge artefacts but rather physical quantities, this section explores what the effect of the GWs passing through a system of test masses is. First, by exploiting the correspondence between a gauge choice and fixing a reference frame, one discusses which frame corresponds to the TT gauge and what the effect of GWs there is. Then, in view of describing the interaction between GWs and GW detectors in chapter 2, one introduces the proper detector frame and repeats the investigation there. Throughout this section, test mass systems are assumed to be outside and far enough from the GW sources, and the linearised GR formalism from section 1.1 is employed.

Two equations play a key role throughout the discussion, namely the geodesic equation and the geodesic deviation equation [39]. The geodesic equation describes the free-fall motion of test bodies in spacetime. For time-like trajectories, its expression is

$$\frac{\mathrm{d}^2 x^\mu}{\mathrm{d}\tau^2} + \Gamma^\mu_{\nu\rho}(x) \frac{\mathrm{d}x^\nu}{\mathrm{d}\tau} \frac{\mathrm{d}x^\rho}{\mathrm{d}\tau} = 0, \tag{1.2.1}$$

where the affine parameter τ is the proper time, and $\Gamma^{\mu}_{\nu\rho}(x)$ is the Christoffel symbol for the metric $g_{\mu\nu}(x)$.The geodesic-deviation equation relates the Riemann curvature tensor to the relative (tidal) acceleration between two neighbouring geodesics. For two time-like geodesics $x^{\mu}(\tau)$ and $x^{\mu}(\tau) + \xi^{\mu}(\tau)$, its form is

$$\frac{\mathrm{D}^2\xi^{\mu}}{\mathrm{D}\tau^2} = -R^{\mu}_{\nu\rho\sigma}\xi^{\rho}\frac{\mathrm{d}x^{\nu}}{\mathrm{d}\tau}\frac{\mathrm{d}x^{\sigma}}{\mathrm{d}\tau}, \tag{1.2.2}$$

where the covariant derivative for a vector field $V^{\mu}(x)$ along the curve $x^{\mu}(\tau)$ is defined as

$$\frac{\mathrm{D}V^{\mu}}{\mathrm{D}\tau} = \frac{\mathrm{d}V^{\mu}}{\mathrm{d}\tau} + \Gamma^{\mu}_{\nu\rho}(x)V^{\nu}\frac{\mathrm{d}x^{\rho}}{\mathrm{d}\tau}. \tag{1.2.3}$$

1.2.1 The TT frame

The reference frame associated with the TT gauge is denoted as the TT frame. To understand the physical interpretation of this frame, one considers a test mass at rest at the proper time $\tau = 0$. Then, by using the previous condition $\mathrm{d}x^i/\mathrm{d}\tau = 0$ at $\tau = 0$, the geodesic equation (1.2.1) becomes

$$\left.\frac{\mathrm{d}^2x^i}{\mathrm{d}\tau^2}\right|_{\tau=0} = -\left.\left[\Gamma^i_{00}\left(\frac{\mathrm{d}x^0}{\mathrm{d}\tau}\right)^2\right]\right|_{\tau=0}. \tag{1.2.4}$$

The expression of Γ^i_{00}, at first order in $h_{\mu\nu}$, can be easily shown to be

$$\Gamma^i_{00} = \frac{1}{2}\left(2\partial_0 h_{0i} - \partial_i h_{00}\right). \tag{1.2.5}$$

This quantity vanishes in the TT gauge, given the conditions on h_{00} and h_{0i} from equation (1.1.13). As a consequence, $\mathrm{d}^2x^i/\mathrm{d}\tau^2 = 0$ at $\tau = 0$ in equation (1.2.4), and ultimately $\mathrm{d}x^i/\mathrm{d}\tau = 0$ at all times. This reveals that, in the TT gauge in linearised theory, particles at rest before the GW arrival remain at rest even after its passage. Similarly, by evaluating the geodesic deviation equation (1.2.2) in this gauge, the coordinate separation $\xi^i(\tau)$ does not change over (proper) time [146]. Hence, as a further consequence, the proper time τ of a test mass at rest in the TT gauge is the same as the coordinate time t, up to $\mathcal{O}\big(h^4\big)$.

The above discussion highlights that the physical effects of GWs cannot be described by what happens to the coordinates, reflecting the invariance of GW under coordinate transformation. The fact that the GW passage does not change coordinates in the TT gauge is solely due to the freedom of choice of these particular coordinates. However, the physical effects of GWs crossing the test masses can still be monitored when examining the proper distances and times. As an example, in the case of two events at $(t_1, \vec{\boldsymbol{x}}_1)$ and $(t_2, \vec{\boldsymbol{x}}_2)$, with $\vec{\boldsymbol{L}} \equiv \vec{\boldsymbol{x}}_2 - \vec{\boldsymbol{x}}_1$ constant in time in the TT gauge and a GW propagating along $\hat{\boldsymbol{k}}$, the proper distance to linear order in h_{ij} is $s \simeq L + h_{ij}(t)\,(L_i\,L_j/2L)$. This implies that (to linear order) the geodesic equation

for proper distances is

$$\ddot{s}_i \simeq \frac{\ddot{h}_{ij}}{2} L_j \simeq \frac{\ddot{h}_{ij}}{2} s_j, \tag{1.2.6}$$

where $s \equiv \hat{L}_i s_i$). Consequently, a possible strategy to detect GWs is time-tracking the round trip of a light beam between two test masses (in the vacuum), given the constant speed of light and the variation of the proper distance at the passage of GWs.

1.2.2 The proper detector frame

The TT frame is not suitable to describe what happens in a detector laboratory, where coordinates are ideally defined by means of a rigid ruler rather than free-falling particles. In addition to that, there are two scales playing an important role when investigating the interaction between GWs and test masses in the laboratory frame with a set of coordinates $(t, \vec{\boldsymbol{x}})$, namely the typical variation scale of the metric L_B and the typical size of the considered region of space $r \equiv |\vec{\boldsymbol{x}}|$.

For a detector whose location is on Earth, which is an accelerated and rotating frame, the metric can be shown to assume, up to $\mathcal{O}\big(r^2\big)$, the following form [151,152]:

$$\begin{aligned} \mathrm{d}s^2 \simeq & - c^2\,\mathrm{d}t^2 \left[1 + \frac{2}{c^2}\vec{\boldsymbol{a}}\cdot\vec{\boldsymbol{x}} + \frac{1}{c^4}\left(\vec{\boldsymbol{a}}\cdot\vec{\boldsymbol{x}}\right)^2 - \frac{1}{c^2}\left(\vec{\boldsymbol{\Omega}}\times\vec{\boldsymbol{x}}\right)^2 + R_{0i0j}\,x^i\,x^j\right] \\ & + 2c\,\mathrm{d}t\,\mathrm{d}x^i\left[\frac{1}{c}\varepsilon_{ijk}\,\Omega^j\,x^k - \frac{2}{3}R_{0jik}\,x^j\,x^k\right] + \mathrm{d}x^i\,\mathrm{d}x^j\left[\delta_{ij} - \frac{1}{3}R_{ikjl}\,x^k\,x^l\right], \end{aligned} \tag{1.2.7}$$

where $\vec{\boldsymbol{a}}$ and $\vec{\boldsymbol{\Omega}}$ are the acceleration of the laboratory with respect to the local free-falling frame and the angular velocity with respect to local gyroscopes, respectively. This form of metric is called called the proper detector frame.

Equation (1.2.7) accounts for several phenomena. The term $2\vec{\boldsymbol{a}}\cdot\vec{\boldsymbol{x}}/c^2$ encodes the inertial acceleration. The $(\vec{\boldsymbol{a}}\cdot\vec{\boldsymbol{x}}/c^2)^2$ one reflects the gravitational redshift. The terms $\left(\vec{\boldsymbol{\Omega}}\times\vec{\boldsymbol{x}}/c\right)^2$ and $\varepsilon_{ijk}\,\Omega^j\,x^k/c$ quantify the Lorentz time dilatation caused by the angular velocity of the laboratory and the Sagnac effect [153–155], respectively. Finally, the terms proportional to the Riemann tensor $R_{\mu\nu\rho\sigma} = \mathcal{O}\big(L_B^{-2}\big)$ encode the effect of the slowly varying background metric and the effect of GWs and enter in the expansion only at $\mathcal{O}\big((r/L_B)^2\big)$. From this, one observes that GWs are competing with many other dominant effects, possibly several orders of magnitude larger and presented below.

At zeroth order in r/L_B, equation (1.2.7) reduces to the flat spacetime metric, where Newtonian intuition applies. This is an important difference compared to the TT frame, where GWs are always present and no expansion in r/L_B is necessary, meaning that the considered region of space has a size smaller than the typical variation scale of the background metric. The first deviations from the flat metric in the detector proper frame arise to linear order in r/L_B, and can be modelled by New-

tonian forces by considering the geodesic equation (1.2.1) adapted to the metric in equation (1.2.7) at $\mathcal{O}(r/L_B)$:

$$\frac{\mathrm{d}^2 x^i}{\mathrm{d}\tau^2} = -a^i - 2\left(\vec{\boldsymbol{\Omega}} \times \vec{\boldsymbol{v}}\right)^i + \frac{f^i}{m} + \mathcal{O}\big(x^i\big), \tag{1.2.8}$$

where $\vec{\boldsymbol{a}} = -\vec{\boldsymbol{g}}$ is the gravity acceleration, $-2\left(\vec{\boldsymbol{\Omega}} \times \vec{\boldsymbol{v}}\right)^i$ the Coriolis force, and f^i represents the external force compensating the gravity acceleration in the laboratory. The terms of $\mathcal{O}\big(x^i\big)$ contain other forces, such as the centrifugal acceleration $\vec{\boldsymbol{\Omega}} \times (\vec{\boldsymbol{\Omega}} \times \vec{\boldsymbol{v}})^i$. Terms proportional to the Riemann tensor appear only from quadratic order in r/L_B, and describe both contributions from the slowly varying Earth gravitational field and the GW one.

The weak effect of GWs can be isolated by considering a frequency band where GW frequency is higher compared to the typical variation timescales of the contributions in equation (1.2.7) linear in $h_{\mu\nu}$. If this condition is true, only terms proportional to the Riemann tensor are retained, and the metric in the detector frame becomes

$$\begin{aligned} \mathrm{d}s^2 \simeq & -c^2\,\mathrm{d}t^2\left[1 + R_{0i0j}\,x^i\,x^j\right] \\ & - 2c\,\mathrm{d}t\,\mathrm{d}x^i\left(\frac{2}{3}R_{0jik}\,x^j\,x^k\right) + \mathrm{d}x^i\,\mathrm{d}x^j\left[\delta_{ij} - \frac{1}{3}R_{ikjl}\,x^k\,x^l\right]. \end{aligned} \tag{1.2.9}$$

This expression of the metric can then be employed in studying the effect of GWs on test masses in the proper detector frame. The process can be simplified by considering the geodesic deviation equation (1.2.2), which can be rewritten as

$$\frac{\mathrm{d}^2\xi^i}{\mathrm{d}\tau^2} = -R^i_{0j0}\xi^j\left(\frac{\mathrm{d}x^0}{\mathrm{d}\tau}\right)^2. \tag{1.2.10}$$

This equation can be further expanded to linear order and simplified in two steps. First, by observing that $\mathrm{d}\tau \sim \mathrm{d}t + \mathcal{O}(h)$. Second, by exploiting the invariance of the Riemann tensor ($R^i_{0j0} = \mathcal{O}(h)$) in the linearised theory to compute it in the TT frame, eventually obtaining

$$\ddot{\xi}^i = \frac{1}{2}\ddot{h}^{TT}_{ij}\,\xi^j. \tag{1.2.11}$$

This equation is the final form of the geodesic deviation equation in the proper detector frame. In its simplicity, it states that the interaction of GWs with a test mass m can be described by means of a Newtonian force

$$F_i = \frac{m}{2}\,\ddot{h}^{TT}_{ij}\,\xi^j, \tag{1.2.12}$$

and hence that the response of the entire detector to GWs can be described using Newtonian physics.

Finally, by employing equation (1.2.11), it is possible to describe the effect of GWs on a system of test masses. This can be easily shown by considering a ring

of test masses, initially at rest and at a distance ξ^i from the centre of the ring, taken to be the origin of the detector frame. As a further simplification of the picture that aims to provide a more intuitive explanation about the naming of GW polarisations, the ring of test masses is assumed to lay in the (x, y) plane and the GW to propagate along the z-direction. Since GWs affects the masses only in the transverse plane, the displacement of the masses is constrained in the (x, y) plane. By considering separately the two cases where only $+$ or $\times$ polarisations are present and assuming $h_{ab}^{TT} \propto h_A \sin(\omega t)$ $(A = +, \times)$, equation (1.2.11) becomes

$$\begin{cases} \delta\ddot{x} = -\frac{h_+}{2}\,(x_0 + \delta x)\;\omega^2\;\sin(\omega t) \\ \delta\ddot{y} = \frac{h_+}{2}\,(y_0 + \delta y)\;\omega^2\;\sin(\omega t) \end{cases} \qquad \begin{cases} \delta\ddot{x} = -\frac{h_\times}{2}\,(y_0 + \delta y)\;\omega^2\;\sin(\omega t) \\ \delta\ddot{y} = -\frac{h_\times}{2}\,(x_0 + \delta x)\;\omega^2\;\sin(\omega t). \end{cases} \tag{1.2.13}$$

It can be noted that $\delta x,\, \delta y \sim \mathcal{O}(h) \ll x_0,\, y_0$. As a consequence, δx and δy can be neglected on the right-hand side of equation (1.2.13), whose integration leads to the solutions

$$\begin{cases} \delta x = -\frac{h_+}{2} x_0\,\omega^2\;\sin(\omega t) \\ \delta y = \frac{h_+}{2} y_0\,\omega^2\;\sin(\omega t) \end{cases} \qquad \begin{cases} \delta x(t) = \frac{h_\times}{2} y_0\,\omega^2\;\sin(\omega t) \\ \delta y(t) = \frac{h_+}{2} x_0\,\omega^2\;\sin(\omega t) \end{cases} \quad . \tag{1.2.14}$$

The resulting deformation of the ring of test masses due to the $+$ or $\times$ polarisations as a function of time is reported in figure 1.2. From this figure, it appears clear that the deformation is the same for both polarisations, except for a relative rotation of $45°$ [7], and that the pattern is invariant under a rotation of $180°$ [8] about the propagation direction of the GW. The line of force associated with the deformations follows a quadrupolar pattern with a shape of a "$+$" and a "$\times$" sign, from which the names "plus" and "cross" polarisation derive.

1.3 Beyond linearised theory: The GW energy-momentum tensor

The discussion about the interaction of GWs with a test mass system above sheds light on the fact that GWs do carry energy. The question that arises from this statement is whether even GWs can be sources of space-time curvature, given that any form of energy contributes to it in GR. To answer this question, the assumption of a flat background metric from linearised theory must be dropped, allowing the spacetime to

[7] The relative inclination of $45°$ between the two polarisation states is connected to the spin of the zero-mass particles associated with the quantum-mechanical description of the GWs. In general, a radiation field of spin S has exactly two orthogonal states of linear polarisation [32, 150], whose relative inclination is an angle $90°/S$. In the case of gravitational radiation, the associated zero-mass particle is the spin-2 graviton, the two orthogonal eigenstates are e_{ij}^{+} and $e_{ij}^{\times}$, and the relative angle is exactly $90°/2 = 45°$.

[8] As above, the invariance under this specific rotation angle comes from the general fact that the classical radiation field of a massless particle of spin S is invariant under a rotation of $360°/S$ about its propagation direction. This leads to the $360°/2 = 180°$ angle in the gravitational radiation case.

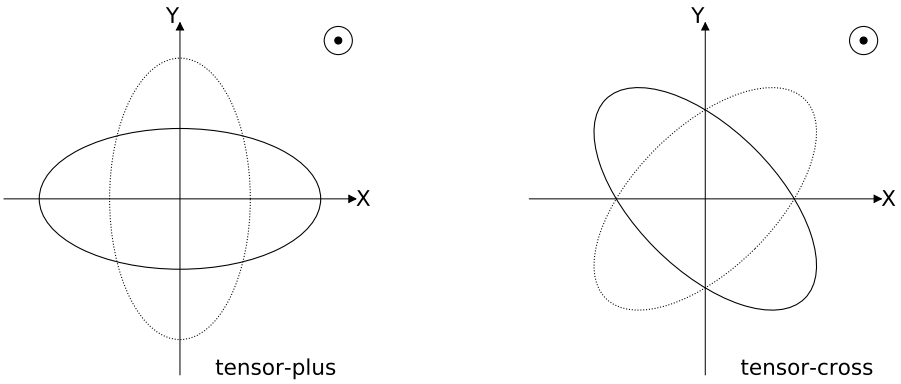

Figure 1.2: GW polarisation effects polarisation effects on a circle of test masses [`my_code`].

be dynamical. This translates into the definition of GWs as perturbations over some curved, dynamical, background metric $\bar{g}_{\mu\nu}(x)$, writing the space-time metric as

$$g_{\mu\nu}(x) = \bar{g}_{\mu\nu}(x) + \delta g_{\mu\nu}(x), \qquad |\delta g_{\mu\nu}(x)| \ll |\bar{g}_{\mu\nu}(x)|. \tag{1.3.1}$$

For consistency with previous notation and to make the connection with linearised theory easier, the above equation can be rewritten in a coordinate system where the diagonal elements of $\bar{g}_{\mu\nu} = \mathcal{O}(1)$ over the region of spacetime of interest, meaning

$$g_{\mu\nu}(x) = \bar{g}_{\mu\nu}(x) + h_{\mu\nu}, \qquad |h_{\mu\nu}(x)| \ll 1. \tag{1.3.2}$$

1.3.1 How to separate GWs from the background?

At first look, the above decomposition of the metric appears not to make possible in general to distinguish which term actually contributes to the background metric and which to the metric fluctuations. This issue resembles again the puzzle of whether GWs can be "gauged away" or are physical, but this time in full GR. This problem can be solved in the case where there is a net separation of scales between the spatial (frequency) variation scale L_B (f_B) of the background $\bar{g}_{\mu\nu}$ and the reduced wavelength (frequency peak) $\lambda\!\!\!^{-}$ (f) of the perturbation. The relation between the scales must allow to identify $h_{\mu\nu}$ as small ripples on a smooth background (high-frequency perturbation of a static or slowly-varying background), leading to the condition

$$\lambda\!\!\!^{-} \ll L_B, \qquad (f \gg f_B)\,. \tag{1.3.3}$$

Within this framework [32, 146, 156], it is possible to investigate how the perturbation $h_{\mu\nu}$ propagates in the background spacetime $\bar{g}_{\mu\nu}$, and how it affects the background metric itself. This will clarify why the perturbation $h_{\mu\nu}$ is called a gravitational wave, and how to properly define the GW energy-momentum tensor, respectively.

The starting point of the discussion is expanding Einstein equations (1.1.1) about the background metric $\bar{g}_{\mu\nu}$. The expansion parameters are $h \equiv \mathcal{O}(|h_{\mu\nu}|)$ and $\lambda\!\!\!^{-}/L_B$

(f_B/f). Moreover, the condition $\lambda\!\!\!^{-}/L_B \ll 1$ ($f_B/f \ll 1$) holds and is denoted as "short-wave expansion". It turns out that it is more convenient to cast Einstein equations in the form

$$R_{\mu\nu} = \frac{8\pi G}{c^4}\left(T_{\mu\nu} - \frac{1}{2}g_{\mu\nu}T\right), \tag{1.3.4}$$

where $T_{\mu\nu}$ and T are the energy-momentum tensor of the matter and its trace, and then expand the Ricci tensor at second order in h

$$R_{\mu\nu} = \bar{R}_{\mu\nu} + R^{(1)}_{\mu\nu} + R^{(2)}_{\mu\nu} + \mathcal{O}\big(h^3\big), \tag{1.3.5}$$

where $\bar{R}_{\mu\nu}$ is the Ricci tensor associated with $\bar{g}_{\mu\nu}$, while $R^{(1)}_{\mu\nu}$ and $R^{(2)}_{\mu\nu}$ are linear and quadratic in $h_{\mu\nu}$, respectively. By inserting the above expression in the Einstein equations (1.3.4), they can be split into two separate sets of equations for low and high momenta (frequency modes) [32, 146, 156]:

$$\bar{R}_{\mu\nu} = -\left[R^{(2)}_{\mu\nu}\right]^{LOW} + \frac{8\pi G}{c^4}\left(T_{\mu\nu} - \frac{1}{2}g_{\mu\nu}T\right)^{LOW} \tag{1.3.6}$$

$$\bar{R}^{(1)}_{\mu\nu} = -\left[R^{(2)}_{\mu\nu}\right]^{HIGH} + \frac{8\pi G}{c^4}\left(T_{\mu\nu} - \frac{1}{2}g_{\mu\nu}T\right)^{HIGH}. \tag{1.3.7}$$

From studying the above equations, it becomes evident why the linearised theory of GR presented in section 1.1 cannot be extended beyond linear order. By evaluating the explicit expressions of $R^{(1)}_{\mu\nu}$ and $R^{(2)}_{\mu\nu}$ (see [32, 146, 150]) in the low-modes equation (1.3.6) in the absence of matter with $T_{\mu\nu} = 0$, it results that $\bar{R}_{\mu\nu} \sim (\partial h)^2 \sim (h/\lambda\!\!\!^{-})^2$. This means that the derivatives of the perturbation impact the curvature of the background metric $\bar{g}_{\mu\nu}$. At the same time, $\bar{R}_{\mu\nu} \sim \partial^2\bar{g}_{\mu\nu} \sim 1/L_B^2$, and hence the curvature determined by GWs can be estimated as [32]

$$h \sim \frac{\lambda\!\!\!^{-}}{L_B}. \tag{1.3.8}$$

Conversely, if $T_{\mu\nu} \neq 0$, the GW contribution to the background curvature is negligible with respect to the one from the matter sources, implying

$$h \ll \frac{\lambda\!\!\!^{-}}{L_B}. \tag{1.3.9}$$

In linearised theory, $\partial\bar{g}_{\mu\nu} \equiv \partial\eta_{\mu\nu} = 0 = 1/L_B$, and therefore any non-zero value of h violates the condition $h \lesssim \lambda\!\!\!^{-}/L_B$. As a consequence, a further systematic expansion in higher orders of h has no domain of validity if the background metric must remain flat. In addition to that, equations (1.3.8) and (1.3.9) make clear that the concept of GW can be defined only if $h \ll 1$, which guarantees $\lambda\!\!\!^{-}/L_B \lesssim 1$, and hence the separation of scales needed to distinguish the GWs from the background spacetime.

1.3.2 Low-modes: GW energy and momentum

Let one examine now the low-modes equation (1.3.6), assuming that there is a sharp separation between the GW length-scale λ (time-scale $1/f$) and the background one L_B ($1/f_B$). Then, it is possible to introduce another length-scale $\bar{l}$ (time-scale $\bar{t}$), satisfying $\lambda \ll \bar{l} \ll L_B$ ($1/f \ll \bar{t} \ll 1/f_B$), and perform an average over a spatial volume (time interval) with characteristic size $\bar{l}$ (time interval $\bar{t}$), denoted in the following as $\langle ... \rangle$. This procedure allows one to average out the fast oscillating modes f with reduced wavelength λ, leaving only low-modes with frequency f_B with reduced wavelength of order L_B. By employing this framework in equation (1.3.6), it is possible to introduce a coarse-grained version of Einstein equations [146, 157]

$$\bar{R}_{\mu\nu} - \frac{1}{2}\bar{g}_{\mu\nu}\bar{R} = \frac{8\pi\, G}{c^4}\left(\bar{T}_{\mu\nu} + t_{\mu\nu}\right), \tag{1.3.10}$$

where $\bar{T}_{\mu\nu}$ is defined from

$$\left\langle T_{\mu\nu} - \frac{1}{2} g_{\mu\nu}\, T \right\rangle = \bar{T}_{\mu\nu} - \frac{1}{2}\bar{g}_{\mu\nu}\,\bar{T}, \tag{1.3.11}$$

and $t_{\mu\nu}$ as

$$t_{\mu\nu} = -\frac{c^4}{8\pi G}\left\langle R^{(2)}_{\mu\nu} - \frac{1}{2}\bar{g}_{\mu\nu} R^{(2)} \right\rangle, \tag{1.3.12}$$

with

$$R^{(2)} = \bar{g}^{\mu\nu} R^{(2)}_{\mu\nu}, \qquad t = \bar{g}^{\mu\nu} t_{\mu\nu} = \frac{c^4}{8\pi G}\left\langle R^{(2)} \right\rangle. \tag{1.3.13}$$

The coarse-grained Einstein equations (1.3.10) describe the dynamics of the background metric $\bar{g}_{\mu\nu}$, which is also the long-wavelength (low-frequency) part of the space-time metric, as a function of $\bar{T}_{\mu\nu}$, whose straightforward physical interpretation is to be the long-wavelength (low-frequency) part of the matter energy-momentum tensor, and the tensor $t_{\mu\nu}$, which in turn depends only on the gravitational field itself and is quadratic in $h_{\mu\nu}$.

The physical meaning of $t_{\mu\nu}$ becomes clear by evaluating it at large distances from the source, where the background metric is approximately flat. By using the explicit expression of $R^{(2)}_{\mu\nu}$ in equation (1.3.12), imposing the Lorentz gauge conditions, and working through some algebra, it is possible to express $t_{\mu\nu}$ as [32, 146]

$$t_{\mu\nu} = \frac{c^4}{32\pi\, G}\left\langle \partial_\mu h_{\alpha\beta}\, \partial_\nu h^{\alpha\beta} \right\rangle. \tag{1.3.14}$$

It is possible to verify under the residual gauge transformation (1.1.4). As a consequence, it must depend only on the physical modes h^{TT}_{ij} and can be identified with

the *effective* energy-momentum tensor [146, 158, 159] that this quantity is invariant[9] of the GWs at a large distance from the source. Also, far from the source, where GR linearised theory holds and $\bar{T}_{\mu\nu} = 0$, the GW energy-momentum tensor satisfies the conservation law $\partial^\mu t_{\mu\nu} = 0$. However, this is no longer true in full GR, where the covariant quantity that is conserved is rather the sum of $\bar{T}_{\mu\nu}$ and $t_{\mu\nu}$. The conservation law assumes the form [32]

$$\bar{D}^\nu \left(\bar{T}_{\mu\nu} + t_{\mu\nu}\right) = 0, \tag{1.3.15}$$

reflecting the fact that there is a continuous exchange of energy-momentum between GWs and the matter sources.

From the expression of the GW energy-momentum tensor in linearised theory, it becomes straightforward to derive the gauge-invariant[10] energy density of GWs

$$t_{00} = \frac{c^2}{32\pi\, G} \left\langle \dot{h}_{ij}^{TT}\, \dot{h}_{ij}^{TT} \right\rangle \tag{1.3.16}$$

which will play a very important role in the incoming chapters (see chapter 3), and related quantities as the GW energy flux, namely the GW energy flow per unit of time through a unit surface far away from the source,

$$\frac{\mathrm{d}^2 E}{\mathrm{d}A\, \mathrm{d}t} = \frac{c^3}{32\pi\, G} \left\langle \dot{h}_{ij}^{TT} \dot{h}_{ij}^{TT} \right\rangle, \tag{1.3.17}$$

and the GW energy spectrum

$$\frac{\mathrm{d}E}{\mathrm{d}f} = \frac{\pi c^3}{4G} f^2\, r^2 \int_{S^2} \mathrm{d}\Omega \left|\tilde{h}(f)\right|^2, \tag{1.3.18}$$

with r the distance from the source and $\mathrm{d}\Omega = \mathrm{d}A\,/r^2$ the solid angle. Similarly, from the GW momentum density t^{0k}, it is possible to show that the GW energy momentum flux is

$$\frac{\mathrm{d}^2 P^k}{\mathrm{d}A\, \mathrm{d}t} = -\frac{c^3}{32\pi\, G} \left\langle \dot{h}_{ij}^{TT}\, \partial^k h_{ij}^{TT} \right\rangle. \tag{1.3.19}$$

1.3.3 High modes: Propagation in curved spacetime

High-mode Einstein equations (1.3.7) can be proved to reduce to equation (1.1.11) in the absence of matter. In the case where instead $T_{\mu\nu} \neq 0$ and the matter dominates

[9] The most general definition of $t_{\mu\nu}$ without averaging is the Landau-Lifshitz energy-momentum pseudotensor [150], where *pseudo* here means that it does not transform as a tensor under all coordinate transformations. However, the numerical values and the transformation properties of the Landau-Lifshitz energy-momentum pseudotensor (in linearised theory) are the same as the quantity in equation (1.3.12) under linear transformations and some additional conditions; see [160] for a detailed discussion. In [159], the Landau-Lifshitz energy-momentum pseudotensor is shown to be invariant (to linear order) under coordinate transformations upon space-time averaging.

[10] Upon space-time averaging [158, 159] and to leading order in $\lambda\!\!\!^{-}/L_B$ [146].

as the main source curvature, implying $h \ll \lambda\!\!\!^{-}/L_B \ll 1$, it is possible to perform a separate expansion in h and $\lambda\!\!\!^{-}/L_B$. By further retaining only linear terms in h and expanding the results in powers of $\lambda\!\!\!^{-}/L_B$, equation (1.3.7) simplifies to [146]

$$R^{(1)}_{\mu\nu} = 0, \tag{1.3.20}$$

which is fully covariant with respect to the background metric $\bar{g}_{\mu\nu}$. The explicit expression in a curved background of the above equation can be found with some algebra and reads [32, 156]

$$\bar{g}^{\rho\sigma}\left(\bar{D}_\rho\bar{D}_\nu h_{\mu\sigma} + \bar{D}_\rho\bar{D}_\mu h_{\nu\sigma} - \bar{D}_\nu\bar{D}_\mu h_{\rho\sigma} - \bar{D}_\rho\bar{D}_\sigma h_{\mu\nu}\right) = 0. \tag{1.3.21}$$

Now, in a similar fashion to what was done in section 1.1 introducing the trace-reverse $\bar{h}_{\mu\nu}$, with $\eta_{\mu\nu}$ replaced by $\bar{g}_{\mu\nu}$, and imposing the (Lorentz) gauge condition $\bar{D}^\nu\bar{h}_{\mu\nu} = 0$, the above equation can be recast as [32, 146, 156]

$$\bar{D}^\rho\bar{D}_\rho\bar{h}_{\mu\nu} + 2\bar{R}_{\mu\rho\nu\sigma}\bar{h}^{\rho\sigma} - \bar{R}_{\mu\rho}\bar{h}^\rho_\nu - \bar{R}_{\nu\rho}\bar{h}^\rho_\mu = 0. \tag{1.3.22}$$

Eventually, by discarding the terms involving the background-metric Riemann and Ricci tensors that are of order higher than $\mathcal{O}\left(h/\lambda\!\!\!^{-2}\right)$, the final expression of equation (1.3.20) is

$$\bar{D}^\rho\bar{D}_\rho\bar{h}_{\mu\nu} = 0. \tag{1.3.23}$$

This equation, together with the Lorentz gauge condition, describes the propagation of $h_{\mu\nu}$ in the limit $\lambda\!\!\!^{-} \ll L_B$, showing that the high-mode Einstein equations (1.3.7) are actually a wave equation for GWs in curved spacetime.

1.4 Gravitational-wave production: Quadrupole formula

After having examined how to describe the energy-momentum carried by GWs, the next question to answer is about the GW generation mechanism and how to describe it. The topic is extremely wide and cannot be covered extensively here, but several reviews exist, such as [161]. In the following, the GW production is discussed within the linearised theory framework, which still allows to catch the main aspects of the process by illustrating them in a simplified way. The initial focus is on weak-field sources of GWs, and the corresponding GW creation formula is derived in flat spacetime. Then, the investigation further restricts itself to low-velocity sources, leading to the introduction of the multipole expansion formalism and the discussion of the first non-zero term of the expansion, namely the quadrupole.

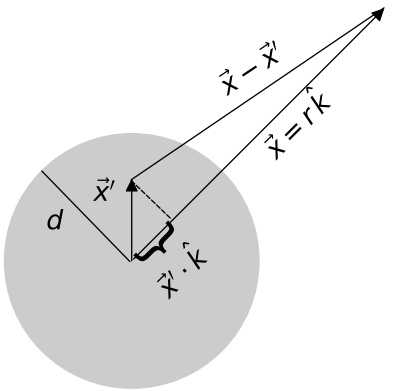

Figure 1.3: Coordinates for the weak-field, low-velocity expansion [`my_code`].

1.4.1 Weak-field sources and low-velocity expansion

Within linearised theory, linearised Einstein equations (1.1.7) in the presence of matter are linear in $h_{\mu\nu}$ and can be solved by means of the Green's function method. Their solution can be expressed in terms of the retarded Green's function, and outside the source and in the TT gauge reads

$$h_{ij}^{TT}(t,\vec{\boldsymbol{x}}) = \frac{4G}{c^4}\Lambda_{ij,kl}(\hat{\boldsymbol{k}})\int \mathrm{d}^3x' \,\frac{1}{|\vec{\boldsymbol{x}}-\vec{\boldsymbol{x}}'|}\,T_{kl}\left(t-\frac{|\vec{\boldsymbol{x}}-\vec{\boldsymbol{x}}'|}{c},\,\vec{\boldsymbol{x}}'\right), \tag{1.4.1}$$

where the integral is over the source volume. By denoting with d the characteristic length scale of the source and restricting to the region of space at a distance, the expansion

$$\left|\vec{\boldsymbol{x}}-\vec{\boldsymbol{x}'}\right| = r - \vec{\boldsymbol{x}'}\cdot\vec{\boldsymbol{k}} + \mathcal{O}\left(\frac{d^2}{r^2}\right) \implies \frac{1}{\left|\vec{\boldsymbol{x}}-\vec{\boldsymbol{x}'}\right|} \sim \frac{1}{r}, \tag{1.4.2}$$

holds (see figure 1.3). In this way, by expanding equation (1.4.1) to linear order in d/r [11], and writing T_{kl} in terms of its Fourier transform (again, to linear order in d/r), it is possible to cast the equation in the form

$$h_{ij}^{TT}(t,\vec{\boldsymbol{x}}) = \frac{4G}{r\,c^5}\Lambda_{ij,kl}(\hat{\boldsymbol{k}})\int_{-\infty}^{+\infty}\frac{\mathrm{d}\omega}{2\pi}\,\tilde{T}_{kl}\left(\omega,\,\omega\frac{\hat{\boldsymbol{k}}}{c}\right)\,e^{-i\omega\left(t-\frac{r}{c}\right)}. \tag{1.4.3}$$

In general, the dominant contributions to the energy-momentum tensor Fourier transform are expected to be large around the characteristic "frequency" of the source internal motion $\omega_s \sim v/d$, where v is the characteristic speed of the source internal matter.

[11] This means that, in linearised theory, GWs are studied at spatial infinity $r \to \infty$ at a fixed time t.

From equation (1.4.3) it is possible to derive the GW energy spectrum by using equation (1.3.18), $\tilde{T}(-k_\mu) = \tilde{T}^*(k_\mu)$ and the properties of $\Lambda_{ij,kl}(\hat{\boldsymbol{k}})$, getting

$$\frac{\mathrm{d}E}{\mathrm{d}\omega} = \frac{G\,\omega^2}{2\pi^2\,c^7} \int \mathrm{d}\Omega\, \Lambda_{ij,kl}(\hat{\boldsymbol{k}})\, \tilde{T}_{ij}\left(\omega,\, \omega\frac{\hat{\boldsymbol{k}}}{c}\right) \tilde{T}^*_{kl}\left(\omega,\, \omega\frac{\hat{\boldsymbol{k}}}{c}\right). \tag{1.4.4}$$

To obtain the total GW energy radiated over the sky, one can invert the above relation in favour of the flux equation (1.3.17), and integrate over $\mathrm{d}\Omega$ by using the identities

$$\int \frac{\mathrm{d}\Omega}{4\pi} k_{i_1} \dots k_{i_{2l}} = \frac{1}{(2l+1)!!} \left(\delta_{i_1 i_2} \dots \delta_{i_{2l-1} i_{2l}} + perm.\right). \tag{1.4.5}$$

Note that, until this point, no assumption has been made about v. This implies that, even though the above equations (1.4.3) for the strain and (1.4.4) for the GW energy spectrum are valid within the weak-field approximation, they hold for both relativistic and non-relativistic sources.

The above expressions can be noticeably simplified in the case of non-relativistic sources, where the assumption $v \ll c$ implies the following condition on the reduced wavelength of the gravitational radiation:

$$ƛ \sim \frac{c}{v}\, d \gg d. \tag{1.4.6}$$

To understand where the non-relativistic condition applies, consider again equation (1.4.1) at $r \gg d$

$$h^{TT}_{ij}(t, \vec{\boldsymbol{x}}) = \frac{1}{r}\,\frac{4G}{c} \Lambda_{ij,kl}(\hat{\boldsymbol{k}}) \int \mathrm{d}^3x'\, T_{kl}\left(t - \frac{r - \vec{\boldsymbol{x}'}\cdot\hat{\boldsymbol{k}}}{c},\, \vec{\boldsymbol{x}}'\right), \tag{1.4.7}$$

with $|\vec{\boldsymbol{x}}'| \leq d$. Now, when considering the Fourier transform of T_{kl}, in addition to it being peaked about ω_s, also the $\omega_s d \ll c$ condition applies. As a consequence, given that T_{kl} is non-vanishing only inside the source, the dominant contribution to h^{TT}_{ij} comes from the modes ω satisfying

$$\frac{\omega}{c}\, \vec{\boldsymbol{x}}' \cdot \hat{\boldsymbol{k}} \leq \frac{\omega_s d}{c} \ll 1. \tag{1.4.8}$$

From the above condition, it is possible to perform a Taylor expansion of T_{kl} about $(t - r/c,\, \vec{\boldsymbol{x}})$ with expansion parameter $\vec{\boldsymbol{x}}' \cdot \hat{\boldsymbol{k}}/c$. Inserting this in equation (1.4.7) yields the low-velocity expansion formula

$$h^{TT}_{ij}(t, \vec{\boldsymbol{x}}) = \frac{4G}{r\,c^4} \Lambda_{ij,kl}(\hat{\boldsymbol{k}}) \left[S^{kl} + \frac{1}{c}\, k_m\, \dot{S}^{kl,m} + \frac{1}{2c^2}\, k_m\, k_p\, \ddot{S}^{ij,mp} + \dots\right]_{\mathrm{ret}}, \tag{1.4.9}$$

where the subscript ret means that the expression is evaluated at the retarded time, and

$$S^{ij,k_1\dots k_n}(t) = \int \mathrm{d}^3x\, T^{ij}(t,\vec{\boldsymbol{x}})\, x^{k_1}\dots x^{k_n} \tag{1.4.10}$$

are the stress-tensor momenta. Equation (1.4.9) can also be rewritten by grouping the terms of the expansion as a function of the energy-density momenta

$$M^{i_1\dots i_n}(t) = \int \mathrm{d}^3x\, T^{00}(t,\vec{\boldsymbol{x}})\, x^{i_1}\dots x^{i_n} \tag{1.4.11}$$

and the linear-momentum-density momenta

$$P^{i,j_1\dots j_n}(t) = \int \mathrm{d}^3x\, T^{0i}(t,\vec{\boldsymbol{x}})\, x^{j_1}\dots x^{j_n} \tag{1.4.12}$$

by using the linearised continuity equation $\partial_\mu T^{\mu\nu} = 0$ and assuming that $T_{\mu\nu}$ vanishes on the boundary ∂V of a volume V larger than the source. As an example, the first two terms of the expansion involving stress-tensor momenta can be rewritten as

$$S^{ij} = \frac{1}{2}\ddot{M}^{ij}, \tag{1.4.13}$$

$$\dot{S}^{ij,k} = \frac{1}{2}\dddot{M}^{ijk} - \ddot{P}^{k,ij}. \tag{1.4.14}$$

1.4.2 Quadrupole moment and radiation

Rewriting equation (1.4.9) in terms of the energy-density and linear-momentum momenta, allows for a better physical understanding of each term of the expansion. The leading term can be obtained by using equation (1.4.13) to perform such substitution together with the properties of $\Lambda_{ij,kl}(\hat{\boldsymbol{k}})$, yielding

$$\left[h_{ij}^{TT}(t,\vec{\boldsymbol{x}})\right]_{\mathrm{quad}} = \frac{2G}{r\,c^4}\,\Lambda_{ij,kl}(\hat{\boldsymbol{k}})\,\ddot{M}^{kl}\left(t-\frac{r}{c}\right) \equiv \frac{2G}{r\,c^4}\ddot{Q}_{ij}^{TT}\left(t-\frac{r}{c}\right), \tag{1.4.15}$$

where

$$Q^{ij} \equiv M^{ij} - \frac{\delta^{ij}}{3}\,M_{kk} = \int \mathrm{d}^3x\ \rho\,(t,\vec{\boldsymbol{x}})\,\left[x^i\,x^j - \frac{r^2}{3}\delta^{ij}\right], \tag{1.4.16}$$

is called quadrupole moment.

The fact that the mass quadrupole is the first non-vanishing term of the expansion and the absence of monopole and dipole terms can be understood by recalling that h_{ij}^{TT} must depend on the time derivative of the multipole moments, since a static source does not emit GWs. The monopole term depends on the mass M of the source, while any dipole term can be sourced only by terms proportional to the linear momentum $\vec{\boldsymbol{P}} = \sum_i m_i\dot{\vec{\mathbf{x}}}_i$ or the angular momentum $\vec{\boldsymbol{L}} = \sum_i \hat{\boldsymbol{r}} \times (m_i\vec{\boldsymbol{v}}_i)$ of the source. Given that $\dot{M} = \dot{\vec{\boldsymbol{P}}} = \dot{\vec{\boldsymbol{L}}} = 0$ in linearised theory, neither monopole nor dipole grav-

itational radiation may exist. Even if these conservation laws no longer hold in the full theory of GR (what is conserved is the total energy-momentum tensor that includes gravitational-field contributions), it is still possible to show that there cannot be radiation from either monopole or dipole terms[12].

Now, by means of equation (1.4.15), it is possible to derive the expressions for the two GW polarisations. The simplest way to do that is to start in a reference frame (x', y', z') where the GW propagation direction is $\hat{\boldsymbol{k}} = \hat{\boldsymbol{z}}'$ and perform a rotation to a generic frame (x, y, z) (see figure 1.1). The final result turns out to be

$$\begin{aligned} h_+(t;\theta,\phi) = \frac{G}{r\,c^4}\Big[& \ddot{M}_{11}\left(\cos^2\phi - \sin^2\phi\,\cos^2\theta\right) + \ddot{M}_{13}\,\sin\phi\,\sin(2\theta) \\ & + \ddot{M}_{22}\left(\sin^2\phi - \cos^2\phi\,\cos^2\theta\right) + \ddot{M}_{23}\,\cos\phi\,\sin(2\theta) \\ & - \ddot{M}_{33}\,\sin^2\theta - \ddot{M}_{12}\,\sin(2\phi)\,\left(1+\cos^2\theta\right)\Big], \end{aligned} \tag{1.4.17}$$

$$\begin{aligned} h_\times(t;\theta,\phi) = \frac{G}{r\,c^4}\Big[& \left(\ddot{M}_{11} - \ddot{M}_{22}\right)\,\sin(2\phi)\,\cos\theta + 2\ddot{M}_{12}\,\cos(2\phi)\,\cos\theta \\ & - 2\ddot{M}_{13}\,\cos\phi\,\sin\theta + 2\ddot{M}_{23}\,\sin\phi\,\sin\theta\Big], \end{aligned} \tag{1.4.18}$$

which allows to evaluate the quadrupole-radiation angular distribution once M_{ij} is known.

Equation (1.4.15) can be used to rapidly derive other quantities, such as the GW radiated energy, angular momentum, and other effects, in the quadrupole approximation. The celebrated quadrupole formula for the total radiated power [25, 26, 40] can be obtained from the equation (1.3.17) for the GW energy flux by using the expression for $\left[h_{ij}^{TT}(t,\vec{\boldsymbol{x}})\right]_{\rm quad}$ in equation (1.4.15), and integrating the resulting expression over the solid angle $\mathrm{d}\Omega$, leading to

$$P_{\rm quad} = \frac{G}{5c^5}\left\langle \dddot{Q}_{ij}\,\dddot{Q}_{ij}\right\rangle, \tag{1.4.19}$$

again evaluated at the retarded time. The expression for the energy spectrum in the quadrupole approximation follows from the above equation by writing the quadrupole moment in terms of its Fourier transform and integrating with respect to time, yielding

$$\left(\frac{\mathrm{d}E}{\mathrm{d}f}\right)_{\rm quad} = \frac{2G}{5c^5}\,(2\pi)^6 f^6 \tilde{Q}_{ij}(\omega)\,\tilde{Q}^*_{ij}(\omega)\,. \tag{1.4.20}$$

Similarly, the variation of linear momentum in time results from the insertion of equation (1.4.15) in equation (1.3.19) for the GW linear-momentum flux, and what is ob-

[12] This is actually related to a more general theorem stating that [32], if a classical radiation field has associated a massless spin S quantum particle, all terms with $l < S$ in a (multipole) spherical harmonics expansion vanish, independently from the nature of the source. In the case of gravitational radiation, the quantum counterpart is the graviton with spin 2, and hence the quadrupole $l = 2$ must be the first term in the expansion.

tained is

$$\left(\frac{\mathrm{d}P^i}{\mathrm{d}t}\right)_{\mathrm{quad}} = -\frac{G}{8\pi c^5}\int \mathrm{d}\Omega\, \dddot{Q}^{TT}_{ab}\,\partial^i \ddot{Q}^{TT}_{ab} = 0, \tag{1.4.21}$$

where the integral vanishes due to the integrand being odd under spatial reflection $\vec{\boldsymbol{x}} \to -\vec{\boldsymbol{x}}$. As a consequence, there is no linear-momentum loss in the quadrupole approximation; while a non-zero result can be obtained at higher order in the expansion from the interference of multipoles with different parity. Another radiated quantity of interest is the total angular momentum, which is also the sum of the radiated orbital angular momentum of the GWs and the spin of the field. From the definition of these quantities together with equation (1.4.15), after some algebra, the resulting rates of orbital angular momentum and spin losses due to GW emission are

$$\left(\frac{\mathrm{d}L^i}{\mathrm{d}t}\right)_{\mathrm{quad}} = -\frac{c^3}{32\pi G}\,\epsilon^{ijk}\int \mathrm{d}\Omega\, r^2\,\left\langle \dot{h}^{TT}_{ab}\, x^j \partial_k h^{TT}_{ab}\right\rangle = \frac{2G}{15c^5}\,\epsilon^{ijk}\left\langle \ddot{Q}_{ja}\dddot{Q}_{ka}\right\rangle, \tag{1.4.22}$$

$$\left(\frac{\mathrm{d}S^i}{\mathrm{d}t}\right)_{\mathrm{quad}} = \frac{c^3}{16\pi G}\,\epsilon^{ijk}\int \mathrm{d}\Omega\, r^2\,\left\langle \dot{h}^{TT}_{ak}\, x^j h^{TT}_{ak}\right\rangle = \frac{4G}{15c^5}\,\epsilon^{ijk}\left\langle \ddot{Q}_{ja}\ddot{Q}_{ka}\right\rangle. \tag{1.4.23}$$

Then the total angular momentum carried away by GWs per unit time is

$$\left(\frac{\mathrm{d}J^i}{\mathrm{d}t}\right)_{\mathrm{quad}} = \left(\frac{\mathrm{d}L^i}{\mathrm{d}t}\right)_{\mathrm{quad}} + \left(\frac{\mathrm{d}S^i}{\mathrm{d}t}\right)_{\mathrm{quad}} = \frac{2G}{5c^5}\,\varepsilon^{ijk}\left\langle \ddot{Q}_{jl}\,\dddot{Q}_{kl}\right\rangle. \tag{1.4.24}$$

Equations (1.4.19), (1.4.21), and (1.4.24) reflect that a GW at a distance r from the source and time t carries energy and momentum, which were extracted from the source at the retarded time $t - r/c$ [13]. Using the fact that the energy balance argument holds in linearised theory, together with the assumption of non-relativistic sources in the multipole expansion, the dynamics of the source may be described by Newtonian mechanics at the lowest order. As a consequence, the back-reaction of the GW on the source can be expressed as a force $\vec{\boldsymbol{F}}$ and a corresponding torque $\vec{\boldsymbol{T}}$, such that

$$\frac{\mathrm{d}E_{\mathrm{source}}}{\mathrm{d}t} = -\left(\frac{\mathrm{d}E}{\mathrm{d}t}\right)_{\mathrm{quad}} = \left\langle F^i \dot{v}_i\right\rangle \tag{1.4.25}$$

$$\frac{\mathrm{d}L^i_{\mathrm{source}}}{\mathrm{d}t} = -\left(\frac{\mathrm{d}L^i}{\mathrm{d}t}\right)_{\mathrm{quad}} = \left\langle T^i\right\rangle, \tag{1.4.26}$$

where the force and torsion per unit volume $\mathrm{d}F^i/\mathrm{d}V$ and $\mathrm{d}T^i/\mathrm{d}V$ have been introduced, respectively. The formulae for the force and the torque components can be found by expressing explicitly the quadrupole Q_{ij} and imposing the continuity equa-

[13] This is true in linearised theory, but the picture is more complex in full GR, where non-linear effects must be accounted for in the GW propagation from the source to the far-away region. Due to these effects, the GW consists of a wavefront, moving at light speed, and a delayed tail; see [162, 163] for more details.

tion of the energy-momentum tensor, leading to

$$F_i = -\frac{2G}{c^5}\, m\, x_j^{(\mathrm{cm})}\, \frac{\mathrm{d}^5 Q_{ij}}{\mathrm{d}t^5}, \tag{1.4.27}$$

$$T_i = -\frac{2G}{5c^5}\, \epsilon_{ijk} Q_{jl} \frac{\mathrm{d}^5 Q_{kl}}{\mathrm{d}t^5}, \tag{1.4.28}$$

where equation (1.4.27) is evaluated in the centre-of-mass frame. The Newtonian potential associated with the back-reaction force and torsion is

$$\Phi(t, \vec{\boldsymbol{x}}) = \frac{G}{c^5}\, x_i^{(\mathrm{cm})}\, x_j^{(\mathrm{cm})} \frac{\mathrm{d}^5 Q_{ij}}{\mathrm{d}t^5}\,(t)\,, \tag{1.4.29}$$

which is also known as the Burke-Thorne potential [164] and acts as a correction to the near-source metric coefficient h_{00} in the post-Newtonian formalism. By inserting equations (1.4.27) and (1.4.28) in the expectation values in equations (1.4.25) and (1.4.26), and integrating by parts (where boundary terms are averaged out), it is possible to recover, up to an expected overall "-" sign, equations (1.4.19) and (1.4.24)

$$\langle F_i \rangle = -\frac{G}{5c^5} \left\langle \dddot{Q}_{jl}\, \ddot{Q}_{kl} \right\rangle, \tag{1.4.30}$$

$$\langle T_i \rangle = -\frac{2G}{5c^5}\, \varepsilon^{ijk} \left\langle \ddot{Q}_{jl}\, \dddot{Q}_{kl} \right\rangle. \tag{1.4.31}$$

Beyond the quadrupole formula

Before passing to some practical examples of GW emission whose main features can be caught in the quadrupole approximation, it is useful to make some remarks. The quadrupole formula is just the first term of the expansion in equation (1.4.9), which can be reorganised in a systematic multipole expansion in a symmetric trace-free form (see [161, 165] as reference) or in terms of tensor spherical harmonics. The systematic multipole expansion allows one to divide the contributions to the GW emission in two kinds: the momenta of the energy density of the source (which, at leading order in v/c are equivalent to the mass momenta), such as the mass quadrupole or, at next-to-leading order, the mass octupole, and the momenta of the angular momentum density of the source, such as the current quadrupole at next-to-leading order. The systematic multiple expansion allows to describe additional features of the GW emission from a source (as an example, the first contribution to the linear momentum loss from the integral over the solid angle of equation (1.3.19) comes from the interference of the quadrupole term and the mass octupole plus current quadrupole one); however, it is still limited to non-relativistic sources in the weak-field approximation. Nonetheless, when the dynamic of a system is entirely determined by gravitational forces (as in the case of a self-gravitating system of astrophysical interest), the weak-field approximation is no longer independent from the low-velocity expansion (1.4.9), and the spacetime cannot be considered flat beyond the lowest order. In that case, the correct formalism to employ in order to describe the GW emission of the system is the post-

Newtonian formalism, for which a vast literature exists to be consulted [148, 166, 167] (or numerical relativity in case of strong field regime [148]).

1.5 Gravitational-wave emission: Some examples

Even though the quadrupole approximation is just the first term of the multipole expansion and assumes sources to be non-relativistic, it can still provide very useful pieces of information about the GW emission from the system of interest. In the following, two simple examples that can be applied to astrophysical systems (which will be useful later in parts II and III) are examined: the emission of GWs from a non-relativistic binary system and from a rotating rigid body.

1.5.1 Inspiral of compact binaries

Consider a non-relativistic binary system whose components can be treated as non-spinning, point-like bodies (this description may suit black holes and compact stars in first approximation). The masses of the components are m_1 and m_2, and their positions are $\vec{x}_1$ and $\vec{x}_2$, with an orbital radius R. The inspiral of the binary system is easier to study in the centre-of-mass (CM) frame, where the problem simplifies to a one-body problem with mass $\mu = m_1 m_2/(m_1 + m_2)$ orbiting (in the x-y plane) around a body with mass $M = m_1 + m_2$ fixed in the CM of the binary system at a relative distance $\vec{r} = \vec{r}_1 - \vec{r}_2$. In the case of circular orbits, the orbital angular velocity ω_s can be expressed as a function of the orbital radius through the third Kepler's law

$$\omega_s^2 = \frac{G\,M}{R^3}. \tag{1.5.1}$$

To evaluate the GW amplitudes in the quadrupole approximation, it is necessary to note that the quadrupole moment of a non-relativistic two-body system can be expressed in the CM frame as

$$Q^{ij}(t) = \mu \left[r^i\,(t)\; r^j\,(t) - \frac{r^2\,(t)}{3}\delta^{ij} \right]. \tag{1.5.2}$$

This expression can then be plugged in equations (1.4.17) and (1.4.18) for the $h_+(t)$ and $h_\times$ amplitudes, which turns out to be

$$h_+(t) = \frac{1}{r}\,\frac{4G\mu\omega_s^2 R^2}{c^4}\,\left(\frac{1+\cos^2\theta}{2}\right)\,\cos(2\omega_s t_{\rm ret} + 2\phi), \tag{1.5.3}$$

$$h_\times(t) = \frac{1}{r}\,\frac{4G\mu\omega_s^2 R^2}{c^4}\,\cos\theta\,\sin(2\omega_s t_{\rm ret} + 2\phi). \tag{1.5.4}$$

Then, rewriting R as a function of ω_s through equation (1.5.1), the above equations become

$$h_+(t) = \frac{4}{r}\left(\frac{G\,\mathcal{M}_c}{c^2}\right)^{5/3}\left(\frac{\pi\,f_{\rm gw}}{c}\right)^{2/3}\left(\frac{1+\cos^2\theta}{2}\right)\cos(2\pi f_{\rm gw}t_{\rm ret}+2\phi) \tag{1.5.5}$$

$$h_\times(t) = \frac{4}{r}\left(\frac{G\,\mathcal{M}_c}{c^2}\right)^{5/3}\left(\frac{\pi\,f_{\rm gw}}{c}\right)^{2/3} cos\theta\,\sin(2\pi f_{\rm gw}t_{\rm ret}+2\phi), \tag{1.5.6}$$

where the GW frequency $f_{\rm gw} = \omega_{\rm gw}/(2\pi) = 2\omega_s/(2\pi)$ and the chirp mass

$$\mathcal{M}_c = \mu^{3/5}M^{2/5} = \frac{(m_1\,m_2)^{3/5}}{(m_1+m_2)^{1/5}} \tag{1.5.7}$$

have been introduced. Then the total GW radiated power can be obtained from the quadrupole formula (1.4.19) by inserting the above equations (1.5.5) and (1.5.6) for the $h_+(t)$ and $h_\times$ amplitudes, leading to

$$P = \frac{32c^5}{5G}\left(\frac{G\,\mathcal{M}_c\,\omega_{\rm gw}}{2c^3}\right)^{10/3}. \tag{1.5.8}$$

The next step is to determine the frequency evolution of the GW signal over time and the corresponding frequency spectrum. Given that the binary system is radiating away energy as GW, its orbital radius must decrease with time, and consequently the angular velocity, hence the radiated GW power, must increase. The energy loss, protracted over a sufficiently long timescale, will eventually lead to the coalescence of the binary system. A rigorous description of the inspiral-merger-ringdown process would require the introduction of post-Newtonian formalism and numerical relativity; see [167]. This is far beyond the scope of this section, and hence the description is limited to the inspiral phase in the Newtonian approximation. Until this point, the motion of the binary-system components has been assumed to be in a fixed, circular Keplerian orbit. However, due to the above-mentioned energy loss, this framework is no longer valid, and what is employed is the *quasi-circular motion* regime. The description in this regime is reasonable as long as the following condition

$$\dot{\omega}_s \ll \omega_s^2 \implies \left|\dot{R}\right| \ll \omega_s R \tag{1.5.9}$$

holds. In this way, the orbit is approximated to be circular with a slowly-varying radius and an energy

$$E_{\rm orbit} = -\frac{G\,m_1\,m_2}{2R} = -\left[\frac{\mathcal{M}_c^5(2\pi G\,f_{\rm gw})^2}{32}\right]^{1/3}. \tag{1.5.10}$$

The time variation of the orbital energy $\mathrm{d}E_{\rm orbit}/\mathrm{d}t$ must be equal in module to the total GW radiated power in equation (1.5.8). Equating this to quantities enables to

obtain a differential equation for the GW frequency evolution over time

$$\dot{f}_{\rm gw} = \frac{96}{5}\pi^{8/3}\left(\frac{G\,\mathcal{M}_c}{c^3}\right)^{5/3} f_{\rm gw}^{11/3}, \tag{1.5.11}$$

whose solution is given by

$$f_{\rm gw} = \frac{1}{\pi}\left(\frac{5}{256}\frac{1}{\tau}\right)^{3/8}\left(\frac{G\,\mathcal{M}_c}{c^3}\right)^{-5/8}, \tag{1.5.12}$$

where $\tau \equiv t_{\rm coal} - t$ quantifies the time to the coalescence time $t_{\rm coal}$, at which $f_{\rm gw}$ formally diverges.

However, before reaching $t_{\rm coal}$, the binary components merge below a critical distance, and no divergence actually happens. Moreover, both the quasi-circular motion regime and the Newtonian approximation break down before the critical distance for the merger is reached. The scale at which the breakdown happens can be estimated by the innermost circular orbit (ISCO) in the case of the Schwarzschild metric [32]:

$$r_{\rm ISCO} = \frac{6GM}{c^2}. \tag{1.5.13}$$

The GW frequency at the end of the inspiral phase of a binary coalescence can then be estimated as the emitted one when the system reaches the ISCO, given by

$$f_{\rm ISCO,gw} = \frac{1}{3\sqrt{6}\,(2\pi)}\frac{c^3}{GM}. \tag{1.5.14}$$

In the slowly-varying circular orbits and Newtonian approximation formalism, the reaching of the ISCO frequency corresponds to a peak in the frequency spectrum of the emitted GW energy, which in this framework can be easily obtained from equation (1.5.10) as

$$\frac{{\rm d}E}{{\rm d}f} = \frac{\pi^{2/3}}{3G}\left(G\mathcal{M}_c\right)^{5/3} f^{-1/3}. \tag{1.5.15}$$

This summarises the main aspects of the inspiral phase of a binary coalescence with circular orbits. However, the corrections to the quadrupole formula (and hence the above quantities) in the case of elliptic orbits assume the simple form (see [168] for the full derivation)

$$P = \frac{32G^4\mu^2M^3}{5c^5a^5}\,f\left(e\right), \qquad f\left(e\right) = \frac{1}{\left(1-e^2\right)^{7/2}}\left(1 + \frac{73}{24}e^2 + \frac{37}{96}e^4\right), \tag{1.5.16}$$

where e and a are the eccentricity and the semi-major axis of the orbits, respectively. In addition to the above formula, it is also possible to find a relative simple relation between a and e of an elliptic orbit with initial eccentricity e_0 and semi-major axis a_0

as [169]

$$a\left(e\right)=a_{0}\frac{g(e)}{g(e_{0})},\qquad g\left(e\right)=\frac{e^{12/19}}{1-e^{2}}\left(1+\frac{121}{304}e^{4}\right)^{870/2299}. \tag{1.5.17}$$

This equation implies that, due to GW back-reaction, the eccentricity decreases quite fast, circularising the orbit and recovering the slowly-varying circular orbit regime.

To conclude this part about the inspiral phase of compact binary coalescence, let remark that real-world binary coalescence may happen at cosmological distances. As a consequence, the redshift z will affect the frequency and amplitude of the emitted GWs. The full calculation to account for this effect results in a simple substitution to be made in equations (1.5.5) and (1.5.6) for the observed polarisation amplitudes and the successive formulas, namely [146]

$$f_{\rm gw}\to\frac{f_{\rm gw}}{1+z}\qquad\mathcal{M}_{c}\to\left(1+z\right)\mathcal{M}_{c}\qquad\frac{1}{r}\to\frac{1}{d_{L}(z)}, \tag{1.5.18}$$

where $d_L(z)$ is the luminosity distance.

1.5.2 Radiation from rotating rigid bodies

The production of GWs from a rotating rigid body can be used to describe the main aspects of rotating astrophysical sources, such as isolated neutron stars. For sake of simplicity, the case of a rigidly rotating ellipsoid about one of its principal axes of inertia is considered. The body frame is identified by the set of coordinates (x_1', x_2', x_3'). In this frame, the ellipsoid inertia tensor is diagonal, meaning $I'_{ij}=\mathrm{diag}(I_1,I_2,I_3)$. The body is assumed to be rotating with angular velocity $\omega_{\rm rot}$ along the x_3' axis.

The description of the emitted gravitational waves is performed in a fixed reference frame, with coordinates (x_1, x_2, x_3). The origin of the fixed frame is the same as the body frame, namely the centre of mass of the body, and $x_3 = x_3'$. It is possible to pass from the body frame moment of inertia to the fixed frame one by means of the time-dependent rotation matrix $R_3(\omega_{\rm rot}t)$, such that $I = R^T I' R$. By an explicit evaluation of the moment-of-inertia-tensor components I_{ij}, it is possible to observe that they differ from the energy-density momenta M_{ij} in (1.4.11) just by an overall minus sign and a constant term (namely the trace), which is irrelevant when considering time derivatives. Then, by using the quadrupole approximation equations (1.4.18) and (1.4.17), the GW polarisation amplitudes observed at a distance r from the source, with a line of sight forming an angle $\iota = \theta$ with the source spin, and oriented in such a way that $\phi = 0$, turn out to be

$$h_{+}=\frac{1}{r}\frac{4G{\omega_{\rm rot}}^{2}}{c^{4}}\left(I_{1}-I_{2}\right)\frac{1+\cos^{2}\iota}{2}\cos(2\omega_{\rm rot}), \tag{1.5.19}$$

$$h_{\times}=\frac{1}{r}\frac{4G{\omega_{\rm rot}}^{2}}{c^{4}}\left(I_{1}-I_{2}\right)\cos\iota\,\sin(2\omega_{\rm rot}). \tag{1.5.20}$$

From the above equation, it can be observed that gravitational radiation can be generated by the rigidly rotating ellipsoid if and only if $I_1 \neq I_2$ and that, in this framework, the GW frequency is again twice the rotational one, namely $f_{\rm gw} = \omega_{\rm gw}/(2\pi) = 2\omega_{\rm rot}/(2\pi) = 2f_{\rm rot}$. The deviation from spherical symmetry of the ellipsoid can be encoded in a quantity called ellipticity ε, defined as

$$\varepsilon \equiv \frac{I_1 - I_2}{I_3}, \tag{1.5.21}$$

and included in the GW amplitudes, which can be compactly rewritten as

$$h_+ = h_0 \left(\frac{1+\cos^2\iota}{2}\right)\cos(2\pi f_{\rm gw} t), \qquad h_\times = h_0 \cos\iota\, \sin(2\pi f_{\rm gw} t), \tag{1.5.22}$$

where

$$h_0 = \frac{4\pi^2 G}{c^4}\,\frac{I_3\, f_{\rm gw}^2}{r}\,\varepsilon. \tag{1.5.23}$$

The faster the ellipsoid rotates, the more intense is the GW signal, since $h_0 \propto f_{\rm gw}^2$. The quadrupole formula for total radiated power follows from equation (1.4.19) as

$$P = \frac{32G}{5c^5}\,\varepsilon^2\, I_3^2\, \omega_{\rm rot}^6. \tag{1.5.24}$$

The emission of GWs has as a consequence the loss of rotational energy over time $\mathrm{d}E_{\rm rot}/\mathrm{d}t = -P$, with $E_{\rm rot} = (1/2) I_3 \omega_{\rm rot}^2$, meaning that the ellipsoid rotational frequency decreases over time. If GW emission is the main mechanism in the rotational energy loss, this *spin-down* can be quantified as

$$\dot{\omega}_{\rm rot} = -\frac{32G}{5c^5}\,\varepsilon^2\, I_3\, \omega_{\rm rot}^5, \tag{1.5.25}$$

and can be used to infer information about the ellipticity in the case of GW detection.

Chapter 2

Ground-based gravitational-wave Interferometers

"Zum Augenblicke dürft ich sagen: Verweile doch, du bist so schön!"
Johann Wolfgang von Goethe, *Faust*

Following the introduction to gravitational waves in the previous chapter, this chapter deals with what technology to use to detect them, focusing on the case of ground-based Michelson interferometers. The chapter proceeds in increasing complexity, starting with a simple Michelson interferometer and ending with a more realistic (but still simplified) version of the existing detectors. The chapter begins by covering how gravitational waves interact with a Michelson interferometer in section 2.1 and deriving the detector antenna patterns and some observable quantities of interest. Then, section 2.2 gets closer to a real-world detector by adding some layers of complexity to the picture, such as Fabry-Perot cavities (to squeeze hundreds of kilometres of optical path in just a few kilometres), the dark fringe detection point (namely the most sensitive detector configuration to gravitational waves), and the consequent control and locking of the detector. Section 2.3 presents the most important noise sources limiting the detector sensitivity and some strategies to adopt to reduce their impact. Eventually, section 2.4 considers the case of Advanced Virgo as a second-generation ground-based gravitational-wave interferometric detector.

2.1 GW detector as a “simple” Michelson interferometer: The interaction with GWs

A Michelson interferometer is an excellent instrument to measure in an extremely precise way the change in the light travel time along its arms, and it may appear natural to use it to detect the passage of GWs and measure their intensity. The layout of a simple interferometer (of the same kind as the one employed by Michelson and Morley in 1887 to probe the non-existence of the ether [170]) is shown in figure 2.1. It

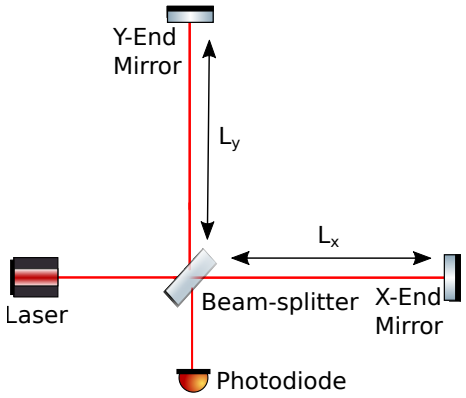

Figure 2.1: A simple Michelson interferometer layout.

consists of a monochromatic light source with a wavelength $\lambda_{\rm L}$, which can be well approximated by a laser; a beam-splitter; two perpendicular arms terminating with a mirror each; and a photodetector. The light is emitted by the source and crosses the beam-splitter that separates it into two beams with equal probability. Each beam travels along one of the interferometer arms, gets reflected back by the mirror, and comes back to the beam-splitter, where it recombines with the other beam. The recombined light is eventually sent to the photodetector that measures its resulting intensity[1].

In the following, one evaluates the expression of the output power for a simple Michelson interferometer in the absence of GWs. This will be the starting point for the discussion about the interaction between GWs and the interferometer, together with the resulting observables. After having been emitted from the source, the input light beam propagates freely and can be described using its electric field with spatial components

$$E_{\rm in} = E_0 e^{-i\omega_{\rm L} t + i\vec{\boldsymbol{k}}_{\rm L}\cdot\vec{\boldsymbol{x}}}, \tag{2.1.1}$$

where $\vec{\boldsymbol{k}}_{\rm L} = 2\pi/\lambda_{\rm L}$ is the wavenumber of the beam, and $\omega_{\rm L} = 2\pi f_{\rm L}$.

Consider the light propagation along the x-arm of length L_x. The beam from the source crosses the beam-splitter, located at the origin of the coordinates $\vec{\boldsymbol{x}} = 0$, at a time t_{0x}, and reaches it back after a round-trip of length $2L_x/c$ at a time $t = t_{0x} + 2L_x/c$. Since the beam is freely propagating, its phase $\exp\{-i\omega_{\rm L} t_0\} = \exp\{-i\omega_{\rm L} t + 2ik_{\rm L} L_x\}$ is conserved, and the electric field acquires an overall $1/2$ from the transmission through the beam-splitter and the reflection at the end-arm mir-

[1] Actually, part of the recombined light travels back in the source direction, and its power gets lost in the configuration assumed here. However, in section 2.2, it will become clear that it is actually possible to recycle this power.

ror[2]. In this way, the output electric field from the x-arm is simply

$$E_{x,\,\mathrm{out}} = -\frac{1}{2}\,E_0 e^{-i\omega_{\mathrm{L}}t+2ik_L L_x}. \tag{2.1.2}$$

The expression for the output electric field that crosses the beam splitter at a time t_{0y}, makes a round-trip along the y-arm of length L_y, and reaches the beam-splitter again at $t = t_{0y}+2L_y/c$, can be obtained by replacing x with y, and flipping the sign in front of E_0 in the above equation. Then, the overall output field $E_{\mathrm{out}} = E_{x,\,\mathrm{out}} + E_{y,\,\mathrm{out}}$ turns out to be

$$\begin{aligned} E_{\mathrm{out}} &= -iE_0\, e^{-i\omega_{\mathrm{L}}t+ik_{\mathrm{L}}(L_x+L_y)}\,\sin\left[k_L\,(L_y-L_x)\right] \\ &\equiv -iE_0\, e^{-i\omega_{\mathrm{L}}t+2ik_L L}\,\sin\left(k_L\Delta L\right), \end{aligned} \tag{2.1.3}$$

where one has defined the common (i.e, average) arm length (CARM) $L \equiv (L_x + L_y)/2$, and the difference of the arm lengths (DARM) $\Delta L \equiv (L_y - L_x)$. From the above equation, it is straightforward to show that the output power reaching the photodetector is

$$P_{\mathrm{out}} \propto |E_{\mathrm{out}}|^2 = E_0^2\,\sin^2\left[k_L\,(L_y-L_x)\right]. \tag{2.1.4}$$

This makes it clear that any variation in the arm length (and consequently in the DARM) also corresponds to a variation in the power at the photodetector.

Consider now a GW passing across the interferometer. It is possible to catch some key aspects of this process without a detailed and rigorous calculation by observing that the GW net effect is to change the time the light takes to perform a round-trip in the interferometer arms.The travel-time variation for the x-arm (y-arm) is encoded in the interval of time ΔT_x (ΔT_y), resulting in an additional phase term in equation (2.1.2) for the x-arm electric field, which becomes

$$\begin{aligned} E_{x,\,\mathrm{out}} &= -\frac{1}{2}\,E_0 e^{-i\omega_{\mathrm{L}}t+2ik_L L_x+i\omega_{\mathrm{L}}\Delta T_x} \\ &= -\frac{1}{2}\,E_0 e^{-2i\omega_{\mathrm{L}}t+ik_L L+ik_L\Delta L+i\omega_{\mathrm{L}}T+i\omega_{\mathrm{L}}(\Delta T_x-\Delta T_y)/2} \\ &= -\frac{1}{2}\,E_0 e^{-2i\omega_{\mathrm{L}}t+ik_L L+i\phi_0+i\omega_{\mathrm{L}}T+i\Delta\phi_x}, \end{aligned} \tag{2.1.5}$$

where in the second line $T \equiv (\Delta T_x + \Delta T_y)/2$, while in the last line $\phi_0 \equiv k_{\mathrm{L}}\Delta L$, and $\Delta\phi_x \equiv \omega_{\mathrm{L}}\left(\Delta T_x - \Delta T_y\right)/2$. Analogously, the equation for the y-arm is

$$E_{y,\,\mathrm{out}} = +\frac{1}{2}\,E_0 e^{-i\omega_{\mathrm{L}}t+2ik_L L-i\phi_0+i\omega_{\mathrm{L}}T+i\Delta\phi_y}, \tag{2.1.6}$$

[2]In the case of an equal probability amplitude beam-splitter, the reflected light gains a factor $r_x = +1/\sqrt{2}$ for the x-arm ($r_y = -1/\sqrt{2}$ for the y-arm), while the transmitted one gains a factor $t = 1/\sqrt{2}$ for both arms. Finally, a multiplication by -1 is necessary to include the reflection from the mirrors at the ends of the arms.

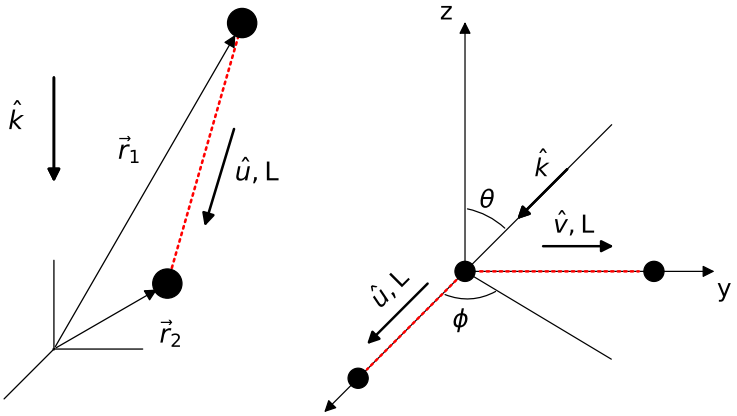

Figure 2.2: Coordinate systems for the evaluation of the single-arm (left) and the Michelson interferometer responses (right) to the passage of a plane GW [`my_code`].

where $\Delta\phi_y = -\Delta\phi_x$. In this way, the resulting electric field at the output is

$$E_{\rm out} = -iE_0\, e^{-i\omega_{\rm L}t + 2ik_L L + i\omega_{\rm L}T}\, \sin\left[\phi_0 + \Delta\phi_x\right], \tag{2.1.7}$$

and, consequently, the output power is

$$\begin{aligned} P_{\rm out} \propto E_0^2\, \sin^2\left[\phi_0 + \Delta\phi_x\right] &= \frac{E_0^2}{2}\, \left[1 - \cos^2\left(2\phi_0 + 2\Delta\phi_x\right)\right] \\ &= \frac{E_0^2}{2}\, \left[1 - \cos^2\left(2\phi_0 + \Delta\phi_{\rm Mich}\right)\right], \end{aligned} \tag{2.1.8}$$

where $\Delta\phi_{\rm Mich} \equiv \Delta\phi_x - \Delta\phi_y = 2\Delta\phi_x$. By comparing equations (2.1.7) and (2.1.8) with equations (2.1.3) and (2.1.4), respectively, it is confirmed that the overall effect of GW is an additional phase $\Delta\phi_{\rm Mich}$ in the output, which can also be interpreted as an effective change in the lengths of the interferometer arms.

The explicit evaluation of the additional phase in equations (2.1.7) and (2.1.8) can be performed in the TT gauge for ease of calculation. The first step is the evaluation of the response of a single interferometer arm to a GW propagating in the direction $\hat{\boldsymbol{k}}$ in the coordinate system in figure 2.2. The beam-splitter and the end-mirror position in this frame are identified with the vectors $\vec{\boldsymbol{r}}_1$ and $\vec{\boldsymbol{r}}_2$, respectively. In turn, the detector arm is directed along $\hat{\boldsymbol{u}} \equiv (\vec{\boldsymbol{r}}_2 - \vec{\boldsymbol{r}}_1)/L_u$. The derivation of the response can be done for a plane GW (the TT-gauge labels are understood in the following)

$$h_{ij}(t) = h_{ij} e^{-2\pi i\, f_{\rm gw} t}. \tag{2.1.9}$$

The passage of the GW affects the trajectory of the photons of the light beam $\vec{\boldsymbol{r}}_\gamma(t) = \vec{\boldsymbol{r}}_1 + \vec{\boldsymbol{u}}(t)$. The corresponding line-element for the photon is

$$0 = ds^2 = -c^2\,\mathrm{d}t^2 + |\mathrm{d}\vec{\mathbf{u}}|^2\left(1 + h_{ij}(t)\hat{u}^i\hat{u}^j\right), \tag{2.1.10}$$

and consequently, the time interval can be approximated as

$$dt = \frac{\pm|\mathrm{d}\vec{\mathbf{u}}|}{\sqrt{1 + h_{ij}(t)\hat{u}^i\hat{u}^j}} \approx \pm|\mathrm{d}\vec{\mathbf{u}}|\left(1 - \frac{1}{2}h_{ij}(t)\hat{u}^i\hat{u}^j\right), \tag{2.1.11}$$

where the "+" solution holds for a beam travelling from the beam-splitter to the mirror and the "−" one on the way back. Integrating the "+" solution between t_{0u} and t_{1u} yields the time of flight of the light from the beam-splitter to the end-mirror as

$$\begin{aligned}
&t_{1u} - t_{0u} = \frac{L_u}{c} + \frac{1}{2}\int_{t_{0u}}^{t_{1u}} \mathrm{d}t' h_{ij}\left(t' - \frac{\vec{\boldsymbol{k}}\cdot\vec{\boldsymbol{r}}_\gamma(t')}{c}\right)\\
=&\frac{L_u}{c} + \frac{1}{2}\,h_{ij}\,\hat{u}^i\,\hat{u}^j\,e^{-2\pi i f_{\rm gw}\left(-\frac{\vec{\boldsymbol{k}}\cdot\vec{\boldsymbol{r}}_1}{c}\right)}\int_{t_{0u}}^{t_{1u}}\mathrm{d}t' e^{-2\pi i f_{\rm gw}\left(t' - \frac{\vec{\boldsymbol{k}}\cdot\vec{\boldsymbol{u}}(t')}{c}\right)}\\
\approx&\frac{L_u}{c} + \frac{1}{2}\,h_{ij}\,\hat{u}^i\,\hat{u}^j\,e^{-2\pi i f_{\rm gw}\left(-\frac{\vec{\boldsymbol{k}}\cdot\vec{\boldsymbol{r}}_1}{c}\right)}\int_{t_{2u}-2L_u/c}^{t_{2u}-L_u/c}\mathrm{d}t' e^{-2\pi i f_{\rm gw}\left[t' - \vec{\boldsymbol{k}}\cdot\hat{\boldsymbol{u}}\left(t' - t_{2u} + \frac{2L_u}{c}\right)\right]},
\end{aligned} \tag{2.1.12}$$

where the photon trajectory has been approximated with the unperturbed one, with $\vec{\boldsymbol{u}}(t) = c(t - t_0)\hat{\boldsymbol{u}}$, $t_{0u} \approx t_{2u} - 2L_u/c$, and similarly $t_{1u} \approx t_{2u} - L_u/c$, since the integrand is already linear in h_{ij}[3]. Similarly, by integrating the "−" solution between t_{1u} and t_{2u} and using $\vec{\boldsymbol{u}}(t) = [L - c(t - t_1)]\,\hat{\boldsymbol{u}}$, the time interval to travel from the end-mirror back to the beam-splitter can be obtained as

$$\begin{aligned}
&t_{2u} - t_{1u} = \frac{L_u}{c} + \frac{1}{2}\int_{t_{1u}}^{t_{2u}} \mathrm{d}t' h_{ij}\left(t' - \frac{\vec{\boldsymbol{k}}\cdot\vec{\boldsymbol{r}}_\gamma(t')}{c}\right)\\
\approx&\frac{L_u}{c} + \frac{1}{2}\,h_{ij}\,\hat{u}^i\,\hat{u}^j\,e^{-2\pi i f_{\rm gw}\left(-\frac{\vec{\boldsymbol{k}}\cdot\vec{\boldsymbol{r}}_1}{c}\right)}\int_{t_{2u}-L_u/c}^{t_{2u}}\mathrm{d}t' e^{-2\pi i f_{\rm gw}\left[t' - \vec{\boldsymbol{k}}\cdot\hat{\boldsymbol{u}}\left(\frac{L_u}{c} - t' + t_2 - \frac{L_u}{c}\right)\right]}.
\end{aligned} \tag{2.1.13}$$

[3]To be fair, this assumption (which follows a pedagogical derivation that can be found in many reviews and books [146]) does not hold in general because it is neglecting the lensing of the photon path by the GWs [171]. Yet, this assumption leads to the correct final results in the TT gauge, where fortuitous cancellations make spatial path perturbations irrelevant; see [172] (where the mistake was noticed for the first time) for a detailed discussion.

Through an explicit evaluation of the two integrals, some algebra, and manipulations, the round-trip time can be expressed as[4]

$$T_{\vec{\boldsymbol{u}},r_1 t}(t_{2u}) = t_{2u} - t_{0u} = \frac{2L_u}{c} + h_{ij}\,\frac{\hat{u}^i\,\hat{u}^j}{2}\,\frac{L_u}{c} e^{-2\pi i f_{\rm gw}\left(t_{2u}-\frac{\vec{\boldsymbol{k}}\cdot\vec{\boldsymbol{r}}_1}{c}\right)} \times\Bigg\{ \mathrm{sinc}\left[\frac{L_u}{c}\,f_{\rm gw}\,\left(1+\vec{\boldsymbol{k}}\cdot\hat{\boldsymbol{u}}\right)\right] e^{-\pi i f_{\rm gw}\frac{L_u}{c}\left(1-\vec{\boldsymbol{k}}\cdot\hat{\boldsymbol{u}}\right)} + \mathrm{sinc}\left[\frac{L_u}{c}\,f_{\rm gw}\,\left(1-\vec{\boldsymbol{k}}\cdot\hat{\boldsymbol{u}}\right)\right] e^{\pi i f_{\rm gw}\frac{L_u}{c}\left(1+\vec{\boldsymbol{k}}\cdot\hat{\boldsymbol{u}}\right)}\Bigg\} e^{-2\pi i f_{\rm gw}\frac{2L}{c}}. \quad (2.1.14)$$

By comparison with equation (2.1.2), the time difference in the travel path is

$$\Delta T_{\vec{\boldsymbol{u}},r_1 t}(t) = h_{ij}\,\frac{\hat{u}^i\,\hat{u}^j}{2}\mathcal{T}_{\vec{\boldsymbol{u}},r_1 t}(f_{\rm gw},\hat{\boldsymbol{k}}\cdot\hat{\boldsymbol{u}})\,e^{-2\pi i f_{\rm gw}\left(t_{u2}-\frac{\vec{\boldsymbol{k}}\cdot\vec{\boldsymbol{r}}_1}{c}\right)}, \quad (2.1.15)$$

where

$$\mathcal{T}_{\vec{\boldsymbol{u}},r_1 t}(f_{\rm gw},\hat{\boldsymbol{k}}\cdot\hat{\boldsymbol{u}}) \equiv \frac{L_u}{c}\,e^{-2\pi i f_{\rm gw}\frac{2L}{c}} \times\Bigg\{ \mathrm{sinc}\left[\frac{L_u}{c}\,f_{\rm gw}\,\left(1+\vec{\boldsymbol{k}}\cdot\hat{\boldsymbol{u}}\right)\right] e^{-\pi i f_{\rm gw}\frac{L_u}{c}\left(1-\vec{\boldsymbol{k}}\cdot\hat{\boldsymbol{u}}\right)} + \mathrm{sinc}\left[\frac{L_u}{c}\,f_{\rm gw}\,\left(1-\vec{\boldsymbol{k}}\cdot\hat{\boldsymbol{u}}\right)\right] e^{\pi i f_{\rm gw}\frac{L_u}{c}\left(1+\vec{\boldsymbol{k}}\cdot\hat{\boldsymbol{u}}\right)}\Bigg\}. \quad (2.1.16)$$

A similar expression holds for the other arm along $\vec{\boldsymbol{v}}$. Combining the travel times like in equations (2.1.5), with $t_{2u} = t_{2v} \equiv t$, leads to

$$\begin{aligned}\Delta T(t) &\equiv \Delta T_{\vec{\boldsymbol{u}},r_1 t}(t) - \Delta T_{\vec{\boldsymbol{v}},r_1 t}(t)\\ &= h_{ij}\frac{1}{2}\left[\hat{u}^i\,\hat{u}^j\mathcal{T}_{\vec{\boldsymbol{u}},r_1 t}(f_{\rm gw},\hat{\boldsymbol{k}}\cdot\hat{\boldsymbol{u}}) - \hat{v}^i\,\hat{v}^j\mathcal{T}_{\vec{\boldsymbol{v}},r_1 t}(f_{\rm gw},\hat{\boldsymbol{k}}\cdot\hat{\boldsymbol{v}})\right] e^{-2\pi i f_{\rm gw}\left(t-\frac{\vec{\boldsymbol{k}}\cdot\vec{\boldsymbol{r}}_1}{c}\right)}\\ &\equiv h_{ij}F^{ij}_{\rm timing}\left(f_{\rm gw},\,\hat{\boldsymbol{k}}\right) e^{-2\pi i f_{\rm gw}\left(t-\frac{\vec{\boldsymbol{k}}\cdot\vec{\boldsymbol{r}}_1}{c}\right)}, \end{aligned} \quad (2.1.17)$$

where the timing response to a GWs with arbitrary direction and polarisation of the Michelson interferometer $F^{ij}_{\rm timing}\left(f_{\rm gw},\,\hat{\boldsymbol{k}}\right)$ has been introduced in the last line [5]. The timing response can be easily converted to the phase and strain responses of a Michel-

[4] Here and in the following, the convention for the normalised cardinal sine function is $\mathrm{sinc}(x) = \sin(\pi x)/(\pi x)$.

[5] The first derivation of the response function for a generic laser-based detector was done in the case of spacecraft doppler tracking by Estabrook and Wahlquist in 1975, see [173], and is different from the one proposed here and flawless. An equivalent derivation in the case of ground-based interferometers, based on the rigorous solution of the geodetic equation, is available in [172], while an even shorter derivation for a generic laser detector, which takes advantage of the metric symmetry and the related Killing vectors, is proposed in [171]

son interferometer as

$$F^{ij}_{\rm phase}\left(f_{\rm gw},\,\hat{\boldsymbol{k}}\right) = \omega_{\rm L} F^{ij}_{\rm timing}\left(f_{\rm gw},\,\hat{\boldsymbol{k}}\right), \tag{2.1.18}$$

$$F^{ij}_{\rm strain}\left(f_{\rm gw},\,\hat{\boldsymbol{k}}\right) = \frac{F^{ij}_{\rm timing}\left(f_{\rm gw},\,\hat{\boldsymbol{k}}\right)}{2L/c}. \tag{2.1.19}$$

Furthermore, expanding h_{ij} in the polarisation basis (see equation (1.1.23)) in equation (2.1.19) allows one to define the antenna patterns for the strain response to the $+$ and $\times$ polarisations, and unpolarised GW, respectively, as

$$F_+(f_{\rm gw},\,\vec{\boldsymbol{k}}) \equiv F^{ij}_{\rm strain}(f_{\rm gw},\,\hat{\boldsymbol{k}})\, e^+_{ij}(\hat{\boldsymbol{k}}), \tag{2.1.20}$$

$$F_\times(f_{\rm gw},\,\vec{\boldsymbol{k}}) \equiv F^{ij}_{\rm strain}(f_{\rm gw},\,\hat{\boldsymbol{k}})\, e^\times_{ij}(\hat{\boldsymbol{k}}), \tag{2.1.21}$$

$$\mathcal{F}(f_{\rm gw},\,\vec{\boldsymbol{k}}) \equiv \sqrt{\left|F_+(f_{\rm gw},\,\vec{\boldsymbol{k}})\right|^2 + \left|F_\times(f_{\rm gw},\,\vec{\boldsymbol{k}})\right|^2} \tag{2.1.22}$$

The antenna patterns present a non-trivial dependence on the GW frequency. However, in the case of ground-based interferometers, where $f_{\rm gw} L_u/c \ll 1$ (*small-antenna limit*), this dependence may be neglected, and the antenna patterns assume the simplified form (obtained by expressing the polarisation tensors $e_{\hat{\boldsymbol{k}}}$ and the incoming GW direction $\hat{\boldsymbol{k}} = -\hat{\boldsymbol{n}}$ as a function of the angles θ and ϕ, see equations (1.1.25) and (1.1.27))

$$F_+(\theta,\phi) = \frac{\left(1+\cos^2\theta\right)}{2}\,\cos\left(2\phi\right), \tag{2.1.23}$$

$$F_\times(\theta,\phi) = \cos\theta\,\sin\left(2\phi\right). \tag{2.1.24}$$

To further account for the GW polarisation angle ψ (see figure 1.1 and equation (1.1.28)), it is sufficient to use the transformation properties of the polarisation tensors under a rotation, obtaining

$$F_+(\theta,\phi,\psi) = \frac{1}{2}\,\left(1+\cos^2\theta\right)\,\cos\left(2\phi\right)\,\cos\left(2\psi\right) - \cos\theta\,\sin\left(2\phi\right)\sin\left(2\psi\right) \tag{2.1.25}$$

$$F_\times(\theta,\phi,\psi) = \frac{1}{2}\,\left(1+\cos^2\theta\right)\,\cos\left(2\phi\right)\,\sin\left(2\psi\right) + \cos\theta\,\sin\left(2\phi\right)\cos\left(2\psi\right). \tag{2.1.26}$$

An illustration of the antenna patterns $F_+(\theta,\phi,\psi=0)$ and $F_\times(\theta,\phi,\psi=0)$ is shown in figure 2.3, from which it appears clear that a single detector has some blind directions[6].

[6]This is the reason why a network of detectors is necessary, namely to cover the entire sky with a network response function as much isotropically as possible.

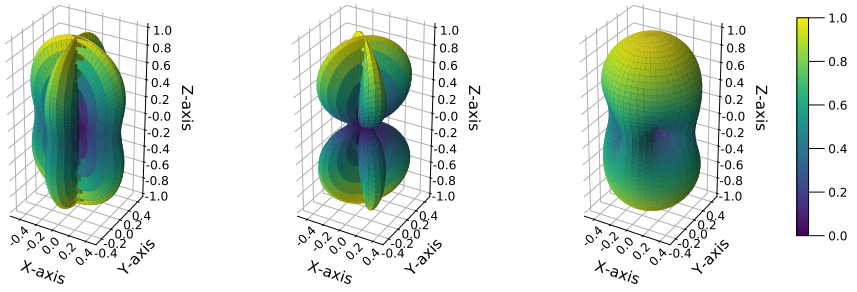

Figure 2.3: (From left to right) Antenna patterns $F_+(f_{\rm gw},\,\vec{\boldsymbol{k}})$, $F_\times(f_{\rm gw},\,\vec{\boldsymbol{k}})$, and $\mathcal{F}(f_{\rm gw},\,\vec{\boldsymbol{k}})$ in the small antenna limit $f_{\rm gw}L_u/c \ll 1$, assuming the detector arm directed along $\hat{\boldsymbol{u}} = \hat{\boldsymbol{x}}$ and $\hat{\boldsymbol{v}} = \hat{\boldsymbol{y}}$, and a GW coming from a sky-direction $\hat{\boldsymbol{n}} = -\hat{\boldsymbol{k}} = \hat{\boldsymbol{z}}$.

Closing the digression about the antenna patterns, the explicit expressions for $\Delta T_{\vec{\boldsymbol{u}},r_1 t}(t)$ and $\Delta T_{\vec{\boldsymbol{v}},r_1 t}(t)$ can be inserted in equation (2.1.5) (removing the assumption about $\vec{\boldsymbol{r_1}} = \vec{\boldsymbol{0}}$, $\hat{\boldsymbol{u}} = \hat{\boldsymbol{x}}$) and used to derive again (2.1.7) and (2.1.8), where now

$$\begin{aligned}\Delta\phi_{\rm Mich}(t) &= \omega_{\rm L}\left(\Delta T_{\vec{\boldsymbol{u}},r_1 t}(t) - \Delta T_{\vec{\boldsymbol{v}},r_1 t}(t)\right)\\ &= h_{ij}F^{ij}_{\rm phase}\left(f_{\rm gw},\,\hat{\boldsymbol{k}}\right)\,e^{-2\pi i f_{\rm gw}\left(t-\frac{\vec{\boldsymbol{k}}\cdot\vec{\boldsymbol{r}}_1}{c}\right)} \equiv |\Delta\phi_{\rm Mich}|\,e^{-2\pi i f_{\rm gw}\left(t-\frac{\vec{\boldsymbol{k}}\cdot\vec{\boldsymbol{r}}_1}{c}\right)}.\end{aligned} \tag{2.1.27}$$

The quantity $|\Delta\phi_{\rm Mich}|$ is the observable (or rather one of the possible observables) that allows one to detect and characterise a GW and is desirable to be as large as possible. By observing that $|\Delta\phi_{\rm Mich}|$ is proportional to terms like $(f_{\rm L}L/c)\,\mathrm{sinc}[(f_{\rm gw}L/c)(1 \pm \hat{\boldsymbol{u}}\cdot\hat{\boldsymbol{k}})] \propto (f_{\rm L}/f_{\rm gw})\sin[(\pi f_{\rm gw}L/c)(1 \pm \hat{\boldsymbol{u}}\cdot\hat{\boldsymbol{k}})]$, it can be maximised by setting the argument of the sine function to $\pi/2$. This translates into the following condition on the interferometer arm length:

$$L \simeq 750\,\mathrm{km}\left(\frac{100\,\mathrm{Hz}}{f_{\rm gw}}\right)\left(\frac{2}{1 \pm \hat{\boldsymbol{u}}\cdot\hat{\boldsymbol{k}}}\right). \tag{2.1.28}$$

Building a simple Michelson interferometer of such arm length on Earth is not feasible; therefore, a way to "fold" this path in a shorter-arm interferometer must be found, as is illustrated in the next section.

To conclude this section, it is worthy to consider again equation (2.1.5) and expand it to the first order in $\Delta T_{\vec{\boldsymbol{u}},r_1 t}(t)$:

$$\begin{aligned}E_{x,\,\rm out} &= -\frac{1}{2}\,E_0 e^{-i\omega_{\rm L}t + 2ik_L L_u + i\omega_{\rm L}\Delta T_{\vec{\boldsymbol{u}},r_1 t}(t)}\\ &\approx -\frac{1}{2}\,E_0 e^{-i\omega_{\rm L}t + 2ik_L L_u}\left[1 + i\omega_L \Delta T_{\vec{\boldsymbol{u}},r_1 t}(t)\right]\\ &= -\frac{1}{2}\,E_0 e^{2ik_L L_u}\left[e^{-i\omega_{\rm L}t} + i\omega_L\,|\Delta T_{\vec{\boldsymbol{u}},r_1 t}|\,e^{-2\pi i f_{\rm gw}\left(-\frac{\vec{\boldsymbol{k}}\cdot\vec{\boldsymbol{r}}_1}{c}\right)}e^{-i(\omega_{\rm L}+\omega_{\rm gw})t}\right],\end{aligned} \tag{2.1.29}$$

from which it appears that, beside the original electric field with frequency ω_L (the "carrier"), there is another electromagnetic wave at frequency $\omega_L + \omega_{\rm gw}$ (a "sideband"). Actually, given that a generic GW at frequency $f_{\rm gw}$ can be decomposed in a sum of two plane waves with frequencies $\pm f_{\rm gw}$ (take as the easiest example the case where equation (2.1.9) is a (co)sine wave), two sidebands are actually induced by its passage, at frequencies $\omega_L \pm \omega_{\rm gw}$ and with amplitude $\omega_{\rm L}|\Delta T_{\vec{u},r_1t}| \sim \mathcal{O}(h_{ij})$ with respect to the one of the carrier.

2.2 Towards a real GW detector: Fabry-Perot cavities, diffraction, and control system

The previous section ends with two noticeable statements from the response of the interferometer to the GW passage. First, equation (2.1.28) makes explicit that a simple Michelson interferometer arm should be hundreds of kilometres long to best measure GWs with a frequency of $100\,\mathrm{Hz}$. Second, equation (2.1.29) highlights the creation of sidebands in the light beam as a consequence of the GW passage. This section covers how to reduce the length of the interferometer to the known km-long one and how to deal with the sidebands. This requires the addition of some components and controls in the optical layout of the interferometer, getting closer to a real ground-based GW interferometer while generating new complications and challenges.

2.2.1 Fabry-Perot cavities

The most intuitive action that can be undertaken to reduce the length of an interferometer is "folding" the optical path of the light in the arms, making it bounce back and forth multiple times before recombining the two beams. Historically, the first solution to be considered for such a scope was the so-called "delay-line" [82, 83], where the trajectories of the bouncing light between the mirrors do not superimpose. Yet, this system presents the drawback of requiring very large mirrors [174] to reach the $\mathcal{O}(100)$ bounces for a 750 km effective optical length. An alternative solution, which does not require impractically broad mirrors [175], has been implemented by transforming the interferometer arms into Fabry-Perot cavities [84, 85].

A simplified scheme of the Fabry-Perot cavity is shown in figure 2.4. It consists of two parallel mirrors that, for the time being, are considered to be plane and of infinite transverse length. The first mirror is modelled as having real reflection and transmission coefficients r_1 and t_1 when the light propagates from the interior of the mirror towards the cavity, and $r_1' = -r_1$ and $t_1' = -t_1$ when going from the cavity towards the mirror. The energy loss is encoded in the coefficient p_1, defined by

$$r_1^2 + t_1^2 = 1 - p_1^2. \tag{2.2.1}$$

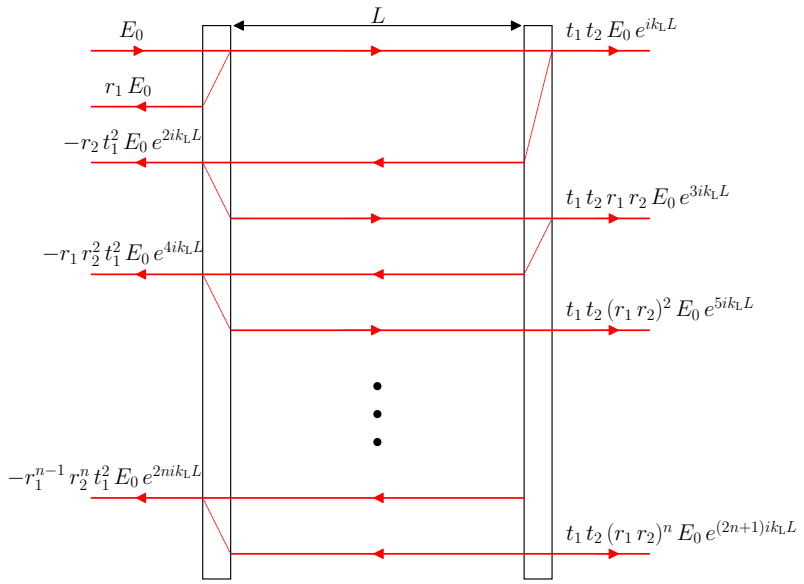

Figure 2.4: Simplified scheme of a Fabry-Perot cavity electric field reflection and transmission [`my_code`]. The phases $e^{2nk_\mathrm{L}L}$ and $e^{(2n+1)k_\mathrm{L}L}$ are not acquired during free propagation and are relative to beam entered in the cavity at times $t_0 - 2nL/c$ and $t_0 - (2n-1)L/c$ [146].

Similar coefficients $(r_2, t_2, r_2', t_2', p_2)$ are assumed for the second mirror, so that $r_2' = -r_2$ when the light propagates from the cavity towards the second mirror and is reflected back.

By fixing the coordinate system in such a way that the first (left) mirror is at $x = 0$ and the second (right) mirror at $x = L$, and an input electric field reaching the first mirror at time t_0

$$E_\mathrm{in}(t, x) = E_0 e^{-i\omega_\mathrm{L}t_0 + ik_\mathrm{L}x} = E_0 e^{-i\omega_\mathrm{L}t_0}, \tag{2.2.2}$$

it is not difficult to obtain the expressions for the reflected electric field outside the cavity [7]

$$E_\mathrm{refl} = E_0 e^{-i\omega_\mathrm{L}t_0}\,\frac{r_1 - r_2\,(1-p_1)\,e^{2ik_\mathrm{L}L}}{1 - r_1 r_2\,e^{2ik_\mathrm{L}L}}, \tag{2.2.4}$$

[7] The reflected electric field outside the cavity is the sum of the electric field $E_\mathrm{refl}^{(0)}$ that the first mirror has reflected at time t_0 and the ($n \to +\infty$ limit of the) electric fields $E_\mathrm{r}^{(n)}$ that entered the cavity at $t_n = t_0 - 2nk_\mathrm{L}L$ and have performed n round-trips before getting transmitted from the first mirror outside the cavity

$$E_\mathrm{r}^{(0)} = r_1 E_\mathrm{in}, \qquad E_\mathrm{r}^{(n)} = \left[-r_1^{n-1} r_2^n t_1^2 e^{2nik_\mathrm{L}L}\right]\,E_\mathrm{in}. \tag{2.2.3}$$

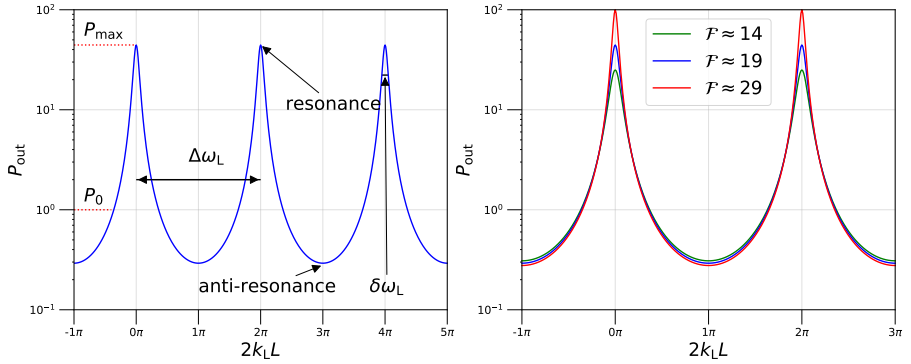

Figure 2.5: (Left) Visualisation of the output power spectrum for $r_1 r_2 = 0.85$ in $2k_L L$ units and the related spectral quantities. (Right) Effect of $\mathcal{F}$ on the output power [`my_code`].

the transmitted electric field outside the cavity [8]

$$E_{\rm t} = E_0 e^{-i\omega_{\rm L} t_0} \frac{t_1 t_2\, e^{ik_{\rm L}L}}{1 - r_1 r_2\, e^{2ik_{\rm L}L}}, \tag{2.2.6}$$

and the electric field inside the cavity at the left mirror ($x = 0$)[9]

$$E_{\rm cav}(x=0) = E_0 e^{-i\omega_{\rm L} t_0} \frac{t_1\, e^{ik_{\rm L}L}}{1 - r_1 r_2\, e^{2ik_{\rm L}L}}, \tag{2.2.7}$$

to which the electric field inside the cavity at the right mirror is related as $E_{\rm cav}(x = L) = e^{ik_{\rm L}L} E_{\rm cav}(x = 0)$.

From the above equations, it becomes clear that, if r_1 and r_2 coefficients are close to one, the cavity presents a set of resonances at $2k_{\rm L}L = 2\pi n$, with $n \in \mathbb{Z}$. This is illustrated in figure 2.5 By using $k_{\rm L} = c/\omega_{\rm L}$, the distance between two consecutive maxima in the power spectrum is

$$\Delta\omega_{\rm L} = \frac{\pi c}{L}, \tag{2.2.8}$$

which is also called *free spectral range*. Another relevant quantity that can be read from the power spectrum (by expanding the denominator of the modulus of equation (2.2.4), (2.2.6), or (2.2.7)) is the full width of a peak at half maximum

$$\delta\omega_{\rm L} = \frac{c}{L} \frac{1 - r_1 r_2}{\sqrt{r_1 r_2}}. \tag{2.2.9}$$

[8] Similarly to the $E_{\rm r}$ case, the transmitted field outside the cavity is the sum of the ($n \to +\infty$ limit of the) fields that entered the cavity at $t_n = t_0 - (2n+1)k_{\rm L}L$ and have performed $2n+1$ round-trips before getting transmitted from the second mirror outside the cavity

$$E_{\rm t}^{(n)} = t_1 t_2\, (r_1 r_2)^n\, e^{(2n+1)ik_{\rm L}L}\, E_{\rm in}. \tag{2.2.5}$$

[9] The calculation is the same as in the $E_{\rm t}$ case off a factor t_2.

The ratio between the free spectral range and the full width at half maximum is called *finesse* $\mathcal{F} \equiv \Delta\omega_{\rm L}/\delta\omega_{\rm L}$, namely

$$\mathcal{F} = \frac{\pi\sqrt{r_1 r_2}}{1 - r_1 r_2}. \tag{2.2.10}$$

The physical meaning of the finesse can be related to the *storage time* τ_s, the average time spent by the light inside the cavity. The expression of the storage time and its relation to the finesse has a simple form in the case where $r_2 = 1$ and r_1 is close to unity, namely [10]

$$\tau_s = \frac{2L}{c}\frac{1}{1 - r_1^2} \simeq \frac{L}{c}\frac{\mathcal{F}}{\pi}. \tag{2.2.12}$$

Both the finesse and the storage time play an important role in describing the interaction of a Fabry-Perot cavity with a GW. Namely, at the lowest order in an $\omega_{\rm gw}\tau_s$ expansion, two Fabry-Perot cavities are equivalent to a Michelson interferometer with arm length $(2/\pi)\mathcal{F}$ [11]. However, the result of the full calculation, which accounts for the GW-induced sidebands for a generic $\omega_{\rm gw}\tau_s$ in the TT gauge, shows that the module of the FP cavity phase shift is actually [176, 177]

$$|\Delta\phi_{\rm FP}| \simeq \frac{2\mathcal{F}}{\pi}\,|\Delta\phi_{\rm mich}|\,\frac{1}{\sqrt{1 + \left(f_{\rm gw}/f_{\rm p}\right)^2}}, \tag{2.2.14}$$

where f_p is called pole frequency and is defined to be a function of the storage time and, consequently, of the finesse, as

$$f_p \equiv \frac{1}{4\pi\tau_s} \simeq \frac{c}{4\mathcal{F}L}. \tag{2.2.15}$$

In light of this, if $f_{\rm gw} = f_p = 100$ Hz, to reach an optical length equivalent to the 750-km arm length $L_{\rm mich}$ of the Michelson-interferometer in equation (2.1.28), is sufficient to replace the interferometers arms with a FP cavity of length $L_{\rm FP}$ designed in such a way the finesse is approximately

$$\mathcal{F} \simeq \frac{125\pi}{\sqrt{2}}\left(\frac{L_{\rm mich}}{750\,{\rm km}}\right)\left(\frac{3\,{\rm km}}{L_{\rm FP}}\right). \tag{2.2.16}$$

[10] The calculation can be easily executed by observing that the probability of performing n round-trips of duration $2L/c$ before coming out from the first mirror in this framework is simply

$$p(n) \propto r_1^{2n}. \tag{2.2.11}$$

[11] This is because, in the adapted framework, a generic perturbation ϵ around a resonance $2k_{\rm L}L = 2\pi n + \epsilon$ of the reflected field $E_{\rm r}$ reflects in the change in the phase

$$\phi \to \phi + \frac{2\mathcal{F}}{\pi}\epsilon. \tag{2.2.13}$$

In this way, the finesse required for the pivot values (corresponding roughly to the Virgo detector site, see 2.4), is $F \approx 278$ which can be easily surpassed in the current generation of ground-based GW interferometers.

2.2.2 Some real-world complications

Even though Fabry-Perot cavities are a good solution to avoid building hundreds-kilometres-long Michelson interferometers, there are many real-world complications that have not been considered that add several layers of complexity to the interferometer scheme. Some of these aspects and the related emerging problems are briefly discussed in the following. For a more complete list and an exhaustive discussion, see [174, 178, 179].

Diffraction

Until now, in the description of the Michelson interferometer and Fabry-Perot cavities, it has been assumed that the laser beam had a null transverse extent, together with the mirrors being plane and of infinite surface. This is far from reality, where mirrors are finite and the laser beam has a transverse size a, filling a cone of angle $\Delta\theta \sim \lambda_{\mathrm{L}}/a_{\mathrm{L}}$. As a consequence, the laser beam is subject to diffraction when travelling along a longitudinal distance x, becoming larger in the transverse plane by an amount $x\,\Delta\theta \sim x\lambda_{\mathrm{L}}/a_{\mathrm{L}}$. The effects of diffraction become important when the transverse size of the beam becomes much broader than the original. This regime is called *Fraunhofer diffraction*, and the condition can be expressed as

$$x \gg a^2/(\lambda_{\mathrm{L}}). \tag{2.2.17}$$

If the laser wavelength λ_{L} is of $\mathcal{O}(1\,\mu\mathrm{m})$ as for current detectors, the diffraction effects for a km-long Michelson interferometer ($x \sim \mathcal{O}(\mathrm{km})$) cannot be neglected already after a single one-way trip along the arm for a transverse size of a few centimetres. In addition to that, in the presence of Fabry-Perot cavities, there are $\mathcal{O}(100)$ round-trips in the cavity, and in the presence of flat mirrors, the laser envelope would become wider and wider, at the end being dispersed due to a transverse size larger than the mirrors.

By studying the propagation of a beam of finite transverse extent, it becomes clear that diffraction can be circumvented by employing spherical mirrors and Gaussian beams. Gaussian beams are a solution of the propagation equation of the electric field in the vacuum in the Fraunhofer diffraction limit, with expression

$$\begin{aligned} E(x,y,z) =& \frac{\mathcal{E}_0}{\sqrt{1+(x/b)^2}} e^{-\left(y^2+z^2\right)/w^2(x)} \\ & \times \exp\left\{ ik_{\mathrm{L}}\left[x + \frac{x^2+y^2}{2R(x)}\right] - i\arctan\left(x/b\right)\right\}, \end{aligned} \tag{2.2.18}$$

where $b = k_{\mathrm{L}} w_0^2/2$ is called Rayleigh range, with w_0 the width at $x = 0$ of the Gaussian profile $\mathcal{E}(x, y, z)$; $R(x) = x + b^2/x$ is the curvature radius, and $w(x) = w_0\sqrt{1 + (x/b)^2}$ is the width of the profile. The term $\arctan(x/b)$ in the exponential is called the Gouy phase and is an additional factor compared to a plane wave propagation. Gaussian beams have the important property of remaining Gaussian along the propagation, and their wavefront can be well approximated to be spherical. In this way, a Gaussian beam with a curvature radius $R(x = x_0)$ and can be focused back by a spherical mirror with the same curvature radius and converged at $x = x_0$, before re-expanding again and reaching another spherical mirror at $x = -x_0$. As a consequence, the beam is bounced back and forth between the two spherical mirrors without increasing its transverse size.

However, a beam of transverse length can actually be described as a superposition of an orthornormal set of solutions to the propagation equation, called *Hermite-Gaussian* modes TEM_{mn}, of which the Gaussian beam is the 00-mode, identified by a Gouy phase $(m + n + 1)\arctan(x/b)$. Even if interferometer lasers emit predominantly in the mode TEM_{00}, the subdominant contamination from higher modes (mainly TEM_{01} and TEM_{10} modes) [146] reintroduces the diffraction effects and is a source of noise if not properly handled. To get rid of these spurious modes, it is possible to send the laser beam into a Fabry-Perot cavity operating in resonance transmission in correspondence with the Gouy phase of the TEM_{00} mode, which is the only one to be efficiently transmitted. This optical component is called *mode-cleaner* [180] and is used in multiple locations in the optical layouts of current GW interferometers.

Dark fringe detection point

From the previous discussion in section 2.1, the net effect of the GW passage in an interferometer is an addititional, time-dependent phase shift $\Delta\phi_{\mathrm{gw}}(t)$ in the laser phase. The natural question that arises is how this phase can be extracted from the detector output. The answer to this question is less simple than it could be expected, already in the case of a simple Michelson interferometer. Looking back at equation (2.1.8) for this configuration, it follows that the output power at the photodiode is $P(\phi) = P_0 \sin^2\phi$, with $\phi = \phi_0 + \Delta\phi_{\mathrm{gw}}(t)$, where ϕ_0 is an experimentally tunable phase. The value of this phase must be chosen in a way to set the interferometer at the best working point to be sensitive to the small displacement $\phi_0 \to \phi_0 + \Delta\phi_{\mathrm{gw}}$. Naively, a natural choice could be $\phi_0 = \pi/4$, where the variation of the power to a change in the phase $\partial P/\partial\phi_0$ is maximum. However, this option must be excluded, given that this working point would also be extremely sensitive to the laser-power fluctuations $P_0 \to P_0 + \Delta P_0$, which turn out to be dominant with respect to the ones induced by GWs in the frequency range of ground-based interferometers [181].

The turning point in this search for the tiny GW effects is to use the interferometer as an *(active) null instrument* [174]. A null instrument is an instrument that is designed to be nearly insensitive to otherwise important noise sources, such as cal-

ibration uncertainties, by recording a zero output in the absence of a signal. The prototype of a null instrument in the literature is the Dicke radiometer [182]. The null-instrumente working point for an interferemoter is called *dark fringe*, and is characterised by choosing $\phi_0 = 0$, where $P = 0$ in the absence of GWs. However, this choice implies that also $\partial P/\partial\phi_0 = 0$. Consequently, an input power change due to GWs in the dark fringe can be at most only $\Delta P = \mathcal{O}\big(h^2\big)$, which appears apparently impossible to detect given the already small h magnitude. Nonetheless, real detectors operate on the dark fringe, meaning solutions to address this problem do indeed exist.

Without going into detail, a possible solution is to have extremely accurate control of the laser-power fluctuation, allowing the dark fringe detection scheme to work [146]. Alternatively, a time-dependent phase modulation can be introduced in the input signal [71], as example by making it cross a (dielectric) material with a time-dependent refraction index (realised through Pockels cells [183]) from an applied electric field $E_{\rm appl} \propto \cos(2\pi f_{\rm mod} t)$, with $f_{\rm mod} \sim$ few MHz [174]. The net effect of the phase modulation is the generation of sidebands with frequencies $f_{\pm,\,n} = f_{\rm L} \pm n f_{\rm mod}$, with n integer. However, in the limit of perfectly reflecting mirrors and equal-arms interferometer, both the carrier and the sidebands can be shown to be on the dark fringe, raising the issue of how to get rid of the sideband contamination. The solution is surprisingly simple, and it is sufficient to introduce a small asymmetry (called *Schnupp asymmetry* [184]) in the arm lengths $\Delta L = n\lambda_{\rm L}$, in such a way that only the carrier is at the dark fringe. This is crucial when a GW with frequency $f_{\rm gw}$ passes by, and, even though the carrier is in the dark fringe, the output acquires a term that is linear in h (its physical origin is the beating between the carrier and the sidebands, and it oscillates with a frequency approximately equal to $f_{\rm mod} \gg f_{\rm gw}$, [146]). This result is remarkable because the interferometer is still being used as a null instrument, but now it is sensitive to a signal linear in h, making its measurement easier compared to the naive picture, where the perturbation had to be of $\mathcal{O}\big(h^2\big)$. In addition to that, the signal is encoded in a high-frequency term, where the noise from laser power fluctuations is much smaller (due to it being proportional to $1/f$, see next section 2.3). A similar result can also be reached in the case of a Fabry-Perot cavity, where the Schnupp asymmetry is not in the cavity lengths but rather in the distances between the beam-splitter and the input mirrors.

Simplified optical layout, controls and locking

The final pieces that need to be briefly discussed to get closer to a realistic GW interferometer are some additions to the optical layout and how to control and lock the interferometer at the dark fringe with all the Fabry-Perot cavities at resonance.

A first additional feature to the optical layout is the *power-recycling*. Given that the detector operates at the dark fringe, the light of the carrier at frequency $f_{\rm L}$ is reflected back from the beam-splitter to the laser and would be wasted. To avoid that, the solution is to place a "recycling" mirror that reflects the light back towards

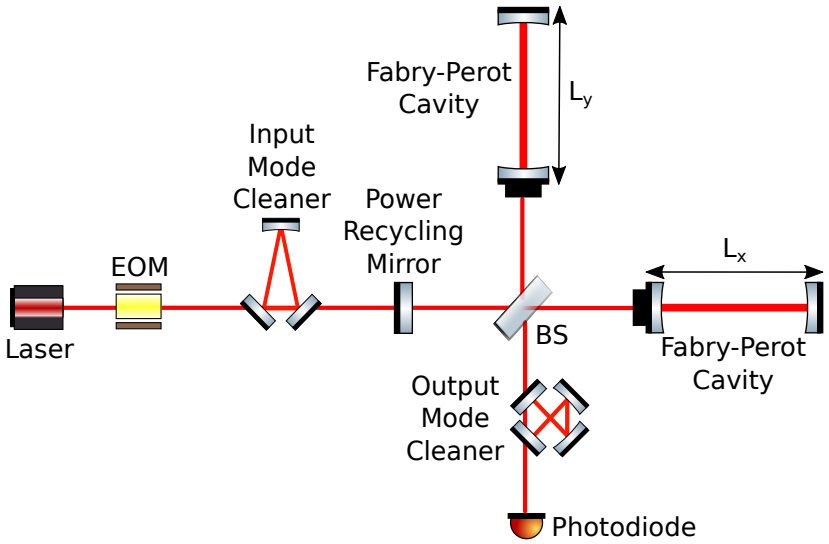

Figure 2.6: Simplified optical layout of a GW interferometer realised using Inkscape [185] and the GWOptics component library [186].

the beam-splitter [177, 187]. With this setup, a new Fabry-Perot cavity is created between the power-recycling mirror and the "equivalent interferometer mirror". This new cavity can then be arranged to be on resonance and, in combination with the other two, increase noticeably the power of the laser light in the interferometer (this is also important to deal with shot noise; see next section 2.3). A second additional feature is an output mode cleaner. This is necessary to get rid of the spurious non-TEM_{00} modes that arise from mirror imperfections and misalignements when the laser bounces back and forth in the cavities. The resulting optical layout, which is visible in figure 2.6 and is still simplified with respect to the one of a real interferometer (see section 2.4), is the basic one for a realistic description of a GW interferometer.

The scheme of the overall optical layout owes its high sensitivity to the laser light being resonant with the Fabry-Perot cavities. However, on resonance, the system is extremely sensitive to any change in the cavity length L, and must remain "locked" in such a configuration, with the interferometer at the dark-fringe working point at the same time,in the absence of any GW signal. The techniques necessary to realise what was just exposed fall in the field of *feedback control systems*. A feedback control system can be simplified to consist minimally of a sensor and an actuator. The former measures a quantity of interest and sends back an error signal with the difference of the measure from the desired value. The latter provides feedback by correcting the error. In the case of a Fabry-Perot cavity, the error signal can be generated and handled by employing the Pound-Drever-Hall locking scheme [188–190], originally invented to stabilise the wavelength of a laser in a Fabry-Perot cavity of fixed length [191]. The key point is the usage of modulated light, which generates a beating term between the carrier (which is on resonance and acquires a phase $\exp\{i\Delta\phi\}$ in case

of any displacement from it) and the sidebands (which are off resonance and hence insensitive to any displacements) in the output power when there is a displacement. The beating term is linear in the deviation $\Delta\phi$ and can then be used as an error signal. As a consequence, it is possible to use the signal to lock the wavelength λ_{L} of the laser to the cavity length. This makes it evident that the detection scheme on dark fringe is nothing but a variation of the Pound-Drever-Hall locking scheme, where it is actually the Fabry-Perot cavity length (which can be opportunely tuned for a Michelson inteferometer) that is locked to the wavelength of the laser.

Concluding, the interferometer locking procedure can be summarised as follows [192]: first, the laser is locked to the length of one arm's Fabry-Perot cavity, and then the stabilised laser is used to lock the second arm's cavity to it[12]. The net effect of this procedure is that the displacement of one arm is measured in units of the other arm's length. In this way, the locking procedure allows all the interferometer Fabry-Perot cavities to operate on resonance. Then, to ensure that the beams recombine at dark fringe, the error signal sent to the actuator is generated by the Schupp asymmetry of the arm lengths and the usage of modulated light, also known as the "Schnupp locking" technique [184]. In the whole procedure, the hard part is to bring the interferometer from a free state to a locked, controlled stage, relying on the availability of extremely responsive control systems. Once the interferometer is locked at its working point, it can be kept in such a configuration for a relatively long period of time.

2.3 Noise sources for ground-based inteferometers

After having illustrated the simplified setup of a GW interferometer, it is natural to evaluate the sensitivity of such an instrument to GWs. The task is less straightforward than it could seem at first glance, given the necessity of carefully identifying, quantifying, and characterising a plethora of noise sources (see figure 2.9 to see an example of several noises limiting the detector sensitivity in the case of Advanced Virgo). This topic is quite wide (see, for example, [181] for quantum noises and [193] for displacement (and other) noises) and cannot be extensively covered here. Therefore, this section is limited to an overview of the most important noise sources.

2.3.1 Shot noise

Given a laser with frequency f_{L}, N_γ photons impact the photodetector in a time T, with an average power

$$P = \frac{1}{T} N_\gamma \hbar \omega_{\mathrm{L}}. \tag{2.3.1}$$

[12] More precisely, the laser is locked to the common arm mode, where the two arms move symmetrically, while the GW detection takes place in the differential arm mode, where the two arms move antisymmetrically [146].

The shot noise arises from the fluctuations in the power ΔP induced by the fluctuation in the number of photons reaching the photodetector ΔN_γ. This fluctuation can be easily evaluated by observing that N_γ is Poisson distributed, and its fluctuation (standard deviation) is simply $\Delta N_\gamma = \sqrt{N_\gamma}$, leading to a fluctuation in power

$$(\Delta P)_{\rm shot} = \frac{1}{T}\sqrt{N_\gamma}\hbar\omega_{\rm L} = \sqrt{\frac{\hbar\omega_{\rm L}}{T}\,P}, \tag{2.3.2}$$

where equation (2.3.1) was used in the second equality.

The fluctuation in power due to shot noise needs to be compared with the one that would arise from a GW signal. For a simple Michelson interferometer with a working point $\phi_0 = \pi/4$ [13], the fluctuation in power induced by a GW follows from equation (2.1.8) $\Delta P_{\rm gw} = P_0\,\Delta\phi_{\rm Mich}/2$. By equating this quantity to equation (2.3.2), the equivalent GW phase shift $\Delta\phi_{\rm Mich}$ induced by shot noise follows as

$$\frac{P_0}{2}\,\Delta\phi_{\rm Mich} = \frac{\sqrt{N_\gamma}}{T}\,\hbar\omega_{\rm L} \implies \Delta\phi_{\rm Mich} = \frac{1}{\sqrt{N_\gamma}}, \tag{2.3.3}$$

where $P = P_0/2$ at $\phi_0 = \pi/4$ and equation (2.3.1) is used in the first and second equality, respectively. An alternative, more effective way of expressing the shot-noise effect is to use the phase strain spectral density[14]

$$S^{1/2}_{\Delta\phi}(f) = \sqrt{\frac{2T}{N_\gamma}} = \sqrt{\frac{2\hbar\omega_{\rm L}}{P}}. \tag{2.3.6}$$

Eventually, by dividing the above equation by the transfer function of the cavity from equation (2.2.14), one can obtain the shot noise spectral density for a Fabry-Perot cavity

$$S^{1/2}_n(f)\Big|_{\rm shot} = \sqrt{\frac{2\hbar\omega_{\rm L}}{P}}\,\frac{\lambda_{\rm L}\sqrt{1+(f/f_{\rm p})^2}}{8\mathcal{F}L} \tag{2.3.7}$$

[13] The choice of a working point not being at the dark fringe here is dictated by the fact that, in general, there are other noises that do not vanish at the dark fringe. Also, this makes the dark fringe not a good working point for a simple Michelson interferometer, for which no phase modulation of the laser is present. Conversely, if only laser shot noise were present, dark fringe would be the optimal working point, even in the absence of phase modulation.

[14] Given a random variable $X(t)$, its (one-sided) spectral density $S_X(f)$ is defined from

$$\langle X(t)X(t')\rangle = \frac{1}{2}\int_{-\infty}^{+\infty} {\rm d}f\, S_X(f)\, e^{-2\pi i f(t-t')}. \tag{2.3.4}$$

In the simple case where $\langle X(t)X(t')\rangle = X_0\delta(t-t')$, for $t = t'$ and a finite observation time T, the spectral density expression simplifies to

$$S_X(f) = 2T\left\langle X^2(t)\right\rangle. \tag{2.3.5}$$

To include the effect of the photodetector efficiency η and the factor C gained from the power recycling, it is sufficient to rescale $P_0 \to \eta C P_0 \equiv \eta P_{\rm bs}$ in the above equation.

2.3.2 Radiation pressure

Equation (2.3.7) suggests that shot noise can be easily lowered by increasing the power of the laser or the gain from the power-recycling process. However, the shot noise is not the only noise associated with the laser in the interferometer. In fact, before reaching the photodetector, the laser is reflected at least once by a mirror. The reflection process, given the impinging of the laser photons on the mirror and the laser power fluctuations, causes a stochastic radiation pressure force on the mirror. By comparison with equation (2.3.2), it becomes evident that this force is proportional to $\sqrt{P_0}$, in contrast to the shot noise decreasing as $1/\sqrt{P_0}$. This means that increasing the laser power to decrease the shot noise would result in an enhancement of the radiation pressure noise, which eventually would dominate. Before hinting at a possible solution to this issue (see incoming subsection), it is necessary to first derive a simplified formula for the strain sensitivity to the radiation-pressure noise.

The first step is to evaluate the spectral density of the force fluctuations on the mirrors. These are induced by the laser momentum transfer to the mirror and can be formulated in terms of laser power fluctuation as $\Delta F = 2\Delta P/c$. By using (2.3.2) for an observation time T, the explicit expression reads

$$\Delta F = 2\sqrt{\frac{\hbar\omega_{\rm L} P}{c^2 T}}. \tag{2.3.8}$$

From the fact that this quantity is related to the fluctuation in the number of photons ΔN_γ, which is frequency-independent, it follows that the spectral density $S_{\rm F}(f)$ must be flat in frequency, namely

$$S_{\rm F}^{1/2}(f) = 2\sqrt{\frac{2\hbar\omega_{\rm L} P}{c^2}}. \tag{2.3.9}$$

This spectral density can be easily converted to the one of a M-mass mirror displacement by observing that, in the first approximation, $F = M\ddot{x}$, and hence $\tilde{F}(f) = -M(2\pi f)^2\tilde{x}$, meaning

$$S_x^{1/2}(f) = \frac{2}{M(2\pi f)^2}\sqrt{\frac{2\hbar\omega_{\rm L} P}{c^2}}. \tag{2.3.10}$$

The next step is to convert the above formula to the radiation pressure strain spectral density in the case of a Fabry-Perot cavity, which is heuristically presented in the following. First, from the observation of the anti-correlation of the Poissonian distributions of the laser photons in the two interferometer arms (meaning that more photons are in one arm, the less are in the other one), equation (2.3.10) gets multiplied by a factor of 2. Second, (2.3.10) must be converted to strain spectral density

units. This, for a simple Michelson interferometer, translates in the division by the (common) arm length L, the transfer function from length variation to strain from $\Delta L = hL$. The last step is to account for the Fabry-Perot cavity properties, resulting in an amplification factor of $2\mathcal{F}/\pi$ for the effective displacement of a mirror (or arm length) compared to the simple Michelson interferometer case and a decrease in power by a factor $[1 + (f/f_{\rm p})^2]$ to account for the mirror vibrating at a frequency f displacing the cavity off-resonance. In this way, the strain spectral density for the radiation pressure noise is [15]

$$\begin{aligned} S_n^{1/2}(f)\Big|_{\rm rad} &= \frac{2}{L}\frac{2\mathcal{F}}{\pi}\frac{S_x^{1/2}(f)}{\sqrt{1+(f/f_{\rm p})^2}} \\ &= \frac{16\sqrt{2}\mathcal{F}}{M\,L(2\pi f)^2}\sqrt{\frac{\hbar}{2\pi}\frac{P_{\rm bs}}{\lambda_{\rm L}c}}\frac{1}{\sqrt{1+(f/f_{\rm p})^2}}, \end{aligned} \tag{2.3.11}$$

where in the second equality the explicit expression for $S_x^{1/2}(f)$ was used (replacing P_0 with $P_{\rm bs}$), together with $\omega_{\rm L} = 2\pi c/\lambda_{\rm L}$.

2.3.3 The standard quantum limit

The combination of the laser shot and the radiation-pressure noises is usually called *optical read-out noise*, whose spectral density is

$$S_n(f)\Big|_{\rm opt} = S_n(f)\Big|_{\rm shot} + S_n(f)\Big|_{\rm rad}. \tag{2.3.12}$$

From the plot in figure 2.7 showing the total spectral density and the individual contributions from shot and radiation-pressure noise for a specific configuration, it becomes evident that the quantum nature of these noises and the Heisenberg uncertainty principle [194] are in action[16] in equation (2.3.12). The fact that it is necessary to account for quantum effects when measuring the position of macroscopic bodies like the mirror is quite remarkable.

A question arising from this picture is whether it is possible to reduce the optical read-out noise arbitrarily low. Naively, this may not be the case, as it would mean having an equal contribution from shot and radiation-pressure noises at every frequency. This is encoded in what is called *standard quantum limit* [195]. To derive the standard limit, the starting point is the square root of equation (2.3.12) with the explicit

[15] The treatment in the Fabry-Perot cavity has been simplified by taking advantage of some cancellations that happen during the full calculation. To be fair, it should be observed that in a Fabry-Perot cavity with finesse factor $\mathcal{F}$, the light bounces on average $\mathcal{N} = 2\mathcal{F}/\pi$, from which the amplification factor of $\mathcal{O}(\mathcal{N})$ of ΔL. If the cavity is at resonance, an additional phase shift in the reflected light due to the transfer function of the cavity (again of $\mathcal{O}(\mathcal{N})$) must be accounted for. However, this additional factor simplifies out when dividing again by the Fabry-Perot cavity transfer function to compare the result with the effect of a GW.

[16] This can be summarised by the statement that the measurement of the position of a test mass (the mirror) by using photons is spoiled by the non-deterministic recoil in form of radiation-pressure fluctuations.

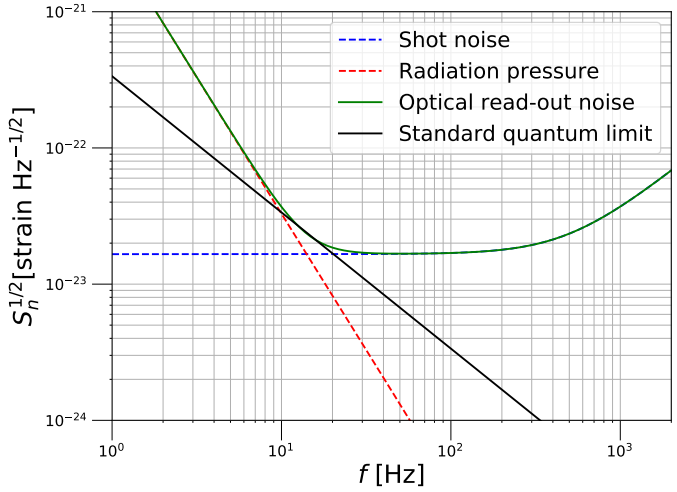

Figure 2.7: Examples of shot noise (blue dotted), radiation pressure noise (red dotted), optical read-out noise (green solid), and standard quantum limit spectral densities for initial Virgo [`my_code`].

expression for the shot and radiation-pressure spectral density, leading to

$$S_n^{1/2}(f;\, f_0)\Big|_{\rm opt} = \frac{1}{\pi f_0 L}\sqrt{\frac{\hbar}{M}}\left[\left(1+\frac{f^2}{f_{\rm p}^2}+\frac{f_0^4}{f^4}\frac{1}{1+f^2/f_{\rm p}^2}\right)\right]^{1/2}, \tag{2.3.13}$$

where

$$f_0 \equiv \frac{8\mathcal{F}}{2\pi}\sqrt{\frac{P_{\rm bs}}{\pi\lambda_{\rm L} c M}} \tag{2.3.14}$$

was introduced. At a fixed frequency f, the standard quantum limit is the value of the spectral density in equation (2.3.13) when minimised with respect to f_0, namely

$$S_{\rm SQL}^{1/2}(f) = \frac{1}{2\pi f L}\sqrt{\frac{8\hbar}{M}}. \tag{2.3.15}$$

It should be stressed that the above expression is a "pseudo-spectral density" [196] rather than a spectral density, since it is the envelope of the minima of the family of functions $S_n^{1/2}(f;\, f_0)\big|_{\rm opt}$. As a consequence, reaching the quantum limit at a given frequency implies that the optical read-out noise at all other frequencies is above this limit, now expressed as[17]

$$S_n(f)\Big|_{\rm opt} = \frac{1}{2}\,S_{\rm SQL}(f)\left[\frac{1}{\mathcal{K}(f)}+\mathcal{K}(f)\right], \tag{2.3.16}$$

[17]This expression holds in the limit where the photodetector efficiency η is equal to one and there is no light modulation, which will add a numerical factor to the shot-noise term.

where

$$\mathcal{K} \equiv \frac{8\omega_{\rm L} P_{\rm bs}}{ML^2}\,\frac{1}{\omega^2(\omega_{\rm p}^2+\omega^2)} \tag{2.3.17}$$

is a dimensionless quantity that is usually used in the literature [197]. To conclude, it is important to remark that it is actually possible to go beyond the standard quantum limit by using quantum non-demolition techniques [181]. Such techniques, as in the case of the frequency-dependent squeezing of light[18] [199, 200], are already implemented in the current generation of advanced ground-based interferometers [201, 202].

2.3.4 Seismic and Newtonian noise

Differently from the optical read-out noise, which is intrinsic to the method employed to detect the displacement of the test masses induced by GWs, seismic and Newtonian noise fall under the "displacement noise" category. These noises are usually characterised by the displacement strain spectral density $S_x^{1/2}(f)$[19]. The complete calculation of each displacement noise involves many technical aspects, which are completely omitted here.

Seismic noise

Seismic noise is the noise associated with the continuous ground motion of the Earth, whose amplitude is of the order of few a microns. As an example, in the 1-10 Hz frequency range, most of the seismic noise comes from daily human activities and local phenomena such as winds. In addition to this, it is also necessary to account for

[18] The electric field $\vec{\boldsymbol{E}}(t,\,\vec{\boldsymbol{x}})$ with a polarisation vector $\vec{\boldsymbol{p}}(t,\,\vec{\boldsymbol{x}})$ can be expressed in the *quadrature picture* as

$$\begin{aligned}\vec{\boldsymbol{E}}(t,\vec{\boldsymbol{x}}) &= E_0\left[a(\vec{\boldsymbol{x}})e^{-i\omega t}+a^*(\vec{\boldsymbol{x}})e^{i\omega t}\right]\,\vec{\boldsymbol{p}}(t,\,\vec{\boldsymbol{x}})\\ &= E_0\left[X_A(\vec{\boldsymbol{x}})\cos(\omega t)-X_P(\vec{\boldsymbol{x}})\sin(\omega t)\right]\,\vec{\boldsymbol{p}}(t,\,\vec{\boldsymbol{x}})\end{aligned} \tag{2.3.18}$$

where $a(\vec{\boldsymbol{x}})$ is the complex amplitude of the field, and

$$X_A(\vec{\boldsymbol{x}}) = \frac{a^*(\vec{\boldsymbol{x}})+a(\vec{\boldsymbol{x}})}{2}, \qquad X_P(\vec{\boldsymbol{x}}) = i\frac{(a^*(\vec{\boldsymbol{x}})+a(\vec{\boldsymbol{x}}))}{2}, \tag{2.3.19}$$

are called *amplitude* and *phase quadrature*, respectively. In a quantum-mechanics picture, the operators associated with the observables $X_A(\vec{\boldsymbol{x}})$ and $X_P(\vec{\boldsymbol{x}})$ are not commutative. As a consequence, the uncertainties of the two observables are related by the Heisenberg uncertainty principle. In practice, the amplitude quadrature couples to the radiation pressure on the mirrors, while the phase-quadrature uncertainty is related to the shot noise. The simplified idea of frequency-dependent squeezing is using a filter cavity to *squeeze* (i.e. reduce the uncertainty of) the quadratures of the vacuum-state of the electric field at the output port of the interferometer in a frequency-dependent way (see [198] for the full details). This makes it possible to reduce the uncertainty on the phase (amplitude) quadrature at high (low) frequencies, hence decreasing the dominant shot (radiation-pressure) noise while increasing the radiation-pressure (shot) noise, which still remains negligible at high (low) frequencies.

[19] The comparison with the equivalent GW amplitude for a Michelson interferometer is straightforward by recalling that, if the arm length L changes by an amount Δx, the corresponding GW amplitude is $\Delta x/L$. This can similarly be understood in terms of $\Delta\phi_{\rm FP}$ for a Fabry-Perot cavity.

a micro-seismic background, which affects a GW interferometer in the form of surface waves, which couple to the interferometer and in turn displace the mirrors. The strain sensitivity usually assumes the form [203]

$$S_x^{1/2}(f)\Big|_{\rm seismic} \simeq A\left(\frac{1\rm Hz}{f^\nu}\right)\ {\rm mHz}^{-1/2}, \tag{2.3.20}$$

with $\nu \simeq 2$ for frequencies above 1 Hz, while $A \sim \mathcal{O}\big(10^{-7}\,{\rm m}\big)$ in a very quiet place. It is easy to realise, by dividing the above equation by $L = 3 - 4\,{\rm km}$, that the noise strain sensitivity is several orders of magnitude above the GW strain. Luckily, seismic noise can be attenuated by building attenuators. An example of an attenuator is a set of pendula in cascade [204, 205], which can attenuate $S_x^{1/2}(f)\,\big|_{\rm seismic}$ by a factor $(f_0^2/f^2)^{2N}$, with $f_0 \ll f$ the resonance frequency of a pendulum and N the number of pendula. The condition on f_0 allows to reduce this noise only at GW frequencies above $\sim 10\,{\rm Hz}$, making it impossible for GW interferometers to search for GWs below this threshold.

Newtonian noise

Newtonian noise describes the effect of the Newtonian gravitational forces of moving bodies, which result in a time-varying gravitational force, also known as "gravity gradient noise". This is mainly due to mass density fluctuations in the ground (from micro-seisms, hence micro-seismic noise) and in the air (from temperature or pressure variations in the atmosphere) that directly couple to the test masses of a GW interferometer [206, 207]. Newtonian noise affects the detector frequency region below 10 Hz [206], the same where seismic noise is also stronger. Differently from seismic noise, which could be attenuated (in theory) arbitrarily, Newtonian noise cannot be removed, given the impossibility of screening gravity (however, some techniques are being developed to this end; see, for example, [208, 209]). Because of this, Newtonian noise provides the ultimate limitation at low frequencies for a ground-based GW inteferometer.

2.3.5 Thermal noise

Thermal (or Brownian) noise arises at $T > 0\,{\rm K}$ due to the thermal kinetic energy of the atoms inducing vibrations in some parts of the detectors, such as suspensions and mirror test masses. The spectral density associated with thermal noise can be characterised by using the *fluctuation-dissipation theorem* [210, 211] [20], which in the

[20] Suppose to have a linear system described by a variable $x(t)$ with $v(t) \equiv \dot{x}(t)$ the velocity and subject to an external force $F(t)$. The equation of motion of the linear system can always be cast in the Fourier domain as

$$\tilde{F}(\omega) = Z(\omega)\tilde{v}(\omega) = -i\omega\, Z(\omega)\tilde{x}(\omega), \tag{2.3.21}$$

where $Z(\omega)$ is called impedance, while its inverse $Y(\omega) = Z^{-1}(\omega)$ admittance. The fluctuation-dissipation theorem asserts that the the real part of the impedance $Z(\omega)$, which encodes the dissipation terms, is related to the (single-sided) power spectrum $S_{\rm F}(\omega)$ of the force causing the (thermal) fluctuations

case of the strain spectral density for the induced displacement Δx reads

$$S_x^{1/2}(f)\Big|_{\text{thermal}} = \frac{\sqrt{k_{\text{B}}T\,\Re\left[Z^{-1}(f)\right]}}{\pi f}. \tag{2.3.23}$$

In general, for a system of mass m and given a normal mode ω_0, the associated impedance is modelled as [212]

$$Z(\omega) = -\frac{im}{\omega}\left[\omega^2 - \omega_0^2 + i\omega_0^2\phi(\omega)\right], \tag{2.3.24}$$

where the dimensionless factor $\phi(\omega) = Q^{-1}$ is named loss-angle, and Q is the quality(Q)-factor [213] [21]. The higher the Q-factor, the lower the damping of the system at resonance. For $\omega \ll \omega_0$, $S_x(\omega) \propto \phi(\omega)/\omega$, while for $\omega \gg \omega_0$, $S_x(\omega) \propto \phi(\omega)/\omega^5$, and finally at resonance, $S_x(\omega) \propto 1/\phi(\omega)$. This means that a material with a small $\phi(\omega)$ will have a narrowly peaked thermal noise at resonance and rapidly decreasing out of it.

Thermal noise may affect the interferometer suspensions through pendulum thermal fluctuations, suspension vertical thermal fluctuations, and violin (normal) modes of the wires. Concerning the test masses, thermal noise may include the Brownian motion of the mirrors, the thermo-elastic fluctuations of the mirror bulk and coating, and the thermo-refractive fluctations in the refraction index of the coatings.

2.4 Advanced Virgo detector

The Advanced Virgo detector [94] is part of the worldwide GW detectors network (see figure 2.8) together with the two Advanced LIGO detectors [90] in the United States, LIGO-Hanford and LIGO-Livinston, KAGRA [95] in Japan, and GEO [122] (to which a new LIGO detector in India [115] will join after its construction towards the end of this decade). The scientific collaborations behind these experiments are members of the International Gravitational-Wave Network (IGWN) [214], and have a memorandum of agreement for full data exchange[22].

---

as

$$S_{\text{F}}(\omega) = 4k_{\text{B}}T\,\Re\left[Z(\omega)\right]. \tag{2.3.22}$$

[21] The quality factor is defined as $Q \equiv f_0/\Delta f$, with f_0 the resonant frequency and Δf the full width of the resonant peak in the frequency response of the system, measured at the level of half of the maximum power.

[22] For groups outside the collaborations, the reconstructed GW data are prepared and publicly released after a latency period at the end of each observing run. The process is handled by the Gravitational-Wave Open Science Centre (GWOSC) [215–217].

	iVirgo+	AdV design
Optical layout (Michelson, FP cavities)	Power Recycled	Dual Recycled
Laser wavelength	1064 nm	1064 nm
Laser power	20 W	175 W
Optical power after IMC	8 W	125 W
Optical power at BS	0.3 kW	4.9 kW
Optical power in arm cavities	6 kW	650 kW
Cavity finesse	50	443
Arm cavity length	3km	3km
Input Mode Length	143.24 m	143.24 m
Power Recycling Cavity Length	11.952 m	11.952 m
Signal Recycling Cavity Length	-	11.952 m
Schnupp asymmetry	85 cm	23 cm
Mirror material	Fused Silica	Fused Silica
Beam Splitter Diameter	55 cm	23 cm
Test mass diameter	35 cm	35cm
Test mass weight	21 kg	42 kg
Test mass flatness	<8 nm RMS	0.5 nm RMS
Coating losses	250 ppm	37.5 ppm
IM/EM ROC	flat/3600 m	1420 m/ 1683 m
Test mass suspensions	Steer Wires	Fused Silica Fibres
Vibration isolation	Super-attenuators	Super-attenuators
Vacuum pressure	10^{-9} mbar	10^{-7} mbar

Table 2.1: Comparison between the main parameters of the Virgo+ interferometer and the Advanced Virgo interferometer in the original design. Data were taken from the Advanced Virgo Technical Design Report [218].

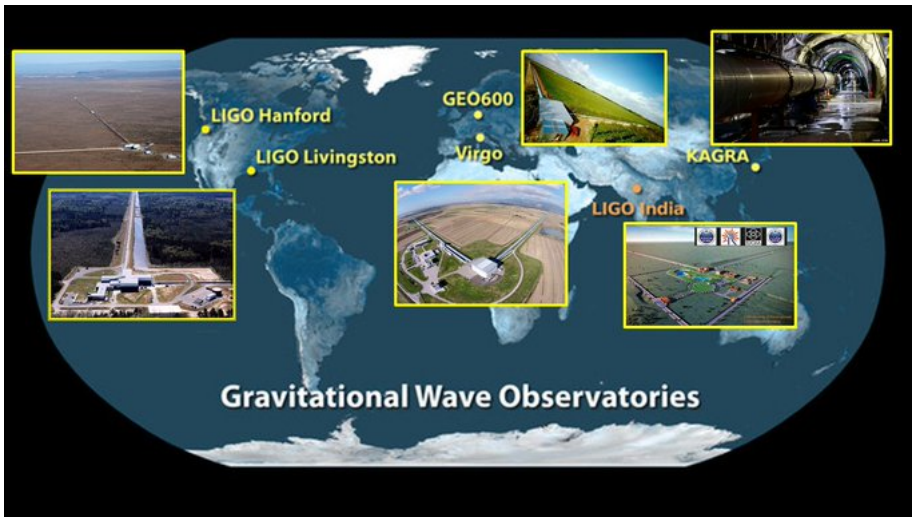

Figure 2.8: Worldwide GW-detector network, showing operating detectors and future ones (taken from LIGO Twitter account).

2.4.1 The detector before O3

Advanced Virgo (AdV) detector is a 3-km arm, Fabry-Perot-enhanced, dual power recycled[23] interferometer located in Cascina, Pisa, Italy. It is an updated version of the Virgo experiment [79, 219] (which in turn was a single power recycled interferometer), designed to improve the sensitivity of the forerunner by one order of magnitude, and hence a CBC detection rate one-thousand times larger. The AdV project was approved and funded in 2009 [220]. Its installation started in mid-2012, following the decommissioning of Virgo+ (the first updated version of Virgo) at the end of the fourth Virgo science run with LIGO in 2011. The construction concluded at the end of 2016, followed by a commissioning period until the end of July 2017. On 1st August 2017, with a 25 Mpc BNS inspiral range sensitivity[24], AdV[25] joined for the last four O2 weeks with LIGO, during which it played an important role in the sky localisation of gravitational wave signals, most importantly in the case of GW170817, the first BNS signal and the only GW signal up to now with an electromagnetic counterpart.

A full list of upgrades foreseen in the original design and AdV sensitivity study are available in the AdV Technical Design Report [218], and [222], respectively, and further summarised in [94] and table 2.1. The net effect of the upgrade from Virgo+ to AdV has been the reduction of quantum noise, with specific focus on the shot noise at

[23]The main addition to the simplified optical layout discussed throughout section 2.2 is a signal recycling cavity between the exit of the beam-splitter and the photodetector.

[24]The inspiral range is defined as the volume- and orientation-averaged distance at which a compact binary coalescence gives a matched filter signal-to-noise ratio of 8 in a single detector [221].

[25]Even though called AdV from now on, AdV was not at its design configuration during O2. Several intermediate steps have been and will be necessary to deal with the problems faced with the introduction of new features during the observing runs after O2; see the rest of this section.

high frequencies (by noticeably increasing the finesse of the Fabry-Perot cavities and the laser power) and radiation pressure noise at low frequencies (by doubling the mass and the thickness of the mirrors), thermal noise from coating thermal noise (by enlarging the laser beam spot size on the test masses and using low-loss and low-absorption coatings), and the reduction of other technical noises. Noticeably, it was not necessary to further improve the vibration isolation system, given the already satisfying seismic isolation provided by the Virgo "Super-Attenuators" [204]. AdV design sensitivity from [90] (where the signal recycling cavity characteristics are tuned to optimise the BNSs detection) is illustrated in figure 2.9. At design, shot noise will be dominant for frequencies higher than 300 Hz, while coating thermal noise will be the main plague in the 50-300 Hz region, and radiation pressure and Newtonian noise are expected to limit low frequencies below 50 Hz.

In the nineteen-month break between O2 and O3, some other hardware upgrades were performed to further improve the interferometer. These can be summarised in four main points [223, 224], namely the re-installation of monolithic suspensions (replacing steel wires suspending arm cavity mirrors with quartz fibres [225]); the increase in the laser power injected into the interferometer (from 10 W to 19 W, aimed to reduce shot noise at high frequencies); the installation of a (phase) squeezed light source [201] (further reduction of shot noise at high frequencies by modifying the properties of the light exiting the interferometer, not foreseen in the original AdV design [94]), and the test installation of an array of seismic sensors (to characterise the seismic noise in view of future Newtonian-noise subtraction methods [208, 209, 226]).

2.4.2 AdV during O3

Simplified optical layout

After the improvements and another commissioning period, AdV joined the O3 run from the beginning of April 2019 to the end of March 2020. A simplified optical layout of AdV during the O3 run is illustrated in figure 2.10. The power-stabilised laser beam (PSL) with wavelength $\lambda_{\mathrm{L}} = 1.064\,\mathrm{nm}$, modulated by the passage through the electro-optic modulator (EOM), is filtered by an input mode cleaner (IMC) realised through a 144-m triangular cavity. Then, after having gone through a partially reflective power recycling (PR) mirror, the beam reaches the beam-splitter (BS) and is split into two perpendicular beams. The beams travel into the "North" and "West" 3-km-long arms hosting the Fabry-Perot cavities, whose test masses are called north input (NI), north end (NE), west input (WI), and west end (WE) mirror. After propagation and storage in the cavities, the two beams recombine at the BS, and the resulting beam directs towards the interferometer output port, while the (phase) squeezed light source is entering the detector. Eventually, the output-port beam is filtered by two output mode-cleaner (OMC) cavities, OMC1 and OMC2, before being detected on the photodetector.

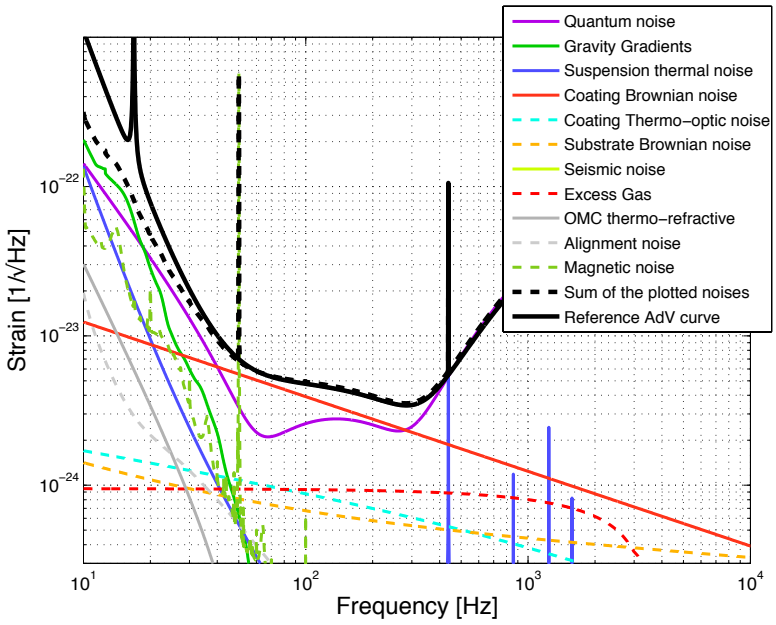

Figure 2.9: Advanced Virgo reference sensitivity (solid black line) and Advanced Virgo noise budget (dashed black line) from [94], where it was computed for a 125-W laser and in the optimal configuration for binary neutron star detection.

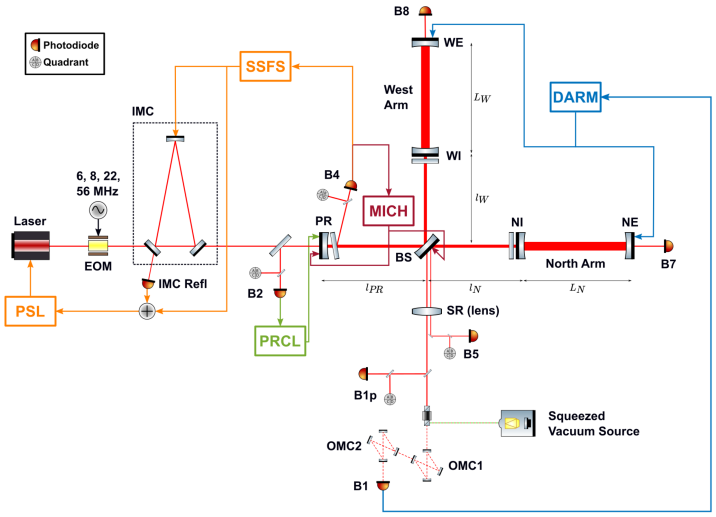

Figure 2.10: AdV simplified optical layout during O3. Figure retrieved from [227].

Controls

The detector is maintained at its global working point by a complex active feedback system, whose details are reported in [227]. The system controls the four main longitudinal degrees of freedom (DOFs) of the AdV detector, namely the difference in length $l_{\mathrm{N}} - l_{\mathrm{W}}$ of the Michelson interferometer short arms (which sets the "dark fringe" optical condition); the power recycling cavity length (PRCL) $l_{\mathrm{PRCL}} + (l_{\mathrm{N}} + L_{\mathrm{W}})/2$ (which must be resonant); the CARM $(L_{\mathrm{N}} + L_{\mathrm{W}})/2$ of the two arm cavities (used as etalon to further stabilise the input-laser frequency); and the DARM $L_{\mathrm{N}} - L_{\mathrm{W}}$ of the two cavity arms (the quantity sensitive to the GW passage). The global control relies on radio-frequency carrier sidebands at 6 MHz, 8 MHz, and 56 MHz [79] generated by an electro-optical modulator (EOM) between the laser source and the IMC. In addition to the global controls, a thermal compensation system (TCS) [228] is installed to compensate for the thermal effects and optical aberrations (such as thermal lensing, thermo-elastic deformations, and elasto-optic effects) due to the power absorption of the mirrors, which can change the optical path length of the laser. The TCS is based on the combined action of Hartmann wavefront sensors, phase cameras, and a CO_2 laser beam [227].

Data quality

At the current stage of the detector, the reconstructed GW strain data stream $h(t)$ is dominated by noise over rare and weak GW signals. The noises can be divided into two main categories. The first category is the instrument fundamental noises, which represent the ultimate limits to its sensitivity and are expected to be stationary and Gaussian [229]. The second category of noises is much wider, with a much richer taxonomy. The most important ones are the noise transients, also known as *glitches*, and the long-lasting noise excesses, known as *spectral lines*. Glitches are usually monitored and classified in the time-frequency domain to distinguish them from transient GW signals. Spectral lines are usually around a particular frequency and can be narrow (i.e. nearly monochromatic) and called *lines*, or wider and called *bumps*. Lines can appear individually or in *combs* (i.e. families of lines separated by a constant frequency interval, related to strict-periodicity signals). Bump structure may vary depending on the source. Both lines and bumps can exhibit *sidebands*, symmetric structures around their main frequency and related to non-linear interactions among different disturbances. These noises can be persistent for the whole observing run or vary in time as a consequence of changes at the detector level. The investigation of these noises happens through hundreds of auxiliary channels acquired by the Virgo data acquisition system (DAQ). To that end, several *DetChar* tools, methods, and procedures exist. For the O3 run, a detailed description of *DetChar* controls and additional environmental noises are available in [223, 224, 230, 231].

	AdV O3	AdV+ Phase I	AdV+ Phase II
Laser power	100 W	130 W	140-150 W
Optical power after IMC	18-26 W	40 W	60-80 W
Arm cavities finesse	450	450	450
IMC finesse	1000	1000	1000
OMC cavity (Finesse)	Double (120)	Single (1000)	Single (1000)
Power recycling gain	39	39	39
Signal recycling	No	Yes	Yes
Beam-splitter	55 cm x 6.5 cm, 34 kg	55 cm x 6.5 cm, 34 kg	55 cm x 6.5 cm, 34 kg
Power recycling mirror	35 cm x 10 cm, 21 kg	35 cm x 10 cm, 21 kg	35 cm x 10 cm, 21 kg
Input mirror	35 cm x 20 cm , 42 kg	35 cm x 20 cm , 42 kg	35 cm x 20 cm , 42 kg
End mirror	35 cm x 20 cm , 42 kg	35 cm x 20 cm , 42 kg	55 cm x 20 cm , 105 kg
ROC I/E Mirror	1420 m / 1683 m	1420 m / 1683 m	1067 m / 1963 m
Signal recycling mirror	-	35 cm x 10 cm, 21 kg	35 cm x 10 cm, 21 kg
Beam size on I/E mirror	49 mm/ 58 mm	49 mm/ 58 mm	49 mm/ 96 mm
Quantum noise reduction	8 dB	12 dB	12 dB
Squeeze type	frequency-independent	frequency-(in)dependent	frequency-dependent
Newtonian Noise reduction	-	1/3	1/3-1/5

Table 2.2: Comparison of the main parameters of AdV, AdV+ Phase I [232] and AdV+ Phase II [233].

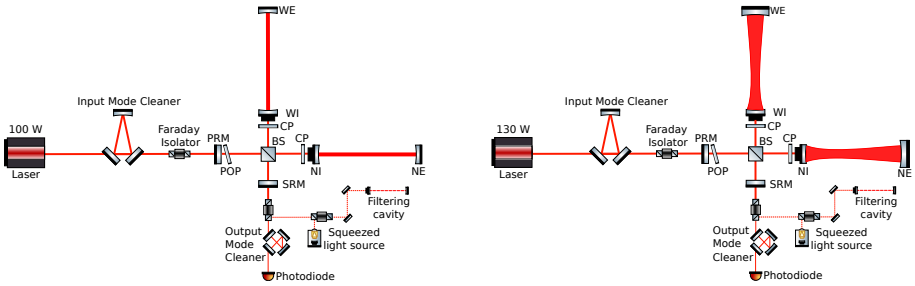

Figure 2.11: Simplified optical layouts of AdV+ Phase I and AdV+ Phase II, adapted from [234] and realised using Inkscape [185] and the GWOptics component library [186].

2.4.3 Towards O4 and future: AdV+ and Virgo_nEXT

Already after the end of O2 in 2017, a further plan for upgrading AdV beyond its design was approved under the name of Advanced Virgo Plus (AdV+). The upgrade is divided into two phases, called AdV+ Phase I and AdV+ Phase II. AdV+ Phase I started after the end of O3 and was completed before the start of O4. The main goals consisted of the reduction of quantum shot and radiation-pressure noises and the implementation of a signal recycling mirror. The reduction of quantum noise has been achieved in two ways, namely by increasing the injected laser power and by implementing a frequency-dependent squeezing source in the interferometer output port. After the installation of the signal-recycling mirror, the properties of the corresponding signal-recycling cavity can be tuned in such a way to improve the detector sensitivity in a desired frequency range. The presence of the addition signal-recycling cavity makes the process of locking and controlling the interferometer more complex, requiring the installation of an Auxiliary Laser System [236]. AdV+ Phase II components are under construction and are expected to be implemented between the end of O4 and the start of O5 observing runs (see figure 2.12 for the expected BNS range sensitivity evolution). The focus of the second phase is the reduction of the thermal noise affecting the mirrors in the mid-range frequency around 100 Hz by changing the beam geometry inside the arm with more than twice as massive end-mirrors and implementing coatings with lower mechanical losses. Moreover, the installation of seismic sensor arrays will allow the subtraction of Newtonian noise from the interferometer output, reducing it by a factor between three and five. A comparison between the optical layout of the two phases is presented in figure 2.11, while the main parameters are in table 2.2. At the end of the upgrade, AdV+ is expected to extend the maximal BNS sensitivity of the detector between 140 and 260 Mpc, depending on the final optical configuration. For more details about the AdV+ project and its status before O4, see [232–234, 237] and [238], respectively.

Further upgrade plans have already been envisaged, when AdV+ will have reached the design layout and sensitivity after the end of O5, and are known under the name of Virgo_nEXT. This final upgrade aims to improve the Virgo detector sensitivity to

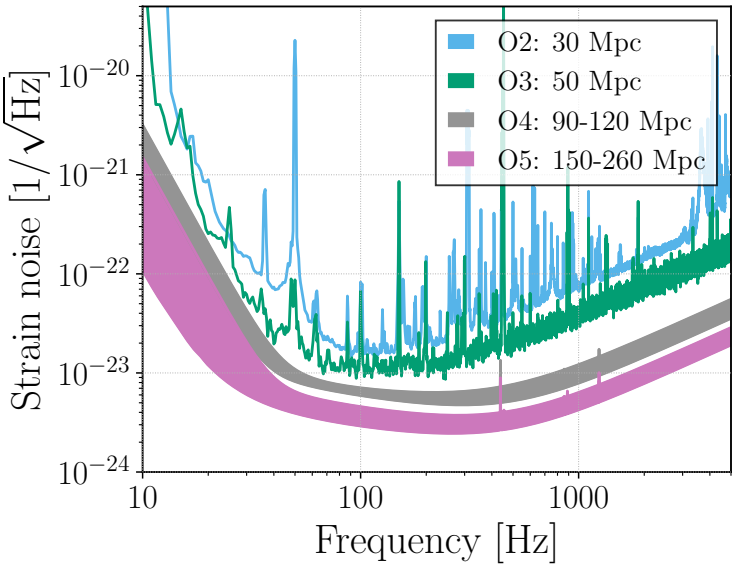

Figure 2.12: Virgo evolving sensitivity according to LVK observing scenarios reported in [235], which differ from the latest one reported in the main text or the ones actually reached where applicable.

extreme limits imposed by its current infrastructure, doubling the BNS sensitivity with respect to O5 up to $\sim$ 500 Mpc. In addition to this, the development and running of this ultimate version of Virgo will allow to bridge the observational time gap between O5 and the start of the operation of future 3rd generation ground-based interferometer detectors like Einstein Telescope [116] and Cosmic Explorer [117] in the next decade, allowing to evolve and test technologies for such detectors.

Part II

Stochastic Gravitational-Wave Background: Astrophysics, Cosmology, and Search Methods

Chapter 3

Stochastic Gravitational-Wave Background: Definition and Taxonomy

"... Così tra questa
immensità s'annega il pensier mio:
e il naufragar m'è dolce in questo mare."

Giacomo Leopardi, *L'Infinito*

After the introduction of gravitational waves and ground-based GW detectors in part I, the focus shifts to the main topic of this thesis, namely stochastic gravitational-wave background (SGWB). This section provides an overview of the SGWBs from different sources and over the GW frequency spectrum. Section 3.1 introduces the concept of SGWB first via everyday-life analogies and then tries to define more formally what an SGWB is and what the related observable quantities of interest are. Then, sections 3.2 and 3.3 present the two main categories of SGWBs, namely the astrophysical and the cosmological ones, presenting the main formulas and sources. Finally, section 3.4 tentatively summarises the bounds and prospects for detection from different experiments covering the GW spectrum.

3.1 What is a Stochastic Gravitational-Wave Background?

3.1.1 An auditory analogy

Defining rigorously what a stochastic gravitational-wave background (SGWB) is can be not as trivial as expected and reveals several subtleties. Hence, before trying to give a proper definition, it can be useful to start with a couple of analogies from everyday life.

Suppose you are at a cocktail party in a crowded room with people who are talking. The superposition of people's voices contains information about how the crowd attending the party is composed (how many males or females there are, age, etc.).

Imagine being in the room, listening to people's conversations to gather as much information as possible about the ensemble properties of the crowd. Talks and voices from people who are close to the listener can be easily heard and understood, but they constitute just a small fraction of the attendants to the party. The more the people are distant from the listener, the more it will be difficult to disentangle their talks from the background (or rather, foreground?) of other people's talks in the room. However, by listening long enough to the blabbering background, it can still be possible to get some information about the average characteristics of people attending the party and how they are grouped inside the room. Alternatively, imagine assisting to an orchestra at a concert. The audience is capable of listening to the melody produced by the overlap of different instruments, even if it is not possible to disentangle the sound from a single instrument in the orchestra ensemble. Still, during the execution, it will still be possible to identify which groups ("populations") of instruments are played at a time, getting an idea of the composition of the orchestra.

The analogy of the cocktail party reflects the current situation of ground-based GW detectors with respect to the CBC population (and, in the near future, to the GW burst-like signal populations): the detector sensitivity allows to detect (listen to) the inspiral-merger-ringdown phase of signals from compact binaries that are sufficiently close to us, while the more distant ones cannot be individually detected either because they are too weak or unresolvable from the gravitational-wave background of CBCs. In addition to that, the duration of the signals in the sensitive ground-based detector band is (much) shorter than the inverse rate of mergers, meaning that the CBC background will be popcorn-like. The time of arrival of the mergers is randomly distributed, and hence, even if the CBC signal is deterministic, the resulting strain from the combination of the CBC population signals will be itself a random variable. This means that the gravitational-wave background signal will be *stochastic* in that sense and can be characterised only by its statistical momenta. The analogy of the orchestra should represent the actual situation with SGWBs from both astrophysical and cosmological populations of persistent/irreducible GW sources. In this case, the SGWB (or rather, the "Symphony of the Universe") will be continuous (and Gaussian due to the central limit theorem) and have multiple components that must be separated to properly identify the ensemble properties of the populations/mechanisms behind the resulting SGWBs.

The two analogies and their real-world counterparts make it clear that the definition of SGWB may depend on whether one considers a population of GW sources as a whole or rather gives the definition from a detector observation perspective[1].

[1]The limited sensitivity of the detectors in a frequency band may not be able to catch all the features of the SGWB. As an example, consider a simplified picture of the SGWB from the BNS coalescence. In the current LIGO-Virgo-KAGRA detectors frequency range (20-2000 Hz), the background can still be considered popcorn-like. However, when considering the future ET frequency range (5-2000 Hz) and sensitivity (which is roughly one order of magnitude better than LVK detectors), the BNS signals will spend much longer time in the detector band. They will overlap and create a continuous foreground of detectable/separable signals and a continuous background of undetectable/unresolvable signals.

3.1.2 Definitions and observables

The standard definition of SGWB is that *a stochastic gravitational-wave background is a random gravitational-wave signal produced by a large number of weak, independent, and unresolved sources* [239]. The attribute "random" means that such a signal can be characterised only statistically, by means of the expectation values of the field variables or, alternatively, of the Fourier components of the metric perturbations. The attributes "weak" and "unresolved" are less straightforward to interpret. This is because, rather than being intrinsic properties of the SGWB, they are entangled in the observational features, such as the detector sensitivity (a signal can be weak for one low-sensitivity detector but not for a high-sensitivity one) or the observation time (a longer observation time may allow to disentangle persistent signals that are otherwise unresolvable for a short observation time if they have peculiar properties and/or the detector has a good sky resolution). According to [240], a way to remove the uncertainty about when an SGWB has the above attributes is to use an operational definition within the contest of Bayesian inference[2].

After the clarification about how to define what an SGWB is, the next step is to understand how to characterise it and what the observable quantities that can be measured are. A natural way to characterise an SGWB is to measure the n-point correlation functions (which in this context are nothing less than the probability distribution moments) of the metric perturbations

$$\langle h_{ab}(t,\vec{\boldsymbol{x}})\rangle\,, \quad \langle h_{ab}(t,\vec{\boldsymbol{x}})\,h_{cd}(t',\vec{\boldsymbol{x}}')\rangle\,, \quad \langle h_{ab}(t,\vec{\boldsymbol{x}})\,h_{cd}(t',\vec{\boldsymbol{x}}')\,h_{ef}(t'',\vec{\boldsymbol{x}}'')\rangle\,, \ldots \tag{3.1.1}$$

where the expectation value $\langle \ldots \rangle$ denotes the ensemble average (or, equivalently, the average over the time and/or space domains if the ergodic hypothesis holds). An analogous formulation of the above equation is possible in terms of the Fourier coefficients of the plane-wave expansion $\tilde{h}_A(f,\,\hat{\boldsymbol{n}})$ in (1.1.23) or the multiple components of the gradient and curl tensor spherical harmonics decomposition $\tilde{a}^{P}_{(lm)}(f)$, with $P = \{G,\,C\}$ (see [241] for conventions and conversion between the two bases).

The expressions of the n-point correlation functions can be simplified noticeably if the SGWB satisfies some specific properties. If the number of sources producing the SGWB is large, then the central limit theorem [242] applies, and the SGWB is Gaussian (in the time/frequency domain). In this case, if the background has a zero mean (an hypothesis that is always possible without loss of generality), all the information about the SGWB is encoded in the 2-point correlation function, since the odd n-point correlation functions are zero and the even n-point correlation functions can be expressed as a function of the 2-point one. Furthermore, if the SGWB is stationary, the n-point correlation functions do not depend on the choice of time origin but rather on the difference between times, e.g. $t - t'$. Finally, a special role is also played by

[2] In this sense, a signal is *stochastic* if preferred over any deterministic signal model in a Bayesian model selection calculation. Similarly, a signal is *resolvable* if decomposable into *separate* (e.g. non-overlapping in either time or frequency) and *individually detectable* signals, again within a Bayesian model selection paradigm.

the source spatial distribution: a cosmological SGWB can be assumed to be isotropic (in first approximation), while an astrophysical one can exhibit anisotropies, giving rise to different statistical distributions and the necessity for different search strategies (see chapters 4 and 5).

Gaussian, stationary, unpolarised SGWB quadratic expectation values

Under the assumption that the SGWB is Gaussian, stationary, and unpolarised, it is sufficient to evaluate the 2-point correlation function of the field perturbation and build observables related to it. By making use of the plane-wave expansion (1.1.23) for $h_{ab}(t,\,\vec{\boldsymbol{x}})$, it is straightforward to express the 2-point correlation function at equal time and position as

$$\begin{aligned}\left\langle h_{ij}(t,\vec{\boldsymbol{x}})\,h^{ij}(t,\vec{\boldsymbol{x}})\right\rangle &= \int_{-\infty}^{\infty}\mathrm{d}f\int_{-\infty}^{\infty}\mathrm{d}f'\int_{\mathcal{S}^2}\mathrm{d}^2\hat{\boldsymbol{n}}\int_{\mathcal{S}^2}\mathrm{d}^2\hat{\boldsymbol{n}}'\,e^{2\pi i f\left(t+\frac{\hat{\boldsymbol{n}}\cdot\vec{\boldsymbol{x}}}{c}\right)}\times\\ &\qquad e^{-2\pi i f'\left(t+\frac{\hat{\boldsymbol{n}}'\cdot\vec{\boldsymbol{x}}}{c}\right)}\sum_{A,\,A'}\left\langle\tilde{h}^*_A(f,\,\hat{\boldsymbol{n}})\,\tilde{h}_{A'}(f',\,\hat{\boldsymbol{n}}')\right\rangle e^A_{ij}\,e^{ij}_{A'}\\ &\equiv\int_{-\infty}^{\infty}\mathrm{d}f\,S_h^{(2)}(f)\equiv\frac{1}{2}\int_{-\infty}^{\infty}\mathrm{d}f\,S_h(f),\end{aligned}\tag{3.1.2}$$

where the last two equalities introduce the two-sided and one-sided strain spectral densities $S_h^{(2)}(f)$ and $S_h(f)$, respectively.

In the case where the SGWB is spatially homogeneous and isotropic[3], the 2-point correlation function of the Fourier coefficients in the plane-wave expansion is

$$\left\langle\tilde{h}^*_A(f,\,\hat{\boldsymbol{n}})\,\tilde{h}_{A'}(f',\,\hat{\boldsymbol{n}}')\right\rangle=\mathcal{C}\,\delta\left(f-f'\right)\,\delta^2\left(\hat{\boldsymbol{n}}-\hat{\mathbf{n}}'\right)\,\delta_{AA'}\,S_h(f),\tag{3.1.3}$$

where $\delta_{AA'}$ is due to the background being unpolarised[4], $\delta(f-f')$ is the stationarity condition in frequency-domain, and $\delta^{(2)}(\hat{\boldsymbol{n}}-\hat{\boldsymbol{n}}')$ follows from the assumption of the spatial homogeneity and isotropy. The normalisation constant $\mathcal{C}$ can be obtained by inserting the above equation in equation (3.1.2) and imposing the last equality, namely

$$S_h(f)=2\int_{\mathcal{S}^2}\mathrm{d}^2\hat{\boldsymbol{n}}\,2\,\mathcal{C}\,S_h(f)=16\pi\,\mathcal{C}\,S_h(f)\implies\mathcal{C}=\frac{1}{16\pi}.\tag{3.1.4}$$

In this way, the normalised 2-point correlation function for a Gaussian, stationary, unpolarised, isotropic SGWB is

$$\left\langle\tilde{h}^*_A(f,\,\hat{\boldsymbol{n}})\,\tilde{h}_{A'}(f',\,\hat{\boldsymbol{n}}')\right\rangle=\frac{\delta\left(f-f'\right)}{2}\,\frac{\delta^2\left(\hat{\boldsymbol{n}}-\hat{\mathbf{n}}'\right)}{4\pi}\,\frac{\delta_{AA'}}{2}\,S_h(f),\tag{3.1.5}$$

[3] In the following, one will denote a spatially homogeneous and isotropic SGWB simply as *isotropic*, for short.

[4] Here, *unpolarised* means that the polarisation modes are statistically independent of one another and have no preferred component [239].

where the first $1/2$ factor is due to the choice of expressing everything as a function of the one-sided strain spectral density[5], while the $1/(4\pi)$ and the second 1/2 factors recall that the one-sided GW strain spectral density is integrated over the sky and summed over both polarisations. If the SGWB is instead anisotropic[6], by defining

$$S_h(f) = \int_{\mathcal{S}_2} \mathrm{d}^2\hat{\boldsymbol{n}}\, \mathcal{P}(f, \hat{\boldsymbol{n}}), \tag{3.1.6}$$

and repeating an analogous procedure to the isotropic one, it is easy to show that the 2-point correlation function becomes

$$\left\langle \tilde{h}^*_A(f,\, \hat{\boldsymbol{n}})\, \tilde{h}_{A'}(f',\, \hat{\boldsymbol{n}}') \right\rangle = \frac{\delta\,(f - f')}{2}\, \delta^2\,(\hat{\boldsymbol{n}} - \hat{\mathbf{n}}')\, \frac{\delta_{AA'}}{2}\, \mathcal{P}(f, \hat{\boldsymbol{n}}). \tag{3.1.7}$$

Characteristic strain, GW energy and flux

Based on the situation and the kind of SGWB model, it can be useful to introduce other observables related to the 2-point correlation function. As an example from the theory, an SGWB can be modelled through the *characteristic strain* $h_c(f)$, related to $S_h(f)$ as

$$h_c(f) \equiv \sqrt{f\, S_h(f)}. \tag{3.1.8}$$

This expression, compared to the naive $\sqrt{S_h(f)}$, has the advantage of being a dimensionless quantity.

Alternatively, it can be useful to observe that the GW energy density is related to the 2-point correlation function by equation (1.3.16). As a consequence, its spectrum $\rho_{\mathrm{gw}}(f)$ can be used to characterise the SGWB, and its definition follows from

$$\begin{aligned}
\rho_{\mathrm{GW}} \equiv & t_{00} = \frac{c^2}{32\pi\, G} \left\langle \dot{h}_{ij}\, \dot{h}^{ij} \right\rangle \\
= & \frac{c^2}{32\pi\, G} \int_{-\infty}^{\infty} \mathrm{d}f \int_{-\infty}^{\infty} \mathrm{d}f' \int_{\mathcal{S}^2} \mathrm{d}^2\hat{\boldsymbol{n}} \int_{\mathcal{S}^2} \mathrm{d}^2\hat{\boldsymbol{n}}'\, (2\pi i\, f)\, e^{2\pi i f\left(t + \frac{\hat{\boldsymbol{n}}\cdot\vec{\boldsymbol{x}}}{c}\right)} \\
& \times (-2\pi i\, f') e^{-2\pi i f'\left(t + \frac{\hat{\boldsymbol{n}}'\cdot\vec{\boldsymbol{x}}}{c}\right)} \sum_{A,\, A'} \left\langle \tilde{h}^*_A(f,\, \hat{\boldsymbol{n}})\, \tilde{h}_{A'}(f',\, \hat{\boldsymbol{n}}') \right\rangle e^A_{ij}\, e^{ij}_{A'} \\
\equiv & \int_0^{\infty} \mathrm{d}f\, \rho_{\mathrm{gw}}(f).
\end{aligned} \tag{3.1.9}$$

However, the GW energy density spectrum is not always the best quantity to measure in the case of an SGWB of cosmological or astrophysical origin. In the case of a cosmological (isotropic) SGWB, similarly to what is done in the CMB case, it is more useful to characterise the background through the frequency spectrum of the

[5] In the case where the two-sided spectral density is used, it is sufficient to perform the substitution $S_h(f) \to 2S^{(2)}_h(f)$ in all the formulas presented here and in the next chapters.

[6] Note that, in the following, one is also tacitly assuming that the radiation from different directions on the sky is uncorrelated with one another [239]. The anisotropy is in the power rather than in the strain.

dimensionless quantity $\Omega_{\rm GW}$. This quantity is defined as the ratio between GW energy density and the today critical energy density $\rho_c \equiv \rho_{c,0}$ needed to close the universe, that is

$$\Omega_{\rm GW} \equiv \frac{\rho_{\rm GW}}{\rho_c} = \int_0^\infty {\rm d}f\, \frac{\rho_{\rm gw}(f)}{\rho_c} = \int_0^\infty \frac{{\rm d}f}{f}\frac{f}{\rho_c}\,\rho_{\rm gw}(f) \equiv \int_0^\infty {\rm d}\ln f\, \Omega_{\rm gw}(f), \tag{3.1.10}$$

where $\rho_c = 3\,H_0^2c^2/(8\pi\,G)$, with H_0 the Hubble parameter today. The frequency spectrum per frequency logarithmic unit $\Omega_{\rm gw}(f)$[7] can then be expressed as a function of $S_h(f)$ and $h_c(f)$ as

$$\begin{aligned}\Omega_{\rm gw}(f) &\equiv \frac{f}{\rho_c}\frac{{\rm d}\rho_{\rm GW}}{{\rm d}f} = f\left(\frac{8\pi\,G}{3\,H_0^2c^2}\right)\left(\frac{c^2}{32\pi\,G}\,4\pi^2f^2\right)(2S_h(f))\\ &= \frac{2\pi^2}{3H_0^2}\,f^3S_h(f) \equiv \frac{2\pi^2}{3H_0^2}\,f^2h_c^2(f).\end{aligned} \tag{3.1.11}$$

This quantity can also be used to characterise an SGWB of astrophysical origin and anisotropic[8], but a more appropriate quantity for a comparison with electromagnetic astrophysics is the GW energy flux $\mathcal{F}_{\rm gw}(f,\,\hat{\boldsymbol{n}})$. Using the definition in equation (1.3.17), it is easy to show that its expression is

$$\mathcal{F}_{\rm gw}(f,\,\hat{\boldsymbol{n}}) = \frac{\pi c^3}{4G}\,f^2\,\mathcal{P}(f,\,\hat{\boldsymbol{n}}). \tag{3.1.13}$$

Quite often, the observable quantities introduced in this section can be approximated to follow a power law in frequency and written as

$$\begin{aligned}&\Omega_{\rm gw}(f) = \Omega_{\rm gw}(f_{\rm ref})\left(\frac{f}{f_{\rm ref}}\right)^\alpha, \quad S_h(f) = S_h(f_{\rm ref})\left(\frac{f}{f_{\rm ref}}\right)^\beta,\\ &h_c(f) = h_c(f_{\rm ref})\left(\frac{f}{f_{\rm ref}}\right)^\gamma, \quad \mathcal{F}_{\rm gw}(f,\hat{\boldsymbol{n}}) = \mathcal{F}_{\rm gw}(f_{\rm ref},\hat{\boldsymbol{n}})\left(\frac{f}{f_{\rm ref}}\right)^\delta,\end{aligned} \tag{3.1.14}$$

where $\alpha = \beta + 3 = (2\gamma + 2) = \delta + 1$. The pivot frequency $f_{\rm ref}$ is usually taken to be the one at which the instrument measuring these quantities is most sensitive. The methods to observe and constrain the properties of an SGWB with ground-based interferometers in the isotropic and anisotropic cases are illustrated in chapters 4 and 5.

[7] $\Omega_{\rm gw}(f)$ in equation (3.1.10) depends on H_0 through ρ_c. An alternative quantity that one can consider and that is independent of the value of H_0 is $h_0^2\,\Omega_{\rm gw}(f)$, where $h_0 \equiv H_0/(100\,{\rm km s^{-1} Mpc^{-1}})$.

[8] In this case, rather than $\Omega_{\rm gw}(f)$, the actual quantity is its angular density

$$\Omega_{\rm gw}(f,\hat{\boldsymbol{n}}) \equiv \frac{f}{\rho_c}\frac{{\rm d}^3\rho_{\rm GW}}{{\rm d}f\,{\rm d}^2\hat{\boldsymbol{n}}} = \frac{2\pi^2}{3H_0^2}\,f^3\mathcal{P}(f,\,\hat{\boldsymbol{n}}) \tag{3.1.12}$$

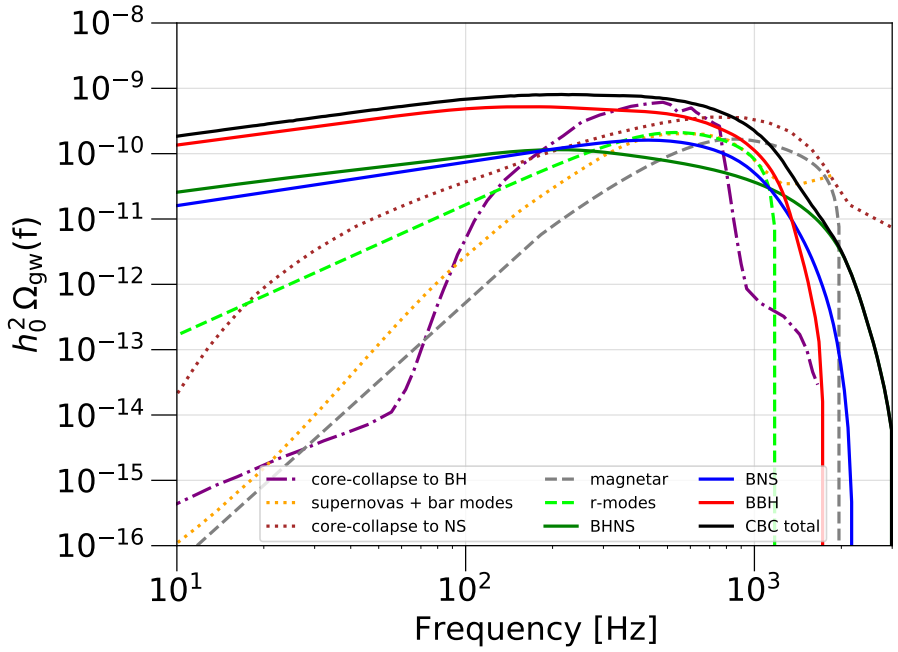

Figure 3.1: Landscape plot for some of the astrophysical SGWBs presented in the main text. The BBH, BNS, BHNS, and total CBC SGWBs are the median values inferred from the GWTC-3 catalogue [93, 247], the magnetar and r-mode ones have been reproduced from [4], while the other ones were retrieved from [243].

3.2 Astrophysical SGWB

A stochastic gravitational-wave background of astrophysical origin is expected to be the result of the superposition of GWs from (unresolvable) sources produced throughout stellar history. Likely, this SGWB is spatially anisotropic, motivated by the fact that the galaxy distribution up to ~ 100 Mpc is concentrated towards the Virgo cluster and the Great Attractor [243]. Moreover, the astrophysical SGWB may not be continuous for some sources, exhibiting non-Gaussianities in the time domain, depending on the ratio between the time interval between two successive GW signals and their average duration, called *duty-cycle*. The detection of an astrophysical SGWB would allow to set noticeable constraints on the ensemble properties of the compact-object population generating it and other important physical parameters of the stellar history, such as the initial mass function [244] and the stellar formation rate. A landscape plot of the $\Omega_{\rm gw}(f)$ spectra for the main astrophysical SGWBs discussed in this section is illustrated in figure 3.1. For a review of the main sources and challenges for their detection and characterisation, see, for example, [243, 245, 246].

3.2.1 Phinney formula and duty cycle

Before making an overview of the main sources of astrophysical SGWB, it is useful to introduce two master formulas used for its characterisation in the frequency and time domains, namely the Phinney formula and the duty-cycle formula.

The Phinney formula [248] (also known unofficially as the "Phinney theorem") allows to compute the amplitude and the spectrum of cosmic SGWB from a broad range of astrophysical[9] sources, including the uncertainties therein. This relation links the SGWB frequency spectrum to the cosmological distribution of discrete GW sources, the total time-integrated energy spectrum of an individual source, and the nowadays comoving number density of remnants. An heuristic derivation of the Phinney formula (for a more rigorous proof, see again [248]) is summarised in the statement that, in any homogeneous and isotropic universe, the GW energy density today $\rho_{\rm GW}$ must be equal to the sum of the energy densities radiated at each redshift, divided by $(1+z)$, with z the redshift, to account for the redshift effects on the gravitational radiation since emission, leading to expression

$$\rho_{\rm GW} \equiv \int_0^\infty \frac{{\rm d}f_s}{f_s} \int_0^\infty {\rm d}z \, \frac{N(z)}{1+z} \, f_s \, \frac{{\rm d}E_{\rm gw}}{{\rm d}f_s}, \tag{3.2.1}$$

where $N(z)$ is the number of events per comoving volume per unit redshift, and $(f_s \, {\rm d}E_{\rm gw}/{\rm d}f_s)$ is the total gravitational radiation energy per logarithmic unit frequency emitted in the cosmic rest frame of the source, with frequency related to the one observed today by $f_s = f(1+z)$. By comparing the above equation for $\rho_{\rm GW} \equiv \rho_c \, \Omega_{\rm GW}$ with equation (3.1.10) defining the spectrum $\Omega_{\rm gw}(f)$, the Phinney formula follows immediately as

$$\rho_c \Omega_{\rm gw}(f) = \frac{\pi^2}{4} \frac{c^2}{G} \, f^2 \, h_c^2(f) = \int_0^\infty {\rm d}z \, \frac{N(z)}{1+z} \left(f_s \, \frac{{\rm d}E_{\rm gw}}{{\rm d}f_s} \right) \Big|_{f_s = f\,(1+z)} . \tag{3.2.2}$$

In the case where multiple families of sources contribute relevantly to the SGWB, the integrand in the above expression must be replaced with a sum over the source types.

The Phinney formula can be refined and also recast as a function of rates and population parameters, which appears to be used more often in nowadays's literature [243, 246]. The starting point of the derivation is observing that $\Omega_{\rm gw}(f)$ is related to the total integrated flux $F_{\rm gw}(f)$, namely

$$\Omega_{\rm gw}(f) = \frac{f}{c\rho_c} F_{\rm gw}(f) = \frac{f}{c\rho_c} \int_\Theta p\,(\theta) \, {\rm d}\theta \int_{z_{\rm min}(\theta)}^{z_{\rm max}(\theta)} \frac{{\rm d}R}{{\rm d}z}\,(\theta, z)\, \Phi_{\rm gw}\,(f, \theta, z)\, {\rm d}z\,, \tag{3.2.3}$$

where $p(\theta)$ is the joint probability distribution of the source properties, with Θ representing the parameter space, ${\rm d}R/{\rm d}z$ is the observed signal rate per unit redshift for sources with parameters θ, and $\Phi_{\rm gw}\,(f, \theta, z)$ is the fluence from a source with param-

[9] This formula can actually be used also for sources of cosmological origin that continued existing during the cosmic history of the Universe, such as cosmic strings and primordial black holes; see next section 3.3

eters θ at redshift z at the observed frequency f. Before commenting on the redshift integration bounds, the above expression is rewritten more similarly to the Phinney formula by observing that the fluence and the rate per unit redshift can be respectively replaced by

$$\Phi_{\rm gw}\left(f,\theta,z\right)=\frac{1}{4\pi r^2(z)}\,\frac{{\rm d}E_{\rm gw}}{{\rm d}f_s}\left(f_s,\theta\right), \tag{3.2.4}$$

with $r(z)$ the proper distance, and

$$\frac{{\rm d}R}{{\rm d}z}\left(z\right)=\frac{R\left(z\right)}{1+z}\,\frac{{\rm d}V}{{\rm d}z}\left(z\right), \tag{3.2.5}$$

where $R(z)$ is the rate per comoving volume[10], ${\rm d}V$ is the comoving volume element and

$$\frac{{\rm d}V}{{\rm d}z}\left(z\right)=4\pi r^2(z)\,\frac{c}{H_0\,E(z)}, \tag{3.2.7}$$

with (for a flat ΛCDM cosmology)

$$E\left(z\right)=\sqrt{\Omega_m\left(1+z\right)^3+\Omega_r\left(1+z\right)^4+\Omega_\Lambda} \tag{3.2.8}$$

encoding the redshift dependence of the comoving volume through cosmic history. In this way, equation (3.2.3) becomes

$$\Omega_{\rm gw}(f)=\frac{f}{\rho_c\,H_0}\int_\Theta p\left(\theta\right){\rm d}\theta\int_{z_{\rm min}(\theta)}^{z_{\rm max}(\theta)}\frac{R\left(\theta,z\right)}{\left(1+z\right)E(z)}\,\frac{{\rm d}E_{\rm gw}(f_s,\theta)}{{\rm d}f_s}\bigg|_{f_s=(1+z)\,f}{\rm d}z\,. \tag{3.2.9}$$

The main difference from the original Phinney formula (3.2.2) is making explicit the integration over the parameter space and setting more structured bounds in the redshift integral[11]. In fact, the lower and upper limits $z_{\rm min}(\theta)$ and $z_{\rm max}(\theta)$ are the minimum and maximum redshifts at which a source with parameters θ can be formed. They depend on the source parameters through the minimum and maximum emission fre-

[10] It should be noticed that, for most astrophysical SGWBs, $R(z)$ can be derived from the cosmic star formation rate SFR(z) (usually expressed in $M_\odot\,{\rm Mpc}^{-3}\,{\rm yr}^{-1}$ units). In this case, where the GW emission starts shortly after the progenitor's birth, it reads

$$R(\theta,\,z)=\lambda(\theta,\,z)\,{\rm SFR}(z), \tag{3.2.6}$$

where $\lambda(\theta,\,z)$ (usually in $M_\odot^{-1}$ units) is the mass fraction converted into the progenitor, which depends on the initial mass function.

[11] The Phinney formula can be recovered by setting $z_{\rm min}(\theta)=0$ and $z_{\rm max}(\theta)=\infty$ and performing the intergral over the parameter space, after which $N(z)\equiv R(z)/E(z)$ and the average source energy spectrum expressions follow.

quencies of the source $f_{s;\,\min}(\theta)$ and $f_{s;\,\max}(\theta)$ as

$$z_{\min}(\theta) = \max\left\{0, \frac{f_{s;\,\min}(\theta)}{f} - 1\right\}, \tag{3.2.10}$$

$$z_{\max}(\theta) = \min\left\{z_{\max}, \frac{f_{s;\,\max}(\theta)}{f} - 1\right\}. \tag{3.2.11}$$

The Phinney formula allows for determining the spectral properties of an astrophysical SGWB in the frequency domain. However, if two SGWBs (such as the ones belonging to the family of compact binary coalescences) have the same frequency dependence in the frequency range of interest, it may be useful to look at their properties in the time domain to break the degeneracy and disentangle them. A quantity that can help with this aim is the *duty cycle* Δ, defined as

$$\Delta = \int_{\Theta} p(\theta)\, \mathrm{d}\theta \int_0^{z_{\max}} \tau_s(\theta)\, (1+z)\, \frac{\mathrm{d}R}{\mathrm{d}z}(z)\, \mathrm{d}z\,, \tag{3.2.12}$$

where $\tau_s(\theta)$ is the duration of a GW signal emitted from a source with parameters θ in the source frame, converted to the observer frame through the $(1+z)$ factor to account for time dilatation. Recalling that the above expression is defined as the ratio between the typical duration of an observed GW signal to the average time integral between successive events, three regimes may be defined[12]:

- $\Delta \gg 1$: The time interval between two successive signals is small compared to the single event duration. The signals overlap, generating a *continuous*, Gaussian (assuming the number of sources is large enough to invoke the Central limit theorem) background.
- $\Delta \ll 1$: The time interval between two consecutive signals is large compared to the single event duration. Long periods of silence separate two signals, resulting in a *shot-noise* background.
- $\Delta \sim 1$: The time interval between two succeeding signals is comparable to their typical duration. Signals may still overlap, but their statistical properties are no longer Gaussian, turning into a *popcorn* background with unpredictable amplitude at detectors.

Some examples of the three regimes are pictured in figure 3.2.

[12] It should be stressed that the duty cycle is not the only quantity that can be used to determine the SGWB properties in the time domain. More specifically, to properly define attributes such as being continuous or generated from unresolvable signals, the *overlap function* $\mathcal{N}(f, \Delta f, z)$ introduced in [249,250] in the case of the CBC SGWB may be more suitable for this scope. In addition to this, the way an SGWB may be observed in a detector is also related to the detector sensitivity, and similar detector-depended quantities accounting for it may need to be defined when making predictions for detection [251].

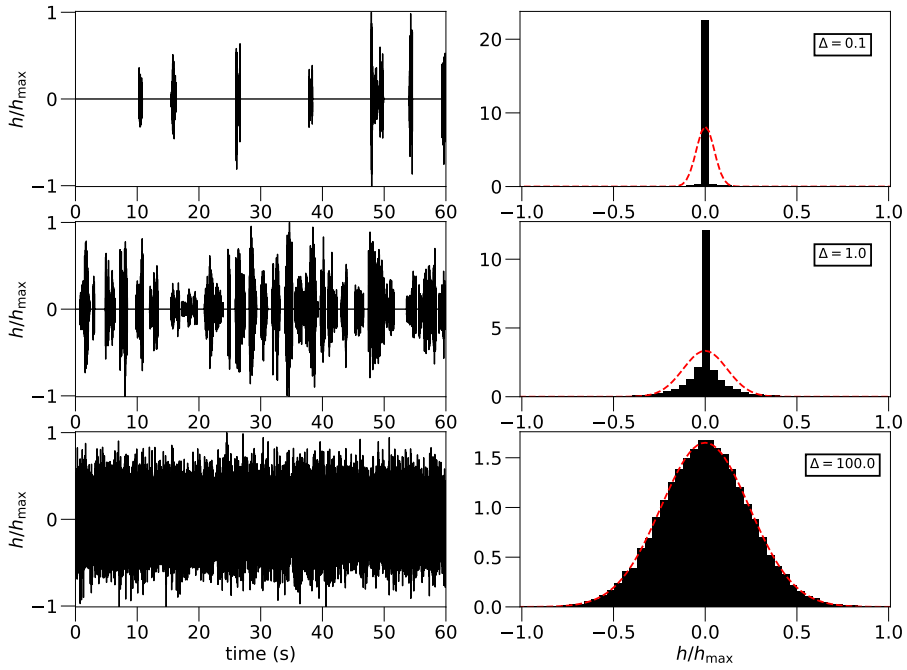

Figure 3.2: Simulated, unphysical, burst-like signals and distributions for different duty cycles $\Delta = 0.1$ (top), $\Delta = 1$ (middle), and $\Delta = 100$ (bottom). The red curves in the histograms show the best-fit Gaussian distributions to the data [`my_code`].

3.2.2 Binary coalescences

Binary coalescences may happen between many different kinds of astrophysical bodies, such as stellar mass black holes (BHs), intermediate mass black holes[13] (IMBHs), massive black holes[14] (MBHs), supermassive black holes[15] (SMBH), neutron stars (NSs), white dwarfs (WDs), and perhaps more exotic compact objects[16], which are ignored[17] in this subsection. Based on the components of the binary, a rich phenomenology arises, covering several orders of magnitudes in frequency from nHz to kHz, divided into three subsections with reference to different categories of experiments (compare with section 3.4) below.

[13] An intermediate mass black hole has mass between $10^2\ M_\odot$ and $\sim 10^4\ M_\odot$ [252].

[14] A massive black hole has a mass between $\sim 10^4\ M_\odot$ and $\sim 10^7\ M_\odot$ [252].

[15] A supermassive black hole has a mass larger than $\sim 10^7\ M_\odot$. Upper bounds on the mass limit are of the order of $\sim 10^{11}\ M_\odot$ from observations [252].

[16] Primordial-black-hole (PBH) binaries are not covered here because they are considered cosmological sources, see section 3.3.

[17] Examples of these more exotic compact objects can be boson/Proca/fermion/quark/grava- stars [253, 254].

Ground-based detectors: $[10 - 10^3]$ Hz

The detection of the first BBH (GW150914 [91]), the first BNS (GW170817 [101]) and the first BHNS (GW200105 [112]) coalescences by the LVK collaboration indirectly confirmed the existence of as many SGWBs from this kind of sources in the 10-1000 Hz band. From the list of the 90 CBC events observed in the first three LVK observing runs [93] it was possible to set constraints on the distributions of some population parameters, such as the mass distribution function, the spin distribution (for BBH), and the merger rates. The summary of these studies is presented in [247]. The most important results in terms of implications for the SGWB from CBCs come from the constraints over the redshift dependence of the merging rates[18] from a hybrid analysis considering both the detected CBCs and the existence of an SGWB in a hyperparametric Bayesian framework [257]. The phenomenological model for the rate is usually assumed to be [247, 258]

$$R(z) = \mathcal{C}(p_1,\, p_2,\, z_{\rm peak}) \frac{r_0 (1+z)^{p_1}}{1 + \left(\frac{1+z}{1+z_{\rm peak}}\right)^{p_1+p_2}}, \tag{3.2.13}$$

where $\mathcal{C}(p_1,\, p_2,\, z_{\rm peak})$ normalisation is such to recover the local rate $r_0 \equiv R(z = 0)$, and $z_{\rm peak}$ the redshift at which the rate peaks, inspired by the peak in the stellar formation rate. At $z < z_{\rm peak}$, $R(z) \sim (1+z)^{p_1}$, and p_1 can be interpreted as the κ from [247], while at $z > z_{\rm peak}$, $R(z) \sim (1+z)^{-p_2}$. Alternatively, it is possible to model the SGWB from these sources by assuming a merger rate model including the formation history of compact binaries, assuming a specific stellar formation rate [259] with a distribution of the time delays t_d between the binary formation and the merger. In the case of BBHs, the stellar formation rate is sometimes further weighted to include metallicity cuts in the birth rate of the BBH progenitors [260]. Prediction for the total CBC SGWB spectrum $\Omega_{\rm gw}(f)$ using the population studies from GWTC-3 [247] is illustrated in figure 3.1, with $\Omega_{\rm CBC}(f = 25\,{\rm Hz}) = 6.9^{+3.0}_{-2.1} \times 10^{-10}$. This SGWB is likely to be the most intense one in the 10-1000 Hz band and is expected to exhibit popcorn-like behaviour in the time domain.

LISA: $[10^{-4} - 10^{-1}]$ Hz

Most of the binary coalescence families are of interest in the LISA band, between 10^{-4} and 10^{-1} Hz. From a multi-frequency-band GW astronomy view, the SGWBs from stellar mass compact binaries (BBHs, BNSs, and NSBHs), already considered in the ground-based detector band, are present here as well but are no longer the dominant ones. Moreover, these SGWBs are now continuous and Gaussian since only the

[18] The mass distribution (unless sharply peaked) may change mildly the overall intensity of the SGWB but has minor effects on the peak position (since the SGWB depends effectively on the average of these population properties in the power-law regime), while the spin distribution has shown to have minor effects compared to the assumption of non-spinning BHs in phenomenological studies [255, 256]. Determining the rates is instead crucial to determine the overall shape and the position of the peak of the SGWB.

early inspiral phase contributes to this band. Recently, the SGWB from (stellar mass) BBHs in the LISA band has been studied in [261] and [262], which have incorporated the uncertainties in the rates and other population properties of the BBHs together with the latest constraints from the LVK [247]. The studies have found the two compatible results $h_0^2\,\Omega_{\rm BBH}(f = 3\,{\rm mHz}) \in [3.2 \times 10^{-13} - 3.2 \times 10^{-12}]$ (population synthesis models [261]) and $h_0^2\,\Omega_{\rm BBH}(f = 3\,{\rm mHz}) \in [5.65 \times 10^{-13} - 1.15 \times 10^{-12}]$ (inferred from LVK GWTC-3 [262]).

Another set of binaries that play an important role in the LISA band are the galactic WD binaries. Due to their high number and the intensity of their quasi-monochromatic, persistent GW signals in the LISA band, these binaries are expected to give rise to a *stochastic gravitational-wave foreground*[19,20] (SGWF) following the spatial distribution of the Milky Way and Gaussian. This signal, together with other galactic binary SGWFs below $\approx 3{\rm mHz}$ (e.g. WDNS and WDBH binaries), acts as an effective additional noise for LISA and will have to be subtracted to unveil the other SGWBs, especially the ones of cosmological origin. The ensemble of more uncommon binaries, such as *extreme mass-ratio inspirals* (EMRIs), *intermediate mass-ratio inspirals* (IMRIs)[21], IMBH binaries, and MBH binaries, may give rise to an SGWB related to the LISA noise curve and mission in a similar way to how the SGWB from stellar mass compact binaries is to the current generation of ground-based interferometric GW observatories [252], being intermittent and likely non-Gaussian.

PTA band: $[10^{-9} - 10^{-7}]$ Hz

The binaries of interest in the PTA band are mainly the SMBH binaries (SMBHBs), involved in the mergers of galaxies and expected to give rise to a continuous SGWB in the lower part of the frequency band. Again, this SGWB of astrophysical origin is expected to be the dominant component [263]. Its detection would validate models predicting the existence of tight SMBHBs and better understand the formation and evolution history of galaxies [264]. Recently, the major PTA consortia have announced the evidence for an SGWB in their data [263, 265–267], whose amplitude if from SMBHB origin would be $\Omega_{\rm gw}(f = 1\,{\rm yr}^{-1}) = 2.4^{+0.7}_{-0.6} \times 10^{-15}$ at 90% confidence level [263].

3.2.3 Isolated neutron stars

Isolated, rotating, non-axisymmetric neutron stars may emit GWs through different mechanisms based on the nature (pulsar, magnetar, gravitar) and age (NS modes instabilities) of the star. These different mechanisms and the corresponding SGWBs are

[19] The choice of using the term *foreground* in contrast to *background* is simply to clarify the relation between this kind of signal and the other noise sources in LISA. This kind of signal can be characterised in the same way as in the case of the SGWB.

[20] This is true also for other galactic binaries, especially below the threshold of 3 mHz [252].

[21] An EMRI and an IMRI are the inspiral phases of the coalescence between a "light" object, such as a WD, a NS, or a stellar mass BH captured by a (super)massive or intermediate mass BH [252].

considered in the original part of this thesis, presented in chapters 7 and 9, corresponding to the two works [2] and [4].

Pulsars

Neutron stars that are observed as pulsars in the radio band are known to rotate with periods down to milliseconds. They are expected to be a detectable source of GWs [268], assuming the GW emission to be due to their deviation from spherical symmetry; see section 1.5.2. Such deviation is usually encoded in the dimensionless parameter called ellipticity (defined in equation (1.5.21)). Given the quasi-monochromatic and persistent nature of the emitted GWs, the SGWB resulting from their superposition is expected to be continuous and Gaussian. A naive estimate of the frequency dependence of the SGWB comes from considering the frequency spectrum associated with the strain in equation (1.5.23), which leads to a frequency spectrum $\mathrm{d}E_{\mathrm{gw}}/\mathrm{d}f \propto f^6$, and $\Omega_{\mathrm{gw}}(f) \propto f^7$ (see chapter 7). However, the actual spectrum may deviate from a power law, given the frequency distribution of the NS population. Moreover, the unknown number of NSs in the Universe makes it difficult to get a precise estimate of the intensity of the SGWB. Nonetheless, such SGWB is expected to be dominated by the GW emission from Galactic NSs (estimated to be between $10^8 - 10^9$ [2]), providing a way to constrain the average ellipticity of such NS population, see chapter 7.

Magnetars

Magnetars are (young) NSs whose crustal magnetic field is extremely large, reaching $10^{10} - 10^{11}$ T (compared to the $\sim 10^8$ T of pulsars), and may be addressed as the source of their deformation, leading to a time-varying quadrupole moment. The magnetar rotation slows down due to the GW emission and the magnetic dipole torque. These two mechanisms both contribute to the GW energy spectrum, which, in the case where the GW emission is negligible as a spin-down mechanism, can be approximated by a power law $\mathrm{d}E_{\mathrm{gw}}/\mathrm{d}f \propto f^3$, and hence $\Omega_{\mathrm{gw}}(f) \propto f^4$ [269] (see chapter 9 for the explicit formulas). If all rotating NS (pulsar, magnetar, and gravitar[22]) emissions were dominated by GWs, the corresponding SGWB would range between $\Omega_{\mathrm{gw}}(f) \sim 10^{-8} - 10^{-7}$ in the $100 - 1000$ Hz band [250], providing an upper bound on the SGWB intensity. If instead all NS were pulsars, this would have the more pessimistic estimate $\Omega_{\mathrm{gw}}(f) \sim 10^{-13} - 10^{-10}$ in the same frequency band [250]. Restricting to magnetars only and assuming that they constitute roughly 10% of the NS population, the estimated SGWB is $\Omega_{\mathrm{gw}}(f) \sim 10^{-10} - 10^{-8}$ [270, 271], again in the $100 - 1000$ Hz band (note that these estimates are more optimistic than those in [250]). These estimates depend on many assumptions and may vary in the literature [250, 269–272]. However, for more realistic assumptions [269], detection of

[22] If a NS emitted only in the GW domain, rather than pulsar or magnetar, it should be called gravitar. However, this term in the literature is sometimes used to denote a NS that emits only in the GW band due to their low magnetic field ($< 10^{-8}$ T [245]), and is kept distinguished here.

SGWB from magnetars seems to be accessible only with third-generation ground-based detectors [116, 117]. In the absence of detection, it will still be possible to constrain several models of magnetar magnetic field configurations and equations of state, see [269] for more details.

Initial instabilities

Neutron stars can emit GWs via the normal modes (as a response of the NS to external perturbations as an elastic body). The taxonomy of the different modes is variegated (f-modes, p-modes, g-modes, r-modes, w-modes, etc.), and the literature is very rich (see [273] as a starting point). The properties of the modes, such as the GW energy spectrum and structure, may change during the existence of the NS. More specifically, the GWs associated with some of these modes can get boosted during the phases that follow the core collapse supernovae to a NS, when the neutron star is actually a proto-neutron star or very young. When it comes to implications for an SGWB, a very promising GW emission mechanism is the one from the r-mode instabilities (belonging to the more general Chandrasekhar-Friedman-Schutz instabilities [274, 275] of a rotating fluid) induced and enhanced by the rotation of a young, hot, rotating NS [276, 277]. The GW emission would make the young NS star lose most of its rotational energy in a timescale of a few years, and the associated SGWB is expected to be continuous and Gaussian [243]. The energy spectrum of the emitted GW can be approximated as a power law $\mathrm{d}E_{\mathrm{gw}}/\mathrm{d}f \propto f$, meaning $\Omega_{\mathrm{gw}}(f) \propto f^2$ [278, 279]. The predicted upper bounds on the $\Omega_{\mathrm{gw}}(f)$ from the early works [278, 279] and the most recent [280] estimate the peak to be $\Omega_{\mathrm{gw}}(f_{\mathrm{peak}}) \sim \text{few} \times 10^{-8}$, where the intensity and position of the peak depend on multiple assumptions on the parameters of the r-modes instability, together with the adopted stellar formation rate.

3.2.4 Core Collapse to Supernovae

At the end of their lives, massive stars may explode as a type II supernova [281], one of the most violent and spectacular processes in the cosmos. Based on the amount of mass ejected during the process, the collapse may end up in a new neutron star or in a black hole. The gravitational radiation released during the process may give rise to two distinguished SGWBs. The waveforms of the GWs and the resulting SGWB are usually obtained via numerical simulations. The general statement about detectability is that they are likely to be accessible to third-generation ground-based detectors.

Core collapse to neutron stars

There have been multiple studies that attempted to address the intensity of the SGWB from supernovae to NSs in the universe and in different phases of the process. This has led to different kinds of predictions for the position of the SGWB peak and its time domain behaviours. As an example, in [282], three different kinds of GW waveforms are considered from numerical relativity models of core collapse, named I, II, and

III for short. The simulations resulted in a popcorn background for I and III and a continuous SGWB for II, with I peaking around 700 Hz at $\Omega_{\rm gw}(f) \approx 3 \times 10^{-12}$, and II and III at 100 Hz and 800 Hz, respectively, with $\Omega_{\rm gw}(f) \approx 10^{-13}$. Other studies [283], which included population III stars[23] together with a delay before the actual supernova explosion and different GW waveforms, found that the signal may be enhanced and last hundreds of milliseconds below 1 Hz, resulting in a Gaussian SGWB in that range. In addition to that, in [285], both population II and III stars are considered in the picture. This results in the SGWB being dominated by supernovae from population II, and it peaked around $10^{-12} \leq h_0^2 \Omega_{\rm gw} \leq 7 \times 10^{-10}$ in the 387-850 Hz frequency band.

Core collapse to black holes

Similar to the core collapse to NSs, the SGWB from the core collapse to BHs comes in many forms and intensities, according to the model used. What is common among the studies realised in the literature is the origin of the SGWB, namely from the superposition of the ring-down modes after the BH formation. Early studies [286, 287] agree in the results when considering all the energy emitted via the $l = m = 2$ dominant quasi-normal mode of the newly born BH. The mode energy spectrum in these studies turns out to be monochromatic, depending on the mass of the BH. The resulting SGWB peak is $\Omega_{\rm gw}(f) = \epsilon \times 10^{-8}$ around 1650 Hz [286], which could be detectable by third-generation detectors for millesimal efficiencies. More recent studies [288] have assumed the energy spectrum to be rather a Gaussian distribution around the mode frequency, leading to enhanced signals even in the presence of lower efficiencies. Other studies have also included more general GW emission mechanisms, leading to $10^{-10} \leq \Omega_{\rm gw} \leq 5 \times 10^{-9}$ in the 50-1000 Hz band in [289], and $\Omega_{\rm gw} \sim 10^{-10}$ between 30 and 100 Hz in the most optimistic case in [290].

3.3 Cosmological SGWB

A cosmological stochastic gravitational-wave background is expected to rise from the superposition of GW signals sourced from phenomena in the (very) early universe. Its detection would allow probing energy scales otherwise inaccessible with other experiments [291]. When dealing with cosmological SGWB, it is important to make a further distinction, namely a primordial, *irreducible* SGWB from inflation [292] and other short-duration phenomena such as first order phase transitions (FOPTs) [293] in the first few instants of universe history, and a (cosmological) SGWB from sources formed in the early universe that are persistent and still exist today, such as cosmic

[23] Population III stars are the predicted first stars formed in the early universe and, hence, the oldest star population [284]. They are characterised by a basically null metallicity, in contrast to the (less old) low-metallicity population II stars in the centre of galaxies and galactic halos and the young, metal-rich population I stars in the arm of spiral galaxies.

strings networks [294] and primordial black holes (PBHs) [295] binaries. In the following, the main arguments about the stochasticity of this background and the master formulas for $\Omega_{\rm gw}(f)$ are sketched. Then, the main sources of primordial and cosmological SGWBs are briefly discussed. A landscape plot with examples of energy spectra for most of the considered sources is illustrated in figure 3.3. An excellent review of all these SGWBs can be found in [296].

3.3.1 Cosmological SGWB properties and spectrum

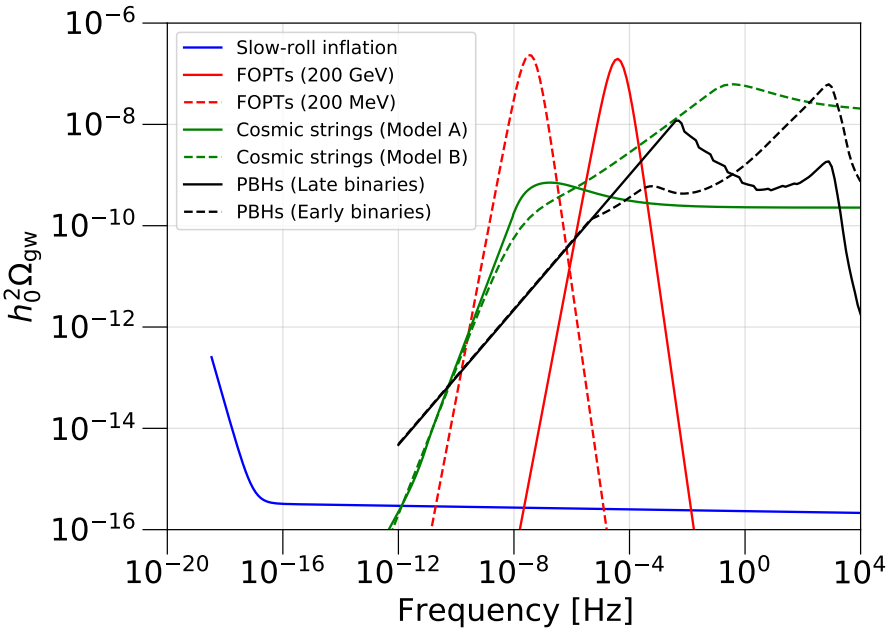

Figure 3.3: Landscape plot with some examples of cosmological SGWBs: slow-roll inflation (blue, $r_{0.05} = 0.07$, $n_T = -r_{0.05}/8$); first order phase transitions (red, $\beta/H_* = 1$, $\alpha = 1$, $v_w = 1$) at 200 GeV (solid) and 200 MeV (dashed), following case 1 from [297]; cosmic strings (green, $G\mu/c^4 = 10^{-11}$) for one cusp from model "A" [298] (solid, credits: Alex Jenkins) and model "B" [299] (dashed, credits: Christophe Ringeval [300]); and early (dashed) and late (solid) primordial black hole binaries (black, $n_s = 0.97$, $f_{\rm PBH} = 1$), following [301].

A rough estimate of the highest energy scale accessible with cosmological GWs follows by considering when the gravitational radiation decouples from the rest of the cosmic fluid elements, namely by equating the interaction rate of GWs $\Gamma(T)$ with the Hubble rate as a function of the temperature $H(T)$, yielding[24] in the radiation-

[24]Equation (3.3.1) assumes a rate $\Gamma(T) = n(T)\,\sigma(T)\,v$, with the number density of particles $n(T) \sim T^3$, cross-section $\sigma(T) \sim GT^2$, and $v = 1$, and the Hubble rate $H(T) \sim T^2/M_{\rm Planck}$.

dominated era [302] (this equation is in natural units $c = 1,\ \hbar = 1$)

$$\frac{\Gamma(T)}{H(T)} \sim \left(\frac{T}{M_{\mathrm{Planck}}}\right)^3, \tag{3.3.1}$$

where M_{Planck} denotes the Planck mass. This means that GWs provide information about energy up to the Planck scale (given current knowledge of gravity). In addition to that, thanks to gravity's intrinsic weakness, the above equation implies that GWs decouple right after they are generated and propagate freely even in the early universe. As a consequence, they carry smoking guns about the generating process and, hence, about the energy and universe epochs that would otherwise be unreachable with colliders and CMB experiments. This makes it clear why the detection of an SGWB with cosmological origin is often referred to as the "Holy Grail" of GW astronomy.

A study of the gravitational-wave propagation through the expanding Friedmann-Lemaître-Robertson-Walker (FLRW) background metric in the more general theory of cosmological perturbation [273, 303] allows to derive expressions for the 2-point correlation function (the cosmological power spectrum $\mathcal{P}_h$) as it would appear nowadays and the SGWB-related observables. Such a calculation (performed in the conformal-time space-Fourier domains and possible only numerically in most cases for persistent sources) is out of the scope of this document; see [296] for the details. However, it is still possible to deduce the general properties that a cosmological SGWB is expected to have via some simple reasoning. A powerful argument is the GW source satisfying causality. Because of that, correlations in cosmological GW signals cannot exist at length or time scales larger than the cosmological horizon at the time of the signal generation. As a consequence, the physical correlation scale of the GW must satisfy $\Delta l_* \leq c\, H_*^{-1}$, and similarly, the time correlation is at most for the interval $\Delta t_* \leq H_*^{-1}$, where the subscript "$_*$" denotes GW production time. This means that the correlation length scale today must satisfy the condition [296]

$$\frac{l_*^{(0)}}{c\, H_0^{-1}} \leq \frac{a_0}{a_* E(z_*)}, \tag{3.3.2}$$

where a_0 and a_* are the scale parameters today and at the emission time, respectively, while $E(z)$ is given in equation (3.2.8). For a (non-persistent[25]) GW source in the radiation-dominated era[26], saturating the above inequality leads to (again in natural

[25] The argument presented below is still valid for sources that continue the GW emission after formation, like in the case of a topological defect. The difference with respect to sources localised in time is that the persistent source power spectrum in frequency is broad-banded rather than narrow-banded.

[26] This allows to approximate the universe expansion as adiabatic, implying the conservation of the entropy per comoving volume [273]

$$g_S(T)\, T^3 a^3(t) = const, \tag{3.3.3}$$

where $g_S(T)$ is the effective number of entropic degrees of freedom at time t. Then, by inserting the above equation in the expression of the radiation energy density [273]

$$\rho_r(T) = \frac{\pi^2}{30}\, g_*(T)\, T^4, \tag{3.3.4}$$

units)

$$\frac{l_*^{(0)}}{H_0^{-1}} \simeq \frac{1}{\sqrt{\Omega_r}} \left(\frac{g_S(T_*)}{g_S(T_0)}\right)^{1/3} \sqrt{\frac{g_*(T_0)}{g_*(T_*)}}\, \frac{T_0}{T_*}$$
$$\simeq 1.3 \times 10^{-11} \left(\frac{100}{g_*(T_*)}\right)^{1/6} \left(\frac{1\,\mathrm{GeV}}{T_*}\right), \tag{3.3.5}$$

where the second approximated equality assumes $T_* > 0.1\,\mathrm{MeV}$, implying $g_*(T_*) = g_S(T_*)$. The above relation clearly manifests that the early-universe GW-signal correlation scale today is tiny compared to the present Hubble scale. Another argument to further corroborate and quantify this fact comes with the evaluation of the number of uncorrelated regions whose independent GW signals reach the observer today. This number can be estimated as the inverse square of the ratio between the correlation length scale at the emission time and the angular diameter distance[27] at that time $\Theta_* = l_*/d_A(z_*)$. This is just the angle subtending l_* at z_*, resulting in $\sim d_A^2(z_p)/l_* = \Theta_*^{-2}$ uncorrelated regions. For the electroweak (EW) phase transition, this number rises to $\geq 10^{24}$ regions emitting independent GW signals superimposing in the one reaching the observer today [296]. This huge number clearly justifies why the field variables $h_{ij}(t, \vec{\boldsymbol{x}})$ must be treated as a random variable[28], making a statistical treatment necessary, and why the GWB is stochastic[29]. Such statistical treatment, describing the variables and related observable quantities in terms of their ensemble average, can be applied only if the *ergodic hypothesis* holds for the observed universe, which would otherwise constitute a single realisation of the ensemble, allowing to exchange ensemble averages with spatial or temporal averages. The assumption of causality made at the beginning and the near homogeneity and isotropy of the universe are sufficient to validate such a hypothesis.

The reasons why an SGWB from the early universe can be well approximated to be Gaussian, stationary, unpolarised, and (statistically) isotropic are now briefly highlighted (see [304] for a more in-depth discussion). Gaussianity is a straightforward consequence of the above discussion about GWB stochasticity, owing to the central limit theorem given the enormous number of emitting uncorrelated regions. Stationarity follows from an evaluation of the time-correlation scales of the GW signals, which are assumed to last much longer than the duration of the observation performed by

where $g_*(T)$ is the effective number of relativistic degrees of freedom, and substituting it in equation (3.3.2), equation (3.3.5) follows.

[27] The angular diameter distance is defined as [273]

$$d_A(z) = \frac{c}{H_0(1+z)} \int_0^z \frac{\mathrm{d}z'}{E(z')}. \tag{3.3.6}$$

[28] In the case of inflation, the above discussion does not apply due to the dimensions of the causally connected regions not being smaller than the causal horizon today. However, inflation is a quantum phenomenon, and consequently $h_{ij}(t, \vec{\boldsymbol{x}})$ are really random variables.

[29] Similar arguments hold even at lower energy scales, such as the one of CMB, and it can also be claimed that stochasticity of the background holds for GW signals sourced in matter-dominated era (up to $z_p \simeq 17$) [296].

experiments (or are not accessible due to the limited resolution of the experimental apparatus). The cosmological SGWB being unpolarised is again supported by the absence of any significant source of parity violation in the observable universe[30]. Finally, statistical homogeneity and isotropy are direct consequences of the observed properties of the universe and of the FLRW spacetime used as a framework during its inflationary and thermal history[31]. Even though this description is satisfied to a good extent, it must be stressed out that there may be exceptions introducing some degree of non-Gaussianity, net polarisation, and anisotropy (mainly in gauge field excitation and interaction scenarios during inflation [296]), which may show up similarly to what happened in the CMB observational history.

To conclude this overview of cosmological SGWB, the expressions for the energy density spectral shape are presented. The derivation of these formulas is usually performed in the conformal-time and momentum space $(\eta, \vec{\boldsymbol{k}})$ by inserting the solution of the equation of motion of $h_A(\eta, \vec{\boldsymbol{k}})$ (more specifically for the *sub-Hubble modes*[32]) in the 2-point correlation functions and then deriving the related quantities in the same space [296]. The observable frequency spectra are then derived by evaluating (with some caveats, see [305]) everything today as a function of the present-day physical frequency $f = kc/(2\pi a_0)$. In the case of short-lived sources, the energy density spectrum observed today is (considering the sub-Hubble modes to be freely propagating after the emission)

$$\Omega_{\rm gw}(k) = \frac{\rho_*}{\rho_c} \left(\frac{a_*}{a_0}\right)^4 \left(\frac{1}{\rho}\frac{{\rm d}\rho_{\rm gw}}{{\rm dln}\, k}\right)\Bigg|_*, \tag{3.3.7}$$

where ρ_* is the total energy density of the universe at the emission time. In the case of short-duration sources producing GWs in the radiation-dominated era, the above equation becomes (in natural units) [296]

$$h_0^2\Omega_{\rm gw}(k) \simeq 1.6\times 10^{-5}\left(\frac{100}{g_*(T_*)}\right)^{1/3}\left(\frac{1}{\rho}\frac{{\rm d}\rho_{\rm gw}}{{\rm dln}\, k}\right)\Bigg|_*, \tag{3.3.8}$$

$$f \simeq 2.6\times 10^{-8}\,{\rm Hz}\,\frac{k}{a_*\,H_*}\left(\frac{g_*(T_*)}{100}\right)^{1/6}\frac{T_*}{\rm GeV}, \tag{3.3.9}$$

giving the amplitude of the GW spectrum and frequency as a function of temperature T_* at the emission time. The above formula shows a remarkable connection between the GW frequency today and the epoch in the early universe where the GW source was operating, which can be put in one-to-one correspondence with the frequency band of different GW experiments. In the case of persistent cosmological GW sources

[30] In addition to that, if no parity-violating source is present, the same equation of motion applies in GR when studying the propagation of GW polarisations in the FLRW spacetime.

[31] This is crucial in the case of short-lived cosmological GW sources, such as the EW phase transition. The GW emission in causally disconnected, and hence uncorrelated, regions happens at the same time exactly due to the temperature being statistically the same everywhere at that time.

[32] Sub-Hubble modes are defined by the condition $aH \ll k$ (in contrast to *super-Hubble modes*, defined by $aH \gg k$), with k the wave-vector number of the mode.

in single or multiple eras, equation (3.3.8) does not have an analytical form, resulting in multiple integrals to be numerically evaluated [305].

3.3.2 Primordial SGWB from inflation

Inflation is a model that predicts an early phase of accelerated expansion in the history of the universe. Historically, the inflationary paradigm emerged as a natural solution to some limits and open problems of the hot big bang framework, namely the *horizon*[33] and the *flatness*[34] *problems*, see [273] as an example. One of the greatest successes of inflation is to explain the origin of primordial density fluctuations that act as seeds of structure formation in the universe. These fluctuations are quantum fluctuations that get amplified during inflation to classical density perturbations [292] and reenter the Hubble radius after the inflationary period, triggering the structure formation via gravitational collapse.

The tensor modes that undergo quantum fluctuations during inflation get stretched to super-Hubble scales and reenter the horizon as a classical, yet stochastic, irreducible gravitational-wave background in the post-inflationary era [306]. The net effect of the resulting SGWB is to produce a net B-mode pattern in the CMB polarisation [307, 308]. Up to today, this prediction from inflation has not been verified yet. The observation of primordial B-modes in the CMB spectrum would be clear evidence of the inflation paradigm and would allow to rule out many of the inflationary models compatible with the data [309]. The prediction of the SGWB energy spectrum today for the standard single-field slow-roll (SFSR) inflation can be approximated [35] as [296, 310]

$$\Omega_{\rm gw}(f) = \frac{3}{128}\,\Omega_r\,\mathcal{P}_h(f)\left[\frac{1}{2}\left(\frac{f_{\rm eq}}{f}\right)^2 + \frac{16}{9}\right], \tag{3.3.10}$$

$$\mathcal{P}_h(f) = r\,\mathcal{P}_{\rm R}(f_*)\left(\frac{f}{f_*}\right)^{n_T}, \tag{3.3.11}$$

where $\mathcal{P}_h$ is the inflationary tensor perturbation power spectrum; $\mathcal{P}_{\mathcal{R}}(f_*) \simeq 2\times10^{-9}$ is the primordial curvature power spectrum evaluated at the pivot frequency $f_* =$

[33] The horizon problem is a consequence of the small anisotropies in CMB temperature even at the lowest multipoles, which correspond to angular-size regions of the order of the whole sky. This would imply that the region of the sky in causal contact must be much larger than the one evaluated in the hot big bang model, starting with a radiation-dominated phase.

[34] The flatness problem arises from the fact that, in a non-flat cosmology, an additional term $\Omega_k(1+z)^2$ appears in equation (3.2.8). This additional term is related to the *curvature* energy density, which, unless very small in the early universe, would be dominating today. This leads to fine-tuned initial conditions on Ω_k, namely the flatness problem.

[35] Equation (3.3.10) is an approximation because its derivation neglects effects such as the radiation-dominated to matter-dominated era transition not being instantaneous; ignoring other phases of universe history such as the late accelerated expansion; treating $g_*(T)$ and $g_S(T)$ as constant; free-streaming neutrinos damping the power spectrum; and more exotic scenarios, such as the presence of a stiff component in the evolution of the universe.

$k_*/(2\pi a_0)$, with $k_* = 0.05\,\mathrm{Mpc}^{-1}$; $f_{\rm eq} = H_0\Omega_m/(\pi\sqrt{2\Omega_r})$ is the frequency entering the horizon at matter-radiation equality, and r and n_t are respectively the tensor-to-scalar ratio and the spectral index that can be constrained via CMB observations. An example of such a (red-tilted, $n_T < 0$) spectrum saturating current CMB bounds is illustrated in figure 3.3. It is possible to observe that due to to its intrinsic weakness, the SGWB from inflation is very unlikely to be detectable with any experiment different from the CMB polarisation. However, there are several models and scenarios beyond the vanilla SRSF inflation that predict an enhanced or blue-tilted ($n_T > 0$) spectrum that may be accessible at higher frequencies of the GW spectrum. See [296] for a review of such mechanisms.

3.3.3 Primordial black holes

Black hole binaries may also have a non-stellar origin, in contrast to the astrophysical ones touched on in subsection 3.2.2. Their constituents, formed in the early universe, are denoted as *primordial black holes* (PBHs). The first predictions about the existence and formation mechanism of these objects were presented in the early works [295, 311–313]. Typically, PBHs appear during the radiation-dominated era, when large density inhomogeneities (generated, for example, during inflation) reenter the horizon and collapse into BH. However, a plethora of similar and alternative mechanisms exist in the literature; see [314, 315] for a comprehensive review.

Differently from their astrophysical counterparts, PBH masses can be as light as 10^{11} kg (this lower limit given from PBH with lower masses being evaporated today through Hawking's radiation), hence subsolar, and span a very broad interval covering roughly 30 orders of magnitude of masses, up to those of SMBHs. In the last couple of decades, PBHs have gained more and more interest as candidates for 1) most (or even all) the (cold) dark matter in galactic halos [316,317]; 2) possibly having already been observed in the LVK band among the known CBCs [318, 319] or hidden as subsolar binary mergers [320,321]; and 3) being seeds for the formation of SMBHs residing in galactic nuclei [322]. In addition to that, PBHs would solve multiple cosmic conundra [323], and multiple observational evidences favouring their existence are slowly emerging [324] in light of the latest constraints [325].

Concerning the SGWB from PBH binaries, it is expected to span a wide frequency band from nHz to thousands of Hz if the PBHs at formation follow a broad mass function. In recent years, it was found that the SGWB would be boosted by assuming a broad mass function from the thermal history of the universe that exhibits a major peak[36] in correspondence of solar mass PBHs [301, 323, 326], leading to comparable rates with those inferred from LVK for astrophysical BBH formed in low metallicity environment [247]. Within this framework, the SGWB intensity makes its detection and probe accessible in the near future with pulsar timing arrays, LISA, and

[36] This peak emerges naturally and corresponds to the drop in the equation of state of the universe due to the QCD phase transition. Secondary peaks about $10^{-5}\,M_\odot$ and $10^{6}\,M_\odot$ are also present, coming from the neutrino decoupling and the electroweak phase transition, see [326] for more details.

the ground-based GW interferometer network. In particular, restricting to the LVK frequency band, the spectrum $\Omega_{\rm gw}(f)$ from PBHs (illustrated in figure 3.3 for two different PBH-binary formation mechanisms) has an intensity comparable with the one from astrophysical CBC. In spite of having different spectral properties, it will be challenging to understand which one will be detected first and how to separate the two contributions. Some studies about combining spectral properties with statistical properties (duty cycle) in the time domain seem to be promising in this direction [251].

3.3.4 First order phase transitions

Phase transitions (PTs) are present everywhere in nature, among which freezing and boiling water, paramagnetic materials becoming ferromagnetic below the Curie temperature, superconductivity, and superfluidity are the most known ones. In their physical description, systems undergoing phase transitions exhibit a discontinuity at some order in the derivatives of their free energy with respect to some thermodynamic variable [327]. Less common PTs are those that have happened in the universe's thermal history, such as the electroweak (EW) and the QCD ones [328] in the standard model of particle physics. These cosmological PTs usually correspond to the appearance or change in the vacuum expectation value of a (scalar) field. If the phase transition is a first-order phase transition[37] (FOPT), a relic SGWB may likely be the only observable that remains after its occurrence. Their detection would allow to prove beyond the standard model scenarios predicting EW and QCD PT to be FOPT, together with other FOPT at higher energies [329, 330] as an alternative or unique way compared to particle colliders.

Cosmological FOPTs are identified by the presence of an energy barrier in the free energy that separates a *false*, symmetric vacuum from the *true*, symmetry-breaking vacuum, which is energetically favoured when temperature decreases. The system (the universe, or rather the field) moves from the false vacuum (favoured at temperatures above a critical one) to the true one through quantum tunnelling or thermal fluctuations. This can be pictured as a nucleation of true-vacuum bubbles expanding and filling the false-vacuum space. As they expand, the false-vacuum free energy is released, being absorbed by the accelerating expanding bubble walls or in the bulk motion of the surrounding plasma as sound waves or magnetic-hydrodynamical turbolences (MHTs). The bulk motion and the bubble collisions towards the end of the PT break spherical symmetry and release energy as GWs, as first pointed out in [293,331].

Surprisingly, the GW emission and the SGWB from a FOPT are characterised by few parameters: the temperature at the GW emission T_* (which can be approximated with the nucleation temperature T_n in absence of supercooling and reheating); the inverse time duration of the PT β (the rate of variation of the nucleation rate) and the related ratio β/H_* (which is inversely proportional to the PT strength); the phase transition strength α (namely the ratio $\rho_{\rm vacuum}/\rho_r^*$ between the vacuum energy density

[37] A first-order phase transition (such as in the case of boiling water) is characterised by a discontinuity in the first derivative free energy of the system (or rather in the potential of the order parameter).

released and the radiation energy density at the GW emission); and the fraction of vacuum energy ending in the kinetic energy of the bubble-wall collisions, sound waves and MHDs κ_i, $i = \{\mathrm{bc},\, \mathrm{sw},\, \mathrm{turb}\}$. This means that the SGWB from FOPTs can be written as the sum of three contributions

$$\Omega_{\mathrm{gw}}(f) = \Omega_{\mathrm{bc}}(f) + \Omega_{\mathrm{sw}}(f) + \Omega_{\mathrm{turb}}(f), \tag{3.3.12}$$

where the expression from a generic component $\Omega_i(f)$, and peak frequency today f_* (in natural units) scales as [296]

$$h_0^2 \Omega_i(f) \sim 1.6 \times 10^{-5} \left(\frac{100}{g_*(T_*)}\right)^{1/3} \left(\frac{H_*}{\beta}\right)^2 \left(\frac{\kappa_i\, \alpha}{1+\alpha}\right)^2, \tag{3.3.13}$$

$$f_{i,\,*} \sim 1.6 \times 10^{-5},\, \mathrm{Hz}\, \frac{\beta}{H_*} \left(\frac{g_*(T_*)}{100}\right)^{1/6} \frac{T}{100\,\mathrm{GeV}}. \tag{3.3.14}$$

The above expressions makes it clear that if the EWPT occurs about $\sim 100\,\mathrm{GeV}$ and is a FOPT (as in some scenarios beyond the standard model), the SGWB spectrum is expected to peak in the LISA frequency range for $1 \lesssim \beta/H_* \lesssim 10^5$. Similarly, a hypothetical QCD FOPT at $\sim 100, \mathrm{MeV}$, would fall in the PTA frequency range. FOPTs from more exotic physical mechanisms can also be probed by ground-based GW inteferometers; see the methods and constraints in [332, 333]. The shape of the $\Omega_i(f)$ spectra is usually approximated by a broken power law (figure 3.3), see as example [297] for the explicit expressions of the individual components.

3.3.5 Topological defects: Cosmic strings

At the end of phase transitions, topological defects (or false vacuum remnants) may be produced based on the topological properties of the vacuum manifolds[38] [294]. Different topological defects of different dimensionalities may be generated, such as the 0-d monopoles, the 1-d cosmic strings, and the 2-d domain walls [294, 334]. Such defects can be local or global, based on the spontaneously broken symmetry during the PT. A generic network of cosmological defects may emit GWs during its time evolution, given the changes in the energy-momentum tensor to maintain the scaling regime. Such continuous emission would produce an irreducible, approximately scale invariant SGWB [335]. However, such a spectrum today does not remain invariant over all frequencies[39], with the frequency associated with the present horizon scale today f_0 and at the matter-radiation equality f_{eq} being the behaviour discriminators. In fact, $\Omega_{\mathrm{gw}}(f) \propto f^3$ for $f \ll f_0$; $\Omega_{\mathrm{gw}}(f) \propto f^{-2}$ for $f > f_0$; and $\Omega_{\mathrm{gw}}(f) \approx \mathrm{const}$ for $f \gg f_{\mathrm{eq}}$ [296].

[38] From a rigorous point of view, topological defects will appear if the vacuum manifold $\mathcal{M}$ presents non-trivial homotopy group $\pi_n(\mathcal{M}) \neq \mathcal{I}$, $n = 0,\, 1,\, 2,\, 3$ [294].

[39] The scale invariance is guaranteed by the scaling regime as long as the source is emitting in the radiation-dominated era. More features are introduced at the matter-radiation equality and by the emission during the matter-dominated era; see [305, 336] for detailed calculations in the case of cosmic strings.

Cosmic strings[40] are classical objects predicted by many field theories, such as great unified theories (GUTs) in the early universe, and can also be formed at the end of inflation [337]. These one-dimensional topological defects, whether global or local, are predicted to present a scaling behaviour[41] characterised by a self-similar evolution of the number density of defects, which is conserved within the causal volume, throughout the cosmic history after their genesis [334]. In the case of a cosmic-string network, its peculiar loop structure[42] allows to emit a significantly higher amount of GWs via loop decay in the case of local cosmic strings [334], superseding the emission due to scaling. In this picture, the cosmic string network is characterised by five parameters [296, 334]: the dimensionless quantity $G\mu/c^4$, related to the string tension (in the Nambu-Goto approximation) μ; the *intercommutation* property $p(=1)$ quantifying the probability of new loop formation when strings (self)interact; the size of the cosmic string loop at birth with respect to the horizon α; the cutoff n_* in the emission spectrum (the amount of the string oscillation harmonics is limited by back-reaction); and the spectral index q of the emission spectrum. The corresponding $\Omega_{\rm gw}$ may be obtained by a mixture of analytical expression and numerical simulations; see, for example, [305, 336]. Another GW emission channel for cosmic strings, related to a non-vanilla SGWB, is the one from the GW bursts emitted during string *kinks* and *cusps* collisions in different combinations (kink-kink, kink-cusp, cusp-cusp) [338]. Kinks are shape discontinuities propagating in the strings at the speed of light, while cusps are highly boosted pieces of a loop where the string folds up [296].

The models describing cosmic-string networks and the related SGWB are variegated, and predictions about the SGWB spectral shape vary based on the combination of the assumed parameters. A similar situation exists when it comes to setting constraints on the SGWB from the cosmic-string networks and inferring string properties, with the methods and the constrained parameters changing accordingly to the experiment frequency range. In spite of this variety, what is common to find in the literature are limits expressed in terms of the string tension $G\mu/c^4$, varying between different experiments. The most stringent bound on this parameter comes from the third observing run of the LIGO-Virgo-KAGRA collaborations [340], with $G\mu/c^4 \lesssim 4 \times 10^{-15}$ for specific benchmark parameters for the models "B" (from [299]) and "C" (an interpolation between model A from [298] and model B) and the benchmark parameters considered there.

[40] The non-trivial homotopy group of the vacuum manifold necessary to give rise to the generation of cosmic strings generation after a PT is $\pi_1(\mathcal{M})$.

[41] In general, only local defects are expected to exhibit a scaling behaviour.

[42] What makes loops peculiar to strings is that they can be split into *small* and *large* loops [338, 339], having a diameter much smaller or much larger than the causal horizon. This distinction in size is not present for other cosmological defects [296].

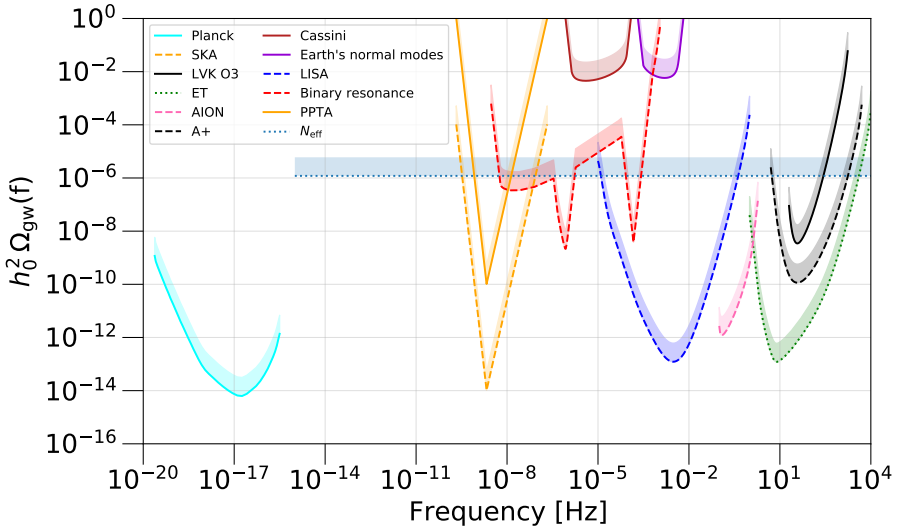

Figure 3.4: Landscape of the existing bounds (solid) and future experiment sensitivities (dashed) to and SGWB across the GW frequency spectrum at 95% confidence, inspired by [341]. The top of the shaded areas denote the SNR=5 power-integrated (PI) sensitivity curves (see section 4.3 for definitions). F.D.L. is indebted to Alex Jenkins for the PI curves of non-ground-based detectors that he used in the review [341].

3.4 Bounds on SGWB and prospects for detection

As mentioned in Prelude 0.3.1, the GW spectrum spans a wide range of frequencies, probed by a plethora of different experiments. The situation is similar for SGWB. The main bounds for a flat vanilla isotropic $\Omega_{\rm gw}$ and sensitivities from different experiments are summarised in this section and figure 3.4. For an extensive review of different kinds of SGWB, related experiments, current efforts, and future prospects, see [245, 296, 341].

3.4.1 Indirect limits

The energy density of SGWB contributes to the total radiation energy in the universe. Radiation energy can be well constrained by the precise measurement of the expansion rate from the Big Bang Nucleosynthesis (BBN) and the photon decoupling process leading to the CMB. These measurements can be easily converted into constraints on the SGWB energy density under the form of bounds on the excessive radiation energy density tolerated at those times. The limits inferred for Ω_{GW} from these measurements are usually expressed in terms of the effective number of neutrino species $N_{\rm eff}$ present in the thermal bath after the electron-positron annihilation or, equivalently, of

the number of neutrino species N_ν before the electron-positron annihilation. This is done by exploiting the conditions

$$h_0^2\,\Omega_{\rm GW} \leq h_0^2\Omega_\gamma\,\frac{7}{8}\left(\frac{4}{11}\right)^{4/3}(N_{\rm eff}-3.046) \simeq 5.6\times10^{-6}\Delta N_{\rm eff}, \tag{3.4.1}$$

$$h_0^2\,\Omega_{\rm GW} \leq h_0^2\Omega_\gamma\,\frac{7}{8}\left(\frac{g_S(T_0)}{g_S(T)}\right)^{4/3}(N_\nu-3)\,\Big|_{T=\rm MeV} \simeq 5.6\times10^{-6}\Delta N_\nu, \tag{3.4.2}$$

where $h_0^2\Omega_\gamma = 2.47\times10^{-5}$, while $g_S(T_0)\simeq 3.91$ and $g_S(T_{=}\rm MeV)\simeq 10.75$, with T_0 the photon temperature today and g_S the effective number of entropic degrees of freedom [296].

Limits on N_ν can be inferred through the BBN predictions of the primordial abundance of light elements, such as deuterium, helium, and lithium. Such abundances would differ from the observed ones if extra radiation were present at the time of BBN. However, due to the degeneracy between N_ν and the baryon-to-photon ratio η_B, better limits on N_ν can be obtained by combining the measured BBN abundances with CMB data, leading to $N_\nu < 3.2$ at 95% confidence level [342], and hence $h_0^2\,\Omega_{\rm GW} < 1.12\times10^{-6}$. This limit only applies to GWs well inside the Hubble radius at the time of BBN, meaning that it holds for frequencies $f \geq 1.5\times10^{-12}$ Hz today [296].

Similar limits on $N_{\rm eff}$ can be obtained from CMB, whose angular scales (e.g. position and amplitude of the acoustic peaks and baryon acoustic oscillations (BAOs)) would be affected by the presence of extra radiation. The implications for the GW energy density have been derived in [343] by combining the data from Planck with CMB lensing, BAOs, and deuterium abundances, yielding $h_0^2\,\Omega_{\rm GW} < 1.2\times10^{-6}$ for adiabatic initial conditions (using homogeneous initial conditions would lead to an improvement by a factor of ~ 5 [296]). These limits hold for a wider frequency range than the BBN one, estimated to be $f > 10^{-15}$ Hz by [344].

3.4.2 Cosmic Microwave Background

The cosmic microwave background can be used to set constraints on the magnitude of $\Omega_{\rm gw}(f)$ in the "Hubble-frequency" range $H_0a_0 < 2\pi f < H_{\rm eq}a_{\rm eq}$ ($3.4\times10^{-19} \lesssim f \lesssim 2.1\times10^{-17}$ Hz [296]) by using its high degree of isotropy in temperature or by measuring its B-mode polarisation. GWs are expected to induce anisotropies in CMB temperature in two ways: first, nowadays GWs with a wavelength of the order of the horizon size will produce a quadrupolar anisotropy (through the Sachs-Wolfe effect [345]); second, today observable fluctuations at smaller angular scales may be caused by GWs at the time of recombination. From CMB observations with the Planck satellite, it is possible to set a bound on the intensity of $\Omega_{\rm gw}(f)$ (see curve labelled with Planck in figure 3.4) that would have changed the observation made [142].

The measurement of B-modes in the CMB polarisation would allow probing the existence of a primordial SGWB such as the one from inflation. GWs alone would

not be capable of inducing a net polarisation in the CMB photons, affecting only their energy (hence temperature). However, due to the photon Thomson scattering at the last scattering surface, the GW passage may induce a net polarisation[43]. The decomposition of the CMB polarisation in E- and B-modes can be recast in terms of the tensor-to-scalar ratio r, which is given by the ratio of the GW power spectrum and the curvature power spectrum and can be connected with the inflaton potential [308]. However, there are several sources of noise that can mimic the GW-induced B-modes that must be taken care of, such as gravitational lensing [308] (which however mainly acts outside the $l \sim 10 - 100$ range of B-modes from GWs) and the material ("dust") present in and about the Milky Way, whose synchrotron emission contaminates the CMB B-modes[44]. Once all the noise sources have been subtracted from the CMB polarisation map, it is possible to set limits on the quantities of interest. Current upper limits from Planck CMB temperature data and baryon acoustic oscillation constrain the tensor-to-scalar ratio $r_{0.05} < 0.07$ at 95% confidence level [348]. When including the data from BICEP/Keck2018, the constraint is tightened down to $r_{0.05} < 0.032$ at 95% confidence level [349].

3.4.3 Pulsar Timing Arrays

Known pulsars are rapidly rotating neutron stars emitting radio pulses due to the misalignment of their rotation axis with respect to the magnetic field. The pulses raised by the sweeping magnetic field exhibit exceptional regularity when averaged over multiple arrival times, making pulsars extremely precise clocks. The first pulsar was discovered in 1967 [350], and the interpretation of pulsars as rapidly spinning neutron stars was presented first in [351].

Given the regularity of the pulses, it is possible to extract information if they present delays over time. Simplifying the picture, this is done by timing their arrival times, subtracting the best fit model of the arrival time, and studying the *timing residuals*. Among the possible causes of change in the time of arrival of the pulses are GWs, which could be searched over using the pulsar timing residuals, as first proposed in [352, 353] (considering the pulsar and the Earth a single interferometer arm) and refined over the years in [354–356]. However, there are many other reasons and phenomena causing the variation in the pulse time of arrival, such as the pulsar spin-down and its derivatives, the dispersion and fluctuations in the dispersion of the signal due to the interstellar medium, uncertainties in the pulsar location and proper motion, and others. All these effects must be accounted for when searching for the presence

[43] The Thomson scattering produces polarised scattered light if the incident electron radiation is not isotropic. In light of the quadrupole anisotropy in the photon distribution due to the presence of (GW) tensor modes, the Thompson-scattered photons get polarised. For more details and rigorous derivation, see, for example, [273].

[44] As an example of how subtle these effects can be, the BICEP2 experiment claimed in 2014 the measurement of primordial B-modes between $30 < l < 150$ [346]. However, these results were challenged by further joint measurements with Planck and proven to be due to galactic dust [347].

of a GW signal in pulsar timing residuals; see [357, 358] for a review of the employed methods.

Among the possible GW signals, the first one that is expected to be observed by PTAs is an SGWB dominated by astrophysical supermassive binary black holes (SMBBHs) inspiral and coalescence in the nHz frequency range [264]. PTAs can also be used to probe multiple SGWBs of cosmological origin, such as cosmic strings. For a detailed review of the astrophysics and cosmology that can be performed with PTAs, see [359]. To detect an SGWB in the nHz range, it is necessary to collect data for multiple years by monitoring as many pulsars as possible at the same time. This allows for understanding whether a common signal is present among the pulsars of the array. Given the presence of common signals from multiple effects, the presence of a higher number of pulsars is crucial to distinguish them from the GW ones whose signature is given by the Hellings and Downs (HD) curve [354] when considering correlation among different pulsar pairs[45]. Results for SGWB searches from PTAs are typically expressed in terms of a power-law power spectral density of timing residuals

$$P_{\rm PTA}(f) = \frac{S_h(f)}{12\pi^2 f^2} = \frac{A_{\rm ref}}{12\pi^2} f_{\rm ref}^{-3} \left(\frac{f}{f_{\rm ref}}\right)^{-n_{\rm PTA}}, \tag{3.4.3}$$

where usually $f_{\rm ref} = {\rm yr}^{-1}$, and $n_{\rm PTA} = 5-\alpha$, (see (3.1.11) for comparison[46]), meaning that $n_{\rm PTA} = 13/3$ for SMBBHs. A detailed description of the search methods for SGWB can be found in [360, 361].

The history of the PTA hunt for an SGWB is longer than the one with ground-based inteferometers, having started in the early 1980s, and is in a much more mature state, getting closer to the first detection. Several international collaborations have been established during the years, with the most known and senior ones being the North American Nanohertz Observatory for Gravitational Waves (NANOGrav) [133], the European Pulsar Timing Array (EPTA) [134], and the Parkes Pulsar Timing Array (PPTA). These collaborations paved the path to the current status of PTAs and have joined together under the aegis of the International Pulsar Timing Array (IPTA), whose members share the data acquired over time. This is important in order to combine the data and improve the significance of their analyses, given that NANOGrav and EPTA have access to pulsars visible only in the boreal hemisphere, while PPTA has access to those in the austral hemisphere. More recently, the Indian Pulsar Timing Array (InPTA) [136] and the future MeerKAT [139] (the SKA precursor [140]) have joined the effort in the IPTA. Moreover, outside the IPTA, important contributions to the field are made by the Chinese Pulsar Timing Array (CPTA), exploiting the world's

[45] The Hellings and Down curve quantifies the reduction in the sensitivity of the search for SGWB in PTAs due to the pulsars not being aligned in the sky and the transfer function along the pulsar-Earth arm [171, 173]. This quantity plays the same role as the *overlap reduction function* has for SGWB searches in the case of ground-based GW detectors; see section 4.2

[46] In the literature, $n_{\rm PTA}$ appears as γ, which here is already used as the exponent for the characteristic strain h_c under the power-law assumption. The relation between the two spectral indices is given by $n_{\rm PTA} = 3 - 2\gamma$.

largest "dish" radio telescope, FAST [138]. A summary of the results from the main collaboration before the 2023 data release is available in [341].

Recently, at the end of June 2023, the main PTA collaborations have separately released their data, accompanying them with relative press conferences and articles [263, 265–267]. A very important announcement was made, namely the presence of multiple lines of evidence for a stochastic signal that is correlated among the pulsars from the pulsar timing data sets collected by the different collaborations. The NANOGrav 15 yr data set paper [263] reported that the correlations of this signal follow the HD curve expected for an SGWB. The presence of an SGWB with a power-law spectrum (HD$^{n_{\rm PTA}}$) is preferred over an only independent-pulsar-noise model with a Bayes factor above 10^{14}, and it is also preferred over a common uncorrelated red noise (CURN$^{n_{\rm PTA}}$) power-law spectrum model with a Bayes factor between 200 and 1000[47,48], depending on spectral modelling choices and the number of considered frequency bins. Assuming that the signal comes from an ensemble of SMBBHs and a fiducial $f^{-2/3}$ characteristic strain (or $n_{\rm PTA} = 13/3$ in equation (3.4.3) for the timing residuals), the strain amplitude at $f_{\rm ref} = 1\,{\rm yr}^{-1}$ is $A_{\rm ref} = 2.4^{+0.7}_{-0.6} \times 10^{-15}$ (90%-confidence Bayesian interval), which is compatible with current astrophysical estimates for the SGWB from SMBBHs [359, 363]. This corresponds to a total integrated energy density $h_0^2\Omega_{\rm GW} = 4.6^{+2.8}_{-2.0} \times 10^{-9}$ in the NANOGrav sensitive frequency band[49].

However, the assumption of a more general model of the timing-residual power with $n_{\rm PTA}$ as a free parameter yields $A_{\rm ref} = 6.4^{+4.2}_{-2.7} \times 10^{-15}$ and $n_{\rm PTA} = 3.2^{+0.6}_{-0.6}$, resulting in a modest tension with $n_{\rm PTA} = 13/3$ for SMBBH SGWB[50]. Moreover, the HD quasi-quadrupolar pattern shows some indications of an additional monopolar signal (which is not preferred over a simple HD pattern only) confined in the 3.95-Hz bin, whose astrophysical or terrestrial origin (e.g. individual inspiralling SMBBH or errors in the chain of timing corrections) remains unknown [263]. This, together with the similarities in the spectral shapes of astrophysical and cosmological SGWBs in the nHz band, makes the determination of the origin of the SGWB from its spectral characterisation challenging [364]. The combination of data from the NANOGrav, EPTA, PPTA, and InPTA (and CPTA if politics allows) collaborations and future PTA observation campaigns will give more insight into this signal and shed light on its astrophysical or cosmological origin.

[47] The value of this Bayes factor is very important because it is the definitive proof that the excess in correlations in the data indeed comes from GWs. The analysis of the 12.5 yr NANOGrav data set had already found such an excess, but there was no conclusive evidence for the HD$^{n_{\rm PTA}}$ interpulsar correlation over a CURN$^{n_{\rm PTA}}$ [362].

[48] Using random phase shifts to remove interpulsar correlations from the data set and build a statistical background distribution for the latter Bayes factor, it was found a p-value equal to 10^{-3} ($\approx 3\sigma$) for the observed Bayes factor. Additionally, a frequency test statistic was built as a weighted sum of interpulsar correlations, yielding p-values equal to 5×10^{-5} ($\approx 3.5\sigma$) and 1.9×10^{-4} ($\approx 4\sigma$) [263].

[49] The official paper [263] assumes $H_0 = 70\,{\rm km\,s^{-1}\,Mpc^{-1}}$, yielding $\Omega_{\rm GW} = 9.3^{+5.8}_{-4.0} \times 10^{-9}$.

[50] Even though the estimation of $n_{\rm PTA}$ is very sensitive to the modelling of the intrinsic red noise and of the interstellar medium timing delay in a few pulsars, the preference for a value smaller than 13/3 may be attributed to astrophysical effects altering the evolution of the SMBBHs.

3.4.4 Space-Doppler Tracking

Timing techniques that are used for GW detection in pulsar timing arrays can also be employed when receiving signals from spacecrafts within the solar system. Historically, the Doppler tracking of spacecrafts for measuring GW was considered and applied even before pulsar timing. This technique was implemented also in searches for SGWB in the low frequency band between 10^{-6} and 10^{-2} Hz, by considering the Earth and the spacecraft as free test masses and attempting measuring the change in the photon frequency due to GW-induced Doppler shift between them. Multiple spacecrafts have been used throughout the years (to list some, Viking, Voyager, Pioneer 10 and 11) but the most stringent limits in the above-mentioned frequency range comes from the Doppler tracking of the Cassini satellite [127]. Using the Cassini data, it was possible to constrain $\Omega_{\rm GW} < 1$, namely $\Omega_{\rm GW} < 0.025$ ($h_0^2\Omega_{\rm GW} \lesssim 0.014$) at a frequency 1.2×10^{-6} Hz using an Hubble parameter today $H_0 = 75$ km/s/Mpc [365].

Even though this kind of measurement bridges the gap between the nHz and the mHz frequencies, which can also be probed by PTAs and future space-based interferometers, its constraints are not sufficient to make any relevant astrophysical or cosmological statement. However, promising prospects for making bounds more stringent and competitive at μHz frequencies are offered by the recently resurrected *binary resonance* method [131,132] (see the PI curve in figure 3.4) that takes advantage of ultra-precise observations of binary systems, such as the binary pulsars or the Earth-Moon system. Alternative proposals to probe the μHz frequencies come from extremely long-baseline space-based interferometers, such as the conceptualised μAres [130].

3.4.5 Space-based interferometers

Space-based interferometers allow probing frequencies below 1 Hz since they are not limited by the seismic noise affecting the ground-based ones. Currently, no space-based interferometer is in orbit, but approved plans for future ones do exist. The most advanced and known one is probably the Laser Interferometer Space Antenna (LISA). According to current plans, it will consist of three drag-free spacecrafts at the vertex of an equilateral triangle of side length 2.5×10^9 m in heliocentric orbits, 20° degrees behind Earth, and a 60° inclination with respect to the ecliptic [128]. With this configuration, it will be able to probe the $10^{-4} - 10^{-1}$ Hz band. The mission was first proposed to ESA/NASA in 1993 and approved only in 2017 by ESA, following the beyond-expectation success of the LISA Pathfinder mission in 2016 that tested LISA technologies [366]. The mission will be adopted by ESA in 2024, and the launch is foreseen for 2035, with the start of (at least) 4.5-year operations in 2037/38. Another mission, in a similar configuration but in high Earth orbit, is the TianQin [129], whose first test satellite, "TianQin-1", was launched at the end of 2019.

Differently from ground-based interferometers, the direct reflection of the laser on mirrors is not feasible because of the large distance between the spacecrafts. As a consequence, each triangle arm is composed of two lasers, in such a way that the received laser beam is locked in phase with the second laser arm and sent back to the other

spacecraft. LISA is designed in such a way to use the techniques from time-delay interferometry, meaning using virtual interferometric observables to effectively reduce the laser noise level [367], and the Sagnac calibration technique to better disentangle the cosmological isotropic SGWB from the instrumental noise [368]. LISA alone cannot perform any cross-correlation search (see chapter 4), and this is a source of complications when it comes to SGWB searches, especially those looking for anisotropies. However, if multiple space-based interferometers are in orbit (as it could be the case with LISA and TianQin), a memorandum of agreement for data sharing (similar to what happens for the ground-based detector network) would enable cross-correlation techniques and be extremely beneficial to this kind of searches.

Concerning sources and sensitivity, SGWB is one of the guaranteed GW signals to be detected and characterised with LISA. More specifically, the signal from all galactic white dwarf binaries (WDBs) will act as anisotropic stochastic gravitational-wave foreground rather than background and will have to be subtracted out of data, in a similar fashion to noise. Once subtracted, the amount of sources and SGWBs accessible to LISA is quite variegated and rich, spanning from the galactic-binary (WDWD, WDNS, NSNS, and stellar mass BHBH) inspirals and the related astropysical SGWBs, passing through extreme mass ratio (EMRI) inspirals (e.g. BHWD binaries) and (super)massive BH binaries [252] to a wide range of cosmological and primordial SGWB, such as (beyond standard model, electroweak) FOPTs, cosmic-string networks, inflation, and PBH binaries [369]. This makes it clear that the component separation of all these signals (individually resolvable ones, persistent and overlapping over time, and SGWBs) will be one of the major data analysis challenges for LISA.

Other two futuristic concepts for spacecraft constellations[51] are the DECi-hertz Inteferometer Gravitational Wave Observatory (DECIGO) [123], and the Big Bang Observer (BBO) [124] probing the 0.1-10 Hz band[52], where the BWD SGWB is absent. Both would operate through four LISA-like spacecraft constellations, two "co-located" in a "David's star" configuration, and the other two disposed ahead and behind of a $2\pi/3$ angle along the same orbit. This configuration would allow them a better angular resolution than LISA, enabling a subtraction of the compact binary foreground [371]. This would allow precise cosmology and tests of general relativity, with a dreamt sensitivity down to $\Omega_{\rm GW} \simeq 10^{-17}$ [124, 372] to detect the irreducible SGWB from inflation.

[51] For completeness, it is important to stress out that there are other proposals that aim to use atom interferometry instead of optical interferometry, such as the Atomic Gravitational-wave Interferometric Sensor AGIS and AGIS-LEO [370]

[52] This band could be accessible to the future generation of ground-based atom interferometers succeeding AION [125] and MAGIS [126]. In particular, the km-long AION proposal is expected to be sensitive down to $\Omega_{gw}(f) \approx 2.7 \times 10^{-12}$ at $f \approx 0.12$ Hz.

3.4.6 Earth, Sun, and Moon Normal Modes

An alternative method to draw bounds on SGWB in the $10^{-4} - 1$ Hz frequency band is measuring the normal modes of the Sun [373], the Earth [374], and the Moon [375]. The best constraints using Sun modes were obtained through helioseismology, leading to $\Omega_{\rm GW} < 4 \times 10^5$ at 0.171 mHz [376], and the observed Sun line of sight velocity, owing to $\Omega_{\rm GW} < 100$ at 10^{-4} Hz. The first results using Earth modes were derived using data from a network of seismometers and considering the correlations of seismometer pairs, assuming the Earth surface to be free and flat in response to GWs. This led to $\Omega_{\rm GW} < 1.2 \times 10^8$ in the $0.05 - 1$ Hz band [377]. The limits in this band were improved using data from the seismometers placed on the Moon during the Apollo mission, translating into $\Omega_{\rm GW} < 1.2 \times 10^{-5}$ between 0.1 Hz and 1 Hz [375]. These are the best upper limits in this frequency range up to now. In the 0.3-5 mHz interval, the usage of data from superconductive gravimeters allowed to take into account the internal structure of the Earth when modelling its response to GWs, making it possible to constrain $\Omega_{\rm GW}$ below unity by studying the Earth normal modes, namely $\Omega < 0.035 - 0.05$ [378]. Looking ahead towards the future, the recent proposal of a Lunar Gravitational-Wave Antenna (LGWA) [379] would allow to improve the limits in the normal-mode frequency range (0.1 mHz-1 Hz) by several orders of magnitude in partnership with LISA [128].

3.4.7 Ground-based interferometers

The ground-based interferometric detectors, presented in chapter 2, can detect SGWB in the few Hz-few kHz range, their sensitivity being ultimately limited by Newtonian noise at low frequencies and laser shot noise at high frequencies. The main candidate as dominant SGWB in this frequency range is the one from CBCs, more specifically from their inspiral phase, as can be seen by comparing figures 3.1 and 3.4, and from the detection of a high number of CBCs [247]. The SGWB from CBCs is expected to appear in the form of a shot-noise-like signal (BBH) and a popcorn-like signal (BNS) in the 20-1726 Hz range of current searches for SGWB with the second-generation LIGO-Virgo-KAGRA detector network.

The situation may change once these detectors reach their design sensitivities, and it will definitely change in the mid-late 2030s when third generation[53] ground-based interferometers such as ET [116] and the two CEs [117] will become operative. Their increased sensitivity (design, ET, CE) and frequency range (ET, down to 1-5 Hz at lower frequencies because underground) will allow them to be sensitive to the earlier, longer-lasting, phase of the inspiral, with the resulting SGWB from the superposition of the BNS signals at those frequencies being a quasi-continuous foreground. Moreover, third-generation detectors will extend the BBH detection horizon to the very

[53] As a remark, there is a proposal for a detector in between the second and third generation ones, namely the Australian NEMO (Neutron-star Extreme Matter Observatory) [380]. This observatory aims to target the high-frequency signals from tidal effects in the late stage of BNS inspirals by using very high laser power.

early time of stellar formation at $z \approx 20$ [381] and beyond [273]. This means that they will be capable of detecting almost every BBH signal with stellar origin in the Universe [382]. This will allow to perform the subtraction of the background/foreground from CBCs [246, 382–385], giving access to some other astrophysical SGWBs discussed in section 3.2 (and perhaps population III stars [246, 386]), and to the faint and elusive cosmological SGWBs down to $\Omega_{GW} = 10^{-13} - 10^{-12}$ within 5 years of observation [382–384, 387].

The current LVK detector network has been searching for an SGWB since 2004, both in isotropic (chapter 4) and anisotropic (chapter 5 and 6) cases, also including searches for non-GR polarisations (which otherwise would need a network of six detectors to be resolved for a transient signal [388], see section 5.4.2), parity violating SGWBs (section 5.4.1), and SGWB from cosmic-string network [340] and other primordial SGWBs [389]. The most recent limits for a (Gaussian, stationary, unpolarised,) isotropic SGWB with a flat energy density spectrum come from the combination of the data from the first three LVK observing runs, resulting in $h_0^2\,\Omega_{GW} \leq 7.8 \times 10^{-9}$ at 95% confidence level at a reference frequency of 25 Hz [258].

3.4.8 Very/Ultra-high-frequency experiments

The possibility of exploring the tens of kHz-THz band of the GW spectrum, possibly free from non-GW phenomena as a noise source, is indeed intriguing. This band would allow to test several exotic cosmological and pre big bang models, including beyond physics standard model and beyond GR theories, and quantum gravity, perhaps even reserving surprises for exotic astrophysical compact objects [119]. The challenges and opportunities from this unknown frequency band are illustrated in the review [120]. Among the past and more recent experiments proposals, it is worth mentioning (in the 1-100 MHz band) the Fermilab holometer [121] (two 39.2m-arm Michelson interferometers with a 0.635-m separation), the QUEST table-top double interferometers [390] (an improvement of the Fermilab holometer technology); the promising optically levitated dielectric sensors for resonant GW searches in the few KHz-300 KHz band [391]; instruments exploiting the inverse Gertsenshtein effect [392] (also known as magnetic conversion) in a broad range of frequencies above GHz [393] and THz regions [394] and its resonance due to polarisation rotation in the 100 MHz region [118], and many more ("speculative") ones [120].

For what concerns SGWB, there are some direct limits from the Fermilab holometer [121], which set 3σ limits $\Omega_{\rm GW} < 5.6 \times 10^{12}$ at 1 MHz and $\Omega_{\rm GW} < 8.4 \times 10^{15}$ at 13 MHz using 130 hours of coincident data [395]. These limits (like others from these kinds of experiments, if existing) are currently not informative, given that they do not accomplish reaching $\Omega_{\rm gw}(f) < 1$. As a consequence, the indirect bounds from the BBN and CMB data are still the best ones for this frequency range.

Chapter 4

Searching for SGWB with ground-based detectors (I): Cross-Correlation methods and Isotropic Search

"On ne voit bien qu'avec le coeur. L'essentiel est invisible pour les yeux."
Antoine de Saint-Exupéry, *Le Petit Prince*

This chapter covers the methods to search for an SGWB with ground-based interferometers, focusing on the case of a Gaussian, stationary, unpolarised, isotropic SGWB. After a brief review of the main challenges in the search for an SGWB, section 4.1 introduces the cross-correlation method and its application to a simple toy model. Then, section 4.2 introduces the interaction of the GW with the detector and defines the notion of *overlap reduction function* (ORF) for a detector pair. Following this, section 4.3 explains how to derive the optimal estimator for the GW energy density for an isotropic SGWB, employing the optimal filtering strategy when analysing the data, and how to evaluate the sensitivity of the search for a power-law energy spectrum. Eventually, section 4.4 summarises the main results from the isotropic-SGWB searches with ground-based interferometric detectors from the first LIGO scientific run to the third LIGO-Virgo-KAGRA observing run.

4.1 The search for SGWB: Cross-correlation methods

The main challenge in detecting SGWB with ground-based GW interferometers (and other experiments as well) comes from the random nature of the signal, mimicking the noise present in a single detector. However, this obstacle can be bypassed if data streams from multiple detectors are available by using cross-correlation techniques. In a nutshell, the cross-correlation method takes the one detector output as a template for the other, accounting for the geometry of the detector pair. The basic idea of using

this practice in the search for a SGWB can be found in several (early) works, such as [354, 396–399].

4.1.1 A simple toy model

Let consider the case of a single sample from two data streams $d_I(t)$, $I = 1, 2$, each containing a Gaussian signal $h(t)$ with zero mean and unknown variance S_h and a Gaussian noise $n_I(t)$ with zero mean and known variance S_{n_I}, namely[1]

$$d_1 = h + n_1, \qquad d_2 = h + n_2. \tag{4.1.1}$$

The problem to solve is to find S_h. This can be done by considering the cross-correlation of the two samples $C_{12} \equiv d_1 d_2$ and evaluating its expectation value, leading to

$$\langle C_{12} \rangle = \langle d_1 d_2 \rangle = \left\langle h^2 \right\rangle + \cancelto{0}{\langle h n_2 \rangle} + \cancelto{0}{\langle n_1 h \rangle} + \langle n_1 n_2 \rangle = \left\langle h^2 \right\rangle + \langle n_1 n_2 \rangle \tag{4.1.2}$$

since the signal h is uncorrelated with the noise n_I. As it will become clear later, the term $\langle n_1 n_2 \rangle$ is in general non-zero owing to the presence of correlated noise. However, in the following, it is assumed that two different detector noises are uncorrelated or can be neglected, and hence $\langle n_1 n_2 \rangle = 0$, meaning that the above equation becomes

$$\langle C_{12} \rangle = \left\langle h^2 \right\rangle \equiv S_h. \tag{4.1.3}$$

In this way, the common signal component has been extracted from the two data streams in the absence of cross-correlated noise[2], finding the cross-correlation to be an estimator for such a quantity. This is true in general, up to some complications that will be included step by step in this chapter.

4.1.2 Maximum-likelihood estimator

The use of cross-correlation as an estimator of S_h turns out naturally in a standard likelihood analysis for Gaussian data sets with a Gaussian template $\bar{h}$ for the stochastic signal. Within this framework, the likelihood in absence of a signal (model $\mathcal{M}_0$) reads ($d \equiv \{d_1, d_2\}$) [407]

$$p\left(d|S_{n_1},\, S_{n_2},\, \mathcal{M}_0\right) = \frac{1}{2\pi\sqrt{S_{n_1}\, S_{n_1}}}\, \exp\left[-\frac{1}{2}\left(\frac{d_1^2}{S_{n_1}} + \frac{d_2^2}{S_{n_2}}\right)\right]. \tag{4.1.4}$$

[1] The assumption of Gaussianity is not strictly necessary for this toy model, but it is fundamental in the maximum likelihood approach shown next.

[2] This is not true in general, where correlated noise, such as the one from Schumann resonances [400, 401] in the case of ground-based interferometers, is present and can impact the search for an SGWB [402–404]. In this scenario, the procedure to extract S_h from the data requires some extra steps; see as example [405, 406].

The likelihood in the presence of a signal (model $\mathcal{M}_1$) is instead

$$p\left(d|S_{n_1},\, S_{n_2},\, \bar{h},\, \mathcal{M}_1\right) = \frac{1}{2\pi\sqrt{S_{n_1}\, S_{n_1}}}\, \exp\left[-\frac{1}{2}\left(\frac{\left(d_1-\bar{h}\right)^2}{S_{n_1}} + \frac{\left(d_2-\bar{h}\right)^2}{S_{n_2}}\right)\right], \tag{4.1.5}$$

where $\bar{h}$ is assumed to be Gaussian distributed, namely

$$p\left(\bar{h}|S_h,\, \mathcal{M}_1\right) = \frac{1}{\sqrt{2\pi\, S_h}}\, \exp\left[-\frac{\bar{h}^2}{2S_h}\right]. \tag{4.1.6}$$

Given the interest in S_h rather than in $\bar{h}$ when performing searches for an SGWB, it is appropriate to marginalise the likelihood over $\bar{h}$, leading to

$$p\left(d|S_{n_1},\, S_{n_2},\, S_h,\, \mathcal{M}_1\right) = \frac{1}{\sqrt{\det\left(2\pi\, C\right)}}\, e^{-\frac{1}{2}\,\sum_{I,J} d_I \left(C^{-1}\right)_{IJ} d_J}, \tag{4.1.7}$$

where

$$C = \begin{pmatrix} S_{n_1}+S_h & S_h \\ S_h & S_{n_2}+S_h \end{pmatrix}. \tag{4.1.8}$$

Then, the maximisation of the likelihood with respect to S_h, S_{n_1}, and S_{n_2} yields the maximum-likelihood estimators

$$\hat{S}_h = d_1 d_2 = C_{12}, \quad \hat{S}_{n_1} = d_1^2 - d_1 d_2, \quad \hat{S}_{n_2} = d_2^2 - d_1 d_2. \tag{4.1.9}$$

This result is remarkable for the following, since it shows that the cross-correlation statistic C_{12} is the maximum-likelihood estimator for a Gaussian stochastic (GW) signal template with zero mean and variance S_h.

4.1.3 Extension to multiple data samples

The extension to multiple data samples $d_{Ii} = h_i + n_{Ii}$ is quite simple in the case where both the stochastic signal and the noises are white (uncorrelated in the discrete time domain) or coloured (correlated in the discrete time domain).

White noise and white signal

In this case, the likelihood for the data $d \equiv d_{1i},\, d_{2i}$ $(i = 1, \ldots N)$ is simply the product of the likelihoods (4.1.4) and (4.1.5). It is straightforward to derive the maximum likelihood estimators for this case, and they turn out to be simply the average of the

single-sample estimators over the N independent data samples[3]

$$\hat{S}_h = \frac{1}{N}\sum_{i=1}^{N} d_{1i}d_{2i}, \quad \hat{S}_{n_1} = \frac{1}{N}\sum_{i=1}^{N} d_{1i}^2 - d_{1i}d_{2i}, \quad \hat{S}_{n_2} = \frac{1}{N}\sum_{i=1}^{N} d_{2i}^2 - d_{1i}d_{2i}. \tag{4.1.11}$$

The variance of the estimator for S_h can also be derived easily, and its expression is

$$\mathrm{Var}(\hat{S}_h) = \frac{S_{n_1}S_{n_2} + (S_{n_1} + S_{n_2})\ S_h + 2S_h^2}{N}, \tag{4.1.12}$$

which in the small signal limit $S_h \ll S_{n_I}$ reduces to $\mathrm{Var}(S_h) \approx S_{n_1}S_{n_2}/N$.

Coloured noise and coloured signal

Within this framework, with the additional assumption of the data being stationary, it turns natural to work in the Fourier domain since the Fourier components are independent. It turns useful to use the one-sided noise power spectral densities $S_{n_1}(f)$, $S_{n_2}(f)$, and $S_h(f)$ [4], defined by

$$\langle \tilde{n}_I^*(f)\tilde{n}_J(f')\rangle = \frac{\delta_{IJ}}{2}\delta(f-f')\,S_{n_I}(f), \quad \left\langle \tilde{h}^*(f)\,\tilde{h}(f')\right\rangle = \frac{1}{2}\delta(f-f')\,S_h(f). \tag{4.1.14}$$

In this way, for N samples from each of the two discretely-sampled data streams $I = 1, 2$ with total duration T, the likelihood for a Gaussian stochastic signal template (over the discrete positive frequencies labelled by $k = 0, 1, \ldots, N/2-1$) reads [407]

$$p(d|S_{n_1},\, S_{n_2},\, S_h,\, \mathcal{M}_1) = \prod_{k=0}^{N/2-1} \frac{1}{\det\left[2\pi\tilde{C}(f_k)\right]}\, e^{-\frac{1}{2}\sum_{I,J}\tilde{d}_I^*(f_k)\left(\tilde{C}(f_k)^{-1}\right)_{IJ}\tilde{d}_J(f_k)}, \tag{4.1.15}$$

where

$$\tilde{C}(f) = \frac{T}{4}\begin{pmatrix} S_{n_1}(f) + S_h(f) & S_h(f) \\ S_h(f) & S_{n_2} + S_h(f) \end{pmatrix}. \tag{4.1.16}$$

[3] If instead the noise variances S_{n_1} and S_{n_2} were known parameters, the maximum likelihood estimator for S_h would include auto-correlation terms for each data stream:

$$\hat{S_h} = \frac{1}{(S_{n_1}+S_{n_2})^2}\left[2S_{n_1}S_{n_2}\frac{1}{N}\sum_{i=1}^{N} d_{1i}d_{2i} + S_{n_2}\left(\frac{1}{N}\sum_{i=1}^{N} d_{1i}^2 - S_{n_1} + S_{n_1}\left(\frac{1}{N}\sum_{i=1}^{N} d_{2i}^2 - S_{n_2}\right)\right)\right]. \tag{4.1.10}$$

[4] Note that, owing to Parseval's theorem [239], the signal power spectral density is related to the time domain variance $\mathrm{Var}(h) \equiv S_h$ by

$$\mathrm{Var}(h) = \int_0^\infty \mathrm{d}f\, S_h(f). \tag{4.1.13}$$

The derivation of the maximum likelihood estimator for S_h is discussed in section 4.3 when searches for isotropic SGWBs with ground-based interferometers are discussed.

4.1.4 Detection statistic

Even though nowadays most SGWB searches are performed within Bayesian formalism (or hybrid frequentist-Bayesian approach, which is equivalent to the full Bayesian in the case of ground-based interferometers [408]), it is instructive to introduce the maximum-likelihood detection statistic[5] associated with the case of N samples of data with uncorrelated white noise and a common white stochastic signal. In the present case, the calculation leads to the result

$$\Lambda_{\rm ML}(d) = \left[1 - \frac{\hat{S}_h^2}{\hat{S}_1 \hat{S}_2}\right]^{-N/2}, \tag{4.1.18}$$

where

$$\hat{S}_1 \equiv \frac{1}{N}\sum_{i=1}^{N} d_{1i}^2 = \hat{S}_h + \hat{S}_{n_1}, \qquad \hat{S}_2 \equiv \frac{1}{N}\sum_{i=1}^{N} d_{2i}^2 = \hat{S}_h + \hat{S}_{n_2} \tag{4.1.19}$$

are the maximum-likelihood estimators of the combined variances[6] $S_1 \equiv S_h + S_{n_1}$ and $S_2 \equiv S_h + S_{n_2}$.

For a comparison with the Bayesian approach, it is suitable to define a frequency $\Lambda(d)$ as twice the logarithm of $\Lambda_{\rm ML}(d)$ [409], namely

$$\Lambda(d) \equiv 2\ln\left(\Lambda_{\rm ML}(d)\right) = -N\ln\left(1 - \frac{\hat{S}_h^2}{\hat{S}_1\hat{S}_2}\right). \tag{4.1.20}$$

In the case of ground-based GW interferometers, where the *small-signal* regime $S_h \ll S_{n_I}$ holds, the above expression noticeably simplifies to

$$\Lambda(d) \approx \frac{\hat{S}_h^2}{\hat{S}_1\hat{S}_2/N} \simeq \frac{\hat{S}_h^2}{\hat{S}_{n_1}\hat{S}_{n_2}/N}. \tag{4.1.21}$$

As it will become clearer in section 4.3, this is just the square of the signal-to-noise ratio (SNR), which plays an important role in understanding whether there is any excess in the data that could be a signal. In addition to that, the detection statistic

[5] In the case of a frequentist statistic approach, the maximum-likelihood detection statistic is defined through the *maximum-likelihood ratio* [239]

$$\Lambda_{\rm ML}(d) = \frac{\max_{\{S_{n_1}, S_{n_2}, S_h\}}\left[p\left(d|S_{n_1}, S_{n_2}, S_h\right)\right]}{\max_{\{S_{n_1}, S_{n_2}\}}\left[p\left(d|S_{n_1}, S_{n_2}\right)\right]} \tag{4.1.17}$$

[6] Note that these estimators depend only on auto-correlated data for each data stream. Hence, in the absence of a signal, they reduce to the maximum-likelihood estimators for the noise variances S_{n_1} and S_{n_2}.

is also related to the *coherence* $\hat{S}_h^2/(\hat{S}_{n_1}\hat{S}_{n_2})$, the normalised cross-correlation of the data from two data streams measuring how well the two data streams match each other.

4.2 Including the GW interaction with the detector

The previous section should have clarified how to measure a common stochastic signal in two stochastic temporal series. However, in the case of SGWB and data from ground-based GW interferometers, the situation is more complex than the one reported previously. The different layers of complexity are presented in the following sections and chapters, starting here with the non-trivial interaction between the SGWB signal and the detectors.

4.2.1 Antenna patterns and detector tensor

The discussion of the response of a Michelson interferometer to the GW passage has already been discussed in detail in section 2.1. Here, the general problem and main results are presented from the SGWB perspective.

Given the weakness of a GW signal $h_{ij}(t, \vec{\boldsymbol{x}})$, the resulting strain $h(t)$ in a detector located at $\vec{\boldsymbol{x}}$ at time t can be approximated to be linear in $h_{ij}(t, \vec{\boldsymbol{x}})$, and described as its convolution with the detector impulse response $F^{ij}(t, \vec{\boldsymbol{x}})$

$$h(t) = (\mathbf{R} * \mathbf{h})\,(t,\, \vec{\boldsymbol{x}}) \equiv \int_{-\infty}^{\infty} \mathrm{d}t' \int \mathrm{d}^3\hat{\boldsymbol{x}}'\, F^{ij}(t',\, \vec{\boldsymbol{x}}')\, h_{ij}(t - t',\, \vec{\boldsymbol{x}} - \vec{\boldsymbol{x}}'). \quad (4.2.1)$$

To recover the framework used in section 2.1, it is sufficient to perform the plane-wave expansion in the above equation and take the Fourier transform of the strain

$$\tilde{h}(f) = \int_{\mathcal{S}^2} \mathrm{d}^2\hat{\boldsymbol{n}}\, F^{ij}(f, \hat{\boldsymbol{n}})\, h_{ij}(f, \hat{\boldsymbol{n}}), \quad (4.2.2)$$

where

$$F^{ij}(f, \hat{\boldsymbol{n}}) = e^{-2\pi i f \hat{\boldsymbol{n}}\cdot\vec{\boldsymbol{x}}/c} \int_{-\infty}^{\infty} \mathrm{d}t' \int \mathrm{d}^3\hat{\boldsymbol{x}}'\, F^{ij}(t',\, \vec{\boldsymbol{x}}') e^{2\pi i f \hat{\boldsymbol{n}}\cdot\vec{\boldsymbol{x}}'/c}. \quad (4.2.3)$$

The explicit expression for a Michelson interferometer strain response F^{ij}_{strain} follows by multiplying equation (2.1.19)[7] by the phase in front of the integral from the above equation, setting $t = 0$, and observing $\hat{\boldsymbol{k}} = -\hat{\boldsymbol{n}}$.

Keeping in mind the non-trivial response of the detectors, the expectation value of the cross-correlation $C_{IJ}(t, t')$ of two detector data streams strains $d_I(t) = h_I(t) +$

[7] Note that the definition of $F^{ij}(f, \hat{\boldsymbol{n}})$ in equation (2.1.19) corresponds to the one for $\bar{F}^{ij}(f,\, \hat{\boldsymbol{n}})$ used in [239]. The change of notation in this and the following chapters is made to obtain a more compact notation when discussing geometrical factors.

$n_I(t)$ and $d_J(t') = h_J(t') + n_J(t')$ in the absence of correlated noise and for a Gaussian, unpolarised, stationary, isotropic SGWB reads

$$\langle C_{IJ}(t,t')\rangle = \langle h_I(t)\, h_J(t')\rangle = \frac{1}{2}\int_{-\infty}^{\infty} \mathrm{d}f\, e^{-2\pi i\, f(t-t')}\Gamma_{IJ}(f)\, S_h(f). \quad (4.2.4)$$

In the above formula, S_h is the one-sided strain spectral density from the expectation values of the Fourier components of the plane-wave expansion presented in equation (3.1.5), while the geometrical factor $\Gamma_{IJ}(f)$ is called the (isotropic) *overlap reduction function* (ORF) [398, 399] for the two detectors I, J.

4.2.2 Overlap reduction function

The overlap reduction function encodes the non-trivial response of the detector pair to the SGWB due to detectors relative separation and orientation, and hence the consequent reduction in sensitivity when performing an SGWB cross-correlation search. Its meaning can be better understood by considering the frequency-domain version of equation (4.2.4)

$$\left\langle \tilde{h}_I^*(f)\, \tilde{h}_J(f')\right\rangle = \frac{1}{2}\delta(f-f')\,\Gamma_{IJ}(f)\, S_h(f), \quad (4.2.5)$$

implying

$$\tilde{C}_{IJ}(f) = \Gamma_{IJ}(f)\, S_h(f), \quad (4.2.6)$$

with $\tilde{C}_{IJ}(f)$ the two-detectors response one-sided cross-spectral density. As a consequence, the ORF can also be interpreted as the transfer function from the SGWB strain spectral density $S_h(f)$ to the detector-pair cross spectral density $\tilde{C}_{IJ}(f)$.

ORF normalisation

The expression of the ORF in equations (4.2.4) and (4.2.5) is usually written in terms of the polarisation-basis response functions $F^A_{IJ}(f, \hat{\boldsymbol{n}})$ from equation (2.1.20)[8] as

$$\Gamma_{IJ}(f) \equiv \frac{1}{8\pi}\sum_{A=+,\times}\int_{\mathcal{S}_2} \mathrm{d}^2\Omega_{\hat{\boldsymbol{n}}}\, F_I^{A\,*}(f,\hat{\boldsymbol{n}})\, F_J^A(f,\hat{\boldsymbol{n}}). \quad (4.2.7)$$

In the case where a single detector is considered, the above expression appears in its auto-correlated response spectral density

$$P_I(f) \equiv \tilde{C}_{II}(f) = \Gamma_{II} S_h(f), \quad (4.2.8)$$

[8] Note that what is written for equation (4.2.3) in relation to (2.1.19) holds here as well.

and assumes the form

$$\Gamma_{II}(f) \equiv \frac{1}{8\pi} \sum_{A=+,\times} \int_{\mathcal{S}_2} \mathrm{d}^2\Omega_{\hat{\boldsymbol{n}}} \left| F_I^A(f, \hat{\boldsymbol{n}}) \right|^2, \tag{4.2.9}$$

which is just the squared modulus of the antenna pattern for the detector response to an unpolarised GW averaged over the whole sky and GW polarisations.

It turns out that it is often useful to use a normalised version of the (isotropic) ORF, denoted by $\gamma_{IJ}(f)$. The normalised expression can be obtained by requiring $\gamma_{IJ}(0) = 1$ for two co-aligned and co-located interferometric detectors. In the case of two equal-arm Michelson interferometers, the fulfilment of this requirement leads to the scaling relation [239]

$$\gamma_{IJ}(f) = \frac{5}{\sin^2\beta} \Gamma_{IJ}(f), \tag{4.2.10}$$

where β is the angle between the interferometer arms.

The small antenna limit

The ORF as written in (4.2.7) depends on four length scales, namely the arm lengths L_I and L_J of the two detectors through the response functions; the distance between the two detectors $s \equiv |\vec{\boldsymbol{x}}_I - \vec{\boldsymbol{x}}_J|$ in the exponential factor; and the GW wavelength $\lambda_{\mathrm{gw}} = c/f_{\mathrm{gw}}$. The solid-angle integral in the ORF equation (4.2.7) must be evaluated numerically in general. However, as seen in chapter 2, for ground-based interferometers, it is possible to use the *small-antenna limit* $fL_I/c \ll 1$ to obtain an analytical formula of the (unnormalised) ORF in terms of Bessel functions (this procedure was first performed in [399] and then, due to the presence of a typographical error, corrected in [410]).

In the small-antenna limit, the strain response function (2.1.19) simplifies to

$$F_I^A(f, \hat{\boldsymbol{n}}) \approx D_I^{ij}\, e_{ij}(\hat{\boldsymbol{n}})\, e^{-2\pi i f \hat{\boldsymbol{n}}\cdot\vec{\boldsymbol{x}}_I/c}, \qquad D_I^{ij} = \frac{1}{2}\left(u_I \otimes u_I - v_I \otimes v_I\right)^{ij}, \tag{4.2.11}$$

where $\vec{\boldsymbol{x}}_I$ identifies the detector I vertex[9] in the system of coordinates in appendix A. In this way, the (isotropic) ORF can be rewritten as

$$\Gamma_{IJ}(f) = D_I^{ij}\, D_J^{kl}\, \Gamma_{ijkl}\left(\Delta\vec{\boldsymbol{x}}\right), \tag{4.2.12}$$

[9] Note that here the position of detectors is assumed to be independent of time. This fact is not true due to the Earth's rotation and orbit, leading to a modulation in the GW signal amplitude and phase. While the effects of the motion can be neglected when considering the ORF in a search for isotropic SGWB (due to the integration over the whole sky and the broad-band nature of the signal), they must be accounted for in searches for anisotropic SGWB.

where Γ_{ijkl} is defined to be

$$\Gamma_{ijkl}\left(\Delta\vec{\boldsymbol{x}}\right) \equiv \sum_{A=+,\times} \int_{\mathcal{S}_2} \mathrm{d}^2\Omega_{\hat{\boldsymbol{n}}}\, e^A_{ij}\left(\hat{\boldsymbol{n}}\right)\, e^A_{kl}\left(\hat{\boldsymbol{n}}\right)\, e^{2\pi i f\, \frac{\Delta\vec{\boldsymbol{x}}\cdot\hat{\boldsymbol{n}}}{c}}, \tag{4.2.13}$$

with $\Delta\vec{\boldsymbol{x}} = \Delta\vec{\boldsymbol{x}}_{IJ} \equiv \vec{\boldsymbol{x}}_I - \vec{\boldsymbol{x}}_J$ the separation vector connecting the detector pair vertices. The above expression shows that, in the small-antenna limit, the dependence of the ORF on the orientation is encoded in the detector tensors D^{ij}_I, $I = 1, 2$, while the dependence on the separation is contained in Γ_{ijkl}. Due to the detector tensors being symmetric and trace-less with respect to the ij indexes, the Γ_{ijkl} inherits the traits of being symmetric under the index exchanges $i \leftrightarrow j$, $k \leftrightarrow l$, $ij \leftrightarrow kl$, and being trace-less with respect to the ij and kl pairs.

By exploiting the symmetry properties of Γ_{ijkl}, its most general expression turns out to be

$$\begin{aligned}\Gamma_{ijkl}\left(\Delta\vec{\boldsymbol{x}}\right) =& A\left(\alpha\right)\delta_{ij}\delta_{kl} + B\left(\alpha\right)\left(\delta_{ik}\delta_{jl} + \delta_{il}\delta_{jk}\right) + C\left(\alpha\right)\left(\delta_{ij}s_k s_l + \delta_{kl}s_i s_j\right) + \\ & D\left(\alpha\right)\left(\delta_{ik}s_j s_l + \delta_{il}s_j s_k + \delta_{jk}s_i s_l + \delta_{jl}s_i s_k\right) + E\left(\alpha\right) s_i s_j s_k s_l,\end{aligned} \tag{4.2.14}$$

where

$$\alpha = \frac{2\pi\, f\, s}{c}, \qquad s \equiv |\Delta\vec{\boldsymbol{x}}|, \qquad \hat{s} \equiv \frac{\Delta\vec{\boldsymbol{x}}}{|\Delta\vec{\boldsymbol{x}}|}. \tag{4.2.15}$$

Then, the contraction of equation (4.2.14) for Γ_{ijkl} with the tensor combinations $\delta^{ij}\delta^{kl}$, $(\delta_{ik}\,\delta_{jl} + \delta_{il}\,\delta_{jk})$, …, $s_i\, s_j\, s_k\, s_l$, yields a linear system in the coefficients A, B, …, E. This system is solvable in terms of scalar integrals involving the contraction of the polarisation tensor product $e^A_{ij}(\hat{\boldsymbol{n}})\, e^A_{kl}(\hat{\boldsymbol{n}})$ with the combinations of d^{ij} and s^i. The analytic evaluation of these integrals leads to (see [410] for more details about the whole calculation)

$$\begin{pmatrix} A\left(\alpha\right) \\ B\left(\alpha\right) \\ C\left(\alpha\right) \\ D\left(\alpha\right) \\ E\left(\alpha\right) \end{pmatrix} = \frac{1}{2\alpha^2} \begin{pmatrix} -5\alpha^2 & 10\alpha & 5 \\ 5\alpha^2 & -10\alpha & 5 \\ 5\alpha^2 & -10\alpha & -25 \\ -5\alpha^2 & 20\alpha & -25 \\ 5\alpha^2 & -50\alpha & 175 \end{pmatrix} \begin{pmatrix} j_0\left(\alpha\right) \\ j_1\left(\alpha\right) \\ j_2\left(\alpha\right), \end{pmatrix} \tag{4.2.16}$$

where $j_0(\alpha)$, $j_1(\alpha)$, and $j_2(\alpha)$ denote the spherical Bessel functions [411]. Finally, by contracting Γ_{ijkl} with the detector tensors, one obtains the analytical formula for the ORF $\Gamma_{IJ}(f)$ in the small-antenna limit, namely:

$$\begin{aligned}\Gamma_{IJ}(f) =& A\left(\alpha\right)\mathrm{Tr}\left(D_I\right)\mathrm{Tr}\left(D_J\right) + 2B\left(\alpha\right) D^{ij}_I D_{Jij} + \\ & C\left(\alpha\right)\left[\mathrm{Tr}\left(D_J\right) D^{ij}_I + \mathrm{Tr}\left(D_I\right) D^{ij}_J\right] s_i s_j + \\ & 4D\left(\alpha\right) D^{ij}_I D_{Ji}{}^{k} s_j s_k + E\left(\alpha\right)\, D^{ij}_J\, D^{kl}_J s_i s_j s_k s_l.\end{aligned} \tag{4.2.17}$$

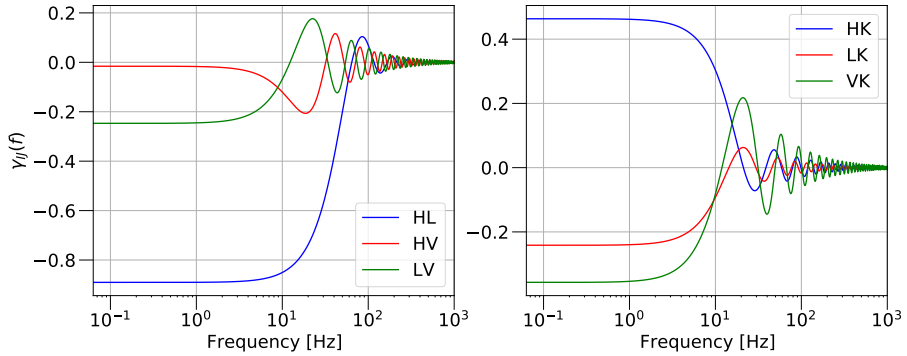

Figure 4.1: Overlap reduction functions for the HLVK detector network, realised with [`my_code`].

It is important to remark that this expression has been obtained solely by using the symmetry properties of Γ_{ijkl} and the detector tensors. By using from the beginning the fact that the detector tensors are trace-less, it would not have been necessary to derive the expressions of $A(\alpha)$ and $C(\alpha)$ since they multiply terms that are zero in this case.

Plots of the normalised ORFs for the strain response of the present detector pairs belonging to the IGWN network are illustrated in figure 4.1. As an example, by considering the ORF of the LIGO Hanford-LIGO Livingston (HL) pair, it is possible to note that the HL ORF is negative at $f = 0$ Hz, due to the relative $90°$ rotation between the two detectors, and with a magnitude less than unity, $|\gamma_{HL}(0)| = 0.89$, due to the $27.2°$ separation between the two detector planes as seen from the centre of the Earth. As a last remark, the first zero of the ORF is around 60 Hz, slightly above $c/(2s) = 50$ Hz, with $s = 3000$ km the distance between the two sites,which corresponds to a GW with a wavelength twice the separation of the two interferometers. From this observation and the sign oscillations of the ORF around its zeroes, it becomes evident that such zeroes represent the transitions between the in- and out-of-phase excitations of the two interferometric detectors.

4.3 Isotropic search

4.3.1 Matched filtering: Some simple examples

The technique of matched filtering is widely used in GW astronomy when analysing data. In the case of SGWB searches, filtering is used in one of its simplest forms, namely to maximise some quantity of interest. Some examples are the detection probability given a fixed false alarm rate; the signal-to-noise ratio referred to some test statistic; or the minimal variance, unbiased estimator of some quantity. Before

proceeding with a direct application of the matched filtering technique for stochastic searches, it is instructive to consider multiple toy models for deterministic signals.

Combining a set of independent measurements

Suppose one has a set of N independent measurements

$$d_i = \theta + n_i, \qquad i = 1, 2, \ldots, N, \tag{4.3.1}$$

where θ is some parameter to be estimated, while n_i are the independent noise terms. For a zero-mean noise with known variance σ_i^2, it is easy to show that $\langle d_i \rangle = \theta$ and $\mathrm{Var}(d_i) = \sigma_i^2$. The goal is to find an estimator $\hat{\theta}$ for θ that is unbiased (meaning $\langle \hat{\theta} \rangle = \theta$) and with minimal variance $\mathrm{Var}(\hat{\theta}) \equiv \sigma_{\hat{\theta}}^2$. This translates into the optimisation problem for the coefficients c_i (the "filters") of the linear combination

$$\hat{\theta} \equiv \sum c_i d_i, \tag{4.3.2}$$

such that (unbiased)

$$\sum_i c_i = 1, \tag{4.3.3}$$

and (minimal variance)

$$\sigma_{\hat{\theta}}^2 = \min_{\{c_i\}} \left[\sum_i c_i^2 \sigma_i^2 \right]. \tag{4.3.4}$$

This is a standard optimisation problem that can be solved by means of the Lagrange multipliers method. The solution for the "filters" c_i is

$$c_i = \frac{\sigma_i^{-2}}{\sum_j \sigma_j^{-2}}, \tag{4.3.5}$$

implying[10]

$$\hat{\theta} = \frac{\sum_i d_i \sigma_i^{-2}}{\sum_j \sigma_j^{-2}}, \tag{4.3.8}$$

$$\sigma^2_{\hat{\theta}} = \frac{1}{\sum_j \sigma_j^{-2}}. \tag{4.3.9}$$

The above expression is a weighted average, where "less noisy" measurements (with smaller variance σ_i^2) have major weights.

Combining correlated measurements

If the N measurements d_i are instead correlated, the covariance matrix is no longer diagonal, having elements

$$\Sigma_{ij} \equiv \langle d_i d_j \rangle - \langle d_i \rangle \langle d_j \rangle . \tag{4.3.10}$$

The procedure to optimise the linear combination (4.3.2) is then the same, with the difference that the condition on the variance now reads[11]

$$\sigma^2_{\hat{a}} = \min_{\{c_i\}} \left[\sum_{i,\,j} c_i c_j \Sigma^2_{ij} \right] . \tag{4.3.11}$$

The solution to the optimisation problem is then the optimal estimator

$$\hat{\theta} = \frac{\sum_{i,\,j} d_i \left(\Sigma\right)^{-1}_{ij}}{\sum_{k,\,l} \left(\Sigma\right)^{-1}_{kl}}, \tag{4.3.12}$$

where the weights $\sum_j (\Sigma^{-1})_{ij}$ replace the σ_i^2 one from the independent measurements case.

[10] This results can also be reached through a maximum-likelihood approach for independent, Gaussian distributed noise n_i, with likelihood function

$$p\left(d|\theta; \{\sigma_i^2\}\right) = \prod_i \frac{1}{\sqrt{2\pi\sigma_i^2}} \exp\left[\frac{1}{2}\,\frac{(d_i-\theta)^2}{2\sigma_i^2}\right]. \tag{4.3.6}$$

The expressions for $\hat{\theta}$ and $\sigma^2_{\hat{\theta}}$ in the main text follow by maximising the above likelihood with respect to the parameter θ, yielding

$$p\left(d|\theta; \{\sigma_i^2\}\right) \propto \exp\left[-\frac{1}{2}\,\frac{(\hat{\theta}-\theta)^2}{2\sigma^2_{\hat{\theta}}}\right]. \tag{4.3.7}$$

[11] In practice, when it comes to stochastic searches, where noise is coloured and data are correlated in the time domain, this formula is actually not necessary. In fact, when passing to the frequency domain, the values for different frequency bins are uncorrelated (assuming the process to be stationary and random). This is a consequence of the Fourier transform acting as a rotation in the data space to a basis where the covariance matrix is diagonal. This is called the *Karhunen-Loeve* transformation [412], and is one of the reasons why signal processing is mostly performed in the frequency domain.

Toy model for a GW signal

The simplest model for a GW signal for a set of independent measurements is assuming that the signal is not simply characterised by a constant parameter θ but also has a "form" h_i such that

$$d_i = \theta\, h_i + n_i, \qquad i = 1, 2, \ldots, N. \tag{4.3.13}$$

The mean $\langle d_i \rangle = \theta\, h_i$ is no longer a constant, introducing an additional layer of complications. However, the compatibility with the framework for independent measurements with a constant signal can easily be recovered by setting

$$\bar{d}_i \equiv d_i / h_i, \tag{4.3.14}$$

and now

$$\left\langle \bar{d}_i \right\rangle = \theta, \qquad \mathrm{Var}(\bar{d}_i) \equiv \bar{\sigma}_i^2 = \sigma_i^2 / h_i^2. \tag{4.3.15}$$

The solution for the optimal estimator immediately follows as

$$\hat{\theta} = \frac{\sum_i \bar{d}_i \bar{\sigma}_i^{-2}}{\sum_j \bar{\sigma}_j^{-2}} = \frac{\sum_i h_i d_i \sigma_i^{-2}}{\sum_j h_i^2 \sigma_j^{-2}}. \tag{4.3.16}$$

The above expression can be found in the literature with the name of *matched filter* [413], since data d_i are projected onto the expected signal profile h_i and weighted with the inverse of the noise variance σ_i^2. The *optimal filter* Q_i for the analysis is encoded in the weight multiplying d_i, namely

$$Q_i \equiv h_i \sigma_i^{-2}. \tag{4.3.17}$$

In the presence of multiple templates h_i, normalised so that $\sum_i h_i^2/\sigma_i^2 = 1$, the signal-to-noise ratio (or its square)

$$\hat{\rho}(h) \equiv \sum_i d_i Q_i \tag{4.3.18}$$

can be used as a detection statistic (and is already maximised by the choice of the optimal filter). If the maximum SNR for a specific template h_i exceeds a threshold ρ_* (with a low enough false-alarm probability), then it is possible to claim the detection of a signal with a profile h_i corresponding to the maximum matched-filter SNR.

4.3.2 Matched filtering: Search for isotropic SGWB

The matched filtering can be adapted for the purpose of searching for a Gaussian, unpolarised, stationary, isotropic SGWB with strain spectral density $S_h(f)$, defined in equation (3.1.5), with a detector pair I, J. The toy model in section 4.1 tacitly

assumes that the two detectors are equal, co-located, and co-aligned, and that the cross-correlation is evaluated at time t.

In the case where this is not true, given an observation time T, the cross-correlation statistic can be defined as an integrated quantity over times[12]

$$\begin{aligned} C_{IJ} &\equiv \int_{-T/2}^{T/2} \mathrm{d}t \int_{-T/2}^{T/2} \mathrm{d}t'\, s_I(t) s_J(t') Q(t,t') \\ &\equiv \int_{-T/2}^{T/2} \mathrm{d}t \int_{-T/2}^{T/2} \mathrm{d}t'\, C_{IJ}(t,t') Q(t,t'), \end{aligned} \tag{4.3.20}$$

where the second integral in time takes into account the time delay, and $Q(t,t')$ is the filter function to be made optimal[13]. In the following, the expression of the optimal filtering is first derived in the *small-signal limit*, where the signal strain spectral density is much smaller than the detector noise power spectral densities, namely $S_h(f) \ll P_{n_I}(f), P_{n_I}(f)$, and then in the general case.

Before passing to the frequency domain, it is useful to observe two points. First, due to the SGWB being stationary in time, the filter $Q(t,t')$ can depend only on a time difference $t-t'$, and hence $Q(t,t') = Q(t-t')$. In this way, the filter is expected to fall off rapidly to zero for time delays $\Delta t = t - t' > d/c$, where d/c is the light time-travel between the two detector vertices. Second, given an observation time $T \gg d/c$, one of the two integral limits in equation (4.3.20) can be changed to get

$$C_{IJ} = \int_{-T/2}^{T/2} \mathrm{d}t \int_{-\infty}^{\infty} \mathrm{d}t'\, s_I(t) s_J(t') Q(t-t'). \tag{4.3.21}$$

Then, passing to the frequency domain

$$\begin{aligned} C_{IJ} &= \int_{-T/2}^{T/2} \mathrm{d}t \int_{-\infty}^{\infty} \mathrm{d}t' \int_{-\infty}^{\infty} \mathrm{d}f \int_{-\infty}^{\infty} \mathrm{d}f' \int_{-\infty}^{\infty} \mathrm{d}f'' \\ &\quad \times\, \tilde{s}_I^*(f)\, e^{2\pi f t}\, \tilde{s}_J(f')\, e^{2\pi f' t'}\, \tilde{Q}(f'')\, e^{2\pi f''(t-t')} \\ &= \int_{-\infty}^{\infty} \mathrm{d}f \int_{-\infty}^{\infty} \mathrm{d}f' \int_{-\infty}^{\infty} \mathrm{d}f''\, \delta_T\left(f-f''\right)\, \delta\left(f'-f''\right)\, \tilde{s}_I^*(f)\, \tilde{s}_J(f')\, \tilde{Q}(f'') \\ &= \int_{-\infty}^{\infty} \mathrm{d}f \int_{-\infty}^{\infty} \mathrm{d}f'\, \delta_T\left(f-f'\right)\, \tilde{s}_I^*(f)\, \tilde{s}_J(f')\, \tilde{Q}(f'), \end{aligned} \tag{4.3.22}$$

[12] In the case where multiple stretches (segments) of duration T are present and each of them is labelled by the time t, the expression for multiple measurements takes the form

$$C_{IJ}(t) \equiv \int_{t-T/2}^{t+T/2} \mathrm{d}t' \int_{t-T/2}^{t+T/2} \mathrm{d}t''\, s_I(t') s_J(t'') Q(t',t''). \tag{4.3.19}$$

[13] Observe that, in the case of identical, co-aligned, co-located detectors, $Q(t,t')$ is simply $\delta(t-t')$.

where the tilde denotes the (short[14]) Fourier transform of a given quantity (note that the filter is real, and hence $\tilde{Q}^*(f) = \tilde{Q}(-f)$), $\delta(f' - f'')$ is the Dirac delta function[15], and $\delta_T(f - f')$ is its finite-time version, defined by

$$\delta_T(f) \equiv \int_{-T/2}^{+T/2} \mathrm{d}t\, e^{-2\pi f t} = T\mathrm{sinc}(\pi f T), \tag{4.3.25}$$

and such that $\delta_T(0) = T$.

As mentioned in the previous subsections, the choice of the optimal filter depends on the quantity to be maximised, which in this case is the signal-to-noise ratio

$$\mathrm{SNR}_{IJ} \equiv \frac{\langle C_{IJ}\rangle}{\sqrt{\mathrm{Var}(C_{IJ})}}. \tag{4.3.26}$$

The calculation of the expectation value of C_{IJ} is straightforward given equation (4.2.5), namely

$$\begin{aligned}
\langle C_{IJ}\rangle =& \int_{-\infty}^{\infty} \mathrm{d}f \int_{-\infty}^{\infty} \mathrm{d}f'\, \delta_T(f - f')\, \langle \tilde{s}_I^*(f)\, \tilde{s}_J(f')\rangle\, \tilde{Q}(f') \\
=& \int_{-\infty}^{\infty} \mathrm{d}f \int_{-\infty}^{\infty} \mathrm{d}f'\, \delta_T(f - f')\, \left\langle \tilde{h}_I^*(f)\, \tilde{h}_J(f')\right\rangle\, \tilde{Q}(f') \\
=& \frac{1}{2}\int_{-\infty}^{\infty} \mathrm{d}f \int_{-\infty}^{\infty} \mathrm{d}f'\, \delta_T(f - f')\, \delta(f - f')\, \Gamma_{IJ}(f)\, S_h(f)\, \tilde{Q}(f') \\
=& \frac{T}{2}\int_{-\infty}^{\infty} \mathrm{d}f\, \Gamma_{IJ}(f)\, S_h(f)\, \tilde{Q}(f),
\end{aligned} \tag{4.3.27}$$

where the second equality uses the fact that signal and noise are uncorrelated and that correlated noise is absent (or negligible); the third one uses the results from equation (4.2.5), and the last equality uses the properties of the Dirac delta function and $\delta_T(0) = T$.

The evaluation of the variance for C_{IJ} is more involved but simplifies noticeably in the small-signal approximation, which assumes the condition $\langle C_{IJ}\rangle = \mathcal{O}(S_h(f)) \ll$

[14]The definition of the short Fourier transform is given by (t here is a label for the short Fourier transform of a segment of duration T)

$$\tilde{s}_I(t; f) \equiv \int_{t-T/2}^{t+T/2} \mathrm{d}t'\, s_I(t'). \tag{4.3.23}$$

The usual Fourier transform is recovered in the limit $T \to \infty$.

[15]The definition employed here for the Dirac delta function is

$$\delta(f) \equiv \int_{-\infty}^{\infty} \mathrm{d}t\, e^{-2\pi f t}. \tag{4.3.24}$$

$P_{n_I}(f), P_{n_I}(f)$:

$$\begin{aligned}
\mathrm{Var}\,(C_{IJ}) \equiv& \left\langle C_{IJ}^2 \right\rangle - \left\langle C_{IJ} \right\rangle^2 \approx \left\langle C_{IJ}^2 \right\rangle \\
=& \int_{-\infty}^{\infty} \mathrm{d}f \int_{-\infty}^{\infty} \mathrm{d}f' \int_{-\infty}^{\infty} \mathrm{d}f'' \int_{-\infty}^{\infty} \mathrm{d}f''' \, \delta_T(f-f') \, \delta_T(f''-f''') \\
& \times \left\langle \tilde{s}_I^*(f) \, \tilde{s}_J(f') \, \tilde{s}_I^*(f'') \, \tilde{s}_J(f''') \right\rangle \tilde{Q}(f) \tilde{Q}(f'') \\
\approx& \int_{-\infty}^{\infty} \mathrm{d}f \int_{-\infty}^{\infty} \mathrm{d}f' \int_{-\infty}^{\infty} \mathrm{d}f'' \int_{-\infty}^{\infty} \mathrm{d}f''' \, \delta_T(f-f') \, \delta_T(f''-f''') \\
& \times \left\langle \tilde{n}_I^*(f) \, \tilde{n}_J(f') \, \tilde{n}_I^*(f'') \, \tilde{n}_J(f''') \right\rangle \tilde{Q}(f) \tilde{Q}(f'') \\
=& \frac{1}{4} \int_{-\infty}^{\infty} \mathrm{d}f \int_{-\infty}^{\infty} \mathrm{d}f' \int_{-\infty}^{\infty} \mathrm{d}f'' \int_{-\infty}^{\infty} \mathrm{d}f''' \, \delta_T(f-f') \, \delta_T(f''-f''') \\
& \times \delta\left(f+f''\right) \, P_{n_I}(f) \, \delta\left(f'+f'''\right) \, P_{n_J}(f') \, \tilde{Q}(f) \, \tilde{Q}(f'') \\
=& \frac{1}{4} \int_{-\infty}^{\infty} \mathrm{d}f \int_{-\infty}^{\infty} \mathrm{d}f' \, \delta_T^2(f-f') \, P_{n_I}(f) \, P_{n_J}(f') \, \tilde{Q}(f) \, \tilde{Q}^*(f') \\
=& \frac{T}{4} \int_{-\infty}^{\infty} \mathrm{d}f \, P_{n_I}(f) \, P_{n_J}(f) \left| \tilde{Q}(f) \right|^2,
\end{aligned} \tag{4.3.28}$$

where the small-signal limit is used to pass from the second to the third line; the Gaussianity condition ($\langle abcd \rangle = \langle ab \rangle \langle cd \rangle \langle ac \rangle \langle bd \rangle + \langle ad \rangle \langle bc \rangle$) together with the independence of the noises and the definition of the (one-sided) noise PSDs

$$\langle \tilde{n}_I^*(f) \tilde{n}_J(f') \rangle = \frac{\delta_{IJ}}{2} \delta\left(f-f'\right) P_{n_I} \tag{4.3.29}$$

to pass from the third to the fourth line; the properties of the Dirac delta function from the fourth to the fifth line; and the substitution[16] of one finite-time delta function with a Dirac delta function together with their properties to obtain the final expression. Summarising

$$\langle C_{IJ} \rangle = \frac{T}{2} \int_{-\infty}^{\infty} \mathrm{d}f \, \Gamma_{IJ}(f) \, S_h(f) \, \tilde{Q}(f) \tag{4.3.30}$$

$$\mathrm{Var}\,(C_{IJ}) \approx \frac{T}{4} \int_{-\infty}^{\infty} \mathrm{d}f \, P_{n_I}(f) \, P_{n_J}(f) \left| \tilde{Q}(f) \right|^2. \tag{4.3.31}$$

Now, the filter optimisation problem is reduced to maximising the SNR with respect to $\tilde{Q}(f)$. The problem can be solved easily by introducing the (positive-definite) inner product $(X,\, Y)$

$$(X,\, Y) \equiv \int_{-\infty}^{\infty} \mathrm{d}f \, X^*(f) \, Y(f) \, P_{n_I}(f) \, P_{n_J}(f), \tag{4.3.32}$$

[16]This substitution is justified by the fact that, for $T \gg d/c$, $\delta_T(f-f')$ is sharply peaked around the region $\Delta f = f - f' \approx T^{-1}$, whose size is much smaller compared to the one on which the functions P_{n_I}, P_{n_I}, $\tilde{Q}(f)$ are changing [304].

with $X(f)$ and $Y(f)$ two complex functions, and observing that

$$\mathrm{SNR} = \frac{\frac{T}{2}\left(\frac{\Gamma_{IJ}(f)\,S_h(f)}{P_{n_I}(f)\,P_{n_J}(f)},\,\tilde{Q}(f)\right)}{\frac{\sqrt{T}}{2}\left(\tilde{Q}(f),\,\tilde{Q}(f)\right)^{1/2}}. \tag{4.3.33}$$

The optimal filter follows immediately as[17]

$$\tilde{Q}(f) = \mathcal{N}\,\frac{\Gamma_{IJ}(f)\,S_h(f)}{P_{n_I}(f)\,P_{n_I}(f)}, \tag{4.3.34}$$

with $\mathcal{N}$ a (real) overall normalisation constant, leading to

$$\mathrm{SNR} = \sqrt{T}\left[\int_{-\infty}^{\infty}\mathrm{d}f\,\frac{\Gamma^2_{IJ}(f)\,S^2_h(f)}{P_{n_I}(f)\,P_{n_I}(f)}\right]^{1/2}. \tag{4.3.35}$$

The above expression for the SNR has two remarkable features. First, it is proportional to the square root of the total observation time T. This basically guarantees that, by observing long enough, it is always possible to extract a weak signal from the dominant noise. Second, the expression of the optimal filter $\tilde{Q}(f)$ depends on the strain spectral density $S_h(f)$ of the SGWB, which is unknown a priori. This means that, instead of a unique optimal filter to perform the analysis, it will be necessary to rather use a set of such filters based on the model of interest. As an example, if the spectral density spectrum can be approximated with a power law $S_h(f) = S_\beta f^\beta$, with S_β a constant (see equation (3.1.14)), which can be reabsorbed in the filter normalisation constant, it is possible to build a set of optimal filters $Q_\beta(f)$, with overall normalisation constants $\mathcal{N}_\beta$ such that $\langle C_{IJ}\rangle = S_\beta\,T$. With this normalisation, the optimal filter functions $\tilde{Q}_\beta$ are completely determined by the exponent β, the overlap reduction function, and the noise spectral density of the two detectors.

The above procedure can be easily adapted to the case where the quantity of interest is $\Omega_{\mathrm{gw}}(f) = \Omega_\alpha f^\alpha$ by simply using equation (3.1.11) linking $S_h(f)$ and $\Omega_{\mathrm{gw}}(f)$,

[17] The problem is equivalent to looking for a vector $\vec{\boldsymbol{Q}}$ maximising the cosine

$$(\vec{\boldsymbol{Q}}\cdot\vec{\boldsymbol{X}})/|\vec{\boldsymbol{Q}}|$$

of the relative angle with another vector $\vec{\boldsymbol{X}}$. The solution here is simply choosing $\vec{\boldsymbol{Q}}//\vec{\boldsymbol{A}}$.

yielding

$$\langle C_{IJ}\rangle = \frac{3H_0^2}{10\pi^2}\frac{T}{2}\int_{-\infty}^{\infty}\mathrm{d}f\,\gamma_{IJ}(f)\,\Omega_{\rm gw}(f)\,f^{-3}\,\tilde{Q}(f), \tag{4.3.36}$$

$$\mathrm{Var}\,(C_{IJ}) \approx \frac{T}{4}\int_{-\infty}^{\infty}\mathrm{d}f\,P_{n_I}(f)\,P_{n_J}(f)\left|\tilde{Q}(f)\right|^2, \tag{4.3.37}$$

$$\tilde{Q}(f) = \mathcal{N}_\Omega\,\frac{\gamma_{IJ}(f)\,\Omega_{\rm gw}(f)}{f^3\,P_{n_I}(f)\,P_{n_I}(f)}, \tag{4.3.38}$$

$$\mathrm{SNR} = \frac{3H_0^2}{10\pi^2}\sqrt{T}\left[\int_{-\infty}^{\infty}\mathrm{d}f\,\frac{\gamma_{IJ}^2(f)\,\Omega_{\rm gw}^2(f)}{f^3\,P_{n_I}(f)\,P_{n_I}(f)}\right]^{1/2}. \tag{4.3.39}$$

where the normalised ORF $\gamma_{IJ}(f)$ was used in place of $\Gamma_{IJ}(f)$ for consistency reasons with literature (see, for example, [258], or next sections).

Beyond the small signal limit

The small-signal limit allows deriving a simple expression for the optimal filter. However, next-generation ground-based detectors, such as ET [116] and Cosmic Explorer [117], may no longer operate in this regime for some SGWB sources.

When the data do not satisfy the small signal limit, the variance is no longer dominated by detector noise contributions (while the expectation value is independent of the relative). By comparison with equation (4.3.28), the quantity to be re-evaluated is $\left\langle C_{IJ}^2\right\rangle$, which now consists of some additional contributions, namely

$$\begin{aligned}\left\langle C_{IJ}^2\right\rangle &= \int_{-\infty}^{\infty}\mathrm{d}f\int_{-\infty}^{\infty}\mathrm{d}f'\int_{-\infty}^{\infty}\mathrm{d}f''\int_{-\infty}^{\infty}\mathrm{d}f'''\,\delta_T(f-f')\,\delta_T(f''-f''')\\ &\quad\times\,\langle\tilde{s}_I^*(f)\,\tilde{s}_J(f')\,\tilde{s}_I^*(f'')\,\tilde{s}_J(f''')\rangle\,\tilde{Q}(f)\tilde{Q}(f'')\\ &= \int_{-\infty}^{\infty}\mathrm{d}f\int_{-\infty}^{\infty}\mathrm{d}f'\int_{-\infty}^{\infty}\mathrm{d}f''\int_{-\infty}^{\infty}\mathrm{d}f'''\,\delta_T(f-f')\,\delta_T(f''-f''')\\ &\quad\times\,\Bigg[\left\langle\tilde{h}_I^*(f)\,\tilde{h}_J(f')\,\tilde{h}_I^*(f'')\,\tilde{h}_J(f''')\right\rangle\\ &\quad+\left\langle\tilde{h}_I^*(f)\,\tilde{n}_J(f')\,\tilde{h}_I^*(f'')\,\tilde{n}_J(f''')\right\rangle+\left\langle\tilde{n}_I^*(f)\,\tilde{h}_J(f')\,\tilde{n}_I^*(f'')\,\tilde{h}_J(f''')\right\rangle\\ &\quad+\,\langle\tilde{n}_I^*(f)\,\tilde{n}_J(f')\,\tilde{n}_I^*(f'')\,\tilde{n}_J(f''')\rangle\Bigg]\tilde{Q}(f)\tilde{Q}(f'').\end{aligned}$$

It is already possible to notice that, in contrast to the small signal limit, the variance also receives contributions from "signal+noise" cross-terms and a "pure signal" variance term. The evaluation of $\left\langle C_{IJ}^2\right\rangle$ does require some lengthy algebra but is not

difficult. At the end of the whole process,the variance has the form

$$\begin{aligned}\mathrm{Var}\left(C_{IJ}\right) \equiv& \left\langle C_{IJ}^2 \right\rangle - \left\langle C_{IJ} \right\rangle^2 \\ =& \frac{T}{4} \int_{-\infty}^{\infty} \mathrm{d}f \left| \tilde{Q}(f) \right|^2 \\ & \times \Big[P_{n_I}(f)\, P_{n_I}(f) + S_h(f) \left(P_{n_I}(f)\, \Gamma_{JJ}(f) + P_{n_J}(f)\, \Gamma_{II}(f) \right) \\ & + S_h^2(f) \left(\Gamma_{II}(f)\, \Gamma_{JJ}(f) + \Gamma_{IJ}(f)^2 \right) \Big]. \end{aligned} \tag{4.3.40}$$

Recasting everything in terms of $\Omega_{\mathrm{gw}}(f)$ and $\gamma_{IJ}(f)$ (observing that $\gamma_{II}(f) \equiv 1$ since the small antenna limit holds), the result is consistent with the one from [410]

$$\begin{aligned}\mathrm{Var}\left(C_{IJ}\right) =& \frac{T}{4} \int_{-\infty}^{\infty} \mathrm{d}f \left| \tilde{Q}(f) \right|^2 \\ & \times \left[P_{n_I}(f)\, P_{n_I}(f) + \frac{3H_0^2}{10\pi^2} \frac{\Omega_{\mathrm{gw}}(f)}{f^3} \left(P_{n_I}(f) + P_{n_J}(f) \right) \right. \\ & \left. + \left(\frac{3H_0^2}{10\pi^2} \frac{\Omega_{\mathrm{gw}}(f)}{f^3} \right)^2 \left(1 + \gamma_{IJ}^2(f) \right) \right] \\ \equiv& \frac{T}{4} \int_{-\infty}^{\infty} \mathrm{d}f \left| \tilde{Q}(f) \right|^2 R(f). \end{aligned} \tag{4.3.41}$$

By repeating the procedure of the small signal case to find the optimal estimator, it is still possible to build an inner product

$$(X,\, Y) \equiv \int_{-\infty}^{\infty} \mathrm{d}f\, X^*(f)\, Y(f)\, R(f), \tag{4.3.42}$$

and find the optimal filter as

$$\tilde{Q}(f) = \mathcal{N}_R \frac{\Omega_{\mathrm{gw}}(f)\, \gamma_{IJ}(f)}{f^3\, R(f)}. \tag{4.3.43}$$

However, complications arise from this point due to the relatively complicated functional dependence of $\tilde{Q(f)}$ on the SGWB spectrum $\Omega_{\mathrm{gw}}(f)$. As a consequence, the space of optimal filters to be considered is enlarged. Already in the case of a power-law SGWB $\Omega_{\mathrm{gw}}(f) = \Omega_\alpha f^\alpha$, the constant Ω_α can no longer be absorbed in the filter normalisation constant, leading to the filter space being parametrised by (α, Ω_α). This translates into more sophisticated search algorithms than those presented in this thesis.

4.3.3 Sensitivity curves for (isotropic) SGWB searches

From the above discussion, it is still not clear how to determine the sensitivity of a detector network to SGWB. For a power-law isotropic SGWB, ad hoc sensitivity curves, known as *power-integrated curves* (PI curves), can be built following the approach

from [414]. The idea is simple and has as a starting point the expression for the optimal SNR in equation (4.3.35) in the small signal limit, extended to a network of $N_{\rm detectors}$ detectors [410, 414], namely

$$\mathrm{SNR} = \sqrt{2T}\left[\int_{f_{\rm min}}^{f_{\rm max}} \mathrm{d}f \sum_{I=1}^{N_{\rm det}} \sum_{J>I}^{N_{\rm det}} \frac{\Gamma_{IJ}^2(f)\, S_h^2(f)}{P_{n_I}(f)\, P_{n_I}(f)}\right]^{1/2}, \tag{4.3.44}$$

where $[f_{\rm min},\, f_{\rm max}]$ is the bandwidth of the network, while the factor $\sqrt{2}$ comes from the symmetry properties of the one-sided spectral density $S_h(f)$. The above expression suggests defining a network effective strain noise PSD $S_{\rm eff}(f)$ as

$$S_{\rm eff}(f) \equiv \left(\sum_{I=1}^{N_{\rm det}} \sum_{J>I}^{N_{\rm det}} \frac{\Gamma_{IJ}^2(f)}{P_{n_I}(f)\, P_{n_J}(f)}\right)^{-1/2} \tag{4.3.45}$$

and also a network effective $\Omega_{\rm eff}$ (and $h_{c,\rm eff}$ based on the sensitivity curve) by using the relation (3.1.11).

The PI curve construction for a power-law $\Omega_{\rm gw}(f) = \Omega(f_{\rm ref};\, \alpha)(f/f_{\rm ref})^{\alpha}$ can be summarised in the following steps[18]:

1) Given a network of detectors, their PSDs P_{n_I}, and the ORFs of the detector pairs, build the effective strain $S_{\rm eff}(f)$ using equation (4.3.45), and convert it to $\Omega_{\rm eff}(f)$ using equation (3.1.11).

2) Choose the observation time $T = T_{\rm obs}$ and the $\mathrm{SNR} = \mathrm{SNR}_*$ the SGWB must be observed with.

3) Under the assumption of a power-law $\Omega_{\rm gw}(f;\, \alpha)$ spectrum, choose a set of spectral indices $\{\vec{\boldsymbol{\alpha}}\}$, a reference frequency $f_{\rm ref}$ (in spite of being necessary for this calculation, its value does not affect the final PI curve).

4) For every α, evaluate

$$\Omega_\alpha \equiv \Omega_{\rm gw}(f_{\rm ref}; \alpha) = \frac{\mathrm{SNR}_*}{\sqrt{2T_{\rm obs}}}\left[\int_{f_{\rm min}}^{f_{\rm max}} \mathrm{d}f\, \frac{(f/f_{\rm ref})^{2\alpha}}{\Omega_{\rm eff}^2(f)}\right]^{-1/2}. \tag{4.3.46}$$

5) At every frequency f, evaluate the PI curve as the envelope of the $\Omega_{\rm gw}(f)$ power-law curves as

$$\Omega_{\rm PI}(f) = \max_{\beta}\left\{\Omega_\beta \left(\frac{f}{f_{\rm ref}}\right)^{\beta}\right\}. \tag{4.3.47}$$

[18]The procedure is totally analogous for $S_h(f)$ and $h_c(f)$ PI curves, using the conversion formula (3.1.14) for the power-law quantities.

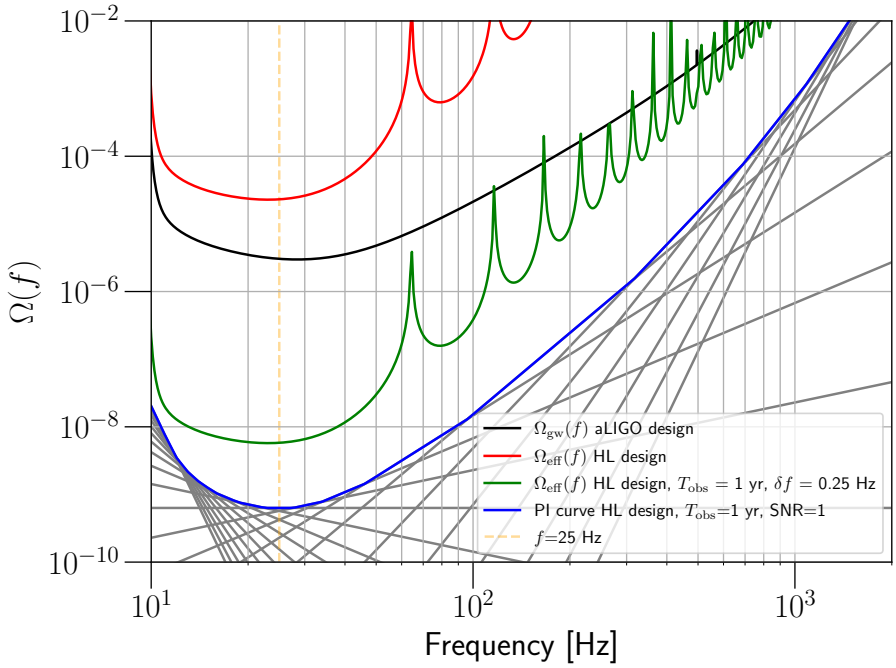

Figure 4.2: $\Omega_{\rm gw}(f)$ sensitivity curves for the HL baseline in the same style as [414], produced using [`my_code`]. The black line is the single-detector sensitivity curve (assumed to be the same for both Hanford and Livingston LIGO detectors) in $\Omega_{\rm gw}(f)$ units. The red curve is the instantaneous $\Omega_{\rm eff}$ sensitivity of the HL baseline. The green curve is again the $\Omega_{\rm eff}$ sensitivity but for an integration over one year with $\delta f = 0.25$Hz. The grey lines are obtained by the integration over frequency for different power laws, assuming an $\mathrm{SNR} = 1$. Finally, the blue curve is the envelope of the grey lines, namely the power-law integrated sensitivity curve.

An example of the PI curve and related quantities for the advanced LIGO detectors is pictured in figure 4.2. The interpretation of the PI curve is the following: any line tangent to the PI curve corresponds to an SGWB following a power-law spectrum with an integrated signal-to-noise ratio SNR_* for an observation time T_{obs}. As a consequence, if the predicted SGWB curve lies below the PI curve, such SGWB is "observed" with $\mathrm{SNR} < \mathrm{SNR}_*$. On the other hand, if it lies above the PI curve, it is "observed" with $\mathrm{SNR} > \mathrm{SNR}_*$. Each of the curves for a power-law model Ω_β can be interpreted as a sensitivity curve for that, and only that, model. This allows, in principle, to extend the concept of an integrated sensitivity curve to models differing from a simple power law by looping over the model parameters $\vec{\boldsymbol{\theta}}$, as long as it is possible to write $\Omega_{\mathrm{gw}}(f) = \Omega_{\mathrm{gw}}(f_{\mathrm{ref}};\, \vec{\boldsymbol{\theta}}) w(f_{\mathrm{ref}};\, \vec{\boldsymbol{\theta}})$, with $w(f_{\mathrm{ref}};\, \vec{\boldsymbol{\theta}}) \equiv \Omega_{\mathrm{gw}}(f)/\Omega_{\mathrm{gw}}(f_{\mathrm{ref}};\, \vec{\boldsymbol{\theta}})$.

4.4 Search for isotropic SGWB: Results from S1 to O3

This section recaps the efforts done with km-long ground-based GW interferometers in searching for a Gaussian, stationary, unpolarised, isotropic SGWB, from the first scientific run (S1) with initial LIGO [415] until the end of the third observing run (O3) with the advanced LIGO [90] and Virgo [94] detectors. The main results are reported in table 4.1.

4.4.1 Optimal estimators for individual frequency bins and hints towards real world complications

Real-world analyses suffer from many more complications and problems compared to those described above, most of which are discussed in chapter 6, where a detailed description of the O3 searches is given. Here, the expressions for the estimator of a generic $\Omega_{\mathrm{ref}} \equiv \Omega_{\mathrm{gw}}(f_{\mathrm{ref}})$ and its uncertainty at a reference frequency (usually chosen as the one at which the detector is most sensitive to) are derived for a discrete set of measurements that need to be combined optimally. This can be done by combining the approach used in the toy model in section 4.3.1 together with the discretised version of what has been presented in the previous section in the small signal limit. Let one consider the case of a segment of duration T, labelled by t, for a detector pair IJ. The cross-correlation spectrum $C_{IJ,\,t\,f}$, with f the discrete frequency label and with frequency resolution Δf, can be written as

$$C_{IJ,\,t\,f} = \Re\left[\tilde{s}^*_{I,\,t\,f}\tilde{s}_{J,\,t\,f}\right]. \tag{4.4.1}$$

Similarly, the discrete covariance matrix $\mathrm{Cov}_{IJ,tff'}$ becomes

$$\mathrm{Cov}_{IJ,tff'} \approx \left\langle \tilde{n}^*_{I\,t\,f}\tilde{n}_{I,\,t\,f'}\right\rangle \left\langle \tilde{n}^*_{J\,t\,f}\tilde{n}_{J,\,t\,f'}\right\rangle = \frac{T}{4}\, P_{n_I,tf}\, P_{n_J,tf}\delta_{ff'}, \tag{4.4.2}$$

Now, by observing that

$$\langle C_{IJ,\,t\,f}\rangle = \frac{T}{2}\,\Gamma_{IJ}(f)\,S_h(f) \equiv \frac{T}{2}\,\Gamma_{IJ}(f)\,S_0(f)w(f)\Omega_{\rm ref}, \tag{4.4.3}$$

where

$$S_0(f) \equiv \frac{3H_0^2}{2\pi^2}\frac{1}{f^3}, \tag{4.4.4}$$

and

$$w(f) \equiv \frac{\Omega_{\rm gw}(f)}{\Omega_{\rm gw}(f_{\rm ref})}, \tag{4.4.5}$$

the correspondence with the notation in the toy model of section 4.3.1 becomes evident, namely

$$\theta \longleftrightarrow \Omega_{\rm ref}, \qquad h_i \longleftrightarrow \frac{T}{2}\,\Gamma_{IJ}(f)\,S_0(f)w(f), \tag{4.4.6}$$

$$d_i \longleftrightarrow C_{IJ,\,t\,f}, \qquad \sigma_i^{-2} \longleftrightarrow \sum_{f'} \mathrm{Cov}^{-1}_{IJ,tff'} \tag{4.4.7}$$

This means that the optimal (narrow-band) estimator for $\Omega_{\rm ref}$ and the relative variance for a segment t at a frequency f can be found by using equation (4.3.16) (note that there is no sum over time or frequencies since this is the estimator for a single segment and a single frequency bin), leading to[19]

$$\hat{\Omega}_{{\rm ref},\,IJ,\,t\,f} = \frac{2}{T}\frac{\Re[\tilde{s}^*_{I\,t\,f}\tilde{s}_{J,\,t\,f'}]}{\Gamma_{IJ}(f)\,S_0(f)\,w(f)}, \tag{4.4.8}$$

$$\sigma^2_{IJ,\,tf} = \frac{1}{2T\,\Delta f}\,\frac{P_{n_I,tf}\,P_{n_J,tf}}{\Gamma^2_{IJ}(f)\,S_0^2(f)\,w^2(f)}. \tag{4.4.9}$$

The optimal (broad-band) estimator and variance can then be obtained by combining these measurements over times, frequencies, and independent baselines using the

[19] Note that in real-world analyses, $T\Delta f \neq 1$ in general, see chapter 6.

weighted sum from section 4.3.1[20] :

$$\hat{\Omega}_{\rm ref} = \frac{\sum_I \sum_{J>I} \sum_{f,\,t} \hat{\Omega}_{{\rm ref},\,IJ,\,t\,f}\, \sigma^{-2}_{IJ,\,tf}}{\sum_I \sum_{J>I} \sum_{f,\,t} \sigma^{-2}_{IJ,\,tf}} \tag{4.4.13}$$

$$\sigma^2 = \frac{1}{\sum_I \sum_{J>I} \sum_{f,\,t} \sigma^{-2}_{IJ,\,tf}}. \tag{4.4.14}$$

4.4.2 The first LIGO scientific run

At the time of the first LIGO scientific run (S1, from 23rd August 2002 to 9th September 2002), the most stringent limits on $\Omega_{\rm GW}$ in the ground-based GW interferometers were from the big bang nucleosyntheisis bound, stating that $h_0^2\,\Omega_{\rm GW} < 10^{-5}$ [416] for frequencies $f > 10^{-8}$ Hz. The most stringent limit from experiments in the 100-1000 Hz band was from the Glasgow-Garching interferometer, namely $h_0^2\,\Omega_{\rm gw}(f) < 3 \times 10^5$ for a flat spectrum (lower bounds, still orders of magnitude above 1, for single frequencies were available from resonant bar detectors, see again [416]). The S1 search for isotropic SGWB made use of a couple of hundred hours of coincident data for the detector pairs H1H2, H1L1, and H2L1, and made use for the first time of the methods (with some complications from analysis in the discrete time and frequency domains and from the real world) presented in this chapter. The analysis set constraints only on a flat $\Omega_{\rm gw}(f) = \Omega_0$ (such as in inflationary or cosmic strings models), given the expectation at the time of a cosmological SGWB being dominant, leading to 90 % confidence level frequentist[21] upper limits $h_0^2\,\Omega_0 < 23 \pm 4.6$ in the frequency range $40 - 314$ Hz [416]. In spite of being still above the order of unit (and hence not informative), this result improved the best previous broad-band results from ground-based GW interferometers by a factor of approximately 10^4, and the best previous narrow-band results from resonant bars by a factor of 3, showing the superiority of km-long interferometers in the search for an SGWB in this frequency range.

[20] For comparison, using the optimal filter approach from the previous section, the continuous version of the broad-band estimator reads

$$\hat{\Omega}_{{\rm ref},\,IJ,\,t} = \frac{2}{T}\,\mathcal{N}_{\rm ref} \int_{-\infty}^{\infty} {\rm d}f\, \frac{\Gamma_{IJ}(f)\, S_0(f) w(f)}{P_{n_I,\,tf}\, P_{n_J,\,tf}} \tag{4.4.10}$$

$$\sigma^2_{\hat{\Omega}_{{\rm ref},\,IJ,\,t}} = \left(T \int_{-\infty}^{\infty} {\rm d}f\, \frac{\Gamma^2_{IJ}(f)\, S_0^2(f)}{P_{n_I,\,tf}\, P_{n_J,\,tf}} \right)^{-1} \tag{4.4.11}$$

$$\mathcal{N}_{\rm ref} \equiv \left(\int_{-\infty}^{\infty} {\rm d}f\, \frac{\Gamma^2_{IJ}(f)\, S_0^2(f)}{P_{n_I,\,tf}\, P_{n_J,\,tf}} \right)^{-1} \tag{4.4.12}$$

[21] This is one of the major differences with modern analyses that adopt the Bayesian approach. Some other relevant differences from the latest analyses are the usage of 90-s-long segments and 0.25-Hz frequency resolution, together with the employment of Tukey windows and the lack of overlapping segments, and some more technical details discussed in the original S1 paper [416].

4.4.3 Bridging the gap with big bang nucleosynthesis

The limits from LIGO S1 were still six orders of magnitude above the constraints from big bang nucleosynthesis; however, it was just a matter of time before the km-long interferometer could improve this limit. Already during the third LIGO scientific run (S3, from 31st October 2003 to 9th January 2004), with roughly 200 hours from H1L1 and H2L1 pairs (H1H2 was excluded due to complications arising from correlated noise), thanks to the improved sensitivity of the detectors, it was possible to improve the limits on Ω_0 from S1 by approximately 10^5 times, down to 90%-confident Bayesian upper limits $h_0^2\,\Omega_0 < 4.4\times10^{-4}$ in the $69-156$ Hz band [417]. This search[22] set limits also in the case of $\alpha = 2$ (referred as "rotating neutron stars") and $\alpha = 3$ (referred as "pre-big-bang cosmology") at 100 Hz, respectively $h_0^2\,\Omega_2 < 4.9 \times 10^{-4}$ and $h_0^2\,\Omega_3 < 4.2 \times 10^{-4}$. The limits over Ω_0 further improved by a factor of roughly 13 during the fourth LIGO scientific run (S4, 22nd February 2005 to 23rd March 2005), down to 90%-confidence Bayesian upper limits $h_0^2\,\Omega_0 < 3.4 \times 10^{-5}$ in the $51 - 150$ Hz band[23] [419].

The fifth LIGO scientific run (S5, from 5th November 2005 to 30th September 2007) was the first one where also Virgo joined for data taking (from 18th May 2007 to 30th September 2007), and multiple baselines were available[24]. Two works are associated with this run: one for the H1, L1, and V1 detectors [389], and one for the two co-located co-aligned Hanford LIGO detectors H1 and H2, both setting limits for Ω_3 at a reference frequency of 900 Hz for an astrophysical SGWB in the frequency range 600-1000 Hz. In the case of H1, L1, and V1, the range choice was dictated by the much better Virgo sensitivity at high frequencies compared to the LIGO Hanford and LIGO Livingston ones. Instead, in the H1 and H2 cases, this choice was forced by too much data contamination from correlated noise at lower frequencies[25]. The 95%-confidence Bayesian upper limits in this frequency band were respectively $h_0^2\,\Omega_3 < 0.16$ [420] for H1, L1 and V1, and $h_0^2\,\Omega_3 < 3.6 \times 10^{-4}$ [421] for H1 and H2. These limits not only improved the previously existing ones from the joint analysis from S4 with bar detectors [422], but also showed the power of the co-located, co-aligned detector pair in stochastic searches.

Finally, with the sixth and last LIGO scientific run (S6, from July 2009 to October 2010 for LIGO, and from July 2009 to January 2010 then from July 2010 to October

[22] Note that the S3 search [417] used Hann widows and the 50% overlapping segments, with annexed complications [418], for the first time. Also, the segment duration was now 60 s, and the non-stationarity (delta sigma) cut is mentioned for the first time and has a 0.2 difference threshold (see chapter 6 for more explanation).

[23] During the S4 analysis [419], different segment durations and frequency resolutions were used, namely 60-s segments and 0.25 frequency bins Hz versus 192-s segments and 0.03125Hz frequency bins. If 60-s segments allow for better sensitivity to noise transients and are better suited for non-stationarity cuts, on the other hand, 192-s segments allow higher frequency resolution and made it possible to better remove the 1 Hz noise combs in the data, limiting the data loss.

[24] H2 is not considered in the counting since it shared the site with H1.

[25] The development of techniques and the complexity of the analysis to account for correlated noise made this work be published three years after the one for H1, L1, and V1, even later than the work associated with the sixth LIGO scientific run.

2010 for Virgo), it was possible to beat for the first time the indirect limits from the big bang nucleosynthesis, making the ground-based GW interferometers the best tool to probe SGWB in the few Hz-kHz range. In fact, during this run, the first one without H2 due to its decommissioning, the 95%-confidence Bayesian upper limits on Ω_0 in the 41.5-169.25 Hz band reached the lower value $h_0^2\,\Omega_0 < 2.6 \times 10^{-6}$ [423]. This run also set the first limits for $\alpha = 0$ in another frequency range, namely $h_0^2\,\Omega_0 < 8.3 \times 10^{-5}$ in 170-600 Hz. Limits were also set for $\alpha = 3$ in two frequency bands: $h_0^2\,\Omega_3 < 6.3 \times 10^{-2}$ at 900-Hz reference frequency in 600-1000 Hz (note that the S5 H1H2 one is still 180 times better than this one), and first one for frequency in 1000-1726 Hz $h_0^2\,\Omega_3 < 0.46$ at 1300-Hz reference frequency.

4.4.4 Advanced detectors: Observing runs

The completion of advanced LIGO and advanced Virgo, leading to an improvement of the sensitivity by one order of magnitude, together with KAGRA joining the effort in O4, has allowed setting more and more stringent bounds on several families of SGWBs[26]. The results from the first LVK observing run (O1, from 18th September 2015, 15:00 UTC, to 12th January 2016, 16:00 UTC) with H1 and L1 detectors allowed to improve the previous upper limits from S6 on a flat energy density spectrum background by a factor around 33 [424], pushing the upper limits down to $h_0^2\,\Omega_0 < 7.9 \times 10^{-8}$ in the 20-85.8 Hz band. In addition to that, in light of the detection of the GW150914 [91] event, limits on the intensity of the SGWB from CBC with spectral index $\alpha = 2/3$ were set, leading to the 95%-confidence Bayesian upper limits $h_0^2\,\Omega_{2/3} < 6.8 \times 10^{-8}$ at a 25 Hz reference frequency within the range 20-98.2 Hz. At the same reference frequency, limits for $\alpha = 3$ were set, namely $h_0^2\,\Omega_3 < 7.9 \times 10^{-9}$ for frequencies between 20 and 305 Hz[27].

The analysis with the data from the second LVK observing run (O2, 30th November 2016, 16:00 UTC, to 25th August 2017) was the first one using the full 20-1726 Hz range to draw results on the intensities of the different SGWBs. The search made use of the data from H1 and L1 detectors, given that Virgo had joined only in the last month of observation, not contributing significantly to this kind of search. The results for the $\alpha = 0$, 2/3, and 3 spectral indexes led to the 95%-confidence Bayesian upper limits (for a flat uniform prior on $\Omega_{\rm ref}$) $h_0^2\,\Omega_0 < 2.8 \times 10^{-8}$, $h_0^2\,\Omega_{2/3} < 2.2 \times 10^{-8}$, and $h_0^2\,\Omega_3 < 3.6 \times 10^{-9}$, improving the ones from O1 at 25 Hz reference frequency by a factor of 2.8, 2.7, and 2.2, respectively [425].

The third LVK observing run (O3, divided into two parts: O3a, from 1st April 2019, 15:00 UTC, to 1st October 2019, 15:00 UTC, and O3b, from 1st November 2019 to 27th March 2020, 17:00 UTC) was the first one where data from all three advanced detectors (H1, L1, and V1) were used to draw constraints on the intensity of the SGWB

[26]Note that the limits presented in the following are all obtained from a uniform prior on Ω_α. The first three observing runs articles [258, 424, 425] present results also for log-uniform priors.

[27]Limits for $\alpha = 3$ were also produced for the range 460-1000 Hz, resulting in $h_0^2\,\Omega_3 < 7.9 \times 10^{-3}$, still 22 times larger than the one obtained in the same range during S5 with the H1 and H2 co-located co-aligned detectors.

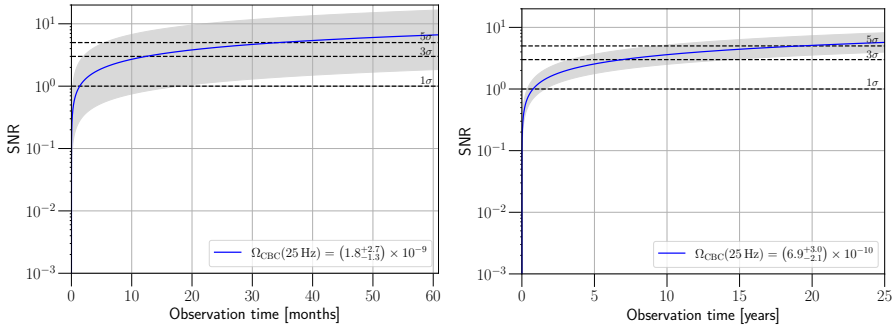

Figure 4.3: SNR as a function of the cumulative observing time, assuming the HL baseline at its design sensitivity and continuous observation [`my_code`]. The blue curves and the shaded regions refer, respectively, to the median value and the uncertainty of the CBC backgrounds from [426] (left panel) and inferred from the GWTC-3 [247] (right panel). The predictions in the left panel agree with those from [426], reaching SNR = 3 in a bit more than one year of observation at design sensitivity for the median value. The prediction from the right panel shows that approximately seven years are required to reach such a threshold for the median value. This behaviour is consistent with the scaling $\mathrm{SNR}_* \propto \sqrt{2T_{\rm obs}}\Omega_\beta$ in section 4.3.3.

energy density. The run was characterised by new data-quality challenges (see chapter 6 for more details). The results from O3 are the most updated and best limits in the 20-1726 Hz band, namely (95%-confidence Bayesian upper limits, uniform prior on Ω_α, at the 25 Hz reference frequency) $\Omega_{\rm ref})$ $h_0^2\,\Omega_0 < 7.8 \times 10^{-9}$, $h_0^2\,\Omega_{2/3} < 5.5 \times 10^{-9}$, and $h_0^2\,\Omega_3 < 6.0 \times 10^{-10}$, improving the O2 ones by a factor of 6.0, 8.8, and 13.1, respectively [258].

The recently started fourth observing run (O4) is the first one where KAGRA data could also be used for stochastic searches. If no evidence for SGWB is found, the improvements to the existing upper limits should be between a factor of 2 and 5 for the spectral index $\alpha = 0$. The most optimistic projections favour the evidence (SNR =3) for excesses from an SGWB (likely from CBCs) in a few years, after LIGO-India [115] will have become operational and the detector network will reach the design sensitivity. An example of such prediction is illustrated in figure 4.3 for two CBC SGWBs in the case of the HL baseline at design sensitivty. This could happen already between the end of this decade and the start of the next one, in the observing periods following O5.

Run	Detectors	α	$\Omega_\alpha^{\rm UL}\, h_0^2$	$f_{\rm ref}$	Confidence	Band
S1 [416]	H1, H2, L1	0	23 ± 4.6	-	90%	40-314 Hz
S3 [417]	H1, H2, L1	0	4.4×10^{-4}	-	90%	69-156 Hz
		2	4.9×10^{-4}	100 Hz	"	73-244 Hz
		3	4.2×10^{-4}	"	"	76-329 Hz
S4 [419]	H1, H2, L1	0	3.4×10^{-5}	-	90%	51-150 Hz
S5 [420]	H1, L1, V1	3	0.16	900 Hz	95%	600-1000 Hz
S5 [421]	H1, H2	3	3.6×10^{-4}	900 Hz	95%	460-1000 Hz
S6 [423]	H1, L1, V1	0	2.6×10^{-6}	-	95%	41.5-169.25 Hz
		3	6.5×10^{-2}	900 Hz	"	600-1000 Hz
		0	8.3×10^{-5}	-	"	170-600Hz
		3	0.46	1300 Hz	"	1000-1726 Hz
O1 [424]	H1, L1	0	7.9×10^{-8}	-	95%	20-85.8 Hz
		2/3	6.0×10^{-8}	25 Hz	"	20-98.2 Hz
		3	7.9×10^{-9}	25 Hz	"	20-305 Hz
		3	7.9×10^{-3}	900 Hz	"	460-1000 Hz
O2 [425]	H1, L1	0	2.8×10^{-8}	25 Hz	95%	20-1726 Hz
		2/3	2.2×10^{-8}	"	"	"
		3	3.6×10^{-9}	"	"	"
O3 [258]	H1, L1, V1	0	7.8×10^{-9}	25 Hz	95%	20-1726 Hz
		2/3	5.5×10^{-9}	"	"	"
		3	6.0×10^{-10}	"	"	"

Table 4.1: Summary of isotropic search results with LIGO and Virgo detectors across the years.

Chapter 5

Searching for SGWB with ground-based detectors (II): Directional Searches and "exotic" backgrounds

"Stat rosa pristina nomine, nomina nuda tenemus"

Umberto Eco, *Il nome della rosa*

This chapter goes beyond the vanilla case of a Gaussian, stationary, unpolarised, isotropic stochastic gravitational-wave background. Sections 5.1 and 5.2 cover, respectively, the searching and the mapping of a Gaussian, stationary, unpolarised, anisotropic SGWB, with the specific cases of *pixel* and *spherical harmonic bases* examined in section 5.3. Then, in section 5.4, it is briefly discussed what happens when removing one of the hypotheses about the SGWB being Gaussian or unpolarised, and what are the techniques that are available or have been proposed in the literature to deal with it.

5.1 Search for anisotropic SGWB: Cross-correlation

As seen in chapter 3, the existence of an SGWB showing anisotropies is well justified, such as in the case of an astrophysical SGWB, which is expected to follow the spatial distribution of the sources. From a 2-point correlation function perspective, the difference between anisotropic and isotropic SGWBs follows from the comparison of equations (3.1.7) and (3.1.5). Concretely, the power-spectral density of anisotropic SGWBs $\mathcal{P}(f, \hat{\boldsymbol{n}})$ exhibits a directional dependence, encoding the GW-power spatial distribution over the sky at a given frequency f.

5.1.1 Optimal filtering

The removal of the hypothesis of isotropy introduces some complications in the search for an SGWB. This section adopts the approach first shown in the pioneering work [427], namely a generalisation of the matched-filter strategy seen in section 4.3 to this case. The starting point is again the expression for the cross-correlation $C_{IJ}(t)$ in equation (4.3.19) for a given chunk of data of length T, labelled by t. After having taken advantage of stationarity in equation (4.3.21) and expressed it as a function of the short Fourier transforms of the data and filter, its expectation value becomes

$$\begin{aligned}\langle C_{IJ}(t)\rangle =& \int_{-\infty}^{\infty} \mathrm{d}f \int_{-\infty}^{\infty} \mathrm{d}f'\, \delta_T\left(f-f'\right)\, \langle \tilde{s}_I^*(f)\, \tilde{s}_J(f')\rangle\, \tilde{Q}(f') \\ =& \int_{-\infty}^{\infty} \mathrm{d}f \int_{-\infty}^{\infty} \mathrm{d}f' \int_{\mathcal{S}^2} \mathrm{d}^2\hat{\boldsymbol{n}} \int_{\mathcal{S}^2} \mathrm{d}^2\hat{\boldsymbol{n}}'\, \delta_T\left(f-f'\right) \\ & \times \sum_{A,A'} F_I^{A\,*}\left(t;\, f,\, \hat{\boldsymbol{n}}\right)\, F_J^{A'}\left(t;\, f',\, \hat{\boldsymbol{n}}'\right)\, \left\langle \tilde{h}_A^*(f,\, \hat{\boldsymbol{n}})\, \tilde{h}_{A'}(f',\, \hat{\boldsymbol{n}}')\right\rangle\, \tilde{Q}(f') \\ =& \frac{T}{2} \int_{-\infty}^{\infty} \mathrm{d}f \int_{\mathcal{S}^2} \mathrm{d}^2\hat{\boldsymbol{n}}\, \gamma_{IJ}(t;\, f,\, \hat{\boldsymbol{n}})\, \mathcal{P}(f,\, \hat{\boldsymbol{n}})\, \tilde{Q}(t;f), \end{aligned} \tag{5.1.1}$$

where

$$\gamma_{IJ}(t;\, f,\, \hat{\boldsymbol{n}}) = \gamma_{IJ}^{(\mathrm{aniso})}(t;\, f,\, \hat{\boldsymbol{n}}) \equiv \frac{1}{2} \sum_A F_I^{A\,*}\left(t;\, f,\, \hat{\boldsymbol{n}}\right)\, F_J^A\left(t;\, f,\, \hat{\boldsymbol{n}}\right) \tag{5.1.2}$$

is the time-dependent geometrical factor that is the counterpart of the ORF[1] in the case of a search for anisotropic SGWBs. Examples at different frequencies of $\gamma_{IJ}(0;\, f,\, \hat{\boldsymbol{n}})$ are illustrated in figure 5.1.

Equation (5.1.1) deserves some comments. In contrast to the isotropic case, where the ORF is independent of time due to the integration over the solid angle in its definition, the geometrical factor $\gamma_{IJ}(t;\, f,\, \hat{\boldsymbol{n}})$ is time dependent[2]. This reflects the fact that the detector vertex positions $\vec{\boldsymbol{x}}_I = \vec{\boldsymbol{x}}_I(t)$, and hence the detector response functions, do change over time due to Earth rotation. As a consequence, the detector pair sweeps "hotspots" and "coldspots" of the anisotropic distribution in the sky through time, and hence the amplitude (and phase) of the resulting SGWB signal is Doppler-modulated in time, with a modulation period equal to one sidereal day [428]. This has important repercussions in the choice of the data-chunk time duration T, over which the short-Fourier transforms $\tilde{s}_I(t;\, f)$ (and $\tilde{h}_I(t;\, f)$) are defined. The duration of the chunks

[1] The relation of $\gamma_{IJ}(t;\, f,\, \hat{\boldsymbol{n}})$ with the isotropic ORF in equation (4.2.7) can easily be seen by the fact that the isotropic ORF is obtained by integrating and averaging (dividing by a $1/(4\pi)$ factor) equation (5.1.2) over the solid angle.

[2] The time dependence can be made explicit in the small-antenna limit by factorising the antenna patterns in a purely geometrical part $\bar{F}_I^A(f,\, \hat{\boldsymbol{n}})$ and in the time-dependent phase, namely

$$\gamma_{IJ}^{(\mathrm{aniso})}(t;\, f,\, \hat{\boldsymbol{n}}) = \frac{1}{2} \sum_A \bar{F}_I^{A\,*}\left(f,\, \hat{\boldsymbol{n}}\right)\, \bar{F}_J^A\left(f,\, \hat{\boldsymbol{n}}\right)\, e^{-2\pi i f \hat{\boldsymbol{n}}\cdot[\vec{\boldsymbol{x}}_I(t) - \vec{\boldsymbol{x}}_J(t)]/c}. \tag{5.1.3}$$

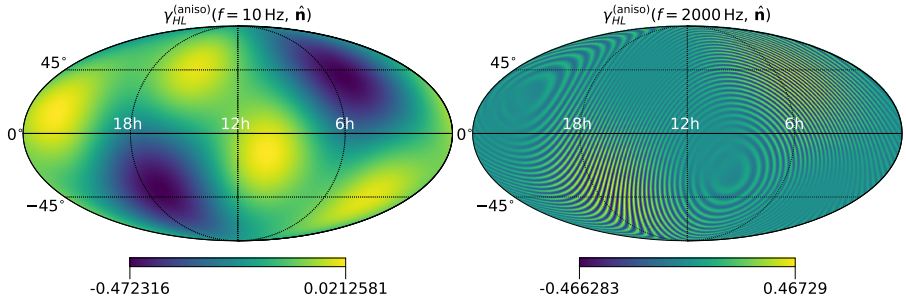

Figure 5.1: Geometrical factor $\gamma_{IJ}^{(\mathrm{aniso})}(f,\,\hat{\mathbf{n}})$ for the HL baseline at 10 Hz and 2000 Hz [`my_code`].

must now account for two time scales, namely the light travel time between the two detectors $\Delta t_{IJ} \equiv |\Delta\vec{\boldsymbol{x}}_{IJ}/c|$ and the rotation period of the Earth $\Delta T_{\mathrm{Earth}}$. The segment duration T must be long enough to avoid correlations between the two detector sites, and hence $T \gg \Delta t_{IJ}$, but at the same time must be shorter than those time scales introducing modulation in the signal due to Earth rotation, and hence $T \ll \Delta T_{\mathrm{Earth}}$. In addition to that, T must be small enough to allow to treat the geometrical factor $\gamma_{IJ}(t;\,f,\,\hat{\boldsymbol{n}})$ as a constant (or average) for that amount of time. Suitable duration for chunks from ground-based detectors turns out to be $10^2\,\mathrm{s} \lesssim T \lesssim 10^3\,\mathrm{s}$ [239].

The geometrical factor and the power spectrum are scalar fields on the 2-sphere, and hence can be decomposed into an orthornormal basis of functions $e_p(\hat{\boldsymbol{n}})$, with p denoting a set of indices such that [429, 430]

$$\mathcal{P}(f,\,\hat{\boldsymbol{n}}) = \sum_p \mathcal{P}_p(f)\,e_p(\hat{\boldsymbol{n}}), \tag{5.1.4}$$

$$\gamma_{IJ}(t;\,f,\,\hat{\boldsymbol{n}}) = \sum_p \gamma_{IJ,\,p}(t;\,f)\,e_p^*(\hat{\boldsymbol{n}}), \tag{5.1.5}$$

$$\int_{\mathcal{S}^2} \mathrm{d}^2\hat{\boldsymbol{n}}\,e_p^*(\hat{\boldsymbol{n}})\,e_{p'}(\hat{\boldsymbol{n}}) = \delta_{pp'}. \tag{5.1.6}$$

By replacing these two quantities in equation (5.1.1) and repeating the procedure for the derivation of the optimal filtering, the general optimal filter for any anisotropic SGWB turns out to be

$$\tilde{Q}(t;\,f) = \mathcal{N}_{\mathrm{aniso}}(t)\frac{\sum_p \gamma_{IJ,\,p}(t;\,f)\,\mathcal{P}_p(f)}{P_{n_1}(f)\,P_{n_2}(f)}, \tag{5.1.7}$$

where $\mathcal{N}_{\mathrm{aniso}}(t)$ is a (segment-dependent) normalisation constant. However, the components $\mathcal{P}_p(f)$ are not known in general, and models must be adopted for these quantities to search for different anisotropic SGWBs. Moreover, the optimal filtering approach alone used in this way does not allow to produce sky maps for $\mathcal{P}(f,\,\hat{\boldsymbol{n}})$. This will be the topic of the next section 5.2.

5.1.2 Modulation in the detector data

As mentioned at the beginning of the section, the signal in the detector is modulated with a period equal to one sidereal day. This symmetry can be exploited to "fold" the detector data when performing a search for anisotropic SGWB [431], as it will be explained in chapter 6. Alternatively, taking advantage of the modulation allows for the design of an analysis evaluating the contribution from each harmonic for a total observation time $T_{\rm obs}$

$$C_{IJ}(t) = \sum_{m=-\infty}^{+\infty} C_{IJ,\,m}\, e^{2\pi i m t/T_{\rm Earth}}, \tag{5.1.8}$$

$$C_{IJ,\,m} = \frac{1}{T_{\rm obs}} \int_0^{T_{\rm obs}} {\rm d}t\, C_{IJ}(t)\, e^{-2\pi i m t/T_{\rm Earth}}. \tag{5.1.9}$$

This symmetry also appears in the geometrical factors $\gamma_{IJ}(t;\, f,\, \hat{\boldsymbol{n}})$ by expanding them in the spherical harmonics basis [427, 429]:

$$\gamma_{IJ}(t;\, f,\, \hat{\boldsymbol{n}}) = \sum_{l=0}^{\infty} \sum_{m=-l}^{m=l} \gamma_{IJ,\,lm}(t;\, f)\, Y^*_{lm}(\hat{\boldsymbol{n}}) \tag{5.1.10}$$

$$\gamma_{IJ,\,lm}(t;\, f) \equiv \int_{\mathcal{S}^2} {\rm d}^2\hat{\boldsymbol{n}}\; \gamma_{IJ}(t;\, f,\, \hat{\boldsymbol{n}})\, Y_{lm}(\hat{\boldsymbol{n}}) = \gamma_{IJ,\,lm}(0;\, f)\, e^{2\pi i m t/T_{\rm Earth}}, \tag{5.1.11}$$

$$\gamma_{IJ,\,lm}(t;\, f) = (-1)^{l+m} \gamma_{IJ,\,l\,-m}(t;\, f), \tag{5.1.12}$$

where the components $\gamma_{IJ,\,lm}(0;\, f)$ can be analytically computed in terms of Bessel functions for ground-based GW interferometric detectors in the small antenna limit; see [427] for the calculation details.

By employing this notation and using the properties of the geometrical factors $\gamma_{IJ,\,lm}(t;\, f)$, it is just a matter of algebra deriving the expectation value and the covariance of the cross-correlation statistic for the m-th harmonic of a time chunk with duration T (in the small-signal approximation):

$$\langle C_m \rangle = \frac{T}{2} \int_{-\infty}^{\infty} {\rm d}f\, \tilde{Q}(t;\, f) \sum_{l=|m|}^{\infty} \gamma_{IJ,\,lm}(0;\, f)\, \mathcal{P}_{lm}(f), \tag{5.1.13}$$

$$\langle C^*_m\, C_{m'} \rangle - \langle C^*_m \rangle\, \langle C_{m'} \rangle \approx \frac{\delta_{mm'}}{T_{\rm obs}} \left(\frac{T}{2}\right)^2 \int_{-\infty}^{\infty} {\rm d}f\, \left|\tilde{Q}(t;\, f)\right|^2 P_{n_1}(t;\, f)\, P_{n_2}(t;\, f), \tag{5.1.14}$$

where $\mathcal{P}_{lm}$ are the spherical harmonic components of the SGWB power spectrum, defined in such a way that

$$\mathcal{P}_{00}(f) = \frac{S_h(f)}{\sqrt{4\pi}}, \qquad \int_{\mathcal{S}^2} {\rm d}^2\hat{\boldsymbol{n}}\, \mathcal{P}_{00}(f) = S_h(f)\, \sqrt{4\pi}. \tag{5.1.15}$$

The resulting SNR expressed in terms of the inner product (4.3.32) is

$$\mathrm{SNR} = \frac{\sqrt{T}\left|\left(\tilde{Q},\ \frac{1}{P_{n_1},P_{n_2}}\sum_{l=|m|}^{\infty}\gamma_{IJ,\,lm}P_{lm}\right)\right|}{\sqrt{\left(\tilde{Q},\,\tilde{Q}\right)}}, \tag{5.1.16}$$

which reduces to the standard expression of the isotropic case in equation (4.3.33) if $\mathcal{P}_{lm}(f) = \delta_{l0}\,\delta_{m0}\,\mathcal{P}_{00}$.

5.2 Search for anisotropic SGWB: Sky mapping

The previous section does not address the problem of how to infer the components $\mathcal{P}_p(f)$ given the measured values of the cross-correlation statistic[3,4] (or its harmonics, in the case where $p = \{lm\}$). This can be done by building the maximum likelihood estimators for the components $\mathcal{P}_p(f)$ of a SGWB power distribution spectrum $\mathcal{P}(f,\,\hat{\boldsymbol{n}})$. From the previous section, the expectation value of the cross-correlation $C_{IJ}(t;\,f)$ at a single frequency is given by

$$\begin{aligned}\langle C_{IJ}(t;\,f)\rangle &= \frac{T}{2}\int_{S^2}\mathrm{d}^2\hat{\boldsymbol{n}}\,\gamma_{IJ}(t;\,f,\,\hat{\boldsymbol{n}})\,\mathcal{P}(f,\,\hat{\boldsymbol{n}})\\ &= \frac{T}{2}\sum_{p}\gamma_{IJ,\,p}(t;\,f)\,\mathcal{P}_p(f) = K_{IJ}\,\mathcal{P},\end{aligned} \tag{5.2.1}$$

where

$$K_{IJ} = K_{IJ,\,t\,f\,p} \equiv \frac{T}{2}\,\gamma_{IJ,\,p}(t;\,f), \tag{5.2.2}$$

and the matrix product is a summation over the 2-sphere basis components p. As in section 4.3, the cross-correlation covariance matrix is nearly diagonal in the small signal limit and in the absence of correlated noise, namely

$$\begin{aligned}N_{t,f,t',f'} &\equiv \mathrm{Cov}(C_{IJ}(t;\,f),\,C_{IJ}(t';\,f'))\\ &\equiv \langle C^{*}_{IJ}(t;\,f),\,C_{IJ}(t';\,f')\rangle - \langle C^{*}_{IJ}(t;\,f)\rangle\,\langle C_{IJ}(t';\,f')\rangle\\ &\approx \frac{T}{4}\delta(t-t')\,\delta(f-f')\,P_{n_I}(t;\,f)\,P_{n_J}(t;\,f).\end{aligned} \tag{5.2.3}$$

Assuming the noise PSD is known (or estimated from the auto-correlated output of each detector) and Gaussian-stationary distributed, the likelihood function of the

[3]The inverse problem and map making for SGWB searches were first addressed in [432], and then refined in [429,433,434]

[4]If cross-correlation statistics are not available due to the lack of a detector network, alternative map-making techniques, such as phase coherent mapping [241,435], can be employed.

cross-correlated data for a given signal model is

$$p(C|\mathcal{P}) \propto \exp\left[-\frac{1}{2}\,(C - K\,\mathcal{P})^{\dagger}\,N^{-1}\,(C - K\,\mathcal{P})\right], \tag{5.2.4}$$

where the IJ indices have been dropped for notational convenience, while the matrix products involve summation over (discrete) times and frequencies t and f and 2-sphere basis components p. The maximum likelihood estimator of $\mathcal{P}$ follows immediately as

$$\hat{\mathcal{P}} = \Gamma^{-1}\,X, \tag{5.2.5}$$

where

$$X \equiv K^{\dagger}N^{-1}C, \qquad \Gamma \equiv K^{\dagger}N^{-1}K \tag{5.2.6}$$

are called *dirty map* and *Fisher (information) matrix*. The dirty map represents the GW sky as observed by a detector pair, while the Fisher matrix acts as a *point spread function*, blurring the sky even in the absence of noise.

The dirty map and Fisher matrix for a network of detectors, after having combined the data over time, frequencies, and independent baselines, are the sum of the individual dirty maps and Fisher matrices, and their explicit expressions read as

$$X \equiv X_p = 4\Delta f \sum_{I}\sum_{I>J}\sum_{t}\sum_{f} \gamma^{*}_{IJ,\,p}(t;\,f)\frac{1}{P_{n_I}(t;\,f)\,P_{n_J}(t;\,f)}\,C_{IJ}(t;f), \tag{5.2.7}$$

$$\Gamma \equiv \Gamma_{pp'} = 2T\Delta f \sum_{I}\sum_{I>J}\sum_{t}\sum_{f} \gamma^{*}_{IJ,\,p}(t;\,f)\frac{1}{P_{n_I}(t;\,f)\,P_{n_J}(t;\,f)}\,\gamma_{IJ,\,p}(t;f). \tag{5.2.8}$$

In the ideal case where the Fisher matrix is invertible, $\hat{\mathcal{P}}$ is an unbiased estimator of $\mathcal{P}$ called *clean map*, namely

$$\langle X\rangle = K^{\dagger}N^{-1}K\,\mathcal{P} \equiv \Gamma\,\mathcal{P} \implies \left\langle\hat{\mathcal{P}}\right\rangle = \mathcal{P}. \tag{5.2.9}$$

Similarly, in the weak-signal limit, the dirty-map and estimator covariance matrices read

$$\left\langle XX^{\dagger}\right\rangle - \langle X\rangle\,\left\langle X^{\dagger}\right\rangle \approx \Gamma, \tag{5.2.10}$$

$$\left\langle\hat{\mathcal{P}}\hat{\mathcal{P}}^{\dagger}\right\rangle - \left\langle\hat{\mathcal{P}}\right\rangle\,\left\langle\hat{\mathcal{P}}^{\dagger}\right\rangle \approx \Gamma^{-1}, \tag{5.2.11}$$

meaning that the Fisher matrix Γ and its inverse Γ^{-1} are the covariance matrices of the dirty and clean maps, respectively.

However, the Fisher matrix is not invertible in general due to *null directions* from the detector antenna patterns blind spots spanning the sky during the observation time. As a consequence, to obtain the clean map, it is necessary to regularise the singular

Fisher matrix. A general procedure that can be used for any $n \times m$ matrix S is the *singular value decomposition* (SVD) [436]. The SVD method allows factorising the matrix as

$$S = U\Sigma V^{\dagger}, \tag{5.2.12}$$

where U and V are $n \times n$ and $m \times m$ unitary matrices, and Σ is a $n \times m$ rectangular matrix with (real, non-negative) singular values along its diagonal and with zeroes everywhere else. In this way, it is possible to define a *pseudo-inverse* matrix S^{+} of S as

$$S^{+} = V\Sigma^{+}U^{\dagger}, \tag{5.2.13}$$

where Σ^{+} is the transposed matrix of S after having substituted non-zero elements along the diagonal with their reciprocal. This matrix coincides with S^{-1} when S is not singular.

By applying the SVD to the Fisher matrix, it turns out that

$$\hat{\mathcal{P}} = \Gamma^{+}X, \tag{5.2.14}$$

which in turns implies

$$\left\langle \hat{\mathcal{P}} \right\rangle = \Gamma^{+}\Gamma\,\mathcal{P}, \tag{5.2.15}$$

$$\left\langle \hat{\mathcal{P}}^{\dagger}\hat{\mathcal{P}} \right\rangle - \left\langle \hat{\mathcal{P}}^{\dagger} \right\rangle \left\langle \hat{\mathcal{P}} \right\rangle \approx \Gamma^{+}. \tag{5.2.16}$$

This shows that $\hat{\mathcal{P}}$ is actually a biased estimator of $\mathcal{P}$ if $\Gamma^{+} \neq \Gamma^{-1}$.

5.3 Pixel basis and SpH basis

Based on the characteristics of the source of interest, it may be preferable to choose different bases over which to expand the geometrical factors and $\mathcal{P}(f,\,\hat{\boldsymbol{n}})$ and apply the maximum likelihood approach described above. Typically, the choice falls on two bases, namely the *pixel basis* and the *spherical harmonics basis*.

5.3.1 Pixel basis

The pixel basis is defined trough the condition

$$\mathcal{P}(f,\,\hat{\boldsymbol{n}}) = \mathcal{P}_{\hat{\boldsymbol{n}}_0}(f)\,\delta^{(2)}(\hat{\boldsymbol{n}} - \hat{\boldsymbol{n}}_0) \Longleftrightarrow e_p(\hat{\boldsymbol{n}}) \equiv \delta^{(2)}(\hat{\boldsymbol{n}} - \hat{\boldsymbol{n}}_0). \tag{5.3.1}$$

From this definition, it becomes natural to employ the pixel basis when searching over a point-like source or an anisotropic SGWB dominated by a restricted ensemble of widely separated point sources. If the number of sources increases, becoming dense enough, the spread function of the detector network causes signals from neighbour-

ing sources to interfere with one another. This makes the pixel basis not suitable to describe SGWBs with extended sources.

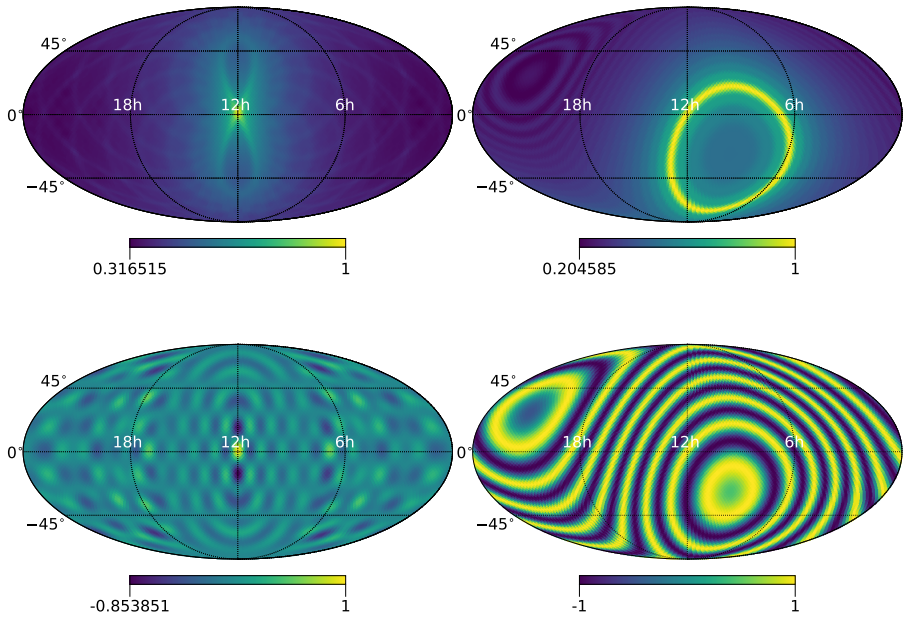

Figure 5.2: Toy models (flat PSDs and constant, isotropic detector response functions) of the HL baseline point-spread functions for a broad-band point-like source located at centre of the map. Units are arbitrary. Top left: broad-band (1-1000 Hz), integrated over one sidereal day. Top right: broad-band (1-1000 Hz) at at time $t = 0$. Bottom left: 375 Hz, integrated over one sidereal day. Bottom right: 375 Hz, at time $t = 0$.

The search technique associated with the pixel basis is known in the literature as *gravitational-wave radiometry* [433, 434, 437] (in analogy with the radiometry techniques used in electromagnetic astronomy and in CMB searches, and to distinguish it from the search employing spherical harmonics as a basis, see the next subsection). The idea behind this technique is to use the Earth rotation synthesis to "point" the detector network towards the desired sky directions by introducing appropriate time delays between the data streams of each detector pair. Every time delay corresponds to the difference in the arrival time of a GW signal at the two detector sites forming the baseline. As a consequence, by cross-correlating the appropriately time-delayed data from two detectors, it is possible to make the GW signal interfere constructively, allowing for the pinpointing of different sky locations. In practice, due to the finite resolution of the individual baselines, which is usually estimated through the diffraction

limit[5] [438]

$$\Delta\theta_{IJ} \approx \frac{\lambda_{\rm gw}}{2|\Delta\vec{\boldsymbol{x}}_{IJ}|} = \frac{c}{2f_{\rm gw}|\Delta\vec{\boldsymbol{x}}_{IJ}|}, \tag{5.3.2}$$

the baselines synthesise the sky into patches rather than individual locations. Moreover, even if the detectors were ideal, with infinite sky resolution and without noise, it would still not be possible to synthesise a point-like source in the sky with a single baseline. This is due to the degeneracy between different locations induced by the time-delay circles (see figure 5.2), with the result that a point-like source is mapped into an eight or tear-drop shape (see again figure 5.2 and these animations).

Using the pixel basis and employing the maximum-likelihood deconvolution from the previous section, it is possible to create a sky atlas at all frequencies of the SGWB anisotropies; see [430,433]. This can be done in a model-independent way by estimating the spatial distribution of a SGWB with a flat strain spectral density $\mathcal{P}(f,\,\hat{\boldsymbol{n}}) = \mathcal{P}(\hat{\boldsymbol{n}})$, which can be later reweighted to the model of interest $\mathcal{P}(f,\,\hat{\boldsymbol{n}})$. This *all-sky all-frequency* approach in the pixel basis can be easily used to recover the results in the case of isotropic SGWBs. This can be done more easily by invoking the assumption of factorisability of $\mathcal{P}(f,\,\hat{\boldsymbol{n}})$ in one frequency-dependent and one angular-dependent factor:

$$\mathcal{P}(f,\,\hat{\boldsymbol{n}}) = \bar{H}(f)\,\mathcal{P}(\hat{\boldsymbol{n}}), \tag{5.3.3}$$

where $\bar{H}(f)$ is the spectral shape of the SGWB, defined in such a way that $\bar{H}(f_{\rm ref}) = 1$ for the choice of a specific reference (pivot) frequency. If the isotropic estimator is in the case of an SGWB with power-law strain spectral density or energy density, $\bar{H}(f)$ is usually defined as [430, 433]

$$\bar{H}(f) \equiv \left(\frac{f}{f_{\rm ref}}\right)^{\beta}, \qquad \beta = \alpha - 3. \tag{5.3.4}$$

[5] For a better estimation of a baseline and, more in general, of a detector network, a careful analysis of the network Fisher matrix should be performed. In this case, the solid angle resolution can be shown to scale inversely proportional to the squared SNR; see, for example, [434, 437].

With these definitions in mind, it is now straightforward to derive the isotropic estimator expressions as[6]

$$\hat{S}_{\rm ref}(f) \equiv \hat{\mathcal{P}}(f) = \sigma^2_{\rm iso}(f)\,\frac{5}{4\pi}\int_{\mathcal{S}^2} {\rm d}^2\hat{\boldsymbol{n}}\,\hat{\mathcal{P}}(f;\hat{\boldsymbol{n}})\,\sigma^{-2}_{\hat{\boldsymbol{n}}}(f), \tag{5.3.6}$$

$$\sigma^{-2}_{\rm iso}(f) = \left(\frac{5}{4\pi}\right)^{-2}\int_{\mathcal{S}^2} {\rm d}^2\hat{\boldsymbol{n}}\int_{\mathcal{S}^2} {\rm d}^2\hat{\boldsymbol{n}}'\,\Gamma_{\hat{\boldsymbol{n}}\hat{\boldsymbol{n}}'}(f), \tag{5.3.7}$$

where

$$\hat{\mathcal{P}}(f;\hat{\boldsymbol{n}}) = \Gamma^{-1}_{\hat{\boldsymbol{n}}\hat{\boldsymbol{n}}'}(f)\,X_{\hat{\boldsymbol{n}}'}(f), \tag{5.3.8}$$

$$\sigma^{-2}_{\hat{\boldsymbol{n}}}(f) = {\rm diag}\left\{\Gamma_{\hat{\boldsymbol{n}}\hat{\boldsymbol{n}}'}(f)\right\}, \tag{5.3.9}$$

$$X_{\hat{\boldsymbol{n}}}(f) = 4\Delta f\sum_I\sum_{J>I}\sum_t \gamma^*_{IJ}(t;\,f,\,\hat{\boldsymbol{n}})\,\frac{\bar{H}(f)}{P_{n_1}(f)\,P_{n_2}(f)}C_{IJ}(t;\,f), \tag{5.3.10}$$

$$\Gamma_{\hat{\boldsymbol{n}}\hat{\boldsymbol{n}}'}(f) = 2T\Delta f\sum_I\sum_{J>I}\sum_t \gamma^*_{IJ}(t;\,f,\,\hat{\boldsymbol{n}})\,\frac{\bar{H}^2(f)}{P_{n_1}(f)\,P_{n_2}(f)}\gamma_{IJ}(t;\,f,\,\hat{\boldsymbol{n}}'). \tag{5.3.11}$$

Similar estimators can be obtained for $\Omega_{\rm gw}(f_{\rm ref},\,\hat{\boldsymbol{n}})$, and for the GW energy flux $\mathcal{F}_{\rm gw}(f,\,\hat{\boldsymbol{n}})$, and the sky-integrated counterparts, by opportunely rescaling and considering the proper frequency dependency in the above equations. It should be noticed that the above (maximum-likelihood) procedure for a detector pair IJ is equivalent to the matched-filter approach with an appropriately normalised cross-correlation statistic

$$C_{IJ}(t;\,f) \equiv \int_{-\infty}^{\infty}{\rm d}f\,Q_{IJ}(t;\,f,\,\hat{\boldsymbol{n}})\,\tilde{s}^*_I(t;\,f)\tilde{s}_J(t;\,f), \tag{5.3.12}$$

with filter function

$$Q_{IJ}(t;\,f,\,\hat{\boldsymbol{n}}) \propto \frac{\gamma_{IJ}(t;\,f\,\hat{\boldsymbol{n}})\,\bar{H}(f)}{P_{n_1}(t;\,f)P_{n_2}(t;\,f)}. \tag{5.3.13}$$

With the matched-filter approach, the estimators $\hat{\mathcal{P}}(\hat{\boldsymbol{n}})$ for a detector network are recovered by summing the individual-baseline statistics (5.3.12) over the times and the independent baselines, using as weights the inverse variances of the individual-baseline statistics [433, 434].

The results from the pixel basis can also be used for other kinds of studies, for example, considering the frequency spectrum from a given sky direction (patch) or

[6]Given that real-world estimators are built starting from discrete quantities, the integrals over the solid angle are replaced by sums over the different directions

$$\int_{\mathcal{S}^2}{\rm d}^2\hat{\boldsymbol{n}}\ldots \to \sum_i \Delta\hat{\boldsymbol{n}}_i, \tag{5.3.5}$$

where $\Delta\hat{\boldsymbol{n}}_i$ is the solid angle element associated with the i-th direction. By employing the HEALPix pixelisation scheme [439], it simplifies to $\Delta\hat{\boldsymbol{n}}_i^{\rm HEALPix} = 4\pi/N_{\rm pix}$, where $N_{\rm pix}$ is the number of pixels in which the sky has been decomposed.

looking for specific sources (*narrow-band radiometer search*) [1]. Alternatively, the broad-band nature of the stochastic signal can be exploited, combining the measurements over frequencies and ignoring the correlation among adjacent pixels (meaning that the Fisher matrix can be approximated to be diagonal) while still retaining directionality and producing sky-maps (*broad-band radiometer search*) [1]. These two kinds of analysis and their implication will be discussed in chapter 6, when presenting the results from the third observing run of the LIGO-Virgo-KAGRA collaboration [1].

5.3.2 Spherical harmonic basis

The spherical harmonic decomposition (SHD) [429,432] can be used as an alternative to the pixel basis when the sources generating the SGWB have a non-negligible angular extension and pixel-to-pixel correlation cannot be neglected. This can be the case of a SGWB of cosmological origin, where the employment of the spherical harmonic basis allows for the inheritance of many of the techniques used in CMB studies.

The signal model assumes the GW power is expanded up to some maximal $l_{\max}$ as

$$\mathcal{P}(f, \hat{\boldsymbol{n}}) = \sum_{l=0}^{l_{\max}} \sum_{m=-l}^{l} \mathcal{P}_{lm}(f, \hat{\boldsymbol{n}})\, Y_{lm}(\hat{\boldsymbol{n}}). \tag{5.3.14}$$

The cutoff in the l-modes expansion can be theoretically motivated, but in practice, it turns out that this limit is more often imposed by the limited angular resolution of the baselines in the detector network. This limit can be estimated again from the diffraction limit in equation (5.3.2), by observing that

$$l_{\max} \approx \frac{\pi}{\Delta\theta} \approx \pi \frac{2 f_{\mathrm{gw}} |\Delta\vec{\boldsymbol{x}}_{IJ}|}{c}, \tag{5.3.15}$$

where f is the maximum frequency at which the GW signal is emitted. Considering the LIGO Hanford-LIGO Livingston baseline, with $|\Delta\vec{\boldsymbol{x}}_{IJ}| \approx 3000\,\mathrm{km}$ and at $f = 500$ Hz, the cutoff is $l_{\max} \approx 30$. If there were no limits on $l_{\max}$, the results from the SHD would be equivalent to those obtained using the pixel basis [429]. For a recent study about ground-based GW detector network angular resolution, see [440].

Similarly to what happens in the radiometer search for a power-law power spectrum, it is possible to build broadband estimators for the $\mathcal{P}_{lm}$ as

$$\hat{\mathcal{P}}_{lm} = (\Gamma_R^{-1})_{lm,\, l'm'}(f) X_{l'm'}(f) \tag{5.3.16}$$

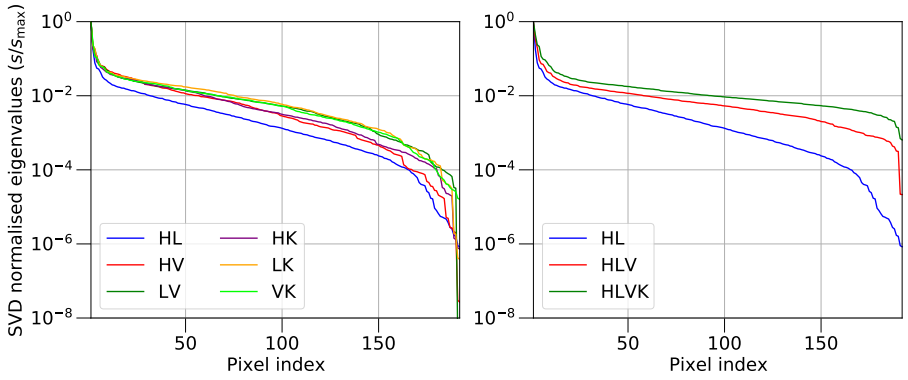

Figure 5.3: Example of singular values for different baselines in the HLVK detector network for $n_{\rm side} = 4$, assuming all detectors having the same flat PSDs and using real geometrical factor [`my_code`]. The pixel index ordering follows the HEALPix ring scheme.

where

$$X_{lm}(f) = 4\Delta f \sum_I \sum_{J>I} \sum_f \sum_t \gamma^*_{IJ,\,lm}(t;\,f) \frac{\bar{H}(f)}{P_{n_1}(f)\,P_{n_2}(f)} C_{IJ}(t;\,f), \quad (5.3.17)$$

$$\Gamma_{lm,\,l'm'} = 2T\Delta f \sum_I \sum_{J>I} \sum_f \sum_t \gamma^*_{IJ,\,lm}(t;\,f) \frac{\bar{H}^2(f)}{P_{n_1}(f)\,P_{n_2}(f)} \gamma_{IJ,\,l'm'}(t;\,f), \quad (5.3.18)$$

that allows to reconstruct the clean map $\mathcal{P}(\hat{\boldsymbol{n}})$ when summed over l and m. An important difference with the standard radiometer search is that here the correlation among different pixels cannot be ignored due to the extended nature of the assumed source. This implies that a regularisation procedure is necessary in order to (numerically) (pseudo-)invert the sparse Fisher matrix due to the detector network blindness to different lm-modes; see figure 5.3 to better visualise the problem. In the standard analyses [1], after having performed the SVD decomposition, the regularisation scheme consists in removing 1/3 of the eigenvalues (namely the ones with the lowest singular values). This choice is somewhat arbitrary and throws away information, but it still allows for good recoveries when dealing with simulated signals [429]. In view of this, other regularisation schemes have been studied in the past few years [440–443] exploring more systematic and flexible treatments case by case, retaining as much information as possible from lm-modes with lower eigenvalues. Nonetheless, it should be noticed (see again figure 5.3) that a natural regularisation happens when multiple detectors, and hence baselines, are included in the network. This is because the additional detectors (and baselines) (partially) fill the blind spots in the combined antenna pattern of the network.

As already mentioned in section 5.2, this "by-hand" regularisation introduces biases in the clean-map estimators. This becomes explicit when expressing the results

in terms of the C_l, measuring the squared angular power in the mode l. The C_l are defined in analogy to what is done for CMB experiments, namely [429, 444]

$$C_l \equiv \frac{1}{2l+1} \sum_{m=-l}^{l} |\mathcal{P}_{lm}|^2, \tag{5.3.19}$$

and their naive estimators are obtained by simply replacing $\mathcal{P}_{lm}$ with the estimators $\hat{\mathcal{P}}_{lm}$, leading to

$$\hat{C}_l \equiv \frac{1}{2l+1} \sum_{m=-l}^{l} \left|\hat{\mathcal{P}}_{lm}\right|^2. \tag{5.3.20}$$

However, the estimators $\hat{\mathcal{P}}_{lm}$ are biased, and hence the $\hat{C}_l$ are biased as well, as can be seen from their expectation value and variance from [429] (in the small-signal approximation):

$$\left\langle \hat{C}_l \right\rangle \approx C_l + \frac{1}{2l+1} \sum_{m} (\Gamma_R^{-1})_{lm,lm}, \tag{5.3.21}$$

$$\mathrm{Var}\left(\hat{C}_l\right) \approx \frac{2}{2l+1} \sum_{m,\,m'} (\Gamma_R^{-1})_{lm,lm'}. \tag{5.3.22}$$

As a consequence, the unbiased estimators are [429]

$$\hat{C}_l = \hat{C}_l^{\mathrm{biased}} - \frac{1}{2l+1} \sum_{m} (\Gamma_R^{-1})_{lm,lm}. \tag{5.3.23}$$

As a final note, it is important to observe that the above formalism of the SHD has been recently extended to an all-sky, all-frequency approach, on the same line as the one used in the pixel domain. This has been introduced in [445] and has improved the reach of the SHD searches, allowing to get and store sky maps from spherical harmonics expansion and enabling the calculation of the corresponding $C_l(f)$ at all frequencies.

5.3.3 λ-statistic and "targeted" searches

The map-making techniques described in the previous and present sections have the disadvantage of requiring the deconvolution of the cross-correlation statistic, hence possibly suffering from numerical errors and artefacts arising from the deconvolution process and/or the problem being ill-posed. In addition to that, the map-making technique does not supply clear methodology about how to claim the presence of a signal in the data, especially in the small-signal regime. The *λ-statistic*, introduced in [429,437], was proven to solve this issue and to be employable as a detection statistic for anisotropic SGWB searches, independently of the basis used for the power spectrum $\mathcal{P}(f, \hat{\boldsymbol{n}})$ decomposition.

The λ statistic for a single baseline is defined as the maximum log-likelihood ratio (MLR) statistic from the likelihood in equation (5.2.4) in the presence of a signal and the corresponding likelihood in the absence of a signal, namely

$$\lambda_{IJ} \equiv \frac{X^{\dagger}_{IJ}\bar{\mathcal{P}}}{\sqrt{\bar{\mathcal{P}}^{\dagger}\Gamma_{IJ}\bar{\mathcal{P}}}}, \tag{5.3.24}$$

where $\bar{P}$ is the template $\mathcal{P}(f,\,\hat{\boldsymbol{n}})$ normalised to unity when integrated over the sky (after having been combined over frequencies), and the matrix-vector product is intended as a sum over times, frequencies, and the 2-sphere components. The above definition can be extended to N_b baselines as

$$\lambda \equiv \frac{\sum_{\mathcal{I}}^{N_b} X^{\dagger}_{\mathcal{I}}\bar{\mathcal{P}}}{\sqrt{\sum_{\mathcal{I}}^{N_b} \bar{\mathcal{P}}^{\dagger}\Gamma_{\mathcal{I}}\bar{\mathcal{P}}}}. \tag{5.3.25}$$

The advantage of the λ-statistic, which is defined in the dirty map space, is that it does not require solving any deconvolution problem (it is still possible to define it also in the clean map space, but this would introduce issues since deconvolution must be done in that case, see [437]).

The λ-statistic can be employed for blind searches for anisotropic SGWB where $\bar{\mathcal{P}}(f,\,\hat{\boldsymbol{n}})$ is unknown. Alternatively, if a template for the SGWB is available, the λ-statistic can be further maximised over different models and parameters for $\mathcal{P}$. In this way, it becomes possible to perform *target directional searches* [446] for anisotropic SGWB with power spectrum

$$\mathcal{P}(f,\,\hat{\boldsymbol{n}}) = \xi\,\bar{H}(f)\,\bar{\mathcal{P}}(\hat{\boldsymbol{n}}), \tag{5.3.26}$$

where ξ a scalar denoting the overall amplitude of the spectrum that depends on the parameters characterising the background. In this case the λ-statistic becomes the SNR related to the unbiased estimator of the overall amplitude, similarly to what happens in searches for deterministic GW signals [429, 437].

$$\hat{\xi} \equiv \frac{X^{\dagger}\bar{\mathcal{P}}}{\bar{\mathcal{P}}^{\dagger}\Gamma\bar{\mathcal{P}}}, \tag{5.3.27}$$

with variance

$$\sigma^2_{\hat{\xi}} \equiv \frac{1}{\bar{\mathcal{P}}^{\dagger}\Gamma\bar{\mathcal{P}}}. \tag{5.3.28}$$

5.4 "Exotic" backgrounds

5.4.1 Polarised backgrounds

The formalism introduced for anisotropic SGWB can be easily adapted to the case of anisotropic, polarised SGWBs (leading to polarisation maps [434]). The 2-point

correlation function in this case reads

$$\left\langle \tilde{h}^{*}_{A}(f,\,\hat{\boldsymbol{n}})\,\tilde{h}_{A'}(f',\,\hat{\boldsymbol{n}}')\right\rangle = \frac{\delta\left(f-f'\right)}{2}\,\delta^{2}\left(\hat{\boldsymbol{n}}-\hat{\mathbf{n}}'\right)\,\mathcal{P}_{AA'}(f,\hat{\boldsymbol{n}}), \tag{5.4.1}$$

where $\mathcal{P}_{AA'}(f,\hat{\boldsymbol{n}})$ is now a polarisation correlation matrix, whose elements can be written as a function of the *Stokes' parameters* I, Q, U, and V [7] that are customarily used in CMB searches:

$$\mathcal{P}_{AA'}(f,\hat{\boldsymbol{n}}) = \frac{1}{2}\begin{pmatrix} I(f,\,\hat{\boldsymbol{n}})+Q(f,\,\hat{\boldsymbol{n}}) & U(f,\,\hat{\boldsymbol{n}})-iV(f,\,\hat{\boldsymbol{n}}) \\ U(f,\,\hat{\boldsymbol{n}})+iV(f,\,\hat{\boldsymbol{n}}) & I(f,\,\hat{\boldsymbol{n}})-Q(f,\,\hat{\boldsymbol{n}}) \end{pmatrix}. \tag{5.4.3}$$

However, early-universe models predicting the existence of SGWBs with a net polarisation (such as pre-inflationary and pre-big-bang ones [448,449]) claim that the associated parity violations would manifest as an asymmetry in the amount of left and right circularly polarised GWs. This implies that the above quantities must be expressed using the circular polarisation basis tensors e^{C}_{ab}, $C=\{R\,L\}$[8], namely

$$\left\langle \tilde{h}^{*}_{C}(f,\,\hat{\boldsymbol{n}})\,\tilde{h}_{C'}(f',\,\hat{\boldsymbol{n}}')\right\rangle = \frac{\delta\left(f-f'\right)}{2}\,\delta^{2}\left(\hat{\boldsymbol{n}}-\hat{\mathbf{n}}'\right)\,\mathcal{P}_{CC'}(f,\hat{\boldsymbol{n}}), \tag{5.4.6}$$

where now

$$\mathcal{P}_{AA'}(f,\hat{\boldsymbol{n}}) = \frac{1}{2}\begin{pmatrix} I(f,\,\hat{\boldsymbol{n}})+V(f,\,\hat{\boldsymbol{n}}) & Q(f,\,\hat{\boldsymbol{n}})-iU(f,\,\hat{\boldsymbol{n}}) \\ Q(f,\,\hat{\boldsymbol{n}})+iU(f,\,\hat{\boldsymbol{n}}) & I(f,\,\hat{\boldsymbol{n}})-V(f,\,\hat{\boldsymbol{n}}). \end{pmatrix} \tag{5.4.7}$$

From the above definition, it is possible to note that $I(f,\,\hat{\boldsymbol{n}})$ is equivalent to the total angular strain spectral density if the SGWBs were unpolarised, while $V(f,\,\hat{\boldsymbol{n}})$ quantifies the degree of asymmetry between the right and left circular polarisation components:

$$\mathcal{P}_{RR}(f,\hat{\boldsymbol{n}})+\mathcal{P}_{LL}(f,\hat{\boldsymbol{n}}) = I(f,\hat{\boldsymbol{n}}), \tag{5.4.8}$$

$$\mathcal{P}_{RR}(f,\hat{\boldsymbol{n}})-\mathcal{P}_{LL}(f,\hat{\boldsymbol{n}}) = V(f,\hat{\boldsymbol{n}}). \tag{5.4.9}$$

[7] Following [447], the Stokes' parameters for a plane, monochromatic wave are defined as

$$\begin{aligned} I &= \left|h^{2}_{+}\right|+\left|h^{2}_{\times}\right|, & Q &= \left|h^{2}_{+}\right|-\left|h^{2}_{\times}\right|, \\ U &= h^{*}_{\times}h_{+}+h^{*}_{+}h_{\times}, & V &= i\left(h^{*}_{\times}h_{+}-h^{*}_{+}h_{\times}\right). \end{aligned} \tag{5.4.2}$$

[8] The circular polarisation basis tensors e^{C}_{ab}, $C=\{R,\,L\}$ can be defined as a function of the $+$ and $\times$ polarisation ones as

$$e^{R}_{ij} \equiv \frac{e^{+}_{ij}+ie^{\times}_{ij}}{\sqrt{2}}, \qquad e^{L}_{ij} \equiv \frac{e^{+}_{ij}-ie^{\times}_{ij}}{\sqrt{2}}, \tag{5.4.4}$$

whose transformation law under a (passive) rotation by an angle ψ reads

$$e^{R}_{ij} \to e^{-2\pi i\psi}e^{R}_{ij}, \qquad e^{L}_{ij} \to e^{2\pi i\psi}e^{L}_{ij}. \tag{5.4.5}$$

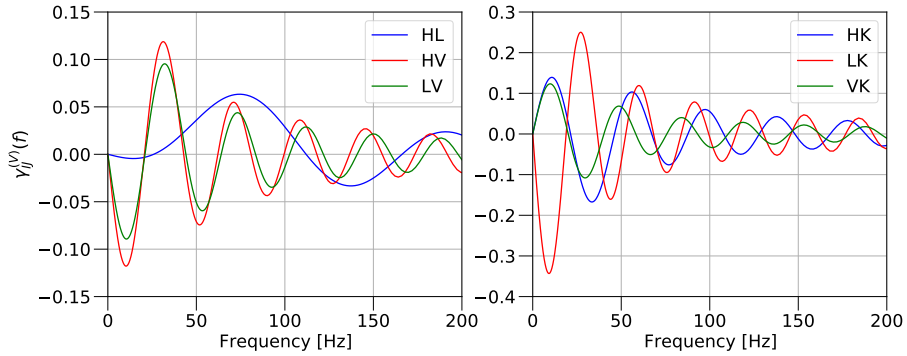

Figure 5.4: $\gamma_{IJ}^{(V)}$ for the HLVK network baselines [`my_code`].

To simplify the picture, one reintroduces the assumption of the SGWB being isotropic, where the circular polarisation matrix assumes a diagonal form, yielding [450, 451]

$$\left\langle \tilde{h}_C^*(f)\, \tilde{h}_{C'}(f') \right\rangle = \frac{\delta\left(f - f'\right)}{2} \frac{\delta^2\left(\hat{\boldsymbol{n}} - \hat{\mathbf{n}}'\right)}{4\pi} S_{h;\,C}(f) \tag{5.4.10}$$

$$S_{h;\,R}(f) \equiv \frac{1}{2}\left(I(f) + V(f)\right), \qquad S_{h;\,L}(f) \equiv \frac{1}{2}\left(I(f) - V(f)\right). \tag{5.4.11}$$

The 2-point correlation function of the signal in a detector pair accounting for the baseline geometry and response becomes

$$\left\langle \tilde{h}_I^*(f) \tilde{h}_J(f) \right\rangle = \frac{1}{2}\,\delta\left(f - f'\right)\left[\Gamma_{IJ}^{(I)}(f)\, I(f) + \Gamma_{IJ}^{(V)}(f)\, V(f)\right], \tag{5.4.12}$$

where the two overlap reduction functions for the I and V Stokes' parameters are

$$\Gamma_{IJ}^{(I)}(f) \equiv \frac{1}{8\pi} \int_{\mathcal{S}^2} \mathrm{d}^2\hat{\boldsymbol{n}} \left[F_I^{+\,*}\left(f, \hat{\boldsymbol{n}}\right) F_J^{+}\left(f, \hat{\boldsymbol{n}}\right) + F_I^{\times\,*}\left(f, \hat{\boldsymbol{n}}\right) F_J^{\times}\left(f, \hat{\boldsymbol{n}}\right)\right], \tag{5.4.13}$$

$$\Gamma_{IJ}^{(V)}(f) \equiv \frac{i}{8\pi} \int_{\mathcal{S}^2} \mathrm{d}^2\hat{\boldsymbol{n}} \left[F_I^{+\,*}\left(f, \hat{\boldsymbol{n}}\right) F_J^{\times}\left(f, \hat{\boldsymbol{n}}\right) - F_I^{\times\,*}\left(f, \hat{\boldsymbol{n}}\right) F_J^{+}\left(f, \hat{\boldsymbol{n}}\right)\right] \tag{5.4.14}$$

with $\Gamma_{IJ}^{(I)}(f)$ being identical to the ordinary ORF $\Gamma_{IJ}(f)$ for an isotropic SGWB in equation (4.2.7). The functional dependence of the two ORFs is illustrated in figure 5.4.

The search for these kinds of SGWBs can be easily designed using the cross-correlation techniques presented in chapter 4, together with the maximum likelihood approach presented in section 5.2 to disentangle the I and V components; see [450, 451] for more detailed explanations. In this case, the formulas of the counterparts of the dirty map and the Fisher matrix differ by the geometrical factors $\gamma_{IJ}(t;\, f,\, \hat{\boldsymbol{n}})$

replaced by $\Gamma^{(I)}_{IJ}(f)$ and $\Gamma^{(V)}_{IJ}(f)$, and the indices running along the directions (or the 2-sphere basis components) substituted by I and V. The most recent results using ground-based detectors to infer constraints over the parity-violation degree $V(f)$, under the assumption of a power law in frequency, are presented in [452].

5.4.2 Non-GR polarisations

Theories beyond general relativity allow six polarisation modes: the $+$ and $\times$ *tensor* modes from GR; the X and Y *vector* (or "shear") modes; and two *scalar* modes: the "breathing" mode B and the longitudinal mode L [453]. Using the triads $\hat{\boldsymbol{n}}$, $\hat{\boldsymbol{l}}$, $\hat{\boldsymbol{m}}$ defined in (1.1.27), the mode tensors in the polarisation basis are[9]

$$\begin{aligned} e^{+}_{ab}(\hat{\boldsymbol{n}}) &= \hat{l}_i\hat{l}_j - \hat{m}_i\hat{m}_j, \qquad & e^{\times}_{ab}(\hat{\boldsymbol{n}}) &= \hat{l}_i\hat{m}_j + \hat{m}_i\hat{l}_j, \\ e^{X}_{ab}(\hat{\boldsymbol{n}}) &= \hat{l}_i\hat{n}_j + \hat{n}_i\hat{l}_j, \qquad & e^{Y}_{ab}(\hat{\boldsymbol{n}}) &= \hat{m}_i\hat{n}_j + \hat{n}_i\hat{m}_j, \\ e^{B}_{ab}(\hat{\boldsymbol{n}}) &= \hat{l}_i\hat{l}_j + \hat{m}_i\hat{m}_j, \qquad & e^{S}_{ab}(\hat{\boldsymbol{n}}) &= \sqrt{2}\,\hat{n}_i\hat{n}_j. \end{aligned} \tag{5.4.15}$$

The effect of each polarisation mode on a set of test masses is illustrated in figure 5.5. The tensor, vector, and scalar nature of the mode can be understood by deriving their transformation laws under a (passive) rotation with angle ψ:

$$\begin{aligned} e^{+}_{ab}(\hat{\boldsymbol{n}}) &\to \cos(2\psi)\, e^{+}_{ab}(\hat{\boldsymbol{n}}) + \sin(2\psi)\, e^{\times}_{ab}(\hat{\boldsymbol{n}}), \\ e^{\times}_{ab}(\hat{\boldsymbol{n}}) &\to -\sin(2\psi)\, e^{+}_{ab}(\hat{\boldsymbol{n}}) + \cos(2\psi)\, e^{\times}_{ab}(\hat{\boldsymbol{n}}), \end{aligned} \tag{5.4.16}$$

$$\begin{aligned} e^{X}_{ab}(\hat{\boldsymbol{n}}) &\to \cos\psi\, e^{X}_{ab}(\hat{\boldsymbol{n}}) + \sin\psi\, e^{Y}_{ab}(\hat{\boldsymbol{n}}), \\ e^{Y}_{ab}(\hat{\boldsymbol{n}}) &\to -\sin\psi\, e^{X}_{ab}(\hat{\boldsymbol{n}}) + \cos\psi\, e^{Y}_{ab}(\hat{\boldsymbol{n}}), \end{aligned} \tag{5.4.17}$$

$$e^{B}_{ab}(\hat{\boldsymbol{n}}) \to e^{B}_{ab}(\hat{\boldsymbol{n}}), \qquad e^{L}_{ab}(\hat{\boldsymbol{n}}) \to e^{L}_{ab}(\hat{\boldsymbol{n}}). \tag{5.4.18}$$

Similarly to what was done in the parity violation case, one considers the case of extra polarisations for a Gaussian, stationary, isotropic SGWB and assumes that it is independently polarised. This means that the 2-point correlation function takes the form

$$\left\langle \tilde{h}^{*}_{A}(f)\, \tilde{h}_{A'}(f') \right\rangle = \frac{\delta\,(f-f')}{2}\, \frac{\delta^2\,(\hat{\boldsymbol{n}}-\hat{\mathbf{n}}')}{4\pi}\, \delta_{AA'}\, S_{h;\,A}(f), \tag{5.4.19}$$

where $A = \{+,\, \times,\, X,\, Y,\, B,\, L\}$. The functions $S_{h;\,A}(f)$ are defined in such a way to recover the one-sided tensor, vector, and scalar strain spectral densities as

$$\begin{aligned} S^{(T)}_{h}(f) &= S_{h;\,+}(f) + S_{h;\,\times}(f), \\ S^{(V)}_{h}(f) &= S_{h;\,X}(f) + S_{h;\,Y}(f), \\ S^{(S)}_{h}(f) &= S_{h;\,B}(f) + S_{h;\,S}(f). \end{aligned} \tag{5.4.20}$$

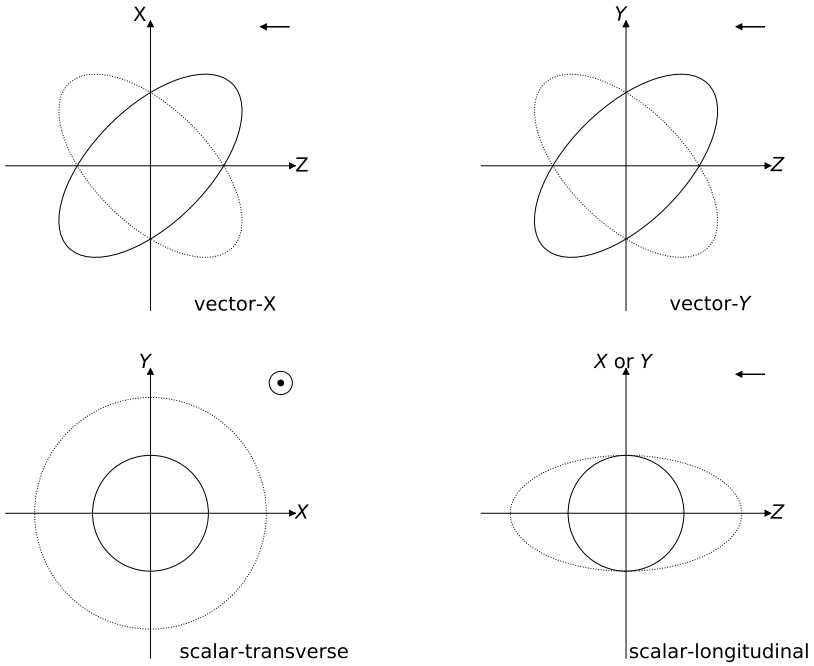

Figure 5.5: Vector and scalar polarisation effects on test mass systems [my_code].

In the following, the SGWB is assumed to be unpolarised in each sector.

The overlap reduction functions can then be defined for each pair of modes as

$$\Gamma_{IJ}^{(T)}(f) \equiv \frac{1}{8\pi} \int_{\mathcal{S}^2} \mathrm{d}^2\hat{\boldsymbol{n}} \left[F_I^{+\,*}(f, \hat{\boldsymbol{n}})\; F_J^{+}(f, \hat{\boldsymbol{n}}) + F_I^{\times\,*}(f, \hat{\boldsymbol{n}})\; F_J^{\times}(f, \hat{\boldsymbol{n}}) \right], \tag{5.4.21}$$

$$\Gamma_{IJ}^{(V)}(f) \equiv \frac{1}{8\pi} \int_{\mathcal{S}^2} \mathrm{d}^2\hat{\boldsymbol{n}} \left[F_I^{X\,*}(f, \hat{\boldsymbol{n}})\; F_J^{X}(f, \hat{\boldsymbol{n}}) + F_I^{Y\,*}(f, \hat{\boldsymbol{n}})\; F_J^{Y}(f, \hat{\boldsymbol{n}}) \right], \tag{5.4.22}$$

$$\Gamma_{IJ}^{(S)}(f) \equiv \frac{1}{8\pi} \int_{\mathcal{S}^2} \mathrm{d}^2\hat{\boldsymbol{n}} \left[F_I^{B\,*}(f, \hat{\boldsymbol{n}})\; F_J^{B}(f, \hat{\boldsymbol{n}}) + F_I^{L\,*}(f, \hat{\boldsymbol{n}})\; F_J^{L}(f, \hat{\boldsymbol{n}}) \right], \tag{5.4.23}$$

and are illustrated in figure 5.6, showing that some ground-based detector pairs (such as HL) are more sensitive to vector modes over tensor and scalar modes than tensor modes. The normalisation of the scalar ORF is not unique in the literature, and the one presented here corresponds to the one from [453][10] in the case $\kappa = 2.5$.

[9] Note that different conventions for the normalisation of e_{ab}^{L} exist in the literature [453, 454].

[10] The factor κ used in [453] is defined as the ratio of the longitudinal mode energy density to the scalar one. For a generic κ, the factor in front of the intergral in $\Gamma_{IJ}^{(S)}(f)$ becomes $3/[4\pi(1+2\kappa)]$.

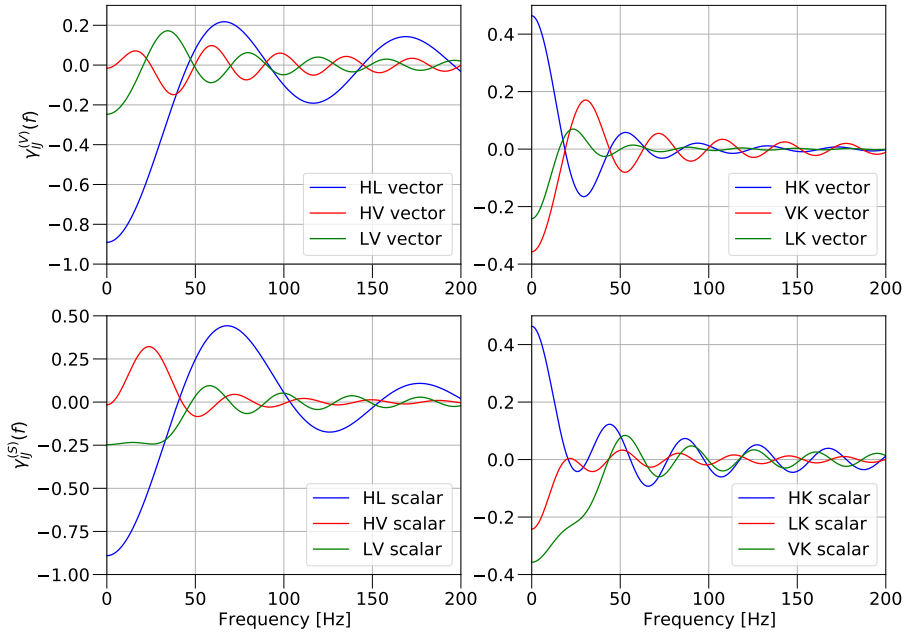

Figure 5.6: ORF corresponding to the vector (top) and scalar (bottom) non-GR polarisations of the HLVK network [`my_code`].

The search to constrain the one-sided spectral densities $S_h^{(T)}(f)$, $S_h^{(V)}(f)$, and $S_h^{(S)}(f)$ makes again use of the Fisher matrix formalism presented before, with the directional indices substituted by $\{T,\, B,\, S\}$ and the geometrical factors by $\Gamma_{IJ}^{(T)}(f)$, $\Gamma_{IJ}^{(V)}(f)$, and $\Gamma_{IJ}^{(S)}(f)$, as presented in [453]. To see how to implement a Bayesian framework that allows for multiple combinations of polarisation to be present at the same time, refer to [454, 455]. The most recent results employing this method for ground-based interferometric detectors frequency range are reported in [258], which uses the data from the first three observing runs from the LIGo-Virgo-KAGRA collaborations and jointly sets the limits $h_0^2\Omega_{\rm gw}^{(T)} \leq 3.0 \times 10^{-9}$, $h_0^2\Omega_{\rm gw}^{(V)} \leq 3.6 \times 10^{-9}$, and $h_0^2\Omega_{\rm gw}^{(S)} \leq 9.7 \times 10^{-9}$ for tensor, vector, and scalar modes, respectively. Recently, the above-mentioned Bayesian formalism has also been extended to anisotropic searches in the spherical harmonics domain [456].

5.4.3 Non-Gaussian backgrounds

Whether a stochastic gravitational-wave background is Gaussian or not is part of the operative definition presented in section 3.1. Assuming to have sufficiently numerous signals overlapping in the time-frequency space and producing confusion noise, Gaussianity is guaranteed as long as the rate of the signals is large enough to invoke the central limit theorem (see [240]). However, as in the case of astrophysical bi-

nary black holes, if the duty cycle of the signal is small, the resulting SGWB will be non-Gaussian but rather intermittent, "popcorn-like".

To search for a non-Gaussian SGWB with cross-correlation techniques, there are two main approaches. The first one consists in including the non-Gaussian nature of the signal in the likelihood by marginalising it over a proper signal model. Then, from the likelihood with or without a signal, it is possible to build frequentist detection statistics by means of the maximum likelihood ratio or by proceeding via a Bayesian model selection. The second approach focuses on deriving frequentist statistics related to the higher-order *moments*[11] of the non-Gaussian distribution, and then use it to perform hypothesis testing. This is usually cast in terms of the third- and fourth-order *cumulants*[12] of the distribution, namely the *skewness* and the (excess) *kurtosis*. This kind of method requires the detector network to be composed of at least three (skewness) and four (kurtosis) detectors. This has become a reality in the last few years and will allow performing these more refined searches; see, for example, [458] and the novel [459, 460].

Likelihood approach

The approach is rather straightforward; assuming Gaussian-stationary noise in the detectors, with a covariance matrix C_n, the likelihood function of observing data $d = \{d_I\}$ in a detector given a model $\bar{h}$ of the signal is

$$p\left(d|\bar{h}, C_n\right) = \frac{1}{\sqrt{\det(2\pi C_n)}} e^{-\frac{1}{2}\sum_{Ii,Jj} n_{Ii}(C^{-1})_{Ii,Jj} n_{Jj}}, \tag{5.4.28}$$

where $n_{Ii} \equiv d_{Ii} - \bar{h}$ are the residuals in the detector I (only noise is expected to be left ideally), must be marginalised over $\bar{h}$

$$p(d|\vec{\theta}_h, \vec{\theta}_n) = \int \mathrm{d}h\, p\left(d|\bar{h}, C_n\right)\, p(\bar{h}|\vec{\theta}_h). \tag{5.4.29}$$

[11] Given a random variable X with probability distribution function $p_X(x)$, the mth-moment of the distribution is defined to be

$$\mu_m \equiv E[X^n] = \langle X^n \rangle \equiv \int_{-\infty}^{\infty} \mathrm{d}x\, p_X(x). \tag{5.4.24}$$

[12] The m-th cumulant κ_m of a probability distribution function can be defined starting from the generating functional (if it exists) [457]

$$K(t) = \ln E\left[e^{tX}\right] \implies \kappa_m \equiv \left.\frac{\mathrm{d}^m K}{\mathrm{d}t^m}\right|_{t=0}. \tag{5.4.25}$$

The first two cumulants coincide with the mean μ and the variance σ^2 of the distribution, while the third- and fourth-order cumulants read

$$\kappa_3 = \mu_3 - \mu_1\mu_2 + 2\mu_1^3, \tag{5.4.26}$$

$$\kappa_4 = \mu_4 - 4\mu_3\mu_1 - 3\mu_2^2 + 12\mu_2\mu_1^2 - 6\mu_1^4. \tag{5.4.27}$$

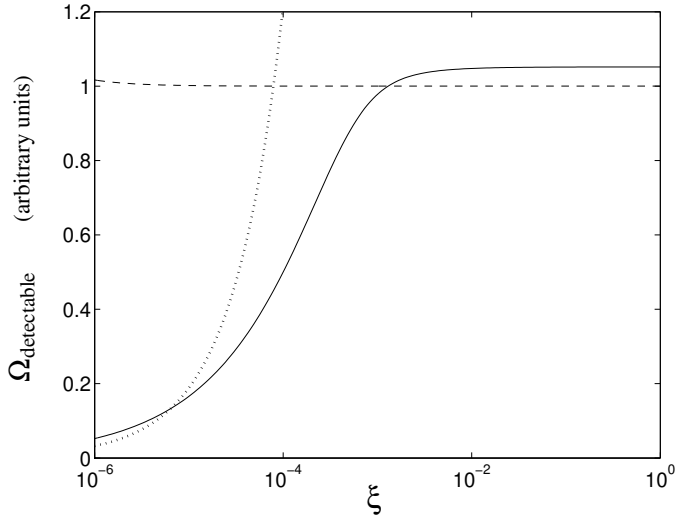

Figure 5.7: Theoretical prediction from [461] about the minimum detectable $\Omega_{\rm detectable}$ for the maximum likelihood statistic (solid), the cross-correlation statistic (dashed), and the burst statistic (dotted) as a function of ξ.

This yields a likelihood function that now depends only on the signal and noise parameters $\vec{\theta}_h$ and $\vec{\theta}_n \equiv C_n$. Several priors have been considered in the literature, more or less complex than the standard Gaussian prior assumed until now (see, for example, equation (4.1.6) in section 4.1 for the toy model). For a comprehensive review, see [239], together with the individual works for each prior [240, 461–463].

An early work trying to include non-Gaussian prior and evaluate the impact on the standard cross-correlation search for an isotropic, intermittent SGWB was [461]. The prior adopted for the signal in this case is

$$p(\bar{h}|\xi,\,\alpha) = \prod_{i=1}^{N}\left[\xi\frac{e^{-\bar{h}_i^2/(2\alpha^2)}}{\sqrt{2\pi\sigma_h^2}} + (1-\xi)\delta(\bar{h}_i)\right], \tag{5.4.30}$$

corresponding to a Gaussian burst occurring with probability $0 \leq \xi \leq 1$ and root-mean-square amplitude α. When $\xi = 1$, meaning that the signal is always present, the vanilla case of a continuous, Gaussian background is recovered. The impact of using this Gaussian-mixture-model likelihood in contrast to the standard isotropic search assuming a Gaussian as a function of the probability of having a signal in the data ξ is illustrated in the figure 5.7. Recently, in [464], the approach used in [461] was resurrected and adapted to a Bayesian framework in a simple case, proposing a stochastic-signal-based search for intermittent SGWBs within the frequency band of ground-based interferometers. This search is currently under development to be extended to real-world data, but its final form will noticeably reduce the time needed to detect popcorn-like SGWBs, such as the one from astrophysical BBHs.

Another approach explored in the past years is the one from [462, 465] that considers a generic likelihood for a non-Gaussian background from the superposition of unresolvable signals. The likelihood reads

$$p(\hat{\mathrm{SNR}}|\xi,\,\vec{\theta}_h,\,\vec{\theta}_n) = \prod_i \left[\xi\, S(\hat{\mathrm{SNR}}_i|\vec{\theta}_h) + (1-\xi)\, B(\hat{\mathrm{SNR}}_i|\vec{\theta}_n)\right] \tag{5.4.31}$$

for a pair of detectors $I,\ J$, taking as data the estimators of the signal-to-noise ratio of the cross-correlated power for a segment duration T and frequency resolution Δf:

$$\widehat{\mathrm{SNR}}_i \equiv \widehat{\mathrm{SNR}}(t;\,f) = \sqrt{\frac{4\Delta f}{T}}\,\frac{\tilde{s}_I^*(t;\,f)\tilde{s}_J(t;\,f)}{\sqrt{P_{n_I}(t\,f)\,P_{n_J}(t\,f)}}. \tag{5.4.32}$$

The probability distributions of the SNR for the signal and noise models S and B are generic in the sense that they are estimated via Monte Carlo simulations and time-slides over real data, respectively. Many progresses have been made in the process of transitioning this kind of search (mainly limited by the required computational power) from theory to reality for ground-based interferometers and will be available to the community in the incoming years.

Cumulant approach

As an example of the cumulant approach, one considers the fourth-order correlation approach from [458] for the detection of non-Gaussian stationary SGWBs. Assuming a four-detector network with detectors $I = 1,\ 2,\ 3,\ 4$, the data in the Fourier domain reads

$$\tilde{d}_I = \tilde{h} + \tilde{n}_I, \qquad \tilde{h} = \tilde{g} + \sum_{i=1}^{N_{\mathrm{burst}}} \tilde{b}_i, \tag{5.4.33}$$

where $\tilde{n}_I$ is the noise in the detector I, $\tilde{g}$ the Gaussian component of the signal, and $\tilde{b}_i$ the non-Gaussian component from the superposition of short-duration burst signals. The bursts are assumed to follow a Poisson statistic such that $\langle n\rangle$ bursts are expected in a segment duration T_{seg}. The fourth-order combination considered is

$$\mathcal{K}_4 \equiv \left\langle \tilde{d}_1^*\tilde{d}_2^*\tilde{d}_3\tilde{d}_4\right\rangle - \left\langle \tilde{d}_1^*\tilde{d}_2^*\right\rangle\left\langle \tilde{d}_3\tilde{d}_4\right\rangle - \left\langle \tilde{d}_1^*\tilde{d}_3\right\rangle\left\langle \tilde{d}_{2^*}\tilde{d}_4\right\rangle - \left\langle \tilde{d}_1^*\tilde{d}_4\right\rangle\left\langle \tilde{d}_2^*\tilde{d}_3\right\rangle. \tag{5.4.34}$$

Assuming the absence of correlated noises between two different detectors and assuming all the bursts have the same mean-square-value $\left\langle \tilde{b}\tilde{b}\right\rangle$, the estimator takes the form

$$\mathcal{K}_4 = \langle n\rangle \left\langle \tilde{b}^*\tilde{b}^*\tilde{b}\tilde{b}\right\rangle. \tag{5.4.35}$$

This depends only on the non-Gaussian component of the signal, as expected. This result holds for co-aligned, co-located, identical detectors. Its generalisation to a real

detector network introduces the expressions for the generalised 4-point overlap reduction functions, namely the sky-average product of the four detector response functions. Moreover, the general formula also involves terms also proportional to the circular polarisation components of the non-Gaussian backgrounds. See the original work [458] for all the details that have been omitted here. Given that a network of four advanced interferometers now exists, it could be possible to apply this method to the data that will be publicly available at the end of the fourth LIGO-Virgo-KAGRA observing run.

Part III

Searching for Stochastic Gravitational-Wave Backgrounds with LIGO and Virgo detectors

Chapter 6

Search for anisotropic gravitational-wave backgrounds using data from Advanced LIGO and Advanced Virgo's first three observing runs

"To control one's own destiny takes a mastermind. To execute the plans takes a fool."

Daniel Keyes, *The Minds of Billy Milligan (The Crowded Room)*

This chapter starts the part of the thesis with the original contributions. It covers the searches for anisotropic SGWBs performed during O3 by the LVK collaboration, resulting in the publication [1], *Phys. Rev. D, vol. 104, no. 2, pp. 022005, 2021*. I was the main analyst for the broad-band radiometer (BBR) search and the writer of the corresponding sections in [1]. I was involved in this analysis and the publication process during the first PhD year, from April 2020 to March 2021. This was the first experience in GW data analysis. I learnt from scratch the flow and the challenges of a search for an SGWB and mastered the usage of the `PyStoch` [466] code used to produce the sky maps for the BBR analysis, starting from the pre-processed folded data sets. I also learnt how to evaluate the statistical significance of the maps and to evaluate upper limits in a Bayesian framework, using the previously existing `MATLAB` codes from O2 and adapting them to the O3 needs. In 2023, I translated those codes into Python as part of the LVK stochastic group's code migration process from `MATLAB` to `Python`.

The chapter begins with an historical overview of past LVK anisotropic searches in section 6.1. Then, in section 6.2, the focus shifts to the O3 observing run, and the main pre-processing and data quality procedures common to all SGWB searches are presented there. The BBR analysis is covered in section 6.3: the folding [431] procedure and the first time usage of the `PyStoch` [466] are highlighted, followed by the exposition of the post-processing methods and the presentation of the results from the

search. Eventually, in section 6.4, the results from the narrow-band radiometer (NBR) search and the spherical harmonic decomposition (SHD) one are briefly mentioned, together with some perspective about the future.

6.1 Previous results

Before considering more in detail the directional analyses performed during O3 [1], it is useful to bridge the gap between the past and the present by examining the history of the searches for a Gaussian, stationary, unpolarised, anisotropic SGWB with km-long ground-based GW interferometers. This kind of analysis is more recent in comparison with the isotropic one and was performed over S4 [467] and S5 [468] data in the initial detector era, and over O1 [469] and O2 [470] data (before O3) in the era of advanced detectors. The main results of the searches throughout the years are reported in table 6.1.

6.1.1 S4 and S5

S4 was the first time that a search for a Gaussian, stationary, unpolarised, anisotropic SGWB was performed with ground-based interferometric GW detectors. The analysis at the time was optimised only to search for point-like sources, using the radiometer techniques [433] implemented in that period. The results of the broad-band (all-sky) search were sky-maps of the upper limits over the reference value of the strain $\mathcal{P}(f,\,\hat{\boldsymbol{n}})$[1] and assuming two different power-law models for the spectral shape $H(f)$[2], with $\beta = -3$ (see (3.1.11) for the conversion to $\Omega_{\rm gw}$) for a scale-invariant, cosmological origin SGWB, and $\beta = 0$ for a flat strain in frequency privileging the frequencies for which interferometer strain sensitivity is higher. These 90%-confidence Bayesian upper limits resulted in H_{-3} ranging in $[1.2\times10^{-48},\,1.2\times10^{-47}]\,\mathrm{Hz}^{-1}$ and H_0 ranging in $[8.5\times10^{-49},\,6.1\times10^{-48}]\,\mathrm{Hz}^{-1}$, at 100-Hz reference frequency and depending on the position of the sky. The same limits have also been expressed in terms of the integrated GW flux (and compared with those inferred from the X-ray emission from binaries) and converted to limits on isotropic SGWB, resulting in a result consistent with what was found in the S4 isotropic search [419]. The S4 run was also the first one where the narrow-band directional analysis was performed. This analysis targets individual "directions" in the sky, usually associated with isolated pulsars or binary pulsars, and performs an unmodelled search ($\beta = 0$) for excesses in the (narrow-band root-mean-square) GW strain $h_0 = \sqrt{X_{\hat{\boldsymbol{n}}_0}(f)}$, with $\hat{\boldsymbol{n}}_0$ the direction of the source of interest. During S4, the only targeted direction was the one associated with the low-mass X-ray binary Scorpius X-1 (Sco-X1) [471, 472], resulting in a 90% confidence

[1] Note that in the most recent analyses [1, 469, 470], limits are expressed directly in terms of the GW energy flux spectrum $\mathcal{F}_{\rm gw}(f)$ or the normalised energy density spectrum $\Omega_{\rm gw}(f)$.

[2] Note that this spectral shape is not normalised to 1, in contrast to $\bar{H}(f)$ introduced in chapter 5 and used in nowadays analyses.

Bayesian upper limit on the $h_0(f)$ spectrum, with $h_0 \leq 3.4 \times 10^{-24}$ at 200 Hz for a 0.25 Hz frequency bin.

The search for anisotropic SGWB during S5 [468] incorporated for the first time an optimised search for extended sources, namely the spherical harmonic decomposition. The problem of regularising the Fisher matrix in a real-world case was first addressed in this analysis, resulting in the 1/3 threshold of the removed eigenvalues that is still used in nowadays searches[3,4]. The (90% Bayesian) limits set by this first SHD search were expressed again in terms of the strain spectral density (and the flux), resulting in $5 - 31 \times 10^{-49}\,\mathrm{Hz}^{-1}\,\mathrm{sr}^{-1}$ for $\beta = -3$ at 100 Hz (in a 40-200 Hz frequency band), and $6 - 35 \times 10^{-49}\,\mathrm{Hz}^{-1}\,\mathrm{sr}^{-1}$ for $\beta = 0$ (in a 40-500 Hz frequency band). The BBR search was performed only in the $\beta = 0$ case, with the strain spectral density bounds in the range $2 - 20 \times 10^{-50}\,\mathrm{Hz}^{-1}$, improving the S4 results by a factor of 30. The S5 NBR search was also enriched by considering additional directions other than Sco-X1, namely those corresponding to the Galactic Centre (GC) [473], and the supernova 1987A (SN1987A) [474]. Among the three sources, the best constraint on the strain was as low as 7×10^{-25} in the most sensitive region, about 160 Hz. In the Sco-X1 case, a factor of 5 improvement with respect to S4 results was observed.

6.1.2 O1 and O2 analyses

As in the case of the isotropic search, the upgrade of the detectors to their advanced configuration allowed for a great improvement in the directional analysis sensitivity. The structure of analyses during O1 and O2 remained essentially the same as in S4 and S5. The main changes came from BBR and SHD searches when presenting the results in the 20-500 Hz search band. They are now expressed only in terms of the GW flux $\mathcal{F}_{\mathrm{gw}}(f, \hat{\boldsymbol{n}})$ (BBR) and the normalised energy density spectrum $\Omega_{\mathrm{gw}}(f, \hat{\boldsymbol{n}})$ (SHD). The values are evaluated at the new 25-Hz reference frequency to account for the change in detector sensitivity. The power-law models are now identified no longer with β but rather with $\alpha = \beta + 3$ for consistency with isotropic searches, and $\alpha = 2/3$ ($\beta = -7/3$) for the CBC case has been added to the analyses. From O1 analysis, the improvements with respect to initial LIGO are quoted to be a factor of 8 in the BBR flux for $\alpha = 3$ and factors of 60 and 4 for the SHD for $\alpha = 0$ and 3, respectively [469]. The NBR search has seen a mean factor of 2 strain-sensitivity improvement in the whole 20-1726 Hz search band, with more than a factor of 10 in the 50-300 Hz band.

For what concerns the O2 search, the only noticeable change in the analysis was the presentation of 95% confidence Bayesian upper limits instead of 90% confidence.

[3] This threshold was chosen in such a way to produce reliably reconstructed maps with minimal bias for a simulated signal. In practice, this choice assumes that, on average, the removed modes do not contain more GW power than the retained ones.

[4] This regularisation is practically implemented by setting 1/3 of the $\mathcal{P}_{lm}$ eigenmodes to zero and setting the corresponding eingenvalues in the variance to the average eigenvalues of the retained modes [468]. This leads to more conservative upper limits compared to the case where the same regularisation scheme is used for both the variance and the $\mathcal{P}_{lm}$.

Run	α	$f_{\rm ref}$	$\mathcal{F}_{\rm gw}^{\rm BBR}$ [erg cm^{-2} s^{-1} Hz^{-1}]	$h_0^2\,\Omega_{\rm gw}^{\rm SHD}$ [sr^{-2}]	Direction	$h_0^{\rm NBR}$ [strain]
S4 [467]	0	100 Hz	$[3.8-38]\times10^{-6}$	-	Sco X-1 (200 Hz)	3.24×10^{-24}
	3	"	$[2.7-19]\times10^{-6}$	-		
S5 [468]	0	100 Hz	-	$[3-19]\times10^{-7}$	Sco X-1 (160 Hz)	7×10^{-25}
S5 [468]	3	"	$[6-60]\times10^{-8}$	$[4-22]\times10^{-7}$	SN 1987A, GC	
O1 [469]	0	25 Hz	$[10-56]\times10^{-8}$	$[1.2-3.5]\times10^{-8}$	Sco X-1 (134.5 Hz)	6.7×10^{-25}
	2/3	"	$[5.1-33]\times10^{-8}$	$[0.9-2.7]\times10^{-8}$	SN 197A (172.5 Hz)	5.5×10^{-25}
	3	"	$[0.1-0.9]\times10^{-8}$	$[0.2-1.3]\times10^{-8}$	GC (172.5 Hz)	7.0×10^{-25}
O2 [470]	0	25 Hz	$[4.4-25]\times10^{-8}$	$[0.4-1.3]\times10^{-8}$	Sco X-1 (184.1 Hz)	4.2×10^{-25}
	2/3	"	$[2.3-14]\times10^{-8}$	$[0.3-1.1]\times10^{-8}$	SN 197A (248.25 Hz)	3.6×10^{-25}
	3	"	$[0.05-0.33]\times10^{-8}$	$[0.09-0.51]\times10^{-8}$	GC (157.3)	4.7×10^{-25}

Table 6.1: Upper limits evolution throughout different runs from S4 to O2. The S4 and S5 results for BBR and SHD are expressed as a function of the quantities used when presenting observing run (O1, O2, O3) results (flux and normalised GW energy density), in contrast to the strain power used in the main text. The best upper limits from the NBR are reported at a reference frequency among different directions (S4 and S5), and over a 1 Hz bands, whose central frequencies are listed.

The median improvement of these limits across the sky ranges in 2.6-2.7 (BBR) and 2.8-3 (SHD) factors over the O1 limits. The analysis was characterised by an unidentified outlier at 36.0625 Hz with a marginal significance of 3σ in the direction of SN1987A in O2 data [470]. The significance of the outlier further decreased when including O1 data, making it identifiable with noise (a fact further confirmed during O3 analysis, where the outlier was not present). The results of the O1 and O2 searches have later on been reproduced in [475], allowing to test the folding techniques described in the next section. The results of the two advanced runs are summarised in table 6.1.

6.2 O3 analysis: data preparation

6.2.1 General information about O3

The third LVK observing run officially started on April 1st 2019, 15:00 UTC, and ended on March 27th 2020, 17:00 UTC. The run was divided into two stretches, O3a and O3b, separated by a month-long pause from October 1st 2019, 15:00 UTC, to November 1st 2019, 15:00 UTC. This latency period was used to perform commissioning and improvements in the detectors involved in the data taking. The detector network during O3 was composed by the advanced LIGO Hanford (H), LIGO Livingston (L) [90], and Virgo (V) [94] detectors. The duty factors of the three detectors during the run were 75%, 77%, and 76%, respectively [224, 476]. For the first time in the advanced-detector era, searches for SGWBs have made use of the data from Virgo as well. This allowed having three baselines for the analyses, HL, HV, and LV, in contrast to the HL one only during the first two observing runs. The implications of the Virgo presence for the analyses are discussed in later sections. The amount of coincident live time was 204.5 days for the HL baseline, 187.5 days for the HV one, and 195.4 days for the LV one. These live times do not take into account any data

quality veto in the time and frequency domains. As hinted in section 4.1, stochastic analyses may be fledged from correlated noise [405], such as the magnetic one from Schumann resonances [400, 401]. To assess the impact of magnetic noise on stochastic searches[5], data from magnetometers at the detector sites were used. More specifically, two LEMI-120 magnetometers [477] were installed at each LIGO detector and two low-noise MFS-06 magnetometers by Metronix [478] at the Virgo site. The magnetometer data were processed in the same way as the strain data to allow better comparison with the SGWB searches; see [258] for more details and possible differences.

6.2.2 Pre-processing

The data streams from the different detectors are pre-processed to build the cross-correlation spectra to be analysed for each baseline. The raw time-series strain data of each detector are first down-sampled from 16384 Hz to 4096 Hz[6] to reduce the memory and computational requirements of the analysis. The detector's most sensitive frequency band is between a few Hz and 2 kHz. The new 4096 Hz sampling frequency results in a 2048 Hz Nyquist frequency, corresponding to the upper bound of the detector sensitivity band. This choice neglects the minor contributions from higher frequencies but still allows retaining the full signal spectra in the data. To avoid aliasing effects, the maximum frequency of the analysis must be chosen to be sufficiently below the Nyquist frequency. From past studies [258, 424, 425], 1726 Hz resulted in a good candidate and is used in the analysis. Following the down-sampling, the data are high-pass filtered through a 16th-order Butterworth filter with an 11 Hz knee frequency. This excludes from the analysis the low-frequency content of the data, dominated by seismic noise, in particular below 10 Hz (see section 2.3). To avoid contamination from residual low-frequency noise, the lower bound of the analysed frequencies is chosen to be 20 Hz. Before performing cross-correlation, the data streams were divided into 192-s-long, 50%-overlapping, Hann-windowed segments. The 192-s segment duration is a trade-off between making it possible to identify (noise) narrow spectral features in the data, minimising the amount of rejected data from non-stationarity tests (see below), and not being affected by the changes in the response functions due to the Earth's rotation. The windowing (together with the high-pass filter) is necessary to limit the spectral leakage of large low-frequency components into the sensitive band. Hann window performs the best but results in losing about 50% of the data per segment. The use of 50% overlapping segments avoids this loss but introduces further correlations in the data to be accounted for later when producing the final cross-correlation spectra (see [418] for the full details). The segments

[5] To be precise, the magnetic-noise budget has been evaluated only for searches for isotropic SGWBs [258, 403, 404]. However, these studies are being extended to the case of searches for anisotropic SGWBs (in preparation).

[6] The magnetometer data are down-sampled from 16384 Hz to 512 Hz and from 2000 Hz to 512 Hz for the LEMI and Metronix magnetometers, respectively. The reason for this lower frequency, compared to the main analysis, is the interest of analysing magnetic data only up to 100 Hz [258].

are then discrete-Fourier transformed, and the resulting spectrum is coarse-grained to the frequency resolution of $1/32$ Hz, which allows for better identification of noise lines and reduces the amount of data removed from time-domain cuts (compared to past choices of a 0.25 Hz frequency resolution; see 4.4). Eventually, the spectra were cross-correlated using the publicly available MATLAB search algorithm [479].

6.2.3 Data quality

The segment cross-correlation spectra (and power spectral densities) cannot be used for the analysis yet due to noise artefacts that may spoil the data. The set of operations that make the data suitable for stochastic searches is called data quality[7]. Data quality leads to time and frequency domain cuts, and new techniques may have to be developed for different detectors and runs.

Time-domain cuts

The data quality in the time domain starts by requiring that both detectors in a baseline are in observing mode without critical issues in the hardware, resulting in the category 1 vetoes common to multiple GW searches [476, 480]. In addition to the category 1 vetoes, the first two weeks (1-16 April 2019) of Hanford detector data were excluded from the analysis due to non-stationarities around the 35.9-Hz and 36.7-Hz calibration lines, and three segments worth of data were removed around the O3 GW events (confirmed and non-retracted ones), since the SGWB is associated with the non-detected events[8]. A further cut in the time domain addresses the non-stationarities (and sometimes non-Gaussianities) present in the data. The cut is implemented in practice by removing the data segments whose power spectral densities differ more than a given threshold, chosen to be 20%, from the ones of the neighbouring segments. The same cut can be specialised for different power-law models describing the detector noises in different frequency ranges and was applied for the spectral indices $\alpha = \{-5,\, 0,\, 3,\, 5\}$, addressing the non-stationarities in the $\sim 15 - 50$ Hz, $\sim 40 - 80$ Hz, $\sim 90 - 500$ Hz, and ≥ 500 Hz bands, respectively [8]. Before O3, this non-stationarity cut was sufficient to cover the data-quality procedure in the time domain. However, due to the presence of very loud glitches during O3 in the LIGO detectors [476], this cut caused the loss of more than 50% of the data. In order to reduce the amount of data lost, the data were further preconditioned by applying a gating procedure. This procedure consisted in identifying the data from LIGO Hanford and LIGO Livingston containing problematic glitches and zeroing them out. This was practically reached by multiplying the data in the segments by an inverse Tukey window when the root-mean-square value of the whitened data in the strain channel exceeded a threshold in the 25-50 Hz or the 70-110 Hz band. For more details about the full procedure, see [481]. The

[7] Note that stochastic searches do not use raw data but rather data that have undergone some cleaning and calibration [258]

[8] Note that the contribution of the resolved events to the SGWB was evaluated to be well below the O3 PI sensitivity curve, $\Omega_{\rm CBC}^{(\rm resolved)} \leq 10^{-10}$ in [258] and actually negligible to the end of the analysis.

gating procedure, in spite of removing short-duration transients from the data, also introduces spectral artefacts around noise lines in frequency; these artefacts do not have an impact on the searches for isotropic SGWB [482] but affect some of the directional searches, namely the NBR analysis. After applying gating (resulting in 0.4% Hanford data and 1% Livingston data being gated), the amount of data removed by time-domain cut is 17.9% in the HL baseline, 22.1% in the HV baseline, and 21.9% in the LV baseline [258], resulting in 169 days, 146 days, and 153 days of live time, respectively [1] (which are incidentally longer than the 129 days of live time used for the first two combined observing runs [470]).

Frequency-domain cuts

After ensuring the goodness of the data in the time domain, data-quality cuts are applied in the frequency domain. The frequency band of the SGWB searches during O3 is between 20 and 1726 Hz. The criteria for analysing or not a frequency bin are mainly two. The first one consists in the presence or absence of calibration lines and other known features in-built with the instrumentation of a single detector, such as power-line harmonics, continuous-wave hardware injections, etc. A tool to determine the bad frequencies for a baseline is the coherence between two channels $I,\ J$

$$\mathrm{Coherence}(f) = \frac{\langle|\tilde{s}_I^*(f)\,\tilde{s}_J(f)|\rangle}{\langle|\tilde{s}_I(f)|^2\rangle\,\langle|\tilde{s}_J(f)|^2\rangle}, \tag{6.2.1}$$

where the expectation value $\langle\rangle$ refers to the average over the analysis segments. This quantity, briefly mentioned at the end of section 4.1, is a useful measure to determine when the correlation in the frequency bin exceeds the one expected from uncorrelated data. Its study is especially helpful to identify narrow-band frequency features to be *notched* from the analysis if correlation with auxiliary channels shows evidence of instrumental contamination [483]. In addition to that, coherence may play an important role when it comes to identifying correlated environmental noise fledgling the baseline [421]. The list of all the frequency bins to be removed is known as the *notch list*. The notch list used in searches for anisotropic SGWB [484] differs from the one used in the isotropic SGWB search [485], given the necessity of removing the additional spectral artefacts appearing at higher frequencies (especially around strong noise lines, such as the calibration ones) after gating the data. The effect of the frequency cuts used for anisotropic SGWB searches is removing approximately 14.8%, 25.2%, and 21.9% percent of the 20-1726 bandwidth from the HL, HV, and LV baselines, respectively.

6.2.4 Folding and PyStoch

For the first time, the procedure of folding [431] was used in an official[9] LVK analysis for anisotropic SGWBs. The idea of folding is simple and takes advantage of the one-sidereal-day temporal symmetry of the data underlying the kernel $K_{IJ,\,t\,f\,p}$ presented in equation (5.2.2). This procedure is 2-sphere basis independent, and hence it can be applied before deconvolving the cross-correlation spectra. The idea behind folding is simple but effective, namely *stacking* the (non-periodic [431] part of the) data over one sidereal day by splitting the summation over time of the segments marked by t. The summation can be split over two contributions by observing $t = i_{\rm day} T_s + t_s$, where $i_{\rm day}$ is an integer index denoting the sidereal day where t lies, t_s is the remainder within the sidereal day $i_{\rm day}$, and $T_s \simeq 86164$ s (23 h 56 min 4 s) is the sidereal-day duration. Explicitly, this means that $\sum_t$ is replaced by $\sum_{i_{\rm day}} \sum_{t_s}$ in equation (5.2.7), with $i_{\rm day}$ running over the total number of sidereal days for which data are processed, and t_s runs over one sidereal day. In practice, while still leading to simple and exact results, the folding procedure becomes more intricate from an algebraic point of view [431] due to the correlation in the spectra of neighbouring segments introduced by the overlapping windows, which makes the noise covariance matrix no longer diagonal [418]. The advantages deriving from folding the data before performing the anisotropic SGWB analyses are multiple: it reduces the computational and memory costs of directional searches by at least a factor equal to the number of sidereal days (since the analyses need to be run only once after folding); it already accounts for the effect of overlapping windows, leading to a further speedup; it makes possible cross-correlation-based searches (such as the all-sky all-frequency search [430]) that were previously precluded by computational cost reasons; and it unifies the pre-processing procedure for all the directional searches, easing the consistency checks among them.

6.3 The broad-band radiometer analysis

6.3.1 Producing maps with PyStoch

The broad-band radiometer (BBR) analysis uses the cross-correlation spectra produced with the methods described in the previous section and searches for anisotropic SGWBs by employing the techniques described in the sections 5.2 and 5.3 in the pixel basis. For the first time in LVK analyses, the BBR analysis made use of the Python-based `PyStoch` pipeline, based on an efficient map-making algorithm [466]. At the time of O3 analysis, `PyStoch` was available only to perform radiometer searches (i.e. in pixel basis, namely BBR and NBR), replacing the part of the MATLAB algorithm [479] dedicated for these kinds of searches used in the past observing runs [469, 470]. The pipeline was designed to take advantage of the folded data struc-

[9] The folding procedure was initially developed and validated on the publicly available S5 data [420, 431]. During the O3 analysis, folded data sets for the O1 and O2 data have been produced and validated [475]

ture[10] together with the standard and efficient HEALPix (Hierarchical Equal-Area iso-Latitude Pixelisation) scheme [439, 486] to further reduce the computational cost and memory requirements of the searches compared to past analyses. Starting from the folded data, which already include data-quality cuts in the time and the frequency[11] domains, `PyStoch` produces the dirty maps and the diagonal Fisher matrices at every time and frequency for a given spectral index α (or a given spectral shape $H(f)$). Then, it sums them as described in section 5.2 to produce the corresponding broad-band quantities for each baseline at a reference frequency $f_{\rm ref}$ as output[12].

6.3.2 Post-processing and significance

Starting from the broad-band dirty map $X_{\hat{\boldsymbol{n}}}$ and diagonal Fisher matrix $\Gamma_{\hat{\boldsymbol{n}}\hat{\boldsymbol{n}}}$, it is possible to deconvolve the dirty map, obtaining the clean map for the *point estimate* of the spatial strain spectral density $\mathcal{P}_{\hat{\boldsymbol{n}}}$. The standard deviation of the estimator at each direction $\sigma_{\hat{\boldsymbol{n}}}$ follows by inverting the diagonal Fisher matrix and taking its square root $[\Gamma_{\hat{\boldsymbol{n}}\hat{\boldsymbol{n}}}]^{-1/2}$. To explore whether there is any excess in the $\mathcal{P}_{\hat{\boldsymbol{n}}}$ map, the signal-to-noise ratio (SNR) maps are evaluated as the ratio of $\mathcal{P}_{\hat{\boldsymbol{n}}}$ to $\sigma_{\hat{\boldsymbol{n}}}$. If the SNR map is consistent with Gaussian noise, it is possible to proceed with the evaluation of the upper limits on $\mathcal{P}_{\hat{\boldsymbol{n}}}$ (or the related quantities such as the flux $\mathcal{F}_{\hat{\boldsymbol{n}}}$ and the dimensionless energy density $\Omega_{\mathrm{gw},\,\hat{\boldsymbol{n}}}$). To check this consistency, the first step consists in the evaluation of the statistical significance of a given map with a certain maximum SNR. In practice, this is reached by computing numerically the maximum SNR distribution by simulating multiple realisations of dirty maps from Gaussian noise coloured with the detector noise encoded in the Fisher matrix[13], and evaluating the p-value of the maximum SNR of interest for a given map. Further tools and operations[14] may have to be applied if the maximum SNR is significant, but they will not be discussed here since this has not happened during O3. Once the presence of a signal has been excluded from the data, it is possible to proceed with the evaluation of the upper limits for each direction. The evaluation of the upper limits adopts the Bayesian approach, using the techniques illustrated in [487], where the posterior is built from the multivariate

[10] Note that `PyStoch` can also be executed using non-folded data, but this would waste most of the speed gained in the analysis from folding the data. Still, this functionality may be useful for consistency checks.

[11] `PyStoch` still allows to perform additional cuts in the frequency domain at this step, if necessary. This was the case during O3, where additional frequency-domain cuts with respect to the isotropic SGWB search were necessary due to the artefacts introduced by gating affecting mainly the NBR search.

[12] Note that the `PyStoch` version available during O3 wasn't enabled yet to save and store the narrow-band sky maps at every frequency, nor optimised to evaluate the full Fisher matrix, assumed to be diagonal for O3 BBR analysis. These additional features are briefly discussed in section 6.4.

[13] Note that the full Fisher matrix is necessary to this goal. During O3, there were no tools available to evaluate such a matrix in the pixel basis due to computational and memory issues. What was done was to obtain the Fisher matrix in the pixel domain via a change of basis operated on the full Fisher matrix available from the analysis in the spherical harmonics base. Operatively, this was reached by using the NEON library part of the more general MATLAB [479] for SGWB searches.

[14] As an example, instead of evaluating the maximum SNR distribution and the corresponding (local) p-value, the general distribution of all SNRs could be computed to obtain a new (global) p-value. See [430] for more details.

			Max SNR (% p-value)				Upper limit ranges (10^{-8})	
α	$\Omega_{\rm gw}$	$H(f)$	HL(O3)	HV(O3)	LV(O3)	O1+O2+O3 (HLV)	O1+O2+O3 (HLV)	O1 + O2 (HL)
0	constant	$\propto f^{-3}$	2.3 (66)	3.4 (24)	3.1 (51)	2.6 (23)	1.7 – 7.6	4.5 – 21
2/3	$\propto f^{2/3}$	$\propto f^{-7/3}$	2.5 (59)	3.7 (14)	3.1 (62)	2.7 (24)	0.85 – 4.1	2.3 – 12
3	$\propto f^{3}$	constant	3.7 (32)	3.6 (47)	4.1 (12)	3.6 (20)	0.013 – 0.11	0.047 – 0.32

Table 6.2: The maximum SNR across all sky positions, its estimated p-value, and the range of the 95% upper limits on gravitational-wave energy flux $F_{\alpha,\Theta}$ [erg cm^{-2} s^{-1} Hz^{-1}] set by the BBR search for each baseline and for the three baselines combined using data from LIGO three observing runs and Virgo O3. The median improvement across the sky compared to limits from O2 analysis is a factor of 3.5 - 3.8, depending on α. The O1+O2 upper limits reported in the last column differ from the upper limits reported in [470] for the reasons explained in the main text.

Gaussian likelihood function for the point estimate $\mathcal{P}_{\hat{\boldsymbol{n}}}$, following a marginalisation over the detectors calibration uncertainties[15].

6.3.3 Results

The results of the O3 BBR analysis for the three different spectral indices $\alpha = 0$, 2/3, and 3 are summarised in table 6.2 and figure 6.1. The sky maps in figure 6.1, where each column refers to a different spectral index, are obtained from the combination of the data from the LIGO-Virgo-KAGRA first three observing runs (O1, O2, and O3) and from all three baselines HL, HV, and LV (note that only O3 data exist for HV and LV analysis). The SNR maps in the upper row are consistent with Gaussian noise (with the p-value of the maximum SNR reported in table 6.2), and hence upper limits on the GW energy flux $\mathcal{F}_{\alpha,\hat{\boldsymbol{n}}}$ at $f_{\rm ref} = 25$ Hz from different sky directions are placed for each α and shown in the bottom row of figure 6.1. The upper-limit evaluation followed the methods mentioned in the previous subsection, employing a flat prior on $\mathcal{P}_{\hat{\boldsymbol{n}}}$ and adopting the amplitude calibration uncertainties of 7.0%, 6.4%, and 5.0% for the Hanford, Livingston, and Virgo detector data [489], respectively.

The maps employ the HEALPix scheme with $n_{\rm side} = 32$ to pixelate the sky, in contrast to the past BBR analyses using a Cartesian grid[16] [468–470]. This choice[17] corresponds to a total of 12288 pixels, each with an area of $\simeq 3\,{\rm deg}^2$. The observed maximum SNRs for different α, their associated p-values, and the 95% confidence Bayesian upper limits on the gravitational-wave flux are reported in table 6.2. The im-

[15] A discussion of the impact of calibration uncertainties on SGWB searches is discussed in detail in [416] and the more recent [488].

[16] More specifically, the grid consisted of 181x360 patches, leading to a much larger number of directions to be analysed (in addition to that, the patches were not equal-area, making arguments based on diffraction limit (5.3.2) more difficult to be applied).

[17] Following the development of the ASAF search (see 6.4) and the related diffraction-limit studies studies, this choice may change during O4, where $n_{\rm side} = 16$, corresponding to 3072 pixels with $\simeq 13\,{\rm deg}^2$ area, is likely to be used instead of $n_{\rm side} = 32$.

			Max SNR (% p-value)				Upper limit range (10^{-9})	
α	$\Omega_{\rm gw}$	$H(f)$	HL(O3)	HV(O3)	LV(O3)	O1+O2+O3 (HLV)	O1+O2+O3 (HLV)	O1 + O2 (HL)
0	constant	$\propto f^{-3}$	1.6 (78)	2.1 (40)	1.5 (83)	2.2 (43)	3.2–9.3	7.8–29
2/3	$\propto f^{2/3}$	$\propto f^{-7/3}$	3.0 (13)	3.9 (0.98)	1.9 (82)	2.9 (18)	2.4–9.3	6.5–25
3	$\propto f^{3}$	constant	3.9 (12)	4.0 (10)	3.9 (11)	3.2 (60)	0.56–3.4	1.9–11

Table 6.3: SHD search results and upper limits on the normalised gravitational-wave energy density $\Omega_\alpha(\Theta)[\mathrm{sr}^{-1}]$ after combining data from LIGO-Virgo's three observing runs [1], as in table 6.2. The median improvement across the sky compared to limits set by the O1+O2 analysis is $2.8 - 3.2$ for the SHD search, depending on α.

provement upon the previous O1+O2 upper limits[18] is by a median factor (across the sky) ranging 3.3-3.5, depending on α. The final combined upper limits are dominated by the HL baseline sensitivity, which is approximately $3 - 10$ times better (depending on alpha) than those of the HV and LV baselines, as can be observed from figure 7 in [1].

6.4 Results from the other analyses and future perspectives

6.4.1 Spherical Harmonics Analysis

The results from the SHD analysis are summarised in table 6.3, following the same scheme as BBR, with the exception of the upper limits on $\Omega_\alpha(f_{\rm ref}, \hat{\boldsymbol{n}})$[19], in contrast to $\mathcal{F}_\alpha(f_{\rm ref}, \hat{\boldsymbol{n}})$, for every α. The improvement compared to the O2 search [470] is by a factor ranging in 2.9-3.3, depending on α. Additionally, the SHD search allows to draw constraints on the C_l, associated with the $\mathcal{P}_{lm}$ and illustrated in figure 6.2, that can be compared with the predictions for the SGWB anisotropies [490–493]. The models considered in the O3 analysis [1] results compatible with the C_l limits, with the experiment non-sensitive enough to draw any constraint on the model predictions. As an example, for $\alpha = 0$, the limit on the kinematic dipole ($l = 1$) is $C_1^{1/2} \leq 2.6 \times 10^{-9}\,\mathrm{sr}^{-1}$, three orders of magnitude higher than the predicted bound $C_1^{1/2} \lesssim \times 10^{-12}\,\mathrm{sr}^{-1}$ from [492].

6.4.2 Narrow-Band Radiometer Analysis

The results from the NBR analysis are summarised in table 6.4. The O3 NBR search targeted three directions in the sky, corresponding to the binary neutron star system

[18] The O1+O2 upper limits in the last column of table 6.2 differ around 5% from those reported in [470]. This is related to the O2 data not having been properly notched in the past and the O1+O2 results having been correctly regenerated during the O3 analysis.

[19] The SHD analysis upper limits can be compared to the BBR one using equations (3.1.11) and (3.1.13) for conversion and scaling the result by the diffraction limit (5.3.2).

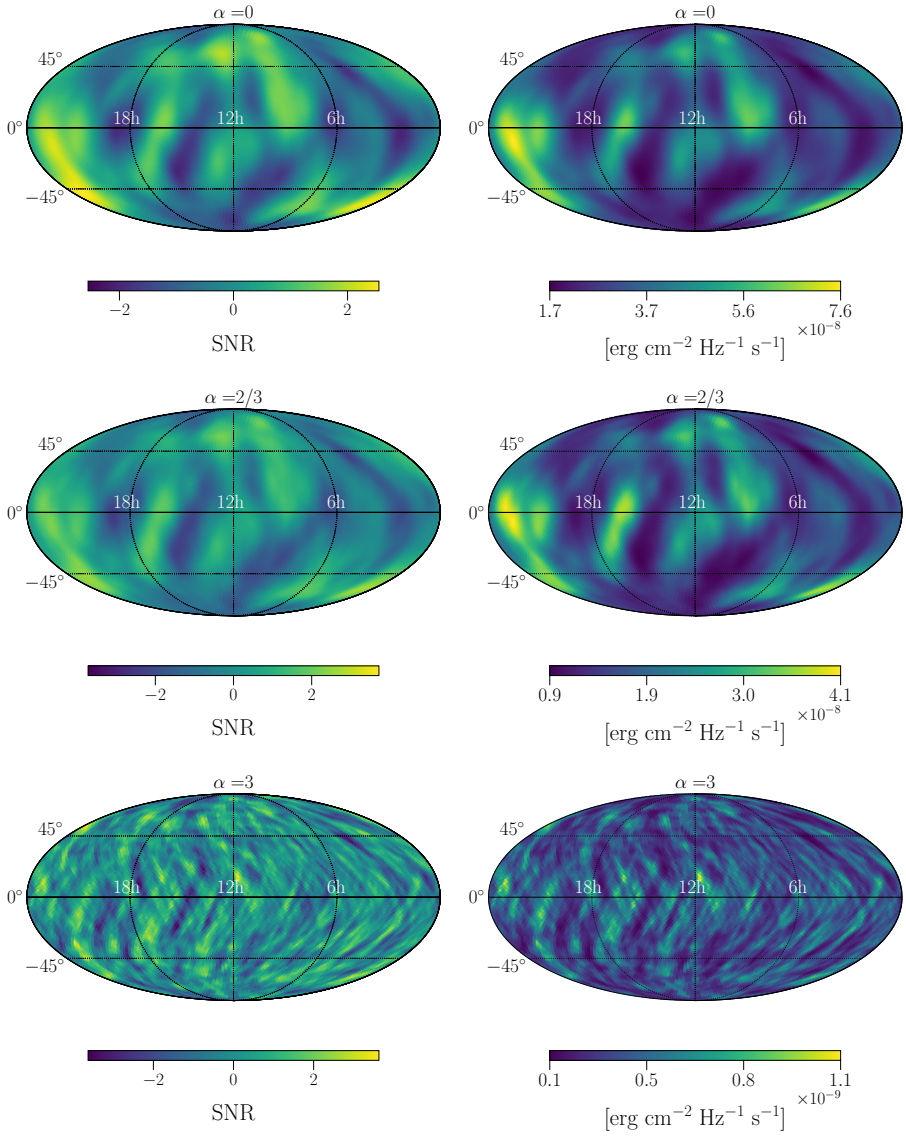

Figure 6.1: Left column: SNR maps from the BBR search for point-like sources. Right column: upper limit (UL) sky maps of the gravitational-wave energy flux. Both sets of maps, presented in equatorial coordinate system, are derived by combining all three LIGO observing runs and the Virgo O3 data. $\alpha = 0,\ 2/3$, and 3 are represented from left to right.

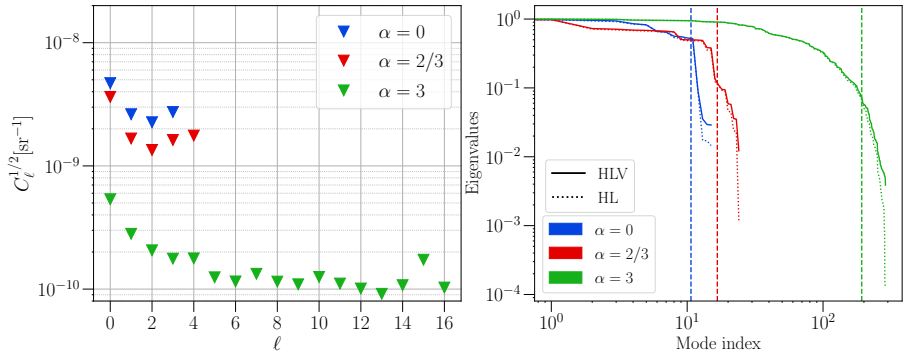

Figure 6.2: Left: SpH-analysis 95% upper limits on C_ℓ for different α using the combined O1+O2+O3 data [1]. Right: Comparison between the Fisher matrix condition numbers for the HL and HLV networks for different values of α, with the vertical dashed lines marking the two-thirds eigenvalue threshold [1].

Direction	Max SNR	p-value (%)	Frequency (Hz) ($\pm$ 0.016 Hz)	Best upper limit (10^{-25})	Frequency band (Hz)
Sco X-1	4.1	65.7	630.31	2.1	189.31 – 190.31
SN 1987A	4.9	1.8	414.0	1.7	185.13 – 186.13
Galactic Center	4.1	62.3	927.25	2.1	202.56 – 203.56

Table 6.4: Left: Maximum SNR, its estimated p-value, and frequency bin of the maximum SNR for each search direction of the NBR search. Right: best 95% confidence-level gravitational-wave strain upper limits achieved, and the corresponding frequency band, for all three sky locations. The best upper limits are taken as the median of the most sensitive 1 Hz band. All these results are derived from the three observing runs of LIGO-Virgo detectors [1].

Scorpius-X1 (sco-x1) [471, 472], the Galactic Centre (GC) [473], and the supernova 1987A (SN 1987A) [474], already studied in the past analyses [469, 470]. The main results of the analysis are reported in table 6.4, where the maximum SNR, its statistical significance, and the corresponding frequency bin are listed for the $h_0(f) = \sqrt{X_{\hat{\boldsymbol{n}}_0}(f)}$ spectrum of each direction. Since no compelling evidence for a signal was found[20], upper limits on h_0[21] were set using the data of O1, O2, and O3. The spectra of the upper limits, together with the 1σ sensitivity, are illustrated in figure 6.3, with the most constraining ones and the corresponding frequency range reported in table 6.4. The upper limits improve the previously existing ones from [470] by a factor ≥ 2.0. Compared to the limits obtained by continuous-wave searches during O1 and O2, these limits are similar or outperformed; see [1] for more details and discussion about how to compare the limits from the two searches.

[20]Note that the O2 outlier in the direction of SN 1987A, at 36.6125 Hz and with an SNR = 5.3, did not appear in O3 data or in the O1+O2+O3 combined data set. This definitely rules out the possibility of the O2 outlier being a persistent GW signal.

[21]The evaluation of the NBR upper limits is more intricate compared to the one for BBR and SHD analyses, given that one is assuming a point-like source, typically a pulsar or a binary system, and corrections for its relative motion and Doppler effect must be included during the post-processing. This leads to the

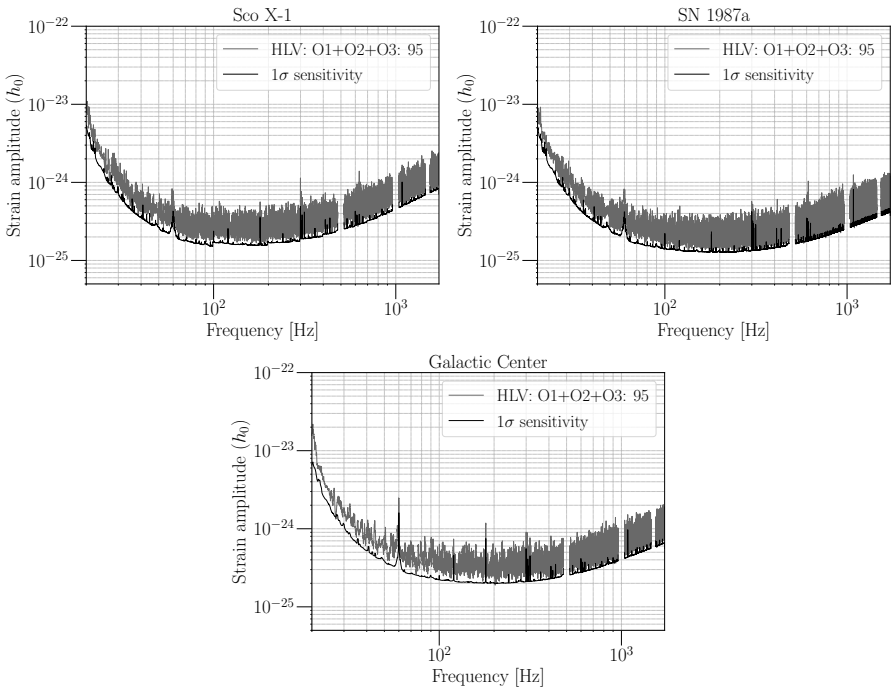

Figure 6.3: The NBR-analysis 95% confidence-level upper limits on the dimensionless strain amplitude h_0 (gray bands) using the data from three observing runs of LIGO-Virgo detectors for Scorpius X-1 (left), SN 1987A (middle) and the Galactic Center (right) [1]. The dark line shows the 1σ sensitivity of the search for each direction.

6.4.3 Future perspectives

The O3 analysis further improved the constraints over SGWB anisotropies, introducing at the same time new tools to improve the speed and quality of the analysis, such as folding [431], which allowed to have a common data set as input for all the three analyses, and `PyStoch` [466], which made even more efficient and user-friendly the BBR and NBR analyses. However, there was (and still is) quite some room for further improving the searches for anisotropic SGWB, both computationally and in terms of the physical implications that can be drawn from its results. During these three years between the end of O3 and the start of O4, several improvements were made. They are briefly listed below, together with their implications and possible applications.

First of all, `PyStoch` functionalities in the pixel domain were further developed, making it possible to store efficiently sky maps at every frequency and, fixed a spectral shape $H(f)$, the broadband full fisher matrix (in contrast to the diagonal one in O3). The first improvement enabled finally to perform an *all-sky all-frequency* (ASAF) directional search for persistent gravitational waves [430]. The ASAF search allows for an unmodelled analysis looking for excesses in the strain spectral density $\mathcal{P}(f, \hat{\boldsymbol{n}})$ at every frequency and direction available. Moreover, the results of such analysis can also be used to recover the results of the NBR analysis by focusing on the spectrum of a single direction in the sky, the BBR ones by combining the narrow-band sky maps over frequency, and even the results of the search for isotropic SGWB by summing over sky directions and frequencies (as shown in equation (5.3.6)) and weighting the data with the spectral shape of interest. The second development allows to make the maximum-SNR p-value evaluation for the BBR maps independent from the SHD results (even though other methods for the p-value evaluation are being considered, such as multiple time-shifting and sky/phase scrambling [430]).

In addition to these pixel domain functionalities, `PyStoch` and ASAF have been extended to the spherical harmonics base [445], allowing for a common pipeline for all the anisotropic SGWB searches to use during O4. The extension of ASAF analysis to the SpH domain makes accessible the computation of the C_l at every frequency, which will play a crucial role in a multi-messenger astronomy scenario, such as in the case of the GW-EM correlation analysis in [494].

Finally, the parameter estimation methods for directional analyses have been extended to infer more details about the properties of the SGWBs of interest, now limited only to the strain spectral density and related quantities. The formalism has been developed for the SHD analysis [495] and recently extended to non-GR polarisation [456]. This machinery, currently limited by computational requirements, will also be extended to the radiometer searches in the upcoming years, with the final goal of doing Bayesian inference in a similar way to what is done in the SGWB isotropic searches [258, 454].

---

presentation of the upper limits combined over multiple frequency bins to avoid Doppler-related spectral leakage of the signal.

Chapter 7

Stochastic gravitational-wave background searches and constraints on neutron-star ellipticity

"Mattia pensava che lui e Alice erano così, due primi gemelli, soli e perduti, vicini ma non abbastanza per sfiorarsi davvero."

Paolo Giordano, *La solitudine dei numeri primi*

This chapter is a reproduction of reference [2], in collaboration with Dr. Jishnu Suresh and Dr. Andrew Lawrence Miller, which was published in *Mon. Not. Roy. Astron. Soc.*, vol. 513, no. 1, pp. 1105–1114, 2022. This project lasted about one year, from its start in April 2021 to its publication in April 2022. F.D.L. was the main author, performing the analysis in sections 7.3 and writing the whole manuscript, with the exception of the introductory part regarding continuous waves. During this project, I learnt how to use the `MATLAB` code `stochastic.m` [479], which used to be the pipeline to perform the pre-processing of every SGWB search within LVK and the post-processing of isotropic SGWB searches before the rise of `pygwb` [8] in `Python`. In this work, we have studied the implications we can draw from the results of an SGWB search in terms of a NS population, reviving and using for the first time the methods from [496] on real data. I also wrote his own code to perform the post-processing part of the analysis in section 7.3.2, starting from the results of `stochastic.m` for the isotropic part of the analysis and from the results of `PyStoch` [466] for the BBR and hotspot parts of the analysis.

Abstract

Rotating neutron stars (NSs) are promising sources of gravitational waves (GWs) in the frequency band of ground-based detectors. They are expected to emit quasi-monochromatic, long-duration GW signals, called continuous waves (CWs), due to their deviations from spherical symmetry. The degree of such deformations, and hence the information about the internal structure of a NS, is encoded in a dimensionless parameter ε called ellipticity. Searches for CW signals from isolated Galactic NSs have shown to be sensitive to ellipticities as low as $\varepsilon \sim \mathcal{O}(10^{-9})$. These searches are optimal

for detecting and characterising GWs from individual NSs, but they are not designed to measure the properties of NSs as a population, such as the average ellipticity $\varepsilon_{\rm av}$. These ensemble properties can be determined by the measurement of the stochastic gravitational-wave background (SGWB) arising from the superposition of GW signals from individually undetectable NSs. In this work, we perform a cross-correlation search for such a SGWB using the data from the first three observation runs of Advanced LIGO and Virgo. Finding no evidence for a SGWB signal, we set upper limits on the dimensionless energy density parameter $\Omega_{\rm gw}(f)$. Using these results, we also constrain the average ellipticity of Galactic NSs and five NS "hotspots", as a function of the number of NSs emitting GWs within the frequency band of the search $N_{\rm band}$. We find $\varepsilon_{\rm av} \lesssim 1.8 \times 10^{-8}$, with $N_{\rm band} = 1.6 \times 10^{7}$, for Galactic NSs, and $\varepsilon_{\rm av} \lesssim [3.5 - 11.8] \times 10^{-7}$, with $N_{\rm band} = 1.6 \times 10^{10}$, for NS hotspots.

7.1 Introduction

Isolated, rotating, non-axisymmetric neutron stars, with a rotational period of the order of milliseconds, are promising sources of GWs for ground-based GW detectors, such as Advanced LIGO [90], Advanced Virgo [94], and KAGRA [95]. Such objects would emit GWs due to deformations on their surfaces, i.e. "mountains" [497], due to a strong internal magnetic field [498], accretion from a companion [499–502] or toroidal perturbations throughout the star, i.e. r-modes [278, 503, 504]. The size of these deformations and the rate at which neutron stars accrete matter are estimated to be small [505]; thus, these processes would emit GWs at an almost fixed frequency by extracting rotational energy from the neutron star on a timescale much longer than the observation time of GW detectors [146]. These are called continuous waves: quasi-monochromatic, long-duration GWs. Methods to search for CWs have been developed [506–509] and are currently used for all-sky [510], directed [511–514], targeted [515–518] and post-merger remnant searches [519–525]. CW methods have even been adapted to search for particle dark matter [526–529], boson clouds around black holes [530–533] and primordial black hole binaries [6, 7], all of which underscore the broad scope of CW physics. However, no method or search mentioned so far for neutron stars or dark matter, no matter how exotic, has allowed us to probe the bulk properties of isolated neutron stars.

Though no CW has been detected yet, each type of CW search has shown promising results. Targeted searches continue to surpass the GW-amplitude spin-down limit, which assumes that all of the rotational energy lost by NSs as they spin-down is through GW radiation [515–517]. Additionally, all-sky and directed searches probe smaller and smaller deformations at galactic-centre distances [534, 535]. The improved sensitivity of these searches over time brings us closer and closer to being able to make a detection of a CW from an isolated NS. Moreover, once we enter the detection era, GWs could be used as a novel messenger to identify new nearby NSs, an alternative to current searches for pulsars in electromagnetic (EM) data, whose average discovery rate is $\simeq 50\,{\rm yr}^{-1}$. However, assuming the Galactic supernovae rate to be $10^{-2}{\rm yr}^{-1}$ [536] and the age of the Milky Way to be 10^{10} yrs, there are roughly $\sim 10^{8}$ NSs [537] in our Galaxy alone. This large number of NSs implies that, even in

the detection era, assuming a CW discovery rate of the same order or even ten times greater than the average electromagnetic one, we would still need centuries to individually detect the majority of the NSs and characterise the Galactic NS population properties. It is also not clear how many isolated NSs would need to be individually detected to make population-based statements. In addition, current CW searches are not yet designed to provide information on NS ensemble properties, even though methods have been developed to combine results from targeted searches for a few hundreds of known pulsars [538–540]. Nonetheless, this is just a small fraction of the larger population considered here, and suggests the need for an alternative strategy to determine such properties that does not rely on measuring GWs from individual NSs.

We attempt to address this problem by searching for an astrophysical stochastic gravitational-wave background (SGWB) [243, 246, 249, 255, 256, 426, 541–552] from the superposition of weak GW signals from individually undetectable pulsars, which could already be observed by current detectors [496]. Its detection and characterisation would provide constraints that are independent and complementary to those inferred from CW (and EM) searches for individual NSs. Moreover, it would give insight into the ensemble properties of NSs by identifying certain traits (e.g. the mean value) of the statistical distributions of the parameters (e.g. the ellipticity), which characterise the population of interest, at once.

In this work, we consider the Galactic-NS population and the NS populations of five "hotspots", i.e. patches of the sky that are expected to have a high number of NSs [543, 553], as potential candidates for our search. For each of these cases, we use cross-correlation [239, 410, 427] methods to search for a SGWB. Cross-correlation allows us to search for a common signal in multiple data streams simultaneously and disentangle it from instrumental noise. From these measurements, we could measure the number of Galactic NSs emitting in a given frequency band and the average ellipticity of that population $\varepsilon_{\rm av}$. However, the search employed in this work finds no evidence of such a background; therefore, we set limits on the SGWB properties and then convert them into constraints on the average ellipticity of each population as a function of the number of NSs emitting GWs within the frequency band of the search.

The paper is organised as follows. In section 7.2, we describe the SGWB signal from isolated, rotating NSs and model the NS population as a function of frequency using the known pulsars from the ATNF catalogue [554]. In section 7.3, we present the cross-correlation techniques and show how to estimate the average ellipticity of a population of pulsars from the results of our search for a SGWB signal. Then, in section 7.4, we illustrate the results of the searches for a SGWB from NSs when using the data from the first three observation runs of Advanced LIGO and Virgo over the population of Galactic NSs, and the NSs of the five hotspots: Virgo, Fornax, Antlia, Centaurus, and Hydra galaxy clusters, which contain thousands of galaxies and are assumed to have roughly 1000 times more NSs than our Galaxy. In addition to that, we express the results as limits on the average ellipticities of the considered populations. Finally, in section 7.5, we summarise and discuss the implications of

our results in terms of possible synergies between CW searches and SGWB ones, and future extensions to this work.

7.2 Modelling the source

The strain amplitude of a GW emitted from an isolated, rotating, non-axi-symmetric NS at a distance d from Earth, with a moment of inertia along the z-axis I_{zz}, and an ellipticity $\varepsilon \equiv \frac{I_{xx}-I_{yy}}{I_{zz}}$, in the quadrupole approximation [146], is given as

$$h_0(f) = \frac{4\pi^2\, G\, \varepsilon\, I_{zz}}{c^4\, d}\, f^2\,, \tag{7.2.1}$$

where G is Newton's gravitational constant, c is the speed of light, and f is the frequency of the emitted GW, which is twice the rotational frequency of the NS. Using equation (7.2.1), it is possible to show that (see appendix 7.6.1) an ensemble of pulsars, whose contributions are summed incoherently, generates a GW power spectral density $S_h(f)$

$$S_h(f) = \frac{32\pi^4 G^2 \left\langle \varepsilon^2 \right\rangle_{\rm NS} \left\langle I_{zz}^2 \right\rangle_{\rm NS}}{5c^8} \left\langle \frac{1}{d^2} \right\rangle_{\rm NS} f^4\, N(f)\,, \tag{7.2.2}$$

where the angular brackets $\langle ... \rangle_{\rm NS}$ denote the ensemble average over the NS population, and $N(f)$ is the number of NSs emitting GWs between frequencies f and $f + df$. To completely determine the frequency dependence of this stochastic signal, we rewrite $N(f)$ as

$$N(f) = N_0\, \Phi(f)\,, \tag{7.2.3}$$

where N_0 is the number of NSs in a given ensemble, and $\Phi(f)$ is the corresponding probability distribution function (PDF) of the NSs frequencies, defined such that

$$N_0 \int_{-\infty}^{\infty} \Phi(f)\, df = N_0\,. \tag{7.2.4}$$

We consider $N_0 \sim 10^8$ when studying the SGWB from Galactic NSs and $N_0 \sim 10^{11}$ when analysing the NS hotspots (extragalactic sources consisting of galaxy clusters). To model $\Phi(f)$, we employ an observation-driven approach [537] and use information about known pulsars available in the ATNF catalogue [554]. We start from the ($\log_{10}$-) frequency distribution of the $\simeq 3000$ pulsars available in the catalogue and obtain the frequency distribution PDF through a Gaussian kernel-density-estimator (KDE) [555]. The resulting $\Phi(f)$ is shown in figure 7.1a. Even though the number of NSs used to construct $\Phi(f)$ is just a tiny fraction of the pulsars within our Galaxy and clusters of galaxies, the frequency distribution is expected to not be significantly biased by selection effects [357, 556] for millisecond pulsars. Moreover, this distribution is consistent with those obtained from population synthesis models [496, 557].

From figure 7.1a, it is interesting to note that $\Phi(f)$ displays a secondary peak at 526 Hz, which incidentally falls within the frequency band to which ground-based GW detectors are sensitive. The unnormalised spectral shape $S_h(f)$ corresponding to the computed $\Phi(f)$ is shown in Figure 7.1b. In this spectrum, due to the dominant contribution from the f^4 term in equation (7.2.2), the peak is shifted to a higher frequency (1688 Hz).

Given $\Phi(f)$ and N_0, we define $N_{\rm band}$ as the "in-band" NS number, which quantifies the number of NSs between a lower frequency $f_{\rm min}$ and a higher frequency $f_{\rm max}$. Thus, we can write $N_{\rm band}$ for the SGWB search described in this work as

$$N_{\rm band} = N_0 \int_{f_{\rm min}}^{f_{\rm max}} \Phi(f)\, df = N_0 \int_{20\,\rm Hz}^{1726\,\rm Hz} \Phi(f)\, df \simeq 0.16\, N_0\,, \tag{7.2.5}$$

where the 20-1726 Hz denotes our chosen frequency band for this search [1]. We analyse this frequency band because current GW detectors are most sensitive to signals arising between 20-1726 Hz [414], and it contains the GW emission band of millisecond pulsars. We also note that only 16% of NSs emit GWs in our chosen frequency band. However, this fraction translates into $\sim 10^7$ and $\sim 10^{10}$ in-band NSs in the galactic and hotspot cases, respectively, all emitting CWs, whose superposition would give rise to a continuous, Gaussian (due to the central limit theorem) SGWB. In this study, we rely on the spectral shape given in equation (7.2.2) to describe the SGWB from NS populations. By assuming a canonical value for $\left\langle I_{zz}^2 \right\rangle_{\rm NS}^{1/2} = 1.1 \times 10^{38} \rm kg\,m^2$, and a fiducial value $\left\langle 1/d^2 \right\rangle_{\rm NS}^{-1/2}$ for each population, we can translate the measurement of a SGWB into constraints on $\varepsilon_{\rm av}$ as a function of $N_{\rm band}$. It is worth noting here that, along with equation (7.2.2), it would be interesting to consider the angular distribution of pulsars to characterise the stochastic GW signal. This is because, from current observations, the Galactic NS angular distribution is likely to be anisotropic, i.e. peaked towards the galactic plane [558], and the hotspots are localised in specific sky regions. However, in this work, we treat the SGWB from Galactic NSs as isotropic and consider the average power strain of the hotspots. Considering all the anisotropies in the SGWB sky would require us to employ the matched-filtering "λ-statistic" proposed in [437] and produce a template bank, which is out of the scope of the present work.

7.3 Search methods

Searches for a SGWB typically characterise the fractional energy density $\Omega_{\rm GW}$ [240, 410, 427, 559], which is defined as the ratio between $\rho_{\rm GW}$, the energy density from all GWs in the Universe, and $\rho_c \equiv \frac{3H_0^2c^2}{8\pi G}$, the critical density needed to have a flat Universe. Here, $H_0 = 67.9\,\rm km\,s^{-1}\,Mpc^{-1}$ [560] is Hubble's parameter today. $\Omega_{\rm GW}$ receives contributions from GWs at all frequencies, and it is natural to study its fre-

[1] The frequency range used in this analysis is consistent with the previous stochastic searches [1, 258]

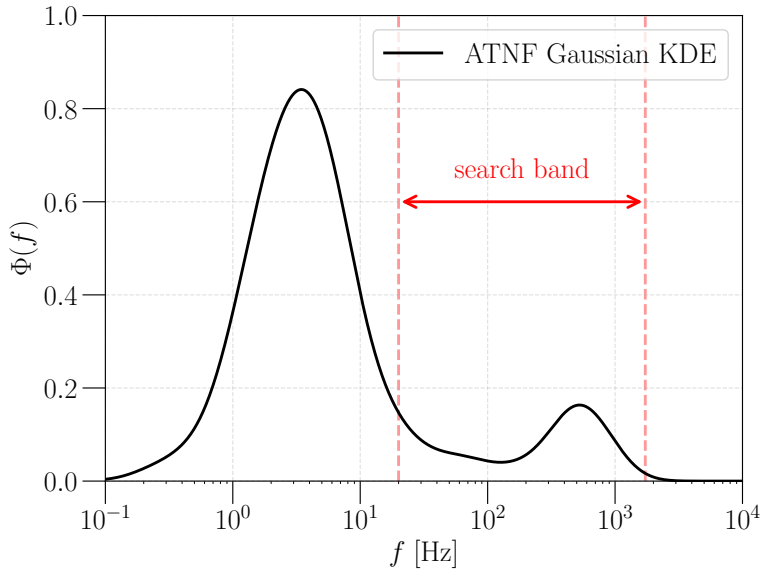

(a) The frequency distribution of the PDF $\Phi(f)$, generated from the ATNF catalogue data. The red-dashed vertical lines show the frequency band 20-1726 Hz used in our search.

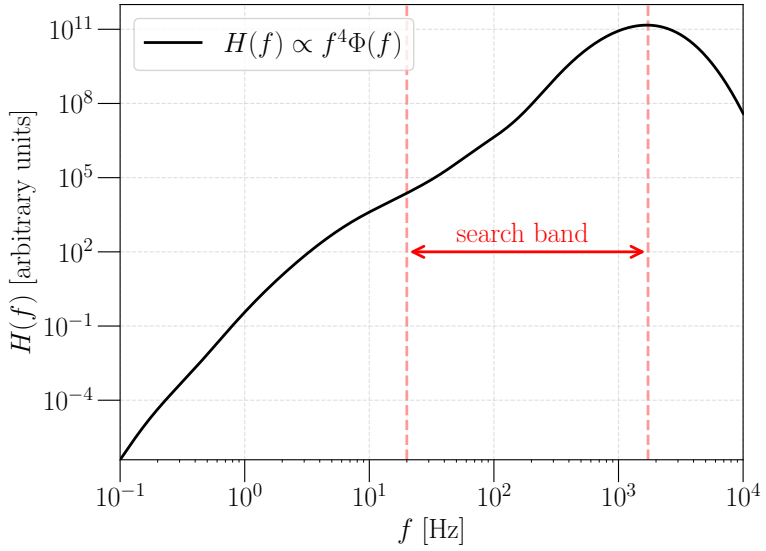

(b) Unnormalised spectral shape $S_h(f)$ as a function of frequency, assuming $\Phi(f)$ derived from a Gaussian KDE using data from the ATNF catalogue. The red-dashed vertical lines show the frequency range that we analyse in our search.

Figure 7.1

quency spectrum

$$\Omega_{\rm gw}(f) = \frac{f}{\rho_c}\,\frac{d\rho_{\rm gw}(f)}{df}\,, \tag{7.3.1}$$

which is related to $S_h(f)$ by

$$\Omega_{\rm gw}(f) = \frac{2\pi^2}{3H_0^2}\,f^3\,S_h(f)\,. \tag{7.3.2}$$

Since we are performing a search that assumes GW sources to be isotropically distributed in the sky, equation (7.3.1) fully characterises the SGWB.

7.3.1 The cross-correlation search for an isotropic SGWB

As illustrated in the above discussion, we first perform a search for a Gaussian, stationary, unpolarised, isotropic SGWB. We use GW strain data from the LIGO-Hanford (H), LIGO-Livingston (L), and Virgo (V) detectors and follow the search procedures in [258]. For each detector pair, called a "baseline IJ" (I, J = H, L, V), we divide the time-series output $s_I(t)$ in segments of duration T, labelled by t, take their Fourier transforms $\tilde{s}_I(t;\,f)$, and calculate a cross-correlation statistic in each segment. Thus, we can define the cross-correlation estimator at every frequency, usually referred to as the "narrow-band estimator", as [239]

$$\hat{\Omega}_{IJ}(t;f) = \frac{2}{T}\,\frac{{\rm Re}[\tilde{s}_I^*(t;f)\,\tilde{s}_J(t;f)]}{\gamma_{IJ}(f)\,S_0(f)}\,, \tag{7.3.3}$$

where $S_0(f) = (3H_0^2)/(10\pi^2 f^3)$, and $\gamma_{IJ}(f)$ is the normalised isotropic overlap reduction function (ORF) [398, 399, 410] of the baseline IJ. The ORF quantifies the reduction in sensitivity due to the geometry of the baseline and its response to the GW signal. The normalisation of the estimator is done in such a way that $\left\langle \hat{\Omega}_{IJ}(t;f) \right\rangle = \Omega_{\rm gw}(f)$ in the absence of correlated noise. The variance associated with the above estimator, in the small signal limit, can be expressed as

$$\sigma^2_{IJ}(t;f) \approx \frac{1}{2T\,\Delta f}\,\frac{P_I(t;f)P_J(t;f)}{\gamma^2_{IJ}(f)\,S_0^2(t;f)}\,, \tag{7.3.4}$$

where $P_I(t;f)$ is the one-sided power spectral density (PSD) in a detector, while Δf denotes the frequency resolution.

Starting from the narrow-band estimator $\hat{\Omega}_{IJ}(t;f)$, we can build a broad-band optimal estimator $\hat{\Omega}_{{\rm ref},\,IJ}$ by combining the cross-correlation spectra from different frequencies with appropriate weight factors. This optimal estimator and the associated

uncertainty can be expressed as

$$\hat{\Omega}_{\mathrm{ref},\,IJ} = \frac{\sum_{k,t} w(f_{\mathrm{k}})\,\hat{\Omega}_{IJ}(t;\,f_{\mathrm{k}})\,\sigma_{IJ}^{-2}(t;\,f_{\mathrm{k}})}{\sum_{k} w^2(f_{\mathrm{k}})\sigma_{IJ}^{-2}(t;\,f_{\mathrm{k}})}\,, \tag{7.3.5}$$

$$\sigma_{IJ}^{-2} = \sum_{k,t} w^2(f_{\mathrm{k}})\,\sigma_{IJ}^{-2}(t;f_{\mathrm{k}})\,, \tag{7.3.6}$$

where f_{k} is a set of discrete frequencies. The weights $w(f)$ can be derived for a generic $\Omega_{\mathrm{gw}}(f)$ following an optimal filtering approach [239]

$$w(f) = \frac{\Omega_{\mathrm{gw}}(f)}{\Omega_{\mathrm{gw}}(f_{\mathrm{ref}})}\,, \tag{7.3.7}$$

where f_{ref} is an arbitrary reference frequency, fixed at $f_{\mathrm{ref}} = 25$ Hz in this analysis to be consistent with [258]. After calculating the cross-correlation statistics for each pair of detectors, we can combine the individual broad-band estimators from independent baselines (HL, HV, LV) as well as past observing runs (O1-HL, O2-HL) to obtain the final estimator $\hat{\Omega}_{\mathrm{ref}}$ and its uncertainty:

$$\hat{\Omega}_{\mathrm{ref}} = \frac{\sum_{IJ} \hat{\Omega}^{\mathrm{ref},\,IJ}\,\sigma_{IJ}^{-2}}{\sum_{IJ}\sigma_{IJ}^{-2}} \tag{7.3.8}$$

$$\sigma^{-2} = \sum_{IJ}\sigma_{IJ}^{-2}\,. \tag{7.3.9}$$

Now, we can recast $\Omega(f)$ in equation (7.3.2) (by means of equation (7.2.2)) and rearranging the terms) in the following form:

$$\Omega_{\mathrm{gw}}(f) = \Omega_{\mathrm{ref}}\left(\frac{f}{f_{\mathrm{ref}}}\right)^7 \frac{\Phi(f)}{\Phi(f_{\mathrm{ref}})}\,. \tag{7.3.10}$$

Finally, after applying the relevant data quality cuts to remove the non-Gaussian features associated with instrumental artifacts [258, 485], we can use the estimators presented in equation (7.3.8) to set upper limits on Ω_{ref} through a Bayesian analysis for the model of interest. To do that, we employ the likelihood

$$p\left(\hat{\Omega}(f_{\mathrm{k}})|\Omega(f_{\mathrm{k}})\right) = \frac{1}{\sqrt{2\pi}\sigma(f_{\mathrm{k}})}\,\exp\left\{\left[-\frac{\left(\hat{\Omega}(f_{\mathrm{k}}) - \Omega(f_{\mathrm{k}})\right)^2}{2\sigma^2(f_{\mathrm{k}})}\right]\right\}, \tag{7.3.11}$$

where $\hat{\Omega}(f_{\mathrm{k}})$ is assumed to be Gaussian distributed in the absence of a signal [239] and $\Omega(f_{\mathrm{k}})$ is the model for the SGWB in equation (7.3.10). Moreover, we can also use the estimator for Ω_{ref} as a starting point to obtain a constraint on $\varepsilon_{\mathrm{av}}$ of a NS population as a function of N_{band}, which will be discussed next.

7.3.2 Constraining the ellipticity of a NS population

Here, we show how to translate the results of the above-presented analysis to build an estimator for the average ellipticity of a NS population. We recall from section 7.2 that we are using fiducial values for $\langle I_{zz}^2 \rangle_{\rm NS}^{1/2}$ and $\langle 1/d^2 \rangle_{\rm NS}^{-1/2}$, while $\varepsilon_{\rm av}$ and $N_{\rm band}$ are left as free parameters for the time being.

Considering equation (7.2.2), along with the frequency range of interest, we can rewrite equation (7.3.2) as

$$\Omega(f) = \frac{64\pi^6 G^2}{3H_0^2} \frac{\langle \varepsilon^2 \rangle_{\rm NS} \langle I_{zz}^2 \rangle_{\rm NS}}{5c^8} \left\langle \frac{1}{d^2} \right\rangle_{\rm NS} f^7 \, N_{\rm band} \, \Phi(f) \, . \tag{7.3.12}$$

Then, by combining the above equation with equations 7.3.7 and 7.3.10, we obtain

$$\Omega(f) = \left(\frac{f}{f_{\rm ref}} \right)^7 \frac{\Phi(f)}{\Phi(f_{\rm ref})} \, \xi \, \langle \varepsilon^2 \rangle_{\rm NS} = w(f) \, \xi \, \langle \varepsilon^2 \rangle_{\rm NS} \ , \tag{7.3.13}$$

where we have introduced $\xi = \xi(N_{\rm band}) \equiv \Omega_{\rm ref} / \langle \varepsilon^2 \rangle_{\rm NS}$, which is just a proportionality constant, once $N_{\rm band}$ is fixed. Within this framework, using equation (7.3.3), the above equation can be recast in terms of different narrow-band estimators:

$$\left(\widehat{\varepsilon^2} \right)_{\rm av} (f_{\rm k}) = \frac{1}{\xi} \frac{\hat{\Omega}_{IJ}(f_{\rm k})}{w(f_{\rm k})} \equiv \frac{\hat{\Omega}_{\rm ref}(f_{\rm k})}{\xi} \, , \tag{7.3.14}$$

where $\hat{\Omega}_{\rm ref}(f_{\rm k})$ is the narrow-band estimator of $\Omega_{\rm ref}$, while $\left(\widehat{\varepsilon^2} \right)_{\rm av} (f_{\rm k})$ is the narrow-band estimator of the average squared ellipticity $\langle \varepsilon^2 \rangle_{\rm NS}$ of the NS population [2].

Starting from the above estimator, we can derive the relation between $\left(\widehat{\varepsilon^2} \right)_{\rm av} (f_{\rm k})$ and the average ellipticity of the NS population along with its estimator. This can be done by writing the expectation value of $\left(\widehat{\varepsilon^2} \right)_{\rm av} (f_{\rm k})$:

$$\left\langle \left(\widehat{\varepsilon^2} \right)_{\rm av} (f_{\rm k}) \right\rangle = \langle \varepsilon^2(f_{\rm k}) \rangle_{\rm NS} \equiv \varepsilon_{\rm av}^2(f_{\rm k}) + \sigma_\varepsilon^2(f_{\rm k}) \, , \tag{7.3.15}$$

where $\varepsilon_{\rm av}(f_{\rm k}) \equiv \langle \varepsilon(f_{\rm k}) \rangle_{\rm NS}$ is the mean value of the ellipticity, while $\sigma_\varepsilon^2(f_{\rm k})$ is the intrinsic variance of the ellipticity distribution. Then, from equation (7.3.15), we can define the biased estimator of the average ellipticity

$$\hat{\varepsilon}_{\rm av}(f_{\rm k}) \equiv \sqrt{\left(\widehat{\varepsilon^2} \right)_{\rm av} (f_{\rm k})} \, . \tag{7.3.16}$$

The bias introduced from the non-zero variance of the ellipticity distribution should be small since the physical ellipticity is a positive-definite quantity. Thus, one can assume $\sigma_\varepsilon(f_{\rm k}) \lesssim \varepsilon_{\rm av}(f_{\rm k})$ and ignore the variance in equation (7.3.15). This choice

[2] The frequencies $f_{\rm k}$ in equation (7.3.14) must be interpreted as labels and not as functional dependence.

translates into more conservative constraints derived from $\hat{\varepsilon}(f_{\rm k})$ [3]. Possible ways to account for the bias, as in the case of a detection of a SGWB from a NS population, would be to estimate $\sigma^2_{\varepsilon}(f_{\rm k})$ from the measurements of individual NSs (such as the ones detected with CW/EM techniques) from theoretical models of the population.

Given the estimator $\hat{\varepsilon}_{\rm av}(f_{\rm k})$, we can derive the associated uncertainty $\sigma_{\hat{\varepsilon}}(f_{\rm k})$ from the likelihood function $p_{\varepsilon}\left(\hat{\varepsilon}_{\rm av}(f_{\rm k})|\varepsilon_{\rm av}(f_{\rm k})\right)$. To obtain this likelihood, we use equations (7.3.13), (7.3.14), and (7.3.16) to express $\Omega(f_{\rm k})$ and $\hat{\Omega}(f_{\rm k})$ as a function of $\varepsilon_{\rm av}(f_{\rm k})$ and $\hat{\varepsilon}_{\rm av}(f_{\rm k})$, and we perform a change of variables in equation (7.3.11). Following this prescription, we obtain the following likelihood function for $\hat{\varepsilon}_{\rm av}(f_{\rm k})$, which is no longer a Gaussian:

$$p_{\varepsilon}\left(\hat{\varepsilon}_{\rm av}(f_{\rm k})|\varepsilon_{\rm av}(f_{\rm k})\right) = \sqrt{\frac{8}{\pi}}\frac{\varepsilon_{\rm av}(f_{\rm k})\,\xi}{\sigma_{\hat{\Omega}}(f_{\rm k})}\,\exp\left\{\left[-\frac{(\hat{\varepsilon}^2_{\rm av}(f_{\rm k})-\varepsilon^2_{\rm av}(f_{\rm k}))^2\,\xi^2}{2\sigma^2_{\hat{\Omega}}(f_{\rm k})}\right]\right\}, \tag{7.3.17}$$

where $\sigma_{\hat{\Omega}}(f_{\rm k})$ is the error corresponding to $\hat{\Omega}_{\rm ref}(f_{\rm k})$. By applying the definition of variance to the above distribution, in the limit $\hat{\varepsilon}_{\rm av}(f_{\rm k}) << 1$, we arrive at:

$$\sigma^2_{\hat{\varepsilon}}(f_{\rm k})|_{\hat{\varepsilon}<<1} \approx \left[\sqrt{\frac{2}{\pi}} - \frac{2^{3/2}\pi}{\Gamma^2(\frac{1}{4})}\right]\frac{\sigma_{\hat{\Omega}}(f_{\rm k})}{\xi} \simeq 0.12\,\frac{\sigma_{\hat{\Omega}}(f_{\rm k})}{\xi}\,. \tag{7.3.18}$$

The derivation and the expression of $\sigma^2_{\hat{\varepsilon}}(f_{\rm k})$ in the general case $\hat{\varepsilon}_{\rm av}(f_{\rm k}) > 0$ are reported in Appendix 7.6.2.

Finally, assuming the ellipticity to be independent of the frequency, the narrow-band estimators $\hat{\varepsilon}_{\rm av}(f_{\rm k})$ can be combined to obtain the optimal broad-band estimator $\hat{\varepsilon}_{\rm opt}$, with a relative uncertainty $\sigma_{\rm opt}$ as

$$\hat{\varepsilon}_{\rm opt} = \frac{\sum_k \hat{\varepsilon}_{\rm av}(f_{\rm k})\,\sigma^{-2}_{\hat{\varepsilon}}(f_{\rm k})}{\sum_k \sigma^{-2}_{\hat{\varepsilon}}(f_{\rm k})}\,, \qquad \sigma_{\rm opt} = \left(\sum_k \sigma^{-2}_{\hat{\varepsilon}}(f_{\rm k})\right)^{-1/2}. \tag{7.3.19}$$

Using equation (7.3.12) and plugging it into the above equation, the optimal estimator depends on the number of in-band NSs, which has been considered as a free parameter in the analysis, through the relation $\hat{\varepsilon}_{\rm opt} \propto N^{-1/2}_{\rm band}$. Hence, the upper limits on the average ellipticity $\varepsilon_{\rm av}$ will also depend on $N_{\rm band}$. In this situation, we could set upper limits on quantities such as $\varepsilon_{\rm av}N^{1/2}_{\rm band}$ or $\varepsilon^2_{\rm av}N_{\rm band}$, which are inherently independent from $N_{\rm band}$. Alternatively, we could evaluate upper limits on $\varepsilon_{\rm av}$ at a reference value of $N_{\rm band}$ and then map them into the $N_{\rm band} - \varepsilon_{\rm av}$ plane. In this paper, we follow the second approach to present constraints on the average ellipticity.

[3] A non-zero $\sigma^2_{\hat{\varepsilon}}(f_{\rm k})$ will increase the intensity of a stochastic signal at a fixed $\varepsilon_{\rm av}(f_{\rm k})$, making its detection easier.

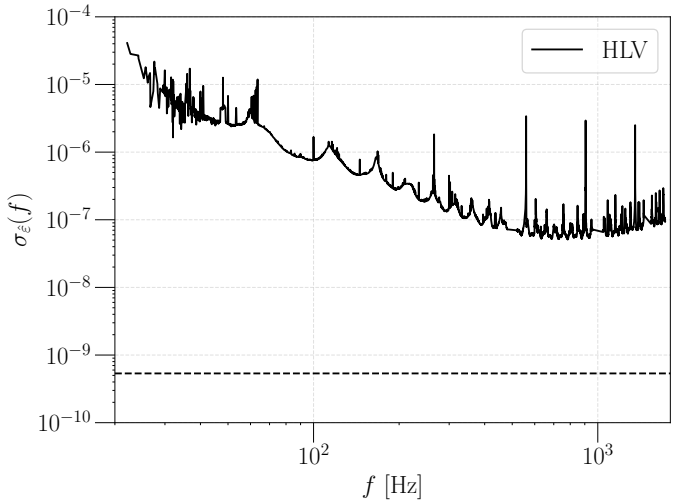

(a) Plot of the 1σ sensitivity to the average ellipticity of Galactic NSs. The solid curve shows the uncertainty $\sigma_\varepsilon(f_\mathrm{k})$ associated with the narrow-band estimators, while the dashed one is the broad-band value of σ_opt. The improvement of the search sensitivity by combining the narrow-band estimators ranges between two and four orders of magnitude. The plot assumes $N_\mathrm{band} = 1.6 \times 10^7$, $\langle 1/d^2 \rangle_\mathrm{NS}^{-1/2} = 6$ kpc, and $\langle I_{zz}^2 \rangle_\mathrm{NS}^{1/2} = 10^{38}\,\mathrm{kg\,m^2}$.

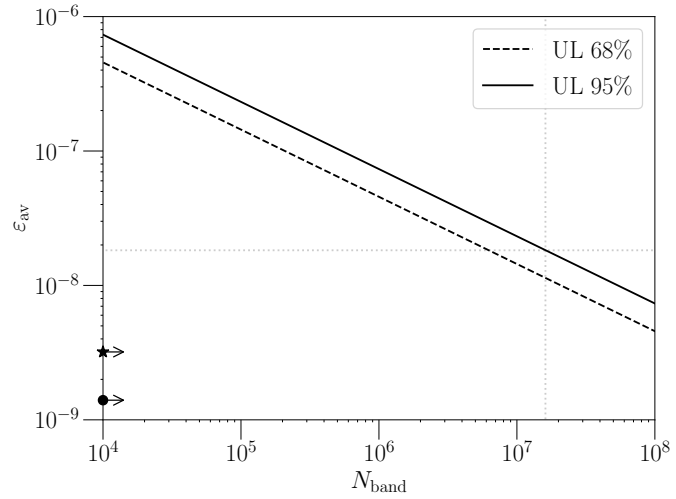

(b) 68% (dashed) and 95% (solid) confidence-level Bayesian upper limits in the $N_\mathrm{band} - \varepsilon_\mathrm{av}$ plane, assuming a log-uniform prior on ε_av. Here, we have set N_band to range from 10^4 and 10^8. The dotted grey lines identify the 95% upper limit on ε_av obtained with the pivot value of in-band NSs, $N_\mathrm{band} = 1.6 \times 10^7$. The star and the circle on the y-axis denote the most recent, lowest upper limits on a single NS ellipticity (*independent of* N_band), respectively $\varepsilon \lesssim 3.2 \times 10^{-9}$ from targeted [515] CW searches and $\varepsilon \lesssim 1.4 \times 10^{-9}$ (assuming 10 pc distance from Earth and a GW frequency of 2047.5 Hz) from all-sky [535] ones.

Figure 7.2

7.4 Results of the analyses

We perform this analysis on publicly available data [216, 217] from the first three observing runs (O1, O2, and O3) of the Advanced LIGO and Virgo detectors. We first search for an isotropic SGWB from Galactic NSs, assuming the model given in equation (7.3.10). Using these search results, we also place upper limits on the average ellipticity of the NS population. Secondly, we consider five clusters of galaxies as hotspots of GWs. By associating a specific patch[4] in the sky to each of them, we again set constraints on the average ellipticity of the NS population starting from the results for the fractional SGWB energy density for each sky patch analysed, $\Omega_{\rm gw}^{\rm patch}(f)$. These results are given in the following subsections.

7.4.1 Galactic NS results

Since our search for an isotropic SGWB from Galactic isolated NSs did not find any evidence for a signal, we set upper limits on $\Omega_{\rm ref}$. These results are subsequently used to constrain $\varepsilon_{\rm av}$ and are listed in table 7.1. The first four columns from the left contain the results for the SGWB background search. The second column shows the value of the cross-correlation statistic and the associated 1σ uncertainty derived from equation (7.3.8). The third and fourth columns present the 95% confidence-level Bayesian upper limits for $\Omega_{\rm ref}$. These upper limits are obtained by marginalising the likelihood function given in equation (7.3.11) over a uniform (third column) and a log-uniform prior (fourth column) on the strength of the SGWB. It is worth noting that the log-uniform prior seems to be the most natural choice since $\Omega_{\rm ref}$ range is expected to span several orders of magnitude and is more sensitive to small signals. The log-uniform prior range was chosen to be between $10^{-18} \leq \Omega_{\rm ref} \leq 10^{-8}$. The upper bound is large enough such that there is no posterior support at that value, while the lower bound cannot be zero for this kind of prior. On the other hand, we have also included the result from the uniform prior case, which leads to more conservative upper limits. In both cases, the estimator for $\Omega_{\rm ref}$, as well as the upper limits, are all of $\mathcal{O}(10^{-14})$. These values are significantly smaller than those for other power-law models for $\Omega_{\rm gw}(f)$, e.g. those reported in [258], since the $\Omega_{\rm gw}$ used in this paper is dominated by the $\sim f^7$ term.

The last two columns in table 7.1 illustrate the limits we have obtained on the average ellipticity at 1σ sensitivity and the corresponding 95% Bayesian upper limits on $\varepsilon_{\rm av}$, using the fiducial value $\left\langle 1/d^2 \right\rangle^{-1/2} = 6\ \mathrm{kpc}$ in equation (7.2.2). The value of the estimator $\hat{\varepsilon}_{\rm opt}$ is of $\mathcal{O}(10^{-11})$, with an associated uncertainty one order of magnitude larger. The improvement in the sensitivity of the search that comes from combining the estimators over frequencies is illustrated in figure 7.2a. Here, the relative uncertainties associated with $\hat{\varepsilon}_{\rm av}(f_{\rm k})$ and $\hat{\varepsilon}_{\rm opt}$ are plotted as a function of frequency.

[4]The methodology to build the sky patches and evaluate the associated average background is presented in appendix 7.6.3, and makes use of the radiometer search [433, 434, 467].

$\Omega(f)$	$\hat{\Omega}_{\rm ref}^{\rm O1+O2+O3}/(10^{-14})$	$\Omega_{\rm ref}^{95\%,\,\rm Uniform}$	$\Omega_{\rm ref}^{95\%,\,\rm Log-uniform}$
$\propto (f)^7\,\Phi(f)$	0.9 ± 1.9	4.5×10^{-14}	2.0×10^{-14}
$\Phi(f)$	$N_{\rm band}$	$\hat{\varepsilon}_{\rm opt}^{\rm O1+O2+O3}/10^{-11}$	$\varepsilon_{\rm Log-uniform}^{95\%}$
ATNF-KDE	1.6×10^7	2.5 ± 53.5	1.8×10^{-8}

Table 7.1: Results of the isotropic search for a SGWB from an ensemble of Galactic NSs using data from the first three LIGO-Virgo-KAGRA observing runs, and the subsequent constraints on the average ellipticity of the Galactic NS population. The top two rows are the results from our search, in which $\Omega(f)$, the cross-correlation statistics, and the upper limits on $\Omega_{\rm ref}$, using a uniform and log-uniform prior, are reported. The bottom two rows encode information about the Galactic NS population, such as $\Phi(f)$ and $N_{\rm band}$, the average ellipticity optimal estimator, and the upper limit obtained by assuming a log-uniform prior on ε between $10^{-12} - 10^{-4}$.

On the other hand, the Bayesian upper limit on the average ellipticity $\varepsilon_{\rm av}$ has been obtained using the likelihood function in equation (7.3.17) by assuming a log-uniform prior in the range $10^{-12} - 10^{-4}$. The obtained constraint is of $\mathcal{O}(10^{-8})$. As discussed in section 7.3.2, the constraint holds only for the representative value of $N_{\rm band}$ that we have explicitly presented here. However, it can be easily mapped into the $N_{\rm band} - \varepsilon_{\rm av}$ plane for different values of in-band NSs. Considering the range $N_{\rm band} \in [10^4 - 10^8]$, we present the 68% and 95% Bayesian upper limits on the average ellipticity in figure 7.2b. In this figure, the pivot value $N_{\rm band} = 1.6 \times 10^7$ is highlighted using a dotted line for an easy comparison. We also report the latest, lowest upper limits on a NS ellipticity from targeted [515] and all-sky [535] CW searches on the y-axis. It is evident from the figure that the resulting $\varepsilon_{\rm av}$, ranging between 10^{-8} and 10^{-6}, follows the $\varepsilon_{\rm av} \propto N_{\rm band}^{-1/2}$ relation, as anticipated in section 7.3.2.

7.4.2 Hotspot results

The search results from five NS GW hotspots and the corresponding constraints on their ellipticities are reported in table 7.2. First, we pixelate the sky by employing the `HEALPix` (Hierarchical Equal Area isoLatitude Pixelation) pixelisation scheme [439,486], with $N_{\rm side} = 16$ (3072 pixels, each one with an extension of $\simeq 13.4\,{\rm deg}^2$). From the right ascension and declination of the hotspot, we identify one pixel and its eight closest neighbours. These collections of pixels will act as a patch in the pixelated sky and are illustrated in figure 7.3. The signal model for each of the hotspots is similar to the one used in the Galactic NS analysis, except for the number of in-band NS (which in this case is $N_{\rm band} = 1.6 \times 10^{10}$) and the distance parameter $\left\langle 1/d^2 \right\rangle_{\rm NS}^{-1/2}$ (values considered are shown in the second column of table 7.2). For each hotspot, we first estimated the $\Omega_{\rm gw}^{\rm patch}(f)$ using the folded data [430, 431, 561] and `PyStoch` pipeline [466], and then followed the method described in section 7.3.2 to derive constraints on the average ellipticity of the NS populations in each of the hotspots.

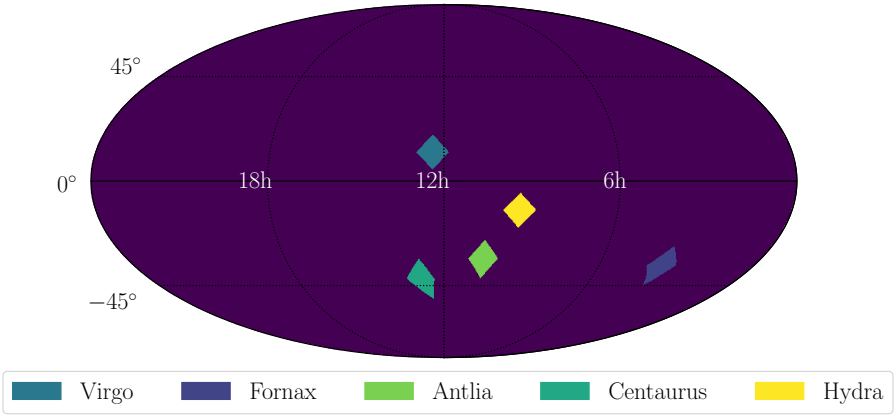

Figure 7.3: The sky-patches associated with the five NS hotspots: Virgo, Fornax, Antlia, Centaurus, and Hydra clusters. Each patch consists of 9 pixels with $N_{\rm side} = 16$: the central one being the one associated with the galaxy cluster, and the eight closest neighbours. The sky map is represented as a Mollweide projection of the sky in ecliptic coordinates.

Within the above framework, we have derived the optimal estimators and the 95% confidence upper limits related to the average ellipticity of the NS populations of the hotspots. These quantities are respectively reported in the third and fourth columns of table 7.2. Because of the absence of any detection, we set upper limits using the same criteria as in the Galactic case. We find that the estimators are of the order of $10^{-10} - 10^{-9}$, whereas the upper limits of the average ellipticity are around $10^{-7} - 10^{-6}$. Comparing the constraints and the relative hotspot distances, we note that the constraints become less stringent when the source is more distant from Earth. By contrasting the hotspot limits with those from Galactic NSs, we observe that the former are one or two orders of magnitude larger than the latter. This difference could arise from several factors, from the model assumed to the characteristics of the ground-based detectors. From a modelling perspective, based on equations 7.2.2 and 7.3.12, the difference between these two kinds of NS populations is encoded in the average of the inverse squared distance of the source from the Earth, the number of in-band NS, and the size of the examined region of the sky. The hotspot populations are estimated to have 10^3 times more NSs compared to the Galactic population but are also 10^3 times more distant from Earth. This means that in light of the model considered and the assumed values, the average ellipticity of the cluster NS population should be $\simeq \sqrt{10^3}$ times the Galactic one, in the naive case where the two SGWB have the same intensity. From the detector perspective, instead, the intrinsic sensitivity of the instrument to the source distance and its position in the sky have an impact. The detector becomes less sensitive the more distant the source of interest is. The sensitivity may get even worse if the source is well localised and spends most of the time in the region of the sky where the detectors have poorly observed modes [239]. Given two populations with different positions and spreads in the sky, analyses of these two areas

Hotspot	$\langle 1/d^2 \rangle_{\rm NS}^{-1/2}$ (Mpc)	$\hat{\varepsilon}_{\rm opt}^{\rm O1+O2+O3}/10^{-9}$	$\varepsilon_{\rm Log-uniform}^{95\%}/10^{-7}$
Virgo	18	0.6 ± 10.6	3.6
Fornax	19	0.5 ± 10.1	3.5
Antlia	40.7	1.5 ± 22.1	7.6
Centaurus	52.4	1.4 ± 27.9	9.6
Hydra	58.3	3.8 ± 34.2	11.8

Table 7.2: Relevant parameters and results of searches for NSs in hotspots. For each cluster of galaxies, a fiducial value of $\langle 1/d^2 \rangle_{\rm NS}^{-1/2}$ (second column), the broad-band estimator $\hat{\varepsilon}_{\rm opt}$ (third column), and the 95% confidence level Bayesian upper limits on the average ellipticity of the population (fourth column) are reported. The upper limits have been obtained by assuming a log-uniform prior between $10^{-12} - 10^{-4}$ over the ellipticities.

may lead to less stringent upper limits for one population with respect to another one, even though the properties of the two populations' original signals are the same. This effect can be mitigated by combining data from multiple detectors (pairs) of a detector network, but it cannot be completely suppressed due to the intrinsic geometry of the network and its interaction with the GW signal. Further studies to evaluate the impact of the model and choice and the detector network characteristics in the recovery of the signal will be the subject of future work.

7.5 Discussions and conclusions

In this work, we have derived constraints on the average ellipticity of a NS population from the results of a cross-correlation-based search for a SGWB. We have considered two classes of NS populations: those in our Galaxy and those in five extragalactic clusters, which we call NS hotspots. We have not found compelling evidence of a SGWB signal from any of the considered sources and hence have set upper limits on the intensity of the background by bounding the energy density parameter $\Omega_{\rm gw}(f)$. These results have then been translated to constraints of the NS average ellipticity, obtained to be as low as $\varepsilon_{\rm av} \lesssim 1.8 \times 10^{-8}$ with $N_{\rm band} = 1.6 \times 10^7$ in the case of Galactic NS and $\varepsilon_{\rm av} \lesssim [3.5-11.8] \times 10^{-7}$ with $N_{\rm band} = 1.6 \times 10^{10}$ for those in galaxy clusters. These constraints obtained using the data from the first three observation runs of Advanced LIGO and Virgo are the first of their kind.

If we consider recent results from CW searches for Galactic NSs, whose lowest limits on NSs ellipticities are $\varepsilon \lesssim 3.2 \times 10^{-9}$ (for J0636+5129) from targeted searches [515] and $\varepsilon \lesssim 1.4 \times 10^{-9}$ (for a NS at 10 pc from Earth and at 2047.5 Hz) from all-sky searches [535], we observe that they are one order of magnitude lower than the values reported here. It is not straightforward to compare these limits, since these analyses constrain different properties of NSs. Targeted CW searches are more sensitive to individual NS properties, such as the ellipticity, but must obtain their limits only based on known pulsars. Moreover, all-sky searches have proven to be compu-

tationally expensive (order of months to run) and can only search in certain parts of the parameter space semi-coherently, which limits their sensitivities to ellipticities of $\mathcal{O}(10^{-7})$ and $\mathcal{O}(10^{-5})$ at $\mathcal{O}(1)$ kpc at high and low frequencies, respectively [535]. Instead, searches for SGWB have become computationally efficient and faster (order of days to run) [258, 431, 466, 484, 562], but their constraining power is weaker compared to targeted CW searches. In addition to that, they have the advantage (once the results are available) of instantaneously identifying the features of an ensemble of known or unknown NSs, which would otherwise require decades or centuries to be determined through individual NS discoveries. Because SGWB and CW searches attempt to answer different physical questions, they can work in synergy. Using the methods of the former, it would be possible to perform rapid, blind all-sky searches for NS signals and transmit the coordinates of possible outliers as inputs to the latter, for a more refined and sensitive search.

In this work, we have restricted ourselves to constrain the average ellipticity of a NS population, given the number of in-band NSs. We have assumed values for the average squared moment of inertia and the average squared inverse distance of the population. We could gain even more information about NS populations by treating these quantities as free parameters. Additionally, we could estimate and set constraints on these quantities through a full Bayesian search, in which priors could be derived from population synthesis simulations. These simulations could also be used to model the NS frequency and angular distributions, which could then be used as an alternative to those derived from the ATNF catalogue, especially in the extragalactic case. Moreover, the inclusion of the angular distribution of the NSs would allow us to perform a template-based matched-filtering search using the λ-statistics from [437], which may set less conservative upper limits. Finally, from the synthesised population, the corresponding SGWB signal could be simulated, and its prospects for detection and characterisation could be examined within the networks of the future detector. Two ways of doing this would be to consider a network, where KAGRA and the future LIGO-India [115] are included, or considering the next-generation interferometers, such as Einstein Telescope [116] and Cosmic Explorer [117], and evaluate their impact on these kinds of searches. These possibilities will be explored in future work.

7.6 Appendix

7.6.1 Derivation of the spectral shape

Here, we present a heuristic procedure to get the expression of the spectral shape $S_h(f)$ in equation (7.2.2). The GW power emitted by a pulsar at a given frequency can be expressed from equation (1.5.24) as

$$P(f) = \frac{32\,\pi^6\,G}{5\,c^5}\varepsilon^2\,I_{zz}^2\,f^6\,, \tag{7.6.1}$$

and is linked to the GW energy density at a distance d from the source through the relation

$$\rho_{\rm gw}(f) = \frac{P(f)}{4\pi\, c\, d^2}\,. \tag{7.6.2}$$

Now, let us consider a population of NSs, each one emitting GW at a frequency f_j and from the direction $\hat{n}_j$, where $j = 1, 2, ..., N_0$ and N_0 is the total number of pulsars. Then, the corresponding GW energy density ratio can be expressed as

$$\begin{aligned}\Omega_{\rm gw}(f,\hat{n}) &= \frac{f}{\rho_c}\sum_{j=1}^{N_0}\frac{P_j}{4\pi c d_j^2}\,\delta(f-f_j)\,\delta^2(\hat{n},\hat{n}_j)\\ &= \frac{f\,\langle P\rangle_{\rm NS}}{4\pi\rho_c\, c}\left\langle\frac{1}{d^2}\right\rangle_{\rm NS} N_0\,\Psi(f,\hat{n})\,,\end{aligned} \tag{7.6.3}$$

where $\Psi(f,\hat{n})$ is the frequency-angular distribution of the NS population. We take the ensemble average over pulsar parameters in the second line of the above equation. Finally, plugging equation (7.6.1) in equation (7.6.3) and using the definition of spectral shape (equation (7.3.12)), we get

$$\begin{aligned}S_h(f) &= \frac{3H_0^2}{2\pi^2 f^3}\int d^2\hat{n}\,\Omega_{\rm gw}(f,\hat{n})\\ &= \frac{32\pi^4\, G^2\,\langle\varepsilon^2\rangle_{\rm NS}\,\langle I_{zz}^2\rangle_{\rm NS}}{5c^8\,\langle d^2\rangle_{\rm NS}} f^4\,\Phi(f)\,N_0\,,\end{aligned} \tag{7.6.4}$$

this is identical to equation (7.2.2) where $\Phi(f) \equiv \int d^2\Omega_{\hat{n}}\,\Psi(f,\hat{n})$.

7.6.2 The ellipticity estimator uncertainty: general case

Here, we derive the expression of the variance $\sigma^2_{\hat{\varepsilon}}(f_{\rm k})$ of the estimator of the average ellipticity $\hat{\varepsilon}_{\rm av}(f_{\rm k})$ in the general case, where $\hat{\varepsilon}_{\rm av}(f_{\rm k}) > 0$. The procedure is not complex conceptually: it is necessary to evaluate the first and second-order expectation values starting from the likelihood in equation (7.3.17) and combine them to get $\sigma^2_{\hat{\varepsilon}}(f_{\rm k})$, but some algebra is required.

From the expressions (where $D_\nu(z)$ is a parabolic cylinder function and we omit the frequency label in the last expression)

$$\begin{aligned}\langle\varepsilon_{\rm av}(f_{\rm k})\rangle &\equiv \int_0^\infty p_\varepsilon\left(\hat{\varepsilon}_{\rm av}(f_{\rm k})|\varepsilon_{\rm av}(f_{\rm k})\right)\varepsilon_{\rm av}\,d\varepsilon_{\rm av}\\ &= \sqrt{\frac{\sigma_{\hat{\Omega}}}{2\xi}}D_{-3/2}\left(-\frac{\hat{\varepsilon}^2_{\rm av}\,\xi}{\sigma_{\hat{\Omega}}}\right)\exp\left[-\frac{\hat{\varepsilon}^4_{\rm av}\,\xi^2}{4\sigma^2_{\hat{\Omega}}}\right]\end{aligned} \tag{7.6.5}$$

and

$$\begin{aligned}\left\langle \varepsilon_{\rm av}^2(f_{\rm k})\right\rangle &\equiv \int_0^\infty p_\varepsilon\left(\hat{\varepsilon}_{\rm av}(f_{\rm k})|\varepsilon({}_{\rm av}f_{\rm k})\right)\varepsilon_{\rm av}^2\, d\varepsilon_{\rm av} \\ &= \sqrt{\frac{2}{\pi}}\frac{\sigma_{\hat{\Omega}}}{\xi}D_{-2}\left(-\frac{\hat{\varepsilon}_{\rm av}^2\,\xi}{\sigma_{\hat{\Omega}}}\right)\exp\left[-\frac{\hat{\varepsilon}_{\rm av}^4\,\xi^2}{4\sigma_{\hat{\Omega}}^2}\right],\end{aligned} \tag{7.6.6}$$

it is straightforward to show

$$\begin{aligned}\sigma_{\hat{\varepsilon}}^2(f_{\rm k}) =& \left\langle \varepsilon_{\rm av}^2(f_{\rm k})\right\rangle - \left\langle \varepsilon_{\rm av}(f_{\rm k})\right\rangle^2 \\ =&\sqrt{\frac{2}{\pi}}\frac{\sigma_{\hat{\Omega}}}{\xi}D_{-2}\left(-\frac{\hat{\varepsilon}_{\rm av}^2\,\xi}{\sigma_{\hat{\Omega}}}\right)\exp\left[-\frac{\hat{\varepsilon}_{\rm av}^4\,\xi^2}{4\sigma_{\hat{\Omega}}^2}\right] - \\ &-\frac{1}{2}\frac{\sigma_{\hat{\Omega}}}{\xi}D_{-3/2}^2\left(-\frac{\hat{\varepsilon}_{\rm av}^2\,\xi}{\sigma_{\hat{\Omega}}}\right)\exp\left[-\frac{\hat{\varepsilon}_{\rm av}^4\,\xi^2}{2\sigma_{\hat{\Omega}}^2}\right].\end{aligned} \tag{7.6.7}$$

The limit $\varepsilon << 1$ in equation (7.3.18) is recovered by observing and using

$$D_\nu(z)|_{z<<1} \approx \frac{2^{-(\nu+2)/2}\,\Gamma\left(-\frac{\nu}{2}\right)}{\Gamma(-\nu)}, \tag{7.6.8}$$

where $\Gamma(z)$ is Euler's Gamma function.

7.6.3 Search for SGWB from NS hotpots

Here, we present how we have derived the limits on $\Omega_{\rm gw}^{\rm patch}(f)$ of a patch in the sky to use as input in section 7.4.2 to get the constraints on the average ellipticity of the NS hotspots.

7.6.4 The directional radiometer search

The directional radiometer search drops the assumption of the SGWB being isotropic [250, 269, 490–493, 563, 564]. This means that the background cannot be simply characterised by considering $\Omega_{\rm gw}(f)$ in equation (7.3.1), but rather the frequency-angular dependent density parameter $\Omega_{\rm gw}(f,\hat{n})$ (measured in $\rm sr^{-1}$):

$$\Omega_{\rm gw}(f,\hat{n}) = \frac{f}{\rho_c}\frac{d^3\rho_{\rm gw}(f,\hat{n})}{df\,d^2\hat{n}} = \frac{2\pi^2}{3H_0^2}\,f^3\,\mathcal{P}(f,\hat{n}), \tag{7.6.9}$$

with $\mathcal{P}(f,\hat{n})$ being the GW strain power.

In order to measure the anisotropies, the radiometer search introduces a maximum-likelihood (ML) estimator [429, 434], as a statistic, at each frequency and each direc-

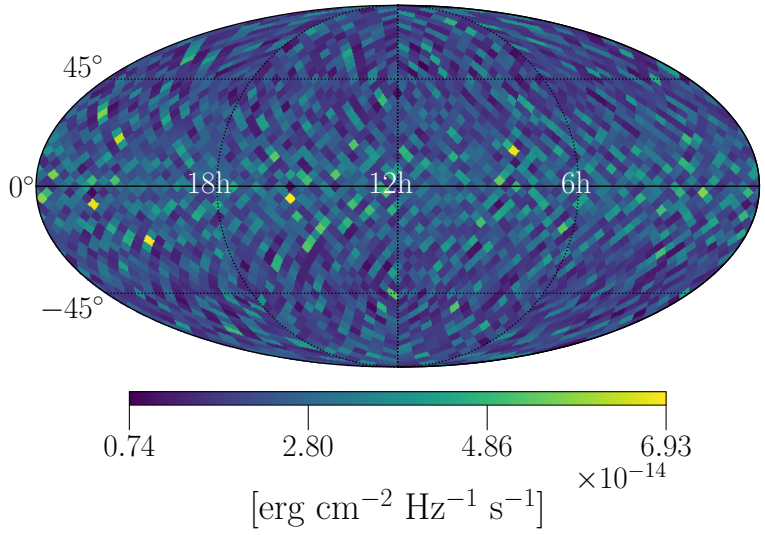

Figure 7.4: Upper limit sky maps on GW energy flux from the broad-band-radiometer analysis for the model $\bar{H}(f)$ in equation (7.6.16). Here the NSs frequency distribution $\Phi(f)$ is the one built from the ATNF catalogue as described in section 7.2. The sky map is represented as a color bar plot on a Mollweide projection of the sky in ecliptic coordinates with $N_{\rm side} = 16$.

tion [430] $\hat{\mathcal{P}}(f,\hat{n})$ with cross-correlation matrix $\sigma_{\hat{n},\hat{n}'}(f)$:

$$\hat{\mathcal{P}}(f,\hat{n}) = \sum_{\hat{n}'} \left[\Gamma_{\hat{n}\hat{n}'}(f)\right]^{-1} X_{\hat{n}'}(f)\,, \tag{7.6.10}$$

$$\sigma_{\hat{n},\hat{n}'}(f) = \left[\Gamma_{\hat{n}\hat{n}'}(f)\right]^{-1/2}\,, \tag{7.6.11}$$

where $X_{\hat{n}'}(f)$ is called "dirty map" and $\Gamma_{\hat{n}\hat{n}'}$ is the Fisher information matrix in the small-signal limit. The summation over $\hat{n}'$ implies integration over the solid angle. The dirty map represents the sky seen through the response of a set of independent baselines IJ, defined as

$$X_{\hat{n}}(f) = T\Delta f\ \mathrm{Re}\sum_{IJ,t} \frac{\left[\gamma_{IJ}(t;f)\right]^*_{\hat{n}}\ \hat{C}_{IJ}(t;f)}{P_I(t;f)\,P_J(t;f)}\,, \tag{7.6.12}$$

where $\hat{C}_{IJ}(t;f) \equiv (2/T)\,\tilde{s}^*_I(t;f)\,\tilde{s}_J(t;f)$ is the cross-correlation spectral density, while $\gamma_{IJ}(t;f,\hat{n})$ is the directional overlap reduction function, which is proportional to the isotropic one in equation (7.3.3) when integrated over the sky. The Fisher information matrix encodes the uncertainty in the measurement of the dirty map and is defined as

$$\Gamma_{\hat{n},\hat{n}'}(f) = T\Delta f\ \mathrm{Re}\sum_{IJ,t} \frac{\left[\gamma_{IJ}(t;f)\right]^*_{\hat{n}}\ \left[\gamma_{IJ}(t;f)\right]_{\hat{n}'}}{P_I(t;f)\,P_J(t;f)}\,. \tag{7.6.13}$$

The ML estimator $\hat{\mathcal{P}}(f,\hat{n})$ in equation (7.6.10) involves the inversion of $\Gamma_{\hat{n},\hat{n}'}(f)$, which can be singular in general and must be regularised. However, for point-like sources considered here, we can work by employing the pixel basis

$$\mathcal{P}(f,\hat{n}) \equiv \mathcal{P}(f,\hat{n}')\,\delta^2(\hat{n},\hat{n}')\,, \tag{7.6.14}$$

and ignore the correlation among neighbourhood directions in the sky [1, 430], and the Fisher information matrix is no longer singular and becomes diagonal. With this caveat, the estimator can be used to set upper limits on $\Omega_{\rm gw}(f,\hat{n})$ and related quantities.

7.6.5 SGWB from NS hotspots in the sky

To specialise the framework to our search for a SGWB from NS hotspots, we make the following, standard, ansatz about the factorisability of $\hat{\mathcal{P}}(f,\hat{n})$ in a frequency- and direction-dependent only terms:

$$\mathcal{P}(f,\hat{n}) = \bar{H}(f)\,\mathcal{P}(\hat{n})\,, \tag{7.6.15}$$

where $\bar{H}(f)$ is defined in such a way that $\bar{H}(f_{\rm ref}) = 1$, $\mathcal{P}(\hat{n})$ is the angular distribution of gravitational-wave power to be estimated by the search. For the signal model presented in section 7.3, $\bar{H}(f)$ turns out to be

$$\bar{H}(f) = \left(\frac{f}{f_{\rm ref}}\right)^4 \frac{\Phi(f)}{\Phi(f_{\rm ref})}\,. \tag{7.6.16}$$

Using the above formalism, it is possible to integrate $\hat{\mathcal{P}}(f,\hat{n})$ (or, equivalently, $\hat{\Omega}_{\rm gw}(f,\hat{n})$) over the frequencies to get a set of broad-band estimators $\hat{\mathcal{P}}_{\rm ref}(\hat{n})$, or over the sky directions of a sky patch, to get a set of narrow-band estimators $\hat{\mathcal{P}}^{\rm patch}(f_{\rm k})$, or even both frequencies and direction, getting a broad-band estimator of the SGWB of a sky patch $\hat{\mathcal{P}}^{\rm patch}_{\rm ref}$. The master formulas for the integrated estimator over a set of frequencies and directions, and the relative uncertainty, are given by

$$\hat{\mathcal{P}}^{\rm patch}_{\rm ref} = \frac{\sum_{k,j}\hat{\mathcal{P}}(f_{\rm k},\hat{n}_{\rm j})\,\sigma^{-2}(f_{\rm k},\hat{n}_{\rm j})\,\bar{H}(f)}{\sum_{k,j}\sigma^{-2}(f_{\rm k},\hat{n}_{\rm j})\,\bar{H}(f)^2}\,, \tag{7.6.17}$$

$$\sigma^{\rm patch}_{\rm ref} = \left(\sum_{k,j}\sigma^{-2}(f_{\rm k},\hat{n}_{\rm j})\,\bar{H}(f)^2\right)^{-1/2}\,. \tag{7.6.18}$$

Within this framework, we derive the following quantities: a broad-band estimator for each sky direction $\hat{\mathcal{P}}^{\rm sky}_{\rm ref}(\hat{n})$, a set of narrow-band estimators for each patch $\hat{\mathcal{P}}^{\rm patch}(f_{\rm k})$, and a broad-band estimator for each patch $\hat{\mathcal{P}}^{\rm patch}_{\rm ref}$. The broad-band estimators are evaluated to get information about the SGWB from a NS population, when one allows for an unknown spatial distribution of the population, compared to the isotropic case. These estimators are translated into estimators of the GW energy flux,

given the astrophysical nature of the source,

$$\hat{\mathcal{F}}_{\rm ref}(\hat{n}) = \frac{c^3\pi}{4G}\, f_{\rm ref}^2\, \hat{\mathcal{P}}_{\rm ref}(\hat{n})\,, \tag{7.6.19}$$

at a reference frequency $f_{\rm ref}$, from which the relative ULs are calculated and illustrated in figure 7.4. The narrow-band estimators for every patch, instead, are converted to narrow-band estimators of the density parameter $\hat{\Omega}_{\rm gw}^{\rm patch}(f_{\rm k})$ by means of equation (7.6.9), and are used as input for the evaluation of constraints on the average ellipticity of the different NS populations in section 7.4.2.

Chapter 8

Probing ensemble properties of vortex-avalanche pulsar glitches with a stochastic gravitational-wave background search

「螺旋丸!」

岸本斉史, -ナルト-

This chapter is a reproduction of reference [3], in collaboration with Dr. Jishnu Suresh, Antoine Depasse, Dr. Magdalena Sieniawska, Dr. Andrew Lawrence Miller, and Prof. Giacomo Bruno. The work was published in *Phys. Rev. D*, 107(10):102001, 2023. This project has included all of the CP3 members involved in GW data analysis activities within LVK, aiming at creating synergies between the members. This project lasted from November 2021 to May 2023. I was the main author, performing the analysis in section 8.3 and writing the whole manuscript, with the exception of the introductory part about searches for transient continuous-wave signals following a pulsar glitch. By adapting the methods from chapter 7, we investigate the implications of SGWB search results for glitching pulsars. We initially modelled the SGWB from glitching pulsars using the results from [565]. During the development of this project, I redid the whole calculation and eventually found that the formulas for the SGWB presented in [565] were incorrect (see section 8.6.1). I also wrote the post-processing code used for this analysis and derived the novel (to our knowledge) formulas in section 8.6.2.

Abstract

A stochastic gravitational-wave background (SGWB) is expected to be produced by the superposition of individually undetectable, unresolved gravitational-wave (GW) signals from cosmological and astrophysical sources. Such a signal can be searched with dedicated techniques using the data acquired by a network of ground-based GW detectors. In this work, we consider the astrophysical SGWB resulting from pulsar glitches, which are sudden increases in the rotational pulsar

frequency, within our Galaxy. More specifically, we assume glitches to be associated with quantised, superfluid, vortex-avalanches in the pulsars, and we model the SGWB from the superposition of GW bursts emitted during the glitching phase. We perform a cross-correlation search for this SGWB-like signal employing the data from the first three observation runs of Advanced LIGO and Virgo. Not having found any evidence for a SGWB signal, we set upper limits on the dimensionless energy density parameter $\Omega_{\rm gw}(f)$ for two different power-law SGWBs, corresponding to two different glitch regimes. We obtain $\Omega_{\rm gw}(f) \leq 7.5 \times 10^{-10}$ at 25 Hz for a spectral index 5/2, and $\Omega_{\rm gw}(f) \leq 5.7 \times 10^{-17}$ at 25 Hz for a spectral index 17/2. We then use these results to set constraints on the average glitch duration and the average radial motion of the vortexes during the glitches for the population of the glitching Galactic pulsars, as a function of the Galactic glitch rate.

8.1 Introduction

The third observing run (O3) of the LIGO-Virgo-KAGRA [90, 94, 95] collaboration finished by cataloguing several tens of gravitational waves (GWs) [93] originating from the compact binary coalescence (CBC) of black holes and/or neutron stars (NS). However, CBCs are only one class of GW sources among a broader range of possibilities. One of the interesting source categories yet to be detected is the stochastic gravitational-wave background (SGWB). The SGWB is considered to be a persistent signal resulting from the incoherent superposition of GWs from a large number of sources with cosmological and astrophysical origins. From the astrophysical perspective, there could be several phenomena contributing to the SGWB [243, 246]. These include the superposition of continuous gravitational waves from NSs [2, 437, 446, 543], magnetars [269, 271, 278, 566, 567], core-collapse to supernovae bursts [283, 285, 289, 290, 568, 569], and the superposition of the unresolved astrophysical CBC events [249,255,256,270,570,571]. Even though these astrophysical phenomena can be classified as sources of weak GW signals, their collective and incoherent signals will form a SGWB, and we may be able to observe them with the network of ground-based GW detectors.

From the high precision tracking of the pulsar spins (for a review, see [357,358]), it is observed that the pulsar rotations are generally stable and show a regular trend in the frequency derivative (spin-down). However, it is a well-established observational fact that the rotational frequencies of certain pulsars are subject to sudden increase, which is often accompanied by a change in the spin-down and an exponential recovery of some fraction of the initial frequency jump [572, 573]. These events are generally referred to as *pulsar glitches* [572, 574–576], which will be referred to in short as glitches in this paper. Glitches can produce a non-zero, time-varying quadrupole moment of the NS and, in turn, lead to GW emission. GWs from the pulsar glitches can be naturally divided into two categories: burst-like GWs, during or shortly after the glitch itself [577–579], and continuous GW signals, following the glitch and so-called recovery phase [580–585].

Out of the many theories proposed so far to explain these events, there are two leading models [586, 587], one based on the superfluid pinning model [588, 589] and another related to the crust cracking model [590]. It has been shown that [581] the

crust cracking model is unable to describe the largest glitches, like the one for the Vela pulsar [591]. Thus, in this paper, we will focus on the superfluid pinning/unpinning model, which is consistent with the observations of two types of glitchers: normal and Vela-like [592–594].

The quantum nature of the superfluids is at the core of the glitch model considered in this paper. According to the model, the NS rotation can be attributed to an array of $\sim 10^{18}$ quantised superfluid vortexes [505, 588, 595, 596] that weave the entire NS interior. If vortexes are strongly attracted or 'pinned' to ions in the crust or flux tubes in the core of the star, they cannot move out. This pinning restricts their outward movement when the crust spins down [597]. Thus, the superfluid core stores a higher angular velocity compared to the crust of the NS. This differential lag builds up between these two components. According to the model, a glitch occurs when a few vortexes unpin and cause an avalanche of $\sim 10^7 - 10^{15}$ unpinned outward-moving vortexes [505, 598], abruptly transferring the angular momentum to the crust. The vortex avalanche may cause a series of GW bursts [599] during the rise-time of the glitch and, in turn, may excite one or more families of the NS global modes (such as f-modes, p-modes, g-modes, and w-modes [600]), whose GW counterparts are not considered in this work. Finally, due to non-axisymmetric Ekman flow [580], there may be a continuous periodic signal, close to the NS rotation frequency, that fades during the post-glitch recovery phase.

Searches for continuous waves (CWs) from glitching pulsars [583, 592, 601] are typically performed in three ways: (1) minimally modelling the aftermath of the glitch and searching for "transient" CWs [583, 585, 602], (2) ignoring the glitches and analysing the periods before and after them [603, 604], and (3) allowing a small mismatch between the electromagnetic (EM) and GW frequency about the time of the glitch [516]. In the most recent observing run of the LIGO-Virgo-KAGRA (LVK) collaboration, CWs due to quadrupolar [516] and r-mode [605] GW emission from the most active known glitcher, PSR J0537-6910 have been searched for. Furthermore, in [518], a search for transient CWs from six glitching pulsars was also performed, in which a "window function" model [583] was used to define the post-glitch period where GWs are emitted [602], resulting in upper limits on the signal strain amplitude as a function of possible post-glitch relaxation duration but not constraining other parameters of the glitches.

GW burst searches are unmodeled analyses that typically hunt short duration [340, 606–609] (milliseconds to a few seconds) or long duration [610–616] (longer than a few seconds) GW transients, whose waveforms are not well-modelled enough and not suited for matched filtering. Pulsar glitches enter the first category, namely short-duration bursts. The first direct search for the GW burst counterpart of a pulsar glitch was performed targeting the 2006 Vela pulsar glitch [608], looking for a signal associated with oscillations of the fundamental quadrupole mode excited by the glitch. Recently, in the third observing run of the LVK collaboration, all-sky searches have been performed for short-duration [578] GW bursts. In all these cases, finding no evidence of GWs, constraints were placed on the individual glitch properties.

Standard GW searches have not been able to detect any CW or burst-like GW signal that can be associated with a single pulsar glitch. However, there is a third kind of GW signal that can be associated with an ensemble of glitching pulsars: a SGWB. Searching for a SGWB from pulsar glitches can be motivated by the number of known pulsars and observed pulsar glitches in the EM domain. Pulsar catalogues (ATNF[1] [554] and Jodrell Bank[2] [573]) encode the information about the parameters of more than 600 pulsar glitches from a fraction of the known ~ 3000 pulsars. This means that, from the discovery of the first pulsar until today, 0.2 glitches per pulsar have been observed. If this proportion is the same when considering the expected $\mathcal{O}(10^8) - \mathcal{O}(10^9)$ [617, 618] neutron stars in the Milky Way, one can assume that around $2 \times \mathcal{O}(10^7) - \mathcal{O}(10^8)$ glitch may have happened in that period of time. These numbers suggest that a SGWB could emerge from the superposition of the GW signals from pulsar glitches.

The detection and characterisation of this SGWB would allow to provide complementary information to the one from GW and EM searches for individual glitches since it would give access to the properties of glitches and glitching pulsars as a population and does not require individual-glitch observations. In this work, we aim to characterise and constrain the SGWB from the superposition of burst-like GW signals associated with vortex-avalanche during the glitches of Galactic pulsars, assuming the superfluid pinning/unpinning model as the glitch source while being agnostic with respect to the overall number of pulsars in the population. To search for such SGWB, we use cross-correlation methods [239, 410], which allow us to search for a common signal in multiple data streams simultaneously and disentangle it from instrumental noise. From the results of the search, which does not show any evidence for a SGWB signal, we derive constraints on the average glitch duration $\tau_{\rm av}$ and the average radial motion of the vortexes during the glitches $\Delta r_{\rm av}$ for the population of the glitching Galactic pulsars. This approach is a novel way to probe the astrophysical properties of pulsar glitches.

This paper is organised as follows: in section 8.2, we present the model for the SGWB from vortex-avalanches pulsar glitches; in section 8.3, we illustrate the search methods; and in section 8.4, we report the results of the analyses. Inferring from these results, we also set constraints on the ensemble properties of the pulsar glitches. These are detailed in the same section. We conclude the paper by discussing the implications of these results and the possible extensions in section 8.5.

8.2 Stochastic Gravitational-Wave Background from vortex-avalanches pulsar glitches

A SGWB arising from the superposition of GW bursts from Galactic pulsar glitches may present characteristic features in the space and time domains. It may be expected

[1] https://www.atnf.csiro.au/research/pulsar/psrcat/glitchTbl.html
[2] https://www.jb.man.ac.uk/ pulsar/glitches.html

to follow the angular distribution of the Galactic NSs, which is peaked in the Galactic plane [558], and hence exhibit anisotropic patterns. In addition, given the large number of glitches and invoking the central limit theorem, the background may be argued to be Gaussian. Nonetheless, given the relatively short duration of the glitches, this may result in it being non-continuous in the time domain. All these aspects are not very known and are worth to be discussed and explored in detail. However, in this first attempt to search for a SGWB from pulsar glitches using LVK data, we will be working under the simplifying assumption that the SGWB can be described as Gaussian, stationary, and isotropic. We will discuss in section 8.4 how this may affect the results of the analysis, and we leave the study of the spatial and temporal features of the background for dedicated works in the future.

Under these assumptions, the SGWB can be characterised by measuring and studying the frequency spectrum of $\Omega_{\rm GW}$, which is the ratio between the GW energy density $\rho_{\rm GW}$ and the critical energy density needed to have a flat Universe $\rho_c \equiv \frac{3H_0^2c^2}{8\pi G}$, with G Newton's gravitational constant, c the speed of light, and $H_0 = 67.9\,\mathrm{km\,s^{-1}\,Mpc^{-1}}$ [560] the Hubble parameter today:

$$\Omega_{\rm gw}(f) = \frac{f}{\rho_c}\,\frac{\mathrm{d}\rho_{\rm gw}(f)}{\mathrm{d}f}, \tag{8.2.1}$$

where f is the frequency of the GWs. We consider the above equation in the case of the NS glitches and derive the expression for $\Omega_{\rm gw}(f)$ [565]. A detailed calculation is shown in the appendix 8.6.1. This leads to the approximation of $\Omega_{\rm gw}(f)$ as a power-law in frequency for two different regimes of glitches from unpinning vortexes:

$$\Omega_{\rm gw}(f) \approx \left(\frac{\Theta}{10^2\,\mathrm{s^{-1}}}\right)^2 \left(\frac{\langle 1/D^2\rangle_{\rm NS}}{1/(6\,\mathrm{kpc})^2}\right) \times \begin{cases} 1.09\times10^{-27}\left(\frac{\langle 1/\tau^5\rangle_{\rm NS}}{1/(10^{-2}\,\mathrm{s})^5}\right)\left(\frac{\langle \Delta r^2\rangle_{\rm NS}}{(10^{-2}\,\mathrm{m})^2}\right)\left(\frac{f}{25\,\mathrm{Hz}}\right)^{5/2}, & \tilde{\omega} \ll \Delta\tilde{r} \\ 2.74\times10^{-17}\left(\frac{\langle \tau\rangle_{\rm NS}}{10^{-2}\,\mathrm{s}}\right)\left(\frac{f}{25\,\mathrm{Hz}}\right)^{17/2}, & \tilde{\omega} \gg \Delta\tilde{r} \end{cases} \tag{8.2.2}$$

where $\langle\cdots\rangle_{\rm NS}$ denotes the ensemble average over the glitching NS population; Θ is the total glitch rate of Galactic NSs; D represents the distance of the sources from the observer; τ is the glitch duration (i.e. the duration of the emitted GW burst during the vortex-avalanche), and Δr is the radial displacement of a vortex during a glitch. In the above equation, $\Delta\tilde{r} \equiv \Delta r/R_s$ with $R_s = 10^4\,\mathrm{m}$ the average NS radius; and $\tilde{\omega} \equiv \omega\tau$ with ω the NS angular velocity. The two regimes of interest are associated with different conditions on $\tilde{\omega}$ and $\Delta\tilde{r}$. One of them, $\tilde{\omega} \ll \Delta\tilde{r}$ (with $\Delta\tilde{r} \ll 1$), is such that the azimuthal motion of the vortexes is negligible compared to their radial one. This happens when the vortex travel time is much shorter compared to the NS rotation period [565]. The second regime corresponds to the condition $\tilde{\omega} \gg \Delta\tilde{r}$ (with

$\tilde{\omega} \ll 1$) and reflects a scenario where a larger contribution to GW strain comes from the azimuthal vortex motion with respect to the radial one.

If we consider Galactic sources only and want to get a rough estimate of the intensity of the resulting SGWB, we may adopt the pivot values for the parameters (see [565]) as given in equation (8.2.2). In such a way, the resulting SGWB turns out to be smaller than other astrophysical SGWBs [243, 258] (such as the one from binary black hole coalescences, expected to be $\Omega_{\rm gw}(25\,{\rm Hz}) \sim 5\times10^{-10}$ [247]). However, given the large uncertainty in the parameters from the small number of observed glitches from (Galactic) NSs, the amplitude of the background may change drastically, given some observational constraints on the glitch properties. As an example, for the case $\tilde{\omega} \ll \Delta\tilde{r}$, if the (average) glitch duration was 10^{-3} or $10^{-4}\,{\rm s}$ and the (average) radial displacement $1\,{\rm m}$, this would lead to a boost in the SGWB amplitude by a factor of 10^9 and 10^{14}, respectively, with respect to the result obtained from equation (8.2.2) for the pivot values.

8.3 Search Methods

8.3.1 Cross-correlation statistic and search for SGWB

We perform the search for a Gaussian, stationary, unpolarised, and isotropic SGWB. To that aim, we analyse the time-series data from the first three observing runs (O1, O2, and O3) of the Advanced LIGO-Hanford (H) and LIGO-Livingston (L) detectors and the Advanced Virgo (V) detector. We first apply time and frequency domain cuts, identically to what was done in [258, 485]. Then, we perform the cross-correlation search, following the procedures outlined below [258], with a publicly available algorithm implementation [479] written in `MATLAB`.

For each "baseline", i.e. a detector pair IJ ($I, J =$ H, L, V), we split the time-series output $s_I(t)$ into segments of duration T, labelled by t, evaluate their Fourier transforms $\tilde{s}_I(t;\, f)$ and obtain a segment-dependent cross-correlation statistic. Thus, we can define the following "narrow-band" cross-correlation estimator at every frequency as [239]

$$\hat{\Omega}_{IJ}(t;f) = \frac{2}{T}\,\frac{{\rm Re}[\tilde{s}^*_I(t;f)\,\tilde{s}_J(t;f)]}{\gamma_{IJ}(f)\,S_0(f)}\,, \tag{8.3.1}$$

where the asterisk (*) denotes the complex conjugate, $S_0(f) = (3H_0^2)/(10\pi^2 f^3)$, and $\gamma_{IJ}(f)$ is the normalised overlap reduction function [398,399,410] that quantifies the reduction in sensitivity due to the geometry of the baseline IJ and its response to the GW signal. The normalisation of the above-defined cross-correlation statistic is chosen in such a way that $\left\langle \hat{\Omega}_{IJ}(t;f) \right\rangle_{\rm time} = \Omega_{\rm gw}(f)$ in the absence of correlated noise. In the small signal limit, the variance of the above estimator can be expressed

as

$$\sigma^2_{IJ}(t;f) \approx \frac{1}{2T\,\Delta f}\frac{P_I(t;f)P_J(t;f)}{\gamma^2_{IJ}(f)\,S^2_0(t;f)}\,, \tag{8.3.2}$$

where $P_I(t;f)$ is the one-sided power spectral density in a detector, and Δf is the frequency resolution.

Given the broad-band nature of the expected signal, we can obtain the corresponding "broad-band" estimator $\hat{\Omega}_{IJ}$ by combining the cross-correlation spectra from different frequencies with appropriate weight factors. This optimal estimator and the associated variance can be expressed as

$$\hat{\Omega}_{\mathrm{ref},\,IJ} = \frac{\sum_{k,t} w(f_\mathrm{k})\,\hat{\Omega}_{IJ}(t;\,f_\mathrm{k})\,\sigma^{-2}_{IJ}(t;\,f_\mathrm{k})}{\sum_k w^2(f_\mathrm{k})\sigma^{-2}_{IJ}(t;\,f_\mathrm{k})}\,, \tag{8.3.3}$$

$$\sigma^{-2}_{IJ} = \sum_{k,t} w^2(f_\mathrm{k})\,\sigma^{-2}_{IJ}(t;f_\mathrm{k})\,, \tag{8.3.4}$$

where f_k is a set of discrete frequencies. The weights $w(f)$ can be derived for a generic $\Omega_\mathrm{gw}(f)$ following an optimal filtering approach [239, 258]

$$w(f) = \frac{\Omega_\mathrm{gw}(f)}{\Omega_\mathrm{gw}(f_\mathrm{ref})}\,, \tag{8.3.5}$$

where f_ref is an arbitrary reference frequency. In this analysis, we fixed this as $f_\mathrm{ref} = 25$ Hz (these choices are in agreement with the one reported in Ref. [258]). The optimal estimator and associated variance for a set of individual, independent ($J > I$) baselines can be obtained as follows:

$$\hat{\Omega}_\mathrm{ref} = \frac{\sum_{IJ}\hat{\Omega}^{\mathrm{ref},\,IJ}\,\sigma^{-2}_{IJ}}{\sum_{IJ}\sigma^{-2}_{IJ}} \tag{8.3.6}$$

$$\sigma^{-2} = \sum_{IJ}\sigma^{-2}_{IJ}\,, \tag{8.3.7}$$

where results from previous observing runs may be included in the sum as separate baselines. Here, we combine HL-O1, HL-O2, HL-O3, HV-O3, and LV-O3. Eventually, in the absence of a detection, we can set upper limits on $\Omega_\mathrm{ref} \equiv \Omega_\mathrm{gw}(f_\mathrm{ref})$ through a Bayesian analysis for any model of interest using the estimators presented in equations (8.3.6) and (8.3.7). To do that, we employ the likelihood

$$p\left(\hat{\Omega}(f_\mathrm{k})|\Omega(f_\mathrm{k})\right) = \frac{1}{\sqrt{2\pi}\sigma(f_\mathrm{k})}\,\exp\left[-\frac{\left(\hat{\Omega}(f_\mathrm{k})-\Omega(f_\mathrm{k})\right)^2}{2\sigma^2(f_\mathrm{k})}\right]\,, \tag{8.3.8}$$

where $\Omega(f_\mathrm{k})$ is the model for the SGWB in equation (8.2.2) and $\hat{\Omega}(f_\mathrm{k})$ is assumed to be Gaussian distributed in the absence of a signal [239]. Additionally, we can also use

the estimator for $\Omega_{\rm ref}$

$$\hat{\Omega}_{\rm ref}(f_{\rm k}) \equiv \frac{\hat{\Omega}_{IJ}(f_{\rm k})}{w(f_{\rm k})} \tag{8.3.9}$$

as a starting point to constrain the average glitch duration $\tau_{\rm av}$ and the average vortex radial displacement $\Delta r_{\rm av}$ of an ensemble of glitching NSs, which will be discussed next in detail.

8.3.2 Constraining $\tau_{\rm av}$ and $\Delta r_{\rm av}$ from a NS population

Here, we show how to utilise the results of the cross-correlation search to derive an estimator for an average quantity $q_{\rm av} \equiv \langle q \rangle_{\rm NS}$ of a NS population. The method that we present is generic (under some assumptions), and we use it to obtain the estimators for $\tau_{\rm av}$ and $\Delta r_{\rm av}$ and constrain them in the two regimes $\tilde{\omega} \ll \Delta\tilde{r}$ and $\tilde{\omega} \gg \Delta\tilde{r}$.

First, we assume that $\Omega_{\rm gw}(f)$ depends on the quantity of interest q through the ensemble average of its n-th power $\langle q^n \rangle_{\rm NS}$ only. In this way, we can recast equation (8.3.5) as follows:

$$\Omega_{\rm gw}(f) = \xi_q \, w(f) \, \langle q^n \rangle_{\rm NS} \, , \tag{8.3.10}$$

where $\xi_q \equiv \xi_q(\vec{\pi}) = \Omega_{\rm ref} / \langle q^n \rangle_{\rm NS}$ is a proportionality constant, once the set of parameters characterising the SGWB $\vec{\pi}$ are fixed, while $n \in \mathbb{R}_0$ (if $n = 0$, we are estimating $\Omega_{\rm ref}$, which is already discussed in the previous subsection). Within this framework, using equation (8.3.1), we can rewrite the above equation as

$$\widehat{\langle q^n \rangle}_{\rm av}(f_{\rm k}) = \frac{1}{\xi_q} \frac{\hat{\Omega}_{IJ}(f_{\rm k})}{w(f_{\rm k})} \equiv \frac{\hat{\Omega}_{\rm ref}(f_{\rm k})}{\xi_q} \, , \tag{8.3.11}$$

where $\hat{\Omega}_{\rm ref}(f_{\rm k})$ is the narrow-band estimator of $\Omega_{\rm ref}$, while $\widehat{\langle q^n \rangle}_{\rm av}(f_{\rm k})$ is the narrow-band estimator of $\langle q^n \rangle_{\rm NS}$ (note that the frequencies $f_{\rm k}$ in the equation are labels and not a functional dependence).

Now, we want to relate $\widehat{\langle q^n \rangle}_{\rm av}(f_{\rm k})$ with the narrow-band estimator for $q_{\rm av}$. This can be achieved by considering the expectation value of $\widehat{\langle q^n \rangle}_{\rm av}(f_{\rm k})$ and its dependence on $q_{\rm av}$:

$$\left\langle \widehat{\langle q^n \rangle}_{\rm av}(f_{\rm k}) \right\rangle = \langle q^n(f_{\rm k}) \rangle_{\rm NS} = (q_{\rm av})^n(f_{\rm k}) + \cdots \, , \tag{8.3.12}$$

where $(\cdots)$ stands for terms involving the intrinsic (central) statistical moments of the statistical distribution of the quantity of interest q. As an example for $n = 2$, $\langle \widehat{\langle q^2 \rangle}_{\rm av}(f_{\rm k}) \rangle = \left\langle q^2(f_{\rm k}) \right\rangle_{\rm NS} = (q_{\rm av})^2(f_{\rm k}) + {\rm Var}(q)(f_{\rm k})$, and the (unknown) bias is encoded in the (unknown) population variance ${\rm Var}(q)$. Following this, we define the biased estimator for $q_{\rm av}$

$$\hat{q}_{\rm av}(f_{\rm k}) \equiv \left[\widehat{\langle q^n \rangle}_{\rm av}(f_{\rm k}) \right]^{1/n} , \tag{8.3.13}$$

where the bias introduced by the other moments is assumed to be negligible (given q being positive definite and peaked around some reference value). The bias could be accounted for in the case of the observation of SGWB from a population of NS glitches by estimating the higher-order moments of the distribution from individual glitch observations or from theoretical models. Given the above expression for $\hat{q}_{\rm av}(f_{\rm k})$, we can derive its uncertainty $\sigma_{\hat{q}}(f_{\rm k})$ if we know the likelihood function $p_q\left(\hat{q}_{\rm av}(f_{\rm k})|q_{\rm av}(f_{\rm k})\right)$. The formula of the likelihood can be obtained in two steps: first, by using equations (8.3.10), (8.3.11), and (8.3.13), we express $\Omega(f_{\rm k})$ and $\hat{\Omega}(f_{\rm k})$ as a function of $q_{\rm av}(f_{\rm k})$ and $\hat{q}_{\rm av}(f_{\rm k})$; second, we perform a change of variables in equation (8.3.8). In this way, we get the likelihood function for $\hat{q}_{\rm av}(f_{\rm k})$, which is no longer a Gaussian:

$$p_q\left(\hat{q}_{\rm av}(f_{\rm k})|q_{\rm av}(f_{\rm k})\right) = \sqrt{\frac{2}{\pi}}\,\frac{|n|\;q_{\rm av}^{n-1}(f_{\rm k})\,\xi_q}{\sigma_{\hat{\Omega}}(f_{\rm k})}\;\exp\left[-\frac{\left(\hat{q}_{\rm av}^{n}(f_{\rm k})-q_{\rm av}^{n}(f_{\rm k})\right)^2\,\xi_q^2}{2\sigma_{\hat{\Omega}}^2(f_{\rm k})}\right], \tag{8.3.14}$$

where $\sigma_{\hat{\Omega}}(f_{\rm k})$ is the standard deviation corresponding to $\hat{\Omega}_{\rm ref}(f_{\rm k})$. By applying the definition of variance, we then get (we omit frequency labels in the right-hand side of the equation and observe that $n<-2$ or $n>0$)

$$\begin{aligned}\sigma_{\hat{q}}^2(f_{\rm k}) = &\sqrt{\frac{2}{\pi}}\left(\frac{\sigma_{\hat{\Omega}}}{\xi_q}\right)^{2/n}\Gamma\left(\frac{n+2}{n}\right)D_{\left(-\frac{n+2}{n}\right)}(z)\,e^{-z^2/4}\\ &-\left[\sqrt{\frac{2}{\pi}}\left(\frac{\sigma_{\hat{\Omega}}}{\xi_q}\right)^{1/n}\Gamma\left(\frac{n+1}{n}\right)D_{\left(-\frac{n+1}{n}\right)}(z)\,e^{-z^2/4}\right]^2,\end{aligned} \tag{8.3.15}$$

where $D_{(\nu)}(z)$ is a parabolic cylinder function, and $z\equiv-\hat{q}_{\rm av}^{n}(f_{\rm k})\,\xi_q/\sigma_{\hat{\Omega}}(f_{\rm k})$. A derivation of the above equation can be found in appendix 8.6.2. Given $\hat{q}_{\rm av}(f_{\rm k})$ and $\sigma_{\hat{q}}^2(f_{\rm k})$, assuming $q_{\rm av}$ to be independent of the frequency, we finally obtain the optimal, broad-band estimator $\hat{q}_{\rm opt}$, with the relative uncertainty $\sigma_{q,\,\rm opt}$ as

$$\hat{q}_{\rm opt} = \frac{\sum_k \hat{q}_{\rm av}(f_{\rm k})\,\sigma_{\hat{q}}^{-2}(f_{\rm k})}{\sum_k \sigma_{\hat{q}}^{-2}(f_{\rm k})}, \tag{8.3.16}$$

$$\sigma_{\hat{q},\,\rm opt} = \left[\sum_k \sigma_{\hat{q}}^{-2}(f_{\rm k})\right]^{-1/2}. \tag{8.3.17}$$

8.4 Results

We search for an isotropic SGWB resulting from the superposition of GWs from NS glitches from the Galactic population of pulsars, assuming the model in equation (8.2.2), recast in the form $\Omega_{\rm gw}(f)=\Omega_{\rm ref}\,(f/f_{\rm ref})^{\alpha}$. We perform the analysis on data from the first three observing runs (O1, O2, and O3) of the Advanced LIGO and Virgo detectors, which are publicly available [216, 217], and follow the methods described in [258]. Using the results of the search, which do not provide any evidence

$\Omega_{\rm gw}(f)$	$\hat{\Omega}_{\rm ref}^{\rm O1+O2+O3}$	$\Omega_{\rm ref}^{95\%,\,\rm Uniform}$	$\Omega_{\rm ref}^{95\%,\,\rm Log-uniform}$
$\propto f^{5/2}$	$(-1.2 \pm 1.5) \times 10^{-9}$	2.4×10^{-9}	7.5×10^{-10}
$\propto f^{17/2}$	$(3.8 \pm 2.5) \times 10^{-17}$	8.3×10^{-17}	5.7×10^{-17}

Table 8.1: Results of the isotropic search for a SGWB from Galactic-NS glitches using data from the first three LIGO-Virgo-KAGRA observing runs. The first row is relative to the regime $\tilde{\omega} \ll \Delta\tilde{r}$, while the second row is relative to the regime $\tilde{\omega} \gg \Delta\tilde{r}$. The four columns are the results from our search, in which the frequency scaling of $\Omega_{\rm gw}(f)$ (first column), the cross-correlation statistics (second column), and the upper limits on $\Omega_{\rm ref}$, using a uniform (third column) and log-uniform (fourth column) prior, are reported.

of a signal, we set constraints on the population parameters of the pulsar glitches. The results and their relative implications are presented in the following subsections.

8.4.1 Search for SGWB

The search has not found any evidence for a SGWB signal. Hence, we set upper limits on $\Omega_{\rm ref}$. The results are summarised in table 8.1. The second column of this table contains the value of the cross-correlation statistic and the associated uncertainty, which have been obtained using equation (8.3.6). The third and fourth columns show the 95% confidence-level Bayesian upper limits for $\Omega_{\rm ref}$. These upper limits are obtained by marginalising the likelihood function in equation (8.3.8) over a uniform (third column) and a log-uniform prior (fourth column) on the magnitude of the SGWB. The choice of a log-uniform prior may seem the most natural since the $\Omega_{\rm ref}$ range is expected to span several orders of magnitude. The log-uniform prior range was chosen to be between $10^{-13} \leq \Omega_{\rm ref} \leq 10^{-5}$ for $\alpha = 5/2$ and $10^{-20} \leq \Omega_{\rm ref} \leq 10^{-8}$ for $\alpha = 17/2$. The lower bound was chosen to be of the same order of magnitude as the expected reach of the next-generation ground-based detectors [258, 414]. The upper bound was chosen in such a way that the upper limits on $\Omega_{\rm ref}$ did not change noticeably when choosing a broader range, reflecting our lack of information about $\Omega_{\rm ref}$ a priori. Even though the choice of the uniform prior translates to more conservative upper limits, we have included those results as well, choosing its range to be the same as the log-uniform one. In the case $\alpha = 5/2$, the estimator for $\Omega_{\rm ref}$ and the upper limits for the uniform prior are of $\mathcal{O}(10^{-9})$, while the ones from the log-uniform prior are of $\mathcal{O}(10^{-10})$. In the case $\alpha = 17/2$ instead, they are of $\mathcal{O}(10^{-17})$ and are several orders of magnitude smaller than the $\alpha = 5/2$ case and the power-law models considered in Ref. [258]: this is expected for this kind of power law, given the definition of $\hat{\Omega}_{\rm ref}$ and equation (8.3.5).

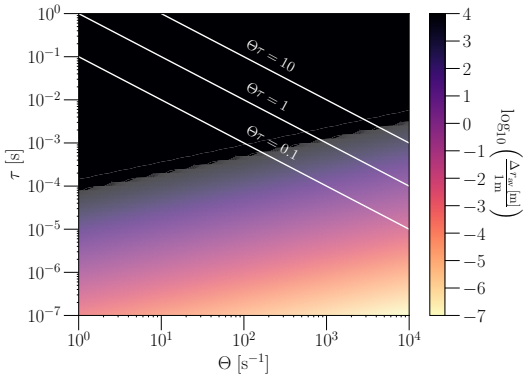

(a) ($\tilde{\omega} \ll \Delta\tilde{r}$): 95% Bayesian upper limits over $\Delta r_{\rm av}$ in the $\Theta - \tau$ plane, assuming a log-uniform prior on $\Delta r_{\rm av}$. We choose $\tau \in [10^{-7}, 1]\,\rm s$ and $\Theta \in [1, 10^4]\,\rm s^{-1}$. The white lines divide the plane into the regions limited by $\Theta\tau = 0.1,\ 1,\ 10$.

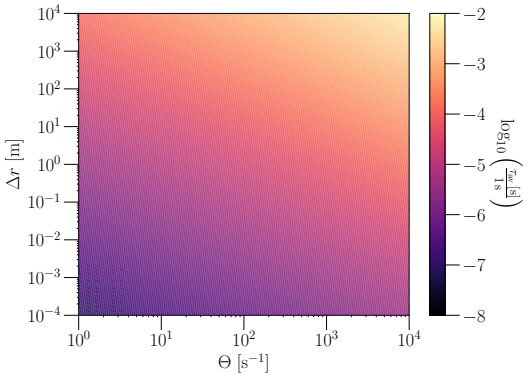

(b) $\tilde{\omega} \ll \Delta\tilde{r}$: 95% Bayesian lower limits over $\tau_{\rm av}$ in the $\Theta - \Delta r$ plane, assuming a log-uniform prior on $\tau_{\rm av}$.We choose $\Delta r \in [10^{-4}, 10^4]\,\rm m$ and $\Theta \in [1, 10^4]\,\rm s^{-1}$.

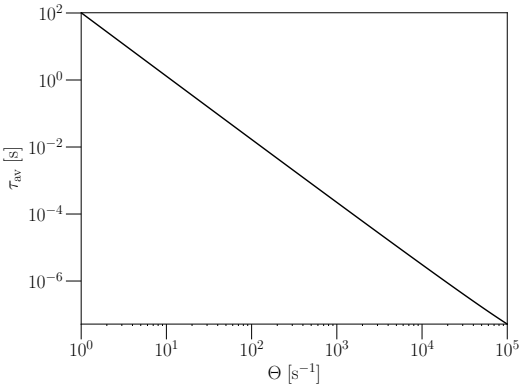

(c) ($\tilde{\omega} \gg \Delta\tilde{r}$): 95% Bayesian upper limits over $\tau_{\rm av}$ as a function of Θ, assuming a log-uniform prior on $\tau_{\rm av}$ and choosing $\Theta \in [1, 10^5]\,\rm s^{-1}$.

Figure 8.1

8.4.2 Implications for $\tau_{\rm av}$ and $\Delta r_{\rm av}$

$\tilde{\omega} \ll \Delta\tilde{r}$

In this regime, by fixing $\left\langle 1/D^2 \right\rangle_{\rm NS}^{-1/2} = 6\,{\rm kpc}$ as the reference value for Galactic pulsars, equation (8.2.2) depends on three unknown parameters: the total Galactic NS glitching rate Θ, the (effective) glitch duration $\tau \equiv \left\langle 1/\tau^5 \right\rangle_{\rm NS}^{-1/5}$, and the (effective) vortex radial motion $\Delta r \equiv \left\langle \Delta r^2 \right\rangle_{\rm NS}^{1/2}$. Following the approach described in 8.3.2, we derive Bayesian upper limits for $\Delta r_{\rm av}$ (keeping Θ and τ as free parameters) and $\tau_{\rm av}$ (keeping Θ and Δr as free parameters). The results are summarised in figures 8.1a and 8.1b.

Figure 8.1a illustrates the upper limits over $\Delta r_{\rm av}$ as a function of Θ and τ, where we choose a log-uniform prior for $\Delta r_{\rm av}$ in the interval $[10^{-7}, 10^{4}]\,{\rm m}$. The upper bound of the prior is dictated by the fact that $\Delta r_{\rm av} < R_S \simeq 10^4\,{\rm m}$, while the lower bound is chosen to be small enough that there is no posterior support at the lower end of the prior range. The constraints over $\Delta r_{\rm av}$ span the range $(10^{-7} - 10^{4})\,{\rm m}$ and become more and more stringent the higher the total glitch rate and the lower the average glitch duration are, as expected from equation (8.2.2). As a reference, we consider the case where $\Theta = 10^2\,{\rm s}^{-1}$ and $\tau = 10^{-2}\,{\rm s}$, resulting in $\Delta r_{\rm av} \leq 9.5 \times 10^3\,{\rm m}$. We observe that the upper limits over $\Delta r_{\rm av}$ in the black region of figure 8.1a (corresponding to most of the considered parameter space) are not informative, given the information $\Delta r_{\rm av} \leq 10^4\,{\rm m}$ is already encoded in the choice of the prior.

Figure 8.1b shows the constraints over $\tau_{\rm av}$, as a function of Θ and Δr, where a log-uniform prior with range $[10^{-10}, 10^{2}]\,{\rm s}$ is used for $\tau_{\rm av}$. The limits over $\tau_{\rm av}$ are interpreted as lower bounds over the average glitch duration, given $\Omega_{\rm gw}(f) \propto \left\langle 1/\tau^5 \right\rangle_{\rm NS}$ as in equation (8.2.2). We note that they cover the range $(10^{-8} - 10^{-2})\,{\rm s}$, and become more stringent (i.e. the minimal average glitch duration becomes higher) when Δr and Θ increase, as expected again from equation (8.2.2). Considering as references $\Theta = 10^2\,{\rm s}^{-1}$ and $\Delta r = 10^{-2}\,{\rm m}$, we obtain $\tau_{\rm av} \geq 3.7 \times 10^{-6}\,{\rm s}$.

It is important to highlight the meaning of regions in which the parameter space is divided in figure 8.1a. These regions are delimited by the conditions $\Theta\tau = 0.1,\, 1,\, 10$. The quantity $\Theta\tau \equiv \Delta$ is called *duty-cycle* and can be used to infer the statistical properties in the time domain of the SGWB. Given a collection of events emitting GWs, the duty cycle is defined as the ratio between the average duration of the events and the average time between two successive events. If $\Delta \gg 1$, the SGWB is continuous and Gaussian, while if $\Delta \ll 1$, the SGWB is shot-noise-like. In the intermediate regime $\Delta \approx 1$, the resulting SGWB is "popcorn"-like and is no longer Gaussian [243]. The distinction in figure 8.1a among the regions of the parameter space corresponding to different regimes is relevant to comment on the analysis result since it assumes the SGWB to be continuous and Gaussian, which means $\Delta \gg 1$. In the regions where this condition is not respected, current search techniques may still detect the SGWB, but the overall process requires longer observation periods (see [461] and section (8.1) in [239] for detailed review and discussions). Currently, no searches that

allow considering the non-continuous or non-Gaussian nature of the SGWB are available. Still, methods and formalism for such searches have been proposed in the last few years [459, 465] and are under development [460, 464].

$\tilde{\omega} \gg \Delta\tilde{r}$

In this regime, equation (8.2.2) does not depend on Δr. Therefore, using the same methods as above, we derive constraints on $\tau_{\rm av}$ only. We also employ the same priors for $\tau_{\rm av}$ as in the $\tilde{\omega} \ll \Delta\tilde{r}$ regime.

The results are illustrated in figure 8.1c. In contrast to figure 8.1b, the limits over τ in figure 8.1c are interpreted as upper limits, given $\Omega_{\rm gw}(f) \propto \langle\tau\rangle_{\rm NS}$. The constraints span the range $(10^{-7} - 10^{2})\,\mathrm{s}$, and become more stringent with Θ increasing, in agreement with equation (8.2.2). In the reference case with $\Theta = 10^{2}\,\mathrm{s}^{-1}$, the result is $\tau_{\rm av} \leq 1.7 \times 10^{-2}\,\mathrm{s}$.

8.5 Discussions and Conclusions

In this work, we have derived constraints on some ensemble properties of a glitching pulsar population from the results of a cross-correlation-based search for SGWB. Throughout this analysis, we have restricted ourselves to the Galactic pulsars, assuming for simplicity the resulting SGWB to be isotropic. We have also considered two glitch regimes in the vortex-avalanche paradigm: $\tilde{\omega} \ll \Delta\tilde{r}$, where the GWs emission is dominated by the radial displacement of the vortexes during the avalanche, and $\tilde{\omega} \gg \Delta\tilde{r}$, where the dominant contribution to the GW strain is given by the vortex azimuthal displacement. These two regimes give rise to SGWBs that differ in their power-law modelling. We have not found any evidence in favour of the presence of a SGWB and hence have drawn upper limits on the energy density parameter $\Omega_{\rm gw}(f)$. These results have been translated into constraints on the average radial vortex displacement and the average glitch duration as a function of the total glitch rate of Galactic pulsars. In the $\tilde{\omega} \ll \Delta\tilde{r}$ regime, we have obtained upper limits on $\Delta r_{\rm av}$ in the range $[10^{-7}\,\mathrm{m} - 10^{4}\,\mathrm{m}]$ and lower limits on $\tau_{\rm av}$ spanning $[10^{-8}\,\mathrm{s} - 10^{-2}\,\mathrm{s}]$; while in the $\tilde{\omega} \gg \Delta\tilde{r}$ case, we have drawn upper limits on $\tau_{\rm av}$ in the range $[10^{-7}\,\mathrm{s} - 10^{2}\,\mathrm{s}]$. These results have been obtained using the data from the first three observation runs of Advanced LIGO and Virgo and are the first of their kind.

We have observed that the limits on $\Delta r_{\rm av}$ become informative (i.e. $\Delta r_{\rm av} \ll 10^{4}$ m) only in the region of parameter space where the SGWB is non-continuous in the time domain. In addition to that, the lower and upper limits on $\tau_{\rm av}$ in both regimes confirm that the SGWB is intermittent. On the other hand, the search assumes the SGWB to be continuous in the time domain, which makes it not the most efficient one [461,464] for this specific search for a SGWB from Galactic pulsar glitches. Even though methods optimised for probing such intermittent SGWBs exist [461, 464, 465], yet no machinery is available as of today.

What we have done in this work can be repeated for other glitch models and may help in constraining their parameters. This approach can be useful to improve our knowledge of (Galactic) pulsar glitch ensemble properties in the absence of direct observations in the GW domain and in spite of the limited number of EM glitching-pulsar observations (several orders of magnitude below the number of pulsars in our Galaxy). This indicates that our search, which aims at detecting a SGWB signal, is complementary to the EM observations and the searches looking for GW signals from individual glitches. First, this search (like other GW searches) is sensitive to quantities that are not accessible (such as the radial motion of the vortexes) or are poorly constrained (such as the glitch duration) with EM observations. Second, in contrast to burst-like GWs and CWs searches, the SGWB search has the advantage of instantaneously identifying features ($\Delta r_{\rm av}$, $\tau_{\rm av}$) of a known population of glitching pulsars, which would otherwise require decades or centuries to be determined through individual measurements of GW from pulsar glitches. If all the above searches could detect the GWs from pulsar glitches, we would have an ideal platform to implement hierarchical search strategies. On one hand, ongoing and future EM-radio missions like UTMOST, MeerKAT, SKA, FAST, and CHIME [619–623] would allow the detection of many more glitches and could deliver crucial information about the glitch phase itself, as well as the relaxation phase. On the other hand, information about the glitching pulsars is passed to complementary burst-like and CW-transient GW searches that could, in principle, allow for the multi-messenger astronomy of the glitch phenomenon using data from ground-based GW detectors. In the case of GW detection, we could combine the parameters determined by these two searches with those of EM observations to improve the measurements and infer the statistical distributions of these quantities, using them as an auxiliary channel to the implications from the SGWB search.

Finally, we point out some possible ways of extending this work. As mentioned earlier, throughout this work, we have restricted ourselves to the glitches from Galactic pulsars and assumed the SGWB to be isotropic. If we relax the assumption of isotropy by including the spatial distribution of Galactic NSs, we may perform a targeted search for a SGWB from pulsar glitches that make use of a template-based matched-filtering statistic [437, 446]. This approach is expected to provide more insight into pulsar glitch properties. Alternatively, keeping the hypothesis of isotropy, we may consider the resulting SGWB from extra-galactic pulsar populations. In this case, the duty cycle $\Theta\tau \propto D^3$, resulting in a SGWB that could be dominated by GWs from extra-galactic pulsar glitches. However, more efforts, including extensive simulations, are required in this case, given our very limited knowledge about these populations. Besides these two points, it is also worth mentioning that, recently, there have been several efforts in connecting glitch rates to physical glitch models and modelling the relationships between glitch size and waiting times [624–628], and in linking Galactic pulsar glitch rates to the characteristic age of the pulsars [629]. This additional information, together with the techniques employed in [629], could be used to estimate Θ from pulsar catalogues and hence to better model and characterise the SGWB, breaking the degeneracy of Θ with the other pulsar parameters we have con-

sidered in this paper. These possibilities, together with the effect on the analysis from the inclusion of (future) detectors like KAGRA [95], LIGO-India [115], Einstein Telescope [116], and Cosmic Explorer [117] in the detector network, will be considered in future works.

8.6 Appendix

8.6.1 Derivation of $\Omega_{\rm gw}(f)$

In this appendix, we elaborate on the derivation of equation (8.3.10) for $\Omega_{\rm gw}(f)$. We start by deriving the expression of the GW strain for a single unpinning vortex. Then we average it over the vortex parameters to get the resulting strain for an individual pulsar glitch. Finally, we apply the definition of $\Omega_{\rm gw}$, average over the glitch-size distribution of the Galactic NS, and obtain equation (8.3.10) in the regimes $\tilde{\omega} \ll \Delta\tilde{r}$ and $\tilde{\omega} \gg \Delta\tilde{r}$. The calculation we present below follows [565], although we correct a few errors that we highlight in our presentation.

Single vortex GW signal strain

The far-field metric perturbation in the transverse-traceless (TT) gauge, $h_{ij}^{TT}(t)$, can be written as a linear combination of time derivatives of mass multipoles $I^{lm}(t)$ and current multipoles $S^{lm}(t)$. In this work, we neglect the contribution from mass multipoles, assuming the matter distribution inside the pulsar to be incompressible and axisymmetric. Hence, we can rewrite the GW strain as a superposition of the current multipoles only

$$h_{ij}^{TT}(t) = \frac{G}{c^4\, D} \sum_{l=2}^{\infty} \sum_{m=-l}^{m=l} T_{ij}^{\mathrm{B2},\, lm} \frac{\partial^l\, S^{lm}}{\partial\, t^l}(t), \tag{8.6.1}$$

where G is Newton's gravitational constant, c the speed of light, D the distance from the source to the observer, $T_{ij}^{\mathrm{B2},\,\mathrm{lm}}$ the ("pure spin 2, magnetic type") tensor spherical harmonics [161], and t the retarded time. The current multipole moment of order $(l,\, m)$ $S^{lm}(t)$, for a fluid with velocity $\vec{v}$ and density ρ (assumed to be $3 \times 10^{17}\,\mathrm{kg\,m^{-3}}$), can be expressed as [161, 630]

$$S^{lm} = \frac{c_l}{c^{l-1}} \int_{\mathcal{V}} d^3x\, Y_{lm}^*\, r^l\, \vec{x} \cdot \left[\vec{\nabla} \times (\rho\, \vec{v})\right], \tag{8.6.2}$$

where

$$c_l = -\frac{32\,\pi}{(2l+1)!!} \sqrt{\frac{l+2}{2l\,(l-1)\,(l+1)}}, \tag{8.6.3}$$

and

$$Y_{lm}(\theta,\varphi) = \sqrt{\frac{(2l+1)\,(l-m)!}{4\pi\,(l+m)!}}\, e^{i\,m\varphi}\, P_l^m(\cos\theta), \tag{8.6.4}$$

with $P_l^m(\cos\theta)$ the associated Legendre function.

The fluid is further assumed to be irrotational and the flow to be purely azimuthal, leading to the following vorticity for vortex singularities [565]:

$$\vec{\nabla}\times\vec{v} = \kappa\,\delta^{(2)}\,(\vec{x}_T - \vec{x}_{v,\,T})\hat{z}, \tag{8.6.5}$$

where κ is the quantum of circulation, taken to be $\kappa = 10^{-7}\,\mathrm{m}^2\,\mathrm{s}^{-1}$ [565], while $\vec{x}_T$ and $\vec{x}_{v,\,T}$ are the equatorial coordinate of the NS and the equatorial vortex position. The leading term to the strain is the current quadrupole $l = 2$, whose only non-vanishing terms are $m = \pm 1$ given the above assumptions. By switching from Cartesian coordinates $(\mathrm{x},\mathrm{y},\mathrm{z})$ to the cylindrical ones $(R,\,\phi,\,z)$, it is possible to obtain the following expression

$$S^{21}(t) = \frac{1}{c}\sqrt{\frac{512\pi}{405}}\rho\,\kappa\,e^{-i\,\phi_v(t)}R_v(t)\left[R_s^2 - R_v^2(t)\right]^{3/2}, \tag{8.6.6}$$

where $R_v(t) = R_0 + d(t)$ and $\phi_v(t) = \phi_0 + \omega t$ are the radial and azimuthal positions of the vortex, with R_0 and ϕ_0 the positions before unpinning, R_s is the pulsar radius, and $\omega = 2\pi f$ the angular velocity of the pulsar. The radial trajectory $d(t)$ can be modelled as follows

$$d(t) = \begin{cases} 0, & t < t_g \\ \int_{t_g}^{t_g+t} v(t')\,dt', & t_g < t < t_g + \tau \\ \Delta r, & t > t_g + \tau \end{cases} \tag{8.6.7}$$

where t_g is the time at which the vortex starts moving, τ is the glitch duration, Δr is the (average) radial distance covered by the vortex between unpinning and repinning, and $v(t')$ is the speed profile of the vortex. In the following, we assume a parabolic speed profile $v(t') = 6\,\Delta r\,t'\,(\tau - t')/\tau^3$. By plugging equation (8.6.6) in equation (8.6.1), one gets the following expression for the strain from a single vortex ($K_0 \equiv \frac{G}{c^5\,D}\sqrt{\frac{512\pi}{405}}\rho\,\kappa$)

$$h_{ij}^{TT}(t;\,\omega,\,R_0,\,\phi_0) = T_{ij}^{\mathrm{B2},\,21}\,K_0\,\frac{\partial^2}{\partial t^2}\left[e^{-i\phi_v(t)}\,R_v(t)\,\left(R_S^2 - R_v^2(t)\right)^{3/2}\right], \tag{8.6.8}$$

For the calculations in the coming sections, it is useful to express the above equations in terms of the dimensionless variables $\tilde{R}_v(t) \equiv R_v(t)/R_s$, $\tilde{\phi}_v(t) \equiv \phi_v(t)/(2\pi)$,

$\tilde{t} \equiv t/\tau$, $\Delta\tilde{r} \equiv \Delta r/R_s$, and $\tilde{f} \equiv f\tau$, hence

$$h_{ij}^{TT}(\tilde{t};\, \tilde{\omega},\, \tilde{R}_0,\, \tilde{\phi}_0) = T_{ij}^{\mathrm{B2,\,21}}\, \tilde{K}_0\, \frac{\partial^2}{\partial \tilde{t}^2} \left[e^{-2\pi i \tilde{\phi}_v(\tilde{t})}\, \tilde{R}_v(\tilde{t})\, \left(1 - \tilde{R}_v^2(\tilde{t})\right)^{3/2} \right] \equiv T_{ij}^{\mathrm{B2,\,21}}\, \tilde{K}_0\, \tilde{h}(\tilde{t}), \tag{8.6.9}$$

where $\tilde{h}(\tilde{t})$ is the second time derivative in the second term, $\tilde{K}_0 \equiv K_0 R_s^4/\tau^2$, $\tilde{R}_0 \in [0, 1 - \Delta\tilde{r}]$, and $\tilde{\phi}_0 \in [0, 1[$, with $\tilde{R}_0 \equiv R_0/R_s$ and $\tilde{\phi}_0 \equiv \phi_0/(2\pi)$.

Vortex avalanche signal

Now that we have the expression for the GW strain from a single vortex, we can derive the one associated with the whole ensemble of unpinning and moving vortexes during a glitch. The population properties of the unpinning vortexes are related to the glitch geometry, more specifically to the (dimensionless) radial ($\tilde{R}_0$) and azimuthal ($\tilde{\phi}_0$) positions, the final vortex radial displacement ($\Delta\tilde{r}$), and the opening angle ($0 < \Delta\tilde{\phi}_0 < 1$) of the vortex avalanche.

Following [565], the probability distribution functions assumed for the initial positions $\tilde{R}_0$ and $\tilde{\phi}_0$ are

$$p(\tilde{R}_0) = \frac{2\tilde{R}_0}{(1 - \Delta\tilde{r})^2} \tag{8.6.10}$$

and

$$p(\tilde{\phi}_0) = \frac{H(\tilde{\phi}_0 + \Delta\tilde{\phi}_0/2) - H(\tilde{\phi}_0 - \Delta\tilde{\phi}_0/2)}{\Delta\tilde{\phi}_0}, \tag{8.6.11}$$

where $H(\cdots)$ is the Heaviside step function, with $\tilde{\phi}_0$ as the bisector of the avalanche. In this way, we can evaluate the expectation value of the GW strain of a vortex during a glitch as

$$[\mu_1]_{ij}\,(t) = \int_0^{1-\Delta\tilde{r}} \mathrm{d}\tilde{R}_0\, p(\tilde{R}_0) \int_{-\Delta\tilde{\phi}_0/2}^{\Delta\tilde{\phi}_0/2} \mathrm{d}\tilde{\phi}_0\, p(\tilde{\phi}_0)\, h_{ij}^{TT}(t). \tag{8.6.12}$$

If we take the average over $\tilde{\phi}_0$, $[\mu_1]_{ij}\,(t) \propto \sin\Big(\Delta\tilde{\phi}_0\,\pi\Big)/(\Delta\tilde{\phi}_0\,\pi)$, which is zero in the case where $\Delta\tilde{\phi}_0 = 1$, corresponding to the so-called creep-like glitches [631], which are not the subject of interest in this paper. Finally, for a glitch involving the unpinning of $\Delta N_v \gg 1$ vortexes, $[\mu_1]_{ij}\,(t)$ are drawn from the same Gaussian distribution owing to the central limit theorem, and the GW strain associated with the whole NS glitch $[h_{\mathrm{glitch}}]_{ij}(t)$ assumes the form

$$[h_{\mathrm{glitch}}]_{ij}(t) = \Delta N_v\, [\mu_1]_{ij}\,(t). \tag{8.6.13}$$

SGWB from vortex-avalanche pulsar glitches

As discussed in the main text, the superposition of individually undetectable, unresolvable GW signals from NS glitches is expected to generate a SGWB. We recast the general formula for $\Omega_{\rm gw}(f)$ in equation (8.2.1) in the following simplified form for an astrophysical SGWB [243, 248, 279]

$$\Omega_{\rm gw}(f) = \frac{f\,\Theta}{\rho_c\,c}\frac{\mathrm{d}^2 E_{\rm gw}}{\mathrm{d}f\,\mathrm{d}A}, \tag{8.6.14}$$

which can be rewritten as [146] ($\mathcal{F}[\cdots]$ denotes the Fourier Transform)

$$\Omega_{\rm gw}(f) = \frac{f\,\Theta\,c^2}{32\,\pi\,G\,\rho_c}\,\left\langle \left| \mathcal{F}[\dot{h}_{ij}](f)\,\mathcal{F}[\dot{h}^{ij}]^*(f) \right| \right\rangle. \tag{8.6.15}$$

In the present case, $\dot{h}^{ij}$ is the time derivative of $[h_{\rm glitch}]_{ij}$ and is expressed as

$$\begin{aligned}\dot{h}^{ij}(t) = \frac{d[h_{\rm glitch}]_{\,ij}}{dt} \approx & T_{ij}^{\mathrm{B2,\,21}}\,K_0\,\frac{R_s^4}{\tau^2}\,\frac{\sin\left(\Delta\tilde{\phi}_0\,\pi\right)}{\Delta\tilde{\phi}_0\,\pi}\,\Delta N_v\,e^{-i\tilde{\omega}\tilde{t}} \\ & \times \begin{cases} \frac{24}{5}\frac{\Delta\tilde{r}}{\tau}, & \tilde{\omega} \ll \Delta\tilde{r} \\ \frac{i\,\pi\tilde{\omega}^3}{16\tau}, & \tilde{\omega} \gg \Delta\tilde{r} \end{cases}. \end{aligned} \tag{8.6.16}$$

From equation (8.6.15), it appears clear that another ensemble average is necessary over the glitching pulsar population of interest. To that aim, we focus on the $\langle\cdots\rangle$ term in equation (8.6.15), which is proportional to the squared modulus of equation (8.6.16), and perform the ensemble average over different parameters.

Given the assumption of isotropy, the averaging over the solid angle involves only tensor spherical harmonics and is straightforward since $\int d\Omega_{\hat{n}}\,T_{ij}^{B2,21}\,(T_{ij}^{B2,21})^* = 1$. Similarly, the average over the dimensionless glitch angular opening $\Delta\tilde{\phi}_0$, here assumed to follow a uniform distribution in the $[0, 1[$ interval, involves the square of the cardinal sine, translating into an approximate factor equal to 0.451412.

The last quantity to average over in equation (8.6.16) is the number of unpinning vortexes ΔN_v. This average procedure can be done more easily in terms of the glitch size $s = \Delta f/f$, which quantifies the variation in the rotation frequency of the pulsar after the glitch and is related to ΔN_v approximately as

$$\frac{\Delta f}{f} \approx \Delta\tilde{r}\frac{\Delta N_v}{N_v}\frac{I_s}{I_c}, \tag{8.6.17}$$

where I_s/I_c is the ratio of the superfluid and crust moments of inertia [574, 631], and $N_v \approx 4\pi^2 f R_s^2/\kappa$ is the total number of vortexes. We also assume the following power-law distribution for s [565, 632, 633], which is supported by the study of multiple glitching pulsars [599] (even though it can be shown not to be universal [599] and

there have been several works on its modeling [624–626, 629]):

$$g(s) = -\frac{1}{2}\left(s_+^{-1/2} - s_-^{-1/2}\right)^{-1} s^{-3/2}, \tag{8.6.18}$$

where s_- and s_+ are the lower and upper bounds on the glitch size. The upper bound corresponds to when all vortexes unpin and can be written as $s_+ = \Delta\tilde{r}(I_s/I_c)$. At the same time, the lower physical bound $s_- \ll s_+$ can be estimated by considering the fractional change due to the outward motion of a single vortex, covering a radial distance equal to the inter-vortex separation $\Delta r \approx \sqrt{\kappa/(4\pi f)}$. From equation (8.6.17) one obtains (assuming $I_s/I_c \sim 10^{-2}$)

$$s_- = \sqrt{\frac{\kappa}{4\pi f}}\,\frac{k}{4\pi^2 R_s^3}\,\frac{I_s}{I_c} \sim 2\times 10^{-30}\left(\frac{f}{100\,\mathrm{Hz}}\right)^{-3/2}. \tag{8.6.19}$$

Now we proceed iwith averaging over the glitch size, which results in ($\Delta N_v = s/s_-$)

$$\int_{s_-}^{s_+} ds\, g(s)\,\Delta N_v^2 \approx \frac{1}{3}\frac{s_+^{3/2}}{s_-^{3/2}} = \frac{N_v^{3/2}}{3} = \frac{1}{3}\left(\frac{f\,R_s^2}{\kappa}\right)^{3/2}. \tag{8.6.20}$$

Finally, by plugging everything in equation (8.6.15) and including an additional $\Theta\tau$ to account for the number of simultaneous pulsars glitching during τ contributing to $\Omega_{\rm gw}(f)$, we obtain (we drop the $\langle ...\rangle_{\rm NS}$ in the below equation)

$$\begin{aligned}\Omega_{\rm gw}(f) \approx & 0.451412\left(\frac{K_0\,R_s^4}{\tau^3}\right)^2\left[\frac{1}{3}\left(\frac{f\,R_s^2}{\kappa}\right)^{3/2}\right](\Theta\tau)\,\frac{\Theta\,f\,c^2}{32\,\pi\,G\,\rho_c}\\ & \times\begin{cases}\frac{576}{25}\frac{\Delta\tilde{r}^2}{R_s^2}, & \tilde{\omega}\ll\Delta\tilde{r}\\ \frac{\pi^2\omega^6\tau^6}{256}, & \tilde{\omega}\gg\Delta\tilde{r}\end{cases}\end{aligned} \tag{8.6.21}$$

which is equivalent to equation (8.2.2) in the main text. It is worth noting that the above equation differs from the one reported in Ref. [565] for both the glitch regimes under consideration (also note that the regimes in that equation are swapped compared to how they were originally defined). For the first case, $\tilde{\omega} \ll \Delta\tilde{r}$, the glitch duration dependency of $\Omega_{\rm gw}(f)$ differs by a factor τ^2. For the other, $\tilde{\omega} \gg \Delta\tilde{r}$, $\Omega_{\rm gw}(f) \propto f^{17/2}$ compared to $\Omega_{\rm gw}(f) \propto f^{13/2}$ from Ref. [565]. The difference arises from the fact that in Ref. [565] $\Omega_{\rm gw}(f) \propto \left|\mathcal{F}[(h_{\rm glitch})_{ij}]\right|^2$ is erroneously used in the very final expression, in contrast to $\Omega_{\rm gw}(f) \propto \left|\mathcal{F}[(\dot{h}_{\rm glitch})_{ij}]\right|^2$ here.

8.6.2 Derivation of Equation (8.3.15)

In this appendix, where we omit the frequency labels for compactness reasons, we provide a derivation of the formula for $\sigma_{\hat{q}}$ in equation (8.3.15), which is a generalisation of equation (3.10) in [496], and equation (B3) in [2]. This can be done by using the definition of variance $\sigma_{\hat{q}}^2 \equiv \langle q_{\rm av}^2\rangle - \langle q_{\rm av}\rangle^2$, and evaluating the first- and second-order

expectation values in the variance definition. We start by evaluating $\langle q_{\rm av}\rangle$:

$$\begin{aligned}
\langle q_{\rm av}\rangle &\equiv \int_0^\infty p_q\left(\hat{q}_{\rm av}(f_{\rm k})|q_{\rm av}(f_{\rm k})\right)\, q_{\rm av}\, {\rm d}q_{\rm av} \\
&= \int_0^\infty {\rm d}q_{\rm av}\, q_{\rm av}\sqrt{\frac{2}{\pi}}\,\frac{|n|\, q_{\rm av}^{n-1}\,\xi_q}{\sigma_{\hat{\Omega}}}\,\exp\left[-\frac{(\hat{q}_{\rm av}^n - q_{\rm av}^n)^2\,\xi_q^2}{2\sigma_{\hat{\Omega}}^2}\right] \\
&= \sqrt{\frac{2}{\pi}}\int_0^\infty {\rm d}t\; t^{1/n}\left(\frac{\sigma_{\hat{\Omega}}}{\xi_q}\right)^{1/n}\exp\left[-\frac{(z+t)^2)}{2}\right] \\
&= \sqrt{\frac{2}{\pi}}\left(\frac{\sigma_{\hat{\Omega}}}{\xi_q}\right)^{1/n}\exp\left(-\frac{z^2}{4}\right)\int_0^\infty {\rm d}t\; t^{1/n}\exp\left(-\frac{t^2}{2}-zt-\frac{z^2}{4}\right) \\
&\equiv \sqrt{\frac{2}{\pi}}\left(\frac{\sigma_{\hat{\Omega}}}{\xi_q}\right)^{1/n}\Gamma\left(\frac{n+1}{n}\right)\exp\left(-\frac{z^2}{4}\right)U\left(\frac{n+2}{2n},\, z\right) \\
&= \sqrt{\frac{2}{\pi}}\left(\frac{\sigma_{\hat{\Omega}}}{\xi_q}\right)^{1/n}\Gamma\left(\frac{n+1}{n}\right)\exp\left(-\frac{z^2}{4}\right)D_{\left(-\frac{n+1}{n}\right)}\left(z\right),\quad n<-1 \text{ or } n>0,
\end{aligned} \tag{8.6.22}$$

where, in the third line, we have defined $t \equiv q_{\rm av}^n\xi_q/\sigma_{\hat{\Omega}}$ and $z \equiv -\hat{q}_{\rm av}^n\xi_q/\sigma_{\hat{\Omega}}$, then, in the fifth line, we have used the following helper function

$$U\left(a,\, z\right) \equiv \frac{\exp\left\{-\frac{z^2}{4}\right\}}{\Gamma\left(a+\frac{1}{2}\right)}\int_0^\infty {\rm d}t\, t^{a-1/2}\exp\left(-\frac{t^2}{2}-zt\right), \qquad {\rm Re}\{a\} > -\frac{1}{2}, \tag{8.6.23}$$

and finally, in the last line, we exploited its relation with the parabolic cylinder function $D_{(\nu)}(z)$ [634]:

$$D_{(\nu)}\left(z\right) = U\left(-\nu-\frac{1}{2},\, z\right). \tag{8.6.24}$$

On a similar line, one can show that

$$\begin{aligned}
\left\langle q_{\rm av}^2\right\rangle &\equiv \int_0^\infty p_q\left(\hat{q}_{\rm av}(f_{\rm k})|q_{\rm av}(f_{\rm k})\right)\, q_{\rm av}^2\, {\rm d}q_{\rm av} \\
&= \int_0^\infty {\rm d}q_{\rm av}\, q_{\rm av}^2\sqrt{\frac{2}{\pi}}\,\frac{|n|\, q_{\rm av}^{n-1}\,\xi_q}{\sigma_{\hat{\Omega}}}\,\exp\left[-\frac{(\hat{q}_{\rm av}^n - q_{\rm av}^n)^2\,\xi_q^2}{2\sigma_{\hat{\Omega}}^2}\right] \\
&= \sqrt{\frac{2}{\pi}}\left(\frac{\sigma_{\hat{\Omega}}}{\xi_q}\right)^{2/n}\Gamma\left(\frac{n+2}{n}\right)\exp\left(-\frac{z^2}{4}\right)D_{\left(-\frac{n+2}{n}\right)}\left(z\right),\quad n<-2 \text{ or } n>0.
\end{aligned} \tag{8.6.25}$$

Eventually, but applying the definition of variance and reinserting the frequency labels, we easily recover equation (8.3.15).

Chapter 9

Searches for a multi-component SGWB: Formalism and Application to Astrophysical SGWBs

「ポケモン ゲットだぜ ！」- *Gotta catch 'em all!*
田尻智, ポケットモンスター

This chapter is a reproduction of reference [4] in collaboration with Dr. Jishnu Suresh and has been accepted for publication by *Phys. Rev. D*. The version of the text that appears in this manuscript differs from the accepted one only in section 9.6, where we have extended the injection study to cover more scenarios. This project started in December 2022 and finished at the end of March 2024, with its acceptance for publication. In this work, we revisit the method from [635] to perform a search for a multi-component SGWB that can jointly estimate the individual components. We further extend the method to jointly derive implications for the population of GW sources inducing the SGWB. I was the main author, performing the analysis in section 9.3 and writing the whole paper. During the project development, I had the chance to learn a lot about SGWB from compact binary coalescences, r-mode initial stabilities in neutron stars, and magnetars, writing the code to derive the spectral shape of the background. Additionally, I developed and automated the whole postprocessing code, which is capable of handling and looping over all the power-law model combinations given a set of components. The code relies on the public `numpyro` [636] python package for Bayesian parameter estimation.

Abstract

The recent start of the fourth observing run of the LIGO-Virgo-KAGRA (LVK) collaboration has reopened the hunt for gravitational-wave (GW) signals, with one compact-binary-coalescence (CBC) signal expected to be observed every few days. Among the signals that could be detected for the first time is the stochastic gravitational-wave background (SGWB) from the superposition of unresolvable GW signals that cannot be detected individually. In fact, multiple SGWBs are likely to arise given the variety of sources, making it crucial to identify the dominant components and assess their origin.

However, most search methods with ground-based detectors assume the presence of one SGWB component at a time, which could lead to biased results in estimating its spectral shape if multiple SGWBs exist. Therefore, a joint estimate of the components is necessary. In this work, we adapt such an approach and analyse the data from the first three LVK observing runs, searching for a multi-component isotropic SGWB. We do not find evidence for any SGWB and establish upper limits on the dimensionless energy parameter $\Omega_{\rm gw}(f)$ at 25 Hz for five different power-law spectral indices, $\alpha = 0,\ 2/3,\ 2,\ 3,\ 4$, jointly. For the spectral indices $\alpha = 2/3,\ 2,\ 4$, corresponding to astrophysical SGWBs from CBCs, r-mode instabilities in young rotating neutron stars, and magnetars, we draw further astrophysical implications by constraining the ensemble parameters $K_{\rm CBC},\ K_{\rm r-modes},\ K_{\rm magnetars}$, defined in the main text.

9.1 Introduction

Gravitational-wave (GW) astronomy with ground-based interferometric detectors is rapidly entering its golden age. Following the first three observing runs (O1, O2, and O3 [231, 637]) of the LIGO-Virgo-KAGRA collaboration [90, 94, 95] (to which in the incoming years the approved LIGO-India [115] will join), around 90 GW signals from compact binary coalescences (CBCs) have been detected by the network and collected in the third Gravitational-Wave Transients Catalogue (GWTC-3 [93]), together with the implications for the compact-binary populations [247]. In addition to that, the fourth LVK observing run (O4) recently started on 24th May 2023. This run is expected to last twenty months (including two months of commissioning the middle) and to have a CBC detection every two to three days [638]. However, due to their intrinsic faintness and the limited detector sensitivity, most of the GW signals cannot be detected individually or resolved. The incoherent superposition of these unresolvable signals is expected to create a persistent stochastic gravitational-wave background (SGWB) signal, which many ongoing experiments aim to probe over a broad range of frequencies. A SGWB can be generated by large variety of phenomena of astrophysical (such as CBCs [249, 255, 256, 541, 571], isolated neutron stars (NSs) [250, 269, 271, 272], NS modes [279, 280, 564], core collapses to supernovae [282, 283, 285, 639, 640], stellar core collapses to black holes [286, 289, 290]) or cosmological (such as cosmic strings [294, 337–339], first order phase transitions [329, 330], primordial black holes [301, 641, 642], domain walls [643, 644], inflation [292, 546, 552], pre big bang models [448, 449, 645]) origin and hence exist as a superposition of different components. As a consequence, after the first SGWB detection, it will be mandatory to identify the dominant components and their origins.

Recently, several collaborations working with pulsar timing arrays (PTAs) have claimed evidence of a SGWB signal within their data [263, 265–267]. Yet, the data need to be more comprehensive to affirm the source of the SGWB excess under the assumption of a single component being present. A ground-based GW detector experiment will face similar issues as data pile up and a SGWB signal emerges. In such a scenario, current searches assuming the presence of a single SGWB component at a time may lead to biased measurements of its intensity if multiple components are present [384, 646, 647]. In light of this, the spectra would need to be estimated jointly,

and component separation methods based on Fisher matrix formalism have already been developed for this scope in the past [635, 648, 649]. In this work, we consider the formalism mentioned above and apply it to the data from the first three LVK observing runs to estimate jointly and set upper limits on the amplitudes of different SGWBs, assuming they are isotropic and their spectral shape follows a power law in frequency. Then, we use the results of the multi-component analysis to derive constraints on ensemble properties of some astrophysical sources associated with a subset of the considered SGWBs, namely the CBCs, NS r-mode instabilities, and magnetars.

The rest of the paper is organised as follows. In section 9.2, we present the astrophysical sources and expressions of the SGWBs of interest. After that, in section 9.3, we discuss the analysis methods for a multi-component SGWB. Then, in section 9.4, we present the results for the SGWB amplitudes and the ensemble properties, comparing them with the single-component results. In the conclusions, we summarise what we have done and present some prospects for improving this work and refining the techniques employed here. In the appendix 9.6, we include an injection study we performed to validate the methods, understand the best procedure to follow in a detection regime, and how to interpret the results in that case.

9.2 Astrophysical stochastic gravitational-wave backgrounds

The astrophysical SGWBs (AGWBs) are those backgrounds whose origin is connected to GW sources formed during the stellar history of the cosmos. Their detection and measurements may give access to properties of astrophysical populations that cannot be observed via electromagnetic astronomy. Like other SGWBs, they can be characterised by means of the dimensionless ratio of the GW energy density $\rho_{\rm gw}$ spectrum per logarithmic frequency unit to the critical energy needed to have a closed Universe ρ_c [410]

$$\Omega_{\rm gw}(f) \equiv \frac{1}{\rho_c}\,\frac{\mathrm{d}\rho_{\rm gw}(f)}{\mathrm{d}\ln f}, \tag{9.2.1}$$

where $\rho_c = 3\,H_0^2 c^2/(8\pi\,G)$, with H_0 the Hubble parameter today, c is the speed of light, and G Newton's gravitational constant.

For astrophysical SGWB, $\Omega_{\rm gw}(f)$ can be expressed in the observer frame using Phinney's formula [248], which we write here as [243, 246]

$$\Omega_{\rm gw}(f) = \frac{f}{\rho_c\,H_0}\int_\Theta p\,(\theta)\,\mathrm{d}\theta \int_{z_{\rm min}(\theta)}^{z_{\rm max}(\theta)} \frac{R\,(\theta,z)}{(1+z)\,E(z)}\,\frac{\mathrm{d}E_{\rm gw}(f_s,\theta)}{\mathrm{d}f_s}\bigg|_{f_s=(1+z)\,f}\mathrm{d}z\,, \tag{9.2.2}$$

where $p(\theta)$ is the joint probability density function of the population parameters, $\mathrm{d}E_{\rm gw}(f_s,\theta)/\mathrm{d}f_s$ is the GW source energy spectrum evaluated in the source frame, $R(\theta,\,z)$ is the source-frame rate per comoving volume, and the dependence on (a flat

ΛCDM ignoring radiation and curvature terms) cosmology is encoded in

$$E(z) = \sqrt{\Omega_m (1+z)^3 + \Omega_\Lambda}. \tag{9.2.3}$$

The bounds in the redshift integral depend on the source parameters through the minimum and maximum emission frequencies of the source $f_{s;\,\min}(\theta)$ and $f_{s;\,\max}(\theta)$ as

$$z_{\min}(\theta) = \max\left\{0, \frac{f_{s;\,\min}(\theta)}{f} - 1\right\}, \tag{9.2.4}$$

$$z_{\max}(\theta) = \min\left\{z_{\max}, \frac{f_{s;\,\max}(\theta)}{f} - 1\right\}. \tag{9.2.5}$$

For the scope of this work, given that many of the distribution functions of the parameters are fledged by uncertainties, we further assume that, in the frequency range of interest, the spectrum $\Omega_{\rm gw}(f)$ depends only on the frequency and on the ensemble averages of the population parameters θ_i of interest[1] through a power-law functional dependence:

$$\Omega_{\rm gw}(f) \approx \xi \left(\frac{f}{f_{\rm ref}}\right)^{\alpha} \prod_i \langle \theta_i^{c_i} \rangle, \tag{9.2.6}$$

where $\langle \ldots \rangle$ denotes the ensemble average, $f_{\rm ref}$ is a pivot frequency, and

$$\xi \equiv \frac{\Omega_{\rm gw}(f_{\rm ref})}{\prod_i \langle \theta_i^{c_i} \rangle} \tag{9.2.7}$$

is an overall normalisation constant.The spectra of the AGWBs considered in the following are illustrated in the landscape plot in figure 9.1.

9.2.1 SGWB from compact binary coalescences

The observation of binary black hole (BBH), binary neutron star (BNS), and binary neutron star black hole (NSBH) merger signals during the LVK first three observing runs has allowed to draw more precise information about the population properties of these objects [93, 247]. The results suggest that the SGWB from CBCs is the dominant one in the ground-based GW detector network's most sensitive frequency band, predicting the energy densities at the reference frequency $f_{\rm ref} = 25\,\mathrm{Hz}$ being $\Omega_{\rm BNS}(25\,\mathrm{Hz}) = 0.6^{+1.7}_{-0.5} \times 10^{-10}$, $\Omega_{\rm NSBH}(25\,\mathrm{Hz}) = 0.9^{+2.2}_{-0.7} \times 10^{-10}$, and $\Omega_{\rm BBH}(25\,\mathrm{Hz}) = 5.0^{+1.4}_{-1.8} \times 10^{-10}$ [247]. The SGWB from these objects can be modelled using equation (9.2.2) by explicitly expressing the energy spectrum of the sources and the merger rate.

[1] The other population parameters, which we are not interested in or whose dependence cannot be written in general in the product of equation (9.2.6), are assumed to be fixed and reabsorbed in the normalisation factor ξ.

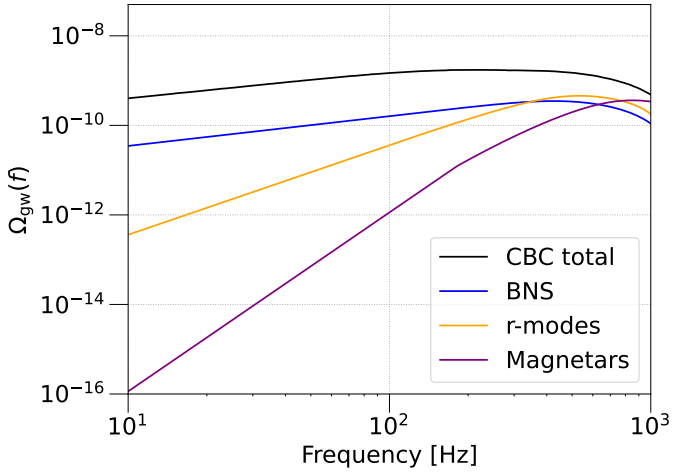

Figure 9.1: Intensity of different astrophysical SGWBs. The black line denotes the median value of the total CBC SGWB as inferred from the GWTC-3 in [247]. The blue line represents the median value of the BNS SGWB, again from [247]. The orange line is the SGWB from r-modes from [280] with our conventions, setting $K = -5/4$ and further scaling equation (9.2.17) to the case where just 1% of the young NSs enters the instability [243]. The purple line is the SGWB from magnetars, using $\varepsilon = 5 \times 10^{-4}$ and $B = 10^{11}$ T, with the other parameters from [270].

It is a standard result that, in the quasi-circular orbit, Newtonian approximation, the energy spectrum of an inspiralling binary is given by

$$\frac{\mathrm{d}E_{\mathrm{gw}}}{\mathrm{d}f} = \frac{\pi^{2/3}}{3G} \left(G\mathcal{M}_c\right)^{5/3} f^{-1/3}. \tag{9.2.8}$$

However, to make predictions about the SGWB from BBHs, it is necessary to consider the full inspiral-merger-ringdown contribution to the energy spectrum, which would otherwise be underestimated. In this case, the above equation is no longer valid, and recent studies [261] for SGWB from BBHs usually make use of the phenomenological waveform at second post-Newtonian order from [650,651] in the limit of non-spinning black holes.

The merger rates for CBCs are intrinsically related to the cosmic stellar formation rate (SFR) [259] through the convolution integral over time delays

$$R(z) = \int \mathrm{d}t_d \, R_f(z_f(z, t_d)) \, P_{t_d}(t_d), \tag{9.2.9}$$

where the dependence on the SFR (usually in $M_\odot \, \mathrm{yr}^{-1} \, \mathrm{Mpc}^{-3}$ units) is implicitly in the formation rate

$$R_f(z_f) = r_0 \frac{\mathrm{SFR}(z_f)}{\mathrm{SFR}(0)} \tag{9.2.10}$$

normalised to the local rate r_0 (usually in $\mathrm{yr}^{-1}\,\mathrm{Gpc}^{-3}$ units), which can be inferred from observations. The most recent results from GWTC-3 [247] suggest that the BNS local merger rate is in the range 10-1700 $\mathrm{yr}^{-1}\,\mathrm{Gpc}^{-3}$, the NSBH one between 7.8 and 140 $\mathrm{yr}^{-1}\,\mathrm{Gpc}^{-3}$, and the BBH one, evaluated at the fiducial redshift $z = 0.2$, to be in the 17.9 and 44 $\mathrm{yr}^{-1}\,\mathrm{Gpc}^{-3}$ interval.

The integral over the time-delays distribution is necessary to account for the time elapsing between the formation of a stellar binary system and its evolution towards a compact binary system. The time-delay distribution is usually assumed to follow a power-law $p_{t_d} \propto t_d^{-1}$ [652], with the maximum time delay equal to the Hubble time and the minimum time delay for BNS and NSBH being 20 Myr and 50 Myr for BBH. In the case of BBH, the merger rate integral may also be further weighted by including a metallicity cut for stars forming at $Z < 0.1\,Z_\odot$ [653, 654]. These aspects and parameters still need to be completely understood and are usually inferred from population syntheses [655] in combination with electromagnetic observations. A recent work [261] considers most of the uncertainties in these parameters and carefully evaluates their impact when predicting the spectrum of a SGWB from BBH and BNS in the ground-based detectors frequency range.

The parameter space in equation (9.2.2) for a compact binary usually ranges between 15 (BBH) and 17 (BNS, NSBH) parameters. Current studies for SGWB from CBCs usually limit to average the rates and the energy spectrum over the two components masses m_1 and m_2 of the binary (in the BBH case, it is possible to include spin as well through the above mentioned phenomenological waveform, but it is usually considered to be zero, spin corrections being small [255, 256]). Population studies from GWTC-3 [247] suggest a preference for a power-law-plus-peak model but do not exclude a broken power-law model for BBH components mass function. The mass function for BNS components is expected instead to exhibit broader features, which for SGWB studies can be taken to be uniformly distributed between 1 and 2.5 $M_\odot$. For NSBH, GWTC-3 studies have used the same mass function for the NS component and a logarithmically uniform distribution of black hole masses between 5 and 50 $M_\odot$.

For this work, when constraining the population properties of a CBC background, we will use a frequency range where this background is well described by the inspiral phase, assuming hence the functional dependence ($j = \mathrm{BBH},\ \mathrm{BNS},\ \mathrm{NSBH}$)

$$\Omega_{\mathrm{gw},\,j}(f) = \xi_j \left(\frac{f}{f_{\mathrm{ref}}}\right)^{2/3} r_{0,\,j} \left\langle \mathcal{M}_c^{5/3} \right\rangle_j \equiv \xi_j \left(\frac{f}{f_{\mathrm{ref}}}\right)^{2/3} K_j, \tag{9.2.11}$$

where the product $K_j \equiv r_{0,\,j} \left\langle \mathcal{M}_c^{5/3} \right\rangle_j$ is assumed to be a free parameter to be constrained. More specifically, we will focus on the whole population of CBCs and constrain an effective $K_{\mathrm{CBC}} \equiv \sum_j K_j$.

9.2.2 Magnetars

Magnetars are neutron stars that are formed with a very intense magnetic field (of the order of $10^{10} - 10^{11}$ T). They were first proposed in [656] as a candidate to explain soft gamma repeaters and anomalous x-ray pulsars. The list of known magnetars is collected in the McGill magnetars catalogue [657]. The intense magnetic field is expected to induce a quadrupolar deformation in the rapidly spinning neutron star, which in turn decelerates through magnetic dipole torque and GW production, with an energy spectrum [269–271]

$$\frac{\mathrm{d}E_{\mathrm{gw}}}{\mathrm{d}f} = I\pi^2 f^3 \left(\frac{5c^2R^6}{192\pi^2GI^2}\frac{4\pi B^2}{\mu_0\varepsilon^2}\,\sin^2\alpha + f^2\right)^{-1}, \quad f \in \left[0 - \frac{2}{P_0}\right], \tag{9.2.12}$$

where I is the magnetar moment of inertia around the rotation axis, R is the magnetar radius, B the (poloidal) magnetic field of the star, ε the dimensionless ellipticity, quantifying the deviation from spherical symmetry, α the "wobble angle" between the magnetar spin and magnetic axes, P_0 the initial rotation period of the magnetar, and μ_0 the vacuum magnetic permeability. The first term in the brackets comes from the rotational energy loss due to electromagnetic dipole radiation, while the second term is due to GW emission. The ellipticity may further depend on the magnetic field in different ways, based on whether the magnetic field configuration is expected to be poloidal-dominated [567], a twisted-torus one [658], or toroidal-dominated [659].

When deriving the expression for the spectrum of the SGWB from magnetars from equation (9.2.2), given that the GW source starts emitting after its birth, it is possible to write the cosmic rate $R(\theta, z)$ as $R_{\mathrm{magnetar}}(\theta, z) = \lambda_{\mathrm{magnetar}}\,\mathrm{SFR}(z)$, where $\lambda_{\mathrm{magnetar}}$ is the fraction per solar mass of the progenitor mass that is converted in magnetars. This quantity can also be written as a function of the mass of the NS progenitors λ_{NS} and the fraction of NSs born as magnetars $f_{\mathrm{magnetars}}$, namely $\lambda_{\mathrm{magnetar}} = f_{\mathrm{magnetars}}\,\lambda_{\mathrm{NS}}$.

The resulting expression of $\Omega_{\mathrm{gw}}(f)$ in the case where the dominant rotational energy loss mechanism is the dipole magnetic torque is then [269, 270]

$$\Omega_{\mathrm{gw}}(f) = \frac{\mathcal{K}}{\rho_c\,H_0}\,f^4 \int_{z_{\mathrm{min}}}^{z_{\mathrm{max}}} \frac{\lambda_{\mathrm{magnetars}}\,\mathrm{SFR}(z)\,(1+z)^2}{E(z)}, \tag{9.2.13}$$

where

$$\mathcal{K} = \frac{192\pi^4 G}{5c^2}\,\frac{\mu_0}{4\pi}\left\langle\frac{1}{R^6}\right\rangle\langle I^3\rangle\,\langle\varepsilon^2\rangle\left\langle\frac{1}{B^2}\right\rangle\left\langle\frac{1}{\sin^2\alpha}\right\rangle. \tag{9.2.14}$$

In the following, we assume the following functional dependence

$$\begin{aligned}\Omega_{\mathrm{gw,\,magnetars}}(f) &= \xi_{\mathrm{magnetars}} \left(\frac{f}{f_{\mathrm{ref}}}\right)^4 \langle \varepsilon^2 \rangle \left\langle \frac{1}{B^2} \right\rangle \\ &\equiv \xi_{\mathrm{magnetars}} \left(\frac{f}{f_{\mathrm{ref}}}\right)^4 K_{\mathrm{magnetars}}, \end{aligned} \tag{9.2.15}$$

where $K_{\mathrm{magnetars}} \equiv \sqrt{\langle \varepsilon^2 \rangle \, \langle 1/B^2 \rangle}$ is assumed to be a free parameter to be constrained.

9.2.3 r-mode instabilities

In the pioneering works [276,277], it was discovered that the emission of gravitational radiation induces instability in the r-modes of young, rapidly rotating NSs. The first studies about the GW emission (and SGWB) related to the r-mode instability were performed in [278, 279], showing that the GW emission can be modelled by two parameters only, namely the angular velocity of the NS Ω and the parameter α, related to the r-modes amplitude $h(t)$ from the $l = m = 2$ current multipole S_{22} dominating the GW emission. After an initial (500-s [278]) phase where Ω is roughly constant and α exponentially grows, the system enters a non-linear hydrodynamic regime, with α reaching a saturation value that lasts around one year and eventually radiates approximately two thirds of the NS rotational energy in GWs, ceasing the r-mode instability [278]. The superposition of the GW signals from young NSs during the year-long non-linear phase can give rise to a continuous SGWB [243, 279, 280].

The expression for $\Omega_{\mathrm{gw}}(f)$ is analogous to the one for SGWB from magnetars, with the main difference within the fraction of initial mass progenitors converted into neutron stars $\lambda_{\mathrm{NS}} = 9 \times 10^{-3} \, M_{\odot}^{-1}$ [243], and the energy spectrum [278]

$$\left.\frac{\mathrm{d}E_{\mathrm{gw}}}{\mathrm{d}f}\right|_{\mathrm{r-modes}} \approx \frac{4}{3} \frac{f}{f_{\mathrm{max}}^2} E_K, \tag{9.2.16}$$

where E_K is the rotational kinetic energy of the NS assuming a Keplerian angular velocity $\Omega_K = 2\sqrt{\pi G \bar{\rho}_{\mathrm{NS}}}/3$ (namely the angular velocity at which the star starts shedding mass at the equator), and f_{max} the corresponding maximal GW frequency[2].

By using the results from more recent studies and simulations about gravitational radiation from r-mode instability [660], which allow for saturation values of α being less than unity, and adapting the resulting expression for $\Omega_{\mathrm{gw}}(f)$ derived in [280] to our notation and convention, it is possible to express the spectrum as (assuming all NSs having a mass equal to $1.4 M_{\odot}$, a radius $R = 12.53$ km, and a polytropic equation of state $p = k\rho^2$ [278–280, 660])

$$\left.\Omega_{\mathrm{gw}}(f)\right|_{\mathrm{r-modes}} = \frac{16\pi^3 c}{3H_0^3} \times 96.7 \times \left\langle \frac{1}{K+2} \right\rangle f^2 \int_{z_{\mathrm{min}}}^{z_{\mathrm{max}}} \mathrm{d}z \, \frac{\mathrm{SFR}(z) \, \lambda_{\mathrm{NS}}}{E(z)} \tag{9.2.17}$$

[2]Note that $E_K \propto \Omega_K^2 \propto f_{\mathrm{max}}^2$, and hence equation (9.2.16) does not depend on f_{max}.

where $(K+2)^{-1} \propto \alpha^2$ when it saturates (see [660] for more details about K definition), with $-5/4 \leq K \ll 10^{13}$. The minimum value $K = -5/4$ corresponds to the smallest amount of differential rotation at the time when the r-mode instability is created, while the upper bound $K \ll 10^{-13}$ encodes the condition that the r-mode angular momentum is much smaller than the angular momentum of the unperturbed star [660]. In the following, when performing the analysis, we consider the following expression for the spectrum

$$\Omega_{\mathrm{gw,\,r-modes}}(f) = \xi_{\mathrm{r-modes}} \left(\frac{f}{f_{\mathrm{ref}}}\right)^2 \left\langle \frac{1}{K+2} \right\rangle \equiv \xi_{\mathrm{r-modes}} \left(\frac{f}{f_{\mathrm{ref}}}\right)^2 K_{\mathrm{r-modes}}, \tag{9.2.18}$$

where the parameter $K_{\mathrm{r-modes}} \equiv \left\langle (K+2)^{-1} \right\rangle$ is the free parameter to be constrained.

9.3 Analysis methods

We perform a search for a Gaussian, stationary, unpolarised and isotropic SGWB, assuming the presence of multiple components $\{\Omega_\alpha(f)\}$ following a power law in frequency, such that

$$\Omega_{\mathrm{gw}}(f) = \sum_\alpha \Omega_\alpha w_\alpha(f), \quad w_\alpha(f) \equiv \frac{\Omega_\alpha(f)}{\Omega_\alpha(f_{\mathrm{ref}})} = \left(\frac{f}{f_{\mathrm{ref}}}\right)^\alpha, \tag{9.3.1}$$

where every component is characterised by an amplitude $\Omega_\alpha \equiv \Omega_\alpha(f = f_{\mathrm{ref}})$, with f_{ref} an arbitrary reference frequency, chosen to be $f_{\mathrm{ref}} = 25$ Hz in the following. We make use of the publicly available [216, 217] time-series data from the first three observing runs (O1, O2, and O3) of the Advanced LIGO-Hanford (H) and LIGO-Livingston (L) detectors and the Advanced Virgo (V) detector. In the same fashion as in [258, 485], we apply both time- and frequency-domain cuts and then perform the cross-correlation search employing the publicly available algorithm in MATLAB [479].

For every detector pair IJ (I, J = H, L, V), called "baseline", we divide the time-series output in segments $s_I(t)$, labelled by t, of duration T, and then we take their short-time Fourier transform $\tilde{s}_I(t;\, f)$, obtaining a segment-dependent cross-correlation statistic spectrum $C_{IJ}(t;f) \equiv \tilde{s}_I^*(t;\, f)\tilde{s}_J(t;\, f)$. In the absence of correlated noise, the expectation value of $C_{IJ}(t;f)$ over the segment can be written as a linear convolution equation

$$\langle C_{IJ} \rangle\,(t;f) = \sum_\alpha K_\alpha(t;f)\,\Omega_\alpha, \qquad \text{or} \qquad \mathbf{C} = \mathbf{K}\cdot\mathbf{\Omega}, \tag{9.3.2}$$

where

$$\mathbf{K} \equiv K_\alpha(t;f) := \frac{T}{2} S_0(f)\gamma_{IJ}(f)w_\alpha(f), \tag{9.3.3}$$

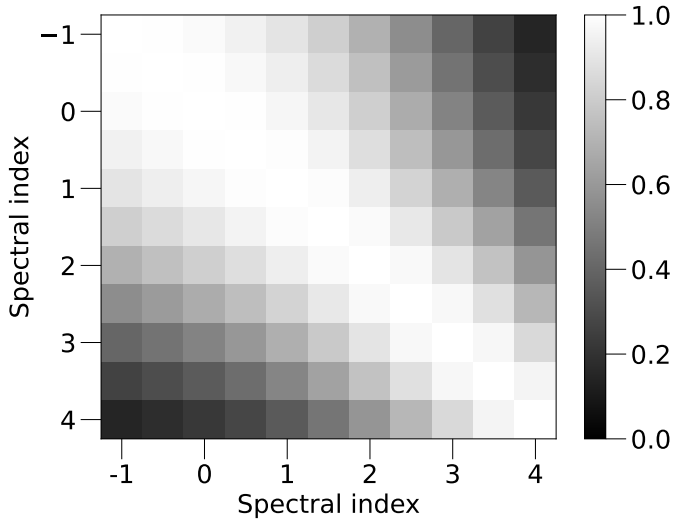

Figure 9.2: Preconditioned Fisher matrix for data from the first three LVK observing runs, showing the couplings among different spectral indices. The diagonal is unity by construction, with the off-diagonal element being smaller than one and positive.

with $S_0(f) = (3H_0^2)/(10\pi^2 f^3)$ and $\gamma_{IJ}(f)$ the normalised overlap reduction function [398, 399, 410] quantifying the reduction in sensitivity due to the geometry of the baseline IJ and its response to the GW signal.

The estimator for $\mathbf{\Omega}$ can be obtained as a maximum-likelihood solution for the convolution equation (9.3.2), namely [635]

$$\hat{\mathbf{\Omega}} = \mathbf{\Gamma}^{-1} \cdot \mathbf{X}, \tag{9.3.4}$$

where

$$\begin{aligned} X_\alpha &= 4\Delta f \sum_{I>J} \sum_{f,\,t} \gamma_{IJ}(f) \frac{w_\alpha(f)\, \tilde{s}_I^*(t;\, f) \tilde{s}_J(t;\, f)}{P_I(t;f)\, P_J(t;f)}, \\ \Gamma_{\alpha\alpha'} &= 2T\Delta f \sum_{I>J} \sum_{f,\,t} \frac{w_\alpha(f)\, w_{\alpha'}(f)\, \gamma_{IJ}^2(f)}{P_I(t;f)\, P_J(t;f)}, \end{aligned} \tag{9.3.5}$$

where $P_I(t;f)$ and $P_J(t;f)$ are the one-sided power spectral densities of the noise in the detectors. The inversion of $\Gamma_{\alpha\alpha'}$ may lead to numerical errors. This can be avoided by preconditioning the matrix as

$$\mathbf{\Gamma} \equiv \Gamma'_{\alpha\alpha'} = \frac{\Gamma_{\alpha\alpha'}}{\sqrt{\Gamma_\alpha \Gamma_{\alpha'}}}, \tag{9.3.6}$$

where $\Gamma_\alpha \equiv \mathrm{diag}\,(\Gamma_{\alpha\alpha'})$. This new coupling matrix can quantify the correlation between different models, as illustrated in figure 9.2. Then the estimator for Ω_α becomes

$$\hat{\Omega}_\alpha = \sum_{\alpha'} \Gamma'^{-1}_{\alpha\alpha'} \frac{X'_{\alpha'}}{\sqrt{\Gamma_\alpha}}, \tag{9.3.7}$$

where $X'_\alpha = X_\alpha/\sqrt{\Gamma_\alpha}$. The covariance matrix and the standard deviation of $\hat{\Omega}_\alpha$ are then

$$\Sigma_{\alpha\alpha'} = \frac{(\Gamma'_{\alpha\alpha'})^{-1}}{\sqrt{\Gamma_\alpha\,\Gamma_{\alpha'}}}, \tag{9.3.8}$$

$$\sigma_\alpha = \left[\sqrt{\mathrm{diag}(\Sigma_{\beta\beta'})}\right]_\alpha . \tag{9.3.9}$$

The likelihood function associated with these estimators can be assumed to be a multivariate Gaussian [635]:

$$\mathcal{L}\left(\hat{\Omega}_\alpha|\Omega_\alpha\right) = \frac{1}{(2\pi)^{N/2}\,(\det\Sigma)^{1/2}}\,\exp\left[-\frac{1}{2}\left(\hat{\Omega}_\alpha - \Omega_\alpha\right)\Sigma^{-1}_{\alpha\alpha'}\left(\hat{\Omega}_{\alpha'} - \Omega_{\alpha'}\right)\right]. \tag{9.3.10}$$

We use the above likelihood function to perform parameter estimation or set bounds on the parameters from the different considered models. The same likelihood function can also be used to estimate the ensemble properties by using equation (9.2.6) and to rewrite the Ω_α model as

$$\Omega_\alpha = \xi_\alpha \prod_i \langle \theta_i^{c_i} \rangle\,. \tag{9.3.11}$$

We have tested the method presented in this section by performing multiple sets of injections in O3 data in the frequency domain; see appendix 9.6 for more details about the most significant ones.

9.4 Results and Discussions

We present the results of the multi-component analysis for the set of spectral indices $\vec{\boldsymbol{\alpha}} = \{0,\, 2/3,\, 2,\, 3,\, 4\}$ and their implications for the ensemble properties of CBCs (in the inspiral phase), pulsar r-mode instabilities, and magnetars.

9.4.1 Power law energy density spectrum

We have performed a search for a Gaussian, stationary, unpolarised, isotropic, multi-component SGWB following the methods presented in the previous section 9.3 and applied them to five spectral indices, namely $\alpha = 0,\, 2/3,\, 2,\, 3,\, 4$. The indices $\alpha = 2/3,\, 2, 4$ are associated with the astrophysical SGWBs produced by CBCs [249, 255, 256, 541, 571], r-mode instabilities in NSs [278–280], and magnetars [269, 271, 272], respectively, as described in section 9.2. The remaining $\alpha = 0,\, 3$ can be associated with other SGWBs with different origins ($\alpha = 0$ to inflationary [292, 546, 552] or cosmic strings [294, 337–339] SGWBs, $\alpha = 3$ to core-collapse to supernova [282,

283, 285, 639, 640] or pre-big bang models [448, 449, 645]), for which we do not draw any additional implication. Moreover, the SGWBs associated with these two spectral indices are usually constrained by searches using the ground-based detectors [258], and it may be interesting to compare the standard results with those of the multi-component analysis method. For the reasons presented in the appendix 9.6 in light of the implications for astrophysical SGWBs, we have restricted the frequency range of the search to 20-100 Hz, where the astrophysical signal $\Omega_{\rm gw}(f)$ can be approximated by a power law[3].

The estimators from analysing every possible combination of spectral indices can be read in table 9.1. The first five lines can be interpreted as results from the single-component analysis. The small difference in the $\alpha = 0,\, 2/3$, and 3 cases from [258] is only to be attributed to the frequency range adopted for our analysis being 20-100 Hz (when we make use of the 20-1726 Hz range used in [258], we recover the same estimators). Compared to the single-component case, the uncertainty in the estimate of the components of the SGWB is, in general, larger in the multi-component analysis, leading to more conservative estimates but still compatible with the single-component ones. Another factor influencing the magnitude of the estimator uncertainties when different combinations of components (with the number of components fixed) are considered is the distance of the spectral indices in the power-law space. As an example of this effect, consider the $\hat{\Omega}_0$ uncertainty in the four combinations $\{\alpha = 0,\, 2/3\}$, $\{\alpha = 0,\, 2\}$, $\{\alpha = 0,\, 3\}$, and $\{\alpha = 0,\, 4\}$, with the second spectral index getting more and "distant" from $\alpha = 0$ and the uncertainty getting lower and lower.

Consistently with previous analyses involving data from the first three LVK observing runs, there is no evidence for a signal in any of the examined combinations of the spectral indices. We have verified this for every combination by performing a Bayesian model comparison between noise-only and signal hypotheses, with the Bayes factor always favouring noise over signal. As a consequence, we have set 95%-confidence Bayesian upper limits $\Omega_\alpha^{95\%}$ for every component for every combination, using a uniform prior between 0 and $10^{-6.5}$ for each of them. The upper limits are summarised in table 9.2. Noticeably, the upper limits become more stringent when including more components in the analysis, following the opposite trend compared to that of the estimator uncertainties. This seems to contradict the naive picture that considering more components should decrease the constraining power of the search. On the other hand, this could be argued by claiming that the power splits among the different components, leading to lower upper limits when more components are included in the analysis, as previously observed in [455]. Alternatively, this trend could also arise from this particular data realisation being noise-dominated [648]. Still, in the presence of a signal (or excesses) in the data, the multi-component analysis provides unbiased estimators and correct parameter estimation results (and hence upper limits), in contrast to the biased single-component ones, see appendix 9.6.

	$\hat{\Omega}_0$	$\hat{\Omega}_{2/3}$	$\hat{\Omega}_2$	$\hat{\Omega}_3$	$\hat{\Omega}_4$
$\alpha = \{0\}$	$(1.5 \pm 7.5) \times 10^{-9}$	-	-	-	-
$\alpha = \{2/3\}$	-	$(2.3 \pm 56.2) \times 10^{-10}$	-	-	-
$\alpha = \{2\}$	-	-	$(-1.3 \pm 2.5) \times 10^{-9}$	-	-
$\alpha = \{3\}$	-	-	-	$(-9.8 \pm 10.3) \times 10^{-10}$	-
$\alpha = \{4\}$	-	-	-	-	$(-4.0 \pm 3.4) \times 10^{-10}$
$\alpha = \{0, 2/3\}$	$(4.4 \pm 4.6) \times 10^{-8}$	$(-3.2 \pm 3.4) \times 10^{-8}$	-	-	-
$\alpha = \{0, 2\}$	$(1.6 \pm 1.4) \times 10^{-8}$	-	$(-5.8 \pm 4.6) \times 10^{-9}$	-	-
$\alpha = \{0, 3\}$	$(9.5 \pm 9.5) \times 10^{-9}$	-	-	$(-1.8 \pm 1.3) \times 10^{-9}$	-
$\alpha = \{0, 4\}$	$(6.1 \pm 8.2) \times 10^{-9}$	-	-	-	$(-5.1 \pm 3.7) \times 10^{-10}$
$\alpha = \{2/3, 2\}$	-	$(1.7 \pm 1.4) \times 10^{-8}$	$(-8.3 \pm 6.1) \times 10^{-9}$	-	-
$\alpha = \{2/3, 3\}$	-	$(8.4 \pm 8.1) \times 10^{-9}$	-	$(-2.1 \pm 1.5) \times 10^{-9}$	-
$\alpha = \{2/3, 4\}$	-	$(5.0 \pm 6.6) \times 10^{-9}$	-	-	$(-5.6 \pm 4.0) \times 10^{-10}$
$\alpha = \{2, 3\}$	-	-	$(7.6 \pm 7.2) \times 10^{-9}$	$(-3.9 \pm 2.9) \times 10^{-9}$	-
$\alpha = \{2, 4\}$	-	-	$(3.1 \pm 4.3) \times 10^{-9}$	-	$(-7.4 \pm 5.8) \times 10^{-10}$
$\alpha = \{3, 4\}$	-	-	-	$(2.4 \pm 3.7) \times 10^{-9}$	$(-1.2 \pm 1.2) \times 10^{-9}$
$\alpha = \{0, 2/3, 2\}$	$(-7.9 \pm 11.4) \times 10^{-8}$	$(9.5 \pm 11.3) \times 10^{-8}$	$(-1.8 \pm 1.5) \times 10^{-8}$	-	-
$\alpha = \{0, 2/3, 3\}$	$(-3.2 \pm 8.3) \times 10^{-8}$	$(3.5 \pm 7.0) \times 10^{-8}$	-	$(-2.9 \pm 2.7) \times 10^{-9}$	-
$\alpha = \{0, 2/3, 4\}$	$(-9.9 \pm 69.8) \times 10^{-9}$	$(1.3 \pm 5.6) \times 10^{-8}$	-	-	$(-6.2 \pm 6.1) \times 10^{-10}$
$\alpha = \{0, 2, 3\}$	$(-1.0 \pm 30.0) \times 10^{-9}$	-	$(8.3 \pm 22.6) \times 10^{-9}$	$(-4.1 \pm 6.4) \times 10^{-9}$	-
$\alpha = \{0, 2, 4\}$	$(4.3 \pm 25.0) \times 10^{-9}$	-	$(1.0 \pm 12.9) \times 10^{-9}$	-	$(-5.9 \pm 10.5) \times 10^{-10}$
$\alpha = \{0, 3, 4\}$	$(6.5 \pm 17.8) \times 10^{-9}$	-	-	$(-1.8 \pm 81.2) \times 10^{-10}$	$(-4.6 \pm 23.2) \times 10^{-10}$
$\alpha = \{2/3, 2, 3\}$	-	$(1.7 \pm 38.8) \times 10^{-9}$	$(6.1 \pm 34.4) \times 10^{-9}$	$(-3.6 \pm 8.4) \times 10^{-9}$	-
$\alpha = \{2/3, 2, 4\}$	-	$(7.7 \pm 30.1) \times 10^{-9}$	$(-1.7 \pm 19.5) \times 10^{-9}$	-	$(-4.5 \pm 12.7) \times 10^{-10}$
$\alpha = \{2/3, 3, 4\}$	-	$(8.1 \pm 18.3) \times 10^{-9}$	-	$(-1.9 \pm 10.4) \times 10^{-9}$	$(-5.6 \pm 280.6) \times 10^{-11}$
$\alpha = \{2, 3, 4\}$	-	-	$(1.6 \pm 2.8) \times 10^{-8}$	$(-1.1 \pm 2.5) \times 10^{-8}$	$(1.5 \pm 4.9) \times 10^{-9}$
$\alpha = \{0, 2/3, 2, 3\}$	$(-3.2 \pm 3.5) \times 10^{-7}$	$(4.1 \pm 4.6) \times 10^{-7}$	$(-1.2 \pm 1.5) \times 10^{-7}$	$(1.9 \pm 2.6) \times 10^{-8}$	-
$\alpha = \{0, 2/3, 2, 4\}$	$(-2.5 \pm 2.7) \times 10^{-7}$	$(3.0 \pm 3.3) \times 10^{-7}$	$(-6.8 \pm 7.6) \times 10^{-8}$	-	$(2.1 \pm 3.1) \times 10^{-9}$
$\alpha = \{0, 2/3, 3, 4\}$	$(-1.5 \pm 1.8) \times 10^{-7}$	$(1.6 \pm 1.9) \times 10^{-7}$	-	$(-2.3 \pm 2.8) \times 10^{-8}$	$(4.5 \pm 6.3) \times 10^{-9}$
$\alpha = \{0, 2, 3, 4\}$	$(-4.0 \pm 6.3) \times 10^{-8}$	-	$(7.6 \pm 9.9) \times 10^{-8}$	$(-4.7 \pm 6.2) \times 10^{-8}$	$(7.1 \pm 10.2) \times 10^{-9}$
$\alpha = \{2/3, 2, 3, 4\}$	-	$(-5.5 \pm 9.6) \times 10^{-8}$	$(9.9 \pm 14.7) \times 10^{-8}$	$(-5.4 \pm 7.8) \times 10^{-8}$	$(7.8 \pm 12.0) \times 10^{-9}$
$\alpha = \{0, 2/3, 2, 3, 4\}$	$(-6.9 \pm 8.9) \times 10^{-7}$	$(9.8 \pm 13.6) \times 10^{-7}$	$(-4.3 \pm 7.1) \times 10^{-7}$	$(1.3 \pm 2.6) \times 10^{-7}$	$(-1.4 \pm 3.0) \times 10^{-8}$

Table 9.1: Estimators from the multi-components analysis in the 20-100 Hz band for the different combinations of the five spectral indices. Horizontal lines divide the table in regions where a fixed number of components is considered for the analysis.

	$\Omega_0^{95\%}$	$\Omega_{2/3}^{95\%}$	$\Omega_2^{95\%}$	$\Omega_3^{95\%}$	$\Omega_4^{95\%}$	$K_{\rm CBC}^{95\%}$	$K_{\rm magnetars}^{95\%}$	$K_{\rm r-modes}^{95\%}$
$\alpha = \{0\}$	1.6×10^{-8}	-	-	-	-	-	-	-
$\alpha = \{2/3\}$	-	1.2×10^{-8}	-	-	-	5.1×10^{4}	-	-
$\alpha = \{2\}$	-	-	4.1×10^{-9}	-	-	-	-	1.3×10^{0}
$\alpha = \{3\}$	-	-	-	1.5×10^{-9}	-	-	-	-
$\alpha = \{4\}$	-	-	-	-	4.5×10^{-10}	-	1.4×10^{-12}	-
$\alpha = \{0, 2/3\}$	1.3×10^{-8}	9.5×10^{-9}	-	-	-	4.2×10^{4}	-	-
$\alpha = \{0, 2\}$	1.4×10^{-8}	-	3.5×10^{-9}	-	-	-	-	1.3×10^{0}
$\alpha = \{0, 3\}$	1.5×10^{-8}	-	-	1.3×10^{-9}	-	-	-	-
$\alpha = \{0, 4\}$	1.5×10^{-8}	-	-	-	4.1×10^{-10}	-	1.3×10^{-12}	-
$\alpha = \{2/3, 2\}$	-	1.0×10^{-8}	3.5×10^{-9}	-	-	4.9×10^{4}	-	1.3×10^{0}
$\alpha = \{2/3, 3\}$	-	1.0×10^{-8}	-	1.3×10^{-9}	-	4.6×10^{4}	-	-
$\alpha = \{2/3, 4\}$	-	1.0×10^{-8}	-	-	4.1×10^{-10}	4.9×10^{4}	1.3×10^{-12}	-
$\alpha = \{2, 3\}$	-	-	3.7×10^{-9}	1.3×10^{-9}	-	-	-	1.3×10^{0}
$\alpha = \{2, 4\}$	-	-	3.9×10^{-9}	-	4.0×10^{-10}	-	1.3×10^{-12}	1.3×10^{0}
$\alpha = \{3, 4\}$	-	-	-	1.3×10^{-9}	4.0×10^{-10}	-	1.3×10^{-12}	-
$\alpha = \{0, 2/3, 2\}$	1.2×10^{-8}	8.4×10^{-9}	3.1×10^{-9}	-	-	4.3×10^{4}	-	1.3×10^{0}
$\alpha = \{0, 2/3, 3\}$	1.2×10^{-8}	8.8×10^{-9}	-	1.2×10^{-9}	-	3.9×10^{4}	-	-
$\alpha = \{0, 2/3, 4\}$	1.3×10^{-8}	8.9×10^{-9}	-	-	3.9×10^{-10}	4.2×10^{4}	1.2×10^{-12}	-
$\alpha = \{0, 2, 3\}$	1.3×10^{-8}	-	3.2×10^{-9}	1.1×10^{-9}	-	-	-	1.3×10^{0}
$\alpha = \{0, 2, 4\}$	1.4×10^{-8}	-	3.3×10^{-9}	-	3.8×10^{-10}	-	1.3×10^{-12}	1.3×10^{0}
$\alpha = \{0, 3, 4\}$	1.4×10^{-8}	-	-	1.2×10^{-9}	3.8×10^{-10}	-	1.2×10^{-12}	-
$\alpha = \{2/3, 2, 3\}$	-	9.0×10^{-9}	3.2×10^{-9}	1.1×10^{-9}	-	4.6×10^{4}	-	1.3×10^{0}
$\alpha = \{2/3, 2, 4\}$	-	9.4×10^{-9}	3.3×10^{-9}	-	3.8×10^{-10}	4.9×10^{4}	1.3×10^{-12}	1.3×10^{0}
$\alpha = \{2/3, 3, 4\}$	-	9.5×10^{-9}	-	1.2×10^{-9}	3.8×10^{-10}	4.4×10^{4}	1.2×10^{-12}	-
$\alpha = \{2, 3, 4\}$	-	-	3.4×10^{-9}	1.2×10^{-9}	3.7×10^{-10}	-	1.3×10^{-12}	1.3×10^{0}
$\alpha = \{0, 2/3, 2, 3\}$	1.2×10^{-8}	7.8×10^{-9}	2.9×10^{-9}	1.1×10^{-9}	-	3.9×10^{4}	-	1.3×10^{0}
$\alpha = \{0, 2/3, 2, 4\}$	1.2×10^{-8}	8.2×10^{-9}	2.8×10^{-9}	-	3.7×10^{-10}	4.1×10^{4}	1.2×10^{-12}	1.3×10^{0}
$\alpha = \{0, 2/3, 3, 4\}$	1.2×10^{-8}	8.3×10^{-9}	-	1.1×10^{-9}	3.6×10^{-10}	3.9×10^{4}	1.2×10^{-12}	-
$\alpha = \{0, 2, 3, 4\}$	1.3×10^{-8}	-	2.9×10^{-9}	1.1×10^{-9}	3.6×10^{-10}	-	1.2×10^{-12}	1.3×10^{0}
$\alpha = \{2/3, 2, 3, 4\}$	-	8.7×10^{-9}	3.0×10^{-9}	1.1×10^{-9}	3.5×10^{-10}	4.4×10^{4}	1.2×10^{-12}	1.3×10^{0}
$\alpha = \{0, 2/3, 2, 3, 4\}$	1.1×10^{-8}	7.6×10^{-9}	2.8×10^{-9}	1.0×10^{-9}	3.4×10^{-10}	3.8×10^{4}	1.2×10^{-12}	1.3×10^{0}

Table 9.2: 95% Bayesian upper limits from the multi-components analysis in the 20-100 Hz band on $\Omega_\alpha^{95\%}$ (to the left of the vertical line) and the related astrophysical parameters $K_i^{95\%}$ (to the right of the vertical line) for the different combinations of the five spectral indices. Horizontal lines divide the table in regions where a fixed number of components is considered for the analysis. The constraints on $\Omega_\alpha^{95\%}$ have been obtained using uniform prior between 0 and $10^{-6.5}$. The constraints on $K_i^{95\%}$ have been obtained using log-uniform prior, see main text. $K_{\rm CBC}$ units are $M_\odot\,{\rm Gpc}^{-3}\,{\rm yr}^{-1}$, $K_{\rm r-modes}$ is dimensionless, and $K_{\rm magnetars}$ is expressed in ${\rm T}^{-1}$.

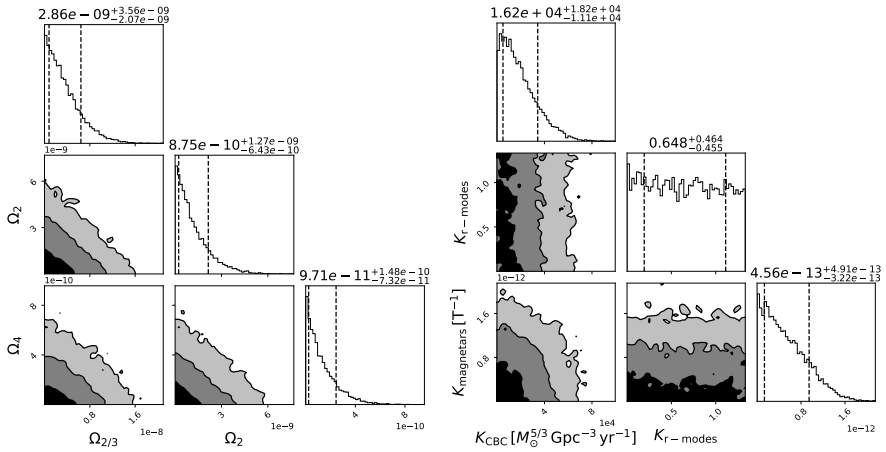

Figure 9.3: Results of the parameter estimation for the $\alpha = 2/3,\, 2,\, 4$ combination in the 20-100 Hz band for power-law Ω_α (left panel) and the corresponding astrophysical parameters (right panel). Contour plots show the 1σ, 2σ, and 3σ credible areas (black, grey, light grey, respectively). The dashed black lines in the histogram panels delimit the 1σ region of the estimated parameters.

9.4.2 Astrophysical parameters

The previous results for the Ω_α can be reinterpreted and translated into constraints on the ensemble properties of the SGWBs of interest, namely from CBCs ($\alpha = 2/3$), r-mode instabilities ($\alpha = 2$), and magnetars ($\alpha = 4$). This can be done in different ways. Suppose the SGWB consists of just one component, and just one ensemble property $\langle\theta^c\rangle$ characterises the background. In that case, it is possible to build an estimator $\widehat{\langle\theta^c\rangle}$ for such quantity (see [2, 3] as examples of this approach) and the associated likelihood to use to draw the Bayesian upper limits. Alternatively, suppose multiple components are present, each having more than one ensemble property. In that case, building the estimator for each property (fixed a component) is generally impossible. The solution is to change the models for Ω_α in the likelihood 9.3.10 with the ones in equation (9.3.11) when performing the parameter estimation or constraining the ensemble properties.

In this work, we have opted for the second approach. Given the absence of signal, we have been able only to constrain the ensemble properties for each component, namely $K_{\rm CBC}$, $K_{\rm r-modes}$, $K_{\rm magnetars}$. The corresponding 95% confidence Bayesian upper limits are reported in table 9.2. To obtain such constraints, we have used uniform priors, with $K_{\rm CBC} \in [0,\, 10^7]\, M_\odot^{5/3}\,{\rm Gpc}^{-3}\,{\rm yr}^{-1}$, $K_{\rm r-modes} \in [10^{-13},\, 4/3]$, and $K_{\rm magnetars} \in [0,\, 10^{-10}]\,{\rm T}^{-1}$, motivated by the limits derived in [247], [660], and [269], respectively. By inspection, we observe that the limits on $K_{\rm r-modes}$ and

[3]Note that, based on the discussion in [258], the choice of this frequency band may limit the search sensitivity for $\alpha > 2/3$, resulting in the upper limits being more conservative.

$K_{\rm magnetars}$ mildly depend on the number of components considered. In contrast, $K_{\rm CBC}$ limits oscillate more, with variations between 5%-25% with respect to the value inferred from the single-component analysis. The reference values that we quote as results of this work are the ones from the $\alpha = \{2/3,\, 2,\, 4\}$ combination, namely $K_{\rm CBC} \leq 4.9 \times 10^4 M_\odot^{5/3}\,{\rm Gpc}^{-3}\,{\rm yr}^{-1}$, $K_{\rm r-modes} \leq 1.3$, and $K_{\rm magnetars} \leq 1.3 \times 10^{-12}\,{\rm T}^{-1}$. The choice of not including $\alpha = 0,\, 3$ for these reference values comes from the injection study presented in the appendix 9.6, assuming only these three components are present or dominant. We examine each of these constraints individually to check whether they are strong enough to have relevant implications for astrophysical populations.

The CBC parameter $K_{\rm CBC}$ is actually a bound over the sum of the products $r_{0,\,j}\langle \mathcal{M}_c^{5/3}\rangle_j$ ($j = {\rm BBH,\, BNS,\, NSBH}$) involving the local rates and the average $5/3$ power of the chirp masses of the individual $\rm BBH,\ BNS,\ and\ NSBH$ populations. Its interpretation and comparison with the recent limits for the CBC population from the GWTC-3 catalogue [247] are not straightforward. This is a limit of the multi-component analysis under the assumption of power-law energy density spectra for $\Omega_{\rm gw}(f)$, which does not allow to remove the degeneracy between SGWBs having the same spectral indices but different ensemble parameters. Further studies about how to break such degeneracy will be the subject of future works, aiming to bring the multi-component analysis beyond the simple power-law assumption.

The r-mode-instability parameter $K_{\rm r-modes} = \langle (K+2)^{-1}\rangle$ can be approximately converted into a limit over $\langle K\rangle$ by taking its inverse and subtracting 2. Doing this for the present upper limit leads to a lower limit for $\langle K\rangle \gtrsim -1.23$. This value is right above $-5/4$, the minimal value that K can assume according to [660] and corresponds to the maximum value of $\Omega_{\rm gw,\,r-modes}$. This limit reflects that not all r-mode instabilities happen with this extreme value for K, usually assumed when doing estimates of the intensity of this kind of SGWB, but does not exclude that individual events in that configuration from happening. Still, the weakness of the constraint does not allow to draw major implications for these phenomena, where uncertainties still dominate many parameters.

The magnetar parameter $K_{\rm magnetars} = \sqrt{\langle \varepsilon^2\rangle\ \langle B^{-2}\rangle}$ suffers from the degeneracy between the average square ellipticity and the average (inverse) square of the (poloidal) magnetic field of the magnetar population. If the magnetar population had an average magnetic field around 10^{10} (10^{11}) T, the corresponding limits on (the square root of the) average (squared) ellipticity would be $\varepsilon \leq 1.3 \times 10^{-2}$ (10^{-1}). Following equations (13) and (14) from [269], this, in turn, would imply the limits on the distortion parameter $\beta \leq 3.5 \times 10^5$ (10^4) for a poloidal-dominated field configuration and the dimensionless parameter $k \leq 1.3 \times 10^6$ (10^5) for a twisted-toroidal field configuration (assuming $\lambda_{\rm magnetars} = 9 \times 10^{-4}\,M_\odot$). However, these constraints are not informative and, together with the other astrophysical uncertainties in the magnetar population, do not allow to draw further implications for the geometry of individual magnetars or on the equation of state of the magnetar population.

9.5 Conclusions

In this work, we have performed a search for a Gaussian, stationary, unpolarised, isotropic stochastic gravitational-wave background with a power-law spectrum in energy density, relaxing the assumption that only one component can be present at a time. We have performed such a search assuming different SGWBs to be present at a time, with spectral indices $\alpha = \{0,\ 2/3,\ 2,\ 3,\ 4\}$ and for all possible combinations, in a 20-100 Hz frequency band. Then, we have inferred the implications for astrophysical SGWBs from compact binary coalescences, young-pulsar r-mode instabilities, and magnetars, corresponding to the spectral indices $\alpha = \{2/3,\ 2,\ 4\}$.

The analysis has not shown evidence of any SGWB, so we have set upper limits on Ω_α at 25-Hz reference frequency for every α combination. We recover the limits from [258] in the single-index case when performing the analysis in the 20-1726 Hz range. When multiple components are present, the limits become more stringent. The derivation of the implications for the ensemble properties of the astrophysical SGWB from CBCs, r-mode instabilities, and magnetars results in constraints over $K_{\rm CBC}$, $K_{\rm r-modes}$, and $K_{\rm magnetars}$, respectively. The bounds are not informative in the case of r-modes and are not competitive with the existing ones in the case of CBCs and magnetars. This fact is further reflected by their mild oscillations in value when considering different α combinations.

The results obtained in this paper may not include additional information compared to the existing ones in the literature, given the weakness of the SGWB components in the data. However, as shown and discussed in the injection study in appendix 9.6, the method employed here will be fundamental to avoid bias and overestimation of the components when getting closer to a detection. The same injection study also highlights the necessity of generalising this method to the case where the SGWB cannot be described by a simple power law and, consequently, introduces bias in the search presented in this work if the signal is strong enough to generate a power excess in the data or be detected. This will allow us to avoid limits on the frequency range used in the search where the power-law regime is no longer applicable. In addition to that, adapting this method to any frequency dependence will also allow us to easily employ it for directional and targeted searches, even in the case where match filtering for the SGWB of interest is used (see, for example, [446]). We reserve such generalisations for future works.

9.6 Appendix: Injection study on O3 data

To test the multi-component search method, we have performed a series of different injections in the O3 data in the frequency domain. This has allowed us to better understand how to interpret the results of the multi-component analysis, compare them with the single-component ones, and test the limit of this formalism for determining the ensemble properties of an SGWB with a frequency-power-law energy density spectrum.

9.6.1 Power-law injections

The first set of injections we present and discuss reproduces a scenario where several components are present, are sufficiently intense to be detectable, and have all the same intensity, for simplicity reasons. The injected signals are characterised by $\{\Omega_\alpha = 1 \times 10^{-6},\, \alpha = 0, 2/3, 2, 3, 4\}$ at 25 Hz, and the analysis is performed in the 20-1726 Hz band. The choice of this broad frequency range allows a better sensitivity of the search for higher α (the O3 public data sets [485] are also available in this range). The results for all possible α combinations in terms of estimators Ω_α and parameter estimation (PE) are summarised in tables 9.3 and 9.4, respectively. The PE results, together with the injected values and the resulting estimators, for the multi-component analysis of the five indices are illustrated in figure 9.4.

We observe that, for any combination, estimators and PE results in tables 9.3 and 9.4 make clear that there are excesses associated with a signal. However, only the combination considering all five indexes does recover the injection correctly, within 1-sigma uncertainty, while the other combinations lead to heavily biased results. In addition to this, by looking at figure 9.4, it is possible to notice the presence of correlation between two different spectral indices in the contour plots, which may lead to degeneracy or bias in the recovery when the signals are not sufficiently intense and/or distant enough in the spectral-index space. Similar results hold for detectable injections where the intensities of the injected Ω_α differ for every α, even by orders of magnitude.

9.6.2 Astrophysical injections

The second set of injections we consider mimics a scenario where the $\Omega_{\mathrm{gw},\,i}(f)$ ($i = 1, 2, \ldots, \mathrm{N_{components}}$) are no longer a power-law in the full search frequency band 20-1726 Hz, as in the case of the astrophysical SGWBs described in section 9.2. In addition to that, the overall intensity of the $\Omega_{\mathrm{gw},\,i}(f)$ is related to the choice of the ensemble properties of the SGWB families that we aim to constrain using the results from the multi-component analysis. In this injection data set, we have injected $\Omega_{\mathrm{gw},\,i}(f)$, with i = BNS, r-modes, magnetars, with population properties $K_{\mathrm{BNS}} \simeq 7.91 \times 10^5\,\mathrm{M}_\odot^{5/3}\,\mathrm{Gpc}^{-3}\,\mathrm{yr}^{-1}$, $K_{\mathrm{r-modes}} = 1 \times 10^3$, and $K_{\mathrm{magnetars}} = 1 \times 10^{-11}$, implying $\Omega_{\mathrm{ref,\,BNS}} \simeq 2.12 \times 10^{-7}$, $\Omega_{\mathrm{ref,\,r-modes}} \simeq 1.69 \times 10^{-7}$, and $\Omega_{\mathrm{ref,\,magnetars}} \simeq 1.79 \times 10^{-8}$, respectively. We have analysed the data set using the same spectral indices as in the main text, namely $\alpha = 0,\, 2/3,\, 2,\, 3,\, 4$, to evaluate the impact of searching for more components than the observable ones in a detection scenario. The results of the injection study are summarised in tables 9.5 and 9.6, containing the estimators for the Ω_α, and the PE results for the ensemble properties.

Unlike the pure power-law case, we cannot use the 20-1726 Hz band to analyse this data set. The $\Omega_{\mathrm{gw},\,i}(f)$ spectra are no longer power-law only in this range, leading

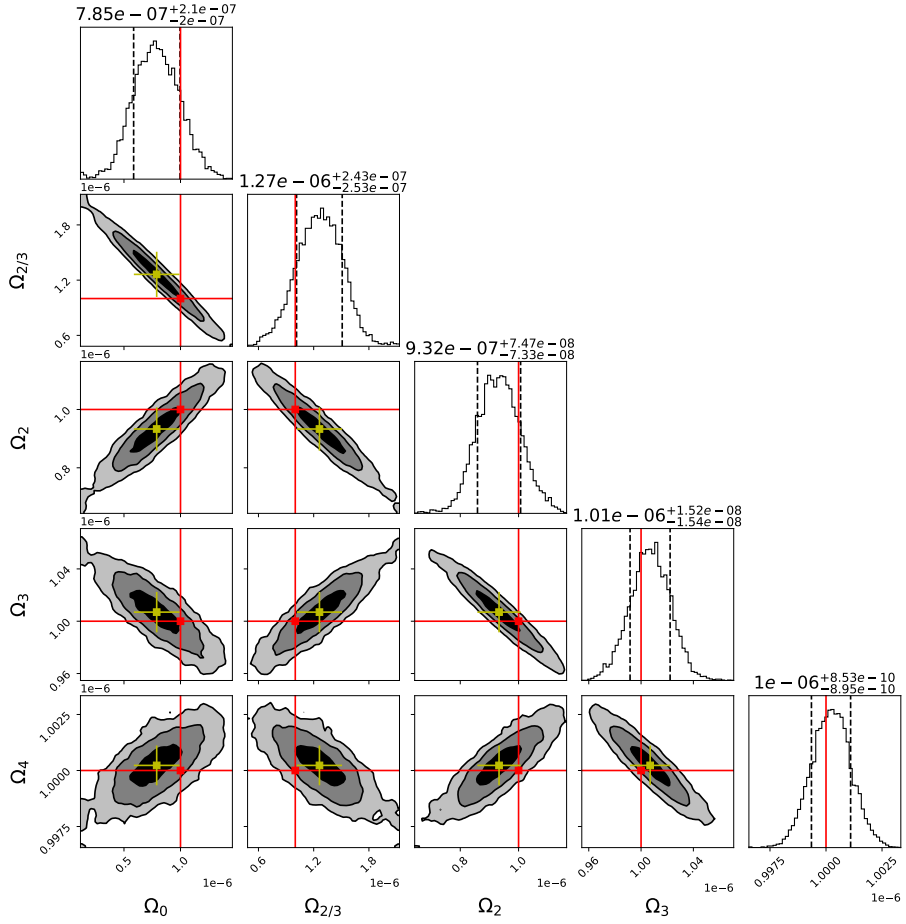

Figure 9.4: Parameter estimation results for the set of the power-law injections in the 20-1726 Hz frequency range, with $\Omega_\alpha = 1 \times 10^{-6}$, $\alpha = 0, 2/3, 2, 3, 4$. Contour plots show the 1σ, 2σ, and 3σ credible areas (black, grey, light grey, respectively). The red lines denote the injected values, while the yellow error bars represent the 1σ uncertainty of the Ω_α estimators form the joint analysis. The dashed black lines in the histogram panels delimit the 1σ region of the estimated parameters.

	$\hat{\Omega}_0 = 1 \times 10^{-6}$	$\hat{\Omega}_{2/3} = 1 \times 10^{-6}$	$\hat{\Omega}_2 = 1 \times 10^{-6}$	$\hat{\Omega}_3 = 1 \times 10^{-6}$	$\hat{\Omega}_4 = 1 \times 10^{-6}$
$\alpha = \{0\}$	$(1.9421 \pm 0.0008) \times 10^{-5}$	-	-	-	-
$\alpha = \{2/3\}$	-	$(1.8066 \pm 0.0006) \times 10^{-5}$	-	-	-
$\alpha = \{2\}$	-	-	$(1.2517 \pm 0.0002) \times 10^{-5}$	-	-
$\alpha = \{3\}$	-	-	-	$(5.6644 \pm 0.0008) \times 10^{-6}$	-
$\alpha = \{4\}$	-	-	-	-	$(1.2263 \pm 0.0002) \times 10^{-6}$
$\alpha = \{0, 2/3\}$	$(-1.5616 \pm 0.0004) \times 10^{-4}$	$(1.3272 \pm 0.0003) \times 10^{-4}$	-	-	-
$\alpha = \{0, 2\}$	$(-3.593 \pm 0.001) \times 10^{-5}$	-	$(2.1759 \pm 0.0004) \times 10^{-5}$	-	-
$\alpha = \{0, 3\}$	$(-9.51 \pm 0.009) \times 10^{-6}$	-	-	$(6.204 \pm 0.001) \times 10^{-6}$	-
$\alpha = \{0, 4\}$	$(7.666 \pm 0.008) \times 10^{-6}$	-	-	-	$(1.1887 \pm 0.0002) \times 10^{-6}$
$\alpha = \{2/3, 2\}$	-	$(-3.873 \pm 0.001) \times 10^{-5}$	$(2.7233 \pm 0.0005) \times 10^{-5}$	-	-
$\alpha = \{2/3, 3\}$	-	$(-9.223 \pm 0.007) \times 10^{-6}$	-	$(6.512 \pm 0.001) \times 10^{-6}$	-
$\alpha = \{2/3, 4\}$	-	$(6.305 \pm 0.006) \times 10^{-6}$	-	-	$(1.1696 \pm 0.0002) \times 10^{-6}$
$\alpha = \{2, 3\}$	-	-	$(-9.975 \pm 0.005) \times 10^{-6}$	$(8.75 \pm 0.002) \times 10^{-6}$	-
$\alpha = \{2, 4\}$	-	-	$(3.518 \pm 0.003) \times 10^{-6}$	-	$(1.0828 \pm 0.0002) \times 10^{-6}$
$\alpha = \{3, 4\}$	-	-	-	$(1.817 \pm 0.002) \times 10^{-6}$	$(9.146 \pm 0.003) \times 10^{-7}$
$\alpha = \{0, 2/3, 2\}$	$(2.2532 \pm 0.001) \times 10^{-4}$	$(-2.5342 \pm 0.0009) \times 10^{-4}$	$(5.085 \pm 0.001) \times 10^{-5}$	-	-
$\alpha = \{0, 2/3, 3\}$	$(9.423 \pm 0.007) \times 10^{-5}$	$(-8.528 \pm 0.005) \times 10^{-5}$	-	$(8.154 \pm 0.002) \times 10^{-6}$	-
$\alpha = \{0, 2/3, 4\}$	$(-2.181 \pm 0.005) \times 10^{-5}$	$(2.273 \pm 0.004) \times 10^{-5}$	-	-	$(1.129 \pm 0.0002) \times 10^{-6}$
$\alpha = \{0, 2, 3\}$	$(2.921 \pm 0.002) \times 10^{-5}$	-	$(-2.585 \pm 0.001) \times 10^{-5}$	$(1.2004 \pm 0.0003) \times 10^{-5}$	-
$\alpha = \{0, 2, 4\}$	$(-9.5 \pm 0.2) \times 10^{-7}$	-	$(3.828 \pm 0.006) \times 10^{-6}$	-	$(1.0748 \pm 0.0002) \times 10^{-6}$
$\alpha = \{0, 3, 4\}$	$(3.361 \pm 0.01) \times 10^{-6}$	-	-	$(1.381 \pm 0.002) \times 10^{-6}$	$(9.729 \pm 0.004) \times 10^{-7}$
$\alpha = \{2/3, 2, 3\}$	-	$(3.607 \pm 0.002) \times 10^{-5}$	$(-3.529 \pm 0.002) \times 10^{-5}$	$(1.3266 \pm 0.0003) \times 10^{-5}$	-
$\alpha = \{2/3, 2, 4\}$	-	$(-1.17 \pm 0.02) \times 10^{-6}$	$(4.06 \pm 0.008) \times 10^{-6}$	-	$(1.0713 \pm 0.0003) \times 10^{-6}$
$\alpha = \{2/3, 3, 4\}$	-	$(2.917 \pm 0.009) \times 10^{-6}$	-	$(1.25 \pm 0.002) \times 10^{-6}$	$(9.856 \pm 0.004) \times 10^{-7}$
$\alpha = \{2, 3, 4\}$	-	-	$(2.611 \pm 0.008) \times 10^{-6}$	$(5.24 \pm 0.04) \times 10^{-7}$	$(1.0299 \pm 0.0005) \times 10^{-6}$
$\alpha = \{0, 2/3, 2, 3\}$	$(-1.528 \pm 0.001) \times 10^{-4}$	$(2.048 \pm 0.002) \times 10^{-4}$	$(-7.069 \pm 0.004) \times 10^{-5}$	$(1.738 \pm 0.0005) \times 10^{-5}$	-
$\alpha = \{0, 2/3, 2, 4\}$	$(1.17 \pm 0.01) \times 10^{-5}$	$(-1.29 \pm 0.01) \times 10^{-5}$	$(5.64 \pm 0.02) \times 10^{-6}$	-	$(1.0547 \pm 0.0003) \times 10^{-6}$
$\alpha = \{0, 2/3, 3, 4\}$	$(-1.55 \pm 0.08) \times 10^{-6}$	$(4.23 \pm 0.07) \times 10^{-6}$	-	$(1.196 \pm 0.004) \times 10^{-6}$	$(9.907 \pm 0.005) \times 10^{-7}$
$\alpha = \{0, 2, 3, 4\}$	$(1.82 \pm 0.03) \times 10^{-6}$	-	$(1.3 \pm 0.02) \times 10^{-6}$	$(9.37 \pm 0.07) \times 10^{-7}$	$(1.0036 \pm 0.0006) \times 10^{-6}$
$\alpha = \{2/3, 2, 3, 4\}$	-	$(2.21 \pm 0.03) \times 10^{-6}$	$(6.7 \pm 0.3) \times 10^{-7}$	$(1.057 \pm 0.009) \times 10^{-6}$	$(9.979 \pm 0.007) \times 10^{-7}$
$\alpha = \{0, 2/3, 2, 3, 4\}$	$(7.9 \pm 2.0) \times 10^{-7}$	$(1.3 \pm 0.2) \times 10^{-6}$	$(9.3 \pm 0.7) \times 10^{-7}$	$(1.01 \pm 0.02) \times 10^{-6}$	$(1.0002 \pm 0.0009) \times 10^{-6}$

Table 9.3: Estimators from the multi-components analysis in the 20-1726 Hz band for the different combinations of the five spectral indices for power-law injection data set, with $\Omega_\alpha = 10^{-6}$. Horizontal lines divide the table in regions where a fixed number of components is considered for the analysis.

	$\Omega_0 = 1 \times 10^{-6}$	$\Omega_{2/3} = 1 \times 10^{-6}$	$\Omega_2 = 1 \times 10^{-6}$	$\Omega_3 = 1 \times 10^{-6}$	$\Omega_4 = 1 \times 10^{-6}$
$\alpha = \{0\}$	$\left(9.999996^{+3e-06}_{-7e-06}\right) \times 10^{-6}$	-	-	-	-
$\alpha = \{2/3\}$	-	$\left(9.999997^{+2e-06}_{-4e-06}\right) \times 10^{-6}$	-	-	-
$\alpha = \{2\}$	-	-	$\left(9.999998^{+1e-06}_{-3e-06}\right) \times 10^{-6}$	-	-
$\alpha = \{3\}$	-	-	-	$\left(5.6644^{+0.0009}_{-0.0008}\right) \times 10^{-6}$	-
$\alpha = \{4\}$	-	-	-	-	$\left(1.2263^{+0.0002}_{-0.0002}\right) \times 10^{-6}$
$\alpha = \{0, 2/3\}$	$\left(6.191^{+0.008}_{-0.008}\right) \times 10^{-6}$	$\left(9.999994^{+5e-06}_{-1e-05}\right) \times 10^{-6}$	-	-	-
$\alpha = \{0, 2\}$	$\left(1.00006^{+0.00011}_{-5e-05}\right) \times 10^{-7}$	-	$\left(9.999998^{+1e-06}_{-3e-06}\right) \times 10^{-6}$	-	-
$\alpha = \{0, 3\}$	$\left(1.00006^{+0.0001}_{-4e-05}\right) \times 10^{-7}$	-	-	$\left(5.6587^{+0.0008}_{-0.0008}\right) \times 10^{-6}$	-
$\alpha = \{0, 4\}$	$\left(7.665^{+0.008}_{-0.007}\right) \times 10^{-6}$	-	-	-	$\left(1.1887^{+0.0002}_{-0.0002}\right) \times 10^{-6}$
$\alpha = \{2/3, 2\}$	-	$\left(1.00007^{+0.00012}_{-6e-05}\right) \times 10^{-7}$	$\left(9.999998^{+1e-06}_{-3e-06}\right) \times 10^{-6}$	-	-
$\alpha = \{2/3, 3\}$	-	$\left(1.00004^{+7e-05}_{-3e-05}\right) \times 10^{-7}$	-	$\left(5.6552^{+0.0008}_{-0.0008}\right) \times 10^{-6}$	-
$\alpha = \{2/3, 4\}$	-	$\left(6.305^{+0.006}_{-0.006}\right) \times 10^{-6}$	-	-	$\left(1.1696^{+0.0002}_{-0.0002}\right) \times 10^{-6}$
$\alpha = \{2, 3\}$	-	-	$\left(1.00002^{+3e-05}_{-1e-05}\right) \times 10^{-7}$	$\left(5.6335^{+0.0008}_{-0.0008}\right) \times 10^{-6}$	-
$\alpha = \{2, 4\}$	-	-	$\left(3.518^{+0.003}_{-0.003}\right) \times 10^{-6}$	-	$\left(1.0828^{+0.0002}_{-0.0002}\right) \times 10^{-6}$
$\alpha = \{3, 4\}$	-	-	-	$\left(1.817^{+0.002}_{-0.002}\right) \times 10^{-6}$	$\left(9.146^{+0.003}_{-0.003}\right) \times 10^{-7}$
$\alpha = \{0, 2/3, 2\}$	$\left(1.00006^{+0.0001}_{-5e-05}\right) \times 10^{-7}$	$\left(1.00007^{+0.00012}_{-5e-05}\right) \times 10^{-7}$	$\left(9.999998^{+1e-06}_{-3e-06}\right) \times 10^{-6}$	-	-
$\alpha = \{0, 2/3, 3\}$	$\left(1.00006^{+9e-05}_{-4e-05}\right) \times 10^{-7}$	$\left(1.00004^{+6e-05}_{-3e-05}\right) \times 10^{-7}$	-	$\left(5.6496^{+0.0008}_{-0.0008}\right) \times 10^{-6}$	-
$\alpha = \{0, 2/3, 4\}$	$\left(5.0^{+0.2}_{-0.3}\right) \times 10^{-6}$	$\left(9.9999903^{+1.74e-06}_{-1e-08}\right) \times 10^{-6}$	-	-	$\left(1.112^{+0.001}_{-0.926}\right) \times 10^{-6}$
$\alpha = \{0, 2, 3\}$	$\left(1.00006^{+9e-05}_{-4e-05}\right) \times 10^{-7}$	-	$\left(1.00002^{+3e-05}_{-1e-05}\right) \times 10^{-7}$	$\left(5.6278^{+0.0008}_{-0.0008}\right) \times 10^{-6}$	-
$\alpha = \{0, 2, 4\}$	$\left(1.0001338^{+4e-07}_{-2e-07}\right) \times 10^{-7}$	-	$\left(9.99996647^{+5e-08}_{-3e-08}\right) \times 10^{-6}$	-	$\left(8.179^{+0.002}_{-0.002}\right) \times 10^{-7}$
$\alpha = \{0, 3, 4\}$	$\left(3.361^{+0.01}_{-0.01}\right) \times 10^{-6}$	-	-	$\left(1.381^{+0.002}_{-0.002}\right) \times 10^{-6}$	$\left(9.729^{+0.004}_{-0.004}\right) \times 10^{-7}$
$\alpha = \{2/3, 2, 3\}$	-	$\left(1.00004^{+6e-05}_{-3e-05}\right) \times 10^{-7}$	$\left(1.00002^{+3e-05}_{-1e-05}\right) \times 10^{-7}$	$\left(5.6243^{+0.0008}_{-0.0008}\right) \times 10^{-6}$	-
$\alpha = \{2/3, 2, 4\}$	-	$\left(1.0118^{+3e-05}_{-2e-05}\right) \times 10^{-7}$	$\left(9.99815^{+4e-06}_{-2e-06}\right) \times 10^{-6}$	-	$\left(8.176^{+0.002}_{-0.002}\right) \times 10^{-7}$
$\alpha = \{2/3, 3, 4\}$	-	$\left(2.917^{+0.008}_{-0.008}\right) \times 10^{-6}$	-	$\left(1.25^{+0.002}_{-0.002}\right) \times 10^{-6}$	$\left(9.856^{+0.004}_{-0.004}\right) \times 10^{-7}$
$\alpha = \{2, 3, 4\}$	-	-	$\left(2.611^{+0.008}_{-0.007}\right) \times 10^{-6}$	$\left(5.24^{+0.04}_{-0.04}\right) \times 10^{-7}$	$\left(1.0299^{+0.0005}_{-0.0005}\right) \times 10^{-6}$
$\alpha = \{0, 2/3, 2, 3\}$	$\left(1.00005^{+9e-05}_{-4e-05}\right) \times 10^{-7}$	$\left(1.00004^{+6e-05}_{-3e-05}\right) \times 10^{-7}$	$\left(1.00002^{+3e-05}_{-1e-05}\right) \times 10^{-7}$	$\left(5.6186^{+0.0008}_{-0.0008}\right) \times 10^{-6}$	-
$\alpha = \{0, 2/3, 2, 4\}$	$\left(1.0013^{+0.0022}_{-0.001}\right) \times 10^{-7}$	$\left(1.0011^{+0.002}_{-0.0008}\right) \times 10^{-7}$	$\left(3.439^{+0.003}_{-0.003}\right) \times 10^{-6}$	-	$\left(1.0846^{+0.0002}_{-0.0002}\right) \times 10^{-6}$
$\alpha = \{0, 2/3, 3, 4\}$	$\left(1.03^{+0.04}_{-0.02}\right) \times 10^{-7}$	$\left(2.829^{+0.009}_{-0.009}\right) \times 10^{-6}$	-	$\left(1.253^{+0.002}_{-0.002}\right) \times 10^{-6}$	$\left(9.853^{+0.004}_{-0.004}\right) \times 10^{-7}$
$\alpha = \{0, 2, 3, 4\}$	$\left(1.82^{+0.03}_{-0.03}\right) \times 10^{-6}$	-	$\left(1.3^{+0.02}_{-0.02}\right) \times 10^{-6}$	$\left(9.37^{+0.07}_{-0.07}\right) \times 10^{-7}$	$\left(1.0036^{+0.0006}_{-0.0006}\right) \times 10^{-6}$
$\alpha = \{2/3, 2, 3, 4\}$	-	$\left(2.21^{+0.03}_{-0.03}\right) \times 10^{-6}$	$\left(6.7^{+0.3}_{-0.3}\right) \times 10^{-7}$	$\left(1.056^{+0.009}_{-0.008}\right) \times 10^{-6}$	$\left(9.979^{+0.006}_{-0.007}\right) \times 10^{-7}$
$\alpha = \{0, 2/3, 2, 3, 4\}$	$\left(7.9^{+2.1}_{-2.0}\right) \times 10^{-7}$	$\left(1.3^{+0.2}_{-0.3}\right) \times 10^{-6}$	$\left(9.3^{+0.7}_{-0.7}\right) \times 10^{-7}$	$\left(1.01^{+0.02}_{-0.02}\right) \times 10^{-6}$	$\left(1.0002^{+0.0009}_{-0.0009}\right) \times 10^{-6}$

Table 9.4: Parameter estimation results from the multi-components analysis in the 20-1726 Hz band for the different combinations of the five spectral indices for power-law injection data set, with $\Omega_\alpha = 10^{-6}$. Horizontal lines divide the table in regions where a fixed number of components is considered for the analysis.

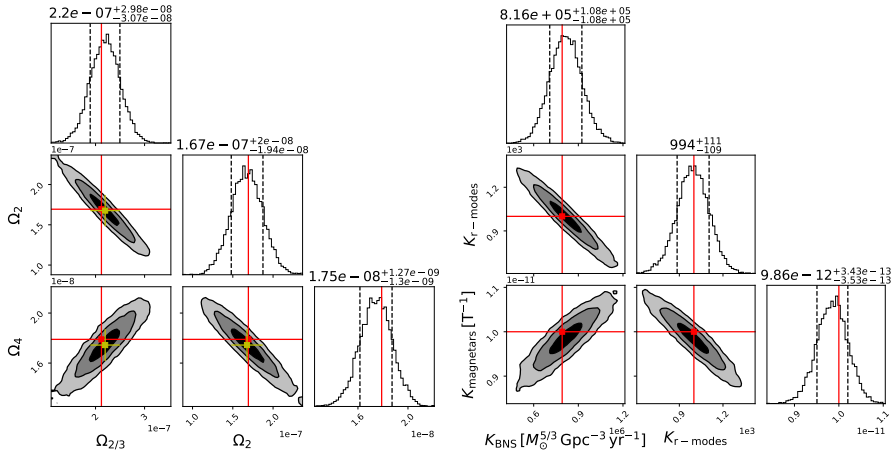

Figure 9.5: Results of the parameter estimation for the $\alpha = 2/3,\ 2,\ 4$ combination in the 20-100 Hz band for the astrophysical injection for BNS, r-modes, and magnetars SGWBs. The left panel shows the recovery of the Ω_α, while the right panel the injected ensemble parameters. Contour plots show the 1σ, 2σ, and 3σ credible areas (black, grey, light grey, respectively). The red lines denote the injected values, while the yellow error bars represent the 1σ uncertainty of the Ω_α estimators form the joint analysis. The dashed black lines in the histogram panels delimit the 1σ region of the estimated parameters.

to the failure in recovering the injected parameters for every combination of spectral indices. To choose the upper bound in the frequencies to employ in the analysis of this data set, we have made a compromise between the (non-)power-law behaviour of the injected signals in the band and the best recovery of the injected parameters. This resulted in the choice of $20 - 100$ Hz, which we have also used for the analysis in the main text.

The results leading to the recovery of the signal and of the injected ensemble parameters have been those associated with performing the multi-component analysis for the set of spectral indices equal to the injected ones (as expected), namely $\alpha = 2/3,\ 2,\ 4$, and are illustrated in figure 9.5. The injection recovery has failed whenever an incorrect number of indices or extra indices were used, leading either to biased signals or even fake recoveries associated with power laws that were not present in the data set.

	$\hat{\Omega}_0$	$\hat{\Omega}_{2/3} = 2.1 \times 10^{-7}$	$\hat{\Omega}_2 = 1.7 \times 10^{-7}$	$\hat{\Omega}_3$	$\hat{\Omega}_4 = 1.8 \times 10^{-8}$
$\alpha = \{0\}$	$(8.68 \pm 0.08) \times 10^{-7}$	-	-	-	-
$\alpha = \{2/3\}$	-	$(7.12 \pm 0.06) \times 10^{-7}$	-	-	-
$\alpha = \{2\}$	-	-	$(3.61 \pm 0.03) \times 10^{-7}$	-	-
$\alpha = \{3\}$	-	-	-	$(1.44 \pm 0.01) \times 10^{-7}$	-
$\alpha = \{4\}$	-	-	-	-	$(4.28 \pm 0.03) \times 10^{-8}$
$\alpha = \{0, 2/3\}$	$(-2.67 \pm 0.05) \times 10^{-6}$	$(2.68 \pm 0.03) \times 10^{-6}$	-	-	-
$\alpha = \{0, 2\}$	$(-1.3 \pm 0.1) \times 10^{-7}$	-	$(3.96 \pm 0.05) \times 10^{-7}$	-	-
$\alpha = \{0, 3\}$	$(3.55 \pm 0.1) \times 10^{-7}$	-	-	$(1.14 \pm 0.01) \times 10^{-7}$	-
$\alpha = \{0, 4\}$	$(5.79 \pm 0.08) \times 10^{-7}$	-	-	-	$(3.21 \pm 0.04) \times 10^{-8}$
$\alpha = \{2/3, 2\}$	-	$(-1.5 \pm 0.1) \times 10^{-7}$	$(4.21 \pm 0.06) \times 10^{-7}$	-	-
$\alpha = \{2/3, 3\}$	-	$(3.03 \pm 0.08) \times 10^{-7}$	-	$(1.04 \pm 0.01) \times 10^{-7}$	-
$\alpha = \{2/3, 4\}$	-	$(4.73 \pm 0.07) \times 10^{-7}$	-	-	$(2.79 \pm 0.04) \times 10^{-8}$
$\alpha = \{2, 3\}$	-	-	$(2.61 \pm 0.07) \times 10^{-7}$	$(4.4 \pm 0.3) \times 10^{-8}$	-
$\alpha = \{2, 4\}$	-	-	$(3.06 \pm 0.04) \times 10^{-7}$	-	$(9.2 \pm 0.6) \times 10^{-9}$
$\alpha = \{3, 4\}$	-	-	-	$(2.62 \pm 0.04) \times 10^{-7}$	$(-4.1 \pm 0.1) \times 10^{-8}$
$\alpha = \{0, 2/3, 2\}$	$(1.4 \pm 0.1) \times 10^{-6}$	$(-1.5 \pm 0.1) \times 10^{-6}$	$(5.9 \pm 0.2) \times 10^{-7}$	-	-
$\alpha = \{0, 2/3, 3\}$	$(4.4 \pm 8.3) \times 10^{-8}$	$(2.7 \pm 0.7) \times 10^{-7}$	-	$(1.05 \pm 0.03) \times 10^{-7}$	-
$\alpha = \{0, 2/3, 4\}$	$(-6.0 \pm 0.7) \times 10^{-7}$	$(9.5 \pm 0.6) \times 10^{-7}$	-	-	$(2.4 \pm 0.06) \times 10^{-8}$
$\alpha = \{0, 2, 3\}$	$(2.6 \pm 0.3) \times 10^{-7}$	-	$(7.6 \pm 2.3) \times 10^{-8}$	$(9.3 \pm 0.6) \times 10^{-8}$	-
$\alpha = \{0, 2, 4\}$	$(1.8 \pm 0.2) \times 10^{-7}$	-	$(2.2 \pm 0.1) \times 10^{-7}$	-	$(1.5 \pm 0.1) \times 10^{-8}$
$\alpha = \{0, 3, 4\}$	$(3.2 \pm 0.2) \times 10^{-7}$	-	-	$(1.35 \pm 0.08) \times 10^{-7}$	$(-6.1 \pm 2.3) \times 10^{-9}$
$\alpha = \{2/3, 2, 3\}$	-	$(3.4 \pm 0.4) \times 10^{-7}$	$(-3.8 \pm 3.4) \times 10^{-8}$	$(1.13 \pm 0.08) \times 10^{-7}$	-
$\alpha = \{2/3, 2, 4\}$	-	$(2.2 \pm 0.3) \times 10^{-7}$	$(1.7 \pm 0.2) \times 10^{-7}$	-	$(1.7 \pm 0.1) \times 10^{-8}$
$\alpha = \{2/3, 3, 4\}$	-	$(3.3 \pm 0.2) \times 10^{-7}$	-	$(8.8 \pm 1.0) \times 10^{-8}$	$(4.4 \pm 2.8) \times 10^{-9}$
$\alpha = \{2, 3, 4\}$	-	-	$(5.0 \pm 0.3) \times 10^{-7}$	$(-1.8 \pm 0.2) \times 10^{-7}$	$(4.4 \pm 0.5) \times 10^{-8}$
$\alpha = \{0, 2/3, 2, 3\}$	$(-8.0 \pm 3.5) \times 10^{-7}$	$(1.4 \pm 0.5) \times 10^{-6}$	$(-3.6 \pm 1.5) \times 10^{-7}$	$(1.7 \pm 0.3) \times 10^{-7}$	-
$\alpha = \{0, 2/3, 2, 4\}$	$(-2.4 \pm 2.7) \times 10^{-7}$	$(5.1 \pm 3.3) \times 10^{-7}$	$(1.0 \pm 0.8) \times 10^{-7}$	-	$(2.0 \pm 0.3) \times 10^{-8}$
$\alpha = \{0, 2/3, 3, 4\}$	$(-3.6 \pm 1.8) \times 10^{-7}$	$(7.0 \pm 1.9) \times 10^{-7}$	-	$(3.8 \pm 2.8) \times 10^{-8}$	$(1.5 \pm 0.6) \times 10^{-8}$
$\alpha = \{0, 2, 3, 4\}$	$(9.9 \pm 6.3) \times 10^{-8}$	-	$(3.5 \pm 1.0) \times 10^{-7}$	$(-8.6 \pm 6.2) \times 10^{-8}$	$(2.9 \pm 1.0) \times 10^{-8}$
$\alpha = \{2/3, 2, 3, 4\}$	-	$(1.6 \pm 1.0) \times 10^{-7}$	$(2.7 \pm 1.5) \times 10^{-7}$	$(-5.4 \pm 7.8) \times 10^{-8}$	$(2.6 \pm 1.2) \times 10^{-8}$
$\alpha = \{0, 2/3, 2, 3, 4\}$	$(-6.9 \pm 8.9) \times 10^{-7}$	$(1.2 \pm 1.4) \times 10^{-6}$	$(-2.6 \pm 7.1) \times 10^{-7}$	$(1.3 \pm 2.6) \times 10^{-7}$	$(4.3 \pm 30.3) \times 10^{-9}$

Table 9.5: Estimators from the multi-components analysis in the 20-100 Hz band for the different combinations of the five spectral indices for BNS, r-mode, and magnetar SGWB injection data set, with injected parameters $K_{\rm CBC} = 7.91 \times 10^5\, M_\odot\, {\rm Gpc}^{-3}\, {\rm yr}^{-1}$, $K_{\rm r-modes} = 1 \times 10^3$, and $K_{\rm magnetars} = 1 \times 10^{-11}\, {\rm T}^{-1}$. Horizontal lines divide the table in regions where a fixed number of components is considered for the analysis.

	Ω_0	Ω_3	$K_{\rm BNS} = 7.9 \times 10^5\, M_\odot^{5/3}\,{\rm Gpc}^{-3}\,{\rm yr}^{-1}$	$K_{\rm r-modes} = 1 \times 10^3$	$K_{\rm magnetars} = 1 \times 10^{-11}\,{\rm T}^{-1}$
$\alpha = \{0\}$	$\left(8.68^{+0.08}_{-0.08}\right) \times 10^{-7}$	-	-	-	-
$\alpha = \{2/3\}$	-	-	$\left(2.66^{+0.02}_{-0.02}\right) \times 10^6$	-	-
$\alpha = \{2\}$	-	-	-	$\left(2.13^{+0.01}_{-0.01}\right) \times 10^3$	-
$\alpha = \{3\}$	-	$\left(1.44^{+0.01}_{-0.01}\right) \times 10^{-7}$	-	-	-
$\alpha = \{4\}$	-	-	-	-	$\left(1.546^{+0.006}_{-0.006}\right) \times 10^{-11}$
$\alpha = \{0, 2/3\}$	$\left(5.4^{+9.2}_{-4.2}\right) \times 10^{-10}$	-	$\left(2.65^{+0.02}_{-0.02}\right) \times 10^6$	-	-
$\alpha = \{0, 2\}$	$\left(9.9^{+16.6}_{-7.4}\right) \times 10^{-10}$	-	-	$\left(2.13^{+0.01}_{-0.01}\right) \times 10^3$	-
$\alpha = \{0, 3\}$	$\left(3.55^{+0.1}_{-0.1}\right) \times 10^{-7}$	$\left(1.14^{+0.01}_{-0.01}\right) \times 10^{-7}$	-	-	-
$\alpha = \{0, 4\}$	$\left(5.79^{+0.08}_{-0.08}\right) \times 10^{-7}$	-	-	-	$\left(1.339^{+0.008}_{-0.008}\right) \times 10^{-11}$
$\alpha = \{2/3, 2\}$	-	-	$\left(3.2^{+5.2}_{-2.4}\right) \times 10^3$	$\left(2.13^{+0.01}_{-0.01}\right) \times 10^3$	-
$\alpha = \{2/3, 3\}$	-	$\left(1.04^{+0.01}_{-0.01}\right) \times 10^{-7}$	$\left(1.13^{+0.03}_{-0.03}\right) \times 10^6$	-	-
$\alpha = \{2/3, 4\}$	-	-	$\left(1.76^{+0.02}_{-0.02}\right) \times 10^6$	-	$\left(1.248^{+0.009}_{-0.009}\right) \times 10^{-11}$
$\alpha = \{2, 3\}$	-	$\left(4.4^{+0.3}_{-0.3}\right) \times 10^{-8}$	-	$\left(1.54^{+0.04}_{-0.04}\right) \times 10^3$	-
$\alpha = \{2, 4\}$	-	-	-	$\left(1.81^{+0.03}_{-0.03}\right) \times 10^3$	$\left(7.1^{+0.2}_{-0.2}\right) \times 10^{-12}$
$\alpha = \{3, 4\}$	-	$\left(1.438^{+0.01}_{-0.01}\right) \times 10^{-7}$	-	-	$\left(2.9^{+2.2}_{-1.3}\right) \times 10^{-13}$
$\alpha = \{0, 2/3, 2\}$	$\left(1.0^{+1.6}_{-0.8}\right) \times 10^{-9}$	-	$\left(3.2^{+5.3}_{-2.4}\right) \times 10^3$	$\left(2.12^{+0.01}_{-0.02}\right) \times 10^3$	-
$\alpha = \{0, 2/3, 3\}$	$\left(7.7^{+6.7}_{-5.1}\right) \times 10^{-8}$	$\left(1.06^{+0.02}_{-0.02}\right) \times 10^{-7}$	$\left(8.8^{+1.6}_{-2.1}\right) \times 10^5$	-	-
$\alpha = \{0, 2/3, 4\}$	$\left(5.5^{+9.1}_{-4.1}\right) \times 10^{-9}$	-	$\left(1.74^{+0.03}_{-0.03}\right) \times 10^6$	-	$\left(1.249^{+0.009}_{-0.009}\right) \times 10^{-11}$
$\alpha = \{0, 2, 3\}$	$\left(2.6^{+0.3}_{-0.3}\right) \times 10^{-7}$	$\left(9.3^{+0.6}_{-0.6}\right) \times 10^{-8}$	-	$\left(4.5^{+1.3}_{-1.3}\right) \times 10^2$	-
$\alpha = \{0, 2, 4\}$	$\left(1.8^{+0.3}_{-0.2}\right) \times 10^{-7}$	-	-	$\left(1.3^{+0.08}_{-0.08}\right) \times 10^3$	$\left(9.3^{+0.3}_{-0.3}\right) \times 10^{-12}$
$\alpha = \{0, 3, 4\}$	$\left(3.58^{+0.1}_{-0.1}\right) \times 10^{-7}$	$\left(1.13^{+0.02}_{-0.02}\right) \times 10^{-7}$	-	-	$\left(1.1^{+1.1}_{-0.7}\right) \times 10^{-12}$
$\alpha = \{2/3, 2, 3\}$	-	$\left(1.01^{+0.03}_{-0.04}\right) \times 10^{-7}$	$\left(1.07^{+0.05}_{-0.07}\right) \times 10^6$	$\left(7.8^{+9.5}_{-5.6}\right) \times 10^1$	-
$\alpha = \{2/3, 2, 4\}$	-	-	$\left(8.2^{+1.1}_{-1.1}\right) \times 10^5$	$\left(9.9^{+1.1}_{-1.1}\right) \times 10^2$	$\left(9.9^{+0.3}_{-0.4}\right) \times 10^{-12}$
$\alpha = \{2/3, 3, 4\}$	-	$\left(9.2^{+0.9}_{-1.1}\right) \times 10^{-8}$	$\left(1.21^{+0.07}_{-0.06}\right) \times 10^6$	-	$\left(4.4^{+1.6}_{-2.2}\right) \times 10^{-12}$
$\alpha = \{2, 3, 4\}$	-	$\left(2.3^{+3.9}_{-1.7}\right) \times 10^{-9}$	-	$\left(1.79^{+0.03}_{-0.03}\right) \times 10^3$	$\left(6.9^{+0.3}_{-0.4}\right) \times 10^{-12}$
$\alpha = \{0, 2/3, 2, 3\}$	$\left(1.3^{+0.8}_{-0.8}\right) \times 10^{-7}$	$\left(1.0^{+0.05}_{-0.07}\right) \times 10^{-7}$	$\left(6.1^{+2.9}_{-3.3}\right) \times 10^5$	$\left(1.7^{+1.9}_{-1.2}\right) \times 10^2$	-
$\alpha = \{0, 2/3, 2, 4\}$	$\left(7.2^{+6.8}_{-5.0}\right) \times 10^{-8}$	-	$\left(4.9^{+2.4}_{-3.0}\right) \times 10^5$	$\left(1.1^{+0.1}_{-0.1}\right) \times 10^3$	$\left(9.6^{+0.4}_{-0.4}\right) \times 10^{-12}$
$\alpha = \{0, 2/3, 3, 4\}$	$\left(4.9^{+6.1}_{-3.6}\right) \times 10^{-8}$	$\left(9.8^{+0.6}_{-1.1}\right) \times 10^{-8}$	$\left(1.0^{+0.1}_{-0.2}\right) \times 10^6$	-	$\left(3.3^{+1.9}_{-2.0}\right) \times 10^{-12}$
$\alpha = \{0, 2, 3, 4\}$	$\left(2.1^{+0.4}_{-0.3}\right) \times 10^{-7}$	$\left(2.8^{+3.9}_{-2.0}\right) \times 10^{-8}$	-	$\left(1.0^{+0.2}_{-0.4}\right) \times 10^3$	$\left(7.8^{+1.2}_{-2.8}\right) \times 10^{-12}$
$\alpha = \{2/3, 2, 3, 4\}$	-	$\left(3.6^{+3.5}_{-2.6}\right) \times 10^{-8}$	$\left(9.8^{+1.6}_{-1.5}\right) \times 10^5$	$\left(6.0^{+2.9}_{-3.9}\right) \times 10^2$	$\left(8.1^{+1.3}_{-2.2}\right) \times 10^{-12}$
$\alpha = \{0, 2/3, 2, 3, 4\}$	$\left(7.9^{+8.1}_{-5.4}\right) \times 10^{-8}$	$\left(3.9^{+3.9}_{-2.7}\right) \times 10^{-8}$	$\left(6.3^{+2.8}_{-3.6}\right) \times 10^5$	$\left(6.9^{+3.2}_{-4.0}\right) \times 10^2$	$\left(7.7^{+1.4}_{-2.9}\right) \times 10^{-12}$

Table 9.6: Parameter estimation results for astrophysical parameters in the 20-100 Hz band for the different combinations of the five spectral indices for BNS, r-mode, and magnetar SGWB injection data set, with injected parameters $K_{\rm CBC} = 7.91 \times 10^5\, M_\odot\,{\rm Gpc}^{-3}\,{\rm yr}^{-1}$, $K_{\rm r-modes} = 1 \times 10^3$, and $K_{\rm magnetars} = 1 \times 10^{-11}\,{\rm T}^{-1}$. Horizontal lines divide the table in regions where a fixed number of components is considered for the analysis.

Conclusions

「受け継がれた意志、年齢の運命、人々の夢、人々が自由の意味を追求し続ける限り、これらのことは決して止まらない」
ゴールド・ロジャー, ワンピース

The first three observing runs of the LIGO-Virgo-KAGRA (LVK) collaboration, while rich in compact-binary-coalescence detections, have shown no evidence for a stochastic gravitational-wave background (SGWB) signal in their data. However, the new constraints on the SGWB intensity from the LVK isotropic (reference [258] and section 4.4) and anisotropic searches (reference [1] and chapter 6) have noticeably improved the previously existing ones from ground-based detectors in the 20-1726 Hz frequency band. I was not among the contributors to the LVK isotropic searches during O3, but I was the main contributor to one of the LVK O3 anisotropic searches, namely the broad-band radiometer (BBR) search, as illustrated in section 6.3 of chapter 6, employing the methods presented in the first three sections of chapter 5. As it was reported in the main text, the BBR results have improved the previously existing ones by a factor ranging between 3.3 and 3.5, depending on the sky direction and the model considered throughout the analysis. After the start of O4, I am still contributing to the BBR analysis as an analyst, tutor for newcomers, and developer of new code snippets necessary to face the new challenges that may appear during O4, as hinted in the main text.

The rest of the works presented in the third part of the manuscript are short-author-list papers, which I led as the main author. These works are a selection among the projects I have contributed to during the PhD (see "Associated Publications and Contributions") and other research directions (and some LVK collaboration service tasks) that I have explored but have never led to any manuscript or were interrupted. The original works presented in chapters 7, 8, and 9 should not be labelled as a simple reinterpretation of the O3 results to obtain non-informative upper limits about some models. These works, in spite of their exploratory nature and their relative simplicity, are the first ones employing specific techniques and constraining some models using the data from the first three observing runs of the advanced LIGO and advanced Virgo detectors.

Chapter 7, based on [2], puts into practice on real data the idea first introduced in [496] to infer constraints on the average ellipticity of Galactic NSs from the results of the search for isotropic SGWB. In the same work, a suggestion about inferring similar information from an extra-galactic NS hotspot was also proposed in the case of the Virgo cluster, assuming a known spatial distribution. Chapter 7 targets four

additional hotspots other than the Virgo cluster but does not make any assumptions about the NS spatial distributions. The extension of the work that was mentioned in the conclusions of chapter 7, including such distribution, never saw the light given the appearance of [446] a few weeks after the completion of the work.

Chapter 8, based on [3], sets for the first time constraints on two power-law astrophysical SGWBs associated with two different regimes of GW emission during pulsar glitches, and the relative ensemble properties. This work used the model first proposed in [565], deriving the SGWB model from scratch (finding a different expression from [565] as presented in section 8.6.1) and focusing on the case of glitches from Galactic pulsars. This work was not further extended due to me thinking that the model adopted from [565] is too much approximated to describe a realistic SGWB and due to a general lack of insight about pulsar glitch physics.

Finally, chapter 9 applies for the first time the formalism to jointly estimate multiple SGWB amplitudes first presented in [635], and extend it to the joint estimation of the ensemble properties of the populations associated with the SGWBs of interest. This very promising approach, which was tested through an injection study, will become important as one gets closer to the first SGWB detection with ground-based detectors since it is able to distinguish the number of components contributing to the excesses observed in single-component analyses. The goal is to further develop this approach, and I hope to include it in the LVK stochastic searches when the time comes.

Future

In contrast to other GW signal morphologies that are likely to be detected for the first time during the ongoing LVK fourth observing run, the detection of an SGWB with GW ground-based interferometric detectors is likely to still require some more years as the detectors become more and more sensitive and more data piles up. However, the waiting is far from being passive, as new challenges and opportunities appear during the approach towards the first SGWB detection:

- With the increase in network sensitivity and the advent of third-generation detectors, the effects of correlated noise on SGWB searches will no longer be negligible, and new data quality techniques will have to be developed. Tremendous progress has been made in recent years in this field, and the recent PhD thesis by Kamiel Janssens [661] is an excellent compendium of such efforts for correlated magnetic, seismic, and Newtonian noises in SGWB isotropic searches.

- Current searches assume the SGWB to be continuous, while the SGWB from CBCs (likely the first one to be detected) is expected to be intermittent. Multiple methods have started being actively developed in the last decade [464, 465] to account for such an intermittent nature and noticeably accelerate the detection process. However, these methods are not yet ready to be applied to real data, and several efforts are ongoing to overcome this limit.

- Current searches assume that the SGWB is Gaussian, while some models for new physics predict non-Gaussianities to be present. The detection of non-Gaussianities would be a smoking gun for new physics and can be probed by correlating the data of detector triplets and quadruplets at a time. In spite of some initial theoretical methods [458–460], no search has been developed yet, mainly due to the lack of a detector network with more than just two detectors. However, this is no longer the case, and this research field will gain more and more interest in the upcoming years.

- As recent evidence for an SGWB in PTA data has shown [263, 265–267], the hardest questions to answer in a detection-like scenario are probably whether the observed correlated excess is actually an SGWB and whether it is just a single SGWB or multiple ones causing the excess. These challenges for ground-based detectors have started being addressed via the *geodesy method* [661, 662] to validate detection and methods for jointly estimating and separating multiple SGWB components, such as the one in chapter 9.

The above bullet points are just some of the challenges and opportunities to explore for the ground-based detector community when searching for an SGWB. These challenges offer the possibility of collaborating and exploiting other solutions that have been developed to search for an SGWB through the whole GW spectrum. Concluding, there is plenty of work left to do in the incoming years before the first SGWB detection with ground-based detectors.

Appendices

Appendix A

Coordinate system for ground-based GW detectors

"Oui, mais regarde les yeux du Lecteur. Il a vu ton point et il a poursuivi vers la ligne du dessous. Pour lui ce n'est pas qu'un point d'imprimerie dans le livre."
Bernard Werber, *Le Mystère des dieux,*

This appendix presents and summarises the coordinate systems used in chapters 2, 4, and 5 in the calculation of $\vec{\boldsymbol{x}}_I$, $\hat{\boldsymbol{u}}_I$, and $\hat{\boldsymbol{v}}_I$, which are used in the evaluation of response functions and overlap reduction functions, for real-world detectors. This appendix is mainly based on [663] and on [664].

A.1 The wave frame

The position of a GW source in the celestial sphere is identified by the spherical coordinates (θ, ϕ), measured with respect to the Earth's fixed frame. These coordinates are related to the right ascension $\alpha = \phi + \mathrm{GMST}$ (GMST is the Greenwich mean sidereal time at which the signal arrives) and the declination $\delta = \pi/2 - \theta$. The GW signal from the source is additionally characterised by a polarisation angle ψ. The $(\theta,\, \phi,\, \psi)$ frame is called the *wave frame*, identified by the wave frame axes $\hat{\boldsymbol{p}}, \hat{\boldsymbol{q}}, \hat{\boldsymbol{n}}$ in figure 1.1, which in the case $\psi = 0$ reduce to $\hat{\boldsymbol{l}}, \hat{\boldsymbol{m}}, \hat{\boldsymbol{n}}$ in equation (1.1.27).

A.2 Global reference frame

Consider a coordinate system whose origin is the centre of the Earth. The axes of this system are expressed in terms of latitude and longitude $(\varphi,\, \lambda)$, in such a way that the x-axis pierces the Earth at $(0^\circ,\, 0^\circ)$, the y-axis at $(0^\circ,\, 90^\circ E)$, and the z-axis at $(90^\circ N,\, 0^\circ)$. A third coordinate, the elevation h normal to the surface tangent plane, can be used to define any point on Earth uniquely. In the coordinate system $(\varphi,\, \theta,\, h)$, assuming the WGS-84 Earth model [663], the $(x,\, y,\, z)$ coordinates of the detector

vertex $\vec{\boldsymbol{x}}_I = x\,\hat{\boldsymbol{\imath}} + y\,\hat{\boldsymbol{\jmath}} + z\,\hat{\boldsymbol{k}}$ read:

$$\begin{cases} x = [R(\varphi) + h]\cos\varphi\cos\lambda \\ y = [R(\varphi) + h]\cos\varphi\sin\lambda \\ z = \left[\frac{b^2}{a^2}R(\varphi) + h\right]\sin\varphi \end{cases} \tag{A.2.1}$$

$$R(\varphi) = \frac{a^2}{\sqrt{a^2\cos^2\varphi + b^2\sin^2\varphi}} \tag{A.2.2}$$

where $a = 6,378137 \times 10^6$ m and $b = 6,356752314 \times 10^6$ m are the semi-major and semi-major axes of the oblate ellipsoid and $R(\varphi)$ is the local Earth radius.

The position of the detector vertex can also be expressed in terms of $(\varphi,\, \theta,\, h)$ as $\vec{\boldsymbol{x}}_I = \varphi\,\hat{\boldsymbol{\varphi}} + \lambda\,\hat{\boldsymbol{\lambda}} + h\,\hat{\boldsymbol{h}}$, where the unit vectors are related to $(\hat{\boldsymbol{\imath}},\, \hat{\boldsymbol{\jmath}},\, \hat{\boldsymbol{k}})$ as

$$\begin{cases} \hat{\boldsymbol{\lambda}} = -\sin\lambda\,\hat{\boldsymbol{\imath}} + \cos\lambda\,\hat{\boldsymbol{\jmath}} \\ \hat{\boldsymbol{\varphi}} = -\sin\varphi\cos\lambda\,\hat{\boldsymbol{\imath}} - \sin\varphi\sin\lambda\,\hat{\boldsymbol{\jmath}} + \cos\varphi\,\hat{\boldsymbol{k}} \\ \hat{\boldsymbol{h}} = \cos\varphi\cos\lambda\,\hat{\boldsymbol{\imath}} + \cos\varphi\sin\lambda\,\hat{\boldsymbol{\jmath}} + \sin\varphi\,\hat{\boldsymbol{k}} \end{cases} . \tag{A.2.3}$$

These unit vectors point towards East, North, and Up, respectively, and correctly simplify to $(\hat{\boldsymbol{\jmath}},\, \hat{\boldsymbol{k}},\, \hat{\boldsymbol{\imath}})$ when $\vec{\boldsymbol{x}}_I$ is pointing towards the equator ($\varphi = 0°$) and the Greenwich meridian ($\lambda = 0°$).

The above unit vectors are the most natural ones to use to express the detector arm directions $\hat{\boldsymbol{u}}_I$ and $\hat{\boldsymbol{v}}_I$. To be able to do so, one also needs to know the arm north-of-east azimuths $\psi_{u/v}$ (meaning that if the arm points towards East, $\psi_{u/v} = 0°$, while if it points towards North, $\psi_{u/v} = 90°$), and the arm tilts $\omega_{u/v}$ above the horizontal of the tangent plane to $\vec{\boldsymbol{x}}_I$. In the $(\hat{\boldsymbol{\lambda}}, \hat{\boldsymbol{\varphi}}, \hat{\boldsymbol{h}})$ system, the unit vector of the arm $\hat{\boldsymbol{u}}_I$ reads ($\hat{\boldsymbol{v}}_I$ follows by replacing u with v) [664]:

$$\hat{\boldsymbol{u}}_I = \cos\omega_u\cos\psi_u\hat{\boldsymbol{\lambda}} + \cos\omega_u\sin\psi_u\hat{\boldsymbol{\varphi}} + \sin\omega_u\hat{\boldsymbol{h}}. \tag{A.2.4}$$

This expression, combined with equation (A.2.3) to pass to the $(\hat{\boldsymbol{\imath}},\, \hat{\boldsymbol{\jmath}},\, \hat{\boldsymbol{k}})$ system, can then be used to evaluate $\hat{\boldsymbol{u}}_I$ and $\hat{\boldsymbol{v}}_I$ in chapters 2, 4, and 5.

A.3 Summary

To characterise a ground-based GW detector geometry, seven quantities are necessary: the latitude φ, the longitude λ, and the elevation h of the detector vertex, as well as the azimuths $\psi_{u/v}$ and the tilt angle $\omega_{u/v}$ of the detector arms. Once these quantities are known, one can evaluate the components of $\vec{\boldsymbol{x}}_I$ using equation (A.2.1) and the unit vectors $\hat{\boldsymbol{u}}_I$ and $\hat{\boldsymbol{v}}_I$ using equation (A.2.4) in combination with equation (A.2.3). The $\vec{\boldsymbol{x}}_I$, $\hat{\boldsymbol{u}}_I$ and $\hat{\boldsymbol{v}}_I$ quantities are summarised in table A.1 for the current network of ground-based GW detectors.

Detector	$\hat{\boldsymbol{u}}_I$	$\hat{\boldsymbol{v}}_I$	$\vec{\boldsymbol{x}}_I$ [m]
GEO600	(-0.44530676905, 0.86651354130, 0.22551311312)	(-0.62605756776, -0.55218609524, 0.55058372486)	(3856309.94926, 666598.956317, 5019641.41725)
LHO	(-0.2238912154, 0.79983069746, 0.55690487831)	(-0.91397818574, 0.02609403989, -0.40492342125)	(-2161414.92636, -3834695.17889, 4600350.22664)
LLO	(-0.9545746153, -0.14158077340, -0.26218911324)	(0.29774156894, -0.48791033647, -0.82054461286)	(-74276.0447238, -5496283.71971, 3224257.01744)
Virgo	(-0.70045821479, 0.20848948619, 0.68256166277)	(-0.05379255368, -0.96908180549, 0.24080451708)	(4546374.09900, 842989.697626, 4378576.96241)
KAGRA	(-0.3759040, -0.8361583, 0.3994189)	(0.7164378, 0.01114076, 0.6975620)	(-3777336.024, 3484898.411, 3765313.697)
LAO	(0.38496278183, -0.39387275094, 0.83466634811)	(0.89838844906, -0.04722636126, -0.43665531647)	(1348971.15479, 5857428.26577, 2127569.25209)

Table A.1: Summary of the detectors' vertex vectors $\vec{\boldsymbol{x}}_I$ [m] and arm unit vectors $\hat{\boldsymbol{u}}_I$ and $\hat{\boldsymbol{v}}_I$ for LIGO Hanford (LIO), LIGO Livingston (LIO), Virgo, KAGRA from LALDetector.h and the under-construction LIGO India (Aundha, LAO) from [665].

Acknowledgements

Once, I was seven years old, my mama told me
"Go make yourself some friends, or you'll be lonely"
Once, I was seven years old..."

Lukas Graham, *7 Years*

I usually refrain from writing these kinds of acknowledgements, given that I prefer acknowledging people face-to-face on a daily basis if our lives allow for it. However, exceptional times require exceptional measures, namely my usual lengthy and pleonastic style... Now, assuming a more serious tone, let's start!

This PhD is the peak of my Education, which began when I was a six-year-old crybaby who was starting to become self-aware of himself and had no idea what life would have reserved for him. In this spirit, I would like to express my deepest gratitude to two of my primary school teachers, Lucia Imperiale and Carla Golinelli: "Thank you, for teaching me the pleasure to learn and making me live it like a pleasant game, planting in me the seeds of *knowledge lover* that have sprouted across the years, leading me eventually here!" I would like to thank (yet bitterly) all my bullies from "scuola media" (a three-year-long secondary-lower school between five-year-long primary and five-year-long high school in Italy) and my monstrous nemesis, my basketball coach A. C.: "Thank you, for almost breaking me down and giving me so many insecurities to overcome over the years but allowing me to develop such a mental strength and teaching me to deal with *differently distinguished gentlemen and ladies* I have been meeting during my lifetime!" Passing to the high school period, my warm thanks go to all the teachers of the "Internationale Deutsche Abteilung" of the Liceo Galvani, whom I was extremely lucky to have as educators: "Thank you, for always stimulating me with new topics, taught at a level often close to the university one, and thank you for making me really understand what it really means and is the *critical thought* and how to *critically think* in everyday life!" Among all of them, I must make a special acknowledgement to Paola Giacconi, my Mathematics and Physics teacher, who made me fall in love with these subjects and soon realise that Physics was the path I wanted to pursue in my higher education. Now, time for university studies. I express gratitude for my Alma-Mater-Bologna fellows with whom I have spent the three years of the bachelor and the two years of the master, with special thanks to Alessandro, Brando, Riccardo, Roberto, and Valerio for the deeper bounds we formed and all the discussions. Getting closer to this PhD, I would like to thank my master thesis advisor, Prof. Fabio Maltoni, who gave me the possibility of doing part of my

master thesis at UCLouvain and welcomed me at the CP3, where I became aware of this PhD fellowship position, which I applied for and then obtained.

Concerning the people I have met during my PhD, I have another long list of acknowledgements. First and foremost, thanks to my PhD advisor, Professor Giacomo Luca Bruno, for investing in me in spite of my original theory-oriented background and for leaving me the complete freedom to explore my own paths and directions. This has not always been easy since I was learning from scratch, but it has allowed me to learn how to work autonomously and rapidly gain my research independence. I thank him for encouraging me to apply for the prestigious *bourse FRIA*, which I have eventually been awarded and has been my source of funding for most of my PhD duration. Explicitly, **I acknowledge that I have been supported throughout my work by a FRIA (Fonds pour la formation à la Recherche dans l'Industrie et dans l'Agriculture) Grant of the Belgian Fund for Research, F.R.S.-FNRS (Fonds de la Recherche Scientifique-FNRS)**. Thanks to my two mentors: "Mr.PostDoc" Andrew Lawrence Miller (a.k.a. Mr.Io), for showing me how the research world works and supporting me during the first two PhD years in times of CoViD (and all the discussions about topics I am forbidden to mention here), and Dr. Jishnu Suresh, for resurrecting my second half of PhD, teaching me how to do research properly in the stochastic world, and all the extra physics discussions we had. Merci beaucoup à Monsieur "One Ant" Antoine (Depasse?!), pour avoir été là depuis le premier jour et avoir dépassé beaucoup de difficultés ensemble comme étudiants de doctorat pendant les années. Je renouvelle mes remerciements à lui et je remercie aussi Clémentine (Dassy, pas le fruit) pour m'avoir aidé dans l'apprentissage de la langue française (avec de mauvais résultats en jugeant ça que j'écris) et pour m'avoir introduit et accuillé dans la culture belge. Merci aux secrétaires Stéphanie Landrain et surtout à Carinne Mertens : sans votre travail, le CP3 aurait courte vie ! Thanks to all the colleagues of the Belgian Virgo stochastic group for all the meetings and work done together for science and to build this community from scratch! Special thanks to the junior fellows for sharing experiences and fears inside and outside academia (in order of appearance in Belgium): Kamiel, Kevin, Jishnu, Max, Aäron, Guillaume, Alba, Hannah, Stavros, and Deepali. Thanks to Daniele for visiting CP3 from time to time and updating each other about our parallel university lives, and to all the other Italian guys at CP3 (Luca, Angela, Matteo, Paola, Tommaso, Jonathan, Simone, and all the others) for reminding me of my roots and making me refresh my Italian from time to time. Thanks to all the women I have encountered during these four years for their extremely positive impacts on my life and all the discussions about sensitive topics I was not aware of. Special thanks to Carinne, Khawla, Veronika, Francesca, Federica (3x), Magdalena, Emma, Paola, Alba, Morgane, Karljin, and Clémentine (hopefully I am not forgetting anyone else).

Concerning this PhD thesis, thanks to the members of the jury, Professor Fabio Maltoni, Professor Christophe Ringeval, Professor Nick van Remortel, and Professor Nelson Christensen: I had a lot of fun during the private defence, answering all your questions and curiosities! I am grateful to all of you for your enormous work in

reading this manuscript into details, catching the remaining typos and giving advice for improving this thesis (and for allowing me some *poetic licences* here and there)!

Thanks to my friends from my past lives, from high school and before, whom I have failed to stay in contact with but who have always been available in case of need and exchange of opinions and memories during these years: Andrew, Luca, Michelangelo, Francesco, Maria Giulia, Alessandro, Raffaello, Diana, and all the others I have forgotten to mention here, thank you!

Thanks to all those who may have actually reached the end of this (much longer than initially expected) manuscript, passing through *Frustration* and *Boredom* but showing *Resilience* and *Adaptability*, four keywords that describes my (and many other people's through the generations) PhD years.

Finally, the greatest thanks go, of course, to my Italian family, which I could not choose at birth but will be forever as long as we are alive and I am extremely grateful to have. Thanks to my (recently spirited-away) Nonna Franca, who taught me how to read and write (and how to make pasta, of course) in very early times. Dedico questa tesi a te, *o Augusta Vegliarda*! Thanks to my super-duper Mamma Emanuela, la miglior mamma al mondo con il suo amore incondizionato, la sua cucina deliziosa ed il mio punto di riferimento come persona e come donna: "Grazie Mamma, grazie per esserci sempre e per tutte le chiamate che abbiamo fatto in questi anni". Thanks to my Papà Michele, for teaching me what respect is and that even a big man like him can be extremely fragile: "Nonostante tutte le sofferenze, grazie per tutto l'amore che mi hai dato e per tutti i sacrifici fatti che non ho potuto apprezzare in giovane età: anche se non te lo dico abbastanza spesso, sappi che ti voglio bene". To my (once!) little brother, mio Fratello Alessandro: "Non è il nostro compito quello d'avvicinarci, così come non s'avvicinano fra loro il sole e la luna, o il mare e la terra. Noi due, caro amico, siamo il sole e la luna, siamo il mare e la terra. La nostra meta non è di trasformarci l'uno nell'altro, ma di conoscerci l'un l'altro e d'imparare a vedere e a rispettare nell'altro ciò ch'egli è: il nostro opposto e il nostro complemento." (*Narziß und Goldmund*, by Hermann Hesse). Thanks to Federica, who has become a sister over the past (six, almost seven!) years. ~~Thanks to the person who has entered my life during the writing of this thesis, but this is another story...~~

And, last but not least, thanks to me and myselves, for always being there to enrich us with each other, from the past towards the future...

"But at what cost?" ... ... "Everything..."

Felice Del Lodrio, *My young self to my current self*

Bibliography

[1] **KAGRA, Virgo, LIGO Scientific** Collaboration, R. Abbott et al., *Search for anisotropic gravitational-wave backgrounds using data from Advanced LIGO and Advanced Virgo's first three observing runs*, *Phys. Rev. D* **104** (2021), no. 2 022005, [arXiv:2103.08520].

[2] F. De Lillo, J. Suresh, and A. L. Miller, *Stochastic gravitational-wave background searches and constraints on neutron-star ellipticity*, *Mon. Not. Roy. Astron. Soc.* **513** (2022), no. 1 1105–1114, [arXiv:2203.03536].

[3] F. De Lillo, J. Suresh, A. Depasse, et al., *Probing ensemble properties of vortex-avalanche pulsar glitches with a stochastic gravitational-wave background search*, *Phys. Rev. D* **107** (2023), no. 10 102001, [arXiv:2211.16857].

[4] F. De Lillo and J. Suresh, *Estimating Astrophysical Population Properties using a multi-component Stochastic Gravitational-Wave Background Search*, [arXiv:2310.05823].

[5] A. Costantini, F. De Lillo, F. Maltoni, et al., *Vector boson fusion at multi-TeV muon colliders*, *JHEP* **09** (2020) 080, [arXiv:2005.10289].

[6] A. L. Miller, S. Clesse, F. De Lillo, et al., *Probing planetary-mass primordial black holes with continuous gravitational waves*, *Phys. Dark Univ.* **32** (2021) 100836, [arXiv:2012.12983].

[7] A. L. Miller, N. Aggarwal, S. Clesse, and F. De Lillo, *Constraints on planetary and asteroid-mass primordial black holes from continuous gravitational-wave searches*, *Phys. Rev. D* **105** (2022), no. 6 062008, [arXiv:2110.06188].

[8] A. I. Renzini et al., *pygwb: A Python-based Library for Gravitational-wave Background Searches*, *Astrophys. J.* **952** (2023), no. 1 25, [arXiv:2303.15696].

[9] D. Kennefick, *Traveling at the Speed of Thought: Einstein and the Quest for Gravitational Waves*. Princeton University Press, 4, 2007.

[10] K. S. Thorne, *Gravitational radiation.*, in *Three Hundred Years of Gravitation*, pp. 330–458. 1987.

[11] K. Thorne, *Black Holes and Time Warps: Einsteins Outrageous Legacy*. Commonwealth Fund Book Program. WW Norton, 1994.

[12] H. Collins, *Gravity's shadow: The search for gravitational waves*. 2004.

[13] D. Kennefick, *Controversies in the history of the radiation reaction problem in general relativity*, [gr-qc/9704002].

[14] K. S. Thorne, *Gravitational radiation: A New window onto the universe*, [gr-qc/9704042].

[15] C.-M. Chen, J. M. Nester, and W.-T. Ni, *A brief history of gravitational wave research*, *Chin. J. Phys.* **55** (2017) 142–169, [arXiv:1610.08803].

[16] J. L. Cervantes-Cota, S. Galindo-Uribarri, and G.-F. Smoot, *A Brief History of Gravitational Waves*, *Universe* **2** (2016), no. 3 22, [arXiv:1609.09400].

[17] A. Einstein, *Zur Allgemeinen Relativitätstheorie*, *Sitzungsber. Preuss. Akad. Wiss. Berlin (Math. Phys.)* **1915** (1915) 778–786. [Addendum: Sitzungsber.Preuss.Akad.Wiss.Berlin (Math.Phys.) 1915, 799–801 (1915)].

[18] A. Einstein, *Die Grundlage der allgemeinen Relativitätstheorie*, *Annalen der Physik* **354** (Jan., 1916) 769–822.

[19] W. Clifford, *On the Space-Theory of Matter (1870)*, *Beyond Geometry: Classic Papers from Riemann to Einstein* **2** (01, 2007).

[20] H. Poincaré, *La dynamique de l'électron*. A. Dumas, 1913.

[21] G. Nordström, *Zur Theorie der Gravitation vom Standpunkt des Relativitätsprinzips*, *Annalen der Physik* **347** (1913), no. 13 533–554.

[22] A. Einstein, A. Beck, and P. Havas, *The Collected Papers of Albert Einstein: The Berlin years: correspondence, 1914-1918*. The Collected Papers of Albert Einstein. Princeton University Press, 1987.

[23] A. Einstein, *Approximative Integration of the Field Equations of Gravitation*, *Sitzungsber. Preuss. Akad. Wiss. Berlin (Math. Phys.)* **1916** (1916) 688–696.

[24] H. Weyl, *Space-Time-Matter*. E.P. Dutton and Company, 1922.

[25] A. Einstein, *Über Gravitationswellen*, *Sitzungsber. Preuss. Akad. Wiss. Berlin (Math. Phys.)* **1918** (1918) 154–167.

[26] A. S. Eddington, *The propagation of gravitational waves*, *Proc. Roy. Soc. Lond. A* **102** (1922) 268–282.

[27] A. Eddington, *CXVII. The spontaneous loss of energy of a spinning rod according to the relativity theory* , *The London, Edinburgh, and Dublin Philosophical Magazine and Journal of Science* **46** (1923), no. 276 1112–1117.

[28] A. Einstein, M. Born, and H. Born, *The Born-Einstein Letters: Correspondence Between Albert Einstein and Max and Hedwig Born from 1916-1955, with Commentaries by Max Born*. Macmillan, 1971.

[29] M. Born, *Briefwechsel 1916-1955*. Nymphenburger Verlagshandlunger, 1969.

[30] D. Kennefick, *Einstein Versus the Physical Review*, *Physics Today - PHYS TODAY* **58** (09, 2005) 43–58.

[31] A. Einstein and N. Rosen, *On Gravitational waves*, *J. Franklin Inst.* **223** (1937) 43–54.

[32] C. W. Misner, K. S. Thorne, and J. A. Wheeler, *Gravitation*. W. H. Freeman, San Francisco, 1973.

[33] N. Rosen, *Plane polarized waves in the general theory of relativity*, *Phys. Z. Sowjetunion* **12** (1937).

[34] N. Rosen, *On Cylindrical Gravitational Waves*, *Mercier & Kervaire* (1956) 171–175.

[35] N. Rosen, *Does gravitational radiation exist?*, *Gen. Rel. Grav.* **10** (1979) 351–364.

[36] J. Eisenstaedt, *The Low Water Mark of General Relativity, 1925-1955*, in *Einstein and the History of General Relativity* (D. Howard and J. Stachel, eds.), pp. 1–277. Birkhäuser, 1989.

[37] A. Mercier and M. Kervaire, eds., *Fünfzig Jahre Relativitätstheorie, Bern, 11.-16. Juli 1955 : Verhandlungen*. Birkhäuser, Basel, 1956.

[38] C. M. Dewitt and D. Rickles, *The role of gravitation in physics : report from the 1957 chapel hill conference*, 2011.

[39] F. A. E. Pirani, *On the Physical significance of the Riemann tensor*, *Acta Phys. Polon.* **15** (1956) 389–405.

[40] T. Damour, *Gravitational Radiation Reaction in the Binary Pulsar and the Quadrupole-Formula Controversy*, *Phys. Rev. Lett.* **51** (Sep, 1983) 1019–1021.

[41] J. H. Taylor, L. A. Fowler, and P. M. McCulloch, *Measurements of general relativistic effects in the binary pulsar PSR 1913+16*, *Nature* **277** (1979) 437–440.

[42] J. H. Taylor and P. M. McCulloch, *Evidence for the existence of gravitational radiation from measurements of the binary pulsar PSR 1913+16*, in *Ninth Texas Symposium on Relativistic Astrophysics*, vol. 336, pp. 442–446, Feb., 1980.

[43] J. M. Weisberg, D. J. Nice, and J. H. Taylor, *Timing Measurements of the Relativistic Binary Pulsar PSR B1913+16*, *Astrophys. J.* **722** (2010) 1030–1034, [arXiv:1011.0718].

[44] M. Kramer et al., *Tests of general relativity from timing the double pulsar*, *Science* **314** (2006) 97–102, [astro-ph/0609417].

[45] P. C. C. e. a. Freire, *The relativistic pulsar-white dwarf binary PSR J1738+0333 II. The most stringent test of scalar-tensor gravity*, *Mon. Not. Roy. Astron. Soc.* **423** (2012) 3328, [arXiv:1205.1450].

[46] J. Weber, *Detection and Generation of Gravitational Waves*, *Phys. Rev.* **117** (1960) 306–313.

[47] J. Weber, *General Relativity and Gravitational Waves*. New York: Interscience Publishers, 1961.

[48] J. Weber, *Observation of the Thermal Fluctuations of a Gravitational-Wave Detector*, *Phys. Rev. Lett.* **17** (1966) 1228–1230.

[49] J. Weber, *Evidence for discovery of gravitational radiation*, *Phys. Rev. Lett.* **22** (1969) 1320–1324.

[50] J. Weber, *Anisotropy and polarization in the gravitational-radiation experiments*, *Phys. Rev. Lett.* **25** (1970) 180–184.

[51] D. W. Sciama, G. B. Field, and M. J. Rees, *Upper Limit to Radiation of Mass Energy Derived from Expansion of Galaxy*, *Phys. Rev. Lett.* **23** (1969) 1514–1515.

[52] W. H. Press and K. S. Thorne, *Gravitational-wave astronomy*, *Ann. Rev. Astron. Astrophys.* **10** (1972) 335–374.

[53] V. B. Braginskii and V. N. Rudenko, *Relativistic gravitational experiments*, *Usp. Fiz. Nauk* **100** (1970) 395–424.

[54] V. B. Braginskii, A. B. Manukin, E. I. Popov, V. N. Rudenko, and A. A. Khorev, *Search for gravitational radiation of extraterrestrial origin*, *Pisma Zh. Eksp. Teor. Fiz.* **16** (1972) 157–161.

[55] V. B. Braginskii, L. P. Grishchuk, A. G. Doroshkevich, et al., *Electromagnetic detectors of gravitational waves*, *Zh. Eksp. Teor. Fiz.* **65** (1973) 1729–1737.

[56] J. A. Tyson, *Null search for bursts of gravitational radiation*, *Phys. Rev. Lett.* **31** (1973) 326–329.

[57] J. L. Levine and R. L. Garwin, *New negative result for gravitational wave detection, and comparison with reported detection*, *Phys. Rev. Lett.* **33** (1974) 794–797.

[58] V. B. Braginskii, A. B. Manukin, E. I. Popov, V. N. Rudenko, and A. A. Khorev, *Upper limit of the density of extraterrestrial gravitational radiation*, *Zh. Eksp. Teor. Fiz.* **66** (1974) 801–812.

[59] R. L. Forward, *Multidirectional, multipolarization antennas for scalar and tensor gravitational radiation*, *Gen. Rel. Grav.* **2** (1971), no. 2 149–159.

[60] P. Astone et al., *The Gravitational wave detector NAUTILUS operating at T = 0.1-K*, *Astropart. Phys.* **7** (1997) 231–243.

[61] M. Cerdonio et al., *The Ultracryogenic gravitational wave detector AURIGA*, *Class. Quant. Grav.* **14** (1997) 1491–1494.

[62] **International Gravitational Event** Collaboration, P. Astone et al., *Methods and results of the IGEC search for burst gravitational waves in the years 1997 - 2000*, *Phys. Rev. D* **68** (2003) 022001, [astro-ph/0302482].

[63] E. Mauceli, Z. K. Geng, W. O. Hamilton, et al., *The ALLEGRO gravitational wave detector: Data acquisition and analysis*, *Phys. Rev. D* **54** (1996) 1264–1275, [gr-qc/9609058].

[64] D. G. Blair, E. N. Ivanov, M. E. Tobar, et al., *High sensitivity gravitational wave antenna with parametric transducer readout*, *Phys. Rev. Lett.* **74** (1995) 1908–1911.

[65] A. de Waard, L. Gottardi, J. van Houwelingen, A. Shumack, and G. Frossati, *MiniGRAIL, the first spherical detector*, *Class. Quant. Grav.* **20** (2003) S143–S151.

[66] O. D. Aguiar et al., *The Brazilian gravitational wave detector Mario Schenberg: Progress and plans*, *Class. Quant. Grav.* **22** (2005) S209–S214.

[67] M. E. Gertsenshtein and V. I. Pustovoit, *On the Detection of Low Frequency Gravitational Waves*, *Sov. Phys. JETP* **16** (1962) 433.

[68] V. B. Braginskii, *Gravitational radiation and the prospect of its experimental discovery*, *Soviet Physics Uspekhi* **8** (apr, 1966) 513.

[69] G. E. Moss, L. R. Miller, and R. L. Forward, *Photon-noise-limited laser transducer for gravitational antenna*, *Appl. Opt.* **10** (1971) 2495–2498.

[70] R. L. Forward, *Wide Band Laser Interferometer Gravitational Radiation Experiment*, *Phys. Rev. D* **17** (1978) 379–390.

[71] R. Weiss, *Gravitation Research*, "http://hdl.handle.net/1721.1/56271", 1972.

[72] R. Weiss, *Gravitation research*, "http://hdl.handle.net/1721.1/56655", 1977.

[73] D. Shoemaker, R. Schilling, L. Schnupp, et al., *Noise Behavior of the Garching 30-meter Prototype Gravitational Wave Detector*, *Phys. Rev. D* **38** (1988) 423–432.

[74] A. Rudiger, W. Winkler, K. Maischberger, et al., *Plans for a large gravitational wave antenna in Germany*, in *4th Marcel Grossmann Meeting on the Recent Developments of General Relativity*, 1985.

[75] J. Hough, B. J. Meers, G. P. Newton, et al., *A British long baseline gravitational wave observatory. Design study report.*, .

[76] J. Hough et al., *Proposal for a joint German-British interferometric gravitational wave detector*, .

[77] Bordé, Ch. J., *Méthodes optiques de détection des ondes gravitationnelles - préface*, *Ann. Phys. Fr.* **10** (1985), no. 3 R1–R2.

[78] A. Brillet, *Interferometric gravitational wave antennae*, *Annales Phys. (France)* **10** (1985) 219–226.

[79] **Virgo** Collaboration, T. Accadia et al., *Virgo: a laser interferometer to detect gravitational waves*, *JINST* **7** (2012) P03012.

[80] `https://www.ego-gw.it/`.

[81] R. W. P. Drever, *A search for anisotropy of inertial mass using a free precession technique*, *Phil. Mag.* **6** (1961) 683–687.

[82] D. Herriott, H. Kogelnik, and R. Kompfner, *Off-axis paths in spherical mirror interferometers*, *Appl. Opt.* **3** (Apr, 1964) 523–526.

[83] D. R. Herriott and H. J. Schulte, *Folded optical delay lines*, *Appl. Opt.* **4** (Aug, 1965) 883–889.

[84] C. Fabry and A. Perot, *Théorie et applications d'une nouvelle méthode de spectroscopie interférentielle*, *Annales de Chimie et de Physique, 7. Série* **16** (01, 1899).

[85] A. Perot and C. Fabry, *On the Application of Interference Phenomena to the Solution of Various Problems of Spectroscopy and Metrology*, *ApJ* **9** (Feb., 1899) 87.

[86] P. Linsay, P. Saulson, R. Weiss, et al., *A Study of a Long Baseline Gravitational Wave Antenna System*. 1983.

[87] L. Janna, *Black hole blues and other songs from outer space*, 2016.

[88] R. Ruthen, *Catching the wave*, *Scientific American* **266** (1992), no. 3 90–101.

[89] D. Castelvecchi, *Hunt for gravitational waves to resume after massive upgrade*, *Nature* **525** (09, 2015) 301–2.

[90] **LIGO Scientific** Collaboration, J. Aasi et al., *Advanced LIGO*, *Class. Quant. Grav.* **32** (2015) 074001, [arXiv:1411.4547].

[91] **LIGO Scientific, Virgo** Collaboration, B. P. Abbott et al., *Observation of Gravitational Waves from a Binary Black Hole Merger*, *Phys. Rev. Lett.* **116** (2016), no. 6 061102, [arXiv:1602.03837].

[92] D. Castelvecchi, *Gravitational waves: How ligo forged the path to victory*, *Nature* **530** (02, 2016) 261–262.

[93] **KAGRA, Virgo, LIGO Scientific** Collaboration, R. Abbott et al., *GWTC-3: Compact Binary Coalescences Observed by LIGO and Virgo during the Second Part of the Third Observing Run*, *Phys. Rev. X* **13** (2023), no. 4 041039, [arXiv:2111.03606].

[94] **Virgo** Collaboration, F. Acernese et al., *Advanced Virgo: a second-generation interferometric gravitational wave detector*, *Class. Quant. Grav.* **32** (2015), no. 2 024001, [arXiv:1408.3978].

[95] **KAGRA** Collaboration, T. Akutsu et al., *Overview of KAGRA: Detector design and construction history*, *PTEP* **2021** (2021), no. 5 05A101, [arXiv:2005.05574].

[96] **KAGRA** Collaboration, Y. Aso, Y. Michimura, K. Somiya, et al., *Interferometer design of the KAGRA gravitational wave detector*, *Phys. Rev. D* **88** (2013), no. 4 043007, [arXiv:1306.6747].

[97] K. Somiya, *Detector configuration of kagra–the japanese cryogenic gravitational-wave detector*, *Classical and Quantum Gravity* **29** (jun, 2012) 124007.

[98] **KAGRA** Collaboration, K. Somiya, *Detector configuration of KAGRA: The Japanese cryogenic gravitational-wave detector*, *Class. Quant. Grav.* **29** (2012) 124007, [arXiv:1111.7185].

[99] **TAMA** Collaboration, M. Ando et al., *Stable operation of a 300-m laser interferometer with sufficient sensitivity to detect gravitational wave events within our galaxy*, *Phys. Rev. Lett.* **86** (2001) 3950, [astro-ph/0105473].

[100] **LIGO Scientific, Virgo** Collaboration, B. P. Abbott et al., *GW170814: A Three-Detector Observation of Gravitational Waves from a Binary Black Hole Coalescence*, *Phys. Rev. Lett.* **119** (2017), no. 14 141101, [arXiv:1709.09660].

[101] **LIGO Scientific, Virgo** Collaboration, B. P. Abbott et al., *GW170817: Observation of Gravitational Waves from a Binary Neutron Star Inspiral*, *Phys. Rev. Lett.* **119** (2017), no. 16 161101, [arXiv:1710.05832].

[102] G. P. Lamb and S. Kobayashi, *GRB 170817A as a jet counterpart to gravitational wave triggerGW 170817*, *Mon. Not. Roy. Astron. Soc.* **478** (2018), no. 1 733–740, [arXiv:1710.05857].

[103] C. M. et al., *The fermi gamma-ray burst monitor*, *The Astrophysical Journal* **702** (aug, 2009) 791.

[104] E. Kuulkers et al., *INTEGRAL reloaded: Spacecraft, instruments and ground system*, *New Astron. Rev.* **93** (2021) 101629, [arXiv:2106.12446].

[105] **LIGO Scientific, Virgo, Fermi-GBM, INTEGRAL** Collaboration, B. P. Abbott et al., *Gravitational Waves and Gamma-rays from a Binary Neutron Star Merger: GW170817 and GRB 170817A*, *Astrophys. J. Lett.* **848** (2017), no. 2 L13, [arXiv:1710.05834].

[106] **LIGO Scientific, Virgo, 1M2H, Dark Energy Camera GW-E, DES, DLT40, Las Cumbres Observatory, VINROUGE, MASTER** Collaboration, B. P. Abbott et al., *A gravitational-wave standard siren measurement of the Hubble constant*, *Nature* **551** (2017), no. 7678 85–88, [arXiv:1710.05835].

[107] **LIGO Scientific, Virgo** Collaboration, B. P. Abbott et al., *GWTC-1: A Gravitational-Wave Transient Catalog of Compact Binary Mergers Observed by LIGO and Virgo during the First and Second Observing Runs*, *Phys. Rev. X* **9** (2019), no. 3 031040, [arXiv:1811.12907].

[108] **LIGO Scientific, Virgo** Collaboration, R. Abbott et al., *GW190412: Observation of a Binary-Black-Hole Coalescence with Asymmetric Masses*, *Phys. Rev. D* **102** (2020), no. 4 043015, [arXiv:2004.08342].

[109] **LIGO Scientific, Virgo** Collaboration, B. P. Abbott et al., *GW190425: Observation of a Compact Binary Coalescence with Total Mass* $\sim 3.4 M_{\odot}$, *Astrophys. J. Lett.* **892** (2020), no. 1 L3, [arXiv:2001.01761].

[110] **LIGO Scientific, Virgo** Collaboration, R. Abbott et al., *GW190521: A Binary Black Hole Merger with a Total Mass of* $150 M_{\odot}$, *Phys. Rev. Lett.* **125** (2020), no. 10 101102, [arXiv:2009.01075].

[111] **LIGO Scientific, Virgo** Collaboration, R. Abbott et al., *GW190814: Gravitational Waves from the Coalescence of a 23 Solar Mass Black Hole with a 2.6 Solar Mass Compact Object*, *Astrophys. J. Lett.* **896** (2020), no. 2 L44, [arXiv:2006.12611].

[112] **LIGO Scientific, KAGRA, Virgo** Collaboration, R. Abbott et al., *Observation of Gravitational Waves from Two Neutron Star–Black Hole Coalescences*, *Astrophys. J. Lett.* **915** (2021), no. 1 L5, [arXiv:2106.15163].

[113] **LIGO Scientific, Virgo** Collaboration, R. Abbott et al., *GWTC-2: Compact Binary Coalescences Observed by LIGO and Virgo During the First Half of the Third Observing Run*, *Phys. Rev. X* **11** (2021) 021053, [arXiv:2010.14527].

[114] **LIGO Scientific, Virgo** Collaboration, R. Abbott et al., *GWTC-2.1: Deep Extended Catalog of Compact Binary Coalescences Observed by LIGO and Virgo During the First Half of the Third Observing Run*, [arXiv:2108.01045].

[115] M. Saleem et al., *The science case for LIGO-India*, *Class. Quant. Grav.* **39** (2022), no. 2 025004, [arXiv:2105.01716].

[116] M. Punturo et al., *The Einstein Telescope: A third-generation gravitational wave observatory*, *Class. Quant. Grav.* **27** (2010) 194002.

[117] D. Reitze et al., *Cosmic Explorer: The U.S. Contribution to Gravitational-Wave Astronomy beyond LIGO*, *Bulletin of the AAS* **51** (2019), no. 7. https://baas.aas.org/pub/2020n7i035.

[118] A. M. Cruise and R. M. J. Ingley, *A prototype gravitational wave detector for 100 MHz*, *Classical and Quantum Gravity* **23** (oct, 2006) 6185.

[119] A. M. Cruise, *The potential for very high-frequency gravitational wave detection*, *Class. Quant. Grav.* **29** (2012) 095003.

[120] N. Aggarwal et al., *Challenges and opportunities of gravitational-wave searches at MHz to GHz frequencies*, *Living Rev. Rel.* **24** (2021), no. 1 4, [arXiv:2011.12414].

[121] **Holometer** Collaboration, A. Chou et al., *Interferometric Constraints on Quantum Geometrical Shear Noise Correlations*, *Class. Quant. Grav.* **34** (2017), no. 16 165005, [arXiv:1703.08503].

[122] B. Willke et al., *The GEO 600 gravitational wave detector*, *Class. Quant. Grav.* **19** (2002) 1377–1387.

[123] S. S. et al., *The status of DECIGO*, *Journal of Physics: Conference Series* **840** (may, 2017) 012010.

[124] C. Cutler and D. E. Holz, *Ultra-high precision cosmology from gravitational waves*, *Phys. Rev. D* **80** (2009) 104009, [arXiv:0906.3752].

[125] L. B. et al., *AION: an atom interferometer observatory and network*, *Journal of Cosmology and Astroparticle Physics* **2020** (may, 2020) 011.

[126] M. e. a. Abe, *Matter-wave Atomic Gradiometer Interferometric Sensor (MAGIS-100)*, *Quantum Science and Technology* **6** (Oct., 2021) 044003, [arXiv:2104.02835].

[127] J. W. Armstrong, *Low-frequency gravitational wave searches using spacecraft doppler tracking*, *Living Rev. Relativ.* **9** (Jan., 2006) 1.

[128] **LISA** Collaboration, P. Amaro-Seoane et al., *Laser Interferometer Space Antenna*, [arXiv:1702.00786].

[129] **TianQin** Collaboration, J. Mei et al., *The TianQin project: current progress on science and technology*, *PTEP* **2021** (2021), no. 5 05A107, [arXiv:2008.10332].

[130] A. Sesana et al., *Unveiling the gravitational universe at μ-Hz frequencies*, *Exper. Astron.* **51** (2021), no. 3 1333–1383, [arXiv:1908.11391].

[131] D. Blas and A. C. Jenkins, *Bridging the μHz Gap in the Gravitational-Wave Landscape with Binary Resonances*, *Phys. Rev. Lett.* **128** (2022), no. 10 101103, [arXiv:2107.04601].

[132] D. Blas and A. C. Jenkins, *Detecting stochastic gravitational waves with binary resonance*, *Phys. Rev. D* **105** (2022), no. 6 064021, [arXiv:2107.04063].

[133] M. A. McLaughlin, *The North American Nanohertz Observatory for Gravitational Waves*, *Classical and Quantum Gravity* **30** (nov, 2013) 224008.

[134] M. Kramer and D. J. Champion, *The European Pulsar Timing Array and the Large European Array for Pulsars*, *Classical and Quantum Gravity* **30** (nov, 2013) 224009.

[135] R. N. e. a. Manchester, *The Parkes Pulsar Timing Array Project*, *PASA* **30** (Jan., 2013) e017, [arXiv:1210.6130].

[136] B. C. e. a. Joshi, *Precision pulsar timing with the ORT and the GMRT and its applications in pulsar astrophysics*, *Journal of Astrophysics and Astronomy* **39** (Aug., 2018) 51.

[137] G. e. a. Hobbs, *The International Pulsar Timing Array project: using pulsars as a gravitational wave detector*, *Classical and Quantum Gravity* **27** (Apr., 2010) 084013, [arXiv:0911.5206].

[138] R. e. a. Nan, *The Five-Hundred Aperture Spherical Radio Telescope (fast) Project*, *International Journal of Modern Physics D* **20** (Jan., 2011) 989–1024, [arXiv:1105.3794].

[139] M. e. a. Bailes, *The MeerKAT telescope as a pulsar facility: System verification and early science results from MeerTime*, *PASA* **37** (July, 2020) e028, [arXiv:2005.14366].

[140] G. Janssen et al., *Gravitational wave astronomy with the SKA*, *PoS* **AASKA14** (2015) 037, [arXiv:1501.00127].

[141] S. C. U. et al., *Taking the Measure of the Universe: Precision Astrometry with SIM PlanetQuest*, *Publications of the Astronomical Society of the Pacific* **120** (2008), no. 863 38–88.

[142] **Planck** Collaboration, Y. Akrami et al., *Planck 2018 results. X. Constraints on inflation*, *Astron. Astrophys.* **641** (2020) A10, [arXiv:1807.06211].

[143] **BICEP2, Keck Array** Collaboration, P. A. R. Ade et al., *Improved Constraints on Cosmology and Foregrounds from BICEP2 and Keck Array Cosmic Microwave Background Data with Inclusion of 95 GHz Band*, *Phys. Rev. Lett.* **116** (2016) 031302, [arXiv:1510.09217].

[144] K. Kuroda, W.-T. Ni, and W.-P. Pan, *Gravitational waves: Classification, Methods of detection, Sensitivities, and Sources*, *Int. J. Mod. Phys. D* **24** (2015), no. 14 1530031, [arXiv:1511.00231].

[145] C. Bambi, S. Katsanevas, and K. D. Kokkotas, eds., *Handbook of Gravitational Wave Astronomy*. Springer Singapore, 2021.

[146] M. Maggiore, *Gravitational Waves. Vol. 1: Theory and Experiments*. Oxford University Press, 2007.

[147] S. Weinberg, *Gravitation and Cosmology: Principles and Applications of the General Theory of Relativity*. John Wiley and Sons, New York, 1972.

[148] E. Poisson and C. M. Will, *Gravity: Newtonian, Post-Newtonian, Relativistic*. Cambridge University Press, 2014.

[149] J. D. E. Creighton and W. G. Anderson, *Gravitational-wave physics and astronomy: An introduction to theory, experiment and data analysis*. 2011.

[150] L. D. Landau and E. M. Lifschits, *The Classical Theory of Fields*, vol. Volume 2 of *Course of Theoretical Physics*. Pergamon Press, Oxford, 1975.

[151] W.-T. Ni and M. Zimmermann, *Inertial and gravitational effects in the proper reference frame of an accelerated, rotating observer*, *Phys. Rev. D* **17** (1978) 1473–1476.

[152] K. S. Thorne, *The theory of gravitational radiation - an introductory review*, in *Gravitational Radiation*, pp. 1–57, Jan., 1983.

[153] G. Sagnac, *L'ether lumineux demontre par l'effet du vent relatif d'ether dans un interferometre en rotation uniforme.*, *Comptes Rendus* **157** (1913) 708–710.

[154] A. Ashtekar and A. Magnon, *The Sagnac effect in general relativity*, *J. Math. Phys.* **16** (1975) 341–344.

[155] R. Anderson, H. R. Bilger, and G. E. Stedman, *"Sagnac" effect: A century of Earth-rotated interferometers*, *American Journal of Physics* **62** (Nov., 1994) 975–985.

[156] R. A. Isaacson, *Gravitational Radiation in the Limit of High Frequency. I. The Linear Approximation and Geometrical Optics*, *Phys. Rev.* **166** (1968) 1263–1271.

[157] R. A. Isaacson, *Gravitational Radiation in the Limit of High Frequency. II. Nonlinear Terms and the Ef fective Stress Tensor*, *Phys. Rev.* **166** (1968) 1272–1279.

[158] R. L. Arnowitt, S. Deser, and C. W. Misner, *Wave zone in general relativity*, *Phys. Rev.* **121** (1961) 1556.

[159] R. L. Arnowitt, S. Deser, and C. W. Misner, *Coordinate invariance and energy expressions in general relativity*, *Phys. Rev.* **122** (1961) 997.

[160] S. V. Babak and L. P. Grishchuk, *The Energy momentum tensor for the gravitational field*, *Phys. Rev. D* **61** (2000) 024038, [gr-qc/9907027].

[161] K. S. Thorne, *Multipole Expansions of Gravitational Radiation*, *Rev. Mod. Phys.* **52** (1980) 299–339.

[162] L. Blanchet and T. Damour, *Tail-transported temporal correlations in the dynamics of a gravitating system*, *Phys. Rev. D* **37** (Mar, 1988) 1410–1435.

[163] L. Blanchet and T. Damour, *Hereditary effects in gravitational radiation*, *Phys. Rev. D* **46** (1992) 4304–4319.

[164] W. L. Burke and K. S. Thorne, *Gravitational radiation damping*, in *Relativity* (M. Carmeli, S. I. Fickler, and L. Witten, eds.), (Boston, MA), pp. 209–228, Springer US, 1970.

[165] T. Damour and B. R. Iyer, *Multipole analysis for electromagnetism and linearized gravity with irreducible Cartesian tensors*, *Phys. Rev. D* **43** (May, 1991) 3259–3272.

[166] T. Damour, *The problem of motion in Newtonian and Einsteinian gravity.*, in *Three Hundred Years of Gravitation*, pp. 128–198. 1987.

[167] L. Blanchet, *Gravitational Radiation from Post-Newtonian Sources and Inspiralling Compact Binaries*, *Living Rev. Rel.* **17** (2014) 2, [arXiv:1310.1528].

[168] P. C. Peters and J. Mathews, *Gravitational radiation from point masses in a Keplerian orbit*, *Phys. Rev.* **131** (1963) 435–439.

[169] P. C. Peters, *Gravitational Radiation and the Motion of Two Point Masses*, *Phys. Rev.* **136** (Nov, 1964) B1224–B1232.

[170] A. A. Michelson and E. W. Morley, *LVIII. On the relative motion of the earth and the luminiferous Æther*, *The London, Edinburgh, and Dublin Philosophical Magazine and Journal of Science* **24** (1887), no. 151 449–463.

[171] N. J. Cornish, *Alternative derivation of the response of interferometric gravitational wave detectors*, *Phys. Rev. D* **80** (2009) 087101, [arXiv:0910.4372].

[172] L. S. Finn, *The Response of interferometric gravitational wave detectors*, *Phys. Rev. D* **79** (2009) 022002, [arXiv:0810.4529].

[173] F. B. Estabrook and H. D. Wahlquist, *Response of Doppler spacecraft tracking to gravitational radiation.*, *General Relativity and Gravitation* **6** (Oct., 1975) 439–447.

[174] P. R. Saulson, *Fundamentals of Interferometric Gravitational Wave Detectors*. World Scientific, 2nd. ed. ed., 2017.

[175] J. Y. Vinet, C. N. Man, A. Brillet, and B. Meers, *Optimization of Long Baseline Optical Interferometers for Gravitational Wave Detection*, *Phys. Rev. D* **38** (1988) 433–447.

[176] B. J. Meers, *The Frequency response of interferometric gravitational wave detectors*, *Phys. Lett. A* **142** (1989) 465–470.

[177] B. J. Meers, *Recycling in Laser Interferometric Gravitational Wave Detectors*, *Phys. Rev. D* **38** (1988) 2317–2326.

[178] A. Freise and K. Strain, *Interferometer Techniques for Gravitational-Wave Detection*, *Living Rev. Rel.* **13** (2010) 1, [arXiv:0909.3661].

[179] C. Bond, D. Brown, A. Freise, and K. Strain, *Interferometer Techniques for Gravitational-Wave Detection*, *Living Rev. Rel.* **19** (2017) 3, [arXiv:0909.3661].

[180] A. Rüdiger, R. Schilling, L. Schnupp, et al., *A Mode Selector to Suppress Fluctuations in Laser Beam Geometry*, *Optica Acta* **28** (May, 1981) 641–658.

[181] S. Hild, *A Basic Introduction to Quantum Noise and Quantum-Non-Demolition Techniques*, pp. 291–314. Springer International Publishing, Cham, 2014.

[182] R. H. Dicke, *The Measurement of Thermal Radiation at Microwave Frequencies*, *Review of Scientific Instruments* **17** (12, 2004) 268–275.

[183] F. Pockels, *Ueber den Einfluss des elektrostatischen Feldes auf das optische Verhalten piėzoelektrischer Krystalle*, vol. 39. Dieterichsche Verlags-Buchhandlung, 1894.

[184] L. Schnupp, "Presentation at European Collaboration Meeting on Interferometric Detection of Gravitational Waves, Sorrent, Italy, Oct 1988." (unpublished).

[185] `https://inkscape.org/`.

[186] `http://www.gwoptics.org/`.

[187] R. W. P. Drever, *Interferometric detectors for gravitational radiation*, p. 321. North Holland, Amsterdam, 1983.

[188] R. V. Pound, *Electronic Frequency Stabilization of Microwave Oscillators*, *Review of Scientific Instruments* **17** (12, 2004) 490–505.

[189] R. W. P. Drever, J. L. Hall, F. V. Kowalski, et al., *Laser phase and frequency stabilization using an optical resonator*, *Appl. Phys. B* **31** (1983), no. 2 97–105.

[190] E. D. Black, *An introduction to Pound–Drever–Hall laser frequency stabilization*, *American Journal of Physics* **69** (01, 2001) 79–87.

[191] E. D. Black and R. N. Gutenkunst, *An introduction to signal extraction in interferometric gravitational wave detectors*, *American Journal of Physics* **71** (04, 2003) 365–378.

[192] R. W. P. Drever, *Fabry-Perot cavity gravity-wave detectors*, p. 306–328. Cambridge University Press, 1991.

[193] I. Fiori, A. Effler, P. Nguyen, et al., *Environmental Noise in Gravitational-Wave Interferometers*. 2021.

[194] W. Heisenberg, *Über den anschaulichen Inhalt der quantentheoretischen Kinematik und Mechanik*, *Zeitschrift fur Physik* **43** (Mar., 1927) 172–198.

[195] C. Caves, *Quantum-Mechanical Radiation-Pressure Fluctuations in an Interferometer*, *Phys. Rev. Lett.* **45** (1980), no. 2 75–79.

[196] C. M. Caves, *Quantum measurement and chaos*. NATO ASI series. Series B, Physics ; v. 161. Plenum Press, New York, 1987.

[197] H. J. Kimble, Y. Levin, A. B. Matsko, K. S. Thorne, and S. P. Vyatchanin, *Conversion of conventional gravitational wave interferometers into QND interferometers by modifying their input and / or output optics*, *Phys. Rev. D* **65** (2002) 022002, [gr-qc/0008026].

[198] E. Polini, *Broadband quantum noise reduction in AdV+ : from frequency-dependent squeezing implementation to detection losses and scattered light mitigation*. Theses, Université Savoie Mont Blanc, Dec., 2022.

[199] C. M. Caves, *Quantum Mechanical Noise in an Interferometer*, *Phys. Rev. D* **23** (1981) 1693–1708.

[200] A. Brillet, J. Gea-Banaclochet, G. Leuchsf, C. N. Man, and J. Y. Vinet, *Advanced techniques: recycling and squeezing*, p. 369–405. Cambridge University Press, 1991.

[201] **Virgo** Collaboration, F. Acernese et al., *Increasing the Astrophysical Reach of the Advanced Virgo Detector via the Application of Squeezed Vacuum States of Light*, *Phys. Rev. Lett.* **123** (2019), no. 23 231108.

[202] **LIGO Scientific** Collaboration, J. Aasi et al., *Enhancing the sensitivity of the LIGO gravitational wave detector by using squeezed states of light*, *Nature Photon.* **7** (2013) 613–619, [arXiv:1310.0383].

[203] J. R. Peterson, *Observations and modeling of seismic background noise*, tech. rep., 1993. Report.

[204] **Virgo** Collaboration, F. Acernese et al., *First locking of the Virgo central area interferometer with suspension hierarchical control*, *Astropart. Phys.* **20** (2004) 629–640.

[205] G. Ballardin et al., *Measurement of the Virgo superattenuator performance for seismic noise suppression*, *Rev. Sci. Instrum.* **72** (2001) 3643–3652.

[206] J. Harms, *Terrestrial gravity fluctuations*, *Living Reviews in Relativity* **22** (Oct, 2019) 6.

[207] M. G. Beker, J. F. J. van den Brand, E. Hennes, and D. S. Rabeling, *Newtonian noise and ambient ground motion for gravitational wave detectors*, *J. Phys. Conf. Ser.* **363** (2012) 012004.

[208] F. Badaracco and J. Harms, *Optimization of seismometer arrays for the cancellation of Newtonian noise from seismic body waves*, *Class. Quant. Grav.* **36** (2019), no. 14 145006, [arXiv:1903.07936].

[209] J. Harms and K. Venkateswara, *Newtonian-noise cancellation in large-scale interferometric GW detectors using seismic tiltmeters*, *Class. Quant. Grav.* **33** (2016), no. 23 234001.

[210] H. B. Callen and T. A. Welton, *Irreversibility and generalized noise*, *Phys. Rev.* **83** (1951) 34–40.

[211] H. B. Callen and R. F. Greene, *On a Theorem of Irreversible Thermodynamics*, *Phys. Rev.* **86** (1952) 702–710.

[212] P. R. Saulson, *Thermal noise in mechanical experiments*, *Phys. Rev. D* **42** (1990) 2437–2445.

[213] E. M. Purcell, *Electricity and Magnetism*. McGraw-Hill, 1965.

[214] P. Brady, G. Losurdo, and H. Shinkai, *LIGO, Virgo, and KAGRA as the International Gravitational Wave Network*, pp. 1–21. Springer Singapore, Singapore, 2020.

[215] `https://gwosc.org/`.

[216] **LIGO Scientific, Virgo** Collaboration, R. Abbott et al., *Open data from the first and second observing runs of Advanced LIGO and Advanced Virgo*, *SoftwareX* **13** (2021) 100658, [arXiv:1912.11716].

[217] **KAGRA, Virgo, LIGO Scientific** Collaboration, R. Abbott et al., *Open Data from the Third Observing Run of LIGO, Virgo, KAGRA, and GEO*, *Astrophys. J. Suppl.* **267** (2023), no. 2 29, [arXiv:2302.03676].

[218] **Virgo** Collaboration, *Advanced Virgo Technical Design Report*, http://tds.ego-gw.it/ql/?c=8940, 2012.

[219] **Virgo** Collaboration, F. Acernese et al., *The present status of the Virgo central interferometer*, *Class. Quant. Grav.* **19** (2002) 1421–1428.

[220] **Virgo** Collaboration, *Advanced Virgo Baseline Design*, https://tds.virgo-gw.eu/?content=3&r=6616, 2009.

[221] L. S. Finn and D. F. Chernoff, *Observing binary inspiral in gravitational radiation: One interferometer*, *Phys. Rev. D* **47** (1993) 2198–2219, [gr-qc/9301003].

[222] **Virgo** Collaboration, M. Punturo, *Advanced Virgo Sensitivity document*, https://tds.virgo-gw.eu/?content=3&r=9710, 2012.

[223] **Virgo** Collaboration, F. Acernese et al., *Virgo Detector Characterization and Data Quality during the O3 run*, [arXiv:2205.01555].

[224] **Virgo** Collaboration, F. Acernese et al., *Virgo detector characterization and data quality: results from the O3 run*, *Class. Quant. Grav.* **40** (2023), no. 18 185006, [arXiv:2210.15633].

[225] D. Aisa et al., *The Advanced Virgo monolithic fused silica suspension*, *Nucl. Instrum. Meth. A* **824** (2016) 644–645.

[226] M. C. Tringali et al., *Seismic array measurements at Virgo's west end building for the configuration of a Newtonian-noise cancellation system*, *Class. Quant. Grav.* **37** (2020), no. 2 025005, [arXiv:1912.08619].

[227] A. Allocca et al., *Interferometer Sensing and Control for the Advanced Virgo Experiment in the O3 Scientific Run*, *Galaxies* **8** (2020), no. 4 85.

[228] L. Aiello, E. Cesarini, V. Fafone, et al., *Thermal compensation system in advanced and third generation gravitational wave interferometric detectors*, *J. Phys. Conf. Ser.* **1226** (2019), no. 1 012019.

[229] **Virgo** Collaboration, J. Aasi et al., *The characterization of Virgo data and its impact on gravitational-wave searches*, *Class. Quant. Grav.* **29** (2012) 155002, [arXiv:1203.5613].

[230] **Virgo** Collaboration, F. Acernese et al., *Virgo detector characterization and data quality: tools*, *Class. Quant. Grav.* **40** (2023), no. 18 185005, [arXiv:2210.15634].

[231] **Virgo** Collaboration, F. Acernese et al., *The Virgo O3 run and the impact of the environment*, *Class. Quant. Grav.* **39** (2022), no. 23 235009, [arXiv:2203.04014].

[232] https://tds.Virgo-gw.eu/?content=3&r=15777.

[233] https://tds.Virgo-gw.eu/?content=3&r=20962.

[234] R. Flaminio, *Status and plans of the Virgo gravitational wave detector*, *Proc. SPIE Int. Soc. Opt. Eng.* **11445** (2020) 1144511.

[235] **KAGRA, LIGO Scientific, Virgo, Virgo** Collaboration, B. P. Abbott et al., *Prospects for observing and localizing gravitational-wave transients with Advanced LIGO, Advanced Virgo and KAGRA*, *Living Rev. Rel.* **21** (2018), no. 1 3, [arXiv:1304.0670].

[236] C. De Rossi et al., *Development of a Frequency Tunable Green Laser Source for Advanced Virgo+ Gravitational Waves Detector*, *Galaxies* **8** (2020), no. 4 87.

[237] D. Bersanetti, B. Patricelli, O. J. Piccinni, et al., *Advanced Virgo: Status of the Detector, Latest Results and Future Prospects*, *Universe* **7** (2021), no. 9 322.

[238] **Virgo** Collaboration, F. Acernese et al., *Advanced Virgo Plus: Future Perspectives*, *J. Phys. Conf. Ser.* **2429** (2023), no. 1 012040.

[239] J. D. Romano and N. J. Cornish, *Detection methods for stochastic gravitational-wave backgrounds: a unified treatment*, *Living Rev. Rel.* **20** (2017), no. 1 2, [arXiv:1608.06889].

[240] N. J. Cornish and J. D. Romano, *When is a gravitational-wave signal stochastic?*, *Phys. Rev. D* **92** (2015), no. 4 042001, [arXiv:1505.08084].

[241] J. Gair, J. D. Romano, S. Taylor, and C. M. F. Mingarelli, *Mapping gravitational-wave backgrounds using methods from CMB analysis: Application to pulsar timing arrays*, *Phys. Rev. D* **90** (2014), no. 8 082001, [arXiv:1406.4664].

[242] H. Fischer, *A History of the Central Limit Theorem: From Classical to Modern Probability Theory*. 01, 2011.

[243] T. Regimbau, *The astrophysical gravitational wave stochastic background*, *Res. Astron. Astrophys.* **11** (2011) 369–390, [arXiv:1101.2762].

[244] J. M. Scalo, *The Stellar initial mass function*, *Fund. Cosmic Phys.* **11** (1986) 1–278.

[245] N. Christensen, *Stochastic Gravitational Wave Backgrounds*, *Rept. Prog. Phys.* **82** (2019), no. 1 016903, [arXiv:1811.08797].

[246] T. Regimbau, *The Quest for the Astrophysical Gravitational-Wave Background with Terrestrial Detectors*, *Symmetry* **14** (2022), no. 2 270.

[247] **KAGRA, Virgo, LIGO Scientific** Collaboration, R. Abbott et al., *Population of Merging Compact Binaries Inferred Using Gravitational Waves through GWTC-3*, *Phys. Rev. X* **13** (2023), no. 1 011048, [arXiv:2111.03634].

[248] E. S. Phinney, *A Practical theorem on gravitational wave backgrounds*, [astro-ph/0108028].

[249] P. A. Rosado, *Gravitational wave background from binary systems*, *Phys. Rev. D* **84** (2011) 084004, [arXiv:1106.5795].

[250] P. A. Rosado, *Gravitational wave background from rotating neutron stars*, *Phys. Rev. D* **86** (2012) 104007, [arXiv:1206.1330].

[251] M. Braglia, J. Garcia-Bellido, and S. Kuroyanagi, *Tracking the origin of black holes with the stochastic gravitational wave background popcorn signal*, *Mon. Not. Roy. Astron. Soc.* **519** (2023), no. 4 6008–6019, [arXiv:2201.13414].

[252] **LISA** Collaboration, P. A. Seoane et al., *Astrophysics with the Laser Interferometer Space Antenna*, *Living Rev. Rel.* **26** (2023), no. 1 2, [arXiv:2203.06016].

[253] M. Visser, C. Barcelo, S. Liberati, and S. Sonego, *Small, dark, and heavy: But is it a black hole?*, *PoS* **BHGRS** (2008) 010, [arXiv:0902.0346].

[254] V. Cardoso and P. Pani, *Testing the nature of dark compact objects: a status report*, *Living Rev. Rel.* **22** (2019), no. 1 4, [arXiv:1904.05363].

[255] S. Marassi, R. Schneider, G. Corvino, V. Ferrari, and S. Portegies Zwart, *Imprint of the merger and ring-down on the gravitational wave background from black hole binaries coalescence*, *Phys. Rev. D* **84** (2011) 124037, [arXiv:1111.6125].

[256] X.-J. Zhu, E. Howell, T. Regimbau, D. Blair, and Z.-H. Zhu, *Stochastic Gravitational Wave Background from Coalescing Binary Black Holes*, *Astrophys. J.* **739** (2011) 86, [arXiv:1104.3565].

[257] T. Callister, M. Fishbach, D. Holz, and W. Farr, *Shouts and Murmurs: Combining Individual Gravitational-Wave Sources with the Stochastic Background to Measure the History of Binary Black Hole Mergers*, *Astrophys. J. Lett.* **896** (2020), no. 2 L32, [arXiv:2003.12152].

[258] **KAGRA, Virgo, LIGO Scientific** Collaboration, R. Abbott et al., *Upper limits on the isotropic gravitational-wave background from Advanced LIGO and Advanced Virgo's third observing run*, *Phys. Rev. D* **104** (2021), no. 2 022004, [arXiv:2101.12130].

[259] E. Vangioni, K. A. Olive, T. Prestegard, et al., *The Impact of Star Formation and Gamma-Ray Burst Rates at High Redshift on Cosmic Chemical Evolution and Reionization*, *Mon. Not. Roy. Astron. Soc.* **447** (2015) 2575, [arXiv:1409.2462].

[260] N. Langer and C. A. Norman, *On the collapsar model of long gamma-ray bursts: constraints from cosmic metallicity evolution*, *Astrophys. J. Lett.* **638** (2006) L63–L66, [astro-ph/0512271].

[261] L. Lehoucq, I. Dvorkin, R. Srinivasan, C. Pellouin, and A. Lamberts, *Astrophysical uncertainties in the gravitational-wave background from stellar-mass compact binary mergers*, *Mon. Not. Roy. Astron. Soc.* **526** (2023), no. 3 4378–4387, [arXiv:2306.09861].

[262] S. Babak, C. Caprini, D. G. Figueroa, et al., *Stochastic gravitational wave background from stellar origin binary black holes in LISA*, *JCAP* **08** (2023) 034, [arXiv:2304.06368].

[263] **NANOGrav** Collaboration, G. Agazie et al., *The NANOGrav 15 yr Data Set: Evidence for a Gravitational-wave Background*, *Astrophys. J. Lett.* **951** (2023), no. 1 L8, [arXiv:2306.16213].

[264] P. A. Rosado, A. Sesana, and J. Gair, *Expected properties of the first gravitational wave signal detected with pulsar timing arrays*, *Mon. Not. Roy. Astron. Soc.* **451** (2015), no. 3 2417–2433, [arXiv:1503.04803].

[265] **EPTA, InPTA:** Collaboration, J. Antoniadis et al., *The second data release from the European Pulsar Timing Array - III. Search for gravitational wave signals*, *Astron. Astrophys.* **678** (2023) A50, [arXiv:2306.16214].

[266] D. J. Reardon et al., *Search for an Isotropic Gravitational-wave Background with the Parkes Pulsar Timing Array*, *Astrophys. J. Lett.* **951** (2023), no. 1 L6, [arXiv:2306.16215].

[267] H. Xu et al., *Searching for the Nano-Hertz Stochastic Gravitational Wave Background with the Chinese Pulsar Timing Array Data Release I*, *Res. Astron. Astrophys.* **23** (2023), no. 7 075024, [arXiv:2306.16216].

[268] K. Riles, *Searches for continuous-wave gravitational radiation*, *Living Rev. Rel.* **26** (2023), no. 1 3, [arXiv:2206.06447].

[269] C.-J. Wu, V. Mandic, and T. Regimbau, *Accessibility of the stochastic gravitational wave background from magnetars to the interferometric gravitational wave detectors*, *Phys. Rev. D* **87** (2013), no. 4 042002.

[270] T. Regimbau and V. Mandic, *Astrophysical Sources of Stochastic Gravitational-Wave Background*, *Class. Quant. Grav.* **25** (2008) 184018, [arXiv:0806.2794].

[271] S. Marassi, R. Ciolfi, R. Schneider, L. Stella, and V. Ferrari, *Stochastic background of gravitational waves emitted by magnetars*, *Mon. Not. Roy. Astron. Soc.* **411** (2011) 2549, [arXiv:1009.1240].

[272] T. Regimbau and J. A. de Freitas Pacheco, *Cosmic background of gravitational waves from rotating neutron stars*, *Astron. Astrophys.* **376** (2001) 381, [astro-ph/0105260].

[273] M. Maggiore, *Gravitational Waves. Vol. 2: Astrophysics and Cosmology*. Oxford University Press, 3, 2018.

[274] S. Chandrasekhar, *Solutions of two problems in the theory of gravitational radiation*, *Phys. Rev. Lett.* **24** (1970) 611–615.

[275] J. L. Friedman and B. F. Schutz, *Secular instability of rotating Newtonian stars*, *Astrophys. J.* **222** (1978) 281.

[276] N. Andersson, *A New class of unstable modes of rotating relativistic stars*, *Astrophys. J.* **502** (1998) 708–713, [gr-qc/9706075].

[277] J. L. Friedman and S. M. Morsink, *Axial instability of rotating relativistic stars*, *Astrophys. J.* **502** (1998) 714–720, [gr-qc/9706073].

[278] B. J. Owen, L. Lindblom, C. Cutler, et al., *Gravitational waves from hot young rapidly rotating neutron stars*, *Phys. Rev. D* **58** (1998) 084020, [gr-qc/9804044].

[279] V. Ferrari, S. Matarrese, and R. Schneider, *Stochastic background of gravitational waves generated by a cosmological population of young, rapidly rotating neutron stars*, *Mon. Not. Roy. Astron. Soc.* **303** (1999) 258, [astro-ph/9806357].

[280] X.-J. Zhu, X.-L. Fan, and Z.-H. Zhu, *Stochastic Gravitational Wave Background from Neutron Star r-mode Instability Revisited*, *Astrophys. J.* **729** (2011) 59, [arXiv:1102.2786].

[281] S. Woosley and T. Janka, *The physics of core-collapse supernovae*, *Nature Phys.* **1** (2005) 147, [astro-ph/0601261].

[282] E. Howell, D. Coward, R. Burman, D. Blair, and J. Gilmore, *The gravitational wave background from neutron star birth throughout the cosmos*, *MNRAS* **351** (July, 2004) 1237–1246.

[283] A. Buonanno, G. Sigl, G. G. Raffelt, H.-T. Janka, and E. Muller, *Stochastic gravitational wave background from cosmological supernovae*, *Phys. Rev. D* **72** (2005) 084001, [astro-ph/0412277].

[284] N. Tominaga, H. Umeda, and K. Nomoto, *Supernova Nucleosynthesis in Population III 13-50 Solar Mass Stars and Abundance Patterns of Extremely Metal-Poor Stars*, *Astrophys. J.* **660** (2007) 516–540, [astro-ph/0701381].

[285] S. Marassi, R. Schneider, and V. Ferrari, *Gravitational wave backgrounds and the cosmic transition from Population III to Population II stars*, *Mon. Not. Roy. Astron. Soc.* **398** (2009) 293, [arXiv:0906.0461].

[286] V. Ferrari, S. Matarrese, and R. Schneider, *Gravitational wave background from a cosmological population of core collapse supernovae*, *Mon. Not. Roy. Astron. Soc.* **303** (1999) 247, [astro-ph/9804259].

[287] J. C. N. De Araujo, O. D. Miranda, and O. D. Aguiar, *Gravitational wave background from Population III black hole formation*, *Mon. Not. Roy. Astron. Soc.* **330** (2002) 651, [astro-ph/0202037].

[288] X.-J. Zhu, E. Howell, and D. Blair, *Observational upper limits on the gravitational wave production of core collapse supernovae*, *Mon. Not. Roy. Astron. Soc.* **409** (2010) L132–L136, [arXiv:1008.0472].

[289] K. Crocker, V. Mandic, T. Regimbau, et al., *Model of the stochastic gravitational-wave background due to core collapse to black holes*, *Phys. Rev. D* **92** (2015), no. 6 063005, [arXiv:1506.02631].

[290] K. Crocker, T. Prestegard, V. Mandic, et al., *Systematic study of the stochastic gravitational-wave background due to stellar core collapse*, *Phys. Rev. D* **95** (2017), no. 6 063015, [arXiv:1701.02638].

[291] R. Caldwell et al., *Detection of early-universe gravitational-wave signatures and fundamental physics*, *Gen. Rel. Grav.* **54** (2022), no. 12 156, [arXiv:2203.07972].

[292] A. A. Starobinskiĭ, *Spectrum of relict gravitational radiation and the early state of the universe*, *Soviet Journal of Experimental and Theoretical Physics Letters* **30** (Dec., 1979) 682.

[293] E. Witten, *Cosmic Separation of Phases*, *Phys. Rev. D* **30** (1984) 272–285.

[294] T. W. B. Kibble, *Topology of Cosmic Domains and Strings*, *J. Phys. A* **9** (1976) 1387–1398.

[295] S. Hawking, *Gravitationally collapsed objects of very low mass*, *Mon. Not. Roy. Astron. Soc.* **152** (1971) 75.

[296] C. Caprini and D. G. Figueroa, *Cosmological Backgrounds of Gravitational Waves*, *Class. Quant. Grav.* **35** (2018), no. 16 163001, [arXiv:1801.04268].

[297] C. Caprini et al., *Science with the space-based interferometer eLISA. II: Gravitational waves from cosmological phase transitions*, *JCAP* **04** (2016) 001, [arXiv:1512.06239].

[298] J. J. Blanco-Pillado, K. D. Olum, and B. Shlaer, *The number of cosmic string loops*, *Phys. Rev. D* **89** (2014), no. 2 023512, [arXiv:1309.6637].

[299] L. Lorenz, C. Ringeval, and M. Sakellariadou, *Cosmic string loop distribution on all length scales and at any redshift*, *JCAP* **10** (2010) 003, [arXiv:1006.0931].

[300] C. Ringeval and T. Suyama, *Stochastic gravitational waves from cosmic string loops in scaling*, *JCAP* **12** (2017) 027, [arXiv:1709.03845].

[301] E. Bagui and S. Clesse, *A boosted gravitational wave background for primordial black holes with broad mass distributions and thermal features*, *Phys. Dark Univ.* **38** (2022) 101115, [arXiv:2110.07487].

[302] M. Maggiore, *Gravitational wave experiments and early universe cosmology*, *Phys. Rept.* **331** (2000) 283–367, [gr-qc/9909001].

[303] R. H. Brandenberger, H. Feldman, and V. F. Mukhanov, *Classical and quantum theory of perturbations in inflationary universe models*, in *37th Yamada Conference: Evolution of the Universe and its Observational Quest*, pp. 19–30, 7, 1993. [astro-ph/9307016].

[304] B. Allen, *The Stochastic gravity wave background: Sources and detection*, in *Les Houches School of Physics: Astrophysical Sources of Gravitational Radiation*, pp. 373–417, 4, 1996. [gr-qc/9604033].

[305] D. C. N. da Cunha and C. Ringeval, *Interferences in the Stochastic Gravitational Wave Background*, *JCAP* **08** (2021) 005, [arXiv:2104.14231].

[306] L. P. Grishchuk, *Amplification of gravitational waves in an istropic universe*, *Zh. Eksp. Teor. Fiz.* **67** (1974) 825–838.

[307] U. Seljak and M. Zaldarriaga, *Signature of gravity waves in polarization of the microwave background*, *Phys. Rev. Lett.* **78** (1997) 2054–2057, [astro-ph/9609169].

[308] M. Kamionkowski and E. D. Kovetz, *The Quest for B Modes from Inflationary Gravitational Waves*, *Ann. Rev. Astron. Astrophys.* **54** (2016) 227–269, [arXiv:1510.06042].

[309] J. Martin, C. Ringeval, and V. Vennin, *Encyclopædia Inflationaris*, *Phys. Dark Univ.* **5-6** (2014) 75–235, [arXiv:1303.3787].

[310] P. D. Lasky et al., *Gravitational-wave cosmology across 29 decades in frequency*, *Phys. Rev. X* **6** (2016), no. 1 011035, [arXiv:1511.05994].

[311] Y. B. Zel'dovich and I. D. Novikov, *The Hypothesis of Cores Retarded during Expansion and the Hot Cosmological Model*, *Soviet Astron. AJ (Engl. Transl.),* **10** (1967) 602.

[312] B. J. Carr and S. W. Hawking, *Black holes in the early Universe*, *Mon. Not. Roy. Astron. Soc.* **168** (1974) 399–415.

[313] B. J. Carr, *The Primordial black hole mass spectrum*, *Astrophys. J.* **201** (1975) 1–19.

[314] M. Y. Khlopov, *Primordial Black Holes*, *Res. Astron. Astrophys.* **10** (2010) 495–528, [arXiv:0801.0116].

[315] A. Escrivà, F. Kuhnel, and Y. Tada, *Primordial Black Holes*, [arXiv:2211.05767].

[316] G. F. Chapline, *Cosmological effects of primordial black holes*, *Nature* **253** (1975), no. 5489 251–252.

[317] B. Carr and F. Kuhnel, *Primordial black holes as dark matter candidates*, *SciPost Phys. Lect. Notes* **48** (2022) 1, [arXiv:2110.02821].

[318] S. Clesse and J. Garcia-Bellido, *GW190425, GW190521 and GW190814: Three candidate mergers of primordial black holes from the QCD epoch*, *Phys. Dark Univ.* **38** (2022) 101111, [arXiv:2007.06481].

[319] A. Escrivà, E. Bagui, and S. Clesse, *Simulations of PBH formation at the QCD epoch and comparison with the GWTC-3 catalog*, *JCAP* **05** (2023) 004, [arXiv:2209.06196].

[320] K. S. Phukon, G. Baltus, S. Caudill, et al., *The hunt for sub-solar primordial black holes in low mass ratio binaries is open*, [arXiv:2105.11449].

[321] G. Morras et al., *Analysis of a subsolar-mass compact binary candidate from the second observing run of Advanced LIGO*, *Phys. Dark Univ.* **42** (2023) 101285, [arXiv:2301.11619].

[322] J. García-Bellido, *Massive Primordial Black Holes as Dark Matter and their detection with Gravitational Waves*, *J. Phys. Conf. Ser.* **840** (2017), no. 1 012032, [arXiv:1702.08275].

[323] B. Carr, S. Clesse, J. García-Bellido, and F. Kühnel, *Cosmic conundra explained by thermal history and primordial black holes*, *Phys. Dark Univ.* **31** (2021) 100755, [arXiv:1906.08217].

[324] B. Carr, S. Clesse, J. Garcia-Bellido, M. Hawkins, and F. Kuhnel, *Observational Evidence for Primordial Black Holes: A Positivist Perspective*, [arXiv:2306.03903].

[325] B. Carr, K. Kohri, Y. Sendouda, and J. Yokoyama, *Constraints on primordial black holes*, *Rept. Prog. Phys.* **84** (2021), no. 11 116902, [arXiv:2002.12778].

[326] C. T. Byrnes, M. Hindmarsh, S. Young, and M. R. S. Hawkins, *Primordial black holes with an accurate QCD equation of state*, *JCAP* **08** (2018) 041, [arXiv:1801.06138].

[327] P. P. et al, *The physics of phase transitions: Concepts and applications.*, *ChemPhysChem* **4** (2003) 401–402.

[328] S. Iso, P. D. Serpico, and K. Shimada, *QCD-Electroweak First-Order Phase Transition in a Supercooled Universe*, *Phys. Rev. Lett.* **119** (2017), no. 14 141301, [arXiv:1704.04955].

[329] L. Marzola, A. Racioppi, and V. Vaskonen, *Phase transition and gravitational wave phenomenology of scalar conformal extensions of the Standard Model*, *Eur. Phys. J. C* **77** (2017), no. 7 484, [arXiv:1704.01034].

[330] B. Von Harling, A. Pomarol, O. Pujolàs, and F. Rompineve, *Peccei-Quinn Phase Transition at LIGO*, *JHEP* **04** (2020) 195, [arXiv:1912.07587].

[331] C. J. Hogan, *Gravitational radiation from cosmological phase transitions*, *Mon. Not. Roy. Astron. Soc.* **218** (1986) 629–636.

[332] A. Romero, K. Martinovic, T. A. Callister, et al., *Implications for First-Order Cosmological Phase Transitions from the Third LIGO-Virgo Observing Run*, *Phys. Rev. Lett.* **126** (2021), no. 15 151301, [arXiv:2102.01714].

[333] C. Badger et al., *Probing early Universe supercooled phase transitions with gravitational wave data*, *Phys. Rev. D* **107** (2023), no. 2 023511, [arXiv:2209.14707].

[334] A. Vilenkin and E. P. S. Shellard, *Cosmic Strings and Other Topological Defects*. Cambridge University Press, 7, 2000.

[335] L. Krauss, S. Dodelson, and S. Meyer, *Primordial Gravitational Waves and Cosmology*, *Science* **328** (2010) 989–992, [arXiv:1004.2504].

[336] D. Camargo Neves da Cunha, C. Ringeval, and F. R. Bouchet, *Stochastic gravitational waves from long cosmic strings*, *JCAP* **09** (2022) 078, [arXiv:2205.04349].

[337] S. Sarangi and S. H. H. Tye, *Cosmic string production towards the end of brane inflation*, *Phys. Lett. B* **536** (2002) 185–192, [hep-th/0204074].

[338] T. Damour and A. Vilenkin, *Gravitational radiation from cosmic (super)strings: Bursts, stochastic background, and observational windows*, *Phys. Rev. D* **71** (2005) 063510, [hep-th/0410222].

[339] X. Siemens, V. Mandic, and J. Creighton, *Gravitational wave stochastic background from cosmic (super)strings*, *Phys. Rev. Lett.* **98** (2007) 111101, [astro-ph/0610920].

[340] **LIGO Scientific, Virgo, KAGRA** Collaboration, R. Abbott et al., *Constraints on Cosmic Strings Using Data from the Third Advanced LIGO–Virgo Observing Run*, *Phys. Rev. Lett.* **126** (2021), no. 24 241102, [arXiv:2101.12248].

[341] A. I. Renzini, B. Goncharov, A. C. Jenkins, and P. M. Meyers, *Stochastic Gravitational-Wave Backgrounds: Current Detection Efforts and Future Prospects*, *Galaxies* **10** (2022), no. 1 34, [arXiv:2202.00178].

[342] R. H. Cyburt, B. D. Fields, K. A. Olive, and E. Skillman, *New BBN limits on physics beyond the standard model from* ^4He, *Astropart. Phys.* **23** (2005) 313–323, [astro-ph/0408033].

[343] L. Pagano, L. Salvati, and A. Melchiorri, *New constraints on primordial gravitational waves from Planck 2015*, *Phys. Lett. B* **760** (2016) 823–825, [arXiv:1508.02393].

[344] T. L. Smith, E. Pierpaoli, and M. Kamionkowski, *A new cosmic microwave background constraint to primordial gravitational waves*, *Phys. Rev. Lett.* **97** (2006) 021301, [astro-ph/0603144].

[345] R. K. Sachs and A. M. Wolfe, *Perturbations of a cosmological model and angular variations of the microwave background*, *Astrophys. J.* **147** (1967) 73–90.

[346] **BICEP2** Collaboration, P. A. R. Ade et al., *Detection of B-Mode Polarization at Degree Angular Scales by BICEP2*, *Phys. Rev. Lett.* **112** (2014), no. 24 241101, [arXiv:1403.3985].

[347] **BICEP2, Planck** Collaboration, P. A. R. Ade et al., *Joint Analysis of BICEP2/$Keck Array$ and $Planck$ Data*, *Phys. Rev. Lett.* **114** (2015) 101301, [arXiv:1502.00612].

[348] M. Tristram et al., *Planck constraints on the tensor-to-scalar ratio*, *Astron. Astrophys.* **647** (2021) A128, [arXiv:2010.01139].

[349] M. Tristram et al., *Improved limits on the tensor-to-scalar ratio using BICEP and Planck data*, *Phys. Rev. D* **105** (2022), no. 8 083524, [arXiv:2112.07961].

[350] A. Hewish, S. J. Bell, J. D. H. Pilkington, P. F. Scott, and R. A. Collins, *Observation of a rapidly pulsating radio source*, *Nature* **217** (1968) 709–713.

[351] T. Gold, *Rotating neutron stars as the origin of the pulsating radio sources*, *Nature* **218** (1968) 731–732.

[352] M. V. Sazhin, *Opportunities for detecting ultralong gravitational waves*, *Sov. Astron.* **22** (Feb., 1978) 36–38.

[353] S. Detweiler, *Pulsar timing measurements and the search for gravitational waves*, *ApJ* **234** (Dec., 1979) 1100–1104.

[354] R. W. Hellings and G. S. Downs, *Upper limits on the isotropic gravitational radiation background from pulsar timing analysis.*, *ApJL* **265** (Feb., 1983) L39–L42.

[355] R. W. Romani, *Timing a Millisecond Pulsar Array*, pp. 113–117. Springer Netherlands, Dordrecht, 1989.

[356] R. S. Foster and D. C. Backer, *Constructing a Pulsar Timing Array*, *ApJ* **361** (Sept., 1990) 300.

[357] D. R. Lorimer, *Binary and Millisecond Pulsars*, *Living Rev. Rel.* **11** (2008) 8, [arXiv:0811.0762].

[358] A. Lyne and F. Graham-Smith, *Pulsar Astronomy*. Cambridge Astrophysics. Cambridge University Press, 4 ed., 2012.

[359] S. Burke-Spolaor et al., *The Astrophysics of Nanohertz Gravitational Waves*, *Astron. Astrophys. Rev.* **27** (2019), no. 1 5, [arXiv:1811.08826].

[360] S. R. Taylor, *The Nanohertz Gravitational Wave Astronomer*, [arXiv:2105.13270].

[361] B. Allen, *Variance of the Hellings-Downs correlation*, *Phys. Rev. D* **107** (2023), no. 4 043018, [arXiv:2205.05637].

[362] **NANOGrav** Collaboration, Z. Arzoumanian et al., *The NANOGrav 12.5 yr Data Set: Search for an Isotropic Stochastic Gravitational-wave Background*, *Astrophys. J. Lett.* **905** (2020), no. 2 L34, [arXiv:2009.04496].

[363] **NANOGrav** Collaboration, G. Agazie et al., *The NANOGrav 15 yr Data Set: Constraints on Supermassive Black Hole Binaries from the Gravitational-wave Background*, *Astrophys. J. Lett.* **952** (2023), no. 2 L37, [arXiv:2306.16220].

[364] **NANOGrav** Collaboration, A. Afzal et al., *The NANOGrav 15 yr Data Set: Search for Signals from New Physics*, *Astrophys. J. Lett.* **951** (2023), no. 1 L11, [arXiv:2306.16219].

[365] J. W. Armstrong, L. Iess, P. Tortora, and B. Bertotti, *Stochastic gravitational wave background: Upper limits in the 10**-6-Hz 10**-3-Hz band*, *Astrophys. J.* **599** (2003) 806–813.

[366] M. Armano et al., *Sub-Femto- g Free Fall for Space-Based Gravitational Wave Observatories: LISA Pathfinder Results*, *Phys. Rev. Lett.* **116** (2016), no. 23 231101.

[367] F. B. Estabrook, M. Tinto, and J. W. Armstrong, *Time delay analysis of LISA gravitational wave data: Elimination of spacecraft motion effects*, *Phys. Rev. D* **62** (2000) 042002.

[368] C. J. Hogan and P. L. Bender, *Estimating stochastic gravitational wave backgrounds with Sagnac calibration*, *Phys. Rev. D* **64** (2001) 062002, [astro-ph/0104266].

[369] **LISA Cosmology Working Group** Collaboration, P. Auclair et al., *Cosmology with the Laser Interferometer Space Antenna*, *Living Rev. Rel.* **26** (2023), no. 1 5, [arXiv:2204.05434].

[370] J. M. Hogan et al., *An Atomic Gravitational Wave Interferometric Sensor in Low Earth Orbit (AGIS-LEO)*, *Gen. Rel. Grav.* **43** (2011) 1953–2009, [arXiv:1009.2702].

[371] C. Cutler and J. Harms, *BBO and the neutron-star-binary subtraction problem*, *Phys. Rev. D* **73** (2006) 042001, [gr-qc/0511092].

[372] H. Kudoh, A. Taruya, T. Hiramatsu, and Y. Himemoto, *Detecting a gravitational-wave background with next-generation space interferometers*, *Phys. Rev. D* **73** (2006) 064006, [gr-qc/0511145].

[373] S. P. Boughn and J. R. Kuhn, *Limits on a stochastic gravitational wave background from observations of terrestrial and solar oscillations*, *ApJ* **286** (Nov., 1984) 387–391.

[374] F. J. Dyson, *Seismic response of the earth to a gravitational wave in the 1-Hz band*, *Astrophys. J.* **156** (1969) 529–540.

[375] M. Coughlin and J. Harms, *Constraining the gravitational-wave energy density of the Universe in the range 0.1 Hz to 1 Hz using the Apollo Seismic Array*, *Phys. Rev. D* **90** (2014), no. 10 102001, [arXiv:1409.4680].

[376] D. M. Siegel and M. Roth, *An upper bound from helioseismology on the stochastic background of gravitational waves*, *Astrophys. J.* **784** (2014) 88, [arXiv:1401.6888].

[377] M. Coughlin and J. Harms, *Upper Limit on a Stochastic Background of Gravitational Waves from Seismic Measurements in the Range 0.05–1 Hz*, *Phys. Rev. Lett.* **112** (2014), no. 10 101102, [arXiv:1401.3028].

[378] M. Coughlin and J. Harms, *Constraining the gravitational wave energy density of the Universe using Earth's ring*, *Phys. Rev. D* **90** (2014), no. 4 042005, [arXiv:1406.1147].

[379] **LGWA** Collaboration, J. Harms et al., *Lunar Gravitational-wave Antenna*, *Astrophys. J.* **910** (2021), no. 1 1, [arXiv:2010.13726].

[380] K. Ackley et al., *Neutron Star Extreme Matter Observatory: A kilohertz-band gravitational-wave detector in the global network*, *Publ. Astron. Soc. Austral.* **37** (2020) e047, [arXiv:2007.03128].

[381] S. Vitale, W. M. Farr, K. Ng, and C. L. Rodriguez, *Measuring the star formation rate with gravitational waves from binary black holes*, *Astrophys. J. Lett.* **886** (2019), no. 1 L1, [arXiv:1808.00901].

[382] T. Regimbau, M. Evans, N. Christensen, et al., *Digging deeper: Observing primordial gravitational waves below the binary black hole produced stochastic background*, *Phys. Rev. Lett.* **118** (2017), no. 15 151105, [arXiv:1611.08943].

[383] S. Sachdev, T. Regimbau, and B. S. Sathyaprakash, *Subtracting compact binary foreground sources to reveal primordial gravitational-wave backgrounds*, *Phys. Rev. D* **102** (2020), no. 2 024051, [arXiv:2002.05365].

[384] K. Martinovic, P. M. Meyers, M. Sakellariadou, and N. Christensen, *Simultaneous estimation of astrophysical and cosmological stochastic gravitational-wave backgrounds with terrestrial detectors*, *Phys. Rev. D* **103** (2021), no. 4 043023, [arXiv:2011.05697].

[385] B. Zhou, L. Reali, E. Berti, et al., *Subtracting compact binary foregrounds to search for subdominant gravitational-wave backgrounds in next-generation ground-based observatories*, *Phys. Rev. D* **108** (2023), no. 6 064040, [arXiv:2209.01310].

[386] K. Martinovic, C. Perigois, T. Regimbau, and M. Sakellariadou, *Footprints of Population III Stars in the Gravitational-wave Background*, *Astrophys. J.* **940** (2022), no. 1 29, [arXiv:2109.09779].

[387] H. Zhong, R. Ormiston, and V. Mandic, *Detecting cosmological gravitational wave background after removal of compact binary coalescences in future gravitational wave detectors*, *Phys. Rev. D* **107** (2023), no. 6 064048, [arXiv:2209.11877].

[388] C. M. Will, *The Confrontation between General Relativity and Experiment*, *Living Rev. Rel.* **17** (2014) 4, [arXiv:1403.7377].

[389] **LIGO Scientific, Virgo** Collaboration, B. P. Abbott et al., *An Upper Limit on the Stochastic Gravitational-Wave Background of Cosmological Origin*, *Nature* **460** (2009) 990, [arXiv:0910.5772].

[390] S. M. Vermeulen, L. Aiello, A. Ejlli, et al., *An Experiment for Observing Quantum Gravity Phenomena using Twin Table-Top 3D Interferometers*, *Class. Quant. Grav.* **38** (2021), no. 8 085008, [arXiv:2008.04957].

[391] N. Aggarwal, G. P. Winstone, M. Teo, et al., *Searching for New Physics with a Levitated-Sensor-Based Gravitational-Wave Detector*, *Phys. Rev. Lett.* **128** (2022), no. 11 111101, [arXiv:2010.13157].

[392] M. E. Gertsenshtein, *Wave Resonance of Light and Gravitational Waves*, *Sov Phys JEPT* **14** (1961) 84–85.

[393] A. Ringwald, J. Schütte-Engel, and C. Tamarit, *Gravitational Waves as a Big Bang Thermometer*, *JCAP* **03** (2021) 054, [arXiv:2011.04731].

[394] A. Ejlli, D. Ejlli, A. M. Cruise, G. Pisano, and H. Grote, *Upper limits on the amplitude of ultra-high-frequency gravitational waves from graviton to photon conversion*, *Eur. Phys. J. C* **79** (2019), no. 12 1032, [arXiv:1908.00232].

[395] **Holometer** Collaboration, A. S. Chou et al., *MHz Gravitational Wave Constraints with Decameter Michelson Interferometers*, *Phys. Rev. D* **95** (2017), no. 6 063002, [arXiv:1611.05560].

[396] L. P. Grishchuk, *Primordial gravitons and possibility of their observation*, *Soviet Journal of Experimental and Theoretical Physics Letters* **23** (Mar., 1976) 293.

[397] P. F. Michelson, *On detecting stochastic background gravitational radiation with terrestrial detectors*, *MNRAS* **227** (Aug., 1987) 933–941.

[398] N. Christensen, *Measuring the stochastic gravitational radiation background with laser interferometric antennas*, *Phys. Rev. D* **46** (1992) 5250–5266.

[399] E. E. Flanagan, *The Sensitivity of the laser interferometer gravitational wave observatory (LIGO) to a stochastic background, and its dependence on the detector orientations*, *Phys. Rev. D* **48** (1993) 2389–2407, [astro-ph/9305029].

[400] W. O. Schumann, *Über die strahlungslosen Eigenschwingungen einer leitenden Kugel, die von einer Luftschicht und einer Ionosphärenhülle umgeben ist*, *Zeitschrift Naturforschung Teil A* **7** (Feb., 1952) 149–154.

[401] W. O. Schumann, *Über die Dämpfung der elektromagnetischen Eigenschwingungen des Systems Erde - Luft - Ionosphäre*, *Zeitschrift Naturforschung Teil A* **7** (Mar., 1952) 250–252.

[402] K. Janssens, K. Martinovic, N. Christensen, P. M. Meyers, and M. Sakellariadou, *Impact of Schumann resonances on the Einstein Telescope and projections for the magnetic coupling function*, *Phys. Rev. D* **104** (2021), no. 12 122006, [arXiv:2110.14730]. [Erratum: Phys.Rev.D 105, 109904 (2022)].

[403] K. Janssens et al., *Correlated 1–1000 Hz magnetic field fluctuations from lightning over Earth-scale distances and their impact on gravitational wave searches*, *Phys. Rev. D* **107** (2023), no. 2 022004, [arXiv:2209.00284].

[404] K. Janssens, *Prospects for an isotropic gravitational wave background detection with Earth-based interferometric detectors and the threat of correlated noise*, in *57th Rencontres de Moriond on Gravitation*, 5, 2023. [arXiv:2305.02694].

[405] M. W. Coughlin et al., *Subtraction of correlated noise in global networks of gravitational-wave interferometers*, *Class. Quant. Grav.* **33** (2016), no. 22 224003, [arXiv:1606.01011].

[406] P. M. Meyers, K. Martinovic, N. Christensen, and M. Sakellariadou, *Detecting a stochastic gravitational-wave background in the presence of correlated magnetic noise*, *Phys. Rev. D* **102** (2020), no. 10 102005, [arXiv:2008.00789].

[407] N. J. Cornish and J. D. Romano, *Towards a unified treatment of gravitational-wave data analysis*, *Phys. Rev. D* **87** (2013), no. 12 122003, [arXiv:1305.2934].

[408] A. Matas and J. D. Romano, *Frequentist versus Bayesian analyses: Cross-correlation as an approximate sufficient statistic for LIGO-Virgo stochastic background searches*, *Phys. Rev. D* **103** (2021), no. 6 062003, [arXiv:2012.00907].

[409] B. Allen, J. D. E. Creighton, E. E. Flanagan, and J. D. Romano, *Robust statistics for deterministic and stochastic gravitational waves in nonGaussian noise. 2. Bayesian analyses*, *Phys. Rev. D* **67** (2003) 122002, [gr-qc/0205015].

[410] B. Allen and J. D. Romano, *Detecting a stochastic background of gravitational radiation: Signal processing strategies and sensitivities*, *Phys. Rev. D* **59** (1999) 102001, [gr-qc/9710117].

[411] M. Abramowitz and I. A. Stegun, *Handbook of Mathematical Functions with Formulas, Graphs, and Mathematical Tables*. Dover, New York City, ninth dover printing, tenth gpo printing ed., 1964.

[412] C. Maccone, *A simple introduction to the KLT (Karhunen—Loève Transform)*, pp. 151–179. Springer Berlin Heidelberg, Berlin, Heidelberg, 2009.

[413] L. A. Wainstein and V. D. Zubakov, *Extraction of Signals from Noise*. Dover books on physics and mathematical physics. Prentice-Hall, Englewood Cliffs, NJ, 1962.

[414] E. Thrane and J. D. Romano, *Sensitivity curves for searches for gravitational-wave backgrounds*, *Phys. Rev. D* **88** (2013), no. 12 124032, [arXiv:1310.5300].

[415] **LIGO Scientific** Collaboration, B. P. Abbott et al., *LIGO: The Laser interferometer gravitational-wave observatory*, *Rept. Prog. Phys.* **72** (2009) 076901, [arXiv:0711.3041].

[416] **LIGO Scientific** Collaboration, B. Abbott et al., *Analysis of first LIGO science data for stochastic gravitational waves*, *Phys. Rev. D* **69** (2004) 122004, [gr-qc/0312088].

[417] **LIGO Scientific** Collaboration, B. Abbott et al., *Upper limits on a stochastic background of gravitational waves*, *Phys. Rev. Lett.* **95** (2005) 221101, [astro-ph/0507254].

[418] A. Lazzarini and J. D. Romano, *Use of Overlapping Windows in the Stochastic Background Search*, https://dcc.ligo.org/LIGO-T040089/public, 2004.

[419] **LIGO Scientific** Collaboration, B. Abbott et al., *Searching for a Stochastic Background of Gravitational Waves with LIGO*, *Astrophys. J.* **659** (2007) 918–930, [astro-ph/0608606].

[420] **LIGO Scientific, Virgo** Collaboration, J. Abadie et al., *Upper limits on a stochastic gravitational-wave background using LIGO and Virgo interferometers at 600-1000 Hz*, *Phys. Rev. D* **85** (2012) 122001, [arXiv:1112.5004].

[421] **LIGO Scientific, Virgo** Collaboration, J. Aasi et al., *Searching for stochastic gravitational waves using data from the two colocated LIGO Hanford detectors*, *Phys. Rev. D* **91** (2015), no. 2 022003, [arXiv:1410.6211].

[422] **ALLEGRO, LIGO Scientific** Collaboration, B. Abbott et al., *First Cross-Correlation Analysis of Interferometric and Resonant-Bar Gravitational-Wave Data for Stochastic Backgrounds*, *Phys. Rev. D* **76** (2007) 022001, [gr-qc/0703068].

[423] **LIGO Scientific, Virgo** Collaboration, J. Aasi et al., *Improved Upper Limits on the Stochastic Gravitational-Wave Background from 2009–2010 LIGO and Virgo Data*, *Phys. Rev. Lett.* **113** (2014), no. 23 231101, [arXiv:1406.4556].

[424] **LIGO Scientific, Virgo** Collaboration, B. P. Abbott et al., *Upper Limits on the Stochastic Gravitational-Wave Background from Advanced LIGO's First Observing Run*, *Phys. Rev. Lett.* **118** (2017), no. 12 121101, [arXiv:1612.02029]. [Erratum: Phys.Rev.Lett. 119, 029901 (2017)].

[425] **LIGO Scientific, Virgo** Collaboration, B. P. Abbott et al., *Search for the isotropic stochastic background using data from Advanced LIGO's second observing run*, *Phys. Rev. D* **100** (2019), no. 6 061101, [arXiv:1903.02886].

[426] **LIGO Scientific, Virgo** Collaboration, B. P. Abbott et al., *GW170817: Implications for the Stochastic Gravitational-Wave Background from Compact Binary Coalescences*, *Phys. Rev. Lett.* **120** (2018), no. 9 091101, [arXiv:1710.05837].

[427] B. Allen and A. C. Ottewill, *Detection of anisotropies in the gravitational wave stochastic background*, *Phys. Rev. D* **56** (1997) 545–563, [gr-qc/9607068].

[428] M. R. Adams and N. J. Cornish, *Discriminating between a Stochastic Gravitational Wave Background and Instrument Noise*, *Phys. Rev. D* **82** (2010) 022002, [arXiv:1002.1291].

[429] E. Thrane, S. Ballmer, J. D. Romano, et al., *Probing the anisotropies of a stochastic gravitational-wave background using a network of ground-based laser interferometers*, *Phys. Rev. D* **80** (2009) 122002, [arXiv:0910.0858].

[430] **KAGRA, Virgo, LIGO Scientific** Collaboration, R. Abbott et al., *All-sky, all-frequency directional search for persistent gravitational waves from Advanced LIGO's and Advanced Virgo's first three observing runs*, *Phys. Rev. D* **105** (2022), no. 12 122001, [arXiv:2110.09834].

[431] A. Ain, P. Dalvi, and S. Mitra, *Fast Gravitational Wave Radiometry using Data Folding*, *Phys. Rev. D* **92** (2015), no. 2 022003, [arXiv:1504.01714].

[432] N. J. Cornish, *Mapping the gravitational wave background*, *Class. Quant. Grav.* **18** (2001) 4277–4292, [astro-ph/0105374].

[433] S. W. Ballmer, *A Radiometer for stochastic gravitational waves*, *Class. Quant. Grav.* **23** (2006) S179–S186, [gr-qc/0510096].

[434] S. Mitra, S. Dhurandhar, T. Souradeep, et al., *Gravitational wave radiometry: Mapping a stochastic gravitational wave background*, *Phys. Rev. D* **77** (2008) 042002, [arXiv:0708.2728].

[435] J. D. Romano, S. R. Taylor, N. J. Cornish, et al., *Phase-coherent mapping of gravitational-wave backgrounds using ground-based laser interferometers*, *Phys. Rev. D* **92** (2015), no. 4 042003, [arXiv:1505.07179].

[436] V. Klema and A. Laub, *The singular value decomposition: Its computation and some applications*, *IEEE Transactions on Automatic Control* **25** (1980), no. 2 164–176.

[437] D. Talukder, S. Mitra, and S. Bose, *Multi-baseline gravitational wave radiometry*, *Phys. Rev. D* **83** (2011) 063002, [arXiv:1012.4530].

[438] J. D. Monnier, *Optical interferometry in astronomy*, *Rept. Prog. Phys.* **66** (2003) 789–857, [astro-ph/0307036].

[439] K. M. Górski, E. Hivon, A. J. Banday, et al., *HEALPix - A Framework for high resolution discretization, and fast analysis of data distributed on the sphere*, *Astrophys. J.* **622** (2005) 759–771, [astro-ph/0409513].

[440] E. Floden, V. Mandic, A. Matas, and L. Tsukada, *Angular resolution of the search for anisotropic stochastic gravitational-wave background with terrestrial gravitational-wave detectors*, *Phys. Rev. D* **106** (2022), no. 2 023010, [arXiv:2203.17141].

[441] S. Panda, S. Bhagwat, J. Suresh, and S. Mitra, *Stochastic gravitational wave background mapmaking using regularized deconvolution*, *Phys. Rev. D* **100** (2019), no. 4 043541, [arXiv:1905.08276].

[442] D. Agarwal, J. Suresh, S. Mitra, and A. Ain, *Upper limits on persistent gravitational waves using folded data and the full covariance matrix from Advanced LIGO's first two observing runs*, *Phys. Rev. D* **104** (2021), no. 12 123018, [arXiv:2105.08930].

[443] L. Xiao, A. I. Renzini, and A. J. Weinstein, *Model-independent search for anisotropies in stochastic gravitational-wave backgrounds and application to LIGO-Virgo's first three observing runs*, *Phys. Rev. D* **107** (2023), no. 12 122002, [arXiv:2211.10010].

[444] **Planck** Collaboration, N. Aghanim et al., *Planck 2018 results. V. CMB power spectra and likelihoods*, *Astron. Astrophys.* **641** (2020) A5, [arXiv:1907.12875].

[445] D. Agarwal, J. Suresh, S. Mitra, and A. Ain, *Angular power spectra of anisotropic stochastic gravitational wave background: Developing statistical methods and analyzing data from ground-based detectors*, *Phys. Rev. D* **108** (2023), no. 2 023011, [arXiv:2302.12516].

[446] D. Agarwal, J. Suresh, V. Mandic, A. Matas, and T. Regimbau, *Targeted search for the stochastic gravitational-wave background from the galactic millisecond pulsar population*, *Phys. Rev. D* **106** (2022), no. 4 043019, [arXiv:2204.08378].

[447] J. D. Jackson, *Classical Electrodynamics*. Wiley, 1998.

[448] M. Gasperini and G. Veneziano, *Pre - big bang in string cosmology*, *Astropart. Phys.* **1** (1993) 317–339, [hep-th/9211021].

[449] M. Gasperini, *Observable gravitational waves in pre-big bang cosmology: an update*, *JCAP* **12** (2016) 010, [arXiv:1606.07889].

[450] N. Seto and A. Taruya, *Measuring a Parity Violation Signature in the Early Universe via Ground-based Laser Interferometers*, *Phys. Rev. Lett.* **99** (2007) 121101, [arXiv:0707.0535].

[451] N. Seto and A. Taruya, *Polarization analysis of gravitational-wave backgrounds from the correlation signals of ground-based interferometers: Measuring a circular-polarization mode*, *Phys. Rev. D* **77** (2008) 103001, [arXiv:0801.4185].

[452] K. Martinovic, C. Badger, M. Sakellariadou, and V. Mandic, *Searching for parity violation with the LIGO-Virgo-KAGRA network*, *Phys. Rev. D* **104** (2021), no. 8 L081101, [arXiv:2103.06718].

[453] A. Nishizawa, A. Taruya, K. Hayama, S. Kawamura, and M.-a. Sakagami, *Probing non-tensorial polarizations of stochastic gravitational-wave backgrounds with ground-based laser interferometers*, *Phys. Rev. D* **79** (2009) 082002, [arXiv:0903.0528].

[454] T. Callister, A. S. Biscoveanu, N. Christensen, et al., *Polarization-based Tests of Gravity with the Stochastic Gravitational-Wave Background*, *Phys. Rev. X* **7** (2017), no. 4 041058, [arXiv:1704.08373].

[455] **LIGO Scientific, Virgo** Collaboration, B. P. Abbott et al., *Search for Tensor, Vector, and Scalar Polarizations in the Stochastic Gravitational-Wave Background*, *Phys. Rev. Lett.* **120** (2018), no. 20 201102, [arXiv:1802.10194].

[456] L. Tsukada, *Extension of the Bayesian searches for anisotropic stochastic gravitational-wave background with nontensorial polarizations*, *Phys. Rev. D* **108** (2023), no. 12 124042, [arXiv:2308.09020].

[457] P. J. H. Green, *Characteristic Functions By E. Lukacs. [Second Edition. Pp. viii 350. London: Griffin, 1970, £5·50]*, *Journal of the Institute of Actuaries* **97** (1971), no. 1 134–135.

[458] N. Seto, *Non-Gaussianity analysis of GW background made by short-duration burst signals*, *Phys. Rev. D* **80** (2009) 043003, [arXiv:0908.0228].

[459] R. Buscicchio, A. Ain, M. Ballelli, G. Cella, and B. Patricelli, *Detecting non-Gaussian gravitational wave backgrounds: A unified framework*, *Phys. Rev. D* **107** (2023), no. 6 063027, [arXiv:2209.01400].

[460] M. Ballelli, R. Buscicchio, B. Patricelli, A. Ain, and G. Cella, *Improved detection statistics for non-Gaussian gravitational wave stochastic backgrounds*, *Phys. Rev. D* **107** (2023), no. 12 124044, [arXiv:2212.10038].

[461] S. Drasco and E. E. Flanagan, *Detection methods for nonGaussian gravitational wave stochastic backgrounds*, *Phys. Rev. D* **67** (2003) 082003, [gr-qc/0210032].

[462] E. Thrane, *Measuring the non-Gaussian stochastic gravitational-wave background: a method for realistic interferometer data*, *Phys. Rev. D* **87** (2013), no. 4 043009, [arXiv:1301.0263].

[463] L. Martellini and T. Regimbau, *Semiparametric approach to the detection of non-Gaussian gravitational wave stochastic backgrounds*, *Phys. Rev. D* **89** (2014), no. 12 124009, [arXiv:1405.5775].

[464] J. Lawrence, K. Turbang, A. Matas, et al., *A stochastic search for intermittent gravitational-wave backgrounds*, *Phys. Rev. D* **107** (2023), no. 10 103026, [arXiv:2301.07675].

[465] R. Smith and E. Thrane, *Optimal Search for an Astrophysical Gravitational-Wave Background*, *Phys. Rev. X* **8** (2018), no. 2 021019, [arXiv:1712.00688].

[466] A. Ain, J. Suresh, and S. Mitra, *Very fast stochastic gravitational wave background map making using folded data*, *Phys. Rev. D* **98** (2018), no. 2 024001, [arXiv:1803.08285].

[467] **LIGO Scientific** Collaboration, B. Abbott et al., *Upper limit map of a background of gravitational waves*, *Phys. Rev. D* **76** (2007) 082003, [astro-ph/0703234].

[468] **LIGO Scientific** Collaboration, J. Abadie et al., *Directional limits on persistent gravitational waves using LIGO S5 science data*, *Phys. Rev. Lett.* **107** (2011) 271102, [arXiv:1109.1809].

[469] **LIGO Scientific, Virgo** Collaboration, B. P. Abbott et al., *Directional Limits on Persistent Gravitational Waves from Advanced LIGO's First Observing Run*, *Phys. Rev. Lett.* **118** (2017), no. 12 121102, [arXiv:1612.02030].

[470] **LIGO Scientific, Virgo** Collaboration, B. P. Abbott et al., *Directional limits on persistent gravitational waves using data from Advanced LIGO's first two observing runs*, *Phys. Rev. D* **100** (2019), no. 6 062001, [arXiv:1903.08844].

[471] **KAGRA, Virgo, LIGO Scientific** Collaboration, R. Abbott et al., *Search for gravitational waves from Scorpius X-1 with a hidden Markov model in O3 LIGO data*, *Phys. Rev. D* **106** (2022), no. 6 062002, [arXiv:2201.10104].

[472] **LIGO Scientific, KAGRA, Virgo** Collaboration, R. Abbott et al., *Model-based Cross-correlation Search for Gravitational Waves from the Low-mass X-Ray Binary Scorpius X-1 in LIGO O3 Data*, *Astrophys. J. Lett.* **941** (2022), no. 2 L30, [arXiv:2209.02863].

[473] **KAGRA, LIGO Scientific, Virgo** Collaboration, R. Abbott et al., *Search for continuous gravitational wave emission from the Milky Way center in O3 LIGO-Virgo data*, *Phys. Rev. D* **106** (2022), no. 4 042003, [arXiv:2204.04523].

[474] B. J. Owen, L. Lindblom, and L. S. Pinheiro, *First Constraining Upper Limits on Gravitational-wave Emission from NS 1987A in SNR 1987A*, *Astrophys. J. Lett.* **935** (2022), no. 1 L7, [arXiv:2206.01168].

[475] D. Agarwal, J. Suresh, S. Mitra, and A. Ain, *Upper limits on persistent gravitational waves using folded data and the full covariance matrix from Advanced LIGO's first two observing runs*, *Phys. Rev. D* **104** (2021), no. 12 123018, [arXiv:2105.08930].

[476] **LIGO** Collaboration, D. Davis et al., *LIGO detector characterization in the second and third observing runs*, *Class. Quant. Grav.* **38** (2021), no. 13 135014, [arXiv:2101.11673].

[477] https://lemisensors.com/.

[478] https://www.geo-metronix.de/mtxgeo/index.php/mfs-06e-overview.

[479] https://git.ligo.org/stochastic-public/stochastic.

[480] **LIGO Scientific, Virgo** Collaboration, B. P. Abbott et al., *Effects of data quality vetoes on a search for compact binary coalescences in Advanced LIGO's first observing run*, *Class. Quant. Grav.* **35** (2018), no. 6 065010, [arXiv:1710.02185].

[481] J. Zweizig and K. Riles, *Information on self-gating of $h(t)$ used in O3 continuous-wave and stochastic searches*, https://dcc.ligo.org/T2000384/public, 2020.

[482] A. Matas, I. Dvorkin, A. Romero, and T. Regimbau, *Application of gating to stochastic searches in O3*, https://dcc.ligo.org/LIGO-P2000546/public, 2021.

[483] **LSC** Collaboration, P. B. Covas et al., *Identification and mitigation of narrow spectral artifacts that degrade searches for persistent gravitational waves in the first two observing runs of Advanced LIGO*, *Phys. Rev. D* **97** (2018), no. 8 082002, [arXiv:1801.07204].

[484] **LIGO Scientific, Virgo, KAGRA** Collaboration, R. Abbott et al., *Data products and supplemental information for O3 stochastic directional paper*, https://dcc.ligo.org/LIGO-G2002165/public, 2021.

[485] **LIGO Scientific, Virgo, KAGRA** Collaboration, R. Abbott et al., *Data for Upper Limits on the Isotropic Gravitational-Wave Background from Advanced LIGO's and Advanced Virgo's Third Observing Run*, https://dcc.ligo.org/LIGO-G2001287/public, 2021.

[486] A. Zonca, L. Singer, D. Lenz, et al., *healpy: equal area pixelization and spherical harmonics transforms for data on the sphere in Python*, *Journal of Open Source Software* **4** (2019), no. 35 1298.

[487] J. T. Whelan, E. L. Robinson, J. D. Romano, and E. H. Thrane, *Treatment of Calibration Uncertainty in Multi-Baseline Cross-Correlation Searches for Gravitational Waves*, *J. Phys. Conf. Ser.* **484** (2014) 012027, [arXiv:1205.3112].

[488] J. Yousuf, S. Kandhasamy, and M. A. Malik, *Effects of calibration uncertainties on the detection and parameter estimation of isotropic gravitational-wave backgrounds*, *Phys. Rev. D* **107** (2023), no. 10 102002, [arXiv:2301.13531].

[489] L. Sun et al., *Characterization of systematic error in Advanced LIGO calibration*, *Class. Quant. Grav.* **37** (2020), no. 22 225008, [arXiv:2005.02531].

[490] G. Cusin, C. Pitrou, and J.-P. Uzan, *Anisotropy of the astrophysical gravitational wave background: Analytic expression of the angular power spectrum and correlation with cosmological observations*, *Phys. Rev. D* **96** (2017), no. 10 103019, [arXiv:1704.06184].

[491] G. Cusin, I. Dvorkin, C. Pitrou, and J.-P. Uzan, *First predictions of the angular power spectrum of the astrophysical gravitational wave background*, *Phys. Rev. Lett.* **120** (2018) 231101, [arXiv:1803.03236].

[492] A. C. Jenkins and M. Sakellariadou, *Anisotropies in the stochastic gravitational-wave background: Formalism and the cosmic string case*, *Phys. Rev. D* **98** (2018), no. 6 063509, [arXiv:1802.06046].

[493] A. C. Jenkins, M. Sakellariadou, T. Regimbau, and E. Slezak, *Anisotropies in the astrophysical gravitational-wave background: Predictions for the detection of compact binaries by LIGO and Virgo*, *Phys. Rev. D* **98** (2018), no. 6 063501, [arXiv:1806.01718].

[494] K. Z. Yang, J. Suresh, G. Cusin, et al., *Measurement of the cross-correlation angular power spectrum between the stochastic gravitational wave background and galaxy overdensity*, *Phys. Rev. D* **108** (2023), no. 4 043025, [arXiv:2304.07621].

[495] L. Tsukada, S. Jaraba, D. Agarwal, and E. Floden, *Bayesian parameter estimation for targeted anisotropic gravitational-wave background*, *Phys. Rev. D* **107** (2023), no. 2 023024, [arXiv:2208.14421].

[496] D. Talukder, E. Thrane, S. Bose, and T. Regimbau, *Measuring neutron-star ellipticity with measurements of the stochastic gravitational-wave background*, *Phys. Rev. D* **89** (2014), no. 12 123008, [arXiv:1404.4025].

[497] D. I. Jones and N. Andersson, *Gravitational waves from freely precessing neutron stars*, *Mon. Not. Roy. Astron. Soc.* **331** (2002) 203, [gr-qc/0106094].

[498] E. L. Osborne and D. I. Jones, *Gravitational waves from magnetically-induced thermal neutron star mountains*, *Mon. Not. Roy. Astron. Soc.* **494** (2020), no. 2 2839–2850, [arXiv:1910.04453].

[499] G. Ushomirsky, C. Cutler, and L. Bildsten, *Deformations of accreting neutron star crusts and gravitational wave emission*, *Mon. Not. Roy. Astron. Soc.* **319** (2000) 902, [astro-ph/0001136].

[500] G. D. Meadors, E. Goetz, and K. Riles, *Tuning into Scorpius X-1: adapting a continuous gravitational-wave search for a known binary system*, *Class. Quant. Grav.* **33** (2016), no. 10 105017, [arXiv:1512.02105].

[501] B. Haskell and A. Patruno, *Are Gravitational Waves Spinning Down PSR J1023+0038 ?*, *Phys. Rev. Lett.* **119** (2017), no. 16 161103, [arXiv:1703.08374].

[502] N. Singh, B. Haskell, D. Mukherjee, and T. Bulik, *Asymmetric accretion and thermal 'mountains' in magnetized neutron star crusts*, *Mon. Not. Roy. Astron. Soc.* **493** (2020), no. 3 3866–3878, [arXiv:1908.05038].

[503] A. Mytidis, M. Coughlin, and B. Whiting, *Constraining the R-mode Saturation Amplitude From a Hypothetical Detection of R-mode Gravitational Waves From a Newborn Neutron Star: Sensitivity Study*, *Astrophys. J.* **810** (2015) 27, [arXiv:1505.03191].

[504] A. Mytidis, A. A. Panagopoulos, O. P. Panagopoulos, A. Miller, and B. Whiting, *Sensitivity study using machine learning algorithms on simulated r-mode gravitational wave signals from newborn neutron stars*, *Phys. Rev. D* **99** (2019), no. 2 024024, [arXiv:1508.02064].

[505] P. D. Lasky, *Gravitational Waves from Neutron Stars: A Review*, *Publ. Astron. Soc. Austral.* **32** (2015) e034, [arXiv:1508.06643].

[506] K. Riles, *Recent searches for continuous gravitational waves*, *Mod. Phys. Lett. A* **32** (2017), no. 39 1730035, [arXiv:1712.05897].

[507] M. Sieniawska and M. Bejger, *Continuous gravitational waves from neutron stars: current status and prospects*, *Universe* **5** (2019), no. 11 217, [arXiv:1909.12600].

[508] R. Tenorio, D. Keitel, and A. M. Sintes, *Search Methods for Continuous Gravitational-Wave Signals from Unknown Sources in the Advanced-Detector Era*, *Universe* **7** (2021), no. 12 474, [arXiv:2111.12575].

[509] O. J. Piccinni, *Status and Perspectives of Continuous Gravitational Wave Searches*, *Galaxies* **10** (2022), no. 3 72, [arXiv:2202.01088].

[510] **KAGRA, Virgo, LIGO Scientific** Collaboration, R. Abbott et al., *All-sky search for continuous gravitational waves from isolated neutron stars in the early O3 LIGO data*, *Phys. Rev. D* **104** (2021), no. 8 082004, [arXiv:2107.00600].

[511] **LIGO Scientific, Virgo** Collaboration, J. Aasi et al., *Directed search for continuous gravitational waves from the Galactic center*, *Phys. Rev. D* **88** (2013), no. 10 102002, [arXiv:1309.6221].

[512] V. Dergachev, M. A. Papa, B. Steltner, and H.-B. Eggenstein, *Loosely coherent search in LIGO O1 data for continuous gravitational waves from Terzan 5 and the galactic center*, *Phys. Rev. D* **99** (2019), no. 8 084048, [arXiv:1903.02389].

[513] O. J. Piccinni, P. Astone, S. D'Antonio, et al., *Directed search for continuous gravitational-wave signals from the Galactic Center in the Advanced LIGO second observing run*, *Phys. Rev. D* **101** (2020), no. 8 082004, [arXiv:1910.05097].

[514] **LIGO Scientific, Virgo, KAGRA, Virgo** Collaboration, R. Abbott et al., *Searches for Continuous Gravitational Waves from Young Supernova Remnants in the Early Third Observing Run of Advanced LIGO and Virgo*, *Astrophys. J.* **921** (2021), no. 1 80, [arXiv:2105.11641].

[515] **LIGO Scientific, Virgo, KAGRA** Collaboration, R. Abbott et al., *Searches for Gravitational Waves from Known Pulsars at Two Harmonics in the Second and Third LIGO-Virgo Observing Runs*, *Astrophys. J.* **935** (2022), no. 1 1, [arXiv:2111.13106].

[516] **LIGO Scientific, Virgo, KAGRA** Collaboration, R. Abbott et al., *Diving below the spin-down limit: Constraints on gravitational waves from the energetic young pulsar PSR J0537-6910*, *Astrophys. J.* **913** (2021) L27, [arXiv:2012.12926].

[517] **LIGO Scientific, Virgo** Collaboration, R. Abbott et al., *Gravitational-wave Constraints on the Equatorial Ellipticity of Millisecond Pulsars*, *Astrophys. J. Lett.* **902** (2020), no. 1 L21, [arXiv:2007.14251].

[518] **LIGO Scientific, KAGRA, Virgo** Collaboration, R. Abbott et al., *Narrowband Searches for Continuous and Long-duration Transient Gravitational Waves from Known Pulsars in the LIGO-Virgo Third Observing Run*, *Astrophys. J.* **932** (2022), no. 2 133, [arXiv:2112.10990].

[519] **LIGO Scientific, Virgo** Collaboration, B. P. Abbott et al., *Search for gravitational waves from a long-lived remnant of the binary neutron star merger GW170817*, *Astrophys. J.* **875** (2019), no. 2 160, [arXiv:1810.02581].

[520] **LIGO Scientific, Virgo** Collaboration, B. P. Abbott et al., *Search for Post-merger Gravitational Waves from the Remnant of the Binary Neutron Star Merger GW170817*, *Astrophys. J. Lett.* **851** (2017), no. 1 L16, [arXiv:1710.09320].

[521] M. Oliver, D. Keitel, and A. M. Sintes, *Adaptive transient Hough method for long-duration gravitational wave transients*, *Phys. Rev. D* **99** (2019), no. 10 104067, [arXiv:1901.01820].

[522] L. Sun and A. Melatos, *Application of hidden Markov model tracking to the search for long-duration transient gravitational waves from the remnant of the binary neutron star merger GW170817*, *Phys. Rev. D* **99** (2019), no. 12 123003, [arXiv:1810.03577].

[523] A. Miller et al., *Method to search for long duration gravitational wave transients from isolated neutron stars using the generalized frequency-Hough transform*, *Phys. Rev. D* **98** (2018), no. 10 102004, [arXiv:1810.09784].

[524] A. L. Miller et al., *How effective is machine learning to detect long transient gravitational waves from neutron stars in a real search?*, *Phys. Rev. D* **100** (2019), no. 6 062005, [arXiv:1909.02262].

[525] S. Banagiri, L. Sun, M. W. Coughlin, and A. Melatos, *Search strategies for long gravitational-wave transients: hidden Markov model tracking and seedless clustering*, *Phys. Rev. D* **100** (2019), no. 2 024034, [arXiv:1903.02638].

[526] A. Pierce, K. Riles, and Y. Zhao, *Searching for Dark Photon Dark Matter with Gravitational Wave Detectors*, *Phys. Rev. Lett.* **121** (2018), no. 6 061102, [arXiv:1801.10161].

[527] H.-K. Guo, K. Riles, F.-W. Yang, and Y. Zhao, *Searching for Dark Photon Dark Matter in LIGO O1 Data*, *Commun. Phys.* **2** (2019) 155, [arXiv:1905.04316].

[528] A. L. Miller et al., *Probing new light gauge bosons with gravitational-wave interferometers using an adapted semicoherent method*, *Phys. Rev. D* **103** (2021), no. 10 103002, [arXiv:2010.01925].

[529] **LIGO Scientific, KAGRA, Virgo** Collaboration, R. Abbott et al., *Constraints on dark photon dark matter using data from LIGO's and Virgo's third observing run*, *Phys. Rev. D* **105** (2022), no. 6 063030, [arXiv:2105.13085].

[530] C. Palomba et al., *Direct constraints on ultra-light boson mass from searches for continuous gravitational waves*, *Phys. Rev. Lett.* **123** (2019) 171101, [arXiv:1909.08854].

[531] M. Isi, L. Sun, R. Brito, and A. Melatos, *Directed searches for gravitational waves from ultralight bosons*, *Phys. Rev. D* **99** (2019), no. 8 084042, [arXiv:1810.03812]. [Erratum: Phys.Rev.D 102, 049901 (2020)].

[532] L. Sun, R. Brito, and M. Isi, *Search for ultralight bosons in Cygnus X-1 with Advanced LIGO*, *Phys. Rev. D* **101** (2020), no. 6 063020, [arXiv:1909.11267]. [Erratum: Phys.Rev.D 102, 089902 (2020)].

[533] **LIGO Scientific, Virgo, KAGRA** Collaboration, R. Abbott et al., *All-sky search for gravitational wave emission from scalar boson clouds around spinning black holes in LIGO O3 data*, *Phys. Rev. D* **105** (2022), no. 10 102001, [arXiv:2111.15507].

[534] **LIGO Scientific, Virgo** Collaboration, R. Abbott et al., *Search of the early O3 LIGO data for continuous gravitational waves from the Cassiopeia A and Vela Jr. supernova remnants*, *Phys. Rev. D* **105** (2022), no. 8 082005, [arXiv:2111.15116].

[535] **KAGRA, LIGO Scientific, Virgo** Collaboration, R. Abbott et al., *All-sky search for continuous gravitational waves from isolated neutron stars using Advanced LIGO and Advanced Virgo O3 data*, *Phys. Rev. D* **106** (2022), no. 10 102008, [arXiv:2201.00697].

[536] R. Diehl et al., *Radioactive Al-26 and massive stars in the galaxy*, *Nature* **439** (2006) 45–47, [astro-ph/0601015].

[537] B. T. Reed, A. Deibel, and C. J. Horowitz, *Modeling the Galactic Neutron Star Population for Use in Continuous Gravitational-wave Searches*, *Astrophys. J.* **921** (2021), no. 1 89, [arXiv:2104.00771].

[538] X. Fan, Y. Chen, and C. Messenger, *Method to detect gravitational waves from an ensemble of known pulsars*, *Phys. Rev. D* **94** (2016), no. 8 084029, [arXiv:1607.06735].

[539] M. Pitkin, C. Messenger, and X. Fan, *Hierarchical Bayesian method for detecting continuous gravitational waves from an ensemble of pulsars*, *Phys. Rev. D* **98** (2018), no. 6 063001, [arXiv:1807.06726].

[540] M. Buono, R. De Rosa, L. D'Onofrio, et al., *A method for detecting continuous gravitational wave signals from an ensemble of known pulsars*, *Class. Quant. Grav.* **38** (2021), no. 13 135021.

[541] X.-J. Zhu, E. J. Howell, D. G. Blair, and Z.-H. Zhu, *On the gravitational wave background from compact binary coalescences in the band of ground-based interferometers*, *Mon. Not. Roy. Astron. Soc.* **431** (2013), no. 1 882–899, [arXiv:1209.0595].

[542] I. Dvorkin, J.-P. Uzan, E. Vangioni, and J. Silk, *Synthetic model of the gravitational wave background from evolving binary compact objects*, *Phys. Rev. D* **94** (2016), no. 10 103011, [arXiv:1607.06818].

[543] S. Dhurandhar, H. Tagoshi, Y. Okada, N. Kanda, and H. Takahashi, *The cross-correlation search for a hot spot of gravitational waves*, *Phys. Rev. D* **84** (2011) 083007, [arXiv:1105.5842].

[544] S. A. Hughes, *Gravitational wave astronomy and cosmology*, *Phys. Dark Univ.* **4** (2014) 86–91, [arXiv:1405.0504].

[545] G. Cusin, R. Durrer, and P. G. Ferreira, *Polarization of a stochastic gravitational wave background through diffusion by massive structures*, *Phys. Rev. D* **99** (2019), no. 2 023534, [arXiv:1807.10620].

[546] R. Bar-Kana, *Limits on direct detection of gravitational waves*, *Phys. Rev. D* **50** (1994) 1157–1160, [astro-ph/9401050].

[547] J. L. Cook and L. Sorbo, *Particle production during inflation and gravitational waves detectable by ground-based interferometers*, *Phys. Rev. D* **85** (2012) 023534, [arXiv:1109.0022]. [Erratum: Phys.Rev.D 86, 069901 (2012)].

[548] K. Inayoshi, K. Kashiyama, E. Visbal, and Z. Haiman, *Gravitational Wave Backgrounds from Coalescing Black Hole Binaries at Cosmic Dawn: An Upper Bound*, *Astrophys. J.* **919** (2021), no. 1 41, [arXiv:2103.12755].

[549] Y. Watanabe and E. Komatsu, *Improved Calculation of the Primordial Gravitational Wave Spectrum in the Standard Model*, *Phys. Rev. D* **73** (2006) 123515, [astro-ph/0604176].

[550] M. Kamionkowski, A. Kosowsky, and M. S. Turner, *Gravitational radiation from first order phase transitions*, *Phys. Rev. D* **49** (1994) 2837–2851, [astro-ph/9310044].

[551] A. Kosowsky, M. S. Turner, and R. Watkins, *Gravitational radiation from colliding vacuum bubbles*, *Phys. Rev. D* **45** (1992) 4514–4535.

[552] M. S. Turner, *Detectability of inflation produced gravitational waves*, *Phys. Rev. D* **55** (1997) R435–R439, [astro-ph/9607066].

[553] Y. Okada, N. Kanda, S. Dhurandhar, H. Tagoshi, and H. Takahashi, *The cross-correlation search for a hot spot of gravitational waves : Numerical study for point spread function*, *J. Phys. Conf. Ser.* **363** (2012) 012040, [arXiv:1112.3090].

[554] R. N. Manchester, G. B. Hobbs, A. Teoh, and M. Hobbs, *The Australia Telescope National Facility pulsar catalogue*, *Astron. J.* **129** (2005) 1993, [astro-ph/0412641].

[555] P. Virtanen et al., *SciPy 1.0–Fundamental Algorithms for Scientific Computing in Python*, *Nature Meth.* **17** (2020) 261, [arXiv:1907.10121].

[556] D. R. Lorimer et al., *Radio Pulsar Populations*, 3, 2019.

[557] S. A. Story, P. L. Gonthier, and A. K. Harding, *Population synthesis of radio and gamma-ray millisecond pulsars from the Galactic disk*, *Astrophys. J.* **671** (2007) 713–726, [arXiv:0706.3041].

[558] D. R. Lorimer, *The Galactic Millisecond Pulsar Population*, *IAU Symp.* **291** (2013) 237–242, [arXiv:1210.2746].

[559] C. M. F. Mingarelli, S. R. Taylor, B. S. Sathyaprakash, and W. M. Farr, *Understanding $\Omega_{\rm gw}(f)$ in Gravitational Wave Experiments*, [arXiv:1911.09745].

[560] **Planck** Collaboration, P. A. R. Ade et al., *Planck 2015 results. XIII. Cosmological parameters*, *Astron. Astrophys.* **594** (2016) A13, [arXiv:1502.01589].

[561] **LIGO Scientific Collaboration, Virgo Collaboration, and KAGRA Collaboration** Collaboration, *Folded data for first three observing runs of Advanced LIGO and Advanced Virgo*, https://doi.org/10.5281/zenodo.6326656, Mar., 2022.

[562] J. Suresh, A. Ain, and S. Mitra, *Unified mapmaking for an anisotropic stochastic gravitational wave background*, *Phys. Rev. D* **103** (2021), no. 8 083024, [arXiv:2011.05969].

[563] N. Mazumder, S. Mitra, and S. Dhurandhar, *Astrophysical motivation for directed searches for a stochastic gravitational wave background*, *Phys. Rev. D* **89** (2014), no. 8 084076, [arXiv:1401.5898].

[564] P. D. Lasky, M. F. Bennett, and A. Melatos, *Stochastic gravitational wave background from hydrodynamic turbulence in differentially rotating neutron stars*, *Phys. Rev. D* **87** (2013), no. 6 063004, [arXiv:1302.6033].

[565] L. Warszawski and A. Melatos, *Gravitational-wave bursts and stochastic background from superfluid vortex avalanches during pulsar glitches*, *Mon. Not. Roy. Astron. Soc.* **423** (2012) 2058, [arXiv:1203.4466].

[566] C. Cutler, *Gravitational waves from neutron stars with large toroidal B fields*, *Phys. Rev. D* **66** (2002) 084025, [gr-qc/0206051].

[567] S. Bonazzola and E. Gourgoulhon, *Gravitational waves from pulsars: Emission by the magnetic field induced distortion*, *Astron. Astrophys.* **312** (1996) 675, [astro-ph/9602107].

[568] B. Finkel, H. Andresen, and V. Mandic, *Stochastic gravitational-wave background from stellar core-collapse events*, *Phys. Rev. D* **105** (2022), no. 6 063022, [arXiv:2110.01478].

[569] D. M. Coward, R. R. Burman, and D. G. Blair, *Simulating a stochastic background of gravitational waves from neutron star formation at cosmological distances*, *Mon. Not. Roy. Astron. Soc.* **329** (2002) 411–416.

[570] T. Regimbau and J. A. de Freitas Pacheco, *Stochastic background from coalescences of NS-NS binaries*, *Astrophys. J.* **642** (2006) 455–461, [gr-qc/0512008].

[571] C. Wu, V. Mandic, and T. Regimbau, *Accessibility of the Gravitational-Wave Background due to Binary Coalescences to Second and Third Generation Gravitational-Wave Detectors*, *Phys. Rev. D* **85** (2012) 104024, [arXiv:1112.1898].

[572] A. G. Lyne, S. L. Shemar, and F. Graham Smith, *Statistical studies of pulsar glitches*, *Monthly Notices of the Royal Astronomical Society* **315** (07, 2000) 534–542.

[573] C. M. Espinoza, A. G. Lyne, B. W. Stappers, and M. Kramer, *A study of 315 glitches in the rotation of 102 pulsars*, *Mon. Not. Roy. Astron. Soc.* **414** (2011) 1679–1704, [arXiv:1102.1743].

[574] B. Link, R. I. Epstein, and K. A. Van Riper, *Pulsar glitches as probes of neutron star interiors*, *Nature* **359** (1992), no. 6396 616–618.

[575] B. Link, R. I. Epstein, and J. M. Lattimer, *Probing the neutron star interior with glitches*, *Astrophys. Space Sci. Libr.* **254** (2000) 117–126, [astro-ph/0001245].

[576] J. R. Fuentes, C. M. Espinoza, A. Reisenegger, et al., *The glitch activity of neutron stars*, *Astron. Astrophys.* **608** (2017) A131, [arXiv:1710.00952].

[577] D. Lopez, S. Tiwari, M. Drago, et al., *Prospects for detecting and localizing short-duration transient gravitational waves from glitching neutron stars without electromagnetic counterparts*, *Phys. Rev. D* **106** (2022), no. 10 103037, [arXiv:2206.14515].

[578] **KAGRA, Virgo, LIGO Scientific** Collaboration, R. Abbott et al., *All-sky search for short gravitational-wave bursts in the third Advanced LIGO and Advanced Virgo run*, *Phys. Rev. D* **104** (2021), no. 12 122004, [arXiv:2107.03701].

[579] W. C. G. Ho, D. I. Jones, N. Andersson, and C. M. Espinoza, *Gravitational waves from transient neutron star f-mode oscillations*, *Phys. Rev. D* **101** (2020), no. 10 103009, [arXiv:2003.12082].

[580] C. A. van Eysden and A. Melatos, *Gravitational radiation from pulsar glitches*, *Class. Quant. Grav.* **25** (2008) 225020, [arXiv:0809.4352].

[581] L. Keer and D. I. Jones, *Developing a model for neutron star oscillations following starquakes*, *Mon. Not. Roy. Astron. Soc.* **446** (2015) 865–891, [arXiv:1408.1249].

[582] A. Singh, *Gravitational wave transient signal emission via Ekman pumping in neutron stars during post-glitch relaxation phase*, *Phys. Rev. D* **95** (2017), no. 2 024022, [arXiv:1605.08420].

[583] R. Prix, S. Giampanis, and C. Messenger, *Search method for long-duration gravitational-wave transients from neutron stars*, *Phys. Rev. D* **84** (2011) 023007, [arXiv:1104.1704].

[584] G. Yim and D. I. Jones, *Transient gravitational waves from pulsar post-glitch recoveries*, *Mon. Not. Roy. Astron. Soc.* **498** (2020), no. 3 3138–3152, [arXiv:2007.05893].

[585] J. Moragues, L. M. Modafferi, R. Tenorio, and D. Keitel, *Prospects for detecting transient quasi-monochromatic gravitational waves from glitching pulsars with current and future detectors*, *Mon. Not. Roy. Astron. Soc.* **519** (2023), no. 4 5161–5176, [arXiv:2210.09907].

[586] B. Haskell and A. Melatos, *Models of Pulsar Glitches*, *Int. J. Mod. Phys. D* **24** (2015), no. 03 1530008, [arXiv:1502.07062].

[587] M. Ruderman, *Pulsars: structure and dynamics*, *Ann. Rev. Astron. Astrophys.* **10** (1972) 427–476.

[588] P. W. Anderson and N. Itoh, *Pulsar glitches and restlessness as a hard superfluidity phenomenon*, *Nature* **256** (1975) 25–27.

[589] M. A. Alpar, D. Pines, P. W. Anderson, and J. Shaham, *Vortex creep and the internal temperature of neutron stars. I - General theory*, *Astrophys. J.* **276** (Jan., 1984) 325–334.

[590] G. BAYM and D. PINES, *Neutron Starquakes and Pulsar Speedup*, in *Nuclear, Particle and Many Body Physics* (P. M. MORSE, B. T. FELD, H. FESHBACH, and R. WILSON, eds.), pp. 816–835. Academic Press, 1972.

[591] M. A. Alpar, H. F. Chau, K. S. Cheng, and D. Pines, *Postglitch Relaxation of the Crab Pulsar after Its First Four Major Glitches: The Combined Effects of Crust Cracking, Formation of Vortex Depletion Region and Vortex Creep*, *Astrophys. J.* **459** (Mar., 1996) 706.

[592] G. Ashton, R. Prix, and D. I. Jones, *A semicoherent glitch-robust continuous-gravitational-wave search method*, *Phys. Rev. D* **98** (2018), no. 6 063011, [arXiv:1805.03314].

[593] M. A. Alpar, H. F. Chau, K. S. Cheng, and D. Pines, *Postglitch Relaxation of the VELA Pulsar after Its First Eight Large Glitches: A Reevaluation with the Vortex Creep Model*, *ApJ* **409** (May, 1993) 345.

[594] H. F. Chau, P. M. McCulloch, R. Nandkumar, and D. Pines, *Postglitch Relaxation following the Ninth Glitch of the VELA Pulsar*, *ApJ* **413** (Aug., 1993) L113.

[595] N. Andersson and G. L. Comer, *Relativistic fluid dynamics: Physics for many different scales*, *Living Rev. Rel.* **10** (2007) 1, [gr-qc/0605010].

[596] A. G. Muslimov and A. I. Tsygan, *Vortex lines in neutron star superfluids and decay of pulsar magnetic fields*, *Astrophysics and Space Science* **115** (Oct, 1985) 43–49.

[597] V. Khomenko and B. Haskell, *Modelling pulsar glitches: the hydrodynamics of superfluid vortex avalanches in neutron stars*, *Publ. Astron. Soc. Austral.* **35** (2018) 20, [arXiv:1801.01413].

[598] L. Warszawski and A. Melatos, *A Cellular Automaton Model of Pulsar Glitches*, *Mon. Not. Roy. Astron. Soc.* **390** (2008) 175, [arXiv:0806.4738].

[599] A. Melatos, C. Peralta, and J. S. B. Wyithe, *Avalanche dynamics of radio pulsar glitches*, *Astrophys. J.* **672** (2008) 1103, [arXiv:0710.1021].

[600] T. Sidery, A. Passamonti, and N. Andersson, *The dynamics of pulsar glitches: Contrasting phenomenology with numerical evolutions*, *Mon. Not. Roy. Astron. Soc.* **405** (2010) 1061, [arXiv:0910.3918].

[601] G. Ashton, R. Prix, and D. I. Jones, *Statistical characterization of pulsar glitches and their potential impact on searches for continuous gravitational waves*, *Phys. Rev. D* **96** (2017), no. 6 063004, [arXiv:1704.00742].

[602] D. Keitel, G. Woan, M. Pitkin, et al., *First search for long-duration transient gravitational waves after glitches in the Vela and Crab pulsars*, *Phys. Rev. D* **100** (2019), no. 6 064058, [arXiv:1907.04717].

[603] **LIGO Scientific** Collaboration, B. Abbott et al., *Beating the spin-down limit on gravitational wave emission from the Crab pulsar*, *Astrophys. J. Lett.* **683** (2008) L45–L50, [arXiv:0805.4758]. [Erratum: Astrophys.J.Lett. 706, L203–L204 (2009), Erratum: Astrophys.J. 706, L203–L204 (2009)].

[604] **LIGO Scientific, Virgo** Collaboration, B. P. Abbott et al., *Narrow-band search for gravitational waves from known pulsars using the second LIGO observing run*, *Phys. Rev. D* **99** (2019), no. 12 122002, [arXiv:1902.08442].

[605] **LIGO Scientific, Virgo, KAGRA** Collaboration, R. Abbott et al., *Constraints from LIGO O3 Data on Gravitational-wave Emission Due to R-modes in the Glitching Pulsar PSR J0537–6910*, *Astrophys. J.* **922** (2021), no. 1 71, [arXiv:2104.14417].

[606] **LIGO Scientific, Virgo** Collaboration, B. P. Abbott et al., *Optically targeted search for gravitational waves emitted by core-collapse supernovae during the first and second observing runs of advanced LIGO and advanced Virgo*, *Phys. Rev. D* **101** (2020), no. 8 084002, [arXiv:1908.03584].

[607] **LIGO Scientific, Virgo, KAGRA** Collaboration, R. Abbott et al., *Search for gravitational-wave transients associated with magnetar bursts in Advanced LIGO and Advanced Virgo data from the third observing run*, [arXiv:2210.10931].

[608] **LIGO Scientific** Collaboration, J. Abadie et al., *A search for gravitational waves associated with the August 2006 timing glitch of the Vela pulsar*, *Phys. Rev. D* **83** (2011) 042001, [arXiv:1011.1357].

[609] M. Ebersold and S. Tiwari, *Search for nonlinear memory from subsolar mass compact binary mergers*, *Phys. Rev. D* **101** (2020), no. 10 104041, [arXiv:2005.03306].

[610] E. Thrane et al., *Long gravitational-wave transients and associated detection strategies for a network of terrestrial interferometers*, *Phys. Rev. D* **83** (2011) 083004, [arXiv:1012.2150].

[611] **KAGRA, Virgo, LIGO Scientific** Collaboration, R. Abbott et al., *All-sky search for long-duration gravitational-wave bursts in the third Advanced LIGO and Advanced Virgo run*, *Phys. Rev. D* **104** (2021), no. 10 102001, [arXiv:2107.13796].

[612] M. H. P. M. Van Putten, *Directed searches for broadband extended gravitational-wave emission in nearby energetic core-collapse supernovae*, *Astrophys. J.* **819** (2016) 169, [arXiv:1602.03634].

[613] D. Lai and S. L. Shapiro, *Gravitational radiation from rapidly rotating nascent neutron stars*, *Astrophys. J.* **442** (1995) 259, [astro-ph/9408053].

[614] A. L. Piro and C. D. Ott, *Supernova Fallback onto Magnetars and Propeller-Powered Supernovae*, *Astrophys. J.* **736** (2011) 108, [arXiv:1104.0252].

[615] A. L. Piro and E. Thrane, *Gravitational Waves from Fallback Accretion onto Neutron Stars*, *Astrophys. J.* **761** (2012) 63, [arXiv:1207.3805].

[616] **LIGO Scientific, Virgo, KAGRA, CHIME/FRB** Collaboration, R. Abbott et al., *Search for Gravitational Waves Associated with Fast Radio Bursts Detected by CHIME/FRB during the LIGO–Virgo Observing Run O3a*, *Astrophys. J.* **955** (2023), no. 2 155, [arXiv:2203.12038].

[617] R. Narayan, *The Birthrate and Initial Spin Period of Single Radio Pulsars*, *ApJ* **319** (Aug., 1987) 162.

[618] S. B. Popov and M. E. Prokhorov, *Population synthesis in astrophysics*, *Phys. Usp.* **50** (2007), no. 11 1123–1146.

[619] M. Bailes, *The Future of Pulsar Research and Facilities*, *Proceedings of the International Astronomical Union* **13** (2017), no. S337 165–170.

[620] L. Levin et al., *Pulsar Searches with the SKA*, *IAU Symp.* **337** (2017) 171–174, [arXiv:1712.01008].

[621] F. Jankowski et al., *The UTMOST pulsar timing programme I: overview and first results*, *Mon. Not. Roy. Astron. Soc.* **484** (2019), no. 3 3691–3712, [arXiv:1812.04038].

[622] L. Qian, R. Yao, J. Sun, et al., *FAST: Its Scientific Achievements and Prospects*, *The Innovation* **1** (Nov., 2020) 100053, [arXiv:2011.13542].

[623] M. E. Lower et al., *The UTMOST pulsar timing programme – II. Timing noise across the pulsar population*, *Mon. Not. Roy. Astron. Soc.* **494** (2020), no. 1 228–245, [arXiv:2002.12481].

[624] W. Fulgenzi, A. Melatos, and B. D. Hughes, *Radio pulsar glitches as a state-dependent Poisson process*, *Monthly Notices of the Royal Astronomical Society* **470** (06, 2017) 4307–4329, [https://doi.org/10.1093/mnras/stx1353].

[625] J. B. Carlin and A. Melatos, *Long-term statistics of pulsar glitches triggered by a Brownian stress accumulation process*, *Mon. Not. Roy. Astron. Soc.* **494** (2020), no. 3 3383–3391, [arXiv:2004.00168].

[626] J. B. Carlin and A. Melatos, *Long-term Statistics of Pulsar Glitches Due to History-dependent Avalanches*, *Astrophys. J.* **917** (2021), no. 1 1, [arXiv:2105.13588].

[627] B. Haskell, *The effect of superfluid hydrodynamics on pulsar glitch sizes and waiting times*, *Mon. Not. Roy. Astron. Soc.* **461** (2016), no. 1 L77–L81, [arXiv:1603.04304].

[628] J. Middleditch, F. E. Marshall, Q. D. Wang, E. V. Gotthelf, and W. Zhang, *Predicting the Starquakes in PSR J0537-6910*, *Astrophys. J.* **652** (2006) 1531–1546, [astro-ph/0605007].

[629] M. Millhouse, A. Melatos, G. Howitt, et al., *An updated glitch rate law inferred from radio pulsars*, *Mon. Not. Roy. Astron. Soc.* **511** (2022), no. 3 3304–3319, [arXiv:2202.01930].

[630] A. Melatos and C. Peralta, *Gravitational Radiation from Hydrodynamic Turbulence in a Differentially Rotating Neutron Star*, *Astrophys. J.* **709** (2010) 77–87, [arXiv:0911.1609].

[631] M. A. Alpar, K. S. Cheng, and D. Pines, *Vortex Creep and the Internal Temperature of Neutron Stars: Linear and Nonlinear Response to a Glitch*, *Astrophys. J.* **346** (Nov., 1989) 823.

[632] T. E. Harris, *The theory of branching processes*. Die Grundlehren der Mathematischen Wissenschaften, Bd. 119. Springer-Verlag, Berlin, 1963.

[633] E. Daly and A. Porporato, *Intertime jump statistics of state-dependent poisson processes*, *Phys. Rev. E* **75** (Jan, 2007) 011119.

[634] "*NIST Digital Library of Mathematical Functions*." https://dlmf.nist.gov/, Release 1.1.10 of 2023-06-15. F. W. J. Olver, A. B. Olde Daalhuis, D. W. Lozier, B. I. Schneider, R. F. Boisvert, C. W. Clark, B. R. Miller, B. V. Saunders, H. S. Cohl, and M. A. McClain, eds.

[635] A. Parida, S. Mitra, and S. Jhingan, *Component Separation of a Isotropic Gravitational Wave Background*, *JCAP* **04** (2016) 024, [arXiv:1510.07994].

[636] D. Phan, N. Pradhan, and M. Jankowiak, *Composable Effects for Flexible and Accelerated Probabilistic Programming in NumPyro*, 12, 2019. [arXiv:1912.11554].

[637] **aLIGO** Collaboration, A. Buikema et al., *Sensitivity and performance of the Advanced LIGO detectors in the third observing run*, *Phys. Rev. D* **102** (2020), no. 6 062003, [arXiv:2008.01301].

[638] R. W. Kiendrebeogo et al., *Updated Observing Scenarios and Multimessenger Implications for the International Gravitational-wave Networks O4 and O5*, *Astrophys. J.* **958** (2023), no. 2 158, [arXiv:2306.09234].

[639] P. Sandick, K. A. Olive, F. Daigne, and E. Vangioni, *Gravitational Waves from the First Stars*, *Phys. Rev. D* **73** (2006) 104024, [astro-ph/0603544].

[640] X.-J. Zhu, E. Howell, and D. Blair, *Observational upper limits on the gravitational wave production of core collapse supernovae*, *Mon. Not. Roy. Astron. Soc.* **409** (2010) L132–L136, [arXiv:1008.0472].

[641] V. Mandic, S. Bird, and I. Cholis, *Stochastic Gravitational-Wave Background due to Primordial Binary Black Hole Mergers*, *Phys. Rev. Lett.* **117** (2016), no. 20 201102, [arXiv:1608.06699].

[642] S. Clesse, J. García-Bellido, and S. Orani, *Detecting the Stochastic Gravitational Wave Background from Primordial Black Hole Formation*, [arXiv:1812.11011].

[643] X. Martin and A. Vilenkin, *Gravitational wave background from hybrid topological defects*, *Phys. Rev. Lett.* **77** (1996) 2879–2882, [astro-ph/9606022].

[644] H. An and C. Yang, *Gravitational Waves Produced by Domain Walls During Inflation*, [arXiv:2304.02361].

[645] V. Mandic and A. Buonanno, *Accessibility of the pre-big-bang models to ligo*, *Phys. Rev. D* **73** (2006) 063008, [astro-ph/0510341].

[646] C. Ungarelli and A. Vecchio, *Studying the anisotropy of the gravitational wave stochastic background with LISA*, *Phys. Rev. D* **64** (2001) 121501, [astro-ph/0106538].

[647] V. Mandic, E. Thrane, S. Giampanis, and T. Regimbau, *Parameter Estimation in Searches for the Stochastic Gravitational-Wave Background*, *Phys. Rev. Lett.* **109** (2012) 171102, [arXiv:1209.3847].

[648] J. Suresh, D. Agarwal, and S. Mitra, *Jointly setting upper limits on multiple components of an anisotropic stochastic gravitational-wave background*, *Phys. Rev. D* **104** (2021), no. 10 102003, [arXiv:2106.09593].

[649] G. Boileau, A. Lamberts, N. J. Cornish, and R. Meyer, *Spectral separation of the stochastic gravitational-wave background for LISA in the context of a modulated Galactic foreground*, *Mon. Not. Roy. Astron. Soc.* **508** (2021), no. 1 803–826, [arXiv:2105.04283]. [Erratum: Mon.Not.Roy.Astron.Soc. 508, 5554–5555 (2021)].

[650] P. Ajith et al., *A Template bank for gravitational waveforms from coalescing binary black holes. I. Non-spinning binaries*, *Phys. Rev. D* **77** (2008) 104017, [arXiv:0710.2335]. [Erratum: Phys.Rev.D 79, 129901 (2009)].

[651] P. Ajith et al., *Inspiral-merger-ringdown waveforms for black-hole binaries with non-precessing spins*, *Phys. Rev. Lett.* **106** (2011) 241101, [arXiv:0909.2867].

[652] M. Chruslinska, K. Belczynski, J. Klencki, and M. Benacquista, *Double neutron stars: merger rates revisited*, *Mon. Not. Roy. Astron. Soc.* **474** (2018), no. 3 2937–2958, [arXiv:1708.07885].

[653] M. Mapelli, N. Giacobbo, F. Santoliquido, and M. C. Artale, *The properties of merging black holes and neutron stars across cosmic time*, *Mon. Not. Roy. Astron. Soc.* **487** (2019), no. 1 2–13, [arXiv:1902.01419].

[654] M. Chruslinska, G. Nelemans, and K. Belczynski, *The influence of the distribution of cosmic star formation at different metallicities on the properties of merging double compact objects*, *Mon. Not. Roy. Astron. Soc.* **482** (2019), no. 4 5012–5017, [arXiv:1811.03565].

[655] F. Santoliquido, M. Mapelli, N. Giacobbo, Y. Bouffanais, and M. C. Artale, *The cosmic merger rate density of compact objects: impact of star formation, metallicity, initial mass function and binary evolution*, *Mon. Not. Roy. Astron. Soc.* **502** (2021), no. 4 4877–4889, [arXiv:2009.03911].

[656] R. C. Duncan and C. Thompson, *Formation of very strongly magnetized neutron stars - implications for gamma-ray bursts*, *Astrophys. J. Lett.* **392** (1992) L9.

[657] S. A. Olausen and V. M. Kaspi, *The McGill Magnetar Catalog*, *Astrophys. J. Suppl.* **212** (2014) 6, [arXiv:1309.4167].

[658] J. Braithwaite and H. C. Spruit, *Structure of the magnetic fields in A stars and white dwarfs*, *Nature* **431** (2004) 819, [astro-ph/0502043].

[659] L. Stella, S. Dall'Osso, G. Israel, and A. Vecchio, *Gravitational radiation from newborn magnetars*, *Astrophys. J. Lett.* **634** (2005) L165–L168, [astro-ph/0511068].

[660] P. M. Sa and B. Tome, *The Influence of differential rotation on the detectability of gravitational waves from the r-mode instability*, *Phys. Rev. D* **74** (2006) 044011, [gr-qc/0606001].

[661] K. Janssens, *Search for a stochastic gravitational-wave background using a global interferometer network*. PhD thesis, 2023.

[662] K. Janssens, T. A. Callister, N. Christensen, et al., *Gravitational-wave geodesy: Defining false alarm probabilities with respect to correlated noise*, *Phys. Rev. D* **105** (2022), no. 8 082001, [arXiv:2112.03560].

[663] A. Lazzarini et al., *Determination of Global and Local Coordinate Axes for the LIGO Sites*, https://dcc.ligo.org/LIGO-T980044/public, 2001.

[664] W. Anderson et al., *Beam Pattern Response Functions and Times of Arrival for Earthbound Interferometer*, https://dcc.ligo.org/LIGO-T010110/public, 2009.

[665] S. Kandhasamy and S. Bose, *LIGO-India observatory coordinate system for GW analyses*, https://dcc.ligo.org/LIGO-T2000158/public, 2023.